

Transactions of the ASME®

Technical Editor, LEWIS T. WHEELER (1997)

Department of Mechanical Engineering,
University of Houston,
Houston, TX 77204-4792

APPLIED MECHANICS DIVISION

Chairman, T. A. CRUSE
Secretary, A. NEEDLEMAN
Associate Technical Editors,
R. ABEYARATNE (1997)
T. R. AKYLAS (1997)
D. M. BARNETT (1996)
R. BECKER (1998)
S. A. BERGER (1997)
I. M. DANIEL (1996)
W. J. DRUGAN (1997)
J. T. JENKINS (1996)
J. W. JU (1998)
S. KYRIAKIDES (1997)
S. LICHTER (1998)
W. K. LIU (1996)
X. MARKENSCOFF (1997)
M. ORTIZ (1998)
J. N. REDDY (1998)
W. N. SHARPE, JR. (1996)
S. W. SHAW (1997)
M. SHINOZUKA (1997)
M. TAYA (1996)

BOARD ON COMMUNICATIONS

Chairman and Vice-President
R. MATES

Members-at-Large
T. BARLOW, N. H. CHAO, A. ERDMAN,
G. JOHNSON, L. KEER,
E. M. PATTON, S. PATULSKI,
S. ROHDE, R. SHAH, F. WHITE,
J. WHITEHEAD, K. T. YANG

OFFICERS OF THE ASME

President, D. T. KOENIG
Executive Director, D. L. BELDEN
Treasurer, R. A. BENNETT

PUBLISHING STAFF

Managing Director, Engineering
CHARLES W. BEARDSLEY
Director, Technical Publishing
JANET M. WEINRIB
Managing Editor, Technical Publishing
CYNTHIA B. CLARK
Managing Editor, Transactions
CORNELIA MONAHAN
Production Editor
JUDITH SIERANT
Production Assistant
MARISOL ANDINO

Transactions of the ASME, Journal of Applied Mechanics (ISSN 0021-8936) is published quarterly (Mar., June, Sept., Dec.) for \$210.00 per year by The American Society of Mechanical Engineers, 345 East 47th Street, New York, NY 10017.

Second class postage paid at New York, NY and additional mailing office. POSTMASTER: Send address changes to Transactions of the ASME, Journal of Applied Mechanics, c/o THE AMERICAN SOCIETY OF MECHANICAL ENGINEERS, 22 Law Drive, Box 2300, Fairfield, NJ 07007-2300.

CHANGES OF ADDRESS must be received at Society headquarters seven weeks before they are to be effective. Please send old label and new address. **PRICES:** To members, \$40.00, annually; to nonmembers, \$210.00. Add \$30.00 for postage to countries outside the United States and Canada.

STATEMENT from By-Laws. The Society shall not be responsible for statements or opinions advanced in papers or printed in its publications (B7.1, Para. 3). **COPYRIGHT © 1996** by The American Society of Mechanical Engineers. Authorization to photocopy material for internal or personal use under circumstances not falling within the fair use provisions of the Copyright Act is granted by ASME to libraries and other users registered with the Copyright Clearance Center (CCC). Transactional Reporting Service provided that the base fee of \$3.00 per article is paid directly to CCC, Inc., 222 Rosewood Drive, Danvers, MA 01923. Request for special permission or bulk copying should be addressed to Reprints/Permission Department. **INDEXED** by Applied Mechanics Reviews and Engineering Information, Inc. Canadian Goods & Services Tax Registration #126148048.

Journal of Applied Mechanics

Published Quarterly by The American Society of Mechanical Engineers

VOLUME 63 • NUMBER 1 • MARCH 1996

TECHNICAL PAPERS

- 1 A Torsional Contact Problem for an Indented Half-Space
R. Y. S. Pak and F. Abedzadeh
- 7 Stress Concentration Factors at an Elliptical Hole on the Interface Between Bonded Dissimilar Half-Planes Under Bending Moment
Mohamed Salama and Norio Hasebe
- 15 Frictional Contact Between the Surface Wave and a Rigid Strip
O. Y. Zhai
- 21 Viscoplastic Analysis of Adhesive Joints
G. K. Hu, F. Schmit, D. Baptiste, and D. François
- 27 Analysis of High-Speed Rolling With Inertia and Rate Effects
D. Iddan and J. Tirosh
- 38 Thermal Stresses due to a Laser Pulse: Elastic Solution
L. G. Hector, Jr. and R. B. Hetnarski
- 47 A Fractal Model for the Rigid-Perfectly Plastic Contact of Rough Surfaces
T. L. Warren, A. Majumdar, and D. Krajcinovic
- 55 Nonlinear Dynamics of a Rigid Block on a Rigid Base
R. N. Iyengar and D. Roy
- 62 Integral Equations for a Three-Dimensional Crack in an Infinite, Fluid-Filled, Poroelastic Solid With Zero Permeability in One Direction
Michio Kurashige and R. J. Clifton
- 69 Punch Problems for an Anisotropic Elastic Half-Plane
C. W. Fan and Chyanbin Hwu
- 77 The Folding of Triangulated Cylinders, Part III: Experiments
S. D. Guest and S. Pellegrino
- 84 Dynamic Effects of Centrifugal Forces on Turbulence
L. S. Yao and S. Ghosh Moulic
- 95 The Freestream Matching Condition for Stagnation Point Turbulent Flows: An Alternative Formulation
R. Abid and C. G. Speziale
- 101 Dynamic Stability of a Rotor Filled or Partially Filled With Liquid
Wen Zhang, Jiong Tang, and Mingde Tao
- 106 The Hydrodynamic Stability of Pendent Drop Under a Liquid Column
S. P. Lin and Z. W. Zhou
- 110 Hydroelastic Vibration of Rectangular Plates
Moon K. Kwak
- 116 Local Stability of Gyroscopic Systems Near Vanishing Eigenvalues
A. A. Renshaw and C. D. Mote, Jr.
- 121 Stability and Vibration of a Rotating Circular Plate Subjected to Stationary In-Plane Edge Loads
I. Y. Shen and Y. Song
- 128 Exact Boundary Condition Perturbation Solutions in Eigenvalue Problems
R. G. Parker and C. D. Mote, Jr.
- 136 Asymptotic Theory of Broadband Rotor Thrust, Part I: Manipulations of Flow Probabilities for a High Number of Blades
R. Martinez
- 143 Asymptotic Theory of Broadband Rotor Thrust, Part II: Analysis of the Right Frequency Shift of the Maximum Response
R. Martinez
- 149 Analytic Solution of Euler's Equations of Motion for an Asymmetric Rigid Body
P. Tsioras and J. M. Longuski
- 156 Vertical Oscillation of a Bed of Granular Material
C. E. Brennen, S. Ghosh, and C. R. Wassgren
- 162 A Comparison Between the Tiersten Model and O(H) Boundary Conditions for Elastic Surface Waves Guided by Thin Layers
P. Bövik
- 168 Rough Balanced Collisions
J. A. Battile

(Contents continued on Outside Back Cover)

CONTENTS (CONTINUED)

173 The Effect of Water on Thermal Stresses in Polymer Composites
R. M. Sullivan

180 Steady Motions of a Drawn Cable
O. M. O'Reilly

190 Some Phenomena of Cracks Perpendicular to an Interface Between Dissimilar Orthotropic Materials
J. C. Sung, J. Y. Liou, and Y. Y. Lin

204 A Finite Element Analysis of Mode III Quasi-Static Crack Growth at a Ductile-Brittle Interface
S. Omprakash and R. Narasimhan

210 Effective Thermoelastic Moduli of a Unidirectional Fiber Composite Containing Interfacial Arc Microcracks
G. P. Tandon and N. J. Pagano

218 Nonlinear Thermo-Viscoelastic Analysis of Interlaminar Stresses in Laminated Composites
Sung Yi, H. H. Hilton, and M. F. Ahmad

225 A Micromechanical Model for the Fiber Bridging of Macro-Cracks in Composite Plates
G. A. Kardomateas and R. L. Carlson

234 Principles of Localized Buckling for a Strut on an Elastoplastic Foundation
G. W. Hunt and A. Blackmore

DISCUSSION

260 A Treatment of Internally Constrained Materials—Discussion by J. Casey and M. M. Carroll

ANNOUNCEMENTS AND SPECIAL NOTES

6	Society of Engineering Sciences, Inc. Nominations Announcement
26	68th Annual Meeting of The Society of Rheology— Announcement
37	Thermal Stresses '97—Announcement
83	Change of Address form
161	Society of Engineering Science—Student Paper Competition
189	3rd EUROMECH Solid Mechanics Conference—Announcement
241	Worldwide Mechanics Meetings Conference Listing
244	Information for Authors

R. Y. S. Pak

F. Abedzadeh

Department of Civil, Environmental and
Architectural Engineering,
University of Colorado,
Boulder, CO 80309-0428

A Torsional Contact Problem for an Indented Half-Space

This paper is concerned with the torsion of a rigid disk bonded to the bottom of a cylindrical indentation on an elastic half-space. By virtue of Fourier sine and cosine transforms, the mixed boundary value problem in classical elastostatics is shown to be reducible to a pair of integral equations, of which one possesses a generalized Cauchy singular kernel. With the aid of the theory of analytic functions, the inherent fractional-order singularity in the contact problem is rendered explicit. Illustrative results on the torsional stiffness of the base of the indentation and the corresponding contact stress distribution are presented for engineering applications.

1 Introduction

The determination of the response of an elastic medium under the torsional action of a bonded rigid disk has been the subject of numerous investigations owing to its relevance to foundation engineering, soil-structure interaction, mechanical and structural designs, and contact mechanics. As a prominent example of mixed boundary value problems in the theory of elasticity, it has attracted the attention of Reissner and Sagoci (1944), Sagoci (1944), Rostovtsev (1955), Collins (1962), Sneddon (1947, 1966), Gladwell (1969), Erguvan (1988), and Pak and Saphores (1991). In these studies, the supporting solid is idealized as either an elastic half-space or a finite stratum with smooth planar boundary surfaces. For a number of practical applications, however, a more relevant configuration is one where the loading is applied to the foundation medium through the base of a prepared indentation. In geotechnical engineering, such boundary topography is common in most construction projects where the foundations are placed at the bottom of excavations (Fang, 1991). In relation to various manufacturing processes and ground exploration methods, an understanding of the class of mixed boundary value problems associated with an indented medium is conducive to a rational analysis and interpretation of the physical process of drilling, coring, and in-situ testing. Owing to the inherent physical and mathematical complexities involved, however, no exact solution has yet been reported for the indented half-space problem.

In this paper, a formal treatment is presented for the torsional response of a rigid disk bonded to the flat end of a cylindrical hole in a half-space. With the aid of Fourier sine and cosine transforms, it is shown that the mixed boundary value problem can be reduced to a pair of integral equations, of which one possesses a generalized Cauchy-singular kernel. Through an analysis of the kernels of the governing equations, the fractional-order singularity of the interfacial traction associated with the contact problem is directly extracted. Together with the analytical development of some related integrals, a solution procedure is implemented which can incorporate the singular nature of the contact traction explicitly. To facilitate theoretical and engineering applications, results on the influence of the embedment depth on the torsional stiffness of the rigid disk and the contact stress distribution are presented as illustrations.

Contributed by the Applied Mechanics Division of THE AMERICAN SOCIETY OF MECHANICAL ENGINEERS for publication in the ASME JOURNAL OF APPLIED MECHANICS.

Discussion on this paper should be addressed to the Technical Editor, Professor Lewis T. Wheeler, Department of Mechanical Engineering, University of Houston, Houston, TX 77204-4792, and will be accepted until four months after final publication of the paper itself in the ASME JOURNAL OF APPLIED MECHANICS.

Manuscript received by the ASME Applied Mechanics Division, Mar. 14, 1994; final revision, Nov. 4, 1994. Associate Technical Editor: R. Abeyaratne.

2 Formulation of Problem

Of interest in this investigation is the torsional response of a rigid disk bonded to the bottom of a flat-ended cylindrical cavity of radius a and depth l in a homogeneous, isotropic, linear elastic half-space (see Fig. 1). For this axisymmetric problem in cylindrical coordinates, $\tau_{z\theta}$ and $\tau_{r\theta}$ are the only nonzero stresses in the semi-infinite medium. Using T_l to denote the applied torque required to sustain the rotation of the rigid disk about the z -axis by an angle Θ , one may write the loading condition at the base of the hole as

$$T_l = -2\pi \int_0^a r^2 \tau_{z\theta}(r, l) dr \quad (1)$$

such that

$$u(r, l) = \Theta r, \quad r < a. \quad (2)$$

Here, $u(r, z)$ stands for the angular displacement field of the indented solid. Other key requirements for the problem are the traction-free condition for the wall of the cylindrical hole,

$$\tau_{r\theta}(a, z) = 0, \quad 0 \leq z < l, \quad (3)$$

the free-surface condition for the upper plane of the indented half-space,

$$\tau_{z\theta}(r, 0) = 0, \quad r < a, \quad (4)$$

and the regularity condition,

$$u(r, z) \rightarrow 0, \quad \sqrt{r^2 + z^2} \rightarrow \infty. \quad (5)$$

With μ as the shear modulus of the elastic solid, the constitutive relations of relevance are

$$\tau_{z\theta} = \mu \frac{\partial u}{\partial z}, \quad \tau_{r\theta} = \mu r \frac{\partial}{\partial r} \left(\frac{u}{r} \right). \quad (6)$$

Owing to the particular topology of the domain, it is convenient to consider the response of the medium in regions $R_1 = \{(r, \theta, z) | r \geq a, 0 \leq \theta \leq 2\pi, z \geq 0\}$ and $R_2 = \{(r, \theta, z) | r \leq a, 0 \leq \theta \leq 2\pi, z \geq l\}$. With the subscript i denoting the quantities of interest in the i th domain henceforth, the equations of equilibrium for the two regions can be expressed as

$$\frac{\partial^2 u_1}{\partial r^2} + \frac{1}{r} \frac{\partial u_1}{\partial r} - \frac{u_1}{r^2} + \frac{\partial^2 u_1}{\partial z^2} = 0, \quad r > a, z > 0, \quad (7)$$

$$\frac{\partial^2 u_2}{\partial r^2} + \frac{1}{r} \frac{\partial u_2}{\partial r} - \frac{u_2}{r^2} + \frac{\partial^2 u_2}{\partial z^2} = 0, \quad r < a, z > l, \quad (8)$$

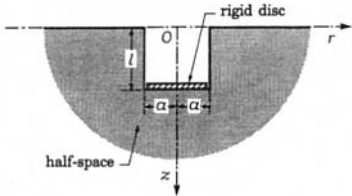


Fig. 1 A rigid disk on an indented half-space

respectively. In terms of the responses of R_1 and R_2 , conditions (2), (3), and (4) imply

$$u_2(r, l) = \Theta r, \quad 0 \leq r < a, \quad (9)$$

$$r \frac{\partial}{\partial r} \left(\frac{u_1}{r} \right) (a, z) = 0, \quad 0 \leq z \leq l, \quad (10)$$

$$\frac{\partial u_1}{\partial z} (r, 0) = 0, \quad r \geq a, \quad (11)$$

while the regularity condition translates to

$$u_i(r, z) \rightarrow 0, \quad \sqrt{r^2 + z^2} \rightarrow \infty, \quad i = 1, 2. \quad (12)$$

To ensure the responses of regions R_1 and R_2 are compatible over their common boundary, one must also require that

$$\tau_{r\theta_1}(a, z) = \tau_{r\theta_2}(a, z), \quad z \geq l \quad (13)$$

and

$$\frac{\partial u_1}{\partial z} (a, z) = \frac{\partial u_2}{\partial z} (a, z), \quad z \geq l. \quad (14)$$

In view of the boundary conditions (9) and (11), it is natural to define the Fourier cosine and sine transforms

$$\tilde{u}_1(r, \xi) = \frac{2}{\pi} \int_0^\infty u_1(r, z) \cos(\xi z) dz, \quad (15)$$

$$\tilde{u}_2(r, \xi) = \frac{2}{\pi} \int_l^\infty u_2(r, z) \sin \xi(z - l) dz. \quad (16)$$

In terms of (15) and (16), the field Eqs. (7) and (8) can be written as

$$\frac{d^2 \tilde{u}_1}{dr^2} + \frac{1}{r} \frac{d\tilde{u}_1}{dr} - \left(\xi^2 + \frac{1}{r^2} \right) \tilde{u}_1 = 0, \quad (17)$$

$$\frac{d^2 \tilde{u}_2}{dr^2} + \frac{1}{r} \frac{d\tilde{u}_2}{dr} - \left(\xi^2 + \frac{1}{r^2} \right) \tilde{u}_2 = -\xi \Theta r, \quad (18)$$

whose general solutions are

$$\tilde{u}_1(r, \xi) = A_1(\xi) K_1(\xi r) + B_1(\xi) I_1(\xi r), \quad (19)$$

$$\tilde{u}_2(r, \xi) = A_2(\xi) K_1(\xi r) + B_2(\xi) I_1(\xi r) + \frac{\Theta r}{\xi}. \quad (20)$$

Here $I_v(x)$ and $K_v(x)$ are the modified Bessel functions of the first and second kind of order v , respectively. For the solution to be bounded at $r = 0$ and ∞ , it is evident that A_1 and B_1 must both be zero. It then follows from the inversion theorems for sine and cosine transforms that the displacement fields in R_1 and R_2 can be represented as

$$u_1(r, z) = \int_0^\infty A_1(\xi) K_1(\xi r) \cos(\xi z) d\xi, \quad r \geq a, \quad z \geq 0. \quad (21)$$

$$u_2(r, z) = \Theta r + \int_0^\infty B_2(\xi) I_1(\xi r) \sin \xi(z - l) d\xi, \quad r \leq a, \quad z \geq l. \quad (22)$$

For further reduction, it is useful to write the shear stress $\tau_{r\theta_1}$ on $r = a$ as

$$\lim_{r \rightarrow a} \mu r \frac{\partial}{\partial r} \left(\frac{u_1}{r} \right) = \mu \chi(z) = \mu \begin{cases} 0, & 0 < z < l \\ \tau(z), & z \geq l \end{cases} \quad (23)$$

where $\tau(z)$ is an unknown function to be determined. According to (13), the solution in R_2 must therefore yield

$$\lim_{r \rightarrow a} \mu r \frac{\partial}{\partial r} \left(\frac{u_2}{r} \right) = \mu \chi(z), \quad z \geq l. \quad (24)$$

On substituting (21) into (23), one finds

$$\lim_{r \rightarrow a} \mu r \frac{\partial}{\partial r} \left(\frac{1}{r} \int_0^\infty A_1(\xi) \cos(\xi z) K_1(\xi r) d\xi \right) = \mu \chi(z),$$

$$z \geq 0. \quad (25)$$

Through the use of the identity

$$r \frac{\partial}{\partial r} \left(\frac{1}{r} K_1(\xi r) \right) = -\xi K_2(\xi r), \quad (26)$$

(25) can be written as

$$-\int_0^\infty \xi A_1(\xi) K_2(\xi a) \cos(\xi z) d\xi = \chi(z). \quad (27)$$

Likewise, with the aid of (22), (24) yields

$$\lim_{r \rightarrow a} \mu r \frac{\partial}{\partial r} \left(\frac{1}{r} \int_0^\infty B_2(\xi) I_1(\xi r) \sin \xi(z - l) d\xi + \Theta \right) = \mu \chi(z), \quad z \geq l. \quad (28)$$

With the identity

$$r \frac{\partial}{\partial r} \left(\frac{1}{r} I_1(\xi r) \right) = \xi I_2(\xi r), \quad (29)$$

it can be shown that (28) reduces to

$$\int_0^\infty \xi B_2(\xi) I_2(\xi a) \sin \xi(z - l) d\xi = \chi(z), \quad z \geq l. \quad (30)$$

Through a formal inversion of (27) and (30), one is thus led to

$$A_1(\xi) = \frac{-2}{\pi \xi K_2(\xi a)} \int_l^\infty \chi(z) \cos(\xi z) dz, \quad (31)$$

$$B_2(\xi) = \frac{2}{\pi \xi I_2(\xi a)} \int_l^\infty \chi(z) \sin \xi(z - l) dz. \quad (32)$$

As a result of (21), (22), (31), (32) and suitable regularity hypotheses on the function $\chi(z)$, one may express

$$\begin{aligned} \frac{\partial u_1}{\partial z} (r, z) &= \frac{1}{\pi} \int_l^\infty (\Phi_K(r, z - \zeta) \\ &\quad + \Phi_K(r, z + \zeta)) \chi(\zeta) d\zeta, \quad r > a, \quad z \geq 0, \end{aligned} \quad (33)$$

$$\begin{aligned} \frac{\partial u_2}{\partial z} (r, z) &= \frac{1}{\pi} \int_l^\infty (\Phi_I(r, \zeta - z) \\ &\quad + \Phi_I(r, \zeta + z - 2l)) \chi(\zeta) d\zeta, \quad r < a, \quad z \geq l, \end{aligned} \quad (34)$$

where

$$\Phi_K(r, d) = \int_0^\infty \frac{K_1(\xi r)}{K_2(\xi a)} \sin(\xi d) d\xi, \quad (35)$$

$$\Phi_I(r, d) = \int_0^\infty \frac{I_1(\xi r)}{I_2(\xi a)} \sin(\xi d) d\xi. \quad (36)$$

With the aid of the foregoing representations, the remaining interfacial condition (14) can be stated as

$$\begin{aligned} & \int_l^\infty (\Phi_I(a^-, \zeta - z) + \Phi_I(a^-, \zeta + z - 2l)) \tau(\zeta) d\zeta \\ &= \int_l^\infty (\Phi_K(a^+, z - \zeta) + \Phi_K(a^+, z + \zeta)) \tau(\zeta) d\zeta, \\ & z \geq l. \end{aligned} \quad (37)$$

In terms of the function $\tau(z)$, an equivalent statement of the loading condition in (1) can also be given by

$$\int_l^\infty \tau(\zeta) d\zeta = \frac{T_l}{2\pi\mu a^2}. \quad (38)$$

As will be illustrated later, (37) is a generalized Cauchy singular integral equation which, together with (38), constitute the primary governing equations for the contact problem.

3 Reduction of Governing Integral Equations

For further reduction of (37), it is useful to note (Pak and Abedzadeh, 1992) that

$$\begin{aligned} & \lim_{r \rightarrow a^+} \int_0^\infty \frac{K_1(\xi r)}{K_2(\xi a)} \sin(\xi d) d\xi \\ &= \int_0^\infty \left(\frac{K_1(\xi a)}{K_2(\xi a)} - 1 \right) \sin(\xi d) d\xi + \frac{1}{d} \end{aligned} \quad (39)$$

and

$$\begin{aligned} & \lim_{r \rightarrow a^-} \int_0^\infty \frac{I_1(\xi r)}{I_2(\xi a)} \sin(\xi d) d\xi \\ &= \int_0^\infty \left(\frac{I_1(\xi a)}{I_2(\xi a)} - 1 \right) \sin(\xi d) d\xi + \frac{1}{d}. \end{aligned} \quad (40)$$

By recourse to (39) and (40), (37) can be written as

$$\begin{aligned} & \int_l^\infty \left[\frac{2}{\zeta - z} + \frac{1}{\zeta + z - 2l} - \frac{1}{\zeta + z} \right] \tau(\zeta) d\zeta \\ &+ \int_l^\infty \left[\int_0^\infty \left(\frac{I_1(\xi a)}{I_2(\xi a)} - 1 \right) (\sin \xi(\zeta - z) \right. \\ &\quad \left. + \sin \xi(\zeta + z - 2l)) d\xi \right] \tau(\zeta) d\zeta \\ &+ \int_l^\infty \left[\int_0^\infty \left(\frac{K_1(\xi a)}{K_2(\xi a)} - 1 \right) (\sin \xi(\zeta - z) \right. \\ &\quad \left. - \sin \xi(\zeta + z)) d\xi \right] \tau(\zeta) d\zeta = 0. \end{aligned} \quad (41)$$

With the definition of the dimensionless parameters

$$\hat{z} = z/a, \quad \hat{l} = l/a, \quad \hat{\zeta} = \zeta/a, \quad (42)$$

and the function

$$\hat{\tau}(\hat{z}) = \tau(z), \quad (43)$$

(41) can finally be stated as

$$\begin{aligned} & \int_l^\infty \left[\frac{2}{\zeta - \hat{z}} + \frac{1}{\zeta + \hat{z} - 2\hat{l}} - \frac{1}{\zeta + \hat{z}} \right] \hat{\tau}(\zeta) d\zeta \\ &+ \int_l^\infty [k_1(\hat{\zeta} - \hat{z}) + k_1(\hat{\zeta} + \hat{z} - 2\hat{l}) \\ &\quad + k_2(\hat{\zeta} - \hat{z}) - k_2(\hat{\zeta} + \hat{z})] \hat{\tau}(\hat{\zeta}) d\hat{\zeta} = 0 \end{aligned} \quad (44)$$

where

$$k_1(d) = \int_0^\infty \left(\frac{I_1(\xi)}{I_2(\xi)} - 1 \right) \sin(\xi d) d\xi, \quad (45)$$

$$k_2(d) = \int_0^\infty \left(\frac{K_1(\xi)}{K_2(\xi)} - 1 \right) \sin(\xi d) d\xi. \quad (46)$$

In terms of (43), (38) can also be expressed in dimensionless form as

$$\int_l^\infty \hat{\tau}(\hat{\zeta}) d\hat{\zeta} = \frac{T_l}{2\pi\mu a^3}. \quad (47)$$

Equations (44) and (47) govern the shear stress distribution $\tau_{r\theta}$ on $r = a$ for $z \geq l$ under the applied torque. Their solutions will, in turn, render the response of the indented medium fully determinate by virtue of (21) (22), (31), and (32).

4 Singular Nature of Solution

As should be evident from the governing integral Eq. (44), the terms $2/(\zeta - \hat{z})$ and $1/(\zeta + \hat{z} - 2\hat{l})$ constitute a generalized Cauchy kernel which is singular if $\zeta = \hat{z}$ or if both ζ and \hat{z} approach the end point \hat{l} . To investigate the singular nature of the solution, it is useful to express

$$\hat{\tau}(\hat{\zeta}) = \frac{\eta(\hat{\zeta})}{(\hat{\zeta} - \hat{l})^\beta}, \quad 0 < \text{Re}(\beta) < 1, \quad (48)$$

and define two sectionally analytic functions

$$\begin{aligned} F_1(\hat{z}) &= \frac{1}{\pi} \int_l^\infty \frac{\hat{\tau}(\hat{\zeta})}{\zeta - \hat{z}} d\hat{\zeta} \\ &= \frac{1}{\pi} \int_l^\infty \frac{\eta(\hat{\zeta})}{(\hat{\zeta} - \hat{z})(\hat{\zeta} - \hat{l})^\beta} d\hat{\zeta}, \end{aligned} \quad (49)$$

$$\begin{aligned} F_2(\hat{z}) &= \frac{1}{\pi} \int_l^\infty \frac{\hat{\tau}(\hat{\zeta})}{\zeta + \hat{z} - 2\hat{l}} d\hat{\zeta} \\ &= \frac{1}{\pi} \int_l^\infty \frac{\eta(\hat{\zeta})}{(\hat{\zeta} + \hat{z} - 2\hat{l})(\hat{\zeta} - \hat{l})^\beta} d\hat{\zeta} \end{aligned} \quad (50)$$

where \hat{z} is extended to the complex plane. From the basic behavior of Cauchy integrals near the end points of the line of integration (Muskhelishvili, 1953), it can be shown as $\hat{z} \rightarrow \hat{l}^+$ on the real axis that,

$$F_1(\hat{z}) = \frac{\eta(\hat{l}) \cot(\pi\beta) e^{\pi i \beta}}{(\hat{z} - \hat{l})^\beta} + F_1^*(\hat{z}), \quad (51)$$

$$F_2(\hat{z}) = \frac{\eta(\hat{l}) e^{\pi i \beta}}{\sin(\pi\beta)(\hat{z} - \hat{l})^\beta} + F_2^*(\hat{z}), \quad (52)$$

where F_1^* and F_2^* satisfy

$$|F_1^*(\hat{z})| < \frac{C_1}{|\hat{z} - \hat{l}|^{\alpha_1}}, \quad |F_2^*(\hat{z})| < \frac{C_2}{|\hat{z} - \hat{l}|^{\alpha_2}}. \quad (53)$$

In the above, C_1 , C_2 , α_1 and α_2 are real positive constants where both α_1 and α_2 are less than $\text{Re}\beta$. Upon substituting (51) and (52) into (44), one can readily conclude that

$$2 \cot(\pi\beta) + \frac{1}{\sin(\pi\beta)} = 0 \quad (54)$$

which yields $\beta = \frac{2}{3}$. This result is consistent with the findings of Williams (1952) for a fixed-free corner problem.

5 Solution of Integral Equations

Central to the mathematical formulation in (44) and (47) are the two kernel functions k_1 and k_2 . By the method of contour integration on the complex ξ -plane, Pak and Abedzadeh (1992) have shown that k_1 and k_2 can be evaluated in the form of

$$k_1(d) = 2\pi - \frac{1}{d} + \pi \frac{e^{-(7/4)\pi d}}{1 - e^{-\pi d}} + \pi \sum_{n=1}^{\infty} (e^{-y_n d} - e^{-(n+(3/4))\pi d}), \quad d \geq 0, \quad (55)$$

and

$$k_2(d) = - \int_0^{\infty} \left(\frac{2}{\pi \xi (J_2^2(\xi) + Y_2^2(\xi))} - 1 \right) e^{-d\xi} d\xi, \quad d \geq 0. \quad (56)$$

The infinite series in (55), whose y_n , $n = 0, \dots, \infty$ denote the non-negative roots of the Bessel function of the first kind J_2 in ascending order with $y_0 = 0$, possesses rapid convergence. On the other hand, with the representation in (56), k_2 can be evaluated effectively by quadrature methods.

With the foregoing developments for k_1 and k_2 , one is now ready to determine the solution of the governing Eqs. (44) and (47). To this end, it is useful to make the transformation

$$v = 1/(\zeta - \hat{l} + 1), \quad x = 1/(\hat{z} - \hat{l} + 1). \quad (57)$$

In terms of (57), (44) and (47) can be expressed as

$$\int_0^1 G(x, v) \hat{\tau}_0(v) dv = 0, \quad 0 \leq v \leq 1, \quad (58)$$

$$\int_0^1 \frac{\hat{l}}{v^2} \hat{\tau}_0(v) dv = \frac{\hat{T}_l}{2\pi}, \quad (59)$$

where

$$G(x, v) = \frac{x}{v} \left[\frac{2}{x - v} + \frac{1}{v + x - 2vx} - \frac{1}{x + v + 2(\hat{l} - 1)vx} \right] + \left(\frac{\hat{l}}{v^2} \right) \left[k_1 \left(\frac{1}{v} - \frac{1}{x} \right) + k_1 \left(\frac{1}{v} + \frac{1}{x} - 2 \right) + k_2 \left(\frac{1}{v} - \frac{1}{x} \right) - k_2 \left(\frac{1}{v} + \frac{1}{x} + 2(\hat{l} - 1) \right) \right], \quad (60)$$

$$\hat{\tau}_0(v) = \hat{\tau} \left(\frac{1}{v} + \hat{l} - 1 \right), \quad (61)$$

$$\hat{T}_l = \frac{T_l}{\mu a^3}. \quad (62)$$

With an even extension of $\hat{\tau}_0$ to the interval of $[-1, 0]$, (58) can be cast as

$$\int_{-1}^1 G(|x|, |v|) \hat{\tau}_0(|v|) dv = 0, \quad -1 \leq x \leq 1. \quad (63)$$

In recognition of the singular behavior of $\hat{\tau}(\hat{z})$ exposed in the preceding section, it is natural to write

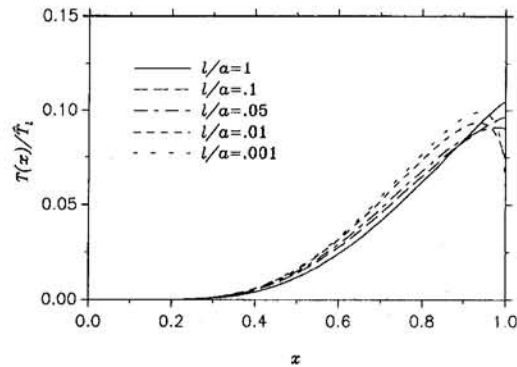


Fig. 2 Solution $T(x)$

$$\hat{\tau}_0(x) = \frac{T(x)}{(1 - x^2)^{2/3}}. \quad (64)$$

Substituting (64) into (63) yields

$$\int_{-1}^1 G(|x|, |v|) \frac{T(|v|)}{(1 - v^2)^{2/3}} dv = 0, \quad -1 \leq x \leq 1. \quad (65)$$

In view of the fractional-order singularities of the integrand at -1 and 1 , and the symmetry of $T(x)$ with respect to 0 , one may expand the solution in terms of Jacobi polynomials $\{P_{2N}^{(\alpha, \beta)}(x)\}$ where $\alpha = \beta = \frac{2}{3}$ (Erdogan, 1979). By the method of collocations, (65) can be reduced to

$$\sum_{k=1}^{2N} W_k G(|x_j|, |v_k|) T(|v_k|) = 0, \quad j = 1, \dots, 2N - 1 \quad (66)$$

where

$$W_k = \frac{-(4N + \alpha + \beta + 2)}{(2N + 1)! (2N + \alpha + \beta + 1)} \times \frac{\Gamma(2N + \alpha + 1) \Gamma(2N + \beta + 1) 2^{\alpha + \beta}}{\Gamma(2N + \alpha + \beta + 1) P_{2N+1}^{(\alpha, \beta)}(v_k) \frac{d}{dv} P_{2N}^{(\alpha, \beta)}(v_k)} \quad (67)$$

and x_j and v_k are the roots of

$$P_{2N-1}^{(1/3, 1/3)}(x_j) = 0, \quad j = 1, \dots, 2N - 1, \quad (68)$$

$$P_{2N}^{(-2/3, -2/3)}(v_k) = 0, \quad k = 1, \dots, 2N, \quad (69)$$

respectively, in descending order. Since the roots x_j and v_k are symmetric with respect to the origin, (66) can be stated as

$$\sum_{k=1}^N W_k G(x_j, v_k) T(v_k) = 0, \quad j = 1, \dots, N. \quad (70)$$

As the root x_N is equal to zero, however, it can be shown that the corresponding N th equation of (70) is automatically satisfied. On the other hand, the loading condition (59) furnishes the inhomogeneous equation

$$\sum_{k=1}^N W_k \frac{T(v_k)}{(v_k)^2} = \frac{\hat{T}_l}{2\pi} \quad (71)$$

which together with (70) form a linear algebraic system whose solution can be computed. Typical solutions for different depths of the hole are given in Fig. 2.

6 Torsional Stiffness

To determine the relationship between the applied torque and the angle of rotation, one can appeal to (21) which can be evaluated at $r = a$ and $z = l$ as

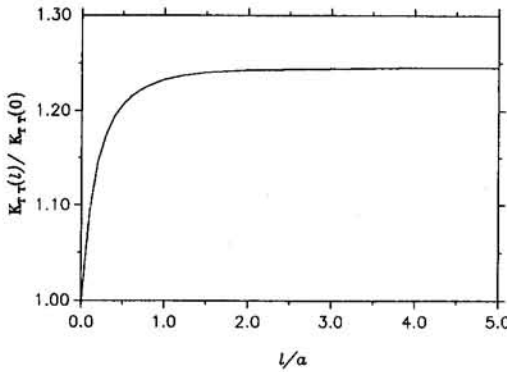


Fig. 3 Torsional stiffness of disk

$$u(a, l) = \frac{a}{\pi} \int_l^\infty [q_2(\hat{l} + \xi) + q_2(\hat{l} - \xi)] \hat{\tau}(\xi) d\xi \quad (72)$$

where

$$q_2(d) = - \int_0^\infty \frac{K_1(\xi)}{\xi K_2(\xi)} \cos(\xi d) d\xi. \quad (73)$$

The numerical evaluation of $q_2(d)$ is facilitated by noting its equivalence to

$$q_2(d) = \int_0^\infty \left(\frac{-2}{\pi \xi^2 (J_2^2(\xi) + Y_2^2(\xi))} + \frac{1 - e^{-\xi}}{\xi} \right) e^{-|d|\xi} d\xi + \ln \left(\frac{|d|}{|d| + 1} \right) \quad (74)$$

by contour integration (Pak and Abedzadeh, 1992). Through the use of (2), (72) and the solution to the governing integral equations, the angular rotation can be found by

$$\Theta = \frac{1}{\pi} \sum_{k=1}^N W_k \left[q_2 \left(\hat{z} + \frac{1}{x_k} + \hat{l} - 1 \right) + q_2 \left(\hat{z} - \frac{1}{x_k} + \hat{l} - 1 \right) \right] T(x_k). \quad (75)$$

The resulting torque-rotation relationship of the disk as a function of the depth of embedment is shown in Fig. 3. As should be apparent from the display, the torsional stiffness

$$K_{TR}(l) = T_l / \Theta \quad (76)$$

assumes, as $l \rightarrow 0$, the value of

$$K_{TR}(0) = (16/3)\mu a^3, \quad (77)$$

which corresponds to the torsional stiffness of a rigid disk bonded to the surface of a complete half-space (Pak and Saphores, 1991). As the hole deepens, however, one can see that the torsional stiffness of its base would rise quite rapidly, although the increase is limited to approximately 25 percent as $l \rightarrow \infty$.

7 Contact Stress Distribution

In accordance with (6) and (34), the contact stress distribution underneath the disk can be represented as

$$\frac{\tau_{z\theta}(r, l)}{\mu} = \frac{2}{\pi} \int_l^\infty k_r(r, \xi - l) \hat{\tau}(\xi) d\xi, \quad r < 1 \quad (78)$$

where

$$k_r(r, d) = \int_0^\infty \frac{I_1(r\xi)}{I_2(\xi)} \sin(\xi d) d\xi, \quad (79)$$

$$\hat{r} = r/a. \quad (80)$$

As can be easily deduced from (40), (48), (54), and (78), $\tau_{z\theta}(r, l)$ has a singularity of the order $\frac{2}{3}$ as $r \rightarrow a$ for $l > 0$.

For the evaluation of the kernel (79), one can prove by contour integration that

$$k_r(r, d) = 2\pi r + \pi \sum_{n=1}^\infty \frac{J_1(ry_n)}{J_1(y_n)} e^{-y_n d}, \quad r < 1. \quad (81)$$

Equation (81) can be used to compute k_r accurately for intermediate and large values of d . For smaller or zero values of the argument, however, the following representation is more effective:

$$k_r(r, d) = \left(\frac{b_1 d (1 - b_1^2/2)}{2(1 - b_1^2)r^{3/2}} - \frac{3d}{b_1 r^{1/2}} \right) E(b_1) + \left(\frac{3b_1 dr^{1/2}}{4} + \frac{3d}{r^{1/2}} \left(\frac{1}{b_1} - \frac{b_1}{2} \right) - \frac{b_1 d}{2r^{3/2}} \right) F(b_1) + \frac{3r}{2} \left(1 - \frac{b_1^2}{b_2} \right)^{1/2} (1 - b_2)^{1/2} \Pi(b_1, b_2) + \int_0^\infty \left(\frac{I_1(r\xi)}{I_2(\xi)} - \frac{5}{4} \xi K_1(\xi) I_1(r\xi) - \frac{3}{4} \xi K_3(\xi) I_1(r\xi) \right) \sin(\xi d) d\xi, \quad r < 1 \quad (82)$$

where

$$b_1^2 = \frac{4r}{(1+r)^2 + d^2}, \quad b_2 = \frac{4r}{(1+r)^2}, \quad (83)$$

$$E(b) = \int_0^{\pi/2} \sqrt{1 - b^2 \sin^2 \phi} d\phi, \quad (84)$$

$$F(b) = \int_0^{\pi/2} \frac{1}{\sqrt{1 - b^2 \sin^2 \phi}} d\phi, \quad (85)$$

$$\Pi(b_1, b_2) = \int_0^{\pi/2} \frac{1}{\sqrt{1 - b_1^2 \sin^2 \phi (1 - b_2 \sin^2 \phi)}} d\phi. \quad (86)$$

In the above, $E(b)$, $F(b)$ and $\Pi(b_1, b_2)$ can be evaluated as standard complete elliptic integrals of the first, second, and third

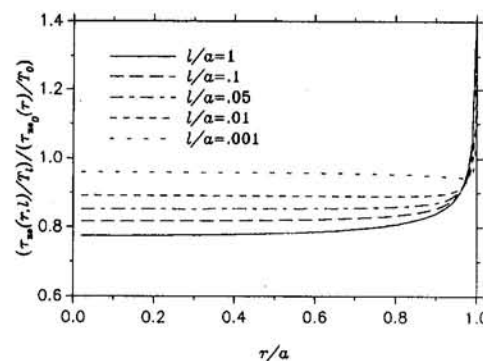


Fig. 4 Contact shear stress distribution

kinds, respectively, while the integral in (82) can be computed accurately by quadrature.

With the aid of the foregoing procedures, the contact shear stress distribution can be determined by

$$\frac{\tau_{z\theta}(r, l)}{\mu} = \frac{2}{\pi} \sum_{k=1}^N W_k T(v_k) \frac{1}{v_k^2} k_r \left(f, \frac{1}{v_k} \right). \quad (87)$$

Typical results are shown in Fig. 4 where they are normalized by the contact stress distribution

$$\frac{\tau_{z\theta_0}(r)}{T_0} = \frac{3r}{4\pi a^3 \sqrt{a^2 - r^2}} \quad (88)$$

for a rigid disk acting on the surface of an unindented half-space (Pak and Saphores, 1991). As $l \rightarrow 0$, one can see that the solution for the indented half-space would approach the one for a smooth half-space except for some boundary layer effects at the edge of the disk. The latter phenomenon can, however, be anticipated in view of the difference in the fundamental singularities inherent in the two boundary value problems.

Acknowledgment

The support provided by the U.S. National Science Foundation through Grant BCS-8958402 is gratefully acknowledged.

References

Collins, W. D., 1962, "The Forced Torsional Oscillations of an Elastic Half-Space and an Elastic Stratum," *Proceedings of London Mathematical Society*, Vol. 12, pp. 226-244.

Erdogan, F., 1979, "Mixed Boundary-Value Problems in Mechanics," *Mechanics Today*, Vol. 4, Pergamon Press, pp. 1-86.

Erguvan, M. E., 1988, "An Axisymmetric Fundamental Solution and the Reissner-Sagoci Problem for an Internally Loaded Non-Homogeneous Transversely Isotropic Half-Space," *International Journal of Engineering Science*, Vol. 26, pp. 77-84.

Fang, H. Y., 1991, *Foundation Engineering Handbook*, 2nd ed., Van Nostrand Reinhold, New York.

Gladwell, G. M. L., 1969, "The Forced Torsional Vibration of an Elastic Stratum," *International Journal of Engineering Science*, Vol. 7, pp. 1011-1023.

Muskhelishvili, N. I., 1953, *Singular Integral Equations*, P. Noordhoff N. V.-Groningen, Holland.

Pak, R. Y. S., and Abedzadeh, F., 1992, "Torsional Traction On an Open Finite Cylindrical Cavity," *Proceedings of Royal Society of London*, Vol. A438, pp. 133-144.

Pak, R. Y. S., and Saphores, J.-D. M., 1991, "Torsion of a Rigid Disc in a Half-Space," *International Journal of Engineering Science*, Vol. 29, pp. 1-12.

Reissner, E., and Sagoci, H. F., 1944, "Forced Torsional Oscillations of an Elastic Half-Space, I," *Journal of Applied Physics*, Vol. 15, pp. 652-654.

Rostovtsev, N. A., 1955, "On the Problem of the Torsion of an Elastic Half-Space," *Prikladnaya Matematika i Mekhanika*, Vol. 19, pp. 55-60.

Sagoci, H. F., 1944, "Forced Torsional Oscillations of an Elastic Half-Space, II," *Journal of Applied Physics*, Vol. 15, pp. 655-662.

Sneddon, I. N., 1947, "Note on a Boundary Value Problem of Reissner and Sagoci," *Journal of Applied Physics*, Vol. 18, pp. 130-132.

Sneddon, I. N., 1966, "The Reissner-Sagoci Problem," *Proceedings of Glasgow Mathematical Association*, Vol. 7, pp. 136-144.

Williams, M. L., 1952, "Stress Singularities Resulting From Various Boundary Conditions in Angular Corners of Plates in Extension," *ASME JOURNAL OF APPLIED MECHANICS*, Vol. 19, pp. 526-528.

Mohamed Salama

Norio Hasebe

Department of Civil Engineering,
Nagoya Institute of Technology,
Gokiso-cho, Showa-ku,
Nagoya, 466, Japan

Stress Concentration Factors at an Elliptical Hole on the Interface Between Bonded Dissimilar Half-Planes Under Bending Moment

The problem of thin plate bending of two bonded half-planes with an elliptical hole on the interface and interface cracks on its both sides is presented. A uniformly distributed bending moment applied at the remote ends of the interface is considered. The complex stress functions approach together with the rational mapping function technique are used in the analysis. The solution is obtained in closed form. Distributions of bending and torsional moments, the stress concentration factor as well as the stress intensity factor, are given for all possible dimensions of the elliptical hole, various material constants, and rigidity ratios.

Introduction

In bimaterial structures, damage can occur from holes, scratches, and defects which reduce the load carrying capacity of large categories of structures used in modern technology. The bimaterial system is required to act as a single unit, in that the loads are transmitted from one material to the next through interfaces. The presence of holes or cracks in one of the two materials or at the interface could cause high elevation of local stresses and failure could supervene. The problem of stress concentration around holes at the interface between bonded dissimilar half-planes is a problem of invariable practical interest. The problem of stress concentration around holes in a homogeneous infinite plate is found in a book by Savin (1961) for different shapes of a hole. In the present paper, the formulations given by Savin (1961) for the plate bending in terms of the complex stress functions are used. The focus of the present investigation is on the derivation of a general analytical solution to the problem of thin plate bending of two bonded dissimilar half-planes with an elliptical hole on the interface and interface cracks on its both sides and to employ this solution to determine some physical quantities such as the stress concentration factor. The complex stress functions approach together with the rational mapping function technique are used in the analysis. The problem is considered for a uniformly distributed bending moment applied at the remote ends of the interface. Examples of the distributions of bending and torsional moment along the interface and boundaries of the hole are shown. Stress concentration factor is calculated for all possible hole dimensions, several material constants and rigidity ratios. An expression for the stress concentration factor is derived and its accuracy is investigated. The stress intensity factor is derived for the case when the elliptical hole becomes very sharp and can be considered as a crack penetrating the two materials. Values of the stress intensity factor are expressed in terms of the complex

stress functions and the stress concentration factor, respectively. A comparison between the two expressions is carried out and their accuracy are investigated.

Analytical Method

Figure 1(a) shows two bonded dissimilar half-planes and an elliptical hole with an interface crack on its both sides. The two half-planes are symmetrically bonded along the X -axis which coincides with one of the principal axes of the hole. The material at $Y \geq 0$ is referred to by material 1, while material 2 is that at $Y \leq 0$. Material 1 is rotated about the X -axis as shown in Fig. 1(b) so as to facilitate the analysis scheme which is carried out accordingly. Symbols and subscripts of the components of bending moments, torsional moments, deflections, bending forces, and rotations are indicated by capital letters in Fig. 1(a) and by small letters in Fig. 1(b). A mapping function by means of which materials 1 and 2 in Fig. 1(b) are mapped into the unit circles of the t_j -planes, ($j = 1, 2$) (see Fig. 1(c)), respectively, is expressed as follows:

$$z_j = -ia \frac{1 + t_j}{1 - t_j} - ib\sqrt{2} \frac{\sqrt{1 + t_j^2}}{1 - t_j} \quad (1a)$$

$$z_j = -ia \frac{1 + t_j}{1 - t_j} - \frac{ib\sqrt{2}}{1 - t_j} \times \left[1 + \sum_{l=1}^m \left(\frac{-A_l}{1 + \alpha_l t_j^2} + A_l \right) \right] + C \quad (1b)$$

$$z_j = \omega(t_j) = \frac{E_0}{1 - t_j} + \sum_{k=1}^{N=2m} \frac{E_k}{\zeta_k - t_j} + E_c \quad (1c)$$

where $N = 28$ is used in this paper. The rational mapping function in (1b) is derived from the irrational mapping function of (1a) and then (1b) is expressed in the form of (1c). The procedure of deriving the rational mapping function is not stated in this paper for the sake of briefing, and it has been thoroughly demonstrated in (Hasebe and Inohara, 1980). Values of A_l and α_l of (1b) are given in Table 1 in Hasebe et al. (1994). The bonded boundary is denoted by M , while the unbonded bound-

Contributed by the Applied Mechanics Division of THE AMERICAN SOCIETY OF MECHANICAL ENGINEERS for publication in the ASME JOURNAL OF APPLIED MECHANICS.

Discussion on this paper should be addressed to the Technical Editor, Professor Lewis T. Wheeler, Department of Mechanical Engineering, University of Houston, Houston, TX 77204-4792, and will be accepted until four months after final publication of the paper itself in the ASME JOURNAL OF APPLIED MECHANICS.

Manuscript received by the ASME Applied Mechanics Division, Apr. 14, 1994; final revision, Feb. 25, 1995. Associate Technical Editor: F. Y. M. Wan.

aries are denoted by L_j (see Fig. 1(b)). Points on the interface M of Fig. 1(a) have the same coordinates which corresponds to $t_1 = t_2$ on the unit circles. Thus, the boundary conditions on the interface can be expressed in terms of a single variable σ which satisfies $\sigma = 1/\bar{\sigma}$ on the unit circle. Bending moments, torsional moments, deflections, bending forces, and rotations in Figs. 1(a) and 1(b) are related as

$$M_{Y_1} = -m_{y_1}, \quad M_{Y_2} = m_{y_2}, \quad M_{X_1} = -m_{x_1}, \quad M_{X_2} = m_{x_2} \quad (2a)$$

$$M_{X_1 Y_1} = m_{x_1 y_1}, \quad M_{X_2 Y_2} = m_{x_2 y_2}, \quad W_1 = -w_1, \quad W_2 = w_2 \quad (2b)$$

$$\int P_{Y_1} ds = \int p_{y_1} ds, \quad \int P_{Y_2} ds = \int p_{y_2} ds \quad (2c)$$

$$\frac{\partial W_1}{\partial X_1} = -\frac{\partial w_1}{\partial x_1}, \quad \frac{\partial W_2}{\partial X_2} = \frac{\partial w_2}{\partial x_2}, \quad \frac{\partial W_1}{\partial Y_1} = \frac{\partial w_1}{\partial y_1},$$

$$\frac{\partial W_2}{\partial Y_2} = \frac{\partial w_2}{\partial y_2}. \quad (2d)$$

Moments, forces, deflections, and rotations are calculated in accordance with the stress functions derived in the analytical plane (z_j -planes) of Fig. 1(b), and those on the physical plane (see Fig. 1(a)) are obtained using (2). Bending and torsional moments are given in terms of the complex stress functions $\phi_j(t_j)$, $\psi_j(t_j)$, ($j = 1, 2$) as follows (Savin, 1961):

$$m_{x_j} + m_{y_j} = -4D_j(1 + \nu_j) \operatorname{Re} \left[\frac{\phi'_j(t_j)}{\omega'(t_j)} \right] \quad (3a)$$

$$\begin{aligned} m_{y_j} - m_{x_j} + 2im_{x_j y_j} \\ = 2D_j(1 - \nu_j) \left\{ \frac{\overline{\omega(t_j)}}{\omega'(t_j)} \left[\frac{\phi'_j(t_j)}{\omega'(t_j)} \right]' + \frac{\overline{\psi'_j(t_j)}}{\omega'(t_j)} \right\}. \quad (3b) \end{aligned}$$

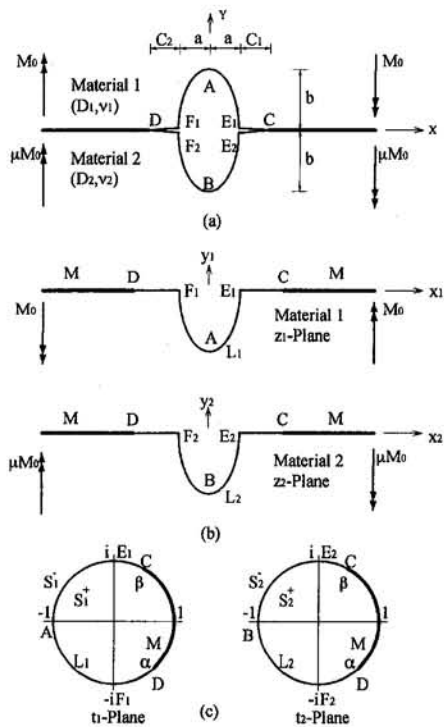


Fig. 1 (a) Geometry and coordinate system of two bonded dissimilar half-planes with an elliptical hole on the interface and interface cracks on its both sides; (b) z_j -planes of materials 1 and 2; (c) unit circles of materials 1 and 2

Since a uniformly distributed bending moment applied at infinity in the X -direction is considered, each of the stress functions is divided into two parts as follows:

$$\phi_j(t_j) = \phi_j^A(t_j) + \phi_j^B(t_j), \quad \psi_j(t_j) = \psi_j^A(t_j) + \psi_j^B(t_j) \quad (4a)$$

where $\phi_j^A(t_j)$ and $\psi_j^A(t_j)$ are the stress functions representing the state of stresses at the remote ends of the half-planes for the uniformly distributed bending moments and are obtained by substituting the values of the applied moments M_0 and μM_0 in (3a) and (3b) as follows:

$$\begin{aligned} \phi_1^A(t_1) &= \frac{M_0}{4D_1(1 + \nu_1)} \omega(t_1), \\ \phi_2^A(t_2) &= \frac{-\mu M_0}{4D_2(1 + \nu_2)} \omega(t_2), \end{aligned} \quad (4b)$$

$$\begin{aligned} \psi_1^A(t_1) &= \frac{M_0}{2D_1(1 - \nu_1)} \omega(t_1), \\ \psi_2^A(t_2) &= \frac{-\mu M_0}{4D_2(1 - \nu_2)} \omega(t_2) \end{aligned} \quad (4c)$$

$$\mu = \frac{D_2(1 - \nu_2^2)}{D_1(1 - \nu_1^2)}. \quad (5)$$

The bending moment applied at material 1 is M_0 , while to keep the continuity of rotations at the remote ends, a bending moment of magnitude μM_0 must be applied at material 2 (see Appendix). The boundary conditions of the external force and rotations are expressed in terms of the two complex stress functions, $\phi_j(t_j)$, $\psi_j(t_j)$, ($j = 1, 2$) as follows (Savin, 1961):

$$\begin{aligned} -\kappa_j \phi_j(\sigma) + \frac{\omega(\sigma)}{\omega'(\sigma)} \overline{\phi'_j(\sigma)} + \overline{\psi_j(\sigma)} &= \frac{1}{D_j(1 - \nu_j)} \\ \times \left[\int_0^s \left(m(s) + i \int_0^s p(s) ds \right) dz + ia_j z + b_j \right] \end{aligned} \quad (6)$$

$$\phi_j(\sigma) + \frac{\omega(\sigma)}{\omega'(\sigma)} \overline{\phi'_j(\sigma)} + \overline{\psi_j(\sigma)} = \left(\frac{\partial w_j}{\partial x_j} + i \frac{\partial w_j}{\partial y_j} \right) \quad (7)$$

where $\kappa_j = (3 + \nu_j)/(1 - \nu_j)$, ν_j is Poisson's ratio, D_j is the flexural rigidity defined by $E_j h_j^3 / [12(1 - \nu_j^2)]$, E_j is Young's modulus, and h_j is the thickness of the plate. The integral with respect to s represents integration along the boundary line. $m(s)$ and $p(s)$ are the bending moment and bending force per unit length along the boundary line, respectively. a_j and b_j are the real and complex constants of integration, respectively, which are set equal to zero in the present paper (Savin, 1961). The complex stress function $\psi_j(t_j)$ is given by analytic continuation of stresses as follows (Muskhelishvili, 1963):

$$\psi_j(t_j) = \kappa_j \overline{\phi_j(1/t_j)} - \frac{\omega(1/t_j)}{\omega'(1/t_j)} \phi'_j(t_j). \quad (8)$$

The boundary condition on L_j is obtained by substituting from (8), (4a), and (4b) in (6) as follows:

$$\begin{aligned} \phi_j^{B+}(\sigma) - \phi_j^{B-}(\sigma) &= \frac{-1}{\kappa_j D_j(1 - \nu_j)} \\ \times \left[\int_{L_j} \left(m(s) + i \int_{L_j} p(s) ds \right) dz \right] &= h_{L_j}(\sigma) \end{aligned} \quad (9)$$

where

$$\phi_j^{A+}(\sigma) = \phi_j^{A-}(\sigma). \quad (10)$$

The superscripts $+$ and $-$ are the limit values of the function $\phi_j(t_j)$ as approaching the boundary from regions S_j^+ and S_j^- ,

respectively, (see Fig. 1(c)). Since the externally applied bending moments are considered by the functions $\phi_j^A(t_j)$ and $\psi_j^A(t_j)$, $h_{L_j}(\sigma) = 0$. The boundary conditions on M are the continuation of moments and rotations. The continuity of stresses is expressed in view of (2) as follows:

$$\begin{aligned} \left[\int_M \left(m_{y_1} + i \int_M p_{y_1} ds \right) dz_1 \right] \\ = - \left[\int_M \left(m_{y_2} - i \int_M p_{y_2} ds \right) dz_2 \right] \quad (11) \end{aligned}$$

which is expressed in terms of the complex stress functions in view of (6) and (8) by

$$\begin{aligned} \phi_1^+(\sigma) - \phi_1^-(\sigma) \\ = - \frac{\kappa_2 D_2(1 - \nu_2)}{\kappa_1 D_1(1 - \nu_1)} [\overline{\phi_2^+(\sigma)} - \overline{\phi_2^-(\sigma)}], \quad (12) \end{aligned}$$

and it can be further simplified using (4a) and (10) as follows:

$$\begin{aligned} \phi_1^{B+}(\sigma) - \phi_1^{B-}(\sigma) \\ = - \frac{\kappa_2 D_2(1 - \nu_2)}{\kappa_1 D_1(1 - \nu_1)} [\overline{\phi_2^{B+}(\sigma)} - \overline{\phi_2^{B-}(\sigma)}]. \quad (13) \end{aligned}$$

Similarly, continuity of rotations along the bonded interface is expressed in view of (2) as follows:

$$\left(\frac{\partial w_1}{\partial x_1} + i \frac{\partial w_1}{\partial y_1} \right) = - \left(\frac{\partial w_2}{\partial x_2} - i \frac{\partial w_2}{\partial y_2} \right). \quad (14)$$

Using (7) and (8), (14) can be written in terms of the complex stress functions by

$$\phi_1^+(\sigma) + \kappa_1 \phi_1^-(\sigma) = -[\overline{\phi_2^+(\sigma)} + \kappa_2 \overline{\phi_2^-(\sigma)}], \quad (15)$$

which is expressed using (4a) and (10) as follows:

$$\begin{aligned} \phi_1^{B+}(\sigma) + \kappa_1 \phi_1^{B-}(\sigma) \\ = -[\overline{\phi_2^{B+}(\sigma)} + \kappa_2 \overline{\phi_2^{B-}(\sigma)}] + D_1(\sigma) \quad (16) \end{aligned}$$

$$D_1(\sigma) = \frac{M_0}{D_1(1 - \nu_1^2)} [\overline{\omega(\sigma)} - \omega(\sigma)]. \quad (17)$$

Since on M we have

$$\omega(\sigma) = \overline{\omega(\sigma)} = \bar{\omega}\left(\frac{1}{\sigma}\right), \quad (18)$$

thus, $D_1(\sigma) = 0$.

Consider the function $\theta_1(t_1)$ defined by

$$\theta_1(t_1) = \phi_1^B(t_1) - \frac{\kappa_2 D_2(1 - \nu_2)}{\kappa_1 D_1(1 - \nu_1)} \overline{\phi_2^B(1/\bar{t}_1)}. \quad (19)$$

Equation (13) can be written in terms of the function $\theta_1(t_1)$ as follows:

$$\theta_1^+(\sigma) - \theta_1^-(\sigma) = 0. \quad (20)$$

The solution of (20) is given by an arbitrary rational function $g_1(t_1)$ (Muskhelishvili, 1963):

$$\theta_1(t_1) = \phi_1^B(t_1) - \frac{\kappa_2 D_2(1 - \nu_2)}{\kappa_1 D_1(1 - \nu_1)} \overline{\phi_2^B(1/\bar{t}_1)} = g_1(t_1). \quad (21)$$

On the boundary, the following relation holds:

$$g_1^+(\sigma) = g_1^-(\sigma) \equiv g_1(\sigma) \quad (22)$$

From (21) the two limit values of $\overline{\phi_2^B(1/\bar{t}_1)}$ are expressed by

$$\overline{\phi_2^{B+}(1/\bar{t}_1)} = \frac{\kappa_1 D_1(1 - \nu_1)}{\kappa_2 D_2(1 - \nu_2)} (\phi_1^{B-}(\sigma) - g_1(\sigma)) \quad (23a)$$

$$\overline{\phi_2^{B-}(1/\bar{t}_1)} = \frac{\kappa_1 D_1(1 - \nu_1)}{\kappa_2 D_2(1 - \nu_2)} (\phi_1^{B+}(\sigma) - g_1(\sigma)). \quad (23b)$$

Substituting (23a) and (23b) in (16), the boundary condition on M is expressed as follows:

$$\phi_1^{B+}(\sigma) + \lambda_1 \phi_1^{B-}(\sigma) = \gamma_1 g_1(\sigma) + h_{1M}(\sigma) \quad (24a)$$

$$h_{1M}(\sigma) = \frac{\kappa_2 D_2(1 - \nu_2)}{\kappa_2 D_2(1 - \nu_2) + \kappa_1 \kappa_1 D_1(1 - \nu_1)} D_1(\sigma) \quad (24b)$$

$$\lambda_1 = \frac{\kappa_1 \kappa_2 D_2(1 - \nu_2) + \kappa_1 D_1(1 - \nu_1)}{\kappa_2 D_2(1 - \nu_2) + \kappa_1 \kappa_1 D_1(1 - \nu_1)} \quad (24c)$$

$$\gamma_1 = \frac{(1 + \kappa_1) \kappa_1 D_1(1 - \nu_1)}{\kappa_2 D_2(1 - \nu_2) + \kappa_1 \kappa_1 D_1(1 - \nu_1)}. \quad (24d)$$

The problem of obtaining $\phi_1^B(t_1)$ is reduced to the Riemann-Hilbert problem of (9) on L_1 and (24a) on M . Similarly, the function $\phi_2^B(t_2)$ can be obtained by merely interchanging the subscripts 1 and 2 in the foregoing derivations. The coefficients of $\phi_2^B(t_2)$ corresponding to (24b), (24c), and (24d) are

$$h_{2M}(\sigma) = \frac{\kappa_1 D_1(1 - \nu_1)}{\kappa_1 D_1(1 - \nu_1) + \kappa_2 \kappa_2 D_2(1 - \nu_2)} D_2(\sigma) \quad (25a)$$

$$\lambda_2 = \frac{1}{\lambda_1} = \frac{\kappa_2 \kappa_1 D_1(1 - \nu_1) + \kappa_2 D_2(1 - \nu_2)}{\kappa_1 D_1(1 - \nu_1) + \kappa_1 \kappa_2 D_2(1 - \nu_2)} \quad (25b)$$

$$\gamma_2 = \frac{(1 + \kappa_1) \kappa_1 D_2(1 - \nu_2)}{\kappa_1 D_1(1 - \nu_1) + \kappa_1 \kappa_2 D_2(1 - \nu_2)}. \quad (25c)$$

Derivation of General Solution

The general solution of Riemann-Hilbert problem is first derived for $\phi_1^B(t_1)$ in the t_1 -plane as follows (Muskhelishvili, 1963):

$$\begin{aligned} \phi_1^B(t_1) = H_1(t_1) + \frac{\gamma_1 \chi_1(t_1)}{2\pi i} \int_M \frac{g_1(\sigma)}{\chi_1^+(\sigma)(\sigma - t_1)} d\sigma \\ + \chi_1(t_1) P_1(t_1) \quad (26a) \end{aligned}$$

$$\begin{aligned} H_1(t_1) = \frac{\chi_1(t_1)}{2\pi i} \int_{L_1} \frac{h_{L_1}(\sigma)}{\chi_1(\sigma)(\sigma - t_1)} d\sigma \\ + \frac{\chi_1(t_1)}{2\pi i} \int_M \frac{h_{1M}(\sigma)}{\chi_1(\sigma)(\sigma - t_1)} d\sigma. \quad (26b) \end{aligned}$$

Noting that $h_{L_1}(\sigma) = 0$. Also, since $D_1(\sigma)$ defined by (17) vanishes, thus, $h_{1M}(\sigma) = 0$, and consequently $H_1(t_1) = 0$ except for the constant of integration. The function $P_1(t_1)$ is an arbitrary rational function. Plemelj function $\chi_1(t_1)$ is defined as follows:

$$\chi_1(t_1) = (t_1 - \alpha)^{m_1} (t_1 - \beta)^{1-m_1} \quad (27a)$$

$$m_1 = 0.5 + i(\ln \lambda_1)/(2\pi). \quad (27b)$$

α and β are the points in the t_1 -plane (and t_2 -plane) corresponding to junctures C and D of boundaries L_j with M . Since $\chi_1(t_1)$ is a multivalued function, the branch $\chi_1(t_1)/t_1 \rightarrow 1$ is chosen for $t_1 \rightarrow \infty$. Plemelj function, $\chi_1(t_1)$ has the following relationships on the boundaries:

$$\chi_1^+(\sigma) = -\lambda_1 \chi_1^-(\sigma) \quad \text{on } M \quad (28a)$$

$$\chi_1^+(\sigma) = \chi_1^-(\sigma) \quad \text{on } L_1. \quad (28b)$$

The function $g_1(t_1)$ is assumed as the summation of two frac-

tional expressions which are regular in S_1^+ and S_1^- , respectively, as follows:

$$g_1(t_1) = \sum_k \frac{a_{1k}}{\xi_{1k} - t_1} + \sum_k \frac{b_{1k}}{\eta_{1k} - t_1} \quad (29)$$

where ξ_{1k} , η_{1k} , a_{1k} , and b_{1k} are unknown complex constants, but the value of $|\xi_{1k}|$ is greater than one and the value of $|\eta_{1k}|$ is less than one. The contour integral of $g_1(t_1)$ of (26a) is changed into line integral surrounding M , and is carried out using the residue theorem as follows:

$$\begin{aligned} & \frac{\gamma_1 \chi_1(t_1)}{2\pi i} \int_M \frac{g_1(\sigma)}{\chi_1^+(\sigma)(\sigma - t_1)} d\sigma \\ &= \frac{\gamma_1 \chi_1(t_1)}{2\pi i(1 + \lambda_1)} \oint_M \frac{g_1(\sigma)}{\chi_1^+(\sigma)(\sigma - t_1)} d\sigma \\ &= \frac{\gamma_1}{(1 + \lambda_1)} \left\{ \sum_k \left(1 - \frac{\chi_1(t_1)}{\chi_1(\xi_{1k})} \right) \frac{a_{1k}}{\xi_{1k} - t_1} \right. \\ & \quad \left. + \sum_k \left(1 - \frac{\chi_1(t_1)}{\chi_1(\eta_{1k})} \right) \frac{b_{1k}}{\eta_{1k} - t_1} \right\}. \quad (30) \end{aligned}$$

The function in (26a), $P_1(t_1)$, is determined by utilizing the regular characteristic of the complex stress function $\psi_1(t_1)$ of (8) in S_1^+ . Substituting (4a) and (4b) in (8) we get

$$\begin{aligned} \psi_1^B(t_1) &= \kappa_1 \overline{\phi_1^B(1/t_1)} - \frac{\bar{\omega}(1/t_1)}{\omega'(t_1)} \phi_1'^B(t_1) \\ & \quad - \frac{M_0}{2D_1(1 - \nu_1)} [\omega(t_1) - \bar{\omega}(1/t_1)]. \quad (31) \end{aligned}$$

Expanding the second term in the right-hand side of (31) in Laurent's series at $t_1 = 1/\zeta_k' \equiv \zeta_k'$, we get

$$\frac{\bar{\omega}(1/t_1)}{\omega'(t_1)} \phi_1'^B(t_1) = - \sum_{k=1}^N \frac{A_{1k} \bar{B}_k \zeta_k'^2}{\zeta_k' - t_1} + \text{regular terms in } S_1^+ \quad (32)$$

where $A_{1k} = \phi_1'^B(\zeta_k')$; $B_k \equiv E_k / \omega'(\zeta_k')$, ($k = 1, 2, \dots, N$).

The first term on the right-hand side of (31) is expressed by substituting (30) in (26a) and expressing $\phi_1^B(t_1)$ in (26a) as $\phi_1^B(1/t_1)$ as follows:

$$\begin{aligned} \overline{\phi_1^B(1/t_1)} &= \overline{\chi_1(1/t_1) P_1(1/t_1)} \\ & \quad + \frac{\gamma_1}{(1 + \lambda_1)} \left[\sum_k \left(1 - \frac{\overline{\chi_1(1/t_1)}}{\chi_1(\xi_{1k})} \right) \frac{\overline{a_{1k}}}{\xi_{1k} - 1/t_1} \right. \\ & \quad \left. + \sum_k \left(1 - \frac{\overline{\chi_1(1/t_1)}}{\chi_1(\eta_{1k})} \right) \frac{\overline{b_{1k}}}{\eta_{1k} - 1/t_1} \right] \\ &= \overline{\chi_1(1/t_1) P_1(1/t_1)} + \frac{\gamma_1}{(1 + \lambda_1)} \\ & \quad \times \sum_k \left(1 - \frac{\chi_2(t_1)}{\chi_2(\xi_{1k}')} \right) \frac{-\overline{a_{1k}} \xi_{1k}'}{\xi_{1k}' - t_1} \\ & \quad + \text{regular terms in } S_1^+ \quad (33) \end{aligned}$$

where

$$\frac{\overline{\chi_1(1/t_1)}}{\chi_1(\xi_{1k})} = \frac{\xi_{1k}' \chi_2(t_1)}{t_1 \chi_2(\xi_{1k}')} \quad (34a)$$

$$\frac{\overline{\chi_1(1/t_1)}}{\chi_1(\eta_{1k})} = \frac{\eta_{1k}' \chi_2(t_1)}{t_1 \chi_2(\eta_{1k}')} \quad (34b)$$

$$\frac{\overline{\chi_1(1/t_1)}}{\chi_1(\zeta_k)} = \frac{\zeta_k' \chi_2(t_1)}{t_1 \chi_2(\zeta_k')} \quad (34c)$$

and $\xi_{1k}' \equiv 1/\zeta_{1k}$; $\eta_{1k}' \equiv 1/\eta_{1k}$; $\zeta_k' \equiv 1/\zeta_k$. Substituting (32) and (33) into (31), the function $\psi_1^B(t_1)$ is expressed with its irregular terms in the unit circle as follows:

$$\begin{aligned} \psi_1^B(t_1) &= \kappa_1 \overline{\chi_1(1/t_1) P_1(1/t_1)} + \frac{\gamma_1 \kappa_1}{(1 + \lambda_1)} \\ & \quad \times \sum_k \left(1 - \frac{\chi_2(t_1)}{\chi_2(\zeta_k')} \right) \frac{-\overline{a_{1k}} \xi_{1k}'}{\xi_{1k}' - t_1} + \sum_{k=1}^N \frac{A_{1k} \bar{B}_k \zeta_k'^2}{\zeta_k' - t_1} \\ & \quad - \frac{M_0}{2D_1(1 - \nu_1)} \sum_{k=1}^N \frac{\bar{E}_k \zeta_k'^2}{\zeta_k' - t_1} \\ & \quad + \text{regular terms in } S_1^+. \quad (35) \end{aligned}$$

The second term in the right-hand side of (35) is regular at $t_1 = \zeta_k'$, while the third and the fourth terms have poles at $t_1 = \zeta_k'$. The function $\psi_1^B(t_1)$ must be regular inside the unit circle and consequently the irregular terms should cancel out. Expanding the first term in the right-hand side of (35) in a Laurent's series at $t_1 = \zeta_k'$ and equating the first, third, and fourth terms to zero, the function $P_1(t_1)$ is finally given by

$$P_1(t_1) = \frac{1}{\kappa_1} \sum_{k=1}^N \frac{\overline{A_{1k}} B_k - \frac{M_0 E_k}{2D_1(1 - \nu_1)}}{\chi_1(\zeta_k)(\zeta_k - t_1)}. \quad (36)$$

The unknown constants of the function $g_1(t_1)$ defined in (29) are obtained using (21) as follows:

$$\begin{aligned} \overline{\phi_1^B(t_1)} &= \frac{\kappa_2 D_2 (1 - \nu_2)}{\kappa_1 D_1 (1 - \nu_1)} \overline{\phi_2^B(1/t_1)} \\ &= \frac{\gamma_1}{1 + \lambda_1} \sum_k \left\{ 1 - \frac{\chi_1(t_1)}{\chi_1(\xi_{1k}')} \right\} \frac{a_{1k}}{\xi_{1k}' - t_1} \\ & \quad + \frac{\kappa_2 D_2 (1 - \nu_2)}{\kappa_1 D_1 (1 - \nu_1)} \frac{\gamma_2}{1 + \lambda_2} \sum_k \left\{ 1 - \frac{\chi_1(t_1)}{\chi_1(\eta_{2k}')} \right\} \frac{\bar{b}_{2k} \eta_{2k}'}{\eta_{2k}' - t_1} \\ & \quad + \frac{1}{\kappa_1} \sum_k \frac{\chi_1(t_1)}{\chi_1(\zeta_k)} \frac{\overline{A_{1k}} B_k - \frac{M_0 E_k}{2D_1(1 - \nu_1)}}{\zeta_k - t_1} + \frac{\gamma_1}{1 + \lambda_1} \\ & \quad \times \sum_k \left\{ 1 - \frac{\chi_1(t_1)}{\chi_1(\eta_{1k}')} \right\} \frac{b_{1k}}{\eta_{1k}' - t_1} + \frac{\kappa_2 D_2 (1 - \nu_2)}{\kappa_1 D_1 (1 - \nu_1)} \frac{\gamma_2}{1 + \lambda_2} \\ & \quad \times \sum_k \left\{ 1 - \frac{\chi_1(t_1)}{\chi_1(\xi_{2k}')} \right\} \frac{\overline{a_{2k}} \xi_{2k}'}{\xi_{2k}' - t_1} + \frac{\kappa_2 D_2 (1 - \nu_2)}{\kappa_1 D_1 (1 - \nu_1)} \frac{1}{\kappa_2} \\ & \quad \times \sum_k \frac{\chi_1(t_1)}{\chi_1(\zeta_k)} \frac{A_{2k} \bar{B}_k \zeta_k'^2 + \frac{\mu M_0 \bar{E}_k \zeta_k'^2}{2D_2(1 - \nu_2)}}{\zeta_k' - t_1}. \quad (37) \end{aligned}$$

The term $\overline{\chi_2(1/t_1)}$ contained in $\overline{\phi_2(1/t_1)}$ is replaced by $\chi_1(t_1)$ as in (34a), (34b), and (34c), where $m_2 = \bar{m}_1$. Relations (19) and (37) which give the function $g_1(t_1)$ are equal. Therefore, their poles in S_1^+ and S_1^- must be equal and the coefficients of each pole are equal as well, which include or exclude the Plemelj functions. Thus, comparing the coefficients of the poles in the two equations, $g_1(t_1)$ is determined as follows:

$$g_1(t_1) = \frac{1}{\kappa_1} \sum_k \frac{\overline{A_{1k}B_k} - \frac{M_0E_k}{2D_1(1-\nu_1)}}{\zeta_k - t_1} + \frac{\kappa_2 D_2(1-\nu_2)}{\kappa_1 D_1(1-\nu_1)} \frac{1}{\kappa_2} \sum_k \frac{A_{2k}\overline{B_k}\zeta_k'^2 + \frac{\mu M_0\overline{E_k}\zeta_k'^2}{2D_2(1-\nu_2)}}{\zeta_k' - t_1}. \quad (38)$$

The complex stress function $\phi_1^B(t_1)$ is obtained by (26a), (30), (36), and (38) and is finally expressed by

$$\begin{aligned} \phi_1^B(t_1) = & \frac{\gamma_1}{1 + \lambda_1} \\ & \times \left[\frac{1}{\kappa_1} \sum_{k=1}^N \left\{ 1 + \frac{1 + \lambda_1 - \gamma_1}{\gamma_1} \frac{\chi_1(t_1)}{\chi_1(\zeta_k)} \right\} \right. \\ & \times \frac{\overline{A_{1k}B_k} - \frac{M_0E_k}{2D_1(1-\nu_1)}}{\zeta_k - t_1} + \frac{\kappa_2 D_2(1-\nu_2)}{\kappa_1 D_1(1-\nu_1)} \frac{1}{\kappa_2} \\ & \left. \times \sum_{k=1}^N \left\{ 1 - \frac{\chi_1(t_1)}{\chi_1(\zeta_k')} \right\} \frac{A_{2k}\overline{B_k}\zeta_k'^2 + \frac{\mu M_0\overline{E_k}\zeta_k'^2}{2D_2(1-\nu_2)}}{\zeta_k' - t_1} \right]. \quad (39) \end{aligned}$$

Similarly, the function $\phi_2^B(t_2)$ is obtained and is expressed by

$$\begin{aligned} \phi_2^B(t_2) = & \frac{\gamma_2}{1 + \lambda_2} \\ & \times \left[\frac{1}{\kappa_2} \sum_{k=1}^N \left\{ 1 + \frac{1 + \lambda_2 - \gamma_2}{\gamma_2} \frac{\chi_2(t_2)}{\chi_2(\zeta_k)} \right\} \right. \\ & \times \frac{\overline{A_{2k}B_k} + \frac{\mu M_0E_k}{2D_2(1-\nu_2)}}{\zeta_k - t_2} + \frac{\kappa_1 D_1(1-\nu_1)}{\kappa_2 D_2(1-\nu_2)} \frac{1}{\kappa_1} \\ & \left. \times \sum_{k=1}^N \left\{ 1 - \frac{\chi_2(t_2)}{\chi_2(\zeta_k')} \right\} \frac{A_{1k}\overline{B_k}\zeta_k'^2 - \frac{M_0\overline{E_k}\zeta_k'^2}{2D_1(1-\nu_1)}}{\zeta_k' - t_2} \right]. \quad (40) \end{aligned}$$

The unknown constants A_{1k} and A_{2k} can be determined using the relations, $A_{1k} = \phi_1^B(\zeta_k')$, $A_{2k} = \phi_2^B(\zeta_k')$, ($k = 1, 2, \dots, N$), and solving $4N$ simultaneous linear system of equations with respect to the real and imaginary parts of A_{1k} and A_{2k} .

Stress Distributions

Two examples of stress distributions are shown for the following parameters; rigidity ratio, $D_2/D_1 = 0.5$, Poisson's ratio of material 1, $\nu_1 = 0.5$, and that of material 2, $\nu_2 = 0.25$. Since the shape is symmetrical with respect to the Y -axis, the distributions are shown for $X \geq 0$. In Fig. 2(a) the hole shape is circular with the lengths of the interface cracks $C_1 = C_2 = a$ while in Fig. 2(b) the hole shape is the ellipse of ratio $b/a = 1.5$ with the length of the interface cracks $C_1 = C_2 = a$. It is obvious that as the ratio a/b decreases (i.e., the ellipse becomes sharper) the maximum values of the bending moments, $M_{\theta 1}$ and $M_{\theta 2}$ increase, then the problem becomes a model of two bonded half-planes with a crack penetrating the two materials. On the boundary M , we have $M_{Y_1} = M_{Y_2} \equiv M_Y$. In addition the following relationship holds among M_{X_1} , M_{X_2} , and M_Y on M , (Hasebe and Salama, 1994a).

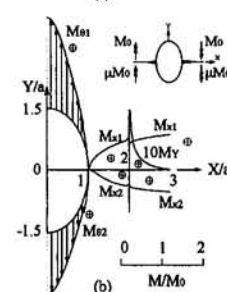
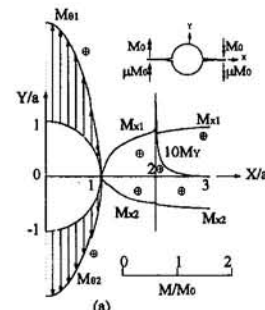


Fig. 2 Distributions of bending and torsional moment along the hole and the interface between the two bonded dissimilar half-planes, $D_2/D_1 = 0.5$; $\nu_1 = 0.5$; $\nu_2 = 0.25$. (a) $C_1/a = C_2/a = 1$; $a/b = 1$. (b) $C_1/a = C_2/a$; $b/a = \frac{2}{3}$.

$$M_{X_2} = \frac{D_2(1 - \nu_2^2)}{D_1(1 - \nu_1^2)} M_{X_1} + \left[\nu_2 - \frac{D_2(1 - \nu_2^2)}{D_1(1 - \nu_1^2)} \nu_1 \right] M_Y \quad (41)$$

Stress Concentration Factor

The stress concentration factor, SCF at points A and B , is calculated for various elliptic holes and is defined by

$$S_A = M_{X_1}^A/M_0, \quad S_B = M_{X_2}^B/\mu M_0 \quad (42)$$

where $M_{X_1}^A$ and $M_{X_2}^B$ are the bending moments at points A and B , respectively. In Fig. 3 the variation of the SCF is shown versus the a/b ratio, and for different values of the rigidity ratio. S_A^* is the SCF at point A for a rigidity ratio equal to $D_2/D_1 = 0.0$.

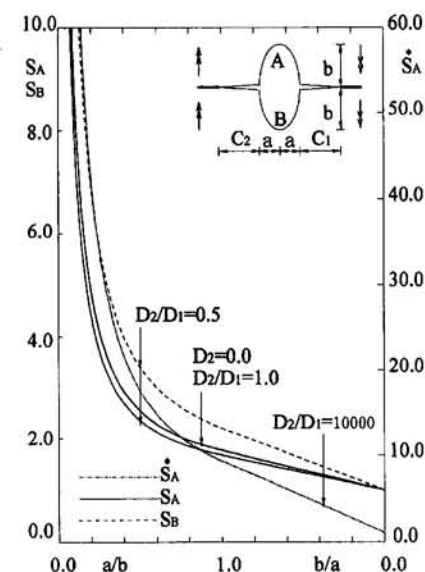


Fig. 3 Stress concentration factors at points A and B for rigidity ratios of $D_2/D_1 = 0, 0.5, 1$ and 10000 , $\nu_1 = \nu_2 = 0.25$ and lengths of interface cracks are $C_1 = C_2 = 0$ and $C_1/a = C_2/a = 4$

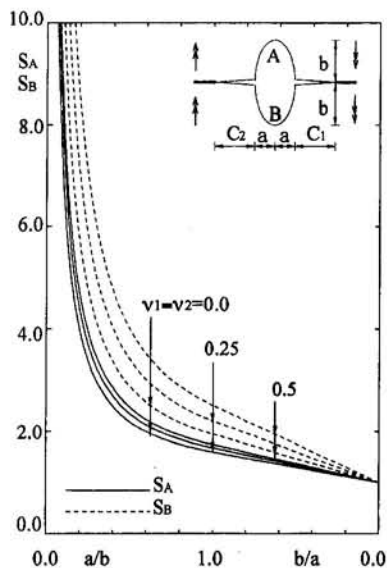


Fig. 4 Stress concentration factors at points A and B for different values of Poisson's ratio and for a rigidity ratio of $D_2/D_1 = 0.5$ and lengths of interface cracks are $C_1 = C_2 = 0$

$D_1 = 10000$ which represents the bending of bonded elastic to rigid materials. The problem of bending of a half-plane with an semi-elliptic hole is demonstrated by the curve $D_2 = 0$ for which the values of S_A coincide with the results of Hasebe (1972). When $D_2 = \infty$ the values of the SCF of material 1 are equal to zero, that is because material 1 is considered fixed at its both ends which are expressed by the line $x_1 = \infty$ and $x_1 = -\infty$ and at these two lines $\partial w_1 / \partial x_1 = 0$. The values of the SCF for $D_2/D_1 = 1$ and $\nu_2 = \nu_1$ are found to be exactly equal with the values given for the case of bending of a homogeneous infinite plate with an elliptic hole by Savin (1961) for which the values of S_A and S_B are equal. The values of S_A are also equal to those of a half-plane and there is no difference in the figure. In order to investigate the dependence of the SCF on the lengths of the interface cracks, two special cases in which the lengths of the interface cracks are given as $C_1 = C_2 = 0$ and $C_1 = C_2 = 4a$ are considered. The values of the SCF are found to have a negligible difference, which can be seen in Fig. 3, corresponding curves are coincident. Also, as the ratio a/b approaches zero, the problem tends to that of bending of two half-planes with a through crack in both materials, for which the SCF represents the stress at the tip of the crack and can be taken as a measure of the stress intensity factor for that particular problem. While, as the ratio b/a approaches zero the problem tends to that of bending of two half-planes with an interface crack for which the SCF in all curves of Fig. 3 approach a value of one. In Fig. 4 the values of the SCF are shown versus a/b and for different values of Poisson's ratio, the solid lines and the dashed lines show the values of the SCF at points A and B, respectively, for a rigidity ratio equal to $D_2/D_1 = 0.5$ and the lengths of the interface cracks are $C_1 = C_2 = 0$. From Figs. 3 and 4, it is clear that the SCF is rather dependent on the Poisson's ratio other than the lengths of the interface cracks.

The SCF of bending of a homogeneous infinite plate with an elliptic hole is given by the following closed form (Savin, 1961):

$$S_{EH} = \frac{M_{\max}}{M_0} = 1 + \frac{2(1+\nu)}{(3+\nu)} \sqrt{\frac{b}{\rho}} \quad (43)$$

where ν is the Poisson's ratio and ρ is the radius of curvature at points A and B, and has the relation $\rho = a^2/b$. A comparison between (43) and our results for the homogeneous case is carried out for some of Poisson's ratios and the ratio of the radius of curvature to the major axes length, b shown in (43), and the results were found to be identical. A general expression for the SCF is derived as follows:

$$SCF = \sum_{j=1}^{\infty} k_j \rho^{n_j} \quad (44)$$

where k_j are the coefficients determined from the boundary conditions and the shape. n_j are the roots of the characteristic equation (Hasebe, 1971; Hasebe and Kutanda, 1978). The first three terms of (44) are considered for an approximate expression as follows:

$$S_A \text{ or } S_B = k_1 \sqrt{\frac{b}{\rho}} + k_2 + k_3 \sqrt{\frac{\rho}{b}} \quad (45)$$

where $n_1 = -0.5$, $n_2 = 0$ and $n_3 = 0.5$ in (44) owing to the elliptical shape of the hole. The coefficients in (45) are determined for different material constants and rigidity ratios and for $C_1 = C_2 = 0$. Using the least squares method and the analytical results, the values of k_1 , k_2 , and k_3 are obtained and are shown in Table 1. The used 100 data for each of S_A and S_B are those of a/b ranges from 0.01 to 1 at an increment of 0.01. The SCF, approximate values and errors of (45) are demonstrated in Table 2. Judging from Table 2, relation (45) is considered as a good approximation.

Stress Intensity Factor

The case of a/b equal to zero represents a through crack in both materials for which the SIF is obtained. The bending and torsional moments are expressed in the vicinity of the crack on the X -axis as follows (Hasebe and Iida, 1979):

$$M_{Y_j} + M_{X_j} = \frac{2}{\sqrt{2r}} \left(k_B^j \cos \frac{\theta}{2} - k_S^j \sin \frac{\theta}{2} \right) \quad (46)$$

$$M_{Y_j} - M_{X_j} + 2iM_{X_j Y_j} = \frac{1}{2(1+\nu_j)\sqrt{2r}} [\{ (7+\nu_j)k_B^j + i(5+3\nu_j)k_S^j \} \exp(-i\theta/2) + (1-\nu_j)(k_B^j - ik_S^j) \times \exp(-5i\theta/2)] \quad (47)$$

where r and θ are the polar coordinates measured, respectively, from the crack tip and from the line of extension of crack. k_B^j and k_S^j are the SIF for bending and torsional of material j , respectively, and they are expressed in terms of the stress functions $\phi_j(t_j)$ as follows:

Table 1 Values of k_1 , k_2 , and k_3 of (46) for S_A for Poisson's ratios of $\nu_1 = \nu_2 = 0$, 0.25, and 0.5

$D_2/D_1 = 0$				$D_2/D_1 = 0.5$				$D_2/D_1 = 10^8$			
$\nu_1 = \nu_2$	0.0	0.25	0.50	0.0	0.25	0.50	0.0	0.25	0.50	0.0	0.25
k_1	0.673	0.772	0.857	0.595	0.674	0.74	3.735	8.092	20.670		
k_2	1.001	1.006	1.011	1.009	1.011	1.012	1.214	1.653	3.294		
k_3	-0.006	-0.010	-0.013	-0.010	-0.012	-0.013	-0.150	-0.405	-1.284		

Table 2 Error percentage between the calculated values of the SCF and (46). $D_2/D_1 = 0.5$, $\nu_1 = \nu_2 = 0.25$ and $C_1 = C_2 = 0$.

ρ/b	S_A	Eq. (46)	Error percent
0.0100	68.4003	68.4209	-0.0302
0.0200	34.7339	34.7156	0.0527
0.0300	23.4969	23.4804	0.0702
0.0400	17.8756	17.8627	0.0719
0.0500	14.5019	14.4921	0.0675
0.1000	7.7526	7.7505	0.0274
0.2000	4.3769	4.3788	-0.0432
0.3000	3.2515	3.2541	-0.0805
0.4000	2.6888	2.6912	-0.0892
0.5000	2.3511	2.3530	-0.0800
0.6000	2.1260	2.1271	-0.0524
0.7000	1.9652	1.9654	-0.0126
0.8000	1.8446	1.8439	0.0376
0.9000	1.7508	1.7491	0.0962
1.0000	1.6758	1.6731	0.1641

$$k_B^j - ik_s^j = -2\sqrt{2}D_j(1 + \nu_j) \exp(-i\delta/2)\phi'_j(t_0)/\sqrt{\omega''(t_0)} \quad (48)$$

where $t_0 = -1$ is the value of t_j on the unit circle which corresponds to the crack tip. δ is the angle between the X -axis and the direction of the crack, $\delta = -\pi/2$ as the crack is in the Y -direction. The following nondimensional SIF is used:

$$F^A = \frac{(3 + \nu_1)}{(1 + \nu_1)} \frac{k_B^j}{M_0 \sqrt{b}}, \quad F^B = \frac{(3 + \nu_2)}{(1 + \nu_2)} \frac{k_B^j}{\mu M_0 \sqrt{b}}. \quad (49)$$

The variation of the SIF of F^A and F^B for materials 1 and 2, respectively, is shown in Fig. 5 versus the rigidity ratio and for different values of Poisson's ratios. The stress intensity factor is related to the SCF at points A and B by

$$K_A = \frac{1}{2} \cdot \frac{3 + \nu_1}{1 + \nu_1} \lim_{\rho \rightarrow 0} \sqrt{\rho} M_{X_1}^A$$

$$K_B = \frac{1}{2} \cdot \frac{3 + \nu_2}{1 + \nu_2} \lim_{\rho \rightarrow 0} \sqrt{\rho} M_{X_2}^B \quad (50)$$

where K_A and K_B are the SIF at points A and B for bending (Hasebe and Kutanda, 1978). A nondimensionalized form of

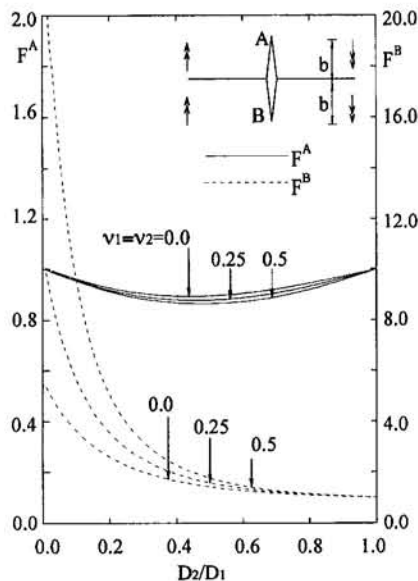


Fig. 5 Stress intensity factors at points A and B versus the flexural rigidity ratios D_2/D_1 , Poisson's ratios of $\nu_1 = \nu_2 = 0, 0.25$ and 0.5 and lengths of interface cracks are $C_1 = C_2 = 0$.

the SIF at points A and B is expressed in terms of the SCF as follows:

$$N_A = \frac{1}{2} \cdot \frac{3 + \nu_1}{1 + \nu_1} \lim_{\rho \rightarrow 0} \sqrt{\rho} M_{X_1}^A / M_0$$

$$N_B = \frac{1}{2} \cdot \frac{3 + \nu_2}{1 + \nu_2} \lim_{\rho \rightarrow 0} \sqrt{\rho} M_{X_2}^B / \mu M_0 \quad (51)$$

where the values of $M_{X_1}^A / M_0$ and $M_{X_2}^B / \mu M_0$ in (51) are the SCF defined by (45). Substituting from (45) into (51), one can see that the term which has influence on the SIF is that containing k_1 . A comparison between (49) and (51) for some cases is carried out and the results show that the values of the SIF obtained by (51) are nearly equal to those of (49).

Conclusions

A general solution to the problem of thin plate bending of partially bonded half-planes with an elliptical hole and interface cracks on its both sides was obtained. The closed-form solution was obtained using the complex stress functions approach developed by Muskhelishvili (1963) and the formulations of Savin (1961) for the thin plate bending together with the rational mapping function technique. Using the technique of the mapping function, it enables us to analyze awkwardly shaped structures and make the analytical solution feasible. For example, if the mapping function of (Hasebe and Iida, 1979) is used, a solution of bonded dissimilar half-planes with a square hole on the interface can be obtained. A comparison between the problem of bending of a homogeneous infinite thin plate with an elliptical hole and the results of this paper for the homogeneous case was carried out. Bending and torsional moment distributions on the boundaries have been obtained and are shown in Figs. 2(a) and 2(b). The relation of (41) among the bending moments, M_{X_1} , M_{X_2} , and M_y on the bonded boundary M is satisfied. The stress concentration factors, S_A and S_B have been obtained for some material constants and rigidity ratios and all dimensions of the elliptical hole. From the figures it is obvious that the length of the interface cracks has a negligible effect on the stress concentration factor, since there were no such loads transmitted between the two materials for the case of loading considered here. The stress concentration factor is shown to vary only for different a/b ratios while Poisson's ratio also shows a small effect. An expression for the stress concentration factor has been obtained by (45) and its accuracy is investigated through a comparison whose results are shown in Table 2. Values of the SIF were derived in two expressions for the case when the ratio a/b tends to zero for which the problem tends to that of bending of two bonded half-planes with a through crack in both the materials.

References

- Hasebe, N., 1971, "Stress Analysis of a Semi-Infinite Plate with a Triangular Notch or Mound," *Proceedings of the Japan Society of Civil Engineers*, No. 194, pp. 29–40 (in Japanese).
- Hasebe, N., 1972, "Stress Analysis of a Semi-Infinite Plate with a Semi-Elliptic Notch," *Bulletin of Nagoya Institute of Technology*, Vol. 24, pp. 295–301 (in Japanese).
- Hasebe, N., and Kutanda, Y., 1978, "Calculation of Stress Intensity Factor From Stress Concentration Factor," *Engineering Fracture Mechanics*, Vol. 10, pp. 215–221.
- Hasebe, N., and Iida, J., 1979, "A Crack Originating From a Triangular Notch on a Rim of a Semi-Infinite Plate Under Transverse Bending," *Engineering Fracture Mechanics*, Vol. 11, pp. 645–652.
- Hasebe, N., and Inohara, S., 1980, "Stress Analysis of a Semi-Infinite Plate with an Oblique Edge Crack," *Ingénieur-Archiv*, Vol. 49, pp. 51–62.
- Hasebe, N., Nakamura, T., and Ito, Y., 1994, "Analysis of the Second Mixed Boundary Value Problem for a Thin Plate," *ASME JOURNAL OF APPLIED MECHANICS*, Vol. 61, pp. 555–559.
- Hasebe, N., and Salama, M., 1994, "Thin Plate Bending Problem of Partially Bonded Bi-material Strips," *Archive of Applied Mechanics* (in Press).
- Muskhelishvili, N. I., 1963, *Some Basic Problems of the Mathematical Theory of Elasticity*, Noordhoff, Groningen.
- Savin, G. N., 1961, *Stress Concentration Around Holes*, Pergamon Press, London.

APPENDIX

Derivation of (5)

Since relation (14) should be satisfied at the remote ends, in terms of the complex stress functions it is expressed by

$$\begin{aligned}\phi_1^A(\sigma) + \frac{\omega(\sigma)}{\omega'(\sigma)} \overline{\phi_1^{A'}(\sigma)} + \overline{\psi_1^A(\sigma)} \\ = - \left[\overline{\phi_2^A(\sigma)} + \frac{\omega(\sigma)}{\omega'(\sigma)} \phi_2^{A'}(\sigma) + \psi_2^A(\sigma) \right]. \quad (52)\end{aligned}$$

Substituting (4b) into (52),

$$\begin{aligned}\frac{M_0}{2D_1(1 - \nu_1^2)} [\omega(\sigma)(1 - \nu_1) + \overline{\omega(\sigma)}(1 + \nu_1)] \\ = \frac{\mu M_0}{2D_2(1 - \nu_2^2)} [\omega(\sigma)(1 + \nu_2) + \overline{\omega(\sigma)}(1 - \nu_2)]. \quad (53)\end{aligned}$$

Noting the relation on the interface of (18), μ is finally expressed as follows:

$$\mu = \frac{D_2(1 - \nu_2^2)}{D_1(1 - \nu_1^2)}. \quad (54)$$

Frictional Contact Between the Surface Wave and a Rigid Strip

O. Y. Zharii

Department of Theoretical and Applied Mechanics,
Kiev University,
64 Vladimirska Street,
Kiev 252017, Ukraine

A problem of frictional contact between a running surface wave and a motionless rigid strip is considered. The corresponding mixed boundary value problem of elastodynamics is reduced to a singular integral equation for the normal stress distribution and a closed-form solution of it has been found. Boundaries of the contact zone are determined from a system of transcendental equations involving trigonometric functions. Also, simple formulae obtained for kinematic characteristics of solution (tangential velocity inside the contact area, velocity and slope of the free surface outside it). The problem considered represents a limiting case of operating ultrasonic motor when it is completely braked by an external tangential load force.

1 Introduction

Precise theoretical modeling of motion and energy transformation in ultrasonic motors is of great interest from both theoretical and practical viewpoints. The general standpoint of the author with this respect has been outlined recently (Zharii and Ulitko, 1992; Zharii, 1993).

One of the most interesting types of motors is a traveling wave ultrasonic motor. Several attempts to develop its model are due to Kurosawa and Ueha (1988), Hirata and Ueha (1993), Suzuki et al. (1990), but as of today, no consistent theory of it has been developed.

In papers by Zharii (1994) and Zharii and Ulitko (1994), two limiting cases of operation of the motor corresponding to cases of vanishing and infinitely large friction have been considered. Both these cases are, of course, unrealistic. But the solutions obtained are surely necessary for the development of grounded ideas concerning nature of motion transformation from elastic waves to rigid bodies in frictional contact.

There is one more limiting case that is worthy of consideration in the course of construction of a complete model of a traveling wave ultrasonic motor. We mean a situation when the tangential load is equal to the pressing force multiplied by a coefficient of dry friction, and consequently, the rotor (rigid strip) is completely braked. In this case, evidently, tangential stresses in each point of contact area are equal in magnitude to the normal pressure multiplied by the friction coefficient. This problem is a direct generalization of the smooth contact problem considered by Zharii and Ulitko (1994).

2 Formulation of a Problem

For theoretical modeling, the stator of an ultrasonic motor is considered as a piezoceramic plate of thickness h : $-h/2 < z < h/2$, polarized in the z -direction. The plate is a half-plane in shape $-\infty < x < \infty, y > 0$ (Fig. 1). Vibrations are excited by the running electric field,

$$E_z = E_0 \cos(kx - \omega t), \quad (1)$$

where k is the wave number, ω is the angular frequency of excitation, and $\lambda = 2\pi/k$ is the wavelength.

Contributed by the Applied Mechanics Division of THE AMERICAN SOCIETY OF MECHANICAL ENGINEERS for publication in the ASME JOURNAL OF APPLIED MECHANICS.

Discussion on this paper should be addressed to the Technical Editor, Professor Lewis T. Wheeler, Department of Mechanical Engineering, University of Houston, Houston, TX 77204-4792, and will be accepted until four months after final publication of the paper itself in the ASME JOURNAL OF APPLIED MECHANICS.

Manuscript received and accepted by the ASME Applied Mechanics Division, Apr. 25, 1994. Associate Technical Editor: T. R. Akylas.

The rotor is modeled by a rigid strip (Zharii, 1994). The equation of motion of the plate in the plane-stress approximation is (Grinchenko et al., 1976, 1989):

$$c_1^2 \operatorname{grad} \operatorname{div} \mathbf{u} - c_2^2 \operatorname{rot} \operatorname{rot} \mathbf{u}$$

$$- (1 + \nu) d_{31} c_1^2 \operatorname{grad} E_z = \frac{\partial^2 \mathbf{u}}{\partial t^2}, \quad (2)$$

where $\mathbf{u} = i u_x(x, y, t) + j u_y(x, y, t)$ is the displacement vector,

$$c_1 = [\rho s_{11}^E (1 - \nu^2)]^{-1/2}, \quad c_2 = [2\rho s_{11}^E (1 + \nu)]^{-1/2} \quad (3)$$

are the longitudinal and transverse wave velocities, and $\nu = -s_{11}^E/s_{22}^E$ is the Poisson's ratio. These and forthcoming notations have been universally accepted (IEEE, 1984; Berlincourt et al., 1964).

Taking into account the specific form of excitation, we pass on to the movable coordinate system, $\xi = x - \omega t/k, y$. In this system, equations of motion (2) become

$$c_1^2 \operatorname{grad} \operatorname{div} \mathbf{u} - c_2^2 \operatorname{rot} \operatorname{rot} \mathbf{u}$$

$$+ i(1 + \nu) d_{31} c_1^2 E_0 k \sin k\xi - \frac{\omega^2}{k^2} \frac{\partial^2 \mathbf{u}}{\partial \xi^2} = 0. \quad (4)$$

In the absence of the rotor, excited in the stator are the running waves of wavelength λ . If now a rigid rotor is pressed to the surface $y = 0$ by means of the force P per unit wavelength and per unit thickness, after decaying of the transient process, contact areas arise (Fig. 1). Also, we suppose that a tangential force of magnitude T acts on the rotor in the positive ξ -direction. When $T = \mu P$, the rotor cannot move under the action of tangential stresses, and tangential stresses inside the contact area are equal in magnitude to the normal pressure multiplied by the friction coefficient μ .

Further we use a dimensionless coordinate $s = k\xi$. Suppose that the contact area covers a segment $\alpha < s < \delta$ (Fig. 2). Within this zone, normal displacement for an absolutely rigid rotor are constant. Therefore, boundary conditions can be written as

$$u_y|_{y=0} = u_0, \quad \tau_{\xi y}|_{y=0} = \mu |\sigma_y|_{y=0} = -\mu \sigma_y|_{y=0}, \quad \alpha < s < \delta. \quad (5)$$

We took here the negative sign because in the slip zone tangential stresses are positive while normal ones should be negative. Also, we suppose that the tangential velocity is negative everywhere inside the contact zone, like in the smooth contact problem (Zharii and Ulitko, 1994). The second of the above equalities is true only when it is so. Stress resultants are

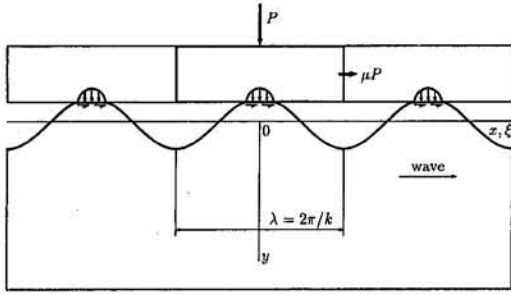


Fig. 1 Geometry of the problem

equal to prescribed normal and tangential forces (both P and T are positive),

$$\int_{\alpha/k}^{\delta/k} \sigma_y d\xi = -P, \quad \int_{\alpha/k}^{\delta/k} \tau_{\xi y} d\xi = T = \mu P. \quad (6)$$

On the free surface, both normal and tangential stresses vanish,

$$\sigma_y|_{y=0} = 0, \quad \tau_{\xi y}|_{y=0} = 0, \\ -\pi < s < \alpha \text{ and } \delta < s < \pi. \quad (7)$$

In the above equations, quantities α and δ are so far undetermined.

3 Derivation of an Integral Equation

Representing unknown contact stresses by the Fourier series,

$$\sigma_y \equiv f(s) = \frac{f_0}{2} + \sum_{n=1}^{\infty} f_n \cos ns + f'_n \sin ns, \\ \tau_{\xi y} \equiv g(s) = \frac{g_0}{2} + \sum_{n=1}^{\infty} g_n \cos ns + g'_n \sin ns \\ = -\mu f(s), \quad -\pi < s < \pi, \quad (8)$$

and taking into account that the latter equality implies proportionality between Fourier coefficients of f and g , we obtain the general solution of (4) in the way similar to that in the previous work (Zharii and Ulitko, 1994). This solution is

$$u_x = (1 + \nu) d_{31} E_0 \frac{k}{\gamma_1^2} \left[(k^2 + \gamma_2^2) \right. \\ \times \left. \frac{-(k^2 + \gamma_2^2)e^{-\gamma_1 y} + 2\gamma_1\gamma_2 e^{-\gamma_2 y}}{\Delta_R} + 1 \right] \sin s + \frac{U_0(y)}{2} \\ + \frac{k}{\rho c_2^2 \Delta_R} \sum_{n=1}^{\infty} \frac{f_n}{n} [-(k^2 + \gamma_2^2)e^{-n\gamma_1 y} + 2\gamma_1\gamma_2 e^{-n\gamma_2 y}] \sin ns \\ + \frac{k}{\rho c_2^2 \Delta_R} \sum_{n=1}^{\infty} \frac{f'_n}{n} [(k^2 + \gamma_2^2)e^{-n\gamma_1 y} - 2\gamma_1\gamma_2 e^{-n\gamma_2 y}] \cos ns \\ - \frac{\gamma_2}{\rho c_2^2 \Delta_R} \sum_{n=1}^{\infty} \frac{\mu f'_n}{n} [2k^2 e^{-n\gamma_1 y} - (k^2 + \gamma_2^2)e^{-n\gamma_2 y}] \cos ns, \\ u_y = (1 + \nu) d_{31} E_0 \\ \times \frac{k^2 + \gamma_2^2 - (k^2 + \gamma_2^2)e^{-\gamma_1 y} + 2k^2 e^{-\gamma_2 y}}{\gamma_1 \Delta_R} \cos s + \frac{V_0(y)}{2}$$

$$+ \frac{\gamma_1}{\rho c_2^2 \Delta_R} \sum_{n=1}^{\infty} \frac{f_n}{n} [-(k^2 + \gamma_2^2)e^{-n\gamma_1 y} + 2k^2 e^{-n\gamma_2 y}] \cos ns \\ + \frac{\gamma_1}{\rho c_2^2 \Delta_R} \sum_{n=1}^{\infty} \frac{f'_n}{n} [-(k^2 + \gamma_2^2)e^{-n\gamma_1 y} + 2k^2 e^{-n\gamma_2 y}] \sin ns \\ - \frac{k}{\rho c_2^2 \Delta_R} \sum_{n=1}^{\infty} \frac{\mu f_n}{n} [-2\gamma_1\gamma_2 e^{-n\gamma_1 y} + (k^2 + \gamma_2^2)e^{-n\gamma_2 y}] \sin ns \\ - \frac{k}{\rho c_2^2 \Delta_R} \sum_{n=1}^{\infty} \frac{\mu f'_n}{n} [2\gamma_1\gamma_2 e^{-n\gamma_1 y} \\ - (k^2 + \gamma_2^2)e^{-n\gamma_2 y}] \cos ns. \quad (9)$$

where, as earlier (Zharii, 1994, Zharii and Ulitko, 1994), we denoted $\gamma_{1,2} = (k^2 - \omega^2/c_{1,2}^2)^{1/2}$ and $\Delta_R = (k^2 + \gamma_2^2)^2 - 4k^2\gamma_1\gamma_2$ as the Rayleigh determinant.

Having written these explicit expressions for displacements, we can calculate the tangential particle velocity $u_x|_{y=0} = -\omega du_x/ds|_{y=0}$ and the half-plane boundary slope $du_y/ds|_{y=0}$. We do this using integral representations of Fourier coefficients that follow from (7) and (8),

$$f_n = \frac{1}{\pi} \int_{\alpha}^{\delta} f(s_1) \cos ns_1 ds_1, \\ f'_n = \frac{1}{\pi} \int_{\alpha}^{\delta} f(s_1) \sin ns_1 ds_1 \quad (10)$$

and the value of sum,

$$\sum_{n=1}^{\infty} \sin ns = \frac{1}{2} \cot \frac{s}{2}. \quad (11)$$

In the result of transformations we obtain

$$u_x|_{y=0} = -V \left[\cos s + \frac{1}{R\kappa A_0} (f(s) + \sigma_0) \right. \\ \left. - \frac{\mu_1}{RA_0} \frac{1}{2\pi} \int_{\alpha}^{\delta} f(s_1) \cot \frac{s_1 - s}{2} ds_1 \right],$$

$$\frac{du_y}{ds}|_{y=0} = U \left[\sin s + \frac{\mu_1}{\kappa A_0} (f(s) + \sigma_0) \right. \\ \left. + \frac{1}{A_0} \frac{1}{2\pi} \int_{\alpha}^{\delta} f(s_1) \cot \frac{s_1 - s}{2} ds_1 \right]. \quad (12)$$

Here

$$U = -(1 + \nu) d_{31} E_0 \frac{(k^2 - \gamma_2^2)(k^2 + \gamma_2^2)}{\gamma_1 \Delta_R}, \\ V = \omega \frac{2k\gamma_2}{k^2 + \gamma_2^2} U \quad (13)$$

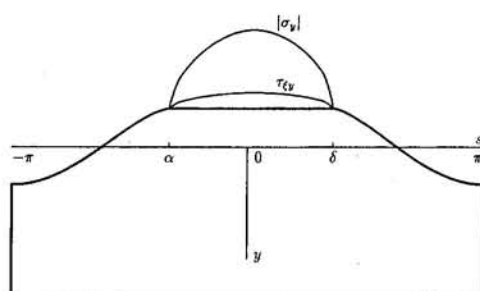


Fig. 2 Normal and tangential stresses

are amplitudes of the vertical displacement and tangential velocity of the boundary $y = 0$ in the absence of a rotor. Other notations mean the amplitude of excitation of a running wave and the pressing force per unit wavelength,

$$A_0 = -(1 + \nu) d_{31} E_0 \cdot \rho c_2^2 \frac{k^2 + \gamma_2^2}{\gamma_1^2}, \quad \sigma_0 = \frac{kP}{2\pi}. \quad (14)$$

Parameters R , κ , and μ_1 are

$$R = \frac{2\sqrt{\gamma_1 \gamma_2}}{k^2 + \gamma_2^2}, \quad \kappa = \frac{\sqrt{\gamma_1 \gamma_2}}{k} \frac{k^2 - \gamma_2^2}{2\gamma_1 \gamma_2 - (k^2 + \gamma_2^2)},$$

$$\mu_1 = \sqrt{\frac{\gamma_2}{\gamma_1}} \mu. \quad (15)$$

Note that all notation coincide with those used earlier by Zharii (1994) and Zharii and Ulitko (1994), with the exception of a new quantity μ_1 and A_0 denoted in those papers by A . Now we use the notation A for an uppercase α for other needs (see below).

Satisfying the kinematic contact condition

$$\frac{du_y}{ds} \Big|_{y=0} = 0, \quad \alpha < s < \delta, \quad (16)$$

that follows from (5), on the base of the second of (12) we come to a singular integral equation with respect to an unknown function $f(s)$:

$$\mu_1 f(s) + \frac{\kappa}{2\pi} \int_{\alpha}^{\delta} f(s_1) \cot \frac{s_1 - s}{2} ds_1$$

$$= -\mu_1 \sigma_0 - \kappa A_0 \sin s, \quad \alpha < s < \delta. \quad (17)$$

Transforming both independent and dependent variables,

$$\eta = \tan \frac{s}{2}, \quad \eta_1 = \tan \frac{s_1}{2}, \quad \varphi(\eta) = f(s) \cos^2 \frac{s}{2}, \quad (18)$$

we reorganize (17) to the standard form,

$$\mu_1 \varphi(\eta) + \frac{\kappa}{\pi} \int_A^{\Delta} \frac{\varphi(\eta_1) d\eta_1}{\eta_1 - \eta} = G(\eta),$$

$$\tan \frac{\alpha}{2} = A < \eta < \Delta = \tan \frac{\delta}{2}. \quad (19)$$

The right-hand side is

$$G(\eta) = -\mu_1 \sigma_0 \frac{1}{1 + \eta^2}$$

$$+ \kappa \sigma_0 \frac{\eta}{1 + \eta^2} - 2\kappa A_0 \frac{\eta}{(1 + \eta^2)^2}. \quad (20)$$

In the transition from (17) to (19) we used the first of static conditions (6) that in terms of the new function φ takes the form

$$\int_A^{\Delta} \varphi(\eta) d\eta = -\pi \sigma_0. \quad (21)$$

4 Solution of the Integral Equation

An exact general solution of Eq. (19) can be written using well-known formulae (see, for example, Mikhlin, 1949). In our case we have

$$\varphi(\eta) = \frac{\mu_1}{\mu_1^2 + \kappa^2} G(\eta) - \frac{\kappa}{\mu_1^2 + \kappa^2} \frac{1}{(\eta - A)^{1-m} (\Delta - \eta)^m}$$

$$\times \frac{1}{\pi} \int_A^{\Delta} \frac{(\zeta - A)^{1-m} (\Delta - \zeta)^m}{\zeta - \eta} G(\zeta) d\zeta$$

$$+ \frac{C}{(\eta - A)^{1-m} (\Delta - \eta)^m}, \quad (22)$$

where C is an arbitrary constant. A new parameter m is determined as

$$m = \frac{1}{2\pi i} \ln \frac{\mu_1 + i\kappa}{\mu_1 - i\kappa}, \quad 0 \leq \operatorname{Re} m < 1. \quad (23)$$

In the problem considered, it is a real number and on the base of the latter equality we may introduce the following useful quantities:

$$\cos m\pi = -\frac{\mu_1}{\sqrt{\mu_1^2 + \kappa^2}}, \quad \sin m\pi = -\frac{\kappa}{\sqrt{\mu_1^2 + \kappa^2}}. \quad (24)$$

An arbitrary constant C can be excluded upon substitution of the general solution (22) into the static condition (21). Integrating under the integral, we use formulae for integrals listed in the Appendix and find that the contribution of $G(\eta)$ vanishes. In the result, we obtain

$$C = -\sigma_0 \sin m\pi. \quad (25)$$

After that, using (A6), we calculate three integrals in (22) originated by the three addends in (20) and obtain an expression for $\varphi(\eta)$ in the form

$$\varphi(\eta) = \frac{\Phi(\eta)}{(\eta - A)^{1-m} (\Delta - \eta)^m}. \quad (26)$$

The right-hand side is singular in form at the ends of the contact area, so we do not write down an explicit formula here (later we will find a more convenient expression).

Demanding that contact stresses and, due to that, φ , are bounded at the ends of the contact area at $\eta = A$ and $\eta = \Delta$, we find that the numerator of this solution must vanish at these points,

$$\Phi(A) = \Phi(\Delta) = 0. \quad (27)$$

These conditions result in a system of transcendental equations that after some transformations takes the form

$$p \sin \frac{m(\delta - \alpha) - 2m\pi}{2} - m \sin m\pi$$

$$\times \sin \frac{\delta - \alpha}{2} \sin \frac{(1+m)\alpha + (1-m)\delta}{2} = 0,$$

$$p \sin \frac{(1-m)(\delta - \alpha) + 2m\pi}{2} - (1-m) \sin m\pi$$

$$\times \sin \frac{\delta - \alpha}{2} \sin \frac{m\alpha + (2-m)\delta}{2} = 0, \quad (28)$$

where $p = -\sigma_0/A_0$.

Making use of the specific form of representation of $\varphi(\eta)$ (26) and conditions (27) expressed by Eqs. (28), we perform an identical transformation

$$\varphi(\eta) = \frac{1}{(\eta - A)^{1-m} (\Delta - \eta)^m}$$

$$\times \left[\Phi(\eta) - \frac{\Delta - \eta}{\Delta - A} \Phi(A) - \frac{\eta - A}{\Delta - A} \Phi(\Delta) \right] \quad (29)$$

and instead of (22) obtain another formula for $\varphi(\eta)$,

$$\varphi(\eta) = \frac{\mu_1}{\mu_1^2 + \kappa^2} G(\eta) - \frac{\kappa}{\mu_1^2 + \kappa^2} (\eta - A)^m (\Delta - \eta)^{1-m} \times \frac{1}{\pi} \int_A^\Delta \frac{G(\zeta) d\zeta}{(\zeta - A)^m (\Delta - \zeta)^{1-m} (\zeta - \eta)}. \quad (30)$$

Calculating integrals in (30) as described in the Appendix (see (A9)) and consistently simplifying the expression obtained using Eqs. (28), we obtain the final formula for $\varphi(\eta)$:

$$\varphi(\eta) = 2A_0 \sin m\pi \cos^m \frac{\alpha}{2} \cos^{1-m} \frac{\delta}{2} (\eta - A)^m \times (\Delta - \eta)^{1-m} \cos^3 \frac{s}{2} \cos \frac{m\alpha + (1-m)\delta + s}{2} \quad (31)$$

and, using the last of (18), find the normal stresses distribution,

$$f(s) = 2A_0 \sin m\pi \sin^m \frac{s - \alpha}{2} \times \sin^{1-m} \frac{\delta - s}{2} \cos \frac{m\alpha + (1-m)\delta + s}{2}. \quad (32)$$

5 Kinematic Characteristics

Applying the transformation (18) to expressions (12), we obtain necessary formulae for the tangential velocity inside the contact area ($\alpha < s < \delta$):

$$\dot{u}_x|_{y=0} = -V \left[\cos s + \frac{\mu_1}{R} \sin s + \frac{1 + \mu_1^2}{RA_0} (\sigma_0 + (\eta^2 + 1)\varphi(\eta)) \right], \quad (33)$$

(here Eq. (19) has been used), and expressions for the velocity and the free surface slope outside the contact zone ($-\pi < s < \alpha$ and $\delta < s < \pi$),

$$\dot{u}_x|_{y=0} = -V \left[\cos s + \frac{\sigma_0}{RA_0} (1 + \mu_1 \kappa \eta) - \frac{\mu_1}{RA_0} (\eta^2 + 1) \frac{1}{\pi} \int_A^\Delta \frac{\varphi(\eta_1) d\eta_1}{\eta_1 - \eta} \right],$$

$$\frac{du_y}{ds}|_{y=0} = U \left[\sin s + \frac{\sigma_0}{\kappa A_0} (\mu_1 - \kappa \eta) + \frac{1}{A_0} (\eta^2 + 1) \frac{1}{\pi} \int_A^\Delta \frac{\varphi(\eta_1) d\eta_1}{\eta_1 - \eta} \right]. \quad (34)$$

Calculating integrals in the latter equations (see formulae (A11) in the Appendix), and again using Eqs. (28), we find simple explicit formulae: inside the contact area

$$\dot{u}_x|_{y=0} = -V \left[\cos s + \frac{\mu_1}{R} \sin s + \mathcal{L} + \frac{1 + \mu_1^2}{R\kappa} \bar{f}(s) \right], \quad (35)$$

and outside it

$$\dot{u}_x|_{y=0} = -V \left[\cos s + \frac{\mu_1}{R} \sin s + \mathcal{L} - \frac{\mu_1}{R} \bar{h}(s) \right],$$

$$\frac{du_y}{ds}|_{y=0} = U \bar{h}(s). \quad (36)$$

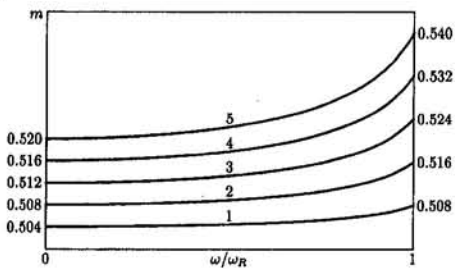


Fig. 3 Frequency dependences of the quantity m for different values of the coefficient of dry friction: (1) $\mu = 0.05$, (2) $\mu = 0.1$, (3) $\mu = 0.15$, (4) $\mu = 0.2$, (5) $\mu = 0.25$

Here $\bar{f}(s)$ means $f(s)/A_0$ and

$$\bar{h}(s) = \begin{cases} -2 \sin^m \frac{\alpha - s}{2} \sin^{1-m} \frac{\delta - s}{2} \\ \times \cos \frac{m\alpha + (1-m)\delta + s}{2}, -\pi < s < \alpha, \\ 2 \sin^m \frac{s - \alpha}{2} \sin^{1-m} \frac{s - \delta}{2} \\ \times \cos \frac{m\alpha + (1-m)\delta + s}{2}, \delta < s < \pi. \end{cases} \quad (37)$$

The constant \mathcal{L} equals

$$\mathcal{L} = \frac{1 + \mu_1^2}{2R\kappa} [m \cos \alpha + (1 - m) \cos \delta - \cos(m\alpha + (1 - m)\delta)]. \quad (38)$$

6 Analysis of Solution

Consider first the quantity m that according to (23) depends on both the friction coefficient and the frequency of excitation. Its value determines the character of stresses (32) and kinematic characteristics (35), (36) near the ends of contact area. Plots of m for different μ are presented in Fig. 3 in the frequency interval from zero to the Rayleigh wave resonant frequency $\omega_R = kc_R$ where c_R is the Rayleigh wave velocity calculated for a given value of Poisson's ratio. All data are calculated for the PZT-4 ceramics having $\nu = 0.33$ and $c_R/c_2 = 0.932$ (Berlincourt et al., 1964).

In the case of frictionless contact we had $m = 0.5$ for all frequencies and plots of stresses and kinematic characteristics were symmetrical with respect to the center of contact area (Zharii and Ulitko, 1994). Now this symmetry disappears: for $\mu > 0$ we have $m > 0.5$. The more is $m - 0.5$ (though this difference is rather small), the brighter is the difference between local distributions of all field quantities near the front point of contact $s = \delta$ (they become sharper) and its back point $s = \alpha$ (they become smoother). It is seen from Fig. 3 that m grows with μ and increases together with ω . It means that working conditions for elastic material become less favorable near the resonant frequency compared to those at low frequencies.

Let us consider transcendental Eqs. (28) determining boundaries of contact area. Asymptotic analysis of them for low values of the loading factor p shows that when $p \ll 1$, approximate formulae are valid:

$$\alpha = -2\sqrt{\frac{1-m}{m} p}, \quad \delta = 2\sqrt{\frac{m}{1-m} p}, \quad (39)$$

therefore $\delta > |\alpha|$. In the smooth contact problem (Zharii and Ulitko, 1994) we had the following relation between the half-length of contact area α_{sm} and parameter p :

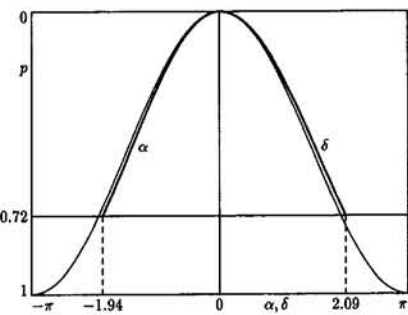


Fig. 4 Boundaries of the contact area in the problems of smooth contact (thin line) and for frictional contact (thick line) at $m = 0.532$ ($\mu = 0.2$, $\omega = kc_R$)

$$\alpha_{sm} = 2 \arcsin \sqrt{p}, \quad \alpha_{sm} = 2\sqrt{p} \quad \text{for } p \ll 1. \quad (40)$$

As $m > 0.5$, we have $\alpha > -\alpha_{sm}$ and $\delta > \alpha_{sm}$.

Analysis of (28) also showed that contact areas merge all together, i.e., $\delta = -\alpha = \pi$ when p takes the value $\sin^2 m\pi < 1$. In the smooth case, as it follows from (40), this occurs at $p = 1$. However, actual values of p for which the solution of the problem is correct, are significantly less than that indicated. Analysis of the tangential velocity distribution (see below) showed that the boundary condition (5) is valid only for $p \leq 0.72$, so quantities α and δ are plotted for these values of p .

In Fig. 4 we plot contact area boundaries in the frictional problem determined by (28) and those in the smooth problem (40). It is seen from the graphs and is confirmed for low p by (39) that the center of contact area is displaced to the right. The maximal relative displacement of it, $\frac{1}{2}(\delta + \alpha)/(\delta - \alpha)$, is equal to 0.032 at the minimal pressure, $p \rightarrow 0$. The length of contact area increases compared to the smooth case: Maximal value of $(\delta - \alpha)/(2\alpha_{sm}) = 1.013$ occurs at the maximal possible value of $p = 0.72$ (see below). These results qualitatively agree with those known for statics (Johnson, 1987).

Using formulae (32), (35), and (36) in Fig. 5 we present normal stress distributions, tangential velocity of the half-plane

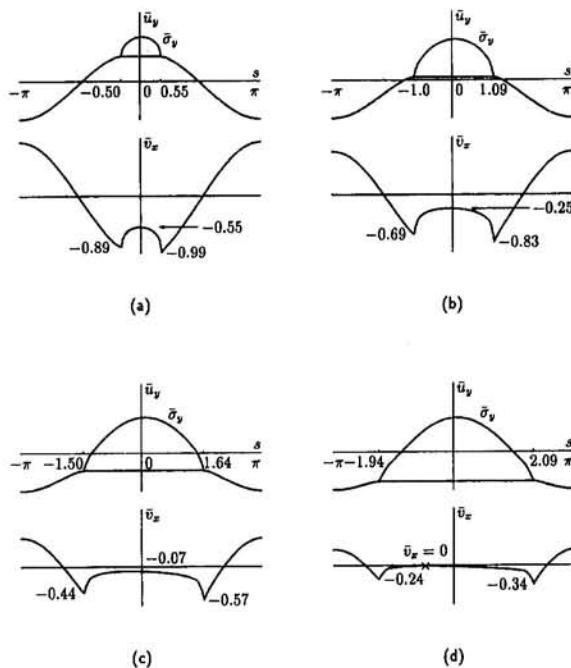


Fig. 5 Vertical displacements of the boundary of the half-plane and normal stress distributions (upper graphs) and tangential velocity of the surface (lower graphs) for values of p : (a) $p = 0.067$, (b) $p = 0.25$, (c) $p = 0.5$, (d) $p = 0.72$; $m = 0.532$ ($\mu = 0.2$, $\omega = kc_R$)

boundary, and the shape of the surface found from the latter of (36), namely

$$u_y = U \left[1 + \int_{-\pi}^s \bar{h}(s_1) ds_1 \right], \quad -\pi \leq s \leq \alpha, \quad (41)$$

$$u_y = U \left[1 - \int_s^\pi \bar{h}(s_1) ds_1 \right], \quad \delta \leq s \leq \pi.$$

Thanks to the proper choice of the integration constant, we eliminated an arbitrary constant that enter the function $U_0(y)$ in (9) and now have $u_y|_{y=0, s=\pm\pi} = U$ irrespective of the value of pressing force P (see Zharii and Ulitko, 1994).

In these graphs we plotted dimensionless quantities $\bar{\sigma}_y = \sigma_y/A_0$, $\bar{u}_y = u_y/U$ and $\bar{v}_x = v_x/V$. As in previous papers we assume, that due to dissipation, U and V achieve large but finite values at the resonant frequency $\omega = kc_R$.

It is seen from Fig. 5 that the amplitude of velocity at the front point of contact $s = \delta$ is bigger than at its back point, $s = \alpha$. As in the smooth case, nonuniformity of the velocity distribution inside the contact area, $|u_x(\delta)|/\min u_x$ increases together with p . At $p = 0.72$ we have $u_x(s) = 0$ at $s = -0.73$ (Fig. 5(d)). When p exceeds this value, we have formally $u_x(s) > 0$ within some interval. Consequently, in this interval $\tau_{\delta y}$ would change its sign. So, for $p > 0.72$, boundary condition (5) and the solution obtained become incorrect.

Conclusions

In this paper, a solution of a new mixed boundary value problem of elastodynamics has been found. The limiting case of it for vanishing friction has been solved by Zharii and Ulitko (1994).

The solution obtained displays several new features. First, asymptotic behavior of stresses and kinematic characteristics is determined by the quantity m that depends on both the friction coefficient and the frequency of excitation. Though deviation of m from its value 0.5 in the smooth problem is small, it causes significant difference between values of the tangential velocity at front and back contact points (see Fig. 5). One more difference is that now the tangential acceleration is infinite in points near the ends of the contact area not only inside it, as in the smooth case, but outside it as well, i.e., at $s \rightarrow \alpha - 0$, $s \rightarrow \delta + 0$ (see (36) and (37)).

This solution gives the necessary information of the structure of an elastic field near the ends of the contact area in the general problem of contact interaction when partial adhesion occurs in the center of the area, and slip near its ends. The problem considered is a limiting case of a general one when due to tangential forces, the adhesion zone shrinks to a point. The very complicated general problem is under investigation now.

References

- Berlincourt, D. A., Curran, D. R., and Jaffe, H. J., 1964, "Piezoelectric and piezomagnetic materials and their function in transducers," *Physical Acoustics*, W. P. Mason, ed., Academic Press, New York, Vol. I, Pt A, pp. 169-270.
- Grinchenko, V. T., Karlash, V. L., Meleshko, V. V., and Ulitko, A. F., 1976, "Investigation of planar vibrations of rectangular piezoceramic plates," *Soviet Applied Mechanics*, Vol. 12, pp. 483-488.
- Grinchenko, V. T., Ulitko, A. F., and Shul'ga, N. A., 1989, "Electroelasticity," *Mechanics of Coupled Fields in Elements of Structures*, Kiev, Naukova Dumka, Vol. 5 (in Russian).
- IEEE, 1984, "An American National Standard: IEEE Standard on piezoelectricity," *IEEE Transactions on Sonics and Ultrasonics*, Vol. SU-31, No. 2, Pt. 2, pp. 1-55.
- Johnson, K., 1987, *Contact mechanics*, Cambridge University Press, Cambridge, MA.
- Hirata, H., and Ueha, S., 1993, "Characteristics estimation of a traveling wave type ultrasonic motor," *IEEE Transactions on Ultrasonics, Ferroelectrics and Frequency Control*, Vol. 40, pp. 402-406.
- Kurosawa, M., and Ueha, S., 1988, "Efficiency of ultrasonic motor using travelling wave," *Journal of the Acoustical Society of Japan*, Vol. 44, pp. 40-46 (in Japanese).

Markushevich, A. I., 1950, *Theory of analytical functions*, Moscow, GITTL (in Russian).

Mikhlin, S. G., 1949, *Integral equations*, Moscow, OGIZ (in Russian).

Suzuki, T., Kamano, T., and Kazuhara, T., 1990, "Modelling of progressive wave type ultrasonic motor," *Japanese Journal of Applied Physics*, Vol. 29, Suppl. 29-1, pp. 194-196.

Uchii, S., 1989, "Present Status of Ultrasonic Motors," *Proceedings of IEEE 1989 Ultrasonic Symposium*, Vol. 2, pp. 749-753.

Zharii, O. Yu., 1993, "Modeling of a Mode Conversion Ultrasonic Motor in the Regime of Slip," *IEEE Transactions on Ultrasonics, Ferroelectrics and Frequency Control*, Vol. 40, pp. 411-417.

Zharii, O. Yu., 1994, "Adhesive Contact Between the Surface Wave and a Rigid Strip," *ASME JOURNAL OF APPLIED MECHANICS*, in press.

Zharii, O. Yu., and Ulitko, A. F., 1992, "Frictional transmission of motion from elastic waves to rigid bodies in contact. Applications to ultrasonic motors," *Euromech-295: Abstracts of lectures*, Nizhny Novgorod, Russia, p. 33.

Zharii, O. Yu., and Ulitko, A. F., 1994, "Smooth Contact Between the Running Rayleigh Wave and a Rigid Strip," *ASME JOURNAL OF APPLIED MECHANICS*, in press.

APPENDIX

Calculation of Cauchy principal value integrals in this work is performed in the same way as in a previous paper (Zharii, 1994). First, we introduce notations

$$q_0(\eta) = 1, \quad q_1(\eta) = \frac{1}{1 + \eta^2}, \quad q_2(\eta) = \frac{\eta}{1 + \eta^2},$$

$$q_3(\eta) = \frac{1}{(1 + \eta^2)^2}, \quad q_4(\eta) = \frac{\eta}{(1 + \eta^2)^2}, \quad (A1)$$

and consider integrals arising in (22),

$$\Psi_r(\eta) = \frac{1}{\pi} \int_A^\Delta \frac{(\zeta - A)^{1-m}(\Delta - \zeta)^m}{\zeta - \eta} q_r(\zeta) d\zeta. \quad (A2)$$

We introduce an auxiliary function of a complex variable z and a complex parameter u ,

$$\mathcal{F}(z) = \frac{(z - A)^{1-m}(z - \Delta)^m}{z - u} q_r(z). \quad (A3)$$

This function is single valued in the complex z -plane cut along the section (A, Δ) connecting its branch points. Calculating the integral of $\mathcal{F}(z)$ along the closed contour L which by pass the segment clockwise we find

$$\frac{1}{2\pi i} \oint_L \mathcal{F}(z) dz = \frac{1}{2\pi i} \int_A^\Delta \mathcal{F}^+(\zeta) d\zeta - \frac{1}{2\pi i} \int_A^\Delta \mathcal{F}^-(\zeta) d\zeta$$

$$= \sin m\pi \Psi(u), \quad (A4)$$

where \mathcal{F}^+ and \mathcal{F}^- are the limiting values of \mathcal{F} on the upper and lower sides of the cut, respectively.

On the other hand, the contour integral in (A4) is equal to the sum of residues of the integrand at points $z = \pm i$, $z = u$ and $z = \infty$ (the latter is nonzero only for $r = 2$).

Applying the Plemelj formula (Markushevich, 1950),

$$\Psi(\eta) = \frac{1}{2} (\Psi^+(\eta) + \Psi^-(\eta)), \quad (A5)$$

(note that the only residue at $z = u$ takes different values at upper and lower sides of the cut) we finally obtain

$$\Psi_r = \frac{1}{\sin m\pi} \left[\sum_{z=\pm i, \infty} \operatorname{res} \mathcal{F}(z) \right]_{u=\eta} + \cot m\pi(\eta - A)^{1-m}(\Delta - \eta)^m q_r(\eta). \quad (A6)$$

These formulae are used for $r = 1, 2, 4$.

In (30) we calculate somewhat different integrals for $r = 1, 2, 4$,

$$\Psi_r(\eta) = \frac{1}{\pi} \int_A^\Delta \frac{(\zeta - A)^{-m}(\Delta - \zeta)^{m-1}}{\zeta - \eta} q_r(\zeta) d\zeta. \quad (A7)$$

Denoting

$$\mathcal{F}(z) = \frac{(z - A)^{-m}(z - \Delta)^{m-1}}{z - u} q_r(z), \quad (A8)$$

in this case we obtain

$$\Psi_r = - \frac{1}{\sin m\pi} \left[\sum_{z=\pm i} \operatorname{res} \mathcal{F}(z) \right]_{u=\eta} + \cot m\pi(\eta - A)^{-m}(\Delta - \eta)^{m-1} q_r(\eta). \quad (A9)$$

In derivation of (25), we used the last formula for $r = 0$ (the sum vanishes) and the following formula:

$$\frac{1}{\pi} \int_A^\Delta \frac{d\zeta}{(\zeta - A)^{1-m}(\Delta - \zeta)^m} = \frac{1}{\sin m\pi}. \quad (A10)$$

Nonsingular integrals arising in (34) can be calculated without use of the Plemelj formula:

$$\frac{1}{\pi} \int_A^\Delta \frac{(\zeta - A)^m(\Delta - \zeta)^{1-m}}{\zeta - \eta} q_r(\zeta) d\zeta = \frac{1}{\sin m\pi} \left[\sum_{z=\pm i} \operatorname{res} \mathcal{F}(z) \right] \pm |\eta - A|^m |\eta - \Delta|^{1-m} q_r(\eta), \quad (A11)$$

where

$$\mathcal{F}(z) = \frac{(z - A)^m(z - \Delta)^{1-m}}{z - \eta} q_r(z). \quad (A12)$$

Either upper or lower sign are taken for $\eta > \Delta$ and $\eta < A$, respectively.

G. K. Hu

Laboratoire MMS-MAT,
URA 850 CNRS Ecole Centrale Paris,
92295 Chatenay Malabry, France

F. Schmit

Centre de Recherche et d'Etudes
d'Arcueil ETCA,
16 bis Avenue Prier de la Cote d'Or,
94114 Arcueil, France

D. Baptiste

D. François

Laboratoire MMS-MAT,
URA 850 CNRS Ecole Central Paris,
92295 Chatenay Malabry, France

Viscoplastic Analysis of Adhesive Joints

The uniaxial constitutive law for an adhesive is studied by constant strain rate tensile, creep and relaxation tests. The S-D effect of the adhesive is taken into account by using the Raghava yielding criterion in a three dimensional constitutive formulation. The obtained constitutive law is then used to analyze a single lap joint and a butt joint by a finite element method. Constant cross head speed tensile and creep loading cases are examined. For a butt joint, the results show that the viscous effect and the influence of the hydrostatic stress must be taken into account due to the variation of the hydrostatic stress and of the loading rate in the adhesive layer as function of its thickness. A comparison with experimental results is also given. A good agreement between viscoplastic calculations and experimental results is obtained for single-lap joints. A reasonable result is obtained for butt joints and the discrepancy is attributed to interfacial debonding.

Introduction

Structural adhesives exhibit some sort of viscoelastic and viscoplastic behavior, especially ductile adhesives at high stress levels and at elevated temperatures. The redistribution of stress and strain in an adhesive joint during viscoelastic-viscoplastic deformation influences considerably the strength of the joints. In addition, adhesives usually exhibit different behavior in tension and in compression (S-D effect), which is associated with the important role of the hydrostatic stress in polymer yielding. In order to calculate more accurately the mechanical behavior of adhesive joints for engineering design, a more complete constitutive formulation for the mechanical behavior of adhesives is needed which accounts for these specific properties of polymeric materials.

The time-dependent behavior of adhesive joints has been studied by a number of investigators. Hayashi (1972) studied analytically the creep properties for a double lap joint. Delale and Erdogan (1981) used the Laplace transformation technique to study a single-lap joint with a viscoelastic adhesive. More recently, Groth (1990) studied viscoplastic stress in a single-lap joint using different rheological models. The S-D effect for adhesives was taken into account by Gali, Dolev, and Ishai (1981) and Raghava, Cadell, and Yeh (1975) for polymeric materials by introducing the influence of hydrostatic stress in the yield criteria. But it seems that little work has been conducted taking into account adhesive viscous and S-D effects for stress analysis in adhesive joints.

This paper presents a stress and strain analysis of adhesive joints using a viscoplastic adhesive model. The experimental study is performed on a commercial adhesive system Hysol EA9309.2. The uniaxial constitutive equation of the adhesive is investigated by constant strain rate, creep, and relaxation tests. The obtained uniaxial law is then generalized to three dimensions by using the Raghava yielding criterion (Raghava, Cadell, and Yeh, 1975), which takes into account the different

behaviors of the adhesive in tension and compression. The obtained constitutive model for the adhesive is used for finite element analysis. The calculated results are then compared with experimental values.

Mechanical Behavior of Bulk Adhesive

The Hysol EA 9309.2 adhesive used in our analysis is a two constituent epoxy system which can be cured at room temperature. To obtain short-term stable mechanical properties, the adhesive was cured for one week at room temperature and post-cured for three days at 50°C.

The uniaxial tensile behavior of the bulk adhesive is determined by using standard ISO 1/2 specimens fabricated from a 1mm plate of hardened adhesive in accordance with NFT91-034 standards.

The mechanical tests, consisting of constant strain-rate tensile, short-term creep, and relaxation tests, are performed at room temperature with a computer controlled testing machine. The strain is measured by a slip gage extensometer. The experimental results are presented in Figs. 1(a) and 1(b), 2 and 3.

These experimental results, as well as loading and unloading tests (Hu, 1991), show that the viscoplastic deformation of the adhesive is very important and that the adhesive displays little strain hardening (Fig. 2). The creep tests (Fig. 1(b)) show that the creep strain is negligible at low stress levels; but at high stress levels, the three stages of creep (primary, secondary, and tertiary) occur. The secondary creep stage dominates most of the adhesive creep life. Therefore, in the following model, only the secondary creep is taken into account. A creep threshold of $\theta = 20$ MPa, based on the creep tests, is proposed, below which the creep strain is neglected.

Based on these considerations, a Norton-type (Lemaitre and Chaboche, 1988) viscoplastic law is used in a uniaxial formulation:

$$\dot{\epsilon} = \left(\frac{\sigma - \theta}{\mu} \right)^k \quad (1)$$

where $\dot{\epsilon}$ is the creep rate at an applied stress σ . μ , k are material constants, which are derived from the creep and the constant strain rate tension tests, giving

$$\mu = 54 \text{ MPa}, \quad k = 8.99.$$

As shown in Figs. 1-3, the uniaxial model can describe well

Contributed by the Applied Mechanics Division of THE AMERICAN SOCIETY OF MECHANICAL ENGINEERS for publication in the ASME JOURNAL OF APPLIED MECHANICS.

Discussion on this paper should be addressed to the Technical Editor, Professor Lewis T. Wheeler, Department of Mechanical Engineering, University of Houston, Houston, TX 77204-4792, and will be accepted until four months after final publication of the paper itself in the ASME JOURNAL OF APPLIED MECHANICS.

Manuscript received by the ASME Applied Mechanics Division, July 26, 1991; final revision, Feb. 16, 1992. Associate Technical Editor: J. W. Rudnicki.

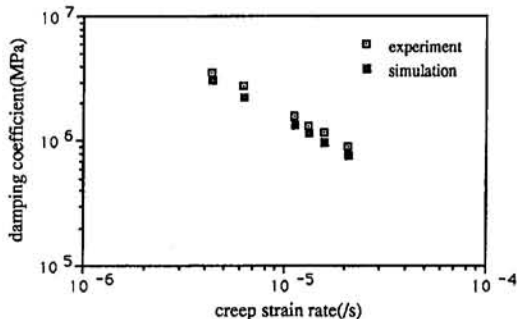


Fig. 1(a) Simulational and experimental creep tests for the bulk adhesive

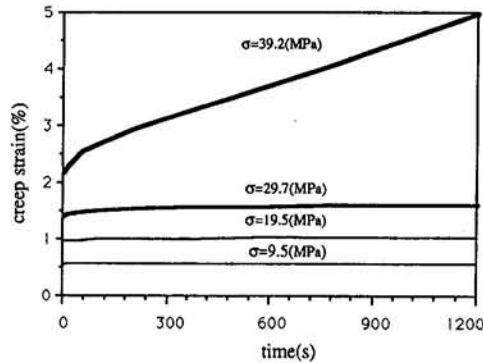


Fig. 1(b) Creep tests for the bulk adhesive

the experimental results for the bulk adhesive (the damping coefficient is defined as $\beta = (\sigma - \theta)/\dot{\epsilon}$). For the relaxation case, it is seen that at lower applied strain levels, there is a difference between the experimental and the calculated curves. This difference comes from the fact that at lower applied strain levels, the primary creep is very important, which is not taken into account in our model.

In the sections which follow, this uniaxial equation is used as the basis for a three-dimensional constitutive formulation.

Three-Dimensional Formulation

In order to analyze the stress distribution in adhesive joints, a three-dimensional constitutive formulation for adhesives is necessary. In our study, the method outlined by Betten (1989) is used and an equivalent stress from the Raghava criterion (Raghava, Cadell, and Yeh, 1975) is proposed to account for the different behaviors of adhesives in tension and compression.

For creep mechanics, the constitutive equation can be written in a general form,

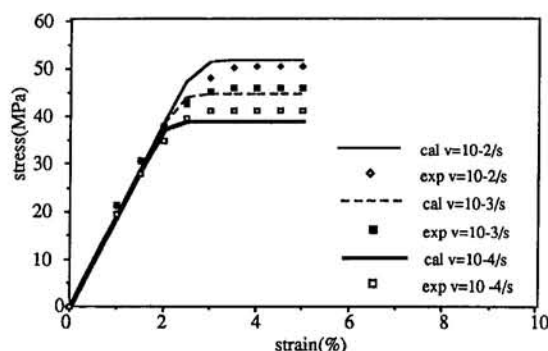


Fig. 2 Simulational and experimental constant strain rate tensile tests

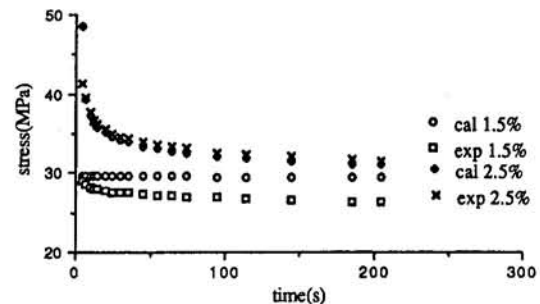


Fig. 3 Simulational and experimental relaxation tests

$$\dot{\epsilon} = \mathbf{f}(\sigma, \omega, \mathbf{A}) \quad (2)$$

where σ is the applied stress tensor, ω the damage tensor, \mathbf{A} the tensor of anisotropy, and $\dot{\epsilon}$ the creep strain rate tensor.

In our case, the anisotropy and the damage of the adhesive are neglected; furthermore the nonlinear stress tensor terms are also neglected for simplification. Under these conditions, Eq. (2) yields:

$$\dot{\epsilon} = \varphi_0 \mathbf{I} + \varphi_1 \mathbf{s} \quad (3)$$

where φ_0 and φ_1 are two scalar coefficients depending only on the experimental data and the stress invariant, \mathbf{s} is the deviatoric part of stress tensor σ ; and \mathbf{I} is the unit tensor. φ_0 and φ_1 are identified from Eqs. (3) and (1), giving:

$$\varphi_0 = \frac{1 - 2\nu}{3\mu^k} (\sigma - \theta)^k \quad (4)$$

$$\varphi_1 = \frac{(1 + \nu)}{\mu^k} \frac{(\sigma - \theta)^k}{\sigma} \quad (5)$$

where ν is the Poisson's ratio and σ is an equivalent stress. In our case, to take into account the S-D effect of the adhesive, an equivalent stress other than that of Von Mises should be defined. For polymeric materials, the Raghava yielding criterion is widely used:

$$J_{2d}^2 + (\sigma_c - \sigma_t)I = \sigma_c \sigma_t \quad (6)$$

with

$$J_{2d} = (1.5s_{ij}s_{ij})^{0.5} \quad (7)$$

$$I = \sigma_{ii} \quad (8)$$

where σ_c and σ_t are the elastic limits in compression and in tension, respectively. From this yielding criterion, the equivalent stress is obtained:

$$\sigma_{eq} = \frac{I(\lambda - 1) + (I^2(\lambda - 1)^2 + 4J_{2d}^2\lambda)^{0.5}}{2\lambda} \quad (9)$$

where λ is defined as σ_c/σ_t .

The general constitutive equation can then be derived from Eqs. (3), (4), (5) and (9):

$$\dot{\epsilon} = \frac{(1 - 2\nu)}{3\mu^k} (\sigma_{eq} - \theta)^k \mathbf{I} + \frac{(1 + \nu)}{\mu^k} (\sigma_{eq} - \theta)^k \frac{\mathbf{s}}{\sigma_{eq}} \quad (10)$$

From Eq. (10), it is found that the Norton constitutive equation is a special case in which incompressibility and the Von Mises equivalent stress are assumed.

This constitutive equation is implemented into the finite element code ZEBULON (Burlet and Cailletaud, 1991). This finite element code is capable of performing linear and nonlinear, static, and dynamic analyses. The Poisson's ratio is a function of deformation, and here, for simplification, we chose $\nu_c = 0.5$ when the adhesive is plastic. λ is taken to be 1.2, as is commonly

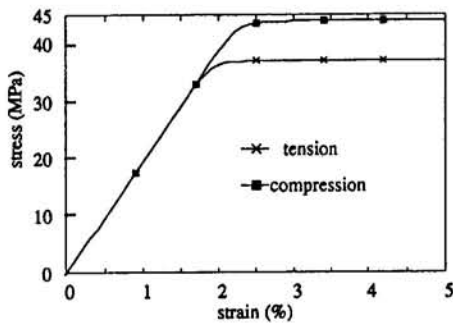


Fig. 4 Calculated tension and compression stress-strain curves at a strain rate 10^{-4} s $^{-1}$ for the bulk adhesive

used for polymeric materials (Adams and Wake, 1984). The uniaxial curves in tension and compression for the adhesive are calculated at a strain rate of 10^{-4} s $^{-1}$ (see Fig. 4) in order to check the finite element code. The result shows that the present constitutive model can reflect the different behaviors of the adhesive in tension and in compression. This constitutive relation is then used to analyze the stress distribution in adhesive joints.

Viscoplastic Stress Analysis of Adhesive Joints

In the following section, a single-lap joint in creep and a butt joint in constant cross head speed tension tests are examined with emphasis on viscous and S-D effect on adhesive joints. The adherent is an aluminium alloy with mechanical constants $E_s = 73000$ MPa, $\nu_s = 0.29$, and the elastic constants for the adhesive are $E_c = 1950$ MPa, $\nu_c = 0.36$.

Single Lap Joint in Creep. The finite element mesh of a single-lap joint is shown in Fig. 5 (the adhesive thickness is 0.5mm). The elements are two-dimensional, eight-node, quadratic elements which can be used for plane-stress, plane-strain, and axisymmetric problems. Geometrical nonlinearity was not included, thus limiting the analysis to material nonlinearity with small displacements. The boundary conditions are shown in Fig. 5. A pressure corresponding to an average shear stress of approximately 20 MPa is applied for a short time, and then it is kept constant on the line AA' (Fig. 5). The calculation is performed under a plane-strain condition.

The distribution of the shear stress and normal stress in the joint at the mid line (x_1) (Fig. 5) is shown in Figs. 6(a) and

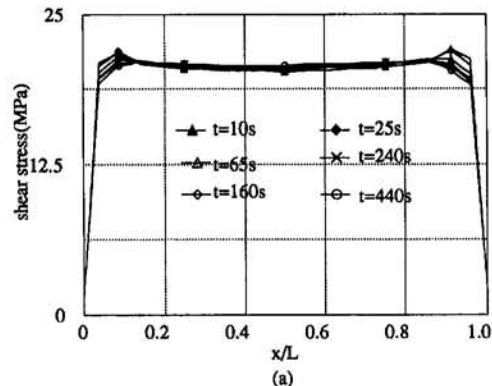


Fig. 6(a) Creep shear stress distribution along the mid-line of single-lap joint

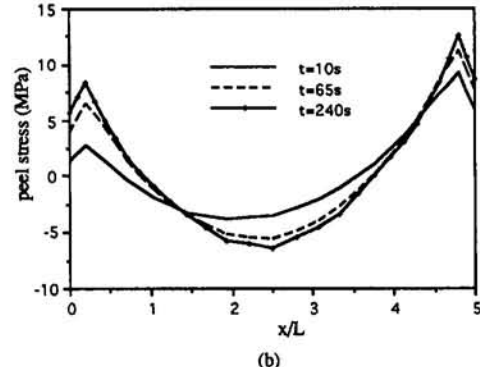


Fig. 6(b) Creep normal stress along the mid-line of single-lap joint

6(b). The shear stress concentration at the joint ends is relaxed by creep. The shear stress tends to be homogeneously redistributed along the joint due to the viscosity of the adhesive. By contrast, the normal stress has a tendency to increase at the joint ends. The asymmetry of the peel stress is due to a small rotation of the applied force line arising from the asymmetry of the joint.

The displacement at the middle of line AA' as a function of time is plotted in Fig. 7. At this loading level, the displacement of the joints continues to increase and creep fracture is unavoidable. This loading level is therefore unacceptable for engineering design. The relaxed shear stress is compensated in the middle of the joint, enhancing the stress level there (Fig. 6(b)). Thus the shear stress (minimum stress) at the midpoint of the joint should always be kept at a value less than the creep limit to avoid creep failure. This is contrary to the ultimate joint strength that is governed by the maximum stress or strain as

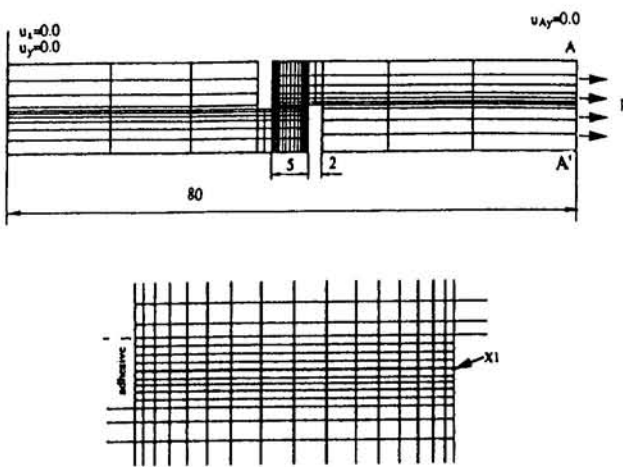


Fig. 5 Finite element analysis of a single-lap joint

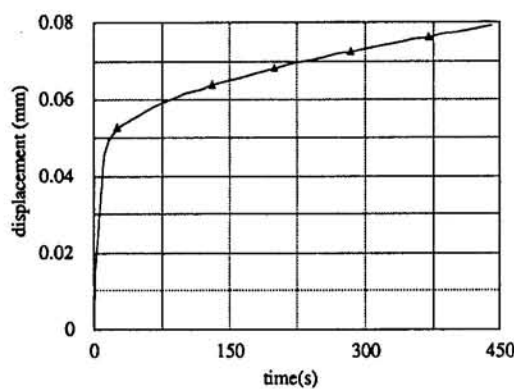


Fig. 7 Displacement evolution as a function of creep time

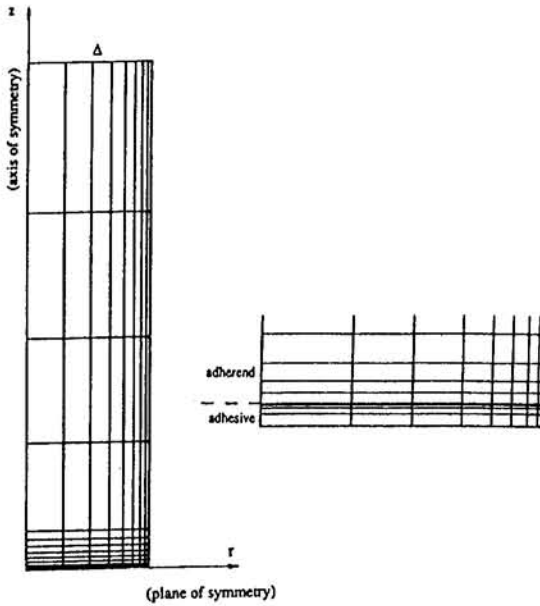


Fig. 8 Finite element analysis of a butt joint

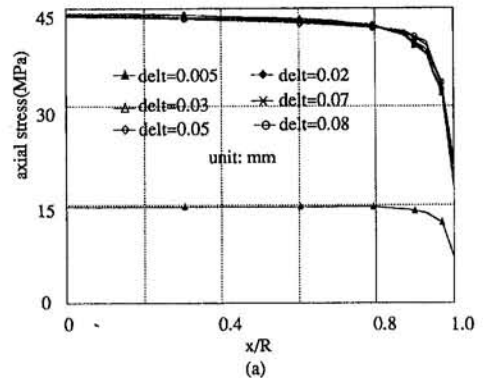
proposed by Hart-Smith (1981). This viscoplastic model can provide a useful tool for creep design of adhesive joints and for studying the viscous influence of adhesive joints.

Butt Joint in Tension. In order to investigate the S-D effect in adhesive joints, a butt joint is examined by a finite element method using the obtained constitutive adhesive model. This kind of joint has been examined by many authors. Adams et al. (1978) studied the elastic case for this type of joint by finite element method; Anderson and DeVries (1989) used fracture mechanics to evaluate the joint strength. This kind of joint is particularly interesting for our analysis. If the cross head speed is kept constant, the loading rate and hydrostatic stress of the adhesive layer changes with varying thickness. These two factors determine the mechanical behavior of the adhesive layer.

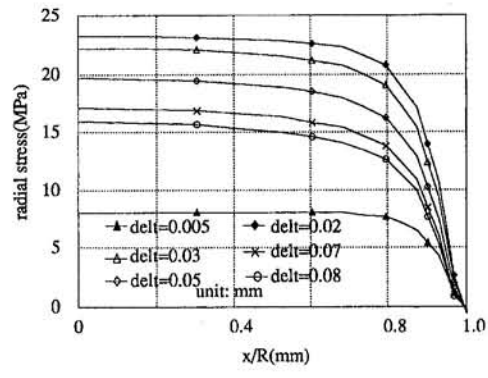
In our analysis, the butt joint consists of two aluminum alloy cylinders bonded with the same adhesive as before. Mechanical behavior is investigated both by a finite element analysis and experimentally. The finite element mesh is shown in Fig. 8. Due to the symmetry, only a quarter of the joint is analyzed. The thickness of the adhesive layer is chosen as 0.5 mm with a cylinder diameter of 10 mm. A displacement of 0.08 mm is applied for 13 seconds, corresponding to a cross head speed of 5×10^{-3} mm/s.

The axial and radial stress distributions are shown at the midplane of the adhesive in Figs. 9(a) and (b). There is little variation in the axial stress σ_{zz} during loading when the adhesive begins to deform plastically. This stress remains almost constant in the joint except near the ends, which are perturbed by the edge singularity. In the central region, the axial stress is slightly higher than the average applied stress needed to satisfy the equilibrium condition. But σ_{rr} decreases with increasing loading. An important hydrostatic stress is induced in the joint due to the difference in Poisson's ratios between the adherents and the adhesive. This stress varies in the same manner as σ_{rr} and it reaches about 28 MPa. The zone influenced by the edge singularity decreases with decreasing adhesive thickness.

The average stress-strain relation of the adhesive layer is also studied as a function of its thickness (see Fig. 10). All of the calculations are performed at the same cross-head speed of 5×10^{-3} mm/s. The results show that the tensile stiffness of a butt joint decreases with increasing adhesive thickness due to the diminution of the hydrostatic stress in the adhesive layer (Fig. 11). The variation of the maximum stress in the adhesive



(a)



(b)

Fig. 9(a) Axial stress distribution along the mid-line of butt joint; (b) radial stress distribution along the mid-line of butt joint

layer is shown in Fig. 11. For a joint with adhesive thickness of 0.1, 0.3, and 0.5 mm, there is very little variation of the maximum stress (this is confirmed experimentally). For the joint with a 3 mm thickness, there is an increase of the maximum stress and this stress decreases when the adhesive thickness is further increased. Finally, the behavior of the bulk adhesive dominates for very large adhesive thicknesses (approximately the diameter of adherent).

This variation comes from competition between the tensile loading rate of the adhesive layer and the hydrostatic stress state as a function of the adhesive thickness during a constant cross-head speed test. In fact, for thinner adhesive thicknesses, the loading rate of the adhesive layer increases and the viscosity has little time to manifest itself. But because the hydrostatic stress is higher, a high equivalent stress (as defined previously) is induced, and it increases the relaxation rate. For the adhesive

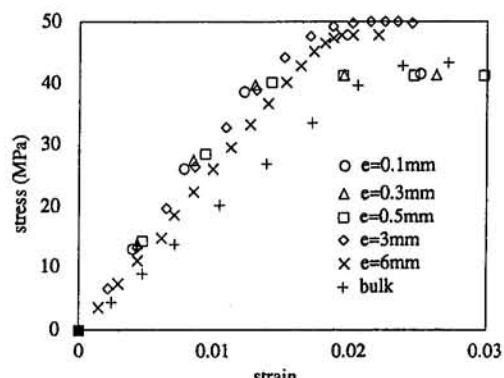


Fig. 10 Average stress and strain relations of adhesive layer as a function of adhesive thickness in a butt joint

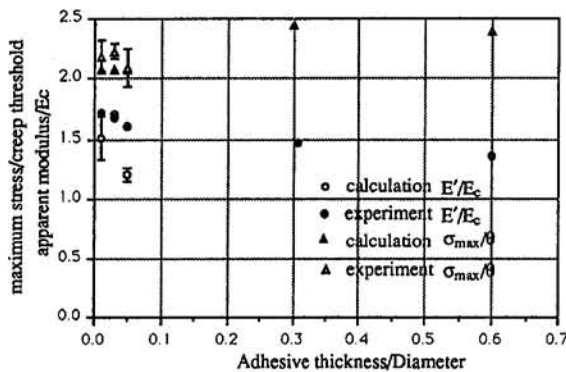


Fig. 11 Butt joint stiffness and maximum average axial stress variations as a function of adhesive thickness

layer of 3mm, the influence of the hydrostatic stress is trivial, and the adhesive behavior is determined mainly by the increasing loading rate.

The variation of the loading rate in the adhesive layers can be estimated. If E_s and l_s represent the Young's modulus and the length of the adherent, respectively, and E_c and l_c those of the adhesive, the total elongation of the adhesive joint (Δl) can be calculated:

$$\begin{aligned}\Delta l &= \Delta l_s + \Delta l_c \\ &= \epsilon_s l_s + \epsilon_c l_c\end{aligned}\quad (11)$$

so that the average deformation rate of the joint is given by:

$$\dot{\delta} = \frac{\Delta l}{l} = \frac{\epsilon_s l_s}{l} + \frac{\epsilon_c l_c}{l}\quad (12)$$

where ϵ_s and ϵ_c are the average strains in the adherents and the adhesive respectively; $\dot{\epsilon}_s$ and $\dot{\epsilon}_c$ denote the average strain rates in the adherents and the adhesive, respectively; $\dot{\delta}$ is the transverse loading rate and l denotes the total joint length.

In the elastic case, the following relation between the strain rate in the adherent and in the adhesive is available:

$$\frac{\dot{\epsilon}_c}{\dot{\epsilon}_s} = \frac{E_s}{E_c}.\quad (13)$$

With Eqs. (12) and (13) the strain rate can then be determined.

In the plastic case, the strain rate in the adherent is taken to be zero since the stress variation in the adherent is almost negligible, and the strain rate in the adhesive layer is calculated by Eq. (12).

For a butt joint having a total joint length of 40mm and an adhesive thickness of 0.5mm, the variation of the loading rate in the adhesive can be three times greater than that initially. When the adhesive is completely plastic, the loading rate is 80 times that of the average loading rate in the joint.

Experimental Comparison

The experimental comparison is performed on both single lap and butt joints at constant cross-head speed loading. The individual specimens are cut and machined from aluminium alloy plates bonded with the adhesive. The cure condition used for the bulk adhesive previously described is adopted. Before bonding, the 2024 T6 aluminium adherents were surface treated with a chromic acid etch to prepare the surfaces.

The tensile tests, using a cross head speed of 1mm/min, are carried out for single lap joints. The average shear strain is measured by an ALTHOF extensometer (Hu, 1991), and the average shear stress is calculated by dividing the applied load by the bonded surface area. The adhesive thickness here is

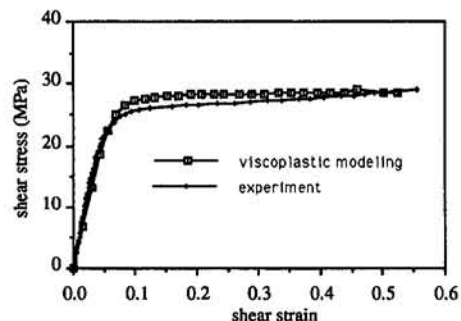


Fig. 12 Comparison between the model and experimental results of a single-lap joint

0.5mm. The comparative result is shown in Fig. 12. A good agreement between the experimental results and the model is obtained.

For butt joints, the mechanical tests are performed at a cross head speed of 5×10^{-3} mm/s. The displacement of the adhesive layer is measured by a slip gage extensometer. The average strain is calculated as being the ratio of the displacement of the adhesive layer to its thickness; the displacement of the adhesive layer is calculated by removing that owing to the adherents from the value measured by the extensometer. The experimental results are compared with the viscoplastic finite element analysis (Fig. 13). A reasonable agreement is also obtained between the model and the experiments. The small discrepancy undoubtedly comes from interfacial debonding that is unaccounted for in the model, but observed in adhesive joints tested in tension within a scanning electron microscope (Hu, 1991). For single-lap joints, only very little localized debonding occurred.

Conclusion

The general constitutive relation of an adhesive was studied experimentally and theoretically to take into account the viscosity and the influence of the hydrostatic stress. The calculated results for adhesive joints using the obtained constitutive equation show that for a single-lap joint under a creep load, the shear stress concentration is relaxed by creep. The relaxed shear stress is compensated by an enhanced shear stress in the central region of the joint. This stress level should always be kept under than the creep limit to prevent creep failure of the joints. For a butt joint subjected to a constant cross-head speed loading, the hydrostatic stress and the loading rate in the adhesive layer varies as a function of the adhesive thickness. The competition between these two factors with varying adhesive thickness is taken into account in the present analyzes. The results show that for thinner joints, the stiffness is more important and the maximum stress varies little (0.1mm to 0.5mm). By increasing the joint thickness, the influence of the hydrostatic stress de-

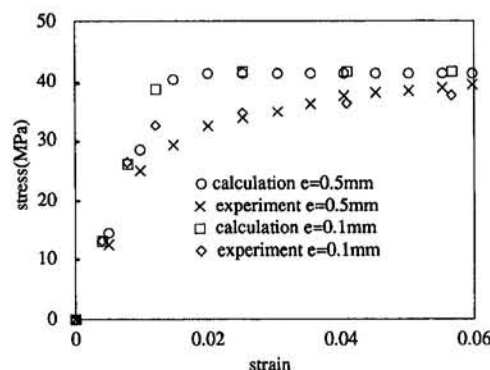


Fig. 13 Comparison between the model and experiment of a butt joint

creases and the influence of the loading rate dominates the behavior. This leads to an increase in the maximum stress in the joint. Finally for very large joint thicknesses (approximately equal to the cylinder diameter), the adhesive bulk material properties are exhibited. The experimental result shows a good agreement with our analyzes for single-lap joints, and a reasonable result is obtained for butt joints. The difference between the model and the experiments for butt joints is probably due to interfacial debonding which is not taken into account in present model.

References

Adams, R. D., Coppendale, J., and Peppiatt, N. A., 1978, "Stress Analysis of Axisymmetric Butt Joints Loaded in Torsion and Tension," *J. of Strain Analysis*, Vol. 13, No. 1, pp. 1-10.

Adams, R. D., and Wake, W. C., 1984, *Structural Adhesive Joints in Engineering*, Elsevier, New York.

Anderson, G. P., and DeVries, K. L., 1989, "Predicting Strength of Adhesive Joints From Test Results," *Int. J. of Fracture*, Vol. 39, pp. 191-200.

Betten, J., 1989, "Generalization of Nonlinear Materials Laws Found in Experiments to Multi-axial States of Stress," *Eur. J. Mech., A/solids* 8, No. 5, pp. 325-339.

Burlet, H., and Cailletaud, G., 1991, "ZEBULON, A Finite Element Code for Nonlinear Materials Behavior," *Eur. Conference on New Advances in Computational Structural Mechanics*, Apr. 2-5, Giens, France.

Delale, F., and Erdogan, F., 1981, "Viscoelastic Analysis of Adhesively Bonded Joints," *ASME JOURNAL OF APPLIED MECHANICS*, Vol. 48, pp. 331-338.

Gali, S., Dolev, G., and Ishai, O., 1981, "An Effective Stress/Strain Concept in the Mechanical Characterization of Structural Adhesive Bonding," *Int. J. Adhesion and Adhesive*, Jan., pp. 135-140.

Groth, H. L., 1990, "Viscoelastic and Viscoplastic Stress Analysis of Adhesive Joint," *Int. J. Adhesion and Adhesive*, Vol. 10, pp. 207-213.

Lemaître, J., and Chaboche, J. L., 1988, "Mécanique des Matériaux Solides," Dunod.

Hart-Smith, L. J., 1981, "Stress Analysis: A Continuum Mechanics Approach," *Developments in Adhesives-2*, Kinloch, ed., Applied Science Publishers, LTD, pp. 1-45.

Hayashi, T., 1972, "Creep Analysis of Bonded Joints," *Composite, Mater. and Structure*, Vol. 1, No. 2, pp. 58-63.

Hu, G. K., 1991, "Approche Théorique et Expérimentale du Comportement Mécanique, de l'Endommagement et de la Rupture des Assemblages Collées," Ph.D, Ecole Centrale Paris.

Raghava, R. S., Cadell, R. M., and Yeh, G. S. V., 1975, "The Macroscopic Yield Behavior of Polymers," *ASME JOURNAL OF APPLIED MECHANICS*, Vol. 8, pp. 225-232.

Analysis of High-Speed Rolling With Inertia and Rate Effects

D. Iddan

Research Scientist.

J. Tirosh

Professor,
Henri Garin Chair,
Mem. ASME

Faculty of Mechanical Engineering,
Technion-Israel Institute of Technology,
Technion City, Haifa 32000
Israel

Limit-analysis procedures for time-dependent materials are utilized for assessing some essential technological parameters in high-speed strip rolling (i.e., the torque, the separation force, the minimal friction required to avoid skidding, maximum allowable speed, etc.). The formulations are quite wide in scope (e.g. they include the inertia of the plastic flow beside the material rate effect) but lack, in general, the rigor of the true bound by reasons to be discussed. The solutions are, by default, considered as "approximate bounds" unless stated differently. Due emphasis is given to the development of a lower bound, infrequently employed in metalworking analysis. It yields relevant information about the process which appears entirely consistent with an independent upper bound solution. In particular, the rate effects are shown (in both solutions) to be characterized by the intensity of two dimensionless groups, known universally as Bingham No. and Euler No. Normally they cannot be ignored at high speeds currently attainable in modern industry, above, say, $u_0 = 50$ [m/s]. For slow speeds, the above solutions constitute rigorous upper and lower bounds. The relative close proximity of the two bounds to experimental data (with copper, aluminum, and steel) and their excellent agreement with the rigid-plastic finite element solution, demonstrate the utility of having these dual bounds simultaneously.

A seemingly useful by-product from the analysis is the ability to predict the onset of skidding at very high speeds. For this sake, an expression is offered for determining the maximum allowable rolling speeds (at the incipient of skidding) in conjunction with the requirement for a certain minimum interfacial friction.

1 Introduction

The effect of high speeds on metalworking plasticity has been surveyed and accentuated by Davies and Austin (1970). In general, such investigations can be approached from two aspects. One aspect is the effect of speed on the material rate-dependent yielding, resulted from the induced high strain rate. This consideration was pioneered by Cristescu and his colleagues (see, for example, Cristescu (1975, 1979) and Durban (1984)), employing a linear viscoplastic constitutive behavior. The second view is to incorporate into the analysis the inertia of the plastic flow in order to get a better estimation of the flow resistance, as suggested by Tirosh and Kobayashi (1976) for rate-independent materials. The present work presents an attempt to apply these two aspects simultaneously on high-speed strip rolling and to "weight" their relative importance on the design of high-speed rolling process. A numerical FEM formulation of such a problem was given by Fontane and Gelin (1991). Other numerical oriented formulations were offered by Chandra (1989) for rate sensitive materials and by Lau et al. (1989) for inertia flows.

A peculiar phenomenon of decreasing loads while increasing rolling speeds was observed experimentally three decades ago by Ford (1947) and attracted attention since then. A partial explanation to this puzzling effect was suggested by Tirosh et al. (1985), based on the supposition that a plastic softening occurs in a narrow self-heated layer beneath the rollers. The analysis in the above paper was restricted to a rolling condition with zero neutral angle, while generally, as resulted from the

present study, the location of the neutral point appears to be a speed-dependent variable. The present solutions will show that by increasing the rolling speed, the neutral point is shifted towards the exit. This makes the process more efficient in the sense that less frictional shear resist the plastic flow beneath the rollers. Consequently, the average pressure on the rollers is gradually decreased, until a limit speed is reached above which skidding is envisaged. The approximate upper bound solution employed here utilizes the new kinematically admissible velocity field of Iddan et al. (1986), which differs from Avitzur's (1968). In parallel, an approximate lower bound solution is suggested, an avenue not considered hitherto. The commonly used "slab method" solutions, i.e., Hoffman and Sachs (1953) and Bland and Ford (1948) can be considered as lower bound solutions. However, they are quite restrictive in the sense that cross sectional planes of the deforming domain are bound to remain planes, and hence unable to account, for example, for the shear stress distribution inside the body. The present solution relaxes this restriction and thus provides, in principle, wider view on phenomena associated with high-speed rolling. The two bounds (which are rigorous under quasi-static condition) appear relatively close one to the other, so that they may replace more elaborate and costly alternatives. Comparisons with experiments of Shida and Awazuhara (1973) and Al-Salehi, Fairbank, and Lancaster (1973) are given with some scatter. On the other hand, the bounding analysis is compared to the finite element solution of Li and Kobayashi (1975). The fine match justifies the use of the derived formulations for predicting the maximum allowable speeds in strip rolling.

2 Constitutive Equation

For limit analysis applications, the relationship between the stress deviator, $s_{ij} = s_{ij}^{(p)} + s_{ij}^{(v)}$ (which is composed of plastic part, $s_{ij}^{(p)}$, and viscous part $s_{ij}^{(v)}$) and the associated strain rate, $\dot{\epsilon}_{ij}$, should be based on an existence of a stress potential. It has been shown to be so by Rice (1970) in certain materials which are characterized by the "over-stress" equation (where the plas-

Contributed by the Applied Mechanics Division of THE AMERICAN SOCIETY OF MECHANICAL ENGINEERS for publication in the ASME JOURNAL OF APPLIED MECHANICS.

Discussion on this paper should be addressed to the Technical Editor, Professor Lewis T. Wheeler, Department of Mechanical Engineering, University of Houston, Houston, TX 77204-4792, and will be accepted until four months after final publication of the paper itself in the ASME JOURNAL OF APPLIED MECHANICS.

Manuscript received by the ASME Applied Mechanics Division, Jan. 14, 1993; final revision, Aug. 11, 1994. Associate Technical Editor: D. M. Parks.

tic flow is activated only when a certain threshold stress is reached) like Perzina's (1963) representation

$$\dot{\epsilon}_{ij} = \gamma F \left(\frac{\sqrt{J_2}}{k} - 1 \right) \frac{s_{ij}}{\sqrt{J_2}}$$

where

$$\begin{aligned} F &> 0 \quad \text{for } \sqrt{J_2} > k \\ F &= 0 \quad \text{for } \sqrt{J_2} \leq k \end{aligned} \quad (1)$$

and $J_2 = \frac{1}{2} s_{ij} s_{ij}$ ($s_{ij} \equiv \sigma_{ij} - \frac{1}{3} \delta_{ij} \sigma_{kk}$), k and γ are material constants.

Nonlinear functions for $F(\dots)$ in (1) may readily be used but presently the linear form (designated as Bingham Material) is mostly used for cold metal working ((Cristescu (1975, 1979) and Tirosh and Sayir (1987)) and will be employed here too, namely

$$\dot{\epsilon}_{ij} = \frac{1}{2\eta} \left[1 - \frac{k}{\sqrt{J_2}} \right] s_{ij} \quad \text{for } \sqrt{J_2} \geq k, \quad (2a)$$

or inversely

$$s_{ij} = \left(2\eta + \frac{k}{\sqrt{I_2}} \right) \dot{\epsilon}_{ij}, \quad (2b)$$

where $I_2 = \frac{1}{2} \dot{\epsilon}_{ij} \dot{\epsilon}_{ij}$, and η represents the "viscosity" of the solid (which is $\eta \equiv (k/\gamma)$). By manipulating with (2b), one can get the Von-Mises' rate-dependent yielding curve as

$$\sqrt{J_2} = k \left(1 + \frac{2\eta\sqrt{I_2}}{k} \right). \quad (2c)$$

In many materials η is a (decreasing) function of (increasing) effective strain-rate $\dot{\epsilon}$, but it is taken as a constant in the presently considered range. At lines of velocity discontinuities (where, due to the extreme high strain rates $\sqrt{I_2} \rightarrow \infty$ and $\eta \rightarrow 0$), we may consider their product in (2c) to reach a finite value. This delicate point, akin to the upper bound formulation, deserves a special study. In the present rolling process we restrict ourselves to the large diameter of the roller (compared to the thickness of the strip) so that the flow is "nearly smooth" and thus avoids the discontinuities. This is one of the reasons why we designate the foregoing analysis as an *approximate bounding analysis* (the second reason, associated with the acceleration, will be given later). Obviously, when the process approaches a quasi-static low speed, the analysis renders *rigorous bounds*. This distinction will be kept throughout.

3 Dynamic Effects

Consider the rolling process shown in Fig. 1. The suggested upper bound solution is based upon the kinematically admissible velocity field of Iddan et al. (1986) portrayed in Fig. 2 and reads

$$\begin{aligned} u_x^* &= \frac{Q}{2} \frac{1}{R + \frac{h_f}{2} - \sqrt{R^2 - x^2}} \\ u_y^* &= \frac{Q}{2} \frac{xy}{\sqrt{R^2 - x^2} \left(R + \frac{h_f}{2} - \sqrt{R^2 - x^2} \right)^2} \end{aligned} \quad (3)$$

where R is the roll radius and

$$Q = \omega R h_f \left(1 + \frac{R \alpha_n^2}{h_f} \right). \quad (4)$$

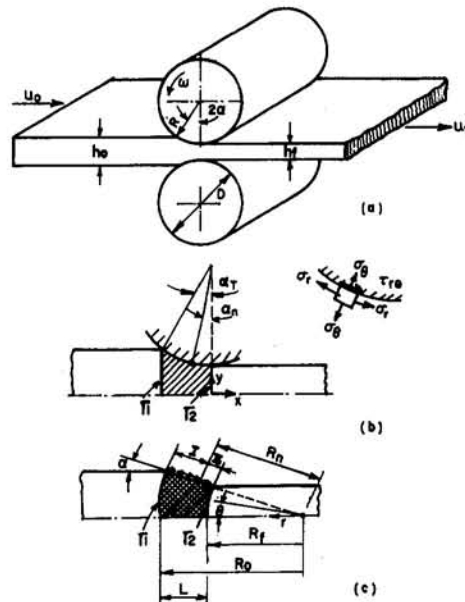


Fig. 1 The geometry of the rolling process: (a) general view, (b) the plastic zone in the upper bound analysis, (c) the plastic zone in the lower bound analysis. The admissible velocity fields used for the two bounds are different.

The extended upper bound functional with due discussion on its approximative character was given by Tirosh and Kobayashi (1976). It reads

$$\begin{aligned} J \leq \int_v s_{ij} \dot{\epsilon}_{ij}^* dv + \int_{s_f} m \sqrt{J_2} [u_i^*] ds \\ + \int_{\Gamma} \sqrt{J_2} [u_i^*] ds + \int_v \rho \dot{u}_i^* u_i^* \end{aligned} \quad (5)$$

where m is the shear factor along the roll/material interface area s_f (namely, $m = \tau/k$), ρ is the material density. $[u_i^*]$ and

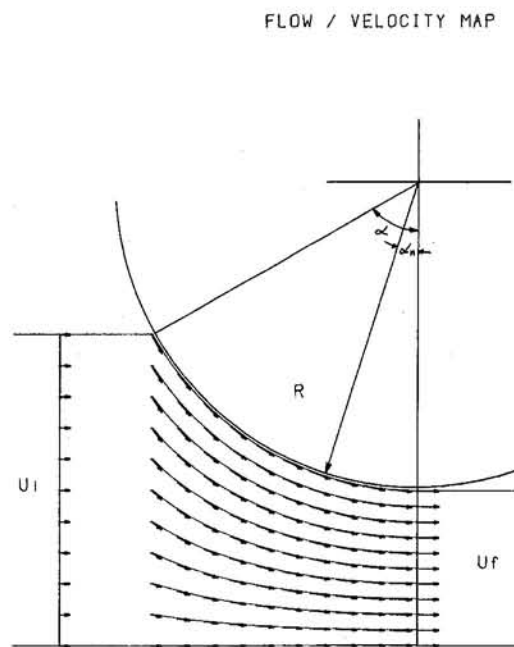


Fig. 2 The smooth kinematically admissible velocity field described in Eq. (3). A line of discontinuity in the velocity field appears only at the entrance (and not at the exit) which may be disregarded when the ratio D/h_0 is $\gg 1$.

$[u_i^*]$ designate the discontinuity in the tangential and normal components across boundaries of velocity discontinuities. ($[u_i^*]$ is finite, $[u_i^*] = 0$). The upper dot denotes the material derivative, whence the acceleration in (5) is

$$\dot{u}_i^* = \frac{\partial u_i^*}{\partial t} + u_j^* u_{i,j}^*. \quad (6)$$

The energy-rate terms on the right-hand side of (5) are all expressed in terms of u^* and its derivatives. The result is in an upper bound to J , (denote as J^*). Since u^* of (3) includes the neutral angle α_n as a free parameter, it will be determined as the angle which minimizes J^* according to

$$\frac{\partial J^*}{\partial \alpha_n} = 0, \quad \frac{\partial^2 J^*}{\partial \alpha_n^2} > 0. \quad (7)$$

The lengthy algebra for expressing J^* and its derivative is omitted here for brevity and given fully in Iddan's thesis (1988). The end result of eliminating α_n from (7) yields

$$\alpha_n = \sqrt{\left(\frac{m}{2a}\right)^2 + \frac{b}{a} - \frac{m}{2a}} \quad (8a)$$

where a and b in (8a) are the following functions:

$$a = N\left(\frac{R}{h_f}\right) \left\{ 4\left(1 + \frac{h_f}{h_0}\right) \sqrt{\frac{h_0 - h_f}{R}} + \left(\frac{h_f}{h_0}\right)^2 \frac{h_0 - h_f}{R} - m\left[1 + 2\frac{h_f}{h_0} - \left(\frac{h_f}{h_0}\right)^2\right] \right\} + 3 \text{Eu} \left[1 - \left(\frac{h_f}{h_0}\right)^2\right] \quad (8b)$$

$$b = \frac{h_f}{2R} \left\{ m \sqrt{\frac{R}{h_f}} \operatorname{tg}^{-1} \sqrt{\frac{h_0}{h_f} - 1} - \ln \frac{h_0}{h_f} - \frac{1}{4} \sqrt{\frac{h_0 - h_f}{R}} - 3 \text{Eu} \left[1 - \left(\frac{h_f}{h_0}\right)^2\right] \right\} - N \left\{ m \left[1 + \left(\frac{h_f}{h_0}\right)^2 - 2\frac{h_f}{h_0}\right] + 4\left(1 + \frac{h_f}{h_0}\right) \sqrt{\frac{h_0 - h_f}{R}} + \left(\frac{h_f}{h_0}\right)^2 \frac{h_0 - h_f}{R} \right\}. \quad (8c)$$

N = (Bingham No.)⁻¹ and Eu = (Euler No.) in (8b) are the basic nondimensional speed parameters of the process defined in this situation as

$$N \equiv \eta \frac{\omega}{k}, \quad \text{Eu} \equiv \rho \omega^2 \frac{R^2}{k}. \quad (8c)$$

The solution (8a) for α_n is valid only for non-negative b . For negative b , one can show that $\alpha_n = 0$. Upon substituting α_n back to the expression of J^* and equating it to the applied work rate ($M\omega$), one gets the approximate upper bound solution for the torque, M , as

$$M = kR^2[G_1 + N \cdot G_2 + \text{Eu} \cdot G_3]. \quad (9)$$

The functions G_1 , G_2 , and G_3 of (9) are derived by Iddan (1988). They are

$$G_1 = \left(\frac{h_f}{R} + \alpha_n^2\right) \left\{ \ln \frac{h_0}{h_f} + \frac{1}{4} \sqrt{\frac{h_0 - h_f}{R}} + m \sqrt{\frac{R}{h_f}} \left[2\operatorname{tg}^{-1} \left(\sqrt{\frac{R}{h_f}} \alpha_n\right) - \operatorname{tg}^{-1} \sqrt{\frac{h_0}{h_f} - 1}\right] \right\} + \left(m \sqrt{\frac{h_0 - h_f}{R}} - 2\alpha_n\right) \quad (10)$$

$$G_2 = \left(1 + \frac{R}{h_f} \alpha_n^2\right)^2 \left\{ 4\left(1 + \frac{h_f}{h_0}\right) \sqrt{\frac{h_0 - h_f}{R}} + \left(\frac{h_f}{h_0}\right)^2 \frac{h_0 - h_f}{R} + m \left[\frac{4}{1 + \frac{R}{h_f} \alpha_n^2} - \frac{2}{\left(1 + \frac{R}{h_f} \alpha_n^2\right)^2} - 2\frac{h_f}{h_0} - 1 + \left(\frac{h_f}{h_0}\right)^2 \right] \right\} \quad (11)$$

$$G_3 = \left[1 + \frac{R}{h_f} \alpha_n^2\right]^3 \left(\frac{h_f}{R}\right) \left[1 - \left(\frac{h_f}{h_0}\right)^2\right]. \quad (12)$$

When relating the interfacial shear stress to the average rolling pressure as $\tau = \mu p$, the approximate upper bound solution for the separation force is

$$F = \frac{M}{\mu R} \frac{1}{\left(1 - 2\frac{\alpha_n}{\alpha_T}\right)} \quad (\alpha_T \text{ is the total contact angle}). \quad (13)$$

By letting the speed approach zero, the reduced expression is a rigorous bound and reads

$$M^{u.b.} = kR^2 G_1, \quad F^{u.b.} = \frac{kRG_1}{\mu \left(1 - 2\frac{\alpha_n}{\alpha_T}\right)} \quad (14)$$

where G_1 is defined in (10) and α_n is defined in (8a).

4 The Viscoplastic Lower Bound

The Admissible Stress Field. The lower bound solution is now extended to include the speed effects via the inertia of the plastic flow. The kinematics which goes with the admissible velocity field in this solution does not have to (but may, if convenient) be similar to the one used in the upper bound solution, and therefore will be denoted differently as $u_i^{(0)}$. Consider a plane strain strip rolling where the arc of contact is replaceable (with a small error) by a line, as in Fig. 1(c). In contrast to the *direct method* of the upper bound any kinematically admissible velocity field will always yield a solution, the lower bound approach (with rate effects) is an *indirect method*. It means that a solution may or may not be reached by the trial stress fields, $\sigma_{ij}^{(0)}$. It depends whether the equation of motion (rather than just the static equilibrium) can be satisfied, which is

$$\sigma_{ij,j}^{(0)} - \rho \dot{u}_i^{(0)} = 0 \quad (15a)$$

where the acceleration field $\dot{u}_i^{(0)}$ is assumed to be derivable from a kinematically admissible velocity field of $u_i^{(0)}$. In addition, the admissible stress field $\sigma_{ij}^{(0)}$ must satisfy the yielding equation

$$J_2^{(0)} = \frac{1}{2} s_{ij}^{(0)} s_{ij}^{(0)} \leq J_2 \quad (\text{where } \sqrt{J_2} \geq k \text{ as in (2c)}) \quad (15b)$$

and the stress boundary conditions

$$\sigma_{ij}^{(0)} n_j = T_i \quad \text{on } sr. \quad (15c)$$

In cases where the stress field is composed from different zones, interfaced by lines of velocity discontinuities, the following "dynamic conditions" should be met across such lines (with notations as in (5));

$$[\sigma_n^{(0)}] = 0, \quad [\sigma_i^{(0)}] = \rho u_n^{(0)} u_i^{(0)}. \quad (15d)$$

At the present analysis, a small angle approximation is used (e.g., relatively low reductions are operated with relatively large roller) such that the stress field is "nearly" continuous and so

are the velocity fields. Thus, the "dynamic jumps" are negligible. The inequality equation of the lower bound theorem (Tirosh and Iddan, 1994) renders

$$\int_{s_u} \sigma_{ij}^{(0)} n_j u_i ds \leq \int_{s_u} T_i u_i ds + \int_V \rho(u_i^{(0)} - u_i) u_i dv. \quad (16)$$

The second term on the right-hand side of (16) is a variation between acceleration fields. It is zero on the boundary, s_u but remains unknown elsewhere, in spite of the steady-state nature of the process. The volume integral of this difference throughout the domain of the flow can be assumed small for any smooth admissible velocity field in V . A possible error of this nature causes us to call the resulted bound as an "approximation" rather than a "rigorous bound" which may only be reached in the limit situation of $u_i^{(0)} \rightarrow 0$.

For the steady-state strip rolling process, Eq. (15a) is hence reduced to

$$\frac{\partial \sigma_r^{(0)}}{\partial r} + \frac{1}{r} \frac{\partial \tau_{r\theta}^{(0)}}{\partial \theta} + \frac{\sigma_r^{(0)} - \sigma_\theta^{(0)}}{r} = \rho u_r^{(0)} \frac{\partial u_r^{(0)}}{\partial r} \quad (17)$$

$$\frac{1}{r} \frac{\partial \sigma_\theta^{(0)}}{\partial \theta} + \frac{\partial \tau_{r\theta}^{(0)}}{\partial r} + 2 \frac{\tau_{r\theta}^{(0)}}{r} = 0. \quad (18)$$

The stress boundary conditions for (17) and (18) depend on the position of the neutral angle as defined in Fig. 1(c). They are given separately at each zone due to their inverse shear direction, namely

$$\tau_{r\theta}^{(0)} = |m\sqrt{J_2^{(0)}}| \quad \text{along the wall:}$$

$$'-' \text{ for } (R_n < r \leq R_0), \quad '+' \text{ for } (R_f < r \leq R_n). \quad (19)$$

Along the plane of symmetry; $\tau_{r\theta}^{(0)} = 0$ for $\theta = 0$.

For the considered cases where the roller's radius is relatively large, say (h_0/R) is $O(10^{-2})$, therefore,

$$\sigma_r^{(0)}(R_0) = \sigma_r(R_0) \approx 0, \quad \sigma_r^{(0)}(R_f) = \sigma_r(R_f) \approx 0. \quad (20)$$

We now choose $u_i^{(0)}$ to satisfy all the kinematical conditions of the flow as u_i^* does in the upper bound analysis of the same problem (Tirosh et al., 1985). Namely

$$u_\theta^{(0)} = u_i^{(0)} = 0 \quad \text{in } V \quad (21)$$

$$u_r^{(0)} = -u_0 \frac{R_0}{r} \cos \theta \approx -u_0 \frac{R_0}{r}. \quad (22)$$

By inserting the above velocity field in (2c), one gets the speed-dependent yielding for this particular problem

$$\sqrt{J_2^{(0)}} = k \left[1 + 2N \left(\frac{R_0}{r} \right)^2 \right] \quad (23)$$

where for this case, the "speed parameter" N is defined as $N = \eta(u_0/R_0 k)$. For time-independent plasticity ($\eta = 0$), the Von-Mises criterion $\sqrt{J_2^{(0)}} = k$ is recovered.

The procedure to get the solution for (17) and (18) is to assume a distribution of the shear stress components in such a way that the stress boundary conditions (19) are satisfied, and then, with this shear distribution, to integrate (17) and (18), subjected to the boundary conditions of (20). The most simple trial supposition is that the shear component vary linearly with the angle, as

$$\tau_r^{(0)} = \pm \left(\frac{m\theta}{\alpha} \right) \sqrt{J_2^{(0)}} \quad (-) \text{ for zone I, } (+) \text{ for zone II} \quad (24)$$

so that (19) is satisfied.

Substituting (24) in (18) and solving for the normalized stress $\hat{\sigma}_\theta$ ($\hat{\sigma}_{ij} \equiv (\sigma_{ij}/k)$) renders

$$\hat{\sigma}_\theta^{(0)} = g(r) \pm m \frac{\theta^2}{\alpha} = g(r) + \text{second-order term} \quad (m\alpha \ll 1) \quad (25)$$

where $g(r)$ is the unknown function to be determined.

Using (25) with (17) with due account of (20), (21), and (22), one gets the stress distribution at each of the zones:

$$\text{I: } \hat{\sigma}_r^{(0)} = -2 \left(\frac{m}{2\alpha} - 1 \right) \left[\ln \frac{R_0}{r} + N \left\{ \left(\frac{R_0}{r} \right)^2 - 1 \right\} \right] + \frac{1}{2} \text{Eu} \left\{ \left(\frac{R_0}{r} \right)^2 - 1 \right\} \quad (26)$$

$$\text{II: } \hat{\sigma}_r^{(0)} = -2 \left(\frac{m}{2\alpha} + 1 \right) \left[\ln \frac{r}{R_f} + N \left\{ \left(\frac{R_0}{R_f} \right)^2 - \left(\frac{R_0}{r} \right)^2 \right\} \right] - \frac{1}{2} \text{Eu} \left\{ \left(\frac{R_0}{R_f} \right)^2 - \left(\frac{R_0}{r} \right)^2 \right\}; \quad (27)$$

the hoop stress in zone I:

$$\hat{\sigma}_\theta^{(0)} = -2 - 2 \left(\frac{m}{2\alpha} - 1 \right) \ln \frac{R_0}{r} - 2N \left\{ \left(\frac{m}{2\alpha} + 1 \right) \left[\left(\frac{R_0}{r} \right)^2 - 1 \right] + 2 \right\} + \frac{1}{2} \text{Eu} \left[\left(\frac{R_0}{r} \right)^2 - 1 \right]; \quad (28)$$

and in zone II:

$$\hat{\sigma}_\theta^{(0)} = -2 - 2 \left(\frac{m}{2\alpha} + 1 \right) \ln \frac{r}{R_f} - 2N \left\{ \left(\frac{m}{2\alpha} + 1 \right) \left[\left(\frac{R_0}{R_f} \right)^2 - \left(\frac{R_0}{r} \right)^2 \right] + 2 \left(\frac{R_0}{r} \right)^2 \right\} - \frac{1}{2} \text{Eu} \left\{ \left(\frac{R_0}{R_f} \right)^2 - \left(\frac{R_0}{r} \right)^2 \right\}. \quad (29)$$

The shear stress (in the two zones with different signs) is

$$\hat{\tau}_{r\theta}^{(0)} = \pm \frac{m\theta}{\alpha} \left[1 + 2N \left(\frac{R_0}{r} \right)^2 \right] \quad (30)$$

where

$$\text{Eu} = \rho \frac{u_0^2}{k}, \quad \text{and} \quad N = \frac{\eta u_0}{kh_0} \sqrt{\frac{2(h_0 - h_f)}{D}}. \quad (31)$$

By letting the speed to approach zero, the *rigorous statically admissible* field for the lower bound theorem is obtained. Thus the static solution is

$$\text{zone I: } \hat{\sigma}_r^{(0)} = -2 \left(\frac{m}{2\alpha} - 1 \right) \ln \frac{R_0}{r} \quad R_n \leq r \leq R_0$$

$$\text{zone II: } \hat{\sigma}_r^{(0)} = -2 \left(\frac{m}{2\alpha} + 1 \right) \ln \frac{r}{R_f} \quad R_f \leq r \leq R_n \quad (32)$$

$$\text{zone I: } \hat{\sigma}_\theta^{(0)} = -2 - 2 \left(\frac{m}{2\alpha} - 1 \right) \ln \frac{R_0}{r} \quad R_n \leq r \leq R_0$$

$$\text{zone II: } \hat{\sigma}_\theta^{(0)} = -2 - 2 \left(\frac{m}{2\alpha} - 1 \right) \ln \frac{r}{R_f} \quad R_f \leq r \leq R_n \quad (33)$$

$$\text{zone I: } \hat{\tau}_{r\theta}^{(0)} = -\frac{m\theta}{\alpha} \quad 0 \leq \theta \leq \alpha, \quad R_n \leq r \leq R_0$$

$$\text{zone II: } \hat{\tau}_{r\theta}^{(0)} = +\frac{m\theta}{\alpha} \quad 0 \leq \theta \leq \alpha, \quad R_f \leq r \leq R_n. \quad (34)$$

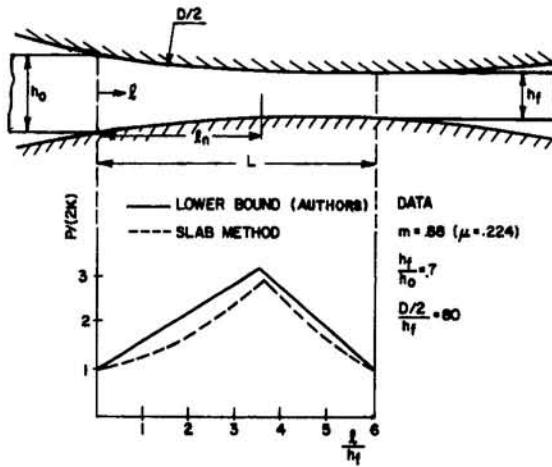


Fig. 3(a) The friction hill in the rolling process. Comparison between the "slab method" (Hoffman and Sachs, 1953) and the author's reduced lower bound solution (namely for $N = Eu = 0$). Note that a higher lower bound means that the solution is closer to reality.

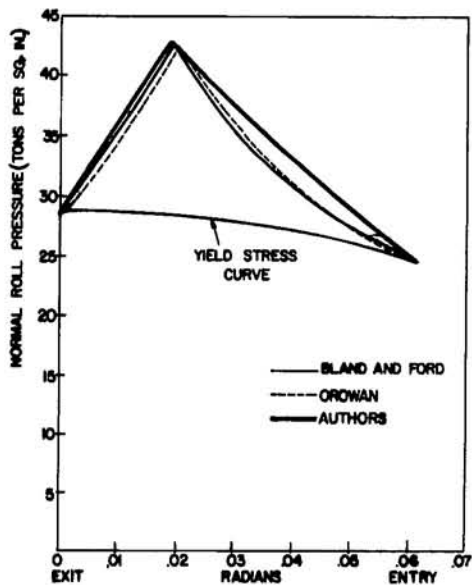


Fig. 3(b) The friction hill in the rolling process. Comparison between the "slab method" (taken from Bland and Ford, 1948) and the authors reduced lower bound solution (namely for $N = Eu = 0$). Data: copper, reduction of 30 percent, friction coefficient of $\mu = 0.086$, $h_0 = 2.54$ mm.

The stress distribution of (33) is compared favorably in Fig. 3 with the "slab method" solution given by Sachs and Hoffman (1953) and Bland and Ford (1948).

5 The Neutral Angle

The neutral point on the strip, beneath the roller, is defined as a point of "no slip" between the strip and the roller. It is located at a distance R_n at which the radial stress of zone I is equal to the radial stress of zone II. Hence, by equating (26) to (27), one gets an implicit equation for R_n . It reads

$$2 \ln \left(\frac{R_0}{R_f} \right) - \frac{m}{\alpha} \ln \left(\frac{R_0 R_f}{R_n^2} \right) + \frac{1}{2} Eu \left[\left(\frac{R_0}{R_f} \right)^2 - 1 \right] + N \left\{ 2 \left[\left(\frac{R_0}{R_f} \right)^2 - 1 \right] + \frac{m}{\alpha} \left[\left(\frac{R_0}{R_f} \right)^2 + 1 - 2 \left(\frac{R_0}{R_n} \right)^2 \right] \right\} = 0. \quad (35)$$

One can obtain from (35) the explicit solution to R_n as

$$R_n \cong R_0 \frac{\left(\frac{R_f}{R_0} \right)^{\left(\frac{1}{2} + \frac{\alpha}{m} \right)}}{e^{\left(\frac{Ta}{2m} \right)}}$$

or

$$h_n \cong h_0 \frac{\left(\frac{h_f}{h_0} \right)^{\left(\frac{1}{2} + \frac{\alpha}{m} \right)}}{e^{\left(\frac{Ta}{2m} \right)}}, \quad (36)$$

or equivalently (via geometrical relationships),

$$\alpha_n^2 \cong 2 \frac{h_0}{D} \left\{ \frac{\left(\frac{h_f}{h_0} \right)^{\left(\frac{1}{2} + \frac{\alpha}{m} \right)}}{e^{\left(\frac{Ta}{2m} \right)}} - \frac{h_f}{h_0} \right\}, \quad (37)$$

where

$$T = \left[\frac{1}{2} Eu - 2N \left(\frac{m}{2\alpha} - 1 \right) \right] \left[\left(\frac{h_0}{h_f} \right)^2 - 1 \right]. \quad (38)$$

For slow speeds one gets

$$h_n \cong h_0 \left(\frac{h_f}{h_0} \right)^{\left(\frac{1}{2} + \frac{\alpha}{m} \right)} \quad (39)$$

$$\alpha_n \cong \left\{ 2 \frac{h_0}{D} \left[\left(\frac{h_f}{h_0} \right)^{\left(\frac{1}{2} + \frac{\alpha}{m} \right)} - \frac{h_f}{h_0} \right] \right\}^{1/2}. \quad (40)$$

A comparison of the neutral angle obtained from the upper bound analysis (Eq. (8)) to the neutral angle obtained from the lower bound analysis (Eq. (37)) is given in Fig. 4 along with three-dimensional analysis of Oh and Kobayashi (1975).

6 The Rolling Torque and Separation Force

The torque (per unit width) is calculated from the totality of the interfacial shear produced by the normal stress distribution (Eq. 28 and 29) and Coulomb friction coefficient according to

$$M = \frac{\mu D}{2} \left[- \int_{R_n}^{R_0} \sigma_b^{(I)} dr + \int_{R_f}^{R_n} \sigma_b^{(II)} dr \right] \quad (41)$$

(zones I and II are designated by superscripts)

which yields

$$M^{U.B.} = \mu k D h_0 \left(\frac{D}{2(h_0 - h_f)} \right)^{1/2} \times \{ (A) + N(B) + Eu(C) \} \quad (42)$$

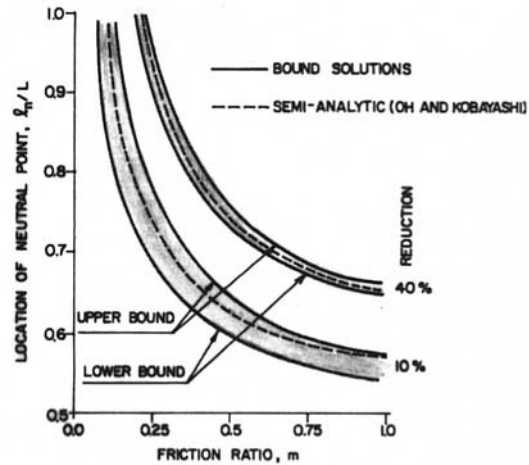


Fig. 4 The location of the neutral point versus the shear factor for various reductions. Comparison of the two reduced bound solutions (upper and lower) with the 3D solution of Oh and Kobayashi (1975) with initial width/thickness ratio of 3.

where $\{A\}$, $\{B\}$, and $\{C\}$ in (42) are

$$A = \frac{h_n}{h_0} \ln \left(\frac{h_0 h_f}{h_n^2} \right) + \frac{m}{2\alpha} \left[1 - \frac{h_f}{h_0} - \frac{h_n}{h_0} \ln \left(\frac{h_0}{h_f} \right) \right] \quad (42a)$$

$$B = \left(1 - \frac{h_n}{h_0} \right) \left[\left(1 + \frac{m}{2\alpha} \right) \left(\frac{h_0}{h_n} - 1 \right) + 2 \right] - \left(\frac{h_0}{h_f} \right)^2 \left(\frac{h_n}{h_0} - \frac{h_f}{h_0} \right) \left[\left(1 + \frac{m}{2\alpha} \right) \left(1 - \frac{h_f}{h_0} \right) + 2 \frac{h_f}{h_n} \right] \quad (42b)$$

$$C = -\frac{1}{4} \left\{ \frac{h_n}{h_0} \left[1 + \left(\frac{h_0}{h_f} \right)^2 \right] - 2 \left(1 + \frac{h_0}{h_f} - \frac{h_0}{h_n} \right) \right\}. \quad (42c)$$

The overall force (per unit width) is readily computed from the same normal stress distribution as

$$F = - \left[\int_{R_f}^{R_0} \sigma_\theta^{(I)} dr + \int_{R_f}^{R_n} \sigma_\theta^{(II)} dr \right] \quad (43a)$$

which yields

$$F^{U.B.} = k \left[\frac{D}{2} (h_0 - h_f) \right]^{1/2} (\{E\} + N\{G\} + Eu\{H\}) \quad (43b)$$

where the expressions $\{E\}$, $\{G\}$, and $\{H\}$ are given as

$$E = 1 + \left(\frac{h_n}{h_0 - h_f} \right) \ln \left(\frac{h_0}{h_f} \right) + \frac{m}{2\alpha} \frac{\left[h_0 + h_f - 2h_n - h_n \ln \left(\frac{h_0 h_f}{h_n^2} \right) \right]}{h_0 - h_f} \quad (44a)$$

$$G = 2 \left\{ \left(\frac{h_0 - h_n}{h_0 - h_f} \right) \left[\left(1 + \frac{m}{2\alpha} \right) \left(\frac{h_0}{h_n} - 1 \right) + 2 \right] + \left(\frac{h_0}{h_f} \right)^2 \left(\frac{h_n - h_f}{h_0 - h_f} \right) \times \left[\left(1 + \frac{m}{2\alpha} \right) \left(1 - \frac{h_f}{h_n} \right) + 2 \frac{h_f}{h_n} \right] \right\} \quad (44b)$$

$$H = -\frac{1}{2} \left\{ 2 \frac{h_0}{h_f} - \frac{h_n}{h_f} \left(1 + \frac{h_0}{h_f} \right) \right\}. \quad (44c)$$

The friction coefficient, μ , for the torque calculation, is related to the friction factor m through their force equivalence relation, as follows:

$$\int_{R_f}^{R_0} \tau_{r\theta}(\alpha) dr = \mu p_{av} (R_0 - R_f) \equiv \mu F_{av} \quad (45)$$

where from (30)

$$\tau_{r\theta}(\alpha) = mk \left[1 + 2N \left(\frac{R_0}{r} \right)^2 \right].$$

The interrelation between μ and m is hence

$$\mu = \frac{m}{\left(\frac{p}{k} \right)_{av}} \left[1 + 2N \left(\frac{h_0}{h_f} \right)^2 \right]. \quad (46a)$$

For nonviscous material it reduces to the regular relation

$$\mu = \frac{m}{\left(\frac{p}{k} \right)_{av}}. \quad (46b)$$

The rolling torque (41) and the separation force (43) varia-

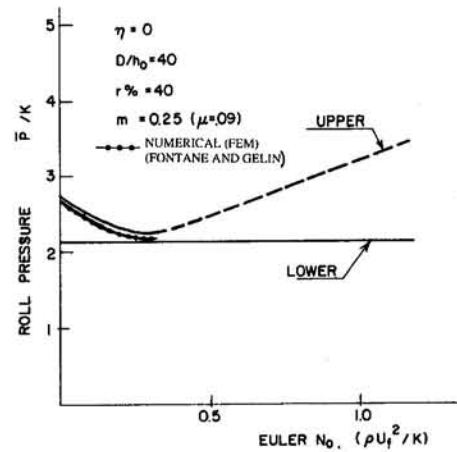


Fig. 5 The average roll pressure as a function of the rolling speed (expressed by the Euler No.). Note the decrease of the roll pressure while increasing the rolling speed in the upper bound solution. This tendency is terminated at the speed at which the neutral angle reaches the rolling exit. From this speed and further on (shown in dashed line) skidding is envisaged. FEM solution of Fontane and Gelin (1991) has an essential resemblance.

tion with respect to the rolling speed are shown in Figs. 5, 6, 7, and 8.

7 Minimum Required Friction and Maximum Allowable Speed

Lower Bound Solution. It is noticed that to ensure $\alpha_n \geq 0$, a minimum allowable shear factor, m_{min} , should be prescribed or else skidding will ensue. For the lower bound solution,

$$m \geq 2\alpha \left[1 + \frac{T}{2 \ln \left(\frac{h_0}{h_f} \right)} \right], \quad \therefore m_{min} = 2\alpha, \quad (47)$$

since, for slow processes, T (defined in (38)) approaches zero.

The condition (47) is equivalent to requiring that the Coulomb friction coefficient should be at least

$$\mu \geq \frac{m_{min}}{\left(\frac{p}{k} \right)_{min}} = \frac{2\alpha}{\left(\frac{p}{k} \right)_{min}}, \quad \therefore \mu_{min} = \alpha \quad (48)$$

since, at $\alpha_n = 0$, $(p/k)_{min} = 2$. The result of (48) agrees qualitatively with observations given by Hoffman and Sachs (1953).

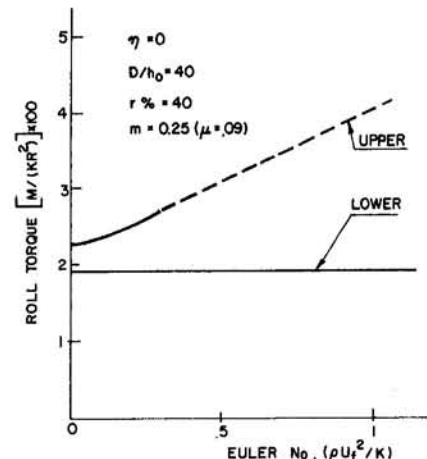


Fig. 6 Bound solutions to the roll torque versus speed. The speed at which skidding is anticipated is shown with dashed line.

At a given speed, the friction prevails at $\alpha_n = 0$ sets the minimum required friction coefficient for safe rolling (i.e., without skidding). Let α_n in (37) be zero and solve for m . This leads to the minimum friction

$$m_{\min}^{(0)} = \sqrt{\frac{h_0 - h_f}{R}} \times \frac{1 + \left(\frac{1}{2} \frac{\rho u_0^2}{k} + 2 \frac{\eta u_0}{kR} \sqrt{\frac{R}{h_0} \left(1 - \frac{h_f}{h_0} \right)} \right) \frac{\left[\left(\frac{h_0}{h_f} \right)^2 - 1 \right]}{2 \ln \left(\frac{h_0}{h_f} \right)}}{1 + \frac{\eta u_0}{kR} \sqrt{\frac{R}{h_0} \left(1 - \frac{h_f}{h_0} \right)} \frac{\left[\left(\frac{h_0}{h_f} \right)^2 - 1 \right]}{\ln \left(\frac{h_0}{h_f} \right)}}. \quad (49)$$

Now, the *maximum allowable rolling speed* (which maintains the minimum friction of (49)), is solved from (49) and reads

$$u_{0\max}^{(0)} = \sqrt{\left(\frac{\bar{b}}{2\bar{\alpha}} \right)^2 + \frac{\bar{c}}{\bar{\alpha}} + \frac{\bar{b}}{2\bar{\alpha}}} \quad (50)$$

where

$$\bar{\alpha} = \frac{\rho}{2k}$$

$$\bar{b} = \frac{2\eta}{kR} \sqrt{\left(\frac{R}{h_0} \right) \left(1 - \frac{h_f}{h_0} \right)} \left(\frac{m}{2\alpha} - 1 \right)$$

$$\bar{c} = 2 \left(\frac{m}{2\alpha} - 1 \right) \ln \left(\frac{h_0}{h_f} \right) / \left[\left(\frac{h_0}{h_f} \right)^2 - 1 \right] \quad (51)$$

and finally

$$u_{f\max}^{(0)} = u_{0\max}^{(0)} \left(\frac{h_0}{h_f} \right). \quad (52)$$

Speeds beyond that may lead to skidding. For example, for nonviscous material, Eqs. (50)-(52) yield the maximum allowable speed as

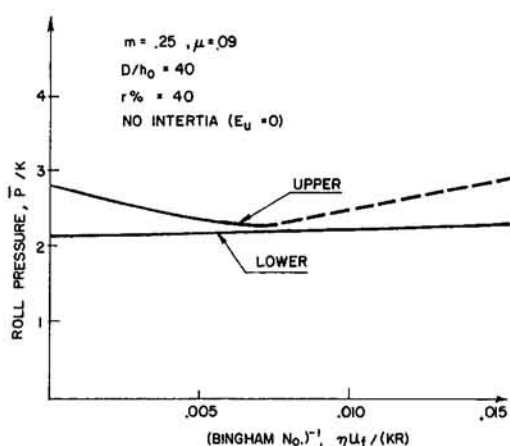


Fig. 7 Bound solutions of the roll pressure for time-dependent material (without inertia), using the Bingham number as the dependent variable. Note the similarity to Fig. 5 where the inertia term (the Euler No.) is used as the dependent variable. The roll pressure is seen to decrease while the rolling speed is progressively increased. It is terminated at the speed at which the neutral point reaches the exit. From this speed on (shown in the dashed line) skidding is envisaged.

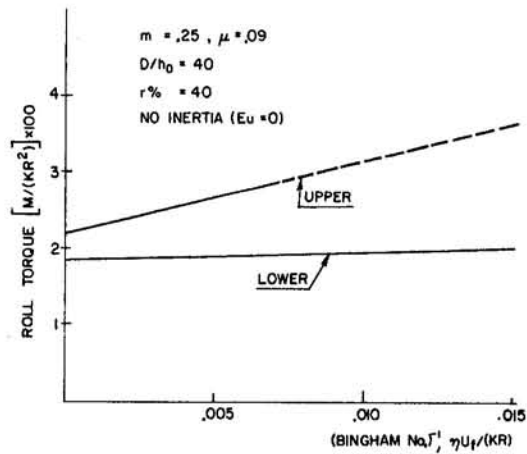


Fig. 8 Bound solutions to the roll torque versus speed, as in Fig. 6, but with Bingham number as the dependent variable rather than the Euler No. The speeds at which skidding is anticipated is shown with a dashed line.

$$u_{f\max}^{(0)} = 2 \left(\frac{h_0}{h_f} \right) \left\{ \left(\frac{m}{2\alpha} - 1 \right) \frac{\ln \left(\frac{h_0}{h_f} \right)}{\left[\left(\frac{h_0}{h_f} \right)^2 - 1 \right]} \frac{k}{\rho} \right\}^{1/2}. \quad (53)$$

Upper Bound Solution. One can estimate the minimum required friction and the maximum allowable speed also from the upper bound solution. Let the expression for $\alpha_n^*(u_f, m, R, h_0, h_f)$ in Eq. (8) be equal to zero to set the limiting condition for nonskidding operation, and solve for m

$$m_{\min}^* = \frac{\frac{h_f}{2R} \left\{ \ln \left(\frac{h_0}{h_f} \right) + \frac{1}{4} \sqrt{\frac{h_0 - h_f}{R}} + \frac{3\rho u_f^2}{k} \left[1 - \left(\frac{h_f}{h_0} \right)^2 \right] \right\}}{\frac{1}{2} \sqrt{\frac{h_f}{R}} \operatorname{tg}^{-1} \sqrt{\frac{h_0}{h_f} - 1} - \frac{\eta u_f}{kR} \left[1 + \left(\frac{h_f}{h_0} \right)^2 - 2 \frac{h_f}{h_0} \right]} + \frac{\frac{\eta u_f}{kR} \left\{ 4 \left(1 + \frac{h_f}{h_0} \right) \sqrt{\frac{h_0 - h_f}{R}} + \left(\frac{h_f}{h_0} \right)^2 \left(\frac{h_0 - h_f}{R} \right) \right\}}{\frac{1}{2} \sqrt{\frac{h_f}{R}} \operatorname{tg}^{-1} \sqrt{\frac{h_0}{h_f} - 1} - \frac{\eta u_f}{kR} \left[1 + \left(\frac{h_f}{h_0} \right)^2 - 2 \frac{h_f}{h_0} \right]}. \quad (54)$$

By letting the process be slow ($u_f \rightarrow 0$), the minimum shear factor becomes

$$m_{\min}^* = \sqrt{\frac{h_f}{R}} \frac{\ln \left(\frac{h_0}{h_f} \right) + \frac{1}{4} \sqrt{\frac{h_0 - h_f}{R}}}{\operatorname{tg}^{-1} \sqrt{\frac{h_0}{h_f} - 1}}. \quad (55)$$

This reduced result is *identical* to Avitzur's solution for quasi-static rolling (1968, Eq. 15.37a) derived from an entirely different velocity field.

The maximum allowable speed is derived from (54) and reads

$$u_{f\max}^* = \sqrt{\left(\frac{\tilde{b}}{2\tilde{\alpha}} \right)^2 + \frac{\tilde{c}}{\tilde{\alpha}} - \frac{\tilde{b}}{2\tilde{\alpha}}}. \quad (56)$$

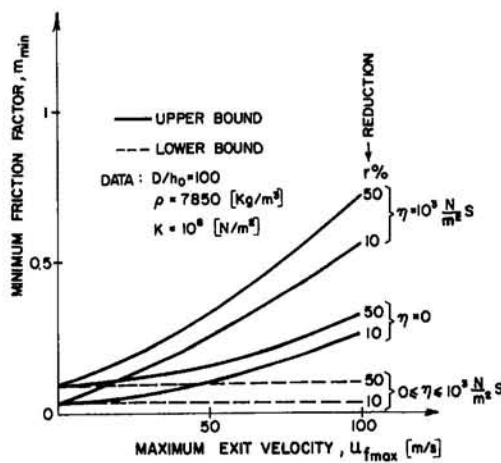


Fig. 9 The minimum allowable friction factor, m , versus the maximum allowable exit speed. It is seen that in order to reach higher rolling speeds one should increase the interfacial shear. This interrelation is not pronounced in the lower bound solution.

where

$$\tilde{a} = \frac{3\rho h_f}{2kR} \left[1 - \left(\frac{h_f}{h_0} \right)^2 \right]$$

$$\tilde{b} = \frac{\eta}{kR} \left\{ 4 \left(1 + \frac{h_f}{h_0} \right) \sqrt{\frac{(h_0 - h_f)}{R}} + \left(\frac{h_f}{h_0} \right)^2 \left(\frac{h_0 - h_f}{R} \right) \right. \\ \left. + m \left[1 + \left(\frac{h_f}{h_0} \right)^2 - 2 \frac{h_f}{h_0} \right] \right\}$$

$$\tilde{c} = \frac{m}{2} \sqrt{\frac{h_f}{R}} \operatorname{tg}^{-1} \sqrt{\frac{h_0}{h_f} - 1} \\ - \frac{h_f}{2R} \left[\ln \left(\frac{h_0}{h_f} \right) + \frac{1}{4} \sqrt{\frac{h_0 - h_f}{R}} \right]. \quad (57)$$

For example, for a nonviscous material, Eqs. (56), (57) yield the maximum allowable speed as

$$u_{f\max}^* = \sqrt{\frac{k}{\rho} \frac{m \sqrt{\frac{R}{h_f}} \operatorname{tg}^{-1} \sqrt{\frac{h_0}{h_f} - 1} - \left[\ln \left(\frac{h_0}{h_f} \right) + \frac{1}{4} \sqrt{\frac{h_0 - h_f}{R}} \right]}{3 \left[1 - \left(\frac{h_f}{h_0} \right)^2 \right]}}. \quad (58)$$

A typical presentation of the interrelation between m_{\min} and $u_{f\max}$ is given in Fig. 9. It explains why higher rolling speeds necessitates higher friction factor with the workpiece.

8 Comparison to Experiments and Finite Element Solution

The hardening behaviour of the tested materials has the following form

$$\sigma = \sigma_0 \left(1 + \frac{\bar{\epsilon}}{b} \right)^n \quad (59)$$

where b , n , and σ_0 are material constants.

As mentioned earlier, to conform with the limit analysis theorems one should use a uniform flow stress in V . This was introduced by the following averaging

$$\bar{\sigma} = \frac{1}{\bar{\epsilon}_f} \int_a^{\bar{\epsilon}_f} \sigma d\bar{\epsilon} = \frac{\sigma_0 b}{(n+1)\bar{\epsilon}_f} \left[\left(1 + \frac{\bar{\epsilon}_f}{b} \right)^{n+1} - 1 \right] \quad (60)$$

where

$$\bar{\epsilon} = \left(\frac{2}{3} \epsilon_{ij} \epsilon_{ij} \right)^{1/2} \quad \text{and} \quad \bar{\epsilon}_f = \frac{2}{\sqrt{3}} \ln \left(\frac{h_0}{h_f} \right). \quad (61)$$

At any specific reduction, the equivalent strain $\bar{\epsilon}$, and subsequently the associated hardening flow stress, $\bar{\sigma}$, were evaluated beforehand, and merged into the final expressions of M and F , as $k = (\bar{\sigma}/\sqrt{3})$.

The bounding solutions (Eqs. (8), (12), (42), and (43)) are compared to experiments with copper and aluminum from Al-Salehi et al. (1973) and with steel from Shida et al. (1973). Corresponding rigid-plastic finite element solutions by Li and Kobayashi (1982) are attached to these Figs. from 10 to 15. The agreement is not too satisfactory in regard to experiments (to be discussed) but very satisfactory with respect to FEM solutions.

9 Results and Discussion

The solutions given here were formulated for *viscoplastic solids undergoing high-speed rolling* with some generalizations and approximations as mentioned in the text. The nature of the solutions does not allow for fine details as residual elasticity (Chandra, 1989), temperature-dependent friction (Lenard, 1989), and the like. Therefore, special occurrences of, for instance, multi normal-pressure peak points (Jesweit, 1989), delamination split ("Alligatoring") of the workpiece (Sherby et al., 1982) etc., cannot be detected. The suggested solutions provide just a general information of what may be changed (if at all) in the design of the process if an increase

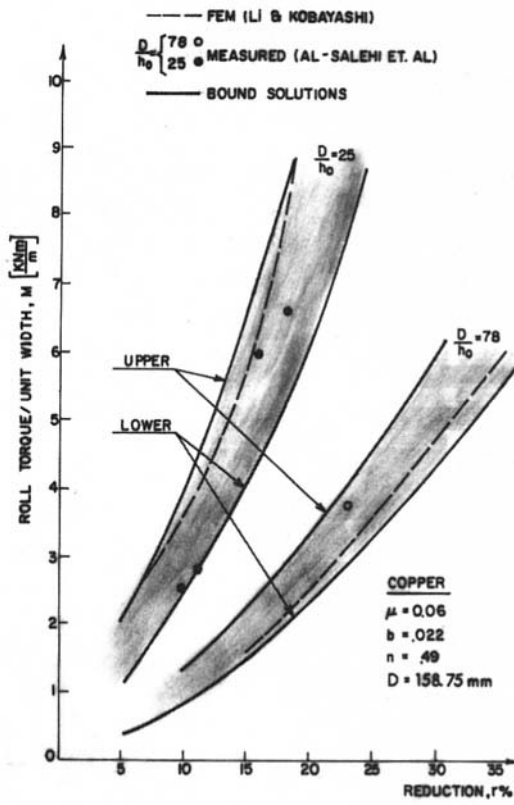


Fig. 10 The roll torque versus reduction. Comparison between FEM solution of Li and Kobayashi (1982) and the bound solutions, along with experiments on copper taken from Al-Salehi, Fairbank, and Lancaster (1973). Data: $\sigma_0 = 70.3 \text{ (N/mm}^2\text{)}$.

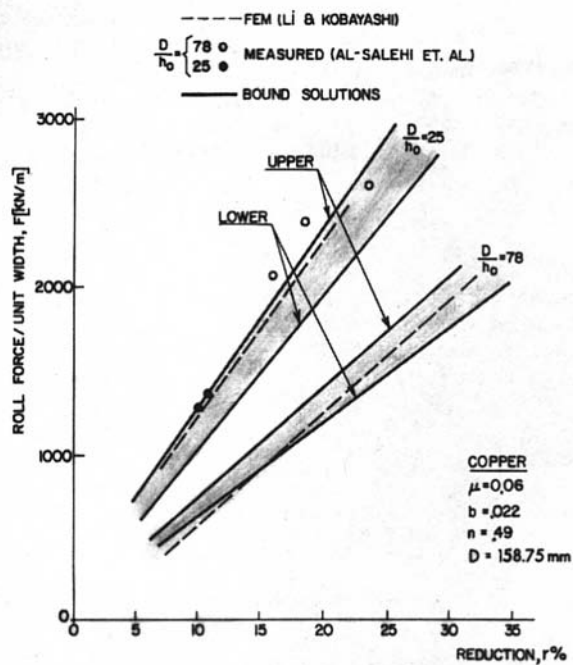


Fig. 11 The roll force versus reduction. Data and references as in Fig. 10. It is seen that at some portion of the curves the lower bound surpasses somewhat the numerical solution (rather than to stay always beneath it). It is believed to be attributed to the difference in the way the frictional shear is used. In the numerical solution the frictional shear is considered independent of the normal stress, whereas in the lower bound analysis (when $N = Eu = 0$) it does depend on the normal stress by a Coulomb-type relationship.

of the rolling speed is anticipated. The solutions are, however, reduced to rigorous bounds (on which practical designs are usually based) by letting the operational speed to approach zero.

It turns out that the suggested approximate solutions appear relatively close to each other and embrace consistently the counterpart numerical rigid-plastic solution of Li and Kobay-

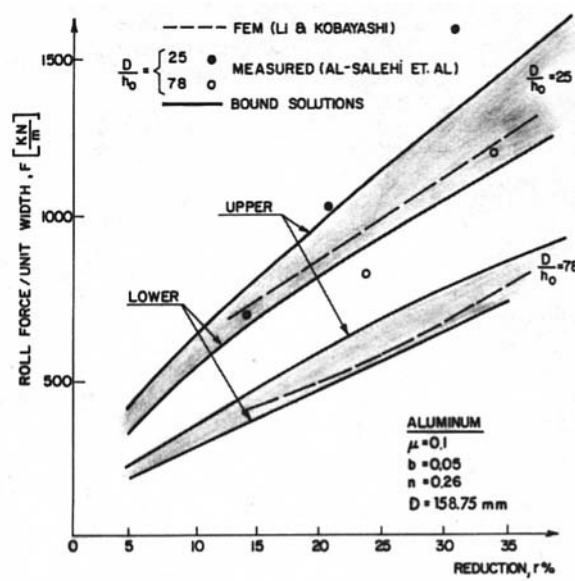


Fig. 13 The roll force versus reduction. References and Data as in Fig. 12.

ashi (1982). The comparisons were done in regard to the position of the neutral angle, (namely, the distance l_n shown in Fig. 3a), the torque (Figs. 10, 12, 14) and the separation force (Figs. 11, 13, 15). The good match of the FEM solution to the presented bounds is exhibited. Experimental data from Al-Salehi et al. (1973) and from Shida et al. (1973) are added to these figures and appear scattered up and down the bounds. This can possibly be attributed to the variation in the friction conditions during the experiments, unaccounted by the analysis, and/or the inadequacy of the Bingham mate-

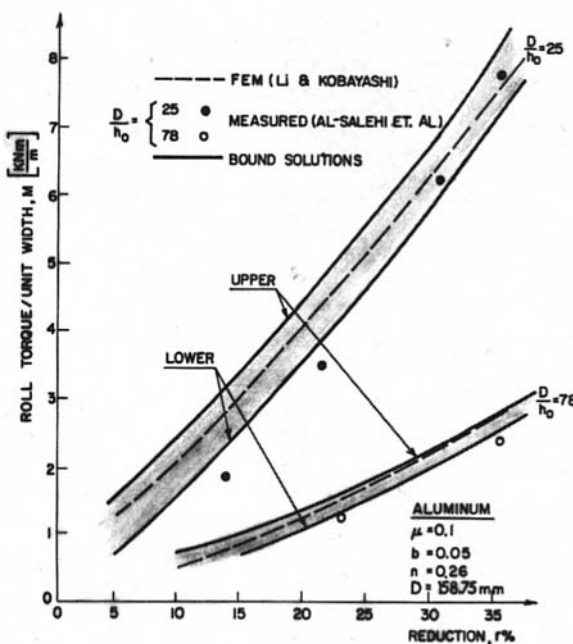


Fig. 12 The roll torque versus reduction. References as in Fig. 10. Data: $\sigma_0 = 50.3$ (N/mm^2).

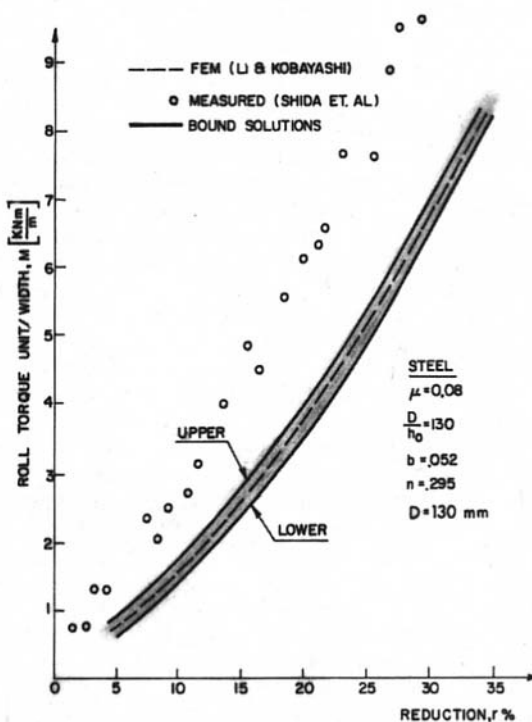


Fig. 14 The roll torque versus reduction. Comparison between FEM solution of Li and Kobayashi (1982) and the bound solutions, along with experiments on steel given by Shida and Awazuhara (1973). Data: $\sigma_0 = 334$ (N/mm^2).

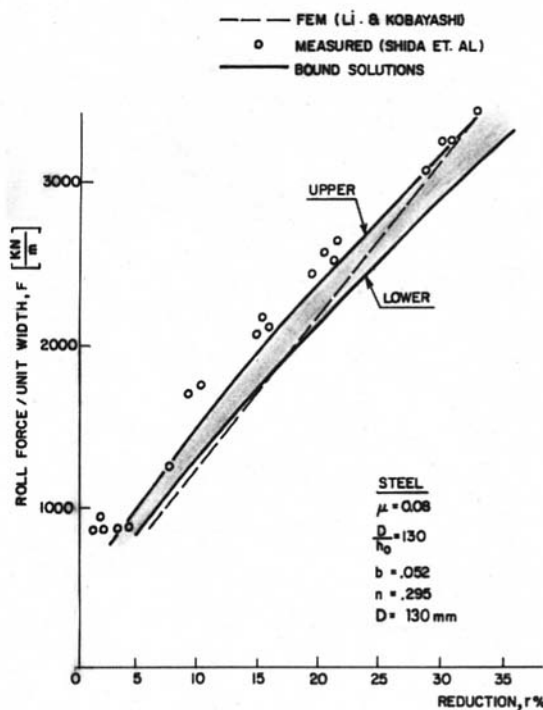


Fig. 15 The roll force versus reduction. References and Data as in Fig. 14. As in Fig. 11 it is seen that at some portion of the curves the lower bound surpasses the FEM solution (rather than to stay beneath it). It is believed to be attributed to the difference in the way the frictional shear is used. In the numerical solution the frictional shear is considered to be independent of the normal stress, whereas in the lower bound analysis ($N = Eu = 0$) it does depend on the normal stress by a Coulomb-type relationship.

rial model to describe the behaviour of the tested materials. The general trend of the scattered data, however, is still an indicative measure of the validity of the suggested solutions.

The speed effect on the separation force and torque appears in Figs. 5, 6, 7, and 8. In these figures the bound solutions are extended beyond their quasi-static range in order to estimate the role plays by the inertia and the material "viscosity." The upper bound solution indicates that the average roll pressure, though not the torque, is reduced with the increase of speed. This kind of observation by Ford (1947) received recently a support from a numerical solution by Fontane and Gelin (1991) who incorporated both inertia and material rate sensitivity into their FEM formulation. The present explanation is that *this phenomenon can be attributed to the shift of the neutral point towards the exit, while the rolling speed is progressively increased*. It relaxes the need to postulate a soft self-heated layer which was as an alternative explanation by the authors (1985).

It is noted that the "maximum allowable speed" phenomenon, anticipated in this work, emerged from the same physical ground as that commonly observed "minimum allowable shear" demand as shown in Fig. 9. They impose the same restriction on the performance of high-speed rolling. For example, when considering a strip of steel ($\rho = 7850$ kg/m^3 , $k = 10^8$ N/m^2), undergoing 40 percent reduction by rollers of dimensions $(D/h_0) = 40$ and shear factor of $m = .25$, the maximum allowable speed is computed (from Eq. 56) to be approximately 60 m/s . The maximum speed can go up if the shear factor, m , and/or (D/h_0) will be increased. When the same material is viscoplastic with, say, $\eta = 10^3$ $[(\text{N/m}^2) \text{ sec}]$ and inertia is ignored, the maximum speed for smooth rolling is then approximately 70 m/s . Again, with higher shear factors and/or larger roll-

diameter, higher limiting speeds can be obtained. A closer experimental study of this complex behavior related to skidding at high speeds is certainly due. Within the framework of the present finding, it seems that the current industrial rolling speeds (which are of the order of 10^2 m/s) are probably on the verge of their maximum utilization.

Acknowledgment

The authors would like to thank the Center for Manufacturing Systems and Robotics Research (CMSR) in the Faculty of Mechanical Engineering at the Technion, Haifa, Israel.

References

- Al-Salehi, F. A. R., Fairbank, T. C., and Lancaster, P. B., 1973, "An Experimental Determination of the Roll Pressure Distribution in Cold Rolling," *International Journal of Mechanical Science*, Vol. 15, pp. 693-710.
- Avitzur, B., 1968, *Metal Forming: Processes and Analysis*, McGraw-Hill, New York, Chapter 15.
- Chandra, A., 1989, "Simulation of Rolling Processes by the Boundary Element Method," *Computational Mechanics*, Vol. 4, pp. 443-451.
- Fontane, J. F., and Gelin, J. C., 1991, "A Finite Element Analysis of High Speed Metal Forming Processes," *Annals of the CIRP*, Vol. 40, No. 1, pp. 277-280.
- Ford, H., 1947, "The Effect of Speed Rolling in the Cold Rolling Processes," *Journal of Iron and Steel Institute*, pp. 380-398.
- Bland, R. D., and Ford, H., 1948, "The Calculation of Roll Force and Torque in Cold Strip Rolling with Tensions," *Proceedings of the Institution of Mech. Engineering*, Vol. 159, pp. 144-150 (taken from H. Ford, *Advance Mechanics of Materials*, John Wiley and Sons, Wiley, p. 601, 1963).
- Cristescu, N., 1975, "Plastic Flow Through Conical Converging Dies, Using a Viscoplastic Constitutive Equation," *International Journal of Mechanical Science*, Vol. 17, pp. 425-433.
- Cristescu, N., and Cleja, S., 1979, "New Trends in Tube and Bar Processing," *Metal Forming Plasticity*, H. Lippmann, ed., Springer-Verlag, New York, pp. 139-159.
- Davies, R., and Austin, E. R., 1970, *Developments in High Speed Metal Forming*, Industrial Press.
- Durban, D., 1984, "Rate Effects in Steady Forming Processes of Plastic Materials," *International Journal of Mechanical Science*, Vol. 26, pp. 293-304.
- Hoffman, O., and Sachs, G., 1953, "Theory of Plasticity for Engineers," McGraw-Hill, New York.
- Iddan, D., 1988, "Dynamic Effects in Forming Processes," Ph.D. Thesis, Technion, Haifa, Israel.
- Iddan, D., Tirosh, J., and Pawelski, O., 1986, "Strip Rolling of Hardening, Rate Sensitive Solids," *Annals of the CIRP*, Vol. 37, No. 1, pp. 151-162.
- Jeswiet, J., 1990, "The Neutral Zone and Temperature at the Roll/Strip Interface," *Annals of the CIRP*, Vol. 39, No. 1, pp. 275-277.
- Lau, A. C. W., Shivpuri, R., and Chou, P. C., 1989, "An Explicit Time Integration Elastic-plastic Finite Element Algorithm for Analysis of High Speed Rolling," *International Journal of Mechanical Science*, Vol. 31, No. 7, pp. 483-497.
- Lenard, J., 1990, "An Experimental Study of Boundary Conditions in Hot and Cold Flat Rolling," *Annals of the CIRP*, Vol. 39, No. 1, pp. 279-282.
- Li, G. J., and Kobayashi, S., 1982, "Rigid-Plastic Finite Element Analysis of Plane Strain Rolling," *ASME Journal of Engineering for Industry*, Vol. 104, pp. 55-64.
- Oh, S. I., and Kobayashi, S., 1975, "An Approximate Method for a Three-Dimensional Analysis of Rolling," *International Journal of Mechanical Science*, Vol. 17, pp. 293-305.
- Perzyna, P., 1963, "The Constitutive Equation for Rate-Sensitive Plastic Materials," *Quarterly of Applied Mathematics*, Vol. 20, pp. 321-329.
- Rice, J. R., 1970, "On the Structure of Stress-Strain Relations for Time-Dependent Plastic Deformation in Metals," *ASME JOURNAL OF APPLIED MECHANICS*, Vol. 92, pp. 728-736.
- Sherby, O. D., de-Jesus, S., Oyama, T., and Miller, A., 1982, "Metal Forming Defects at Large Strain Deformation at Intermediate Temperature," *Plasticity of Metals at Finite Strain*, E. H. Lee and R. L. Mallett, eds., Division of Applied Mechanics, Stanford Univ. Press, pp. 3-22.
- Shida, S., and Awazuhara, H., 1973, "Rolling Load and Torque in Cold Rolling," *Journal of Japan Society for Technology and Plasticity*, Vol. 14, pp. 267-272.
- Tirosh, J., and Iddan, D., 1989, "Technological Implication of High Speed Forming Processes," *Annals of the CIRP*, Vol. 38, pp. 235-238.
- Tirosh, J., and Iddan, D., 1994, "The Dynamics of Fast Metal Forming Processes," *Journal of the Mechanics and Physics of Solids*, Vol. 42, No. 4, pp. 611-628.
- Tirosh, J., Iddan, D., and Pawelski, O., 1985, "The Mechanics of High Speed Rolling of Viscoplastic Materials," *ASME JOURNAL OF APPLIED MECHANICS*, Vol. 50, pp. 309-318.

Tirosh, J., and Kobayashi, S., 1976, "Kinetic and Dynamic Effects on the Upper-Bound Load in Metal Forming Processes," *ASME JOURNAL OF APPLIED MECHANICS*, Vol. 41, pp. 314-318.

Tirosh, J., and Sayir, M., 1987, "High Speed Deep Drawing of Hardening and Rate Sensitive Solids with Small Interfacial Friction," *Journal of the Mechanics and Physics of Solids*, Vol. 35, pp. 479-494.

L. G. Hector, Jr.
Scientific Associate,
Surface Technology Division,
Alcoa Technical Center,
Alcoa Center, PA 15069-0001
Assoc. Mem. ASME

R. B. Hetnarski
James E. Gleason Professor of
Mechanical Engineering,
Rochester Institute of Technology,
Rochester, NY 14623-5604
Fellow ASME

Thermal Stresses due to a Laser Pulse: Elastic Solution

The thermal stress field in an elastic half-space due to a single pulse from a laser is derived for the general case of a mixed-mode structure beam. The mode structure models the output from a cylindrical laser resonator and thus defines a radially symmetric intensity distribution about the beam axis. The functional form of the temporal pulse profile is quite general in that it models the temporal pulse shapes emitted by a laser that is either internally pulsed through radio frequency modulation of its power supply, Q-switched, or mode locked. It also models a continuous beam that is mechanically chopped through external means.

Introduction

The birth of pulsed laser technology in the 1960s extended the usefulness of the laser in materials processing applications. Pulsed lasers are now commonly used in such diverse applications as drilling, scribing, trimming of electric resistors, welding, hardening, quenching, cutting, and surface texturing of metal forming tools (see Nonhof (1988) for an overview of materials processing applications with Nd:YAG lasers, and Steen (1991) for an overview of materials processing applications with CO₂ lasers).

Laser irradiation of a surface produces a heating effect due to the absorption of light energy. Deposition of the laser energy can be either continuous, where there is no interruption of the beam, or pulsed, where beam output from the resonator is interrupted either electronically or mechanically. In a pulsed beam, a significant amount of energy is delivered to a material surface in short time intervals thereby leading to elevated thermal stress levels as the thermal load is absorbed into the substrate. The thermal stress field that results from pulsed laser irradiation is primarily controlled by the temporal pulse profile or distribution of pulse energy in time. An individual pulse typically rises to its peak power in a small interval known as the rise time. After peak power is attained, the pulse decays to minimum energy over a time interval which typically exceeds the rise time and the temporal distribution of energy in the pulse is thus negatively skewed. In other laser resonators, the temporal pulse profile has a near-zero skewness and thus the pulse rise time and decay time are nearly equivalent. The shape of the temporal profile is due to the mechanism that produces the pulses (i.e., electronic, mechanical, acousto-optic, etc.).

The amount of heat delivered in a single laser pulse and the manner in which it is distributed in time governs the thermal stress field in the irradiated material. The thermal stresses can lead to surface and subsurface cracking of a material and hence degrade its performance in a future application. The thermal stress field in a laser-irradiated material is also important in materials processing applications where the goal is to alter the microstructure of the material near its surface (such as in laser hardening). The ability to predict the thermal stress field in a material can also help one to adjust critical process parameters such as pulse repetition rate, pulse train period, peak power per pulse, and depth of focus.

Theoretical and experimental investigations of laser heating of materials and the resulting thermal stress fields began to appear not long after the laser became a significant materials processing tool in the 1960s. For example, Oswald et al. (1971) conducted an experimental investigation of the thermoelastic response of materials such as Al, Ag, Cu, Si, and Ge irradiated with a pulsed laser. Popov et al. (1983) developed an experimental technique to investigate thermally-induced plastic slip with an energy beam. Geller et al. (1986) modeled the thermal stress field in a steel plate quenched with either a laser or an electron beam. Welsh et al. (1988) explored thermal stresses and strains in both an elastic half-space and thin films under steady-state heating with a Gaussian source from a laser. Germanovich et al. (1988) derived the thermoelastic response of a half-space subjected to volumetric heating by a concentrated heat flux for various values of absorption coefficient. Volchenok and Rudin (1989) derived the thermal stress field in a multilayer plate due to the action of a continuous Gaussian surface source.

In this paper we derive the thermal stress field in an elastic half-space due to a single laser pulse, the heat from which is absorbed in the surface plane of the material. The distribution of pulse energy during pulse activation is described by a function that models the temporal pulse profiles from common materials processing lasers, such as a Q-switched Nd:YAG laser or pulsed CO₂ laser. The spatial distribution of heat energy on the material surface is a superposition of the two lowest order modes from a cylindrical laser resonator; these modes result from solution of the standing wave equation for the resonator. The mixed structure is more general since it is a mixture of both the Gaussian mode, where the maximum energy is at the center of the pulse, and the doughnut mode, where the energy is minimum at the pulse center and concentrated in a ring around the pulse center. The problem is thus axisymmetric with respect to the z-axis.

Thermal field

Heat from a laser pulse with temporal profile, $Y(t)$, and radial intensity distribution, $Q(r)$, is absorbed in the surface plane of an elastic half-space (r, θ, z) with the z -axis directed into the half-space. The resulting thermal field, $T = T(r, z, t)$, is derived from the following temperature problem:

$$\frac{\partial^2 T}{\partial r^2} + \frac{1}{r} \frac{\partial T}{\partial r} + \frac{\partial^2 T}{\partial z^2} = \frac{1}{\alpha} \frac{\partial T}{\partial t} \quad \text{for } r > 0, z > 0, t > 0 \quad (1)$$

$$T = 0 \quad \text{at } t = 0, \forall r, z \quad (2)$$

$$\frac{\partial T}{\partial z} = -\frac{Y(t)Q(r)}{K} \quad \text{on } z = 0, t > 0 \quad (3)$$

Contributed by the Applied Mechanics Division of THE AMERICAN SOCIETY OF MECHANICAL ENGINEERS for publication in the ASME JOURNAL OF APPLIED MECHANICS.

Discussion on this paper should be addressed to the Technical Editor, Professor Lewis T. Wheeler, Department of Mechanical Engineering, University of Houston, Houston, TX 77204-4792, and will be accepted until four months after final publication of the paper itself in the ASME JOURNAL OF APPLIED MECHANICS.

Manuscript received by the ASME Applied Mechanics Division, Feb. 18, 1994; final revision, Oct. 26, 1994. Associate Technical Editor: M. Taya.

$$\frac{\partial T}{\partial r} = 0 \quad \text{at} \quad r = 0, t > 0 \quad (4)$$

$$T \rightarrow 0 \quad \text{as} \quad r, z \rightarrow \infty. \quad (5)$$

In Eq. (1), α stands for the thermal diffusivity and in Eq. (3) K represents the thermal conductivity. Note that the assumption of a surface source given by Eq. (3) is appropriate for laser heating of metals where beam absorption occurs to depths of the order of 10 nm to 100 nm (Englisch, 1977).

The solution to Eqs. (1)–(5) may be written as

$$T(r, z, t) = \frac{\alpha}{K} \int_{\tau=0}^t \int_{r'=0}^{\infty} Y(\tau) Q(r') \times g(r, z, t - \tau | r', 0, 0) dr' d\tau \quad (6a)$$

where

$$g(r, z, t - \tau | r', 0, 0) = \frac{2r'}{\pi} \int_{\beta=0}^{\infty} \int_{\eta=0}^{\infty} \beta J_o(\beta r) J_o(\beta r') \times \exp\{-\alpha(\beta^2 + \eta^2)(t - \tau)\} \cos(\eta z) d\eta d\beta \quad (6b)$$

and $Y(t)$ is a dimensionless function of time.

Thermal Stress Problem

The thermoelastic stress field, σ_{ij} , is the sum of particular stresses, σ_{ij}^p , and homogeneous stresses σ_{ij}^h

$$\sigma_{ij} = \sigma_{ij}^p + \sigma_{ij}^h. \quad (7)$$

The particular solution results from the thermal field in the material but does not satisfy all of the boundary conditions. The homogeneous solution (designated with the superscript h) is

superposed onto the particular solution so as to cause the solution to satisfy the following boundary conditions:

$$\sigma_{zz}(r, 0, t) = 0; \quad \sigma_{rz}(r, 0, t) = 0. \quad (8)$$

Stress Field Corresponding to Particular Solution. The particular solution is derived using the method of the displacement potential (Nowacki, 1986). The stress field σ_{ij}^p is derived from the displacement potential, φ , using the following relations:

$$\sigma_{rr}^p = -2\mu \left[\frac{1}{r} \frac{\partial}{\partial r} + \frac{\partial^2}{\partial z^2} \right] \varphi; \quad \sigma_{\theta\theta}^p = -2\mu \left[\frac{\partial^2}{\partial r^2} + \frac{\partial^2}{\partial z^2} \right] \varphi;$$

$$\sigma_{zz}^p = -2\mu \left[\frac{1}{r} \frac{\partial}{\partial r} + \frac{\partial^2}{\partial r^2} \right] \varphi; \quad \sigma_{rz}^p = 2\mu \frac{\partial^2 \varphi}{\partial r \partial z} \quad (9a-d)$$

where $\mu = E/2(1 + \nu)$. Here, μ is the shear modulus, E is Young's modulus, and ν is Poisson's ratio. The displacement potential is related to the thermal field through

$$\nabla^2 \varphi = mT \quad (10a)$$

where

$$m = \left(\frac{1 + \nu}{1 - \nu} \right) \kappa \quad (10b)$$

and κ is the coefficient of linear thermal expansion. Inserting Eqs. (6) into Eq. (10a) and taking the Laplace transform of the resulting expression, with the Laplace transforms denoted by an overbar, gives

Nomenclature

a = dimensionless shape parameter affecting negative skewness of temporal profile	z = normal position variable	$\varphi(r, z, p)$ = Laplace transform of displacement potential
b = dimensionless shape parameter affecting pulse activation time	$C(t; \beta)$ = function defined by Eq. (31)	$\Phi(r, z, t)$ = Love function
c = dimensionless shape parameter affecting positive skewness of temporal profile	$D(t; \beta)$ = function defined by Eq. (33)	Dimensionless quantities
d = characteristic beam radius	E = Young's modulus	r^* = dimensionless radial spatial variable
f = fraction of mode structure containing the Gaussian source	$G(z, t - \tau \beta)$ = function defined by Eq. (18b)	t^* = dimensionless time
$g(r, z, t - \tau r', 0, 0)$ = function defined by Eq. (6b)	K = thermal conductivity	t_r^* = dimensionless pulse rise time
$h(\beta; f)$ = function defined by Eq. (23b)	K_c = parameter related to characteristic beam radius	z^* = dimensionless normal position variable
m = material parameter defined by Eq. (10b)	$Q(r)$ = radial intensity distribution	$G^*(z^*, t^* - \tau^* \beta^*)$ = dimensionless function defined by Eq. (18b)
p = Laplace transform variable	$T(r, z, t)$ = temperature field	$T^*(r^*, z^*, t^*)$ = dimensionless temperature field
q_o = maximum incident flux for Gaussian source	$Y(t)$ = temporal pulse profile (dimensionless)	$Y(\tau^*)$ = temporal profile in terms of dimensionless temporal integration variable
r = radial spatial variable	α = thermal diffusivity	$\sigma_{ij}^*(r^*, z^*, t^*)$ = dimensionless stress field
t = time	β = integration variable	τ^* = dimensionless temporal integration variable
t_r = pulse rise time	η = integration variable	$\psi(r^*, z^*, t^* - \tau^* f)$ = function defined by Eq. (36b)
	κ = coefficient of thermal expansion	
	λ = parameter defined by Eq. (23a)	
	μ = shear modulus	
	ν = Poisson's ratio	
	$\sigma_{ij}(r, z, t)$ = stress field	
	τ = temporal integration variable	
	$\varphi(r, z, t)$ = displacement potential	

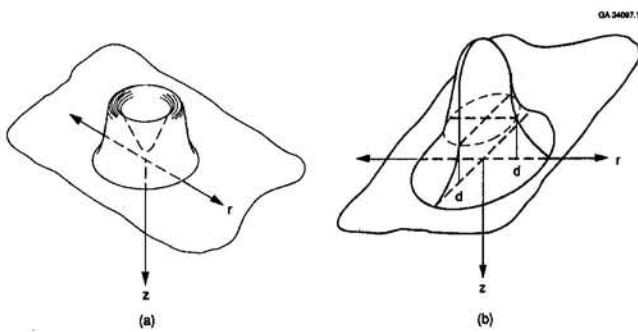


Fig. 1 (a) Mixed source ($f \ll 1$); (b) Gaussian source ($f = 1$)

$$\nabla^2 \bar{\varphi} = \frac{2m\alpha}{\pi K} \int_{r'=0}^{\infty} r' \bar{Y}(p) Q(r') \times \left\{ \int_{\beta=0}^{\infty} \int_{\eta=0}^{\infty} \frac{\beta J_o(\beta r) J_o(\beta r') \cos(\eta z)}{p + \alpha(\beta^2 + \eta^2)} d\eta d\beta \right\} dr'. \quad (11)$$

By inspection, Eq. (11) has the following particular integral:

$$\bar{\varphi} = -\frac{2m\alpha}{\pi K} \int_{r'=0}^{\infty} r' \bar{Y}(p) Q(r') \times \left\{ \int_{\beta=0}^{\infty} \int_{\eta=0}^{\infty} \frac{\beta J_o(\beta r) J_o(\beta r') \cos(\eta z)}{(\beta^2 + \eta^2)[p + \alpha(\beta^2 + \eta^2)]} d\eta d\beta \right\} dr'. \quad (12)$$

Equation (12) may be more conveniently written as

$$\bar{\varphi} = -\frac{2m\alpha}{\pi K} \int_{r'=0}^{\infty} r' \bar{Y}(p) Q(r') \times \left\{ \int_{\beta=0}^{\infty} \beta J_o(\beta r) J_o(\beta r') \left[\int_{\eta=0}^{\infty} \frac{\cos(\eta z)}{p(\beta^2 + \eta^2)} d\eta \right. \right. \\ \left. \left. - \int_{\eta=0}^{\infty} \frac{\cos(\eta z)}{p(\beta^2 + \eta^2)} d\eta \right] d\beta \right\} dr' \quad (13)$$

Evaluation of the integrals over the integration variable η gives

$$\bar{\varphi} = -\frac{m\alpha}{K} \int_{r'=0}^{\infty} r' Q(r') \beta J_o(\beta r) J_o(\beta r') \frac{\bar{Y}(p)}{p} \times \left[\frac{e^{-\beta z}}{\beta} - \frac{\exp\left\{-\sqrt{\frac{p+\alpha\beta^2}{\alpha}} z\right\}}{\sqrt{\frac{p+\alpha\beta^2}{\alpha}}} \right] d\beta dr' \quad (14)$$

In order to lend generality to the problem, the following function is chosen to represent the heat absorbed in the surface plane due to a pulse with mixed mode structure:

$$Q(r) = q_o [f + (1-f) K_c r^2] e^{-(K_c r^2)}. \quad (15)$$

Equation (15) models axial intensity distributions due to many high-power lasers that emit pulses having intensity distributions comprised of complex mixtures of modes. The fraction of the mode structure that contains the Gaussian mode is given by f , where

$$f = \frac{\text{TEM}_{oo}}{\text{TEM}_{oo} + \text{TEM}_{o1*}} \quad \begin{cases} \text{TEM}_{oo} \rightarrow \text{Gaussian mode} \\ \text{TEM}_{o1*} \rightarrow \text{doughnut mode} \\ 0 \leq f \leq 1 \end{cases} \quad (16)$$

and the designation TEM, which stands for transverse electromagnetic, describes the behavior of the laser resonator at its boundaries (Koechner, 1988). Figure 1(a) depicts the pulse

mode structure for $f \ll 1$. Figure 1(b) shows the Gaussian mode which corresponds to $f = 1$. The doughnut mode structure, which is the extreme case of Fig. 1(a), corresponds to $f = 0$. The parameter q_o corresponds to the maximum incident flux for a Gaussian source and contains information about pertinent surface physics, e.g., reflectivity, morphology, etc. The parameter K_c is related to the characteristic beam radius d through $K_c = d^{-2}$. The beam radius d represents the circular boundary within the Gaussian source that contains 63 percent of the total pulse power incident to the surface. Equation (15) results from the Laguerre-Gaussian distribution function which is a solution of the equation for standing waves in the laser resonator (see Koechner, 1988).

Note that the doughnut mode structure is useful for selected heat treating, cutting, and welding applications while the Gaussian mode structure is employed in the vast majority of laser cutting applications (Powell, 1993).

Using Eq. (15), we may write the following integral:

$$\int_{r'=0}^{\infty} r' Q(r') J_o(\beta r') dr' = \frac{q_o}{2K_c} \left[f + (1-f) \left(1 - \frac{\beta^2}{4K_c} \right) \right] e^{-(\beta^2/4K_c)}. \quad (17)$$

Performing the Laplace transform inversion on Eq. (14) and using Eq. (17) gives the desired form of the displacement potential:

$$\varphi = -\frac{m\alpha q_o}{2K_c K} \int_{\beta=0}^{\infty} \left[f + (1-f) \left(1 - \frac{\beta^2}{4K_c} \right) \right] e^{-(\beta^2/4K_c)} J_o(\beta r) \times \int_{\tau=0}^{\infty} Y(\tau) \left\{ e^{-\beta z} - \frac{1}{2} G(z, t-\tau | \beta) \right\} d\tau d\beta \quad (18a)$$

where

$$G(z, t-\tau | \beta) = \left[e^{\beta z} \text{erf} \left\{ \beta \sqrt{\alpha(t-\tau)} + \frac{z}{\sqrt{4\alpha(t-\tau)}} \right\} \right. \\ \left. + e^{-\beta z} \text{erf} \left\{ \beta \sqrt{\alpha(t-\tau)} - \frac{z}{\sqrt{4\alpha(t-\tau)}} \right\} \right. \\ \left. - 2 \sinh(\beta z) \right] \quad (18b)$$

and erf(x) is the error function. The stress field corresponding to the particular solution, derived with Eqs. (9) and (18a), is therefore

$$\sigma_{rr}^p = \lambda \int_{\beta=0}^{\infty} h(\beta; f) \int_{\tau=0}^{\infty} Y(\tau) \left[\left\{ \frac{G}{2} - e^{-\beta z} \right\} \frac{\beta J_1(\beta r)}{r} \right. \\ \left. + \left\{ \beta^2 e^{-\beta z} - \frac{1}{2} \frac{\partial^2 G}{\partial z^2} \right\} J_o(\beta r) \right] d\tau d\beta \quad (19)$$

$$\sigma_{\theta\theta}^p = \lambda \int_{\beta=0}^{\infty} h(\beta; f) \int_{\tau=0}^{\infty} Y(\tau) \left[\left\{ e^{-\beta z} - \frac{G}{2} \right\} \right. \\ \left. \times \left\{ \frac{\beta J_1(\beta r)}{r} - \beta^2 J_o(\beta r) \right\} \right. \\ \left. + \left\{ \beta^2 e^{-\beta z} - \frac{1}{2} \frac{\partial^2 G}{\partial z^2} \right\} J_o(\beta r) \right] d\tau d\beta \quad (20)$$

$$\begin{aligned}\sigma_{zz}^p &= \lambda \int_{\beta=0}^{\infty} h(\beta; f) \int_{\tau=0}^t Y(\tau) \\ &\quad \times \left\{ \frac{G}{2} - e^{-\beta z} \right\} \beta^2 J_o(\beta r) d\tau d\beta \quad (21)\end{aligned}$$

$$\begin{aligned}\sigma_{rz}^p &= -\lambda \int_{\beta=0}^{\infty} h(\beta; f) \int_{\tau=0}^t Y(\tau) \\ &\quad \times \left\{ \beta e^{-\beta z} + \frac{1}{2} \frac{\partial G}{\partial z} \right\} \beta J_1(\beta r) d\tau d\beta \quad (22)\end{aligned}$$

where

$$\lambda = \frac{m\mu\alpha q_o}{K_c K} \quad (23a)$$

and

$$h(\beta; f) = \left[f + (1-f) \left(1 - \frac{\beta^2}{4K_c} \right) \right] e^{-(\beta^2/4K_c)}. \quad (23b)$$

Note that Eqs. (19)–(22) satisfy only one of the boundary conditions since

$$\frac{\partial G}{\partial z} \Big|_{z=0} = -2\beta \quad (24)$$

and hence

$$\sigma_{rz}^p \Big|_{z=0} = 0. \quad (25)$$

However,

$$\sigma_{zz}^p \Big|_{z=0} \neq 0 \quad (26)$$

since

$$G \Big|_{z=0} = 2 \operatorname{erf} \{ \beta \sqrt{\alpha(t-\tau)} \}. \quad (27)$$

In order to remove the unwanted traction, we must superpose an isothermal solution onto Eqs. (19)–(22).

Stress Field Corresponding to Isothermal Solution. The stress field corresponding to the isothermal solution σ_{ij}^h is derived from the Love function $\Phi = \Phi(r, z, t)$ (Nowacki, 1986) using

$$\begin{aligned}\sigma_{rr}^h &= \frac{2\mu}{1-2\nu} \frac{\partial}{\partial z} \left[\nu \nabla^2 - \frac{\partial^2}{\partial r^2} \right] \Phi; \\ \sigma_{\theta\theta}^h &= \frac{2\mu}{1-2\nu} \frac{\partial}{\partial z} \left[\nu \nabla^2 - \frac{1}{r} \frac{\partial}{\partial r} \right] \Phi; \\ \sigma_{zz}^h &= \frac{2\mu}{1-2\nu} \frac{\partial}{\partial z} \left[(2-\nu) \nabla^2 - \frac{\partial^2}{\partial z^2} \right] \Phi; \\ \sigma_{rz}^h &= \frac{2\mu}{1-2\nu} \frac{\partial}{\partial r} \left[(1-\nu) \nabla^2 - \frac{\partial^2}{\partial z^2} \right] \Phi. \quad (28)\end{aligned}$$

The Love function, which satisfies the axisymmetric biharmonic equation, is written in terms of the two unknown functions $C(t; \beta)$ and $D(t; \beta)$ as

$$\Phi = \int_{\beta=0}^{\infty} [C(t; \beta) + z\beta D(t; \beta)] e^{-\beta z} J_o(\beta r) d\beta. \quad (29)$$

The shear stress σ_{rz}^h is

$$\begin{aligned}\sigma_{rz}^h &= \frac{2\mu}{1-2\nu} \int_{\beta=0}^{\infty} [C(t; \beta) + (\beta z - 2\nu) D(t; \beta)] \\ &\quad \times \beta^3 e^{-\beta z} J_1(\beta r) d\beta. \quad (30)\end{aligned}$$

Application of the zero shear stress boundary condition Eq. (8b) gives

$$C(t; \beta) = 2\nu D(t; \beta) \quad (31)$$

The normal stress σ_{zz}^h is

$$\sigma_{zz}^h = \frac{2\mu}{1-2\nu} \int_{\beta=0}^{\infty} D(t; \beta) (1 + \beta z) \beta^3 e^{-\beta z} J_o(\beta r) d\beta \quad (32)$$

Application of the remaining boundary condition Eq. (8a) to the sum of Eqs. (21) and (32) gives

$$\begin{aligned}D(t; \beta) &= \left[\frac{m\alpha q_o (1-2\nu)}{2\beta K_c K} \right] h(\beta; f) \\ &\quad \times \int_{\tau=0}^t Y(\tau) \operatorname{erfc} \{ \beta \sqrt{\alpha(t-\tau)} \} d\tau \quad (33)\end{aligned}$$

The remaining components of the isothermal solution are

$$\begin{aligned}\sigma_{rr}^h &= \frac{2\mu}{1-2\nu} \int_{\beta=0}^{\infty} \left[(1 - \beta z) \beta J_o(\beta r) \right. \\ &\quad \left. - (1 - 2\nu - \beta z) \frac{J_1(\beta r)}{r} \right] \beta^2 e^{-\beta z} D(t; \beta) d\beta \quad (34)\end{aligned}$$

$$\begin{aligned}\sigma_{\theta\theta}^h &= \frac{2\mu}{1-2\nu} \int_{\beta=0}^{\infty} \left[2\nu \beta J_o(\beta r) \right. \\ &\quad \left. + (1 - 2\nu - \beta z) \frac{J_1(\beta r)}{r} \right] \beta^2 e^{-\beta z} D(t; \beta) d\beta. \quad (35)\end{aligned}$$

Dimensionless Formulation. It is convenient to recast the problem in terms of the following dimensionless variables:

$$\begin{aligned}r^* &= r\sqrt{K_c}; \quad z^* = z\sqrt{K_c}; \quad t^* = 4\alpha K_c t; \\ \tau^* &= 4\alpha K_c \tau; \quad \beta^* = \beta/\sqrt{K_c} \\ \sigma_{ij}^* &= \left(\frac{4\sqrt{K_c} K}{m\mu q_o} \right) \sigma_{ij}; \quad T^* = \left(\frac{\sqrt{K_c} K}{q_o} \right) T\end{aligned}$$

The temperature solution Eqs. (6) may be written as

$$T^* = \frac{1}{\sqrt{4\pi}} \int_{\tau^*=0}^{t^*} Y(\tau^*) \psi(r^*, z^*, t^* - \tau^* | f) d\tau^* \quad (36a)$$

where

$$\begin{aligned}\psi(r^*, z^*, t^* - \tau^* | f) &= \left[f + (1-f) \right. \\ &\quad \times \left. \left\{ 1 - \frac{1}{1+t^*-\tau^*} \left(1 - \frac{r^{*2}}{1+t^*-\tau^*} \right) \right\} \right]\end{aligned}$$

$$\begin{aligned}&\exp \left\{ - \left(\frac{r^{*2}}{1+t^*-\tau^*} + \frac{z^{*2}}{t^*-\tau^*} \right) \right\} \\ &\times \frac{1}{\sqrt{t^*-\tau^*} [1+t^*-\tau^*]}. \quad (36b)\end{aligned}$$

The dimensionless thermal stress components are

$$\begin{aligned} \sigma_{rr}^* &= \int_{\beta^*=0}^{\infty} h(\beta^*; f) \int_{\tau^*=0}^{t^*} Y(\tau^*) \left[\left\{ \frac{G^*}{2} - e^{-\beta^* z^*} \right\} \right. \\ &\quad \times \frac{\beta^* J_1(\beta^* r^*)}{r^*} + \left\{ \beta^{*2} e^{-\beta^* z^*} - \frac{1}{2} \frac{\partial^2 G^*}{\partial z^{*2}} \right\} J_o(\beta^* r^*) \\ &\quad + \left\{ (1 - \beta^* z^*) \beta^* J_o(\beta^* r^*) \right. \\ &\quad \left. - (1 - 2\nu - \beta^* z^*) \frac{J_1(\beta^* r^*)}{r^*} \right\} \\ &\quad \times \beta^* e^{-\beta^* z^*} \operatorname{erfc} \left\{ \frac{\beta^* \sqrt{t^* - \tau^*}}{2} \right\} d\tau^* d\beta^* \quad (37) \end{aligned}$$

$$\begin{aligned} \sigma_{\theta\theta}^* &= \int_{\beta^*=0}^{\infty} h(\beta^*; f) \int_{\tau^*=0}^{t^*} Y(\tau^*) \left[\left\{ e^{-\beta^* z^*} - \frac{G^*}{2} \right\} \right. \\ &\quad \times \left\{ \frac{\beta^* J_1(\beta^* r^*)}{r^*} - \beta^{*2} J_o(\beta^* r^*) \right\} \\ &\quad + \left\{ \beta^{*2} e^{-\beta^* z^*} - \frac{1}{2} \frac{\partial^2 G^*}{\partial z^{*2}} \right\} J_o(\beta^* r^*) \\ &\quad + \left\{ 2\nu \beta^* J_o(\beta^* r^*) + (1 - 2\nu - \beta^* z^*) \frac{J_1(\beta^* r^*)}{r^*} \right\} \\ &\quad \times \beta^* e^{-\beta^* z^*} \operatorname{erfc} \left\{ \frac{\beta^* \sqrt{t^* - \tau^*}}{2} \right\} d\tau^* d\beta^* \quad (38) \end{aligned}$$

$$\begin{aligned} \sigma_{zz}^* &= \int_{\beta^*=0}^{\infty} \beta^{*2} h(\beta^*; f) J_o(\beta^* r^*) \int_{\tau^*=0}^{t^*} Y(\tau^*) \\ &\quad \times \left[\frac{G^*}{2} - e^{-\beta^* z^*} + e^{-\beta^* z^*} (1 + \beta^* z^*) \right. \\ &\quad \times \operatorname{erfc} \left\{ \frac{\beta^* \sqrt{t^* - \tau^*}}{2} \right\} d\tau^* d\beta^* \quad (39) \end{aligned}$$

$$\begin{aligned} \sigma_{rz}^* &= - \int_{\beta^*=0}^{\infty} \beta^* h(\beta^*; f) J_1(\beta^* r^*) \int_{\tau^*=0}^{t^*} Y(\tau^*) \\ &\quad \times \left[\beta^* e^{-\beta^* z^*} + \frac{1}{2} \frac{\partial G^*}{\partial z^*} - \beta^{*2} z^* e^{-\beta^* z^*} \right. \\ &\quad \times \operatorname{erfc} \left\{ \frac{\beta^* \sqrt{t^* - \tau^*}}{2} \right\} d\tau^* d\beta^* \quad (40) \end{aligned}$$

where $\operatorname{erfc}(x)$ stands for the complementary error function and G^* and its derivatives are listed in the Appendix.

Temporal Pulse Profile. The temporal profile of the pulse is

$$Y(t^*) = \left(\frac{t^*}{t_r^*} \right)^a \exp \{ -b(t^{*c} - t_r^{*c}) \} \quad (41)$$

where a , b , and c are temporal shape factors that control the extent of negative skewness of the pulse energy in time, pulse activation time, and positive skewness of the pulse energy in time, respectively. These parameters must be chosen so as to

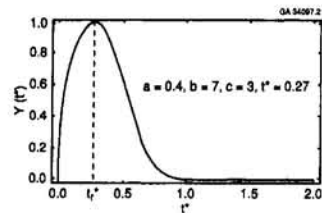


Fig. 2 Model of temporal pulse profile

ensure that the pulse activation time is significantly longer than the rate at which heat propagates through the material. Note that temporal pulse profiles similar to that in Eq. (41) have been proposed by Hetnarski and DeBolt (1991).

Equation (41) models temporal profiles from a laser that is either pulsed through radio frequency modulation of its power supply (Gardner, 1992), *Q*-switched, or mode-locked. It also models output from a laser that emits a continuous beam that is mechanically chopped outside of its resonator (Hector and Sheu, 1993). An oscilloscope trace of the temporal profile of a *Q*-switched Nd:YAG laser using a 6.3-mm diameter crystal may be found in Kim and Hector (1991). A similar trace from a mode locked Nd:YAG laser using a 4-mm diameter crystal may be found in Hector et al. (1992).

The dimensionless pulse rise time, t_r^* , or the time required for the pulse to reach peak power, is

$$t_r^* = \left(\frac{a}{bc} \right)^{c^{-1}}. \quad (42)$$

Results and Discussion

The model temporal profile shown in Fig. 2 was used to generate the thermal stress field in an elastic half-space. Values of a , b , and c were chosen to be 0.4, 7, and 3, respectively, since they give a negatively skewed profile that resembles the temporal output from many pulsed lasers. The dimensionless rise time is calculated from Eq. (42) to be $t_r^* = 0.27$ and the pulse decays to minimum energy by $t^* = 1$. Equations (37)–(40) were evaluated with standard numerical integration routines.

The steady-state thermoelastic response of the half-space due to continuous surface sources is examined first since it will provide a basis against which the more complicated effects due to transient heating may be compared. Figures 3 depict the

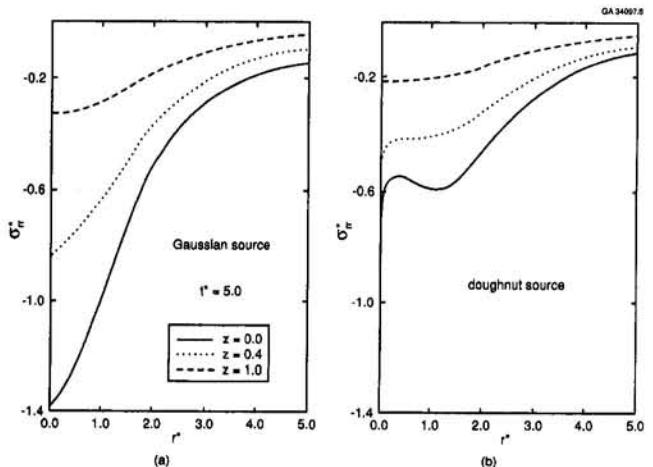


Fig. 3 Steady-state variation of radial stress with radial distance from axis at selected depths and time for (a) $f = 1$; (b) $f = 0$

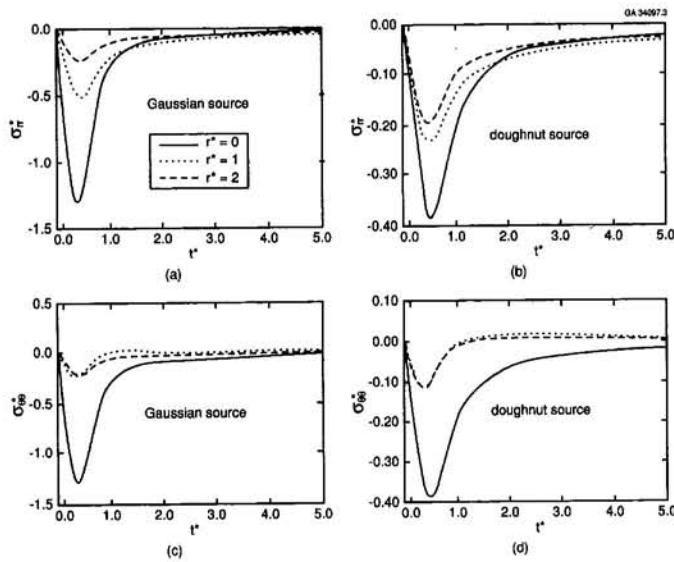


Fig. 4 Evolution of surface stresses at selected radial positions (a) σ_r^* for $f = 1$; (b) σ_r^* for $f = 0$; (c) $\sigma_{\theta\theta}^*$ for $f = 1$; (d) $\sigma_{\theta\theta}^*$ for $f = 0$

steady state radial stress variation with radial distance from the axis and at selected depths, due to Gaussian and doughnut surface sources, for $Y(t^*) = 1$. Figure 3(a) shows that the surface of the material experiences the largest compressive radial stress since surface elements beneath the beam expand against "cooler" surface elements outside of the edge of the beam. Note that the spatial distribution of the radial stress field resembles the radial distribution of the source, as expected. Figure 3(a) is in qualitative agreement with the results of Welsh et al. (1988). Similar observations are appropriate for the radial stress due to the doughnut source (as shown in Fig. 3(b)).

Considered next is the surface stress distribution both in time and with radial position due to heat from a pulse with temporal profile given by Eq. (41) with the specified temporal shape factors. Figures 4 show the evolution of surface stresses σ_r^* and $\sigma_{\theta\theta}^*$ at selected radial positions relative to the center of the pulse. Figures 4(a) and 4(b) compare the radial surface stresses due to the Gaussian source ($f = 1$) and doughnut source ($f = 0$), respectively. As is the case with steady state heating, compressive radial stresses develop on the surface in response to the manner in which energy is deposited to the surface. The radial stress becomes increasingly compressive during the time when the pulse is activated. Shortly after the pulse reaches maximum energy, a maximum compressive stress occurs in the surface beneath the center of the beam followed by a decay to zero stress as the pulse decays to minimum energy. Note that radial positions that are removed from the axis experience a similar variation in radial stress although the maximum compressive stresses are much lower than those at the center. The major difference in the evolution of radial surface stresses due to the Gaussian and doughnut sources is that the magnitude of the maximum compressive stresses due to the latter are considerably less than the former (and hence the reason for the differing vertical scales between Figs. 4(a) and 4(b)). The energy distribution due to the Gaussian source is much more concentrated around the center of the beam. This is why the Gaussian source is the most popular mode structure for materials processing applications. Similar radial surface stress distributions are observed in Figs. 4(c) and 4(d) for $\sigma_{\theta\theta}^*$ due to the Gaussian and doughnut sources.

Figures 5 show the radial distribution of surface stresses at selected times during pulse activation for the Gaussian and doughnut sources. The maximum (compressive) radial surface stress is at the center of the beam since surface elements rapidly

expand in response to the absorbed energy but are constrained by "cooler" surface elements surrounding the center. The radial stress decreases from the center since the energy in the Gaussian source decreases in a similar fashion. Even though the pulse has delivered its peak power by $t^* = 0.27$, the maximum radial stress continues to increase as a short time interval is required for the material to develop thermal stresses in response to the absorbed energy. At times $t^* = 1, 3$, the pulse has decayed to minimum energy and σ_r^* exhibits a corresponding decay back to zero stress. The radial surface stress due to the doughnut source in Fig. 5(b) behaves in a similar fashion except that the maximum compressive stress it creates at the beam center is smaller in magnitude than that due to the Gaussian source in Fig. 5(a). A secondary maximum in compressive stress is reached at a point that is removed from the beam center. This is due to surface elements being compressed in this region in response to the largest energy concentration delivered by the doughnut source.

The imposition of the zero shear stress boundary condition (Eq. 8(b)) allows one to investigate only the radial and circumferential stress distributions in the surface plane. It is of interest to investigate the subsurface stress field since a shear stress distribution is developed and this is the purpose of Figs. 6-8.

Figures 6 show the evolution of the subsurface stress field at a depth $z^* = 1.5$ and at selected radial positions relative to the axis due to heat from a Gaussian source. During pulse activation, elements in the vicinity of the axis develop small tensile radial, circumferential, and shear stresses while experiencing compressive normal stresses. As heat propagates from the surface into the material substrate, shear stresses develop in response to the manner in which the rapid expansion of surface elements is prevented by colder regions in the surface. Hence, subsurface material elements deform as a consequence of the manner in which surface elements deform and from the fact that those elements beneath the surface are further constrained by colder regions deeper into the substrate and by adjacent elements. Elements proximate to the axis deform in the manner shown in the inset figure in Fig. 6(d). Note that the maximum value of σ_{rz}^* on the axis is achieved at a time that is nearly twice the pulse rise time due to the finite time required to heat the material at $z^* = 1.5$, and the material to subsequently deform (see Fig. 6(c)). Also, by symmetry, $\sigma_{rz}^* = 0$ on the axis as indicated by the solid line in Fig. 6(d). As surface elements relax their accumulated strains during pulse decay from peak

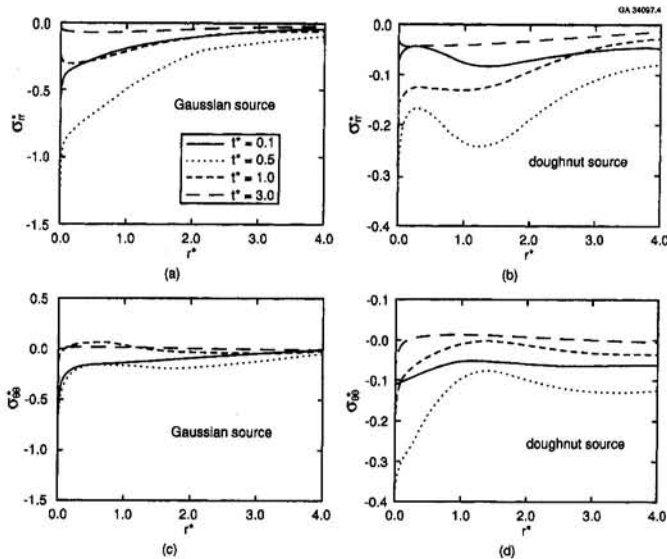


Fig. 5 Radial distribution of surface stresses at selected times (a) σ_r^* for $f = 1$; (b) σ_r^* for $f = 0$; (c) $\sigma_{\theta\theta}^*$ for $f = 1$; (d) $\sigma_{\theta\theta}^*$ for $f = 0$

power, σ_r^* , $\sigma_{\theta\theta}^*$, and $\sigma_{\theta\theta}^*$ subsurface stresses achieve maximum compressive values and then decay to zero.

Figures 7 show the radial distribution of the stress field at $z^* = 1.5$ and selected times due to a Gaussian surface source. Maximum tensile stresses accumulate at points on the axis for both σ_r^* and $\sigma_{\theta\theta}^*$ and decrease along points removed from the axis. Tensile stresses continue to increase along radial positions until the effect of pulse deactivation causes them to gradually decrease to compressive values, as shown by those curves at $t^* = 1, 3$ in Figs. 7(a) and 7(b). Note in Fig. 7(d) that a maximum in the shear stress at $t^* = 0.5$ is reached near $r^* = 1$.

Figure 8(a) shows the axial variation of radial stress due to a Gaussian source at selected times. Extreme values of the subsurface tensile stresses occur as the pulse reaches its rise time and shortly thereafter. Compressive stresses occur during the time when the pulse deactivates. Note that the $t^* = 0.10$,

0.27 curves intersect the ordinate axis at $\sigma_r^* = -0.62, -1.18$, respectively, and thus do not continue on to infinity, as might be inferred from the scale used to plot the figures. Figure 8(b) shows that the radial stress field is compressive at $r^* = 1$ for the times indicated in the figure.

Concluding Remarks

The thermal stress field due to a single laser pulse with specified axial and temporal profiles has been derived for an elastic half-space. Compressive stresses develop in the surface plane of the material while the effect of subsurface shear stresses and a compressive normal stress produces tensile radial and circumferential stress fields near the axis until material response to pulse deactivation occurs.

Although the assumption of an elastic response is reasonable for many laser heated materials, there are situations where a

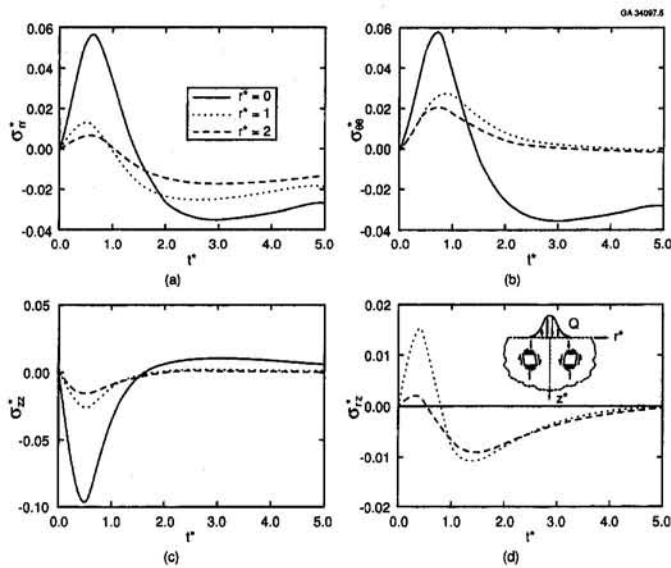


Fig. 6 Evolution of stress field at $z^* = 1.5$ and selected radial positions due to Gaussian source (a) σ_r^* ; (b) $\sigma_{\theta\theta}^*$; (c) $\sigma_{\theta\theta}^*$; (d) $\sigma_{\theta\theta}^*$

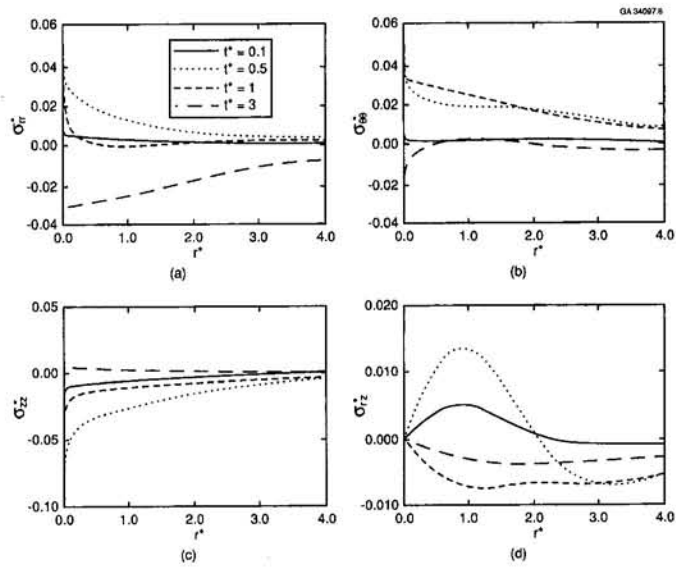


Fig. 7 Radial distribution of stress field at $z^* = 1.5$ and selected times due to Gaussian source (a) σ_r^* ; (b) σ_θ^* ; (c) σ_z^* ; (d) σ_{rz}^*

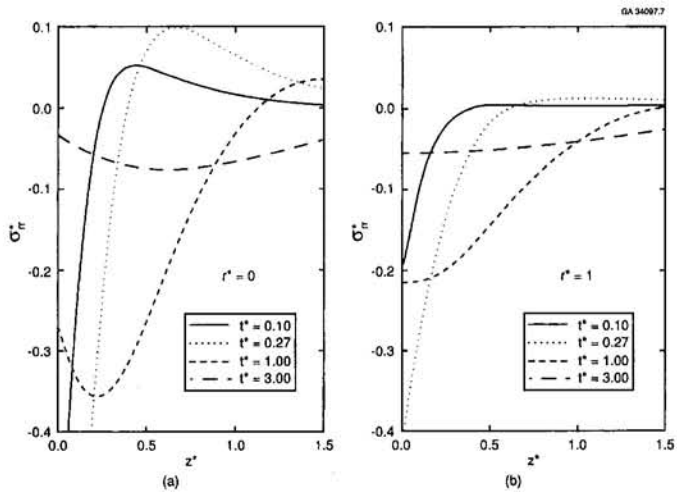


Fig. 8 Axial variation of radial stress due to Gaussian source at selected times for (a) $r^* = 0$; (b) $r^* = 1$

material is preheated to a significant fraction of its melting temperature in order to improve beam coupling to the material. The preheated material is then exposed to a pulsed heat source to effect a metallurgical transformation or to remove small quantities through the thermocapillary effect during melting or through evaporation. In this situation, a viscoelastic constitutive model is more appropriate and work is underway to incorporate viscous effects into the model. It is also the case that very few materials processing applications involve single pulse heating of a material. In the vast majority of applications, a train of pulses is delivered to the surface and hence localized heating and subsequent thermal stresses are much more severe. Models of both stationary and moving pulsed heat sources are currently being developed for this more realistic situation. There are important applications where thin coatings are heated with a pulsed laser. To estimate the thermal stress fields in these situations, a problem where the exposed region is of a finite thickness, rather than semi-infinite, is under development. Finally, many laser processing applications involve material removal and work

is underway to understand the thermal stress distribution in situations where phase change with associated material removal occurs (see Hector and Sheu (1993) and Hector and Sheu (1991) for examples of material removal processes involving a pulsed laser).

Acknowledgment

The authors wish to thank K. B. Lippert of the Applied Math and Computer Technology Division at Alcoa Technical Center for kindly generating Figs. 3-8.

References

- Englisch, W. R., 1977, "Laser Processing of Materials," *Battelle Information Journal*, Vol. 15, pp. 7-19.
- Gardner, P., 1992, Coherent, Inc. private communication with L. G. Hector, Jr.

Geller, M. A., Gorelik, G. E., Pavlyukevich, N. V., and Parnas, A. L., 1986, "Calculation of Temperature and Thermal Stresses in Quenching Steel with Laser and Electron Beams," *Physics and Chemistry of Materials Treatment*, Vol. 20, No. 4, pp. 314-316, (in Russian).

Germanovich, L. N., Kill, I. D., and Tsodokova, N. S., 1988, "Thermoelastic Stresses in a Half-Space Heated by Concentrated Energy Flux," *Applied Mathematics and Mechanics*, Vol. 52, No. 4, pp. 525-533, (in Russian).

Hector, Jr., L. G., Kim, W.-S., and Özisik, M. N., 1992, "Hyperbolic Heat Conduction Due to a Mode-Locked Laser Pulse Train," *International Journal of Engineering Science*, Vol. 30, No. 12, pp. 1731-1744.

Hector, L. G. Jr., and Sheu, S., 1991, Brightness Enhancement with Textured Roll, United States Letters Patent #4,996,113, United States Patent and Trademark Office, Arlington, VA.

Hector, Jr., L. G., and Sheu, S., 1993, "Focused Energy Beam Work Roll Surface Texturing Science and Technology," *Journal of Materials Processing and Manufacturing Science*, Vol. 2, No. 1, pp. 63-117.

Hetnarski, R. B., and DeBolt, F., 1991, "Analysis of Laser Produced Stresses in a Structure," *Proceedings of the Second Pan American Congress of Applied Mechanics*, P. Kittl, D. Mook, G. Reinke, eds., sponsored by the American Academy of Mechanics and published by the PACAM 2 Congress Committee, Valparaiso, Chile, pp. 364-367.

Kim, W.-S., and Hector, Jr., L. G., 1991, "The Influence of Temporal Pulse Profile on Hyperbolic Heat Conduction in Materials Subjected to Repetitively Pulsed Laser Radiation," *Mechanics Research Communications*, Vol. 18, No. 6, pp. 419-428.

Koechner, W., 1988, *Solid-State Laser Engineering*, 2nd ed. Springer-Verlag, New York.

Nonhof, C. J., 1988, *Materials Processing with Nd-Lasers*, Electrochemical Publications Ltd., Ayr, Scotland.

Nowacki, W., 1986, *Thermoelasticity*, 2nd ed. Pergamon, New York.

Oswald, Jr., R. B., McLean, F. B., Schallhorn, D. R., and Buxton, L. D., 1971, "One-Dimensional Thermoelastic Response of Solids to Pulsed Energy Deposition," *Journal of Applied Physics*, Vol. 42, No. 9, pp. 3463-3473.

Popov, V. P., Lanin, A. G., Kolesov, V. S., and Bochkov, A. N., 1983, "Determination of Thermoplastic Surface Strains by the Local Heating Method," *Physics and Chemistry of Materials Processing*, Vol. 17, No. 6, pp. 70-73.

Powell, J., 1993, *CO₂ Laser Cutting*, Springer-Verlag, New York.

Steen, W. M., 1991, *Laser Material Processing*, Springer-Verlag, New York.

Volchenok, I. A., and Rudin, G. I., 1988, "Thermoelastic Stresses in a Multilayer Plate Upon Action of Laser Radiation," *Journal of Engineering Physics*, Vol. 55, No. 5, pp. 1286-1290.

Welsh, L. P., Tuchman, J. A., and Herman, I. P., 1988, "The Importance of Thermal Stresses and Strains Induced in Laser Processing with Focused Gaussian Beams," *Journal of Applied Physics*, Vol. 64, No. 11, pp. 6274-6286.

APPENDIX

Dimensionless Form of G and Associated Derivatives

The dimensionless form of G is G^* , where

$$G^* = \left[e^{\beta^* z^*} \operatorname{erf} \left\{ \frac{\beta^*}{2} \sqrt{t^* - \tau^*} + \frac{z^*}{\sqrt{t^* - \tau^*}} \right\} \right. \\ \left. + e^{-\beta^* z^*} \operatorname{erf} \left\{ \frac{\beta^*}{2} \sqrt{t^* - \tau^*} - \frac{z^*}{\sqrt{t^* - \tau^*}} \right\} \right. \\ \left. - 2 \sinh(\beta^* z^*) \right] \quad (A1)$$

$$\frac{\partial G^*}{\partial z^*} = \beta^* \left[e^{\beta^* z^*} \operatorname{erf} \left\{ \frac{\beta^*}{2} \sqrt{t^* - \tau^*} + \frac{z^*}{\sqrt{t^* - \tau^*}} \right\} \right. \\ \left. - e^{-\beta^* z^*} \operatorname{erf} \left\{ \frac{\beta^*}{2} \sqrt{t^* - \tau^*} - \frac{z^*}{\sqrt{t^* - \tau^*}} \right\} \right. \\ \left. - 2 \cosh(\beta^* z^*) \right] \quad (A2)$$

$$\frac{\partial^2 G^*}{\partial z^{*2}} = \beta^* \left[\frac{4}{\sqrt{\pi(t^* - \tau^*)}} \right. \\ \left. \times \exp \left\{ - \left(\frac{\beta^{*2}}{4} (t^* - \tau^*) + \frac{z^{*2}}{(t^* - \tau^*)} \right) \right\} \right. \\ \left. + \beta^* e^{\beta^* z^*} \operatorname{erf} \left\{ \frac{\beta^*}{2} \sqrt{t^* - \tau^*} + \frac{z^*}{\sqrt{t^* - \tau^*}} \right\} \right. \\ \left. + \beta^* e^{-\beta^* z^*} \operatorname{erf} \left\{ \frac{\beta^*}{2} \sqrt{t^* - \tau^*} - \frac{z^*}{\sqrt{t^* - \tau^*}} \right\} \right. \\ \left. - 2\beta^* \sinh(\beta^* z^*) \right] \quad (A3)$$

T. L. Warren¹

Department of Mechanical and
Aerospace Engineering
Arizona State University,
Tempe, AZ 85287-6106
Assoc. Mem. ASME

A. Majumdar

Department of Mechanical and
Environmental Engineering,
University of California,
Santa Barbara, CA 93106
Assoc. Mem. ASME

D. Krajcinovic

Department of Mechanical and
Aerospace Engineering,
Arizona State University,
Tempe, AZ 85287-6106
Fellow ASME

A Fractal Model for the Rigid-Perfectly Plastic Contact of Rough Surfaces

In this study a continuous asymptotic model is developed to describe the rigid-perfectly plastic deformation of a single rough surface in contact with an ideally smooth and rigid counter-surface. The geometry of the rough surface is assumed to be fractal, and is modeled by an effective fractal surface compressed into the ideally smooth and rigid counter-surface. The rough self-affine fractal structure of the effective surface is approximated using a deterministic Cantor set representation. The proposed model admits an analytic solution incorporating volume conservation. Presented results illustrate the effects of volume conservation and initial surface roughness on the rigid-perfectly plastic deformation that occurs during contact processes. The results from this model are compared with existing experimental load displacement results for the deformation of a ground steel surface.

1 Introduction

The geometry and structure of the interface between two solid surfaces in contact is of fundamental importance to the study of friction, wear, lubrication, and thermal and electrical conductivity. It is well known, that in a general case the actual contact between two real solids is realized only over a small fraction of the surface in a discrete number of areas. Consequently, the real area of contact is only a fraction of the apparent (nominal) area, and the parameters of the actual contact regions depend on the curvature and roughness of the contacting surfaces. Early studies of the contact of rough surfaces are described in Archard (1957), Bowden and Tabor (1951, 1964), and Greenwood and Williamson (1966). More recent studies are due to Johnson (1985), Liu et al. (1986), Chang et al. (1987), Bhushan (1990), Borodich and Mosolov (1991, 1992), Majumdar and Bhushan (1991), Majumdar et al. (1991), Handzel-Powierza et al. (1992), and Bhushan and Majumdar (1992).

In general, the structure of most surfaces appears to be random on a small scale. Statistical parameters such as the root-mean square (r.m.s.) of surface height σ , slope σ' and curvature σ'' are conventionally used to characterize the surface roughness. Several theories based on these parameters have been developed to model rough surfaces in contact. The most popular of these is the Greenwood and Williamson (G & W) (1966) model which is based on the assumption that the surface is composed of hemispherical asperities having equal radii given by $1/\sigma''$. The centers of asperities are distributed normally about the mean plane, and it is assumed that the contacting asperities deform elastically according to the Hertz contact theory. Recently, Chang et al. (1987) modified the original G & W (1966) model to incorporate the effects of volume conservation when an asperity deforms both elastically and plastically. Several other theories of friction, wear, and lubrication based on the G & W (1966) model have been developed, and are discussed

by Bhushan (1990). However, as pointed out by Majumdar and Bhushan (1991), Majumdar et al. (1991), and Bhushan and Majumdar (1992), the parameters σ , σ' , and σ'' are not unique to a surface, and they depend on the resolution and scan length of the roughness measuring instrument. Thus, the assumption of a surface being composed of hemispherical asperities belonging to a single length scale is an over-simplification of the real surface which contains several roughness scales.

The multiscale nature of the surface roughness geometry suggests the use of a fractal representation. Lately the contact of rough surfaces has been approximated by fractal models (Liu et al., 1986; Borodich and Mosolov, 1991, 1992; Majumdar and Bhushan, 1991; Majumdar et al., 1991; Bhushan and Majumdar, 1992). The method developed by Majumdar and Bhushan (1991), Majumdar et al. (1991), and Bhushan and Majumdar (1992) uses the Weierstrass-Mandelbrot function, as described by Mandelbrot (1982), to simulate surface roughness. Modified Hertz equations are then employed to model the elasto-plastic deformation of the surface. In Liu et al. (1986), a fractal surface is constructed using the Cantor set, which is used to simulate the electrical contact properties of a rough surface interface. Similarly, the model developed by Borodich and Mosolov (1991, 1992) is also based on the Cantor set, and provides asymptotic expressions for a fractal die penetrating either a rigid perfectly plastic, or elastic half-space. Hill's solution (Hill, 1950) for a punch in contact with a rigid-perfectly plastic half-space is employed to estimate plastic deformation. For elastic deformation, the surface of the half-space is modeled using a Winkler foundation (Cook and Young, 1985) which corresponds to a distribution of mutually independent linear springs.

As shown by Johnson (1985) and Majumdar et al. (1991), the contact between two rough surfaces may possibly be modeled as the contact of an effective composite surface with a rigid flat surface (see Appendix). Hence, a solution for the deformation of an equivalent surface generated using the Cantor set can be modified for the problem at hand. However, in this study only the case of a single rough surface in contact with a rigid flat surface is considered, therefore, the construction of an effective composite surface is not required. The method developed by Borodich and Mosolov (1991, 1992) is generalized and extended in this paper by allowing the fractal surface to deform. It is assumed that the fractal surface behaves as an ideally rigid-perfectly plastic material, which is in contact with a smooth, rigid, and frictionless half-space. According to this

¹ Currently at Sandia National Laboratories, Albuquerque, NM 87185-0312.

Contributed by the Applied Mechanics Division of THE AMERICAN SOCIETY OF MECHANICAL ENGINEERS for publication in the ASME JOURNAL OF APPLIED MECHANICS.

Discussion on this paper should be addressed to the Technical Editor, Professor Lewis T. Wheeler, Department of Mechanical Engineering, University of Houston, Houston, TX 77204-4792, and will be accepted until four months after final publication of the paper itself in the ASME JOURNAL OF APPLIED MECHANICS.

Manuscript received by the ASME Applied Mechanics Division, Nov. 3, 1993; final revision, Aug. 1, 1994. Associate Technical Editor: J. T. Jenkins.

new model, the material volume below the fractal surface can be conserved during the plastic deformation process. Furthermore, the applied Cantor set representation may also provide a simple framework for examining the effects of asperity interaction during frictional sliding which is a topic of much research.

2 Characterization of a Fractal Surface

Following Borodich and Mosolov (1991, 1992), the Cantor set surface shown in Fig. 1 is constructed by joining the segments obtained from successive stages of the Cantor set. At each stage of construction, the middle sections of the initial segments are removed so that the lengths of the remaining segments are $1/f_x$ times the length of the initial segments, where $f_x > 1$. The depth of the recesses (measured from the last step) at the $(n+1)$ th construction step of the fractal surface is $1/f_z$ times less than the depth at the n th step, where $f_z > 1$. Hence, the horizontal length of the $(n+1)$ th step is

$$L_{n+1} = \left(\frac{1}{f_x}\right) L_n = \left(\frac{1}{f_x}\right)^{n+1} L_0, \quad (1)$$

while the recess depth is

$$h_{n+1} = \left(\frac{1}{f_z}\right) h_n = \left(\frac{1}{f_z}\right)^{n+1} h_0. \quad (2)$$

As pointed out by Mandelbrot (1985) and later by Majumdar et al. (1991), most rough surfaces have a self-affine scaling structure, which implies that length scales change by different amounts in different directions. This is also evident with the case of the structure constructed in Fig. 1. Because of this fact, methods used for self-similar fractals are not in general applicable to self-affine structures as described by Mandelbrot (1985). However, a relationship between the self-affine Cantor set structure, and a self-affine surface profile $z(x)$ may be conjectured through the use of the structure function

$$S(\tau) = \langle [z(x + \tau) - z(x)]^2 \rangle, \quad (3)$$

where $S(\tau)$ physically represents the mean square of the difference in height expected over any spatial distance τ , and $\langle \cdot \rangle$ implies averaging over the statistical ensemble of $z(x)$. It has been shown by Berry (1978) that the structure function for a fractal profile can be expressed in the form

$$S(\tau) = \Lambda^{2D-2} \tau^{4-2D}. \quad (4)$$

In (4), D is the self-affine fractal dimension, and Λ is a charac-

teristic parameter of the fractal function referred to as the topography. The two parameters D and Λ completely characterize the fractal profile and are independent of τ and, thus, scale independent. The self-affine fractal dimension D of a surface profile is dimensionless and falls in the range $1 < D < 2$, while the topography Λ can take on any positive value and has the dimension of length. Furthermore, the r.m.s. height σ of the surface profile is related to the topography through the relation (Feder, 1988)

$$\sigma^2 = \frac{\Lambda^{2D-2} L_c^{4-2D}}{4 - 2D}, \quad (5)$$

where L_c is the correlation length of the profile. Using (3) and (4) and the fact Λ is a constant, it follows that for self-affine scaling

$$\Delta z \sim \Delta x^{2-D}, \quad (6)$$

where $2-D$ is equivalent to the well-known Hurst exponent.

As shown by Borodich and Mosolov (1992), a self-affine fractal dimension for the Cantor set structure in Fig. 1 can be obtained based on statistical considerations. At the n th generation, the Cantor set surface contains $N = s^n$ segments, each of length

$$\delta_n = \left(\frac{1}{s f_x}\right)^n L_0, \quad (7)$$

where the parameter s corresponds to the number of asperities on a repeating segment. For example, the Cantor set surfaces in Figs. 1 and 2 have $s = 2$ and $s = 3$, respectively. Changing the parameter s provides a generalization for the construction of an infinite number of different structures based on the Cantor set independent of the parameters f_x and f_z .

During an iterative step in the construction of the Cantor set surface, scaling in the horizontal direction is

$$\Delta x_{n+1} = \left(\frac{1}{s f_x}\right) \Delta x_n. \quad (8)$$

In the vertical direction, the corresponding fluctuations Δz_n at the n th generation can be defined by considering the probability of obtaining the value

$$z_n = \left(\frac{1}{f_z}\right)^n h_0. \quad (9)$$

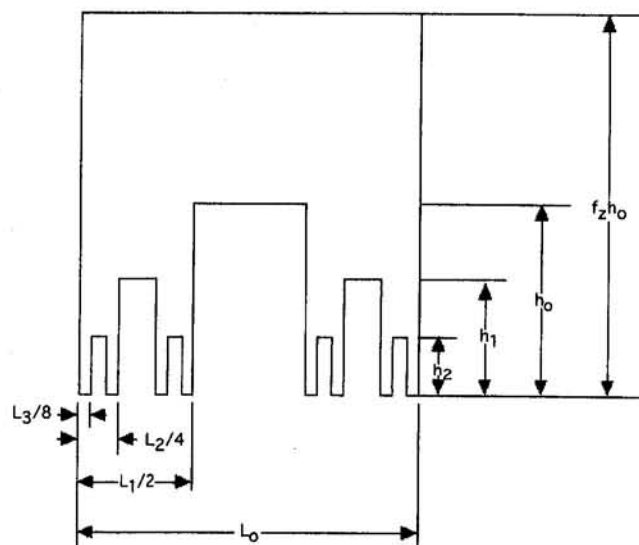


Fig. 1 Fractal surface constructed from the Cantor set with $s = 2$

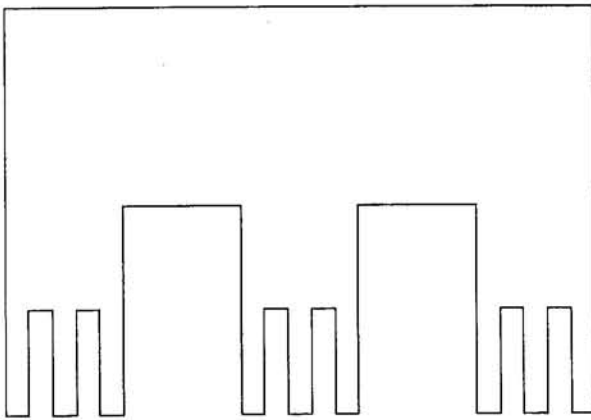


Fig. 2 Cantor set model with $s = 3$

The actual construction of the self-affine Cantor set profile is based on deterministic methods, however, its relation to a surface profile exhibiting fractional Brownian motion requires some statistical considerations. At the n th generation, the support of (9) has a total length $L_n - L_{n+1}$, from which the probability of obtaining z_n is $P(z_n) = (L_n - L_{n+1})/L_0$ and it is found

$$P(z_n) = \left(\frac{1}{f_x}\right)^n \left(1 - \frac{1}{f_x}\right). \quad (10)$$

As shown by Borodich and Mosolov (1992), the fluctuation Δz_n at the n th generation can be obtained by assuming that Δz_n scales as the expected value $z_n P(z_n)$ in which

$$\Delta z_n \sim z_n P(z_n). \quad (11)$$

It then follows that the expected value of the fluctuation at the $(n+1)$ th generation is related to the expected value of the fluctuation at the n th generation through the relation

$$z_{n+1} P(z_{n+1}) = \left(\frac{1}{f_z f_x}\right) z_n P(z_n), \quad (12)$$

such that the segment fluctuations are related as

$$\Delta z_{n+1} = \left(\frac{1}{f_z f_x}\right) \Delta z_n. \quad (13)$$

Using (8) and (13) in (6) provides the relationship

$$\left(\frac{\Delta z_{n+1}}{\Delta z_n}\right) = \left(\frac{\Delta x_{n+1}}{\Delta x_n}\right)^{2-D}, \quad (14)$$

from which the self-affine fractal dimension for the Cantor set surface is obtained as

$$D = 1 - \frac{\ln f_z}{\ln s f_x} + \frac{\ln s}{\ln s f_x}, \quad (15)$$

where $1 < D < 2$. Furthermore, the last term on the right-hand side of (15) defines the fractal dimension D_c of the underlying Cantor set which is the dimension of the collection of an infinite number of points that falls in the range $0 < D_c < 1$, and is uniquely defined through values of s and f_x obtained from a random surface profile.

For the case of a rough surface in contact with an ideally smooth and rigid counter surface, the fractal dimension D along with the parameters L_0 and h_0 can be determined experimentally from a surface profile of the rough surface. The fractal dimension D can be directly obtained from the slope of the structure function of a surface profile that represents a fractional

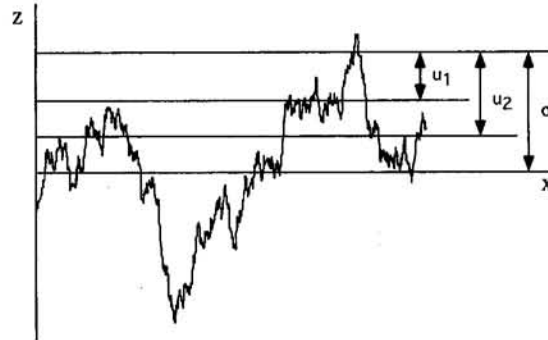


Fig. 3 Fractal surface profile intersected by two planes below the r.m.s. height σ

Brownian process, while L_0 corresponds to the profile length, and h_0 is equal to twice the r.m.s. height σ which can be obtained from the topography. The self-affine fractal dimension of the material specimen is related to the self-affine fractal dimension of the deterministic Cantor set structure through the three geometric parameters s , f_x , and f_z as given in (15), which provides one equation with three unknowns. Two other relations for the parameters f_x and f_z can be obtained by considering the linear area that is in contact with a plane that intersects the experimentally obtained surface profile at two separate locations as illustrated in Fig. 3. These linear areas can be equated with the linear areas obtained using the asymptotic results for the area displacement relation neglecting volume conservation as discussed in the following section. Thus, this result together with D , L_0 , and h_0 completely defines the equivalent Cantor set surface profile of unit depth which approximates a random surface profile of unit depth in a deterministic manner.

For two rough surfaces in contact, the parameters D and Λ would have to be obtained from an effective composite surface profile as described in the Appendix. Through the use of (A5), D and Λ can be determined and an effective composite surface profile can be constructed using the Weierstrass-Mandelbrot function as described by Majumdar et al. (1991). From the simulated Weierstrass-Mandelbrot surface profile, the parameters f_x and f_z can be obtained in the manner described above.

3 Rigid-Perfectly Plastic Deformation Model

According to the proposed fractal surface model, it is assumed that a fractal surface profile of unit depth constructed with the Cantor set and composed of rigid-perfectly plastic material is in contact with a smooth rigid half space as shown

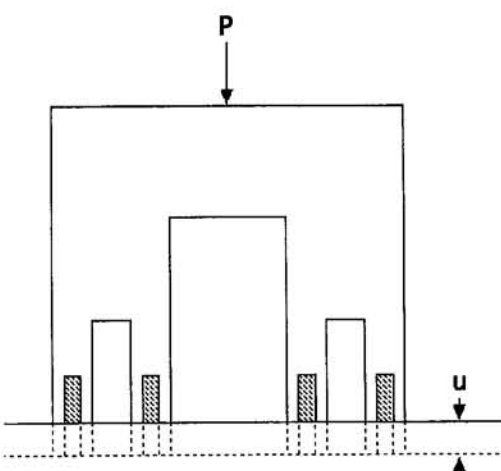


Fig. 4 Deforming Cantor set surface with $s = 2$

in Fig. 4. It is also assumed that the Cantor set surface is independent of the technique used to construct it, and that the limiting (yield) load for plastic deformation (per unit thickness) of the asperities, is

$$P = \sigma_y L. \quad (16)$$

In (16), σ_y is the local value of the yield stress of the deforming rigid-perfectly plastic material in compression, and L is the length of the deforming material in contact with the rigid half-space. The local value of yield stress implies the stress required to produce plastic deformation at the length scale under consideration, and may be different from the value used on the macro scale. It is further assumed that each asperity behaves as a rigid-perfectly plastic axial loaded column and all the material from the $(n+1)$ th generation of asperity pairs flows into the troughs between the asperities when the critical load P_{n+1} is reached for the $(n+1)$ th generation of asperities. The material volume is conserved using this assumption, and simultaneously the height of the n th generation asperities is increased.

With P_{n+1} being the critical load at the $(n+1)$ th generation of asperities and P_n the critical load at the n th generation, the change in load in transition from the $(n+1)$ th generation to the n th generation is

$$\Delta P_{n+1} = P_n - P_{n+1}. \quad (17)$$

In terms of the yield stress σ_y and parameters f_x and L_0 the change in load is

$$\Delta P_{n+1} = \sigma_y (f_x - 1) L_0 \left(\frac{1}{f_x} \right)^{n+1}. \quad (18)$$

In (18), the change in load is proportional to the change in linear area which is consistent with other models for the contact of rough surfaces under the assumption of plastic deformation of asperities (Oden and Martins, 1985). When the load is increased from P_{n+1} to P_n the asperities compress by an amount

$$\Delta u_{n+1} = u_n - u_{n+1}. \quad (19)$$

Here, u_{n+1} is the distance the fractal surface is deformed from its undeformed state due to the load P_{n+1} , and u_n is the distance corresponding to the load P_n . Letting the number of generations of asperities tend to infinity, and simultaneously accounting for volume conservation of the deforming material, the displacements can be expressed by

$$u_n = X H \gamma \left(\frac{1}{f_z} \right)^n, \quad (20)$$

where

$$X = \left(1 - \frac{1}{f_x} \right), \quad \gamma = \sum_{k=0}^{\infty} \left(\frac{1}{f_x f_z} \right)^k, \quad H = f_z h_0. \quad (21)$$

Here, $f_x > 1$ and $f_z > 1$, therefore, the series which defines γ is a geometric series. The expressions X and γ are due to the volume conservation of the plastic deformation process. If volume conservation is neglected the product $X \gamma$ is taken as being equal to unity.

The incremental change in displacement can then be expressed as

$$\Delta u_{n+1} = X H \gamma (f_z - 1) \left(\frac{1}{f_z} \right)^{n+1}. \quad (22)$$

Dividing (18) by (22) gives

$$\frac{\Delta P_{n+1}}{\Delta u_{n+1}} = \frac{\sigma_y (f_x - 1) L_0}{X H \gamma (f_z - 1)} \left(\frac{f_z}{f_x} \right)^{n+1}. \quad (23)$$

In the limit as $n+1 \rightarrow \infty$, (23) can be expressed as the asymptotic derivative

$$\frac{dP}{du} = \frac{\sigma_y (f_x - 1) L_0}{\phi (f_z - 1)} \left(\frac{u}{\phi} \right)^{(\ln f_z / \ln f_x) - 1}, \quad (24)$$

where

$$\phi = X H \gamma. \quad (25)$$

The asymptotic expression relating the load to the plastic deformation is derived by integrating (24), and using the initial condition that $P = 0$ for $u = 0$. Thus,

$$P = \frac{P_0}{\alpha} \left(\frac{f_x - 1}{f_z - 1} \right) \left(\frac{u}{\phi} \right)^\alpha, \quad (26)$$

where

$$P_0 = \sigma_y L_0, \quad \alpha = \frac{\ln f_x}{\ln f_z}. \quad (27)$$

Equation (26) defines the asymptotic load-displacement relation for a rigid-perfectly plastic fractal surface. As was the case with the results obtained by Borodich and Mosolov (1991, 1992), the solution in (26) is based on asymptotic behavior, and will most likely give the best results for $u \ll h_0$. With this result it is observed that within the region of applicability, the expression (15) can be used in conjunction with the expression for α in (27) to provide the relation

$$\alpha = \frac{1 - D_c}{1 + D_c - D}, \quad (\alpha > 0) \quad (28)$$

which is in terms of the fractal dimension D and the Cantor set dimension D_c .

Dividing (26) by σ_y gives the real linear area of contact at any displacement position u . The equality $\phi = f_z h_0$ corresponds to neglecting volume conservation. In this case the linear area displacement relation is

$$A_{mc} = \frac{L_0}{\alpha} \left(\frac{f_x - 1}{f_z - 1} \right) \left(\frac{u}{f_z h_0} \right)^\alpha. \quad (29)$$

Evaluating (29) at two separate values of u and equating the corresponding values of A_{mc} with the linear area from an experimentally obtained surface profile at the respective distances u below the r.m.s. height σ , provides two equations which can be solved for the geometric parameters f_x and f_z . This process should be carried out over a large number of realizations in order to obtain statistically valid values of f_x and f_z . These results can then be used in conjunction with (15) to obtain the value of s which provides a spatial distribution of the asperities. From this result it is seen that the load displacement relation given by (26) can be characterized without use of the fractal dimension D , however, the relation of f_x and f_z to D provides further insight into how the geometric structure of the surface profile being modeled changes with length scale.

A measure of the error involved with neglecting volume conservation during plastic contact can be obtained from the ratio of the applied load with volume conservation to the applied load without volume conservation. Denoting this ratio by κ it is found that

$$\kappa = \left(\frac{1}{X \gamma} \right)^\alpha \geq 1, \quad (30)$$

which is entirely dependent on the geometric parameters f_x and f_z .

4 Results and Discussion

Numerical results are presented in Figs. 5(a-f) for the load-displacement relationship in a nondimensional form for the Cantor set surface shown in Fig. 1. The parameters $s = 2$ and $f_x = 1.5$ were held constant in this illustrative example giving a constant Cantor set dimension $D_c = 0.6309$. Results were obtained with and without volume conservation. It is observed in Fig. 5(a) with $D = 1.1$, that a significantly larger load is required to produce the same displacement if volume conservation is not neglected. This result is also observed in Figs. 5(b-f) as expected. It is further observed that if f_z is less than f_x , the load scales as the displacement to a power less than one. This result is seen in Figs. 5, (a) and (b) which have the lowest values of D , and are physically the smoothest surfaces. By increasing D from 1.2 to 1.3, f_z becomes less than f_x causing the character of the solution to change since the load scales as the displacement to a power greater than one. Physically, an increase in D is equivalent to decreasing f_z (i.e., increasing the height of asperities on each repeating segment) with the other parameters s and f_x held fixed. This result is consistent with curves that exhibit fractional Brownian motion as discussed by Voss (1988), where when the fractal dimension D is increased the curve becomes rougher with sharper peaks. Thus higher fractal dimensions give rise to more sharply peaked asperities which plastically deform at lower loads as observed in Figs. 5(a-f) with the Cantor set model. Increasing D from 1.6 to 1.7 causes f_z to decrease to a value less than one leading to results that are not physically realistic.

Recently, Handzel-Powierza et al. (1992) have conducted surface deformation experiments on face turned, ground, and bead-blasted carbon steel specimens (0.45 percent carbon), which were in contact with a smooth rigid counter specimen. In all cases, the load-displacement relations follow a sigmoidal curve similar to that shown in Fig. 6 which exhibits a comparison of the experimental data obtained by Handzel-Powierza et al. (1992) for the ground specimen with a theoretical prediction obtained using (28). The error in the experimental measurements was determined to be approximately $\pm 0.5 \mu\text{m}$ for the displacements, and $\pm 5 \text{ MPa}$ for the load. In the early stages of deformation, the load scales as the displacement raised to a power greater than one. In the later stages of the deformation process, the curve changes direction and the load scales as the displacement raised to a power less than one, which is consistent with results observed with bulk plastic deformation. Handzel-Powierza et al. (1992) compare the early stages of deformation with a modified version of the G & W (1966) model which only considers elastic deformation of asperities. It is highly probable, however, that on the first loading in the early stages of deformation both elastic and micro-plastic deformation of asperities takes place, with the micro-plastic deformation possibly being much greater than the elastic deformation. With this in mind, it is observed that the Cantor set model can be employed to simulate the results that follow the sigmoidal curve in the early stages of deformation, thus providing a model for micro-plasticity. As shown in Fig. 6, the agreement between the theoretical and experimental results is good in the early stages of loading. For this rough theoretical estimate, the yield stress was taken as 700 MPa for AISI 1045 steel. It was further assumed that the profile fractal dimension is $D = 1.5$ based on the results obtained by Majumdar et al. (1991) for ground stainless steel surfaces. The corresponding Cantor set dimension was assumed to be $D_c = 0.6228$ with $s = 3$ giving $f_x = 1.9455$ and $f_z = 1.2418$. The depth h_0 was taken as $6.6 \mu\text{m}$ which corresponds to twice the r.m.s. height obtained by Handzel-Powierza et al. (1992).

It is found that current surface roughness measuring instruments such as stylus profilometers, optical interferometers, scanning tunneling microscopes, and atomic force microscopes can be employed to obtain surface profiles of desired material

specimens. Spectral techniques can then be applied to these surface profiles to determine if they exhibit fractal characteristics. It has been shown in general (Jossang and Feder, 1992; Warren et al., 1995) that for most fractal surface profiles at any particular length scale the Hurst exponent 2-D satisfies all positive moments used to define the height-difference correlation function (the structure function is the square of the height-difference correlation function defined by the second moment). Thus a multifractal representation is not required to define the fractal surface profile. However, in some cases (Bhushan and Majumdar, 1992; Warren et al., 1993) fractal surface profiles do exhibit different fractal dimensions at different length scales and may require what is referred to as a bifractal or trifractal representation. This type of representation has not been included in the present Cantor set model. However, if desired the model could be modified to incorporate a bifractal or trifractal representation at a later time.

Thus, if a surface profile is fractal and can be represented in terms of a single fractal dimension the formulation for the present Cantor set model is applicable and unique values for the self-affine fractal dimension D , topography Λ , sample length L_0 and parameters f_x and f_z can be determined directly from the measured data. These parameters are used to reconstruct the surface deterministically based on the described Cantor set structure in which the statistics should remain the same since D and Λ are the same for both the real and artificial surfaces. This deterministically constructed Cantor set surface has the advantage in that it allows for techniques known in mechanics which are based on Euclidean geometry to be applied to non-Euclidean geometry since the element on which the technique is applied is Euclidean although the collection of elements is fractal.

Because of the periodicity of the Cantor set model it undergoes the same construction procedure at each hierarchical level producing contact areas that are all the same size. Therefore, it is doubtful that this model will provide an exact simulation of the deformation of a random rough surface. However, the model does admit an analytic solution, and as proposed by Borodich and Mosolov (1992), it may in many cases be that (a) the specific character of a fractal model has little effect on the asymptotic behavior of the process, and (b) the fractal dimension D which provides a measure of the rate at which a surface is changing is of most importance. The solution obtained here provides further insight into the effect that surface structure has on the deformation process, and it also provides indications of the effect that different surface forming processes may have on subsequent surface deformation. Furthermore, in an averaged sense the Cantor set model appears to provide fairly reasonable results, and gives an estimate of the error associated with neglecting volume conservation which is common to many present models.

For future work this present Cantor set model may have the potential to be used in the characterization of frictional sliding of two bodies in contact. In order to describe the frictional sliding phenomenon, it appears imperative to define the spatial distribution of contact areas in order to determine the interaction effects that these areas have with each other. Currently, it appears quite difficult to determine the statistical distribution of contact areas (Majumdar and Bhushan 1991; Majumdar et al. 1991), and even if the distribution is obtained it is not clear as to how it can be applied to study frictional sliding. However, the spatial distribution of contact areas appears to be a natural outcome of this Cantor set model, and even though the distribution of contact areas are periodic, it may provide further insight into the frictional sliding phenomenon.

5 Acknowledgment

The research presented in this paper was made possible by the National Science Foundation Solid Mechanics Program, Di-

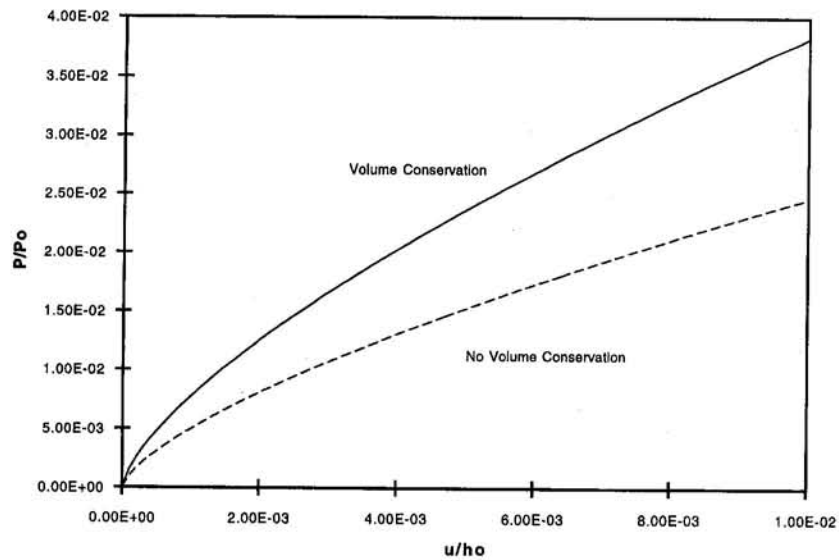


Fig. 5(a)

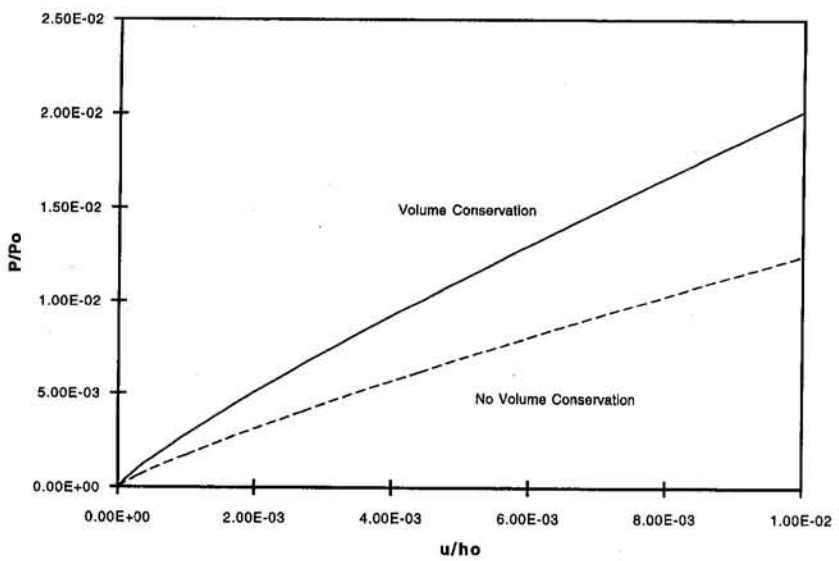


Fig. 5(b)

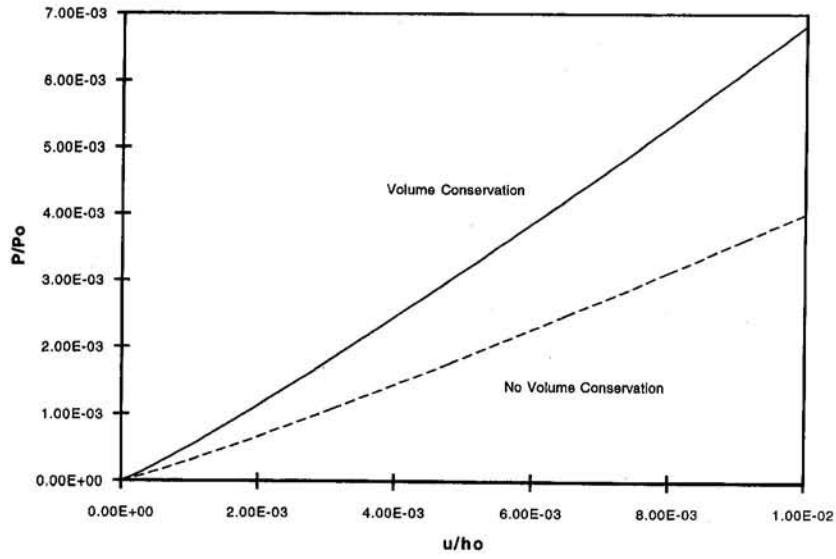


Fig. 5(c)

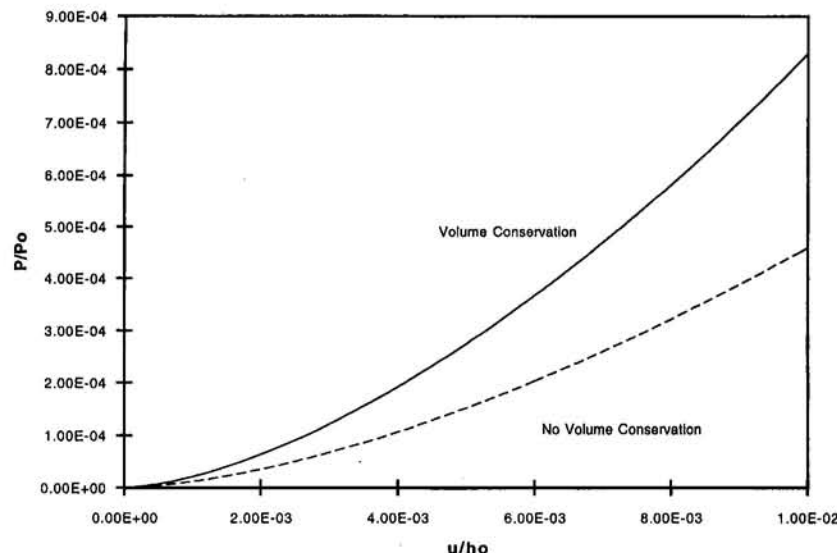


Fig. 5(d)

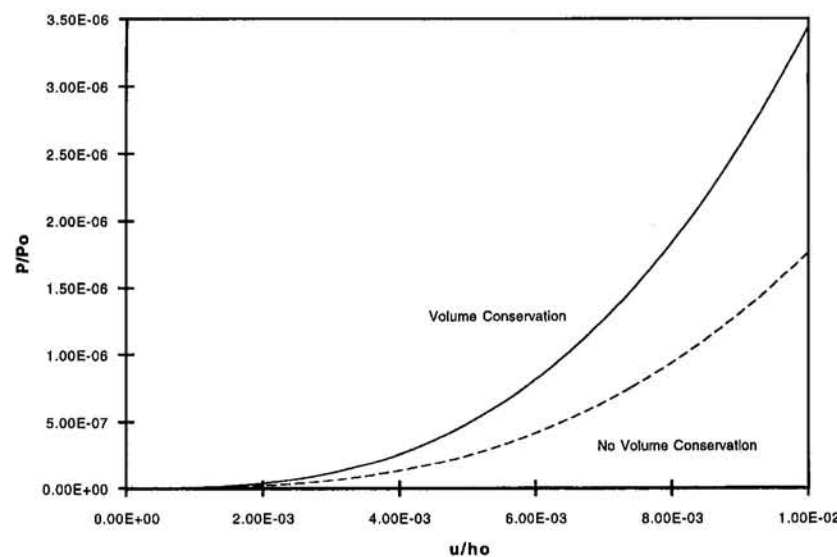


Fig. 5(e)

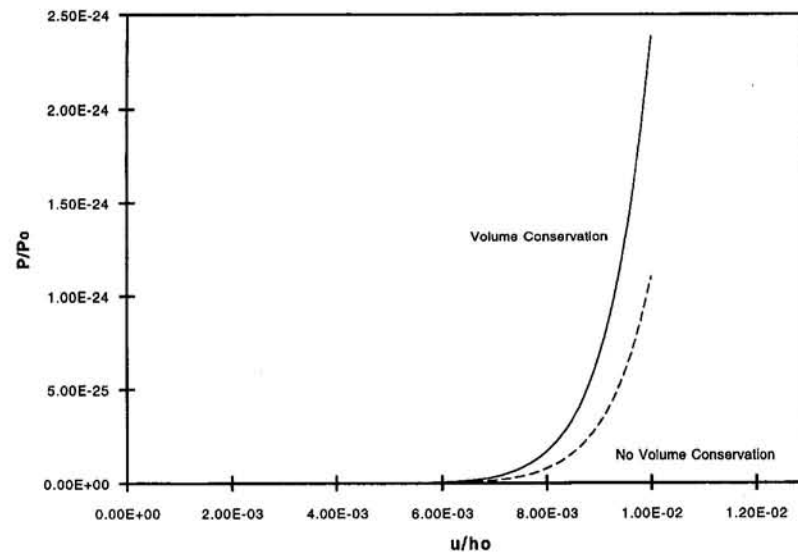


Fig. 5(f)

Fig. 5 Nondimensional load-displacement curves for a Cantor set surface with $s = 2$ and $f_x = 1.5$; (a) $D = 1.1$, (b) $D = 1.2$, and (c) $D = 1.3$, (d) $D = 1.4$, (e) $D = 1.5$, and (f) $D = 1.6$

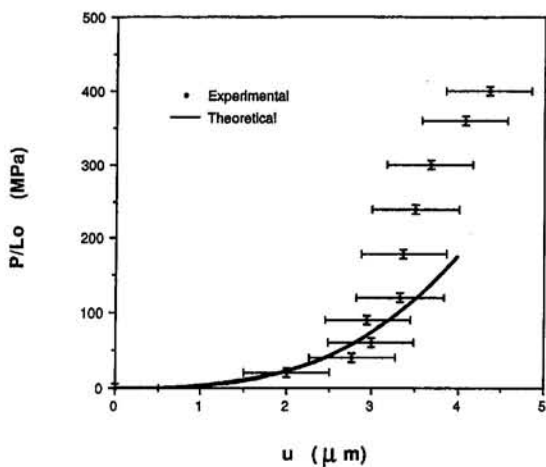


Fig. 6 Experimental and theoretical load-displacement results for a ground medium carbon steel specimen

vision of Engineering research grant awarded to the Department of Mechanical and Aerospace Engineering at the Arizona State University.

References

Archard, J. F., 1957, "Elastic Deformation and the Laws of Friction," *Proc. Roy. Soc. Lond.*, Vol. A243, pp. 190–205.

Berry, M. V., 1979, "Difractals," *J. Phys. A*, Vol. 12, pp. 781–797.

Bhushan, B., 1990, *Tribology and Mechanics of Magnetic Storage Devices*, Springer-Verlag, New York.

Bhushan, B., and Majumdar, A., 1992, "Elastic-Plastic Contact Model for Bifractal Surfaces," *Wear*, Vol. 153, pp. 53–64.

Borodich, F. M., and Mosolov, A. B., 1991, "Fractal Contact of Solids," *Sov. Phys. Tech. Phys.*, Vol. 36, No. 9, pp. 995–997.

Borodich, F. M., and Mosolov, A. B., 1992, "Fractal Roughness in Contact Problems," *J. Appl. Maths. Mech.*, Vol. 56, No. 5, pp. 681–690.

Bowden, F. P., and Tabor, D., 1951, *Friction and Lubrication of Solids: Part I*, Oxford University Press, London.

Bowden, F. P., and Tabor, D., 1964, *Friction and Lubrication of Solids: Part II*, Oxford University Press, London.

Chang, W. R., Etsion, I., and Bogy, D. B., 1987, "An Elastic-Plastic Model for the Contact of Rough Surfaces," *ASME Journal of Tribology*, Vol. 109, pp. 257–263.

Cook, R. D., and Young, W. C., 1985, *Advanced Mechanics of Materials*, Macmillan, New York.

Feder, J., 1988, *Fractals*, Plenum Press, New York.

Greenwood, J. A., and Williamson, J. B. P., 1966, "Contact of Nominally Flat Surfaces," *Proc. Roy. Soc. Lond.*, Vol. A295, pp. 300–319.

Handzel-Powierza, Z., Klimczak, T., and Poljanik, A., 1992, "On the Experimental Verification of the Greenwood-Williamson Model for the Contact of Rough Surfaces," *Wear*, Vol. 154, pp. 115–124.

Hill, R., 1950, *The Mathematical Theory of Plasticity*, Clarendon Press, Oxford, UK.

Johnson, K. L., 1985, *Contact Mechanics*, Cambridge University Press, Cambridge, U.K.

Jossang, T., and Feder, J., 1992, "The Fractal Characterization of Rough Surfaces," *Phys. Scr.*, Vol. T44, pp. 9–14.

Liu, S. H., Kaplan, T., and Gray, L. J., 1986, "Theory of the AC Response of Rough Interfaces," *Fractals in Physics*, L. Pietronero and E. Tosatti, eds., North-Holland, New York, pp. 383–389.

Majumdar, A., and Bhushan, B., 1991, "Fractal Model of Elastic-Plastic Contact Between Rough Surfaces," *ASME Journal of Tribology*, Vol. 113, pp. 1–11.

Majumdar, A., Bhushan, B., and Tien, C. L., 1991, "Role of Fractal Geometry in Tribology," *ASME Advances in Information Storage Systems*, Vol. 1, pp. 231–266.

Mandelbrot, B. B., 1982, *The Fractal Geometry of Nature*, Freeman, San Francisco.

Mandelbrot, B. B., 1985, "Self-affine Fractals and Fractal Dimension," *Phys. Scr.*, Vol. 32, pp. 257–260.

Oden, J. T., and Martins, J. A. C., 1985, "Models and Computational Methods for Dynamic Friction Phenomena," *Comput. Meth. Appl. Mech. Engng.*, Vol. 52, pp. 527–634.

Voss, R. F., 1988, "Fractals in Nature: From Characterization to Simulation," *The Science of Fractal Images*, H. O. Pietgen and D. Saupe, eds., Springer-Verlag, New York, pp. 21–70.

Warren, T. L., Majumdar, A., and Krajcinovic, D., 1995, "Atomic Force Microscope Imaging of the Surface Roughness of SCS and TiB₂ coated SiC Fibers and Uncoated Sapphire Fibers," *Composites*, Vol. 26, pp. 619–629.

APPENDIX

Equivalent Composite Surface

The contact between two rough surfaces can often be modeled as the contact between one equivalent rough surface with a rigid flat plane. For the equivalent rough surface, the structure function $S(\tau)$ is given as (Majumdar et al., 1991)

$$S(\tau) = \langle [z(x + \tau) - z(x)]^2 \rangle, \quad (A1)$$

where

$$z(x) = z_1(x) - z_2(x), \quad (A2)$$

and (*) implies averaging over the statistical ensemble of $z(x)$. In (A2), $z_1(x)$ and $z_2(x)$ correspond to points on the lower and upper surfaces, respectively, which are measured from a reference plane below the lower surface, thus contact occurs when $z(x) \geq 0$. Using (A2) in (A1) gives

$$S(\tau) = \langle [z_1(x + \tau) - z_1(x)]^2 \rangle - 2[z_1(x + \tau) - z_1(x)][z_2(x + \tau) - z_2(x)] + \langle [z_2(x + \tau) - z_2(x)]^2 \rangle. \quad (A3)$$

Since the two surfaces are statistically uncorrelated, the cross product term in (A3) vanishes so that

$$S(\tau) = \langle [z_1(x + \tau) - z_1(x)]^2 + [z_2(x + \tau) - z_2(x)]^2 \rangle, \quad (A4)$$

which reduces to

$$S(\tau) = S_1(\tau) + S_2(\tau). \quad (A5)$$

Therefore the structure function of the equivalent surface is the sum of the structure functions of the individual surfaces.

R. N. Iyengar¹
Professor.

D. Roy¹
Research Fellow.

Department of Civil Engineering,
Indian Institute of Science,
Bangalore 560 012, India

Nonlinear Dynamics of a Rigid Block on a Rigid Base

The planar rocking of a prismatic rectangular rigid block about either of its corners is considered. The problem of homoclinic intersections of the stable and unstable manifolds of the perturbed separatrix is addressed to and the corresponding Melnikov functions are derived. Inclusion of the vertical forcing in the Hamiltonian permits the construction of a three-dimensional separatrix. The corresponding modified Melnikov function of Wiggins for homoclinic intersections is derived. Further, the 1-period symmetric orbits are predicted analytically using the method of averaging and compared with the simulation results. The stability boundary for such orbits is also established.

Introduction

This paper investigates the response of a rigid rectangular block on a rigid base, in planar rocking motion about its corners. This problem has been studied by several investigators in the past. Housner (1963) drew attention to the fact that rocking of blocks is of relevance in earthquake engineering. Spanos and Koh (1984) observed that for slender blocks the equation of motion will be piecewise linear. This property was exploited to construct a symmetric periodic solution. They also conducted detailed numerical work to arrive at a boundary in the parameter space beyond which the block would topple. Hogan (1989, 1990, 1992) in a series of papers has extensively studied the rocking response of blocks. He considered prismatic blocks on a rigid base under sinusoidal excitation. Initially the impacts with the base were assumed to cause no energy dissipation. A variety of periodic orbits and also chaotic motion were found possible. Further improvements, to include damping, have been handled numerically. The piecewise linearity of slender blocks has been used by Hogan also to construct periodic solutions. Tso and Wong (1989a) have used this property to predict the existence and stability of harmonic and subharmonic responses. They followed this study (Wong and Tso, 1989b) by an experimental investigation wherein the existence of three-period and quasi-periodic orbits were demonstrated. Yim and Lin (1991) have extended the study of rocking of slender objects by constructing the Melnikov function. This helps in identifying regions in the parametric space where, chaotic response may be possible. Through numerical studies, they further exhibit the possibility of chaotic behavior in rigid blocks. Shenton and Jones (1991a, 1991b) have considered the periodic slide-rock motion of rigid blocks. Augustin and Sinopoli (1992) have derived the equation of motion of a rocking block including static and kinetic dry friction. They have also delineated the region where rocking is possible as functions of static friction and shape of the block. Recently Lipscombe and Pellegrino (1993) investigated through theory and experiments the effect of bouncing of short blocks after each impact with the base. Their study further highlights the extreme sensitivity of rocking response to geometric imperfections and errors in the relevant parameters occurring in the equation of motion.

¹ Presently at the Central Building Research Institute, Roorkee 247 667, India.
Contributed by the Applied Mechanics Division of THE AMERICAN SOCIETY OF MECHANICAL ENGINEERS for publication in the ASME JOURNAL OF APPLIED MECHANICS.

Discussion on this paper should be addressed to the Technical Editor, Professor Lewis T. Wheeler, Department of Mechanical Engineering, University of Houston, Houston, TX 77204-4792, and will be accepted until four months after final publication of the paper itself in the ASME JOURNAL OF APPLIED MECHANICS.

Manuscript received by the ASME Applied Mechanics Division, Jan. 24, 1994; final revision, Dec. 8, 1994. Associate Technical Editor: P. D. Spanos.

The present study investigates the full nonlinear system without the assumption of slenderness and consequent piecewise linear property. The Melnikov functions for homoclinic intersections of two different types are derived. The effect of vertical base excitation is also included. It is shown that the modified Melnikov function of Wiggins (1988) can be constructed when harmonic vertical and lateral base excitations are simultaneously present. Further an approximate analytical solution is presented for a one period orbit, valid for short blocks also. Numerical results are obtained in the parameter space to illustrate the application of the analytical solutions.

Equation of Motion

The system under consideration is shown in Fig. 1. Under the action of base accelerations $u''(t)$ and $v''(t)$ the prismatic rectangular block rocks about the edge passing through the points O and O_1 . Taking moments of the forces about a corner the equation of motion for the planar rotation θ can be shown to be

$$I\theta'' + I(1 - \nu)\theta'|\theta'|\delta(\theta) + WR \sin(\alpha \operatorname{sgn} \theta - \theta) \\ \times (1 + v''/g) + WR \cos(\alpha \operatorname{sgn} \theta - \theta)u''/g = 0. \quad (1)$$

Here the primes denote derivatives with respect to time, $\delta(\cdot)$ is the Dirac delta function and $\operatorname{sgn}(\cdot)$ is the signum function. I is the moment of inertia of the block about a corner; ν is the coefficient of restitution, defined as the ratio of the angular velocities immediately after and before an impact; W is the weight of the block and R is the distance of the centroid of the cross section from a corner. The angle θ is taken to be positive when the block rotates about the corner O_1 . The base excitations are taken as $u''(t)/g = u_m \sin(\lambda_u t)$ and $v''(t)/g = v_m \sin(\lambda_v t)$. Now introducing the dimensionless parameters $\epsilon_1 = (1 - \nu)$, $\epsilon_2 = WR/I\nu^2$, $\epsilon_3 = u_m \epsilon_2$, $\epsilon_4 = v_m \epsilon_2$, $\Omega = \lambda_v/\lambda_u$ and changing the independent variable to $\tau = \lambda_u t/2\pi$ one gets

$$\ddot{\theta} + \epsilon_1 \dot{\theta} |\dot{\theta}| \delta(\theta) + 4\pi^2 \epsilon_2 \sin(\alpha \operatorname{sgn} \theta - \theta) \\ = -4\pi^2 \epsilon_3 \sin(2\pi\tau) \cos(\alpha \operatorname{sgn} \theta - \theta) \\ - 4\pi^2 \epsilon_4 \sin(2\pi\Omega\tau) \sin(\alpha \operatorname{sgn} \theta - \theta). \quad (2)$$

The above equation is valid only if rocking gets initiated. The condition for initiation of rocking is $\epsilon_3 \geq \epsilon_2(1 - \epsilon_4/\epsilon_2) \times \tan \alpha$. In case the horizontal forcing is absent, the frequency ratio Ω in the above equation is undefined and hence minor modifications are needed. The equation of motion for a block driven by only vertical excitation is taken as

$$\ddot{\theta} + \epsilon_1 \dot{\theta} |\dot{\theta}| \delta(\theta) + 4\pi^2 \epsilon_5 \sin(\alpha \operatorname{sgn} \theta - \theta) \\ = -4\pi^2 \epsilon_6 \sin(2\pi\tau) \sin(\alpha \operatorname{sgn} \theta - \theta). \quad (3)$$

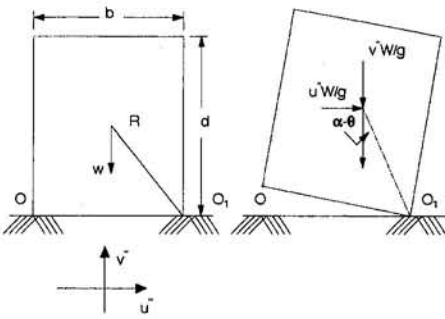


Fig. 1 Rocking rigid block

Here the new dimensionless parameters ϵ_5 and ϵ_6 are defined as $\epsilon_5 = WR/\Delta v^2$, $\epsilon_6 = v_m \epsilon_5$. In this case, in order that rocking gets initiated, the initial conditions should be nonzero and $\epsilon_4 > \epsilon_2$. All the parameters excepting ϵ_2 and ϵ_5 are taken to be small quantities. Further, the time variable τ is replaced by t for convenience.

Vertical Input as a Small Perturbation

Equation (2) which represents the more general case can be recast as

$$\begin{aligned}\dot{\theta}_1 &= f_1 \\ \dot{\theta}_2 &= f_2 + g_2 \\ \dot{\psi} &= 1\end{aligned}\quad (4)$$

where

$$\begin{aligned}f_1 &= \theta_2, f_2 = -4\pi^2\epsilon_2 \sin(\alpha \operatorname{sgn} \theta_1 - \theta_1) \\ g_2 &= -\epsilon_1 \theta_2 |\theta_2| \delta(\theta_1) - 4\pi^2\epsilon_3 \sin(2\pi t) \cos(\alpha \operatorname{sgn} \theta_1 - \theta_1) \\ &\quad - 4\pi^2\epsilon_4 \sin(2\pi \Omega t) \sin(\alpha \operatorname{sgn} \theta_1 - \theta_1).\end{aligned}$$

The Separatrix

The above equations constitute an autonomous Hamiltonian system if $\epsilon_1 = \epsilon_3 = \epsilon_4 = 0$, with

$$H(\theta_1, \theta_2) = 0.5\theta_2^2 + 4\pi^2\epsilon_2 \cos(\alpha \operatorname{sgn} \theta_1 - \theta_1). \quad (5)$$

$$\theta_2 = \dot{\theta}_1$$

The phase plane for such a system is shown in Fig. 2. The system has three singular points, namely a neutrally stable center at $(\theta_1, \theta_2) = (0, 0)$ and a pair of unstable saddle points at $(\theta_1, \theta_2) = (\pm\alpha, 0)$. The saddle points are connected by the separatrix S , which is the level curve corresponding to $H(\pm\alpha, 0) = H_0 = 4\pi^2\epsilon_2$. An explicit expression for S can be found by solving the differential equation

$$0.5\theta_2^2 + 4\pi^2\epsilon_2 \cos(\alpha \operatorname{sgn} \theta_1 - \theta_1) = 4\pi^2\epsilon_2 \quad (6)$$

with the initial condition $\theta_1(0) = 0$. The expressions for the homoclinic trajectories are

$$\begin{aligned}\theta_{1\pm}(t) &= \pm \operatorname{sgn}(t) [\alpha \\ &\quad - 4 \tan^{-1} \{ \exp(-2\pi\epsilon_2^{1/2} t \operatorname{sgn}(t) \tan(\alpha/4)) \}]\end{aligned}\quad (7)$$

$$\begin{aligned}\theta_{2\pm}(t) &= \pm [1 + \tan^2(\alpha/4) \exp(-4\pi\epsilon_2^{1/2} t \operatorname{sgn}(t))]^{-1} \\ &\quad \times [8\pi\epsilon_2^{1/2} \tan(\alpha/4) \exp(-2\pi\epsilon_2^{1/2} t \operatorname{sgn}(t))]\end{aligned}\quad (8)$$

The separatrix S is given by

$$S = \{(\theta_{1+}, \theta_{2+})\} \cup \{(\theta_{1-}, \theta_{2-})\} \cup \{(\alpha, 0)\} \cup \{(-\alpha, 0)\} \quad (9)$$

where $(\alpha, 0)$ and $(-\alpha, 0)$ are the limit points for the trajectories $\theta_{1+}(t)$ and $\theta_{1-}(t)$, respectively, as $t \rightarrow \infty$. It may be noted that in the above derivations, the relations $\operatorname{sgn}(\theta_{1+}) = \operatorname{sgn}(t)$, $\operatorname{sgn}(\theta_{1-}) = -\operatorname{sgn}(t)$ have been used.

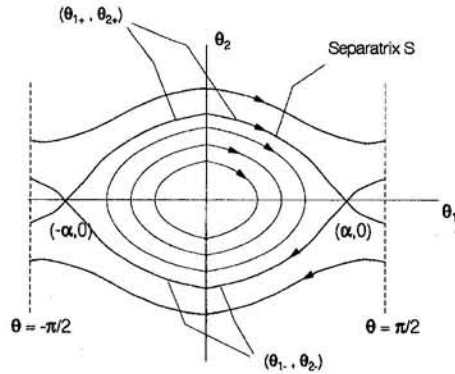


Fig. 2 Phase plane of Eq. (5)

Melnikov Function

For the present problem possibilities of homoclinic intersections of the stable and unstable manifolds exist. In such cases, simple zeros of the associated Melnikov function would indicate transversal intersections between the stable and unstable manifolds. This in turn would hint at the possibility of chaos. Here it may be pointed out that the functions, f_2 and g_2 are C^1 except at $\theta = 0$. Even for such a case, it can be shown that the perturbed homoclinic trajectories are ϵ -close to the unperturbed ones. Further, it may be geometrically demonstrated (Appendix) that transversal intersections between the stable and unstable manifolds are not possible whenever $\theta_1 = 0$. Therefore the transversality arguments (Wiggins, 1990) are not violated. Hence if q' denotes the $O(\epsilon)$ correction to the unperturbed homoclinic trajectory, q , then q' can be expressed piecewise continuously by the first variational equation

$$\begin{aligned}q'(t, t_0) &= \mathbf{D}\mathbf{f} \{q(t - t_0)\} q'(t, t_0) \\ &\quad + \mathbf{g} \{q(t - t_0), t\}, t, t_0 \in (-\infty, 0) \cup (0, \infty) \quad (10)\end{aligned}$$

where \mathbf{f} and \mathbf{g} are vector functions defined as

$$\mathbf{f} = \{f_1 \ f_2\}^T \text{ and } \mathbf{g} = \{g_1 \ g_2\}^T \quad (11)$$

and \mathbf{D} stands for the Jacobian of the vector function \mathbf{f} with respect to its argument q . It may be mentioned that $\theta_1 = t = t_0 = 0$ corresponds to a point of discontinuity where the first variational Eq. (10) is not meaningful.

Now, referring to Fig. 3, it may be argued that two types of transversal intersections are possible. In Type I, stable and

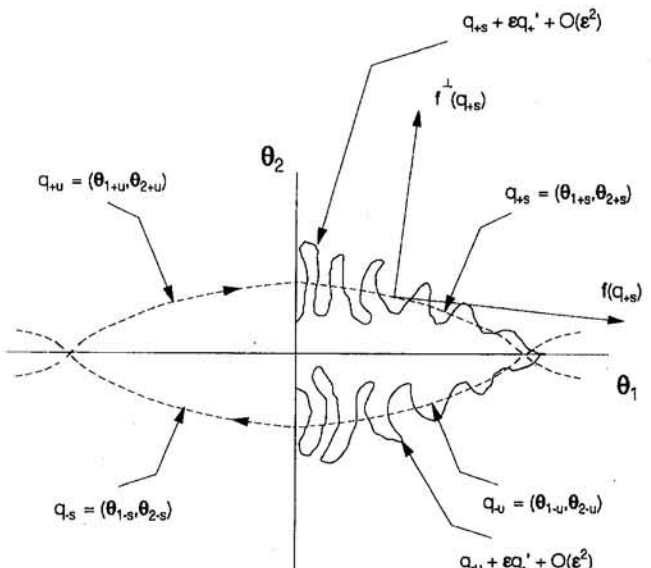


Fig. 3 Poincaré section of the perturbed phase plane of Eq. (4)

unstable manifolds of two different hyperbolic fixed points may intersect. Thus the existence of homoclinic points $p_1 \in {}^e q_{+s} \cap {}^e q_{+u}$ is investigated. On the other hand if $\epsilon_2 \ll 1$, i.e., if the maximum distance of separation of the unperturbed stable and unstable manifolds of the same fixed point is $O(\epsilon)$, then it is possible that homoclinic points of the type $p_2 \in {}^e q_{+s} \cap {}^e q_{-u}$ may exist even under a perturbative field of $O(\epsilon)$. This is referred to as homoclinic intersections of Type II.

Homoclinic Intersections—Type I

With reference to Eq. (4), the Melnikov function may be found from the well-known wedge product (Guckenheimer and Holmes, 1986)

$$M_{h1} = \int_{-\infty}^{\infty} \mathbf{f} \{ \theta_{1+}(t), \theta_{2+}(t) \} \wedge \mathbf{g} \{ \theta_{1+}(t), \theta_{2+}(t), (t + t_0) \} dt. \quad (12)$$

Here the subscript 'h1' stands for homoclinic intersection of Type I. It is noted that the Melnikov function corresponding to $\{\theta_{1-}, \theta_{2-}\}$ would be identical to the above. Now expansion of the right-hand side of Eq. (12) followed by suitable simplification leads to

$$M_{h1} = -8\pi^2\epsilon_1\epsilon_2(1 - \cos \alpha) - 64I_u\pi^3\epsilon_2^{1/2}\epsilon_3 \tan(\alpha/4) \sin(2\pi t_0) - 64I_v\pi^3\epsilon_2^{1/2}\epsilon_4 \tan(\alpha/4) \cos(2\pi\Omega t_0) \quad (13)$$

where

$$I_u = \int_0^{\infty} \{1 + \tan^2(\alpha/4) \exp(-4\pi\epsilon_2^{1/2}t)\}^{-1} \exp(-2\pi\epsilon_2^{1/2}t) \times \cos(2\pi t) \cos[4 \tan^{-1}\{\tan(\alpha/4) \exp(-2\pi\epsilon_2^{1/2}t)\}] dt$$

and

$$I_v = \int_0^{\infty} \{1 + \tan^2(\alpha/4) \exp(-4\pi\epsilon_2^{1/2}t)\}^{-1} \times \exp(-2\pi\epsilon_2^{1/2}t) \sin(2\pi\Omega t) \times \sin[4 \tan^{-1}\{\tan(\alpha/4) \exp(-2\pi\epsilon_2^{1/2}t)\}] dt. \quad (14)$$

In deriving the above expressions for M_{h1} the properties of the separatrix, S , namely, $\theta_{2+}(t) = \theta_{2+}(-t)$, and $\theta_{1+}(t) = -\theta_{1+}(-t)$, have been used. Equation (13) contain I_u and I_v which are infinite integrals. An alternative expression for M_{h1} can be derived which is computationally more convenient by observing that $\theta_{2+}dt = d\theta_{1+}$. Use of this in Eq. (12) leads to

$$M_{h1} = -8\pi^2\epsilon_1\epsilon_2(1 - \cos \alpha) - 8\pi^2\epsilon_3 \sin 2\pi t_0 K_u + 8\pi^2\epsilon_4 \cos(2\pi\Omega t_0) K_v \quad (15)$$

where

$$K_u = \int_0^{\infty} \cos[(1/\epsilon_2^{1/2}) \ln \{\tan(0.25(\alpha - \phi))/\tan(0.25\alpha)\}] \times \cos(\alpha - \phi) d\phi \quad (16)$$

and

$$K_v = \int_0^{\infty} \sin[(\Omega/\epsilon_2^{1/2}) \ln \{\tan(0.25(\alpha - \phi))/\tan(0.25\alpha)\}] \times \sin(\alpha - \phi) d\phi. \quad (17)$$

It is to be noted that the Melnikov function for the combined forcing as given by Eq. (15) is valid only for rational values of Ω . Only in this case, we can find a least common multiplier ψ_c of the time periods of horizontal and vertical excitations given, respectively, by $T_1 = 1.0$ and $T_2 = 1/\Omega$ such that $g_2(\theta_1, \theta_2, t) = g_2(\theta_1, \theta_2, t + \psi_c)$. In case the horizontal excitation is absent, the equation of motion is given by Eq. (3). Again the Melnikov function can be found as

$$M_{h1u} = -8\pi^2\epsilon_1\epsilon_5(1 - \cos \alpha) + 8\pi^2\epsilon_6 \cos(2\pi t_0) L_u. \quad (18)$$

Here L_u is given by

$$L_u = \int_0^{\alpha} \sin[(1/\epsilon_5^{1/2}) \ln \{\tan(0.25(\alpha - \phi))/\tan(0.25\alpha)\}] \times \sin(\alpha - \phi) d\phi \quad (19)$$

Homoclinic Intersection—Type II

It is here assumed that $\epsilon_2 \ll 1$. Referring to Fig. 3, the vector notation $q_+ = (q_{+s} \cup q_{+u}) = (\theta_{1+s}, \theta_{2+s}) \cup (\theta_{1+u}, \theta_{2+u})$ is introduced for the upper half of the unperturbed homoclinic orbit. A similar notation is valid for q_- , the lower half. The subscripts s and u stand for the stable and unstable manifolds. Clearly, the unperturbed homoclinic orbit is given by $q = (q_+ \cup q_-)$. Now a separation vector is defined between the stable and unstable manifolds of the perturbed fixed point as $d(t_0) = [{}^e q_{+s}(t_0) - {}^e q_{-u}(t_0)]$. Here, t_0 is an arbitrary time when the Poincaré section as shown in Fig. 3 is chosen. The time-dependent distance function is

$$\Delta(t, t_0) = \mathbf{f} \{ q_+'(t - t_0) \} \wedge \{ q_+'(t, t_0) - q_-'(t, t_0) \} = \Delta_s(t, t_0) - \Delta_u(t, t_0) \quad (20)$$

so that the Melnikov function for homoclinic intersections would be given by

$$M_{h2}(t_0) = \Delta(t_0, t_0) = \int_{t_0}^{\infty} \Delta_s(t, t_0) dt - \int_{-\infty}^{t_0} \Delta_u(t, t_0) dt. \quad (21)$$

Here, q_+ and q_- are the $O(\epsilon)$ corrections to q_{+s} and q_{-u} given by the first variational equation (10). Now, following Guckenheimer and Holmes (1986), one can show that

$$\dot{\Delta}_s(t, t_0) = \mathbf{f} \{ q_+(t - t_0) \} \wedge \mathbf{g} \{ q_+(t - t_0), t \}. \quad (22)$$

Similarly, taking the time derivative of $\Delta_u(t, t_0)$ and using Eq. (10), one has

$$\begin{aligned} \dot{\Delta}_u(t, t_0) = & \mathbf{D} \mathbf{f} \{ q_+(t - t_0) \} \mathbf{f} \{ q_+(t - t_0) \} \wedge q_-'(t, t_0) \\ & + \mathbf{f} \{ q_+(t - t_0) \} \wedge [\mathbf{D} \mathbf{f} \{ q_-(t - t_0) \} q_-'(t, t_0) \\ & + \mathbf{g} \{ q_-(t - t_0), t \}]. \end{aligned} \quad (23)$$

It is noted here that $\Delta_u(-\infty, t_0) = 0$. Further, in the present problem,

$$f_1(\theta_1, \theta_2) = f_1(\theta_1) = \theta_2$$

and

$$\partial f_2(\theta_{1+}, \theta_{2+})/\partial \theta_{1+} = \partial f_2(\theta_{1-}, \theta_{2-})/\partial \theta_{1-}. \quad (24)$$

Expansion of the right side of Eq. (23), use of the above conditions, and finally substitution of the resulting expressions in Eq. (21) followed by a change of variable from t to $t + t_0$ leads to the following Melnikov function

$$M_{h2} = \int_{0+}^{\infty} \mathbf{f} \{ q_+(t) \} \wedge \mathbf{g} \{ q_+(t), (t + t_0) \} dt + \int_{-\infty}^{-} \mathbf{f} \{ q_+(t) \} \wedge \mathbf{g} \{ q_-(t), (t + t_0) \} dt \quad (25)$$

for homoclinic intersections. Further simplification is possible by noting that along the unperturbed separatrix, $\theta_{1+}(t) = -\theta_{1-}(t)$ and $\theta_{2+}(t) = -\theta_{2-}(t)$. This leads to

$$M_{h2} = -8\pi^2\epsilon_1\epsilon_2(1 - \cos \alpha) - 8\pi^2\epsilon_3 \sin(2\pi t_0)K_u - 8\pi^2\epsilon_4 \sin(2\pi\Omega t_0)K_{uv}. \quad (26)$$

Here

$$K_{uv} = \int_0^\alpha \cos[(\Omega/\epsilon_2^{1/2}) \ln \{\tan(0.25(\alpha - \phi))/\tan(0.25\alpha)\}] \times \sin(\alpha - \phi) d\phi. \quad (27)$$

It is seen that for $\epsilon_4 = 0$, we have $M_{h1} = M_{h2}$. Hence the onset of chaos via Type I and Type II intersections follow the same pattern for blocks driven by only the horizontal acceleration. In case, $\epsilon_3 = 0$, one gets the following expression for the block driven by only a vertical excitation

$$M_{h2v} = -8\pi^2\epsilon_1\epsilon_5(1 - \cos \alpha) - 8\pi^2\epsilon_6 \sin(2\pi t_0)L_{uv} \quad (28)$$

where

$$L_{uv} = \int_0^\alpha \cos[(1/\epsilon_5^{1/2}) \ln \{\tan(0.25(\alpha - \phi))/\tan(0.25\alpha)\}] \times \sin(\alpha - \phi) d\phi. \quad (29)$$

Vertical Input as Parametric Excitation

Wiggins (1988) has developed a method which is more general than that of Melnikov. Parametric excitations with large amplitudes but with small frequencies can be handled by this approach. For this purpose, Eq. (4) is rewritten as

$$\begin{aligned} \dot{\theta}_1 &= f_1 \\ \dot{\theta}_2 &= f_2 + g_2 \\ z &= \Omega \\ \dot{\psi} &= 1. \end{aligned} \quad (30)$$

Here

$$f_1(\theta_1, \theta_2) = \theta_2$$

$$f_2(\theta_1, \theta_2)$$

$$= -4\pi^2\epsilon_2 \sin(\alpha \operatorname{sgn} \theta_1 - \theta_1) \{1 + (\epsilon_4/\epsilon_2) \sin(2\pi z)\}$$

$$\begin{aligned} g_2(\theta_1, \theta_2, \psi) &= -\epsilon_1\theta_2 |\theta_2| \delta(\theta_1) \\ &\quad - 4\pi^2\epsilon_3 \sin(2\pi\psi) \cos(\alpha \operatorname{sgn} \theta_1 - \theta_1) \end{aligned} \quad (31)$$

where z and ψ are modulo $1/\Omega$ and 1, respectively.

Three-Dimensional Separatrix

It is observed that the above system is Hamiltonian when $\epsilon_1 = \epsilon_3 = 0$. The time variable for such a system gets uncoupled from the rest of the equations. The hyperbolic fixed points for this case are $(-\alpha, 0, z)$ and $(\alpha, 0, z)$ for all $\epsilon_4 < \epsilon_2$ and for all z in the interval $(0, 1/\Omega]$. The corresponding phase space is illustrated in Fig. 4. The Hamiltonian is given by the energy functional

$$\begin{aligned} H(\theta_1, \theta_2, z) &= 0.5\theta_2^2 + 4\pi^2\epsilon_2 \cos(\alpha \operatorname{sgn} \theta_1 - \theta_1) \\ &\quad \times \{1 + (\epsilon_4/\epsilon_2) \sin(2\pi z)\}. \end{aligned} \quad (32)$$

To obtain the expressions for the homoclinic trajectories the above equation is solved for $H_0(z) = 4\pi^2\epsilon_2 \{1 + (\epsilon_4/\epsilon_2) \sin(2\pi z)\}$. This leads to

$$\begin{aligned} \theta_{1\pm}(t, z) &= \pm \operatorname{sgn}(t)[\alpha \\ &\quad - 4 \tan^{-1} \{\exp(-2\pi\mu(z)t \operatorname{sgn}(t)) \tan(\alpha/4)\}] \end{aligned} \quad (33)$$

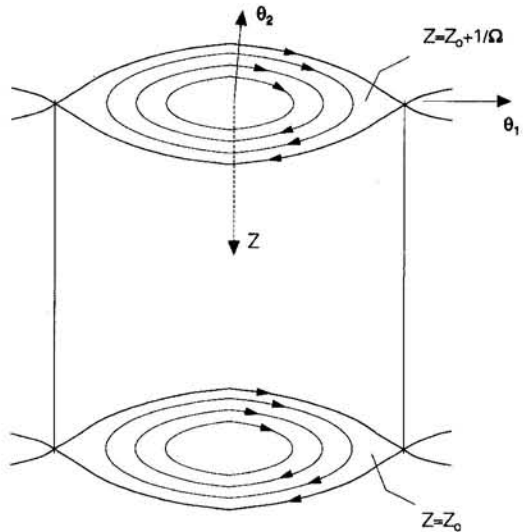


Fig. 4 Phase space for the system of Eqs. (30)

and

$$\begin{aligned} \theta_{2\pm}(t, z) &= \pm [1 + \tan^2(\alpha/4) \exp\{-4\pi\mu(z)t \operatorname{sgn}(t)\}]^{-1} \\ &\quad \times [8\pi\mu(z) \tan(\alpha/4) \exp\{-2\pi\mu(z)t \operatorname{sgn}(t)\}] \end{aligned} \quad (34)$$

where $\mu(z) = [\epsilon_2 \{1 + (\epsilon_4/\epsilon_2) \sin(2\pi z)\}]^{1/2}$.

The separatrix, S , for this case is given by

$$\begin{aligned} S &= \{\theta_{1+}, \theta_{2+}, z\} \cup \{\theta_{1-}, \theta_{2-}, z\} \\ &\cup \{\alpha, 0, z\} \cup \{-\alpha, 0, z\}. \end{aligned} \quad (35)$$

Wiggins's Modified Melnikov Function

In further work, it is assumed that $\Omega \ll 1$. This means that z is a slow time variable. The modified Melnikov function, $M_w(t_0, z)$, which can detect the homoclinic intersections at a three-dimensional Poincaré section based at t_0 as given by Wiggins (1988) is

$$\begin{aligned} M_w(t_0, z) &= \int_{-\infty}^{\infty} (f_1 g_2 - f_2 g_1) dt \\ &\quad + \Omega \int_{-\infty}^{\infty} \{f_1(\partial f_2/\partial z) - f_2(\partial f_1/\partial z)\} t dt. \end{aligned} \quad (36)$$

Here

$$\begin{aligned} f_1 &= f_1\{q(t, z)\}, \quad f_2 = f_2\{q(t, z)\}, \\ g_1 &= g_1\{q(t, z), (t + t_0)\}, \\ g_2 &= g_2\{q(t, z), (t + t_0)\} \quad \text{and} \\ q(t, z) &= \{\theta_1(t, z), \theta_2(t, z)\}. \end{aligned}$$

Use of Eqs. (32), (33), and (34) in Eq. (36) and subsequent simplification leads to

$$\begin{aligned} M_w &= -8\pi^2\epsilon_1\epsilon_2 \{1 + (\epsilon_4/\epsilon_2) \sin(2\pi z)\} (1 - \cos \alpha) \\ &\quad - 8\pi^2\epsilon_3 \sin(2\pi t_0) K_{uw} + 16\pi^2\epsilon_4\Omega \cos(2\pi z) K_{vw}. \end{aligned} \quad (37)$$

The integrals K_{uw} and K_{vw} are given by

$$\begin{aligned} K_{uw} &= \int_0^\alpha \cos[\mu(z) \ln \{\tan(0.25(\alpha - \phi))/\tan(0.25\alpha)\}] \\ &\quad \times \cos(\alpha - \phi) d\phi \end{aligned} \quad (38)$$

$$K_{uv} = \int_0^\alpha [4\pi^2 \epsilon_2 \{ \mu(z) \} \ln \{ \tan(0.25(\alpha - \phi)) / \tan(0.25\alpha) \}] \times \sin(\alpha - \phi) d\phi \quad (39)$$

If $\epsilon_3 = 0$ in Eq. (37), the Melnikov function with only the vertical force acting is obtained.

Numerical Results

First the Melnikov function, M_{h1} , as given by Eq. (15) is considered. Given α , Ω , ϵ_4 , and ϵ_1 , the following relation between ϵ_2 and ϵ_3 is obtained for the zeros of M_{h1}

$$\epsilon_3 = (1/K_u \sin(2\pi t_0) \{ \epsilon_4 \cos(2\pi\Omega t_0) K_v - \epsilon_1 \epsilon_2 (1 - \cos \alpha) \}). \quad (40)$$

Now for any ϵ_2 , one can find $\epsilon_3(t_0)$. The Melnikov boundary M_b in the parameter plane $\epsilon_3 - \epsilon_2$ is defined as the graph of $\inf \{ \epsilon_3(t_0) \}$ versus ϵ_2 . In Figs. 5 and 6, the effect of changing the damping parameter ϵ_1 and the shape parameter α on M_b is shown. These results refer to the case when only the horizontal excitation is acting. In this case, the condition for initiation of rocking would be $\epsilon_3 = \epsilon_2 \tan \alpha$. These rocking initiation curves (RIC) are also shown in these figures. When the effect of vertical excitation is included homoclinic intersections of both the types are possible. For constructing the corresponding Melnikov boundaries one has to search for the zeros of Eqs. (15) and (26) such that $\epsilon_3(t_0)$ is minimized. However, it is not readily possible to fix up such a t_0 that minimizes ϵ_3 in the $\epsilon_3 - \epsilon_2$ plane. It is therefore required to plot several graphs of $\epsilon_3(t_0)$ versus ϵ_2 for various t_0 values and then numerically find out the curve corresponding to $\inf \{ \epsilon_3(t_0) \}$ versus ϵ_2 . This final result is shown in Fig. 7. In Fig. 8, to locate the modified boundary of Wiggins, Eq. (37) is set equal to zero and several graphs of $\inf \{ \epsilon_3(t_0, z) \}$ versus ϵ_2 are plotted for different values of z . The modified boundary M_w corresponds to $z = 0.5$ except for extremely small values of ϵ_2 . This result is also compared in Fig. 8 with the usual Melnikov boundary M_b as given by Eq. (15). For the parameters chosen the modified boundary is weaker than the Melnikov boundary. However, Wiggins' modified approach will be valid for large values of ϵ_4 also.

Symmetric One-Period Orbit

The Melnikov boundary, for which numerical results are presented, divides the parameter space into two regions. Below this boundary only periodic solutions are possible. Above the boundary, however, the solutions are not necessarily periodic. With this in view it would be interesting to ask whether boundaries for specific types of periodic solutions can also be obtained. This requires extensive numerical work and is not under-

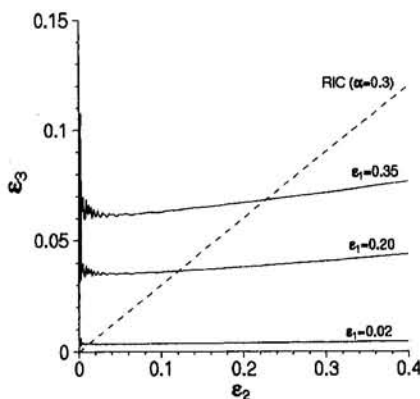


Fig. 5 Effect of damping on M_b , only horizontal forcing $\alpha = 0.3$

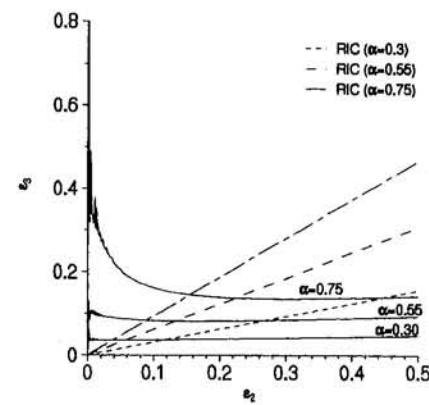


Fig. 6 Effect of shape parameter on M_b , only horizontal forcing $\epsilon_1 = 0.20$

taken here. On the other hand, an analytical solution is found for a symmetric one period orbit. No assumption on the slenderness of the block is made, but the damping is assumed to be small so that, the discontinuity at $\theta = 0$ can be smoothed. The solution valid in the interval $(-\alpha \leq \theta \leq \alpha)$ is taken in the form

$$\theta(t) = A \cos \beta, \dot{\theta}(t) = -2\pi A \sin \beta \quad (41)$$

where, $\beta = 2\pi t + \phi$. If A and ϕ are slowly varying, the classical averaging method leads to

$$\dot{A} = X_1 + X_2 \cos \phi + X_3 \sin \phi \quad (42)$$

$$\dot{\phi} = Y_1 + Y_2 \cos \phi + Y_3 \sin \phi \quad (43)$$

where

$$X_1 = -2\epsilon_1 A^2$$

$$X_2 = \pi \epsilon_3 (J_0 + J_2) \cos \alpha + (8/3) \epsilon_3 \{ J_1 + (7/5) J_3 + (23/35) J_5 \} \sin \alpha$$

$$X_3 = -(4/3) \epsilon_3 J_1 \sin \alpha$$

$$Y_1 = -\pi + 4(\epsilon_2/A) \{ J_0 - (2/3) J_2 - (2/5) J_4 \} \sin \alpha - 2\pi(\epsilon_2/A) J_1 \cos \alpha$$

$$Y_2 = (5/6)(\epsilon_3/A) J_1 \sin \alpha$$

$$Y_3 = \pi(\epsilon_3/A) \{ -J_0 + J_2 \} \cos \alpha + (\epsilon_3/A) \times \{ (-25/6) J_1 \sin \alpha + (16/15) J_3 + (17/210) J_5 \}. \quad (44)$$

Here $J_n(A)$ are Bessel functions of the first kind and order n . While deriving the above expressions the first three terms in the Fourier expansions,

$$\cos(A \cos \beta) = J_0(A) - 2J_2(A) \cos 2\beta + 2J_4(A) \cos 4\beta - \dots$$

$$\sin(A \cos \beta) = 2J_1(A) \cos \beta - 2J_3(A) \cos 3\beta + 2J_5(A) \cos 5\beta - \dots \quad (45)$$

have been retained. In the steady state, $\dot{A} = \dot{\phi} = 0$. This leads to the transcendental equations

$$(X_3 Y_2 - X_2 Y_3)^{-2} \{ (X_2 Y_1 - X_1 Y_2)^2 + (X_3 Y_1 - X_1 Y_3)^2 \} - 1 = 0 \quad (46)$$

$$\tan \phi = (X_3 Y_1 - X_1 Y_3)^{-1} (X_1 X_2 - X_2 Y_1). \quad (47)$$

Solution of these equations leads to the steady-state values of A and ϕ .

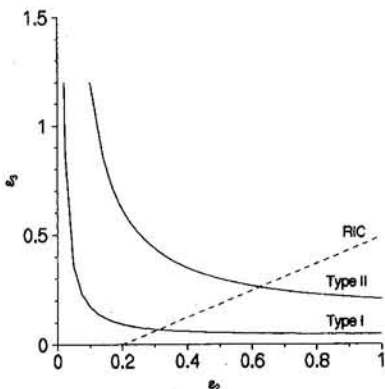


Fig. 7 Effect of vertical excitation on M_b $\epsilon_1 = 0.025$, $\alpha = 0.55$, $\epsilon_4 = 0.2$, $\Omega = 0.2$

An advantage of analytical approaches is that one can perform a stability analysis on the solution. It is easily seen that the divergence of the vector field $V_f = \{f_1(f_2 + g_2)\}^T$ as given by Eq. (4) is

$$\langle \nabla V_f \rangle = -2\epsilon_1\theta_2 \operatorname{sgn}(\theta_2)\delta(\theta_1). \quad (48)$$

Since $\theta_2 \operatorname{sgn}(\theta_2) > 0$, the phase-space of the system contracts by jumps whenever $\theta_1 = 0$. But the assumed continuous one period orbit, given by Eq. (41) cannot account for these jumps in every cycle. However, on an average with the assumed solution the divergence over one cycle is

$$\langle \langle \nabla V_f \rangle \rangle = -2\epsilon_1(1/2\pi) \int_0^{2\pi} (-2\pi A \sin \beta) \times \operatorname{sgn}(\sin \beta)\delta(\cos \beta)d\beta = -4A\epsilon_1. \quad (49)$$

Over a long period of time this average divergence contracts the phase space exponentially by the same amount as given by Eq. (48). Thus the stability of the averaged steady-state solution (A, ϕ) can be studied by considering the variational equation

$$\ddot{v} + 4A\epsilon_1\dot{v} + \{-4\pi^2\epsilon_2 \cos(\alpha \operatorname{sgn} \theta - \theta) + 4\pi^2\epsilon_3 \sin(2\pi t) \sin(\alpha \operatorname{sgn} \theta - \theta)\}v = 0 \quad (50)$$

Here θ is a known periodic function and hence through the eigenvalues of the Floquet transition matrix, one can study whether the variation v grows or decays exponentially. This in turn establishes the stability boundary of the one-period solution given by Eq. (41).

The transcendental Eqs. (46) and (47) have been solved iteratively to obtain several possible symmetric one period solu-

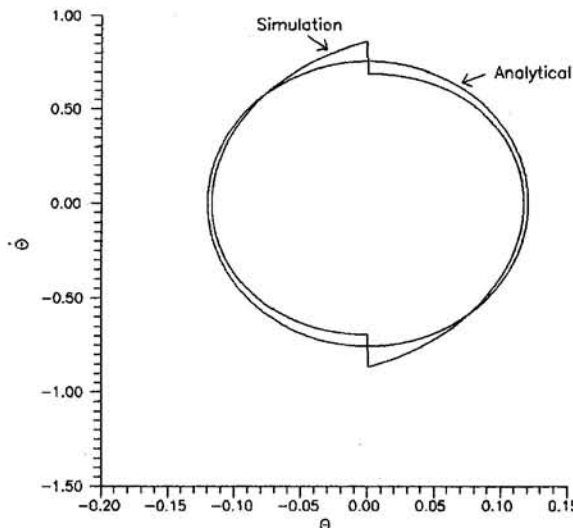


Fig. 9 Numerically and analytically computed symmetric 1-period orbits $\epsilon_1 = 0.2$, $\epsilon_2 = -0.03$, $\epsilon_3 = 0.11$, $\alpha = 0.55$

tions, for a block under only horizontal excitation. In Fig. 9, one such solution is presented and compared with the exact solution numerically obtained using the Runge-Kutta scheme. It is observed that the comparison is very favourable. The stability boundary of these solutions in the parameter plane $(\epsilon_1 - \epsilon_3)$ is presented in Fig. 10 along with the Melnikov boundary for homoclinic intersections of Type I and the corresponding RIC.

Discussion and Conclusions

The purpose of this paper has been to bring into focus the importance of the Melnikov function in understanding the dynamical behavior of a free-standing block rocking on a rigid base. The presence of homoclinic trajectories in the unperturbed phase space allows one to construct the Melnikov function and to check for the possibility of homoclinic intersections, when the system is perturbed by damping and external forcing. In previous studies, the assumption of piecewise linearity has been made to find the Melnikov boundary. Here this assumption has not been used. The effect of vertical excitation has also been included. There are two ways in which the vertical excitation can be handled. First, the amplitude can be taken to be small and thus the excitation can be treated as a small perturbation. The second approach is due to Wiggins wherein, the frequency parameter of the vertical excitation is treated as a small quantity. The Melnikov boundary (M_b) partitions the parameter space such that below the boundary only periodic trajectories are pos-

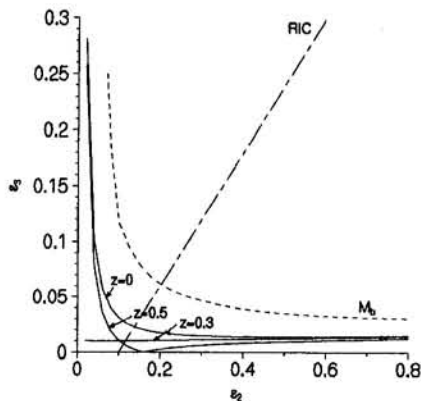


Fig. 8 Wiggin's modified boundary M_{bw} $\epsilon_1 = 0.025$, $\epsilon_4 = 0.1$, $\alpha = 0.55$, $\Omega = 0.1$

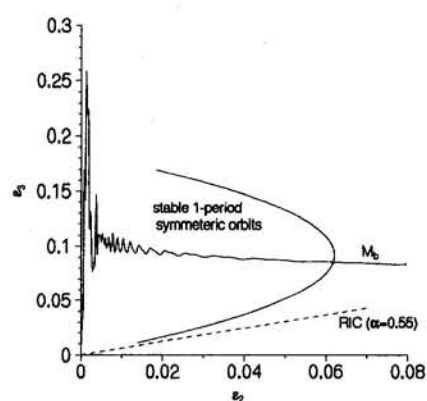


Fig. 10 Stability boundary of 1-period solutions and Melnikov boundary $\epsilon_1 = 0.2$, $\epsilon_4 = 0.0$, $\alpha = 0.55$

sible. In the present problem, an interesting question is the toppling of the block. For this to happen the trajectories have to cross the unperturbed separatrix. Hence, one can take the boundary M_b or the modified boundary M_{bw} as limiting curves below which toppling cannot occur. Thus crossing this boundary in the parameter plane would be a necessary condition for toppling of the block. It is interesting to note that a one period symmetric orbit not hitherto reported in the literature can be analytically obtained. The stability of this solution can also be analytically studied. This provides a further boundary in the (ϵ_2, ϵ_3) parameter plane (Fig. 10) to refine the region where complicated response may be possible. However, the present results provide only necessary conditions. Further structuring of this region to demarcate multiperiod, quasi-period and toppling solutions is necessary. The concept of lobe dynamics and the transport of the points in phase space across the pseudo-separatrix (Wiggins, 1992) may prove useful in studying the toppling characteristics of the block.

References

Giuliano, A., and Sinopoli, A., 1992, "Modelling the Dynamics of Large Block Structures," *Meccanica*, Vol. 27, pp. 195–211.

Guckenheimer, J., and Holmes, P., 1986, *Nonlinear Oscillations, Dynamical Systems and Bifurcations of Vector Fields*, 2nd ed., Springer-Verlag, New York.

Hogan, S. J., 1989, "On the Dynamics of Rigid Block Motion under Harmonic Forcing," *Proceedings of the Royal Society, London*, Vol. A425, pp. 441–476.

Hogan, S. J., 1990, "The Many Steady-state Responses of a Rigid Block under Harmonic Forcing," *Earthquake Engineering and Structural Dynamics*, Vol. 19, pp. 1057–1071.

Hogan, S. J., 1992, "The Effect of Damping on Rigid Block Motion under Harmonic Forcing," *Proceedings of the Royal Society, London*, Vol. A437, pp. 97–108.

Housner, W. G., 1963, "The Behaviour of Inverted Pendulum Structures During Earthquakes," *Bulletin of the Seismological Society of America*, Vol. 53, pp. 403–417.

Lipscombe, P. R., and Pellegrino, S., 1993, "Free Rocking of Prismatic Blocks," *Journal of Engineering Mechanics*, ASCE, Vol. 119, pp. 1387–1410.

Shenton, III, H. W., and Jones, N. P., 1991a, "Base Excitation of Rigid Bodies. I. Formulation," *Journal of Engineering Mechanics*, ASCE, Vol. 117, pp. 2286–2306.

Shenton, III, H. W., and Jones, N. P., 1991b, "Base Excitation of Rigid Bodies. II. Periodic Slide-rock Response," *Journal of Engineering Mechanics*, ASCE, Vol. 117, pp. 2307–2328.

Spanos, P. D., and Koh, A. S., 1984, "Rocking of Rigid Blocks due to Harmonic Shaking," *Journal of Engineering Mechanics*, ASCE, Vol. 110, pp. 1627–1642.

Tso, W. K., and Wong, C. M., 1989a, "Steady-state Rocking Response of Rigid Blocks, Part I," *Earthquake Engineering and Structural Dynamics*, Vol. 18, pp. 89–109.

Tso, W. K., and Wong, C. M., 1989b, "Steady-state Rocking Response of Rigid Blocks, Part II," *Earthquake Engineering and Structural Dynamics*, Vol. 18, pp. 110–120.

Wiggins, S., 1988, "On the Detection and Dynamical Consequences of Orbits Homoclinic to Hyperbolic Periodic Orbits and Normally Hyperbolic Invariant Tori in a Class of Ordinary Differential Equations," *SIAM Journal of Applied Mathematics*, Vol. 48, pp. 262–285.

Wiggins, S., 1990, *Applied Nonlinear Dynamical Systems and Chaos*, Springer-Verlag, New York.

Wiggins, S., 1992, *Chaotic Transport in Dynamical Systems*, Springer-Verlag, New York.

Yim, S. C. S., and Lin, H., 1991, "Nonlinear Impact and Chaotic Response of Slender Rocking Objects," *Journal of Engineering Mechanics*, ASCE, Vol. 117, pp. 2079–2100.

APPENDIX

Proposition A1

Let $q_s(t - t_0)$ and $q_s(t, t_0)$ denote the unperturbed and perturbed stable homoclinic trajectories for the system of Eq. (4) on a Poincaré section based at t_0 . Let $q_s(t_0, t_0) - q_s(0) = O(\epsilon)$. Then $q_s(t, t_0) - q_s(t - t_0) = O(\epsilon) \forall t \in (t_0, \infty)$.

A similar proposition holds true for the unstable homoclinic trajectory with time reversed.

Proof. Let \mathbf{f} and \mathbf{g} be vector-valued functions as given by Eq. (11). The function \mathbf{g} may be equivalently represented as

$$\mathbf{g}(\mathbf{q}_s, t, \epsilon) = \epsilon \bar{\mathbf{g}}(\mathbf{q}_s, t, \epsilon). \quad (A1)$$

This leads to

$$\begin{aligned} |\mathbf{q}_s(t, t_0) - q_s(t - t_0)| &\leq |\mathbf{q}_s(t_0, t_0) - q_s(0)| \\ &+ \int_{t_0}^t |\mathbf{f}(\mathbf{q}_s(\xi, t_0)) - \mathbf{f}(q_s(\xi - t_0))| d\xi \\ &+ \epsilon \int_{t_0}^t |\bar{\mathbf{g}}(\mathbf{q}_s(\xi, t_0), \xi, t)| d\xi. \end{aligned} \quad (A2)$$

Referring to Eq. (4), the function $\bar{\mathbf{g}}$ may be decomposed as

$$\bar{\mathbf{g}} = \bar{\mathbf{g}}^c + \bar{\mathbf{g}}^d \quad (A3)$$

where

$$\bar{\mathbf{g}}^d = \{0 - \theta_2 | \theta_2 | \delta(\theta_1)\}^T. \quad (A4)$$

Since \mathbf{f} and $\bar{\mathbf{g}}^c$ are C^0 functions, hence $\exists M \geq 0$, and $L \geq 0$, such that in an interval $[t_0, t_1]$, where $t_1 > t_0$ and $t_1 - t_0 = O(1)$,

$$|\bar{\mathbf{g}}^c(\mathbf{q}_s, t, \epsilon)| \leq M$$

and

$$|\mathbf{f}(\mathbf{q}_s(\xi)) - \mathbf{f}(q_s(\xi))| \leq L |\mathbf{q}_s(\xi) - q_s(\xi)|. \quad (A5)$$

Further, let there be I impacts of the block with the ground in $[t_0, t_1]$. It may then be readily shown that

$$\int_{t_0}^t |\bar{\mathbf{g}}^d(\mathbf{q}_s(\xi), \xi, \epsilon)| d\xi = K, \quad (A6)$$

where $K = \sum_{i=0}^I |\theta_{2i}|_{\theta_{1i}=0}$.

In other words, K is the sum of the absolute velocities at impacts. Substitution of (A6) and (A7) in (A3) followed by the use of Gronwall's lemma leads to

$$\begin{aligned} |\mathbf{q}_s - q_s| &\leq [|\mathbf{q}_s(t_0, t_0) - q_s(0)| \\ &+ \epsilon(K + M/L)] \exp[L(t - t_0)]. \end{aligned} \quad (A7)$$

Hence \exists a constant Q independent of ϵ , such that $|\mathbf{q}_s - q_s| = O(\epsilon)$ for $t_0 \leq t \leq t_0 + Q/L$. Since \mathbf{q}_s is a stable manifold, $|\mathbf{q}_s - q_s| = O(\epsilon)$ for $t_0 \leq t < \infty$. \square

Proposition A2

A transversal intersection of \mathbf{q}_s and \mathbf{q}_u is not possible at $\theta_1 = 0$.

Proof. \mathbf{q}_s and \mathbf{q}_u has a transversal intersection at a point p , iff

$$T_p(\mathbf{q}_s) + T_p(\mathbf{q}_u) = R^2. \quad (A8)$$

At $\theta_1 = 0$, \mathbf{q}_s and \mathbf{q}_u undergo a jump along the θ_2 -axis. Therefore the only way \mathbf{q}_s and \mathbf{q}_u may intersect is along a line on the θ_2 -axis. Let $p' \in \mathbf{q}_s \cap \mathbf{q}_u$ be one such intersection. Then

$$T_{p'}(\mathbf{q}_s) + T_{p'}(\mathbf{q}_u) = R^1. \quad \square \quad (A9)$$

Michio Kurashige

Department of Mechanical Engineering,
Iwate University,
Morioka 020, Japan

R. J. Clifton

Division of Engineering,
Brown University,
Providence, RI 02912
Mem. ASME.

Integral Equations for a Three-Dimensional Crack in an Infinite, Fluid-Filled, Poroelastic Solid With Zero Permeability in One Direction

Fundamental solutions for an instantaneous point force and an instantaneous fluid point source are derived for an infinite, fluid-saturated, poroelastic solid with zero permeability in one direction. Applying these solutions and Cleary's reciprocal theorem to the three-dimensional problem of a pressurized plane crack yields two integral equations, which relate normal tractions and fluid pressure on the crack faces to crack opening and fluid injection rate per unit fracture area. An important application of these equations is the prediction of hydraulic fractures induced during waterflooding of reservoirs to enhance gas and oil recovery. Zero permeability in one direction may be a good approximation for the case in which the reservoir is sandwiched between two impermeable rock layers.

Introduction

In our previous paper (Kurashige and Clifton, 1992), a pair of integral equations was derived for the three-dimensional problem of a pressurized plane crack in an infinite, isotropic, homogeneous, fluid-saturated, poroelastic solid with isotropic permeability, using the known fundamental solutions (Cleary, 1977) for a point force and a fluid point source. These integral equations relate normal tractions and pore fluid pressure on the crack faces to the crack opening and fluid volume supply rate per unit fracture area. These equations were intended to apply to the prediction of hydraulic fractures induced during waterflooding—a technique used to enhance the recovery of gas and oil by injecting water into some wells to force gas and oil to neighboring wells. Numerical solutions based on these equations were obtained recently for the water flooding case (Clifton and Wang, 1991).

The aim of the present paper is to obtain a similar pair of integral equations for a pressurized plane crack in an infinite, elastically isotropic, homogeneous, fluid-saturated, poroelastic solid having zero permeability in one direction. Because reservoirs of gas and oil are sandwiched between impermeable formations, the water injected into the reservoir from the well bore or from the induced fracture flows mainly in the horizontal direction, when the height of the fracture is comparable to the height of the reservoir, as in most cases except at early times. Therefore, the assumption of zero permeability in the vertical direction but non-zero permeability in the horizontal directions may be a good approximation for many cases of practical importance.

In the first half of the paper, fundamental solutions are obtained for an instantaneous point force and an instantaneous fluid volume source in such an infinite solid with vanishing

permeability in one direction. Using these solutions for the stress field resulting from an infinitesimal segment of a dislocation line (Clifton and Abou-Sayed, 1979; Kurashige and Clifton, 1992), the second half has derived the required pair of integral equations.

Basic Equations

Let us consider an elastically isotropic, homogeneous, fluid-saturated, poroelastic solid having zero permeability in one direction. Denote total stress, pore fluid pressure, average strain, pore fluid volume change per unit total volume, and pore fluid volume flux by σ_{ij} , p , ϵ_{ij} , ΔV , q_i , respectively. Constitutive equations for such a poroelastic material are given by (Cleary, 1977)

$$\sigma_{ij} = L_{ijpq}\epsilon_{pq} - \alpha p\delta_{ij} \\ = 2G\left(\epsilon_{ij} + \frac{\nu}{1-2\nu}\epsilon_{kk}\delta_{ij}\right) - \alpha p\delta_{ij}, \quad (1)$$

$$\Delta V = \frac{3(\nu_u - \nu)}{2GB(1 + \nu_u)(1 + \nu)}\left(\sigma_{kk} + \frac{3}{B}p\right), \quad (2)$$

$$q_x = -\kappa \frac{\partial p}{\partial x}, \quad q_y = 0, \quad q_z = -\kappa \frac{\partial p}{\partial z}, \quad (3)$$

where α is Biot's coefficient of effective stress given by

$$\alpha = \frac{3(\nu_u - \nu)}{B(1 + \nu_u)(1 - 2\nu)}, \quad (4)$$

and G , B , ν , ν_u , κ are the shear modulus, Skempton's pore pressure coefficient, drained and undrained Poisson's ratios, and permeability in the x and z -directions. We have made the zero-permeability direction coincident with the y -axis of the Cartesian coordinates (x_i) or (x , y , z) so that the pore fluid flux vanishes in the y -direction as in Eqs. (3). In what follows, we will use either (x_i) or (x , y , z) depending on which is more convenient.

Contributed by the Applied Mechanics Division of THE AMERICAN SOCIETY OF MECHANICAL ENGINEERS for publication in the ASME JOURNAL OF APPLIED MECHANICS.

Discussion on this paper should be addressed to the Technical Editor, Professor Lewis T. Wheeler, Department of Mechanical Engineering, University of Houston, Houston, TX 77204-4792, and will be accepted until four months after final publication of the paper itself in the ASME JOURNAL OF APPLIED MECHANICS.

Manuscript received by the ASME Applied Mechanics Division, Jan. 14, 1994; final revision, Dec. 1, 1994. Associate Technical Editor: J. T. Jenkins.

Since we shall deal with the quasi-static case with body force f_i and fluid volume source r^F per unit volume, the equilibrium equations and the pore fluid diffusion equation are

$$\sigma_{ij,j} + f_i = 0, \quad (5)$$

$$q_{i,i} + \partial \Delta V / \partial t = r^F. \quad (6)$$

As in the linear theory of elasticity, the average strains are defined in terms of the average displacement u_i by

$$\epsilon_{ij} = \frac{1}{2}(u_{i,j} + u_{j,i}). \quad (7)$$

In the above and what follows, the usual summation convention holds for repeated indices, unless otherwise mentioned, and commas denote partial differentiation.

Equations (1) through (7) constitute a full system of governing equations for an elastically isotropic, fluid-saturated, poroelastic solid with zero permeability in the y -direction. After some manipulations with these equations, the equilibrium equations and the diffusion equation are expressed in terms of the displacements and the pore fluid pressure as follows:

$$\nabla^2 u_i + \frac{1}{1-2\nu} u_{j,jl} - \frac{\alpha}{G} p_{,i} = -\frac{1}{G} f_i, \quad (8)$$

$$\begin{aligned} \left(\nabla^2 - \frac{1}{c} \frac{\partial}{\partial t} \right) \left(u_{j,j} + \frac{\alpha_1}{G} p \right) - \frac{\alpha_2}{G} \frac{\partial^2 p}{\partial y^2} \\ = -\frac{\alpha_0}{G} f_{j,j} - \frac{1}{\alpha c} r^F, \quad (9) \end{aligned}$$

where

$$\begin{aligned} \alpha_0 &= \frac{1-2\nu}{2(1-\nu)}, & \alpha_1 &= \frac{3(1-2\nu_u)}{2B(1+\nu_u)}, \\ \alpha_2 &= \frac{3(1-2\nu)(1-\nu_u)}{2B(1+\nu_u)(1-\nu)}, \\ \alpha_3 &= \frac{\nu_u - \nu}{2(1-\nu_u)(1-\nu)}. \end{aligned} \quad (10)$$

Although it has not appeared in Eqs. (8) and (9), α_3 is defined in (10) for later use.

Fourier and Laplace Transforms

Fourier and Laplace transforms and their inverse transforms are used in the following sections. For an arbitrary function $f(x_j, t)$, and for Fourier transform and Laplace transform parameters denoted by ξ_j (corresponding to x_j) and s , the transforms and their inverses are defined as follows:

$$\hat{f}(\xi_j, t) = \frac{1}{\sqrt{(2\pi)}} \int_{-\infty}^{\infty} f(x_j, t) \exp(i\xi_j x_j) dx_j, \quad (\text{no sum on } j) \quad (11)$$

$$f(x_j, t) = \frac{1}{\sqrt{(2\pi)}} \int_{-\infty}^{\infty} \hat{f}(\xi_j, t) \exp(-ix_j \xi_j) d\xi_j, \quad (\text{no sum on } j) \quad (12)$$

$$f^*(x_j, s) = \mathcal{L}[f(x_j, t)] = \int_0^{\infty} f(x_j, t) \exp(-st) dt, \quad (13)$$

$$f(x_j, t) = \frac{1}{2\pi i} \int_{\text{Br}} f^*(x_j, s) \exp(st) ds, \quad (14)$$

where Br means the Bromwich integral path. Furthermore, the triple Fourier transform will be expressed by the same raised hat symbol used for the single Fourier transform.

Fundamental Solution for Instantaneous Point Fluid Volume Source

Consider an instantaneous point fluid volume source with unit intensity at the origin of the Cartesian coordinate system (x_i) at time $t = 0$. The associated forcing fields are

$$r^F = \delta(x)\delta(y)\delta(z)\delta(t), \quad f_i = 0, \quad (15)$$

where $\delta(\cdot)$ denotes the Dirac delta function. Note that, since the permeability vanishes in the y -direction but not in the other directions, the fundamental solution for the fluid source is axially symmetric about the y -axis. Taking into account Eq. (15), and applying the triple Fourier and Laplace transforms to Eqs. (8) and (9), one obtains, with the help of the relation $\alpha\alpha_0 + \alpha_1 = \alpha_2$,

$$\hat{p}^* = \frac{1}{(2\pi)^{3/2}} \frac{G/(\alpha\alpha_2)}{c(\xi_1^2 + \xi_3^2) + s}, \quad (16)$$

$$\hat{u}_j^* = \frac{1}{(2\pi)^{3/2}} \frac{\alpha_0/\alpha_2}{c(\xi_1^2 + \xi_3^2) + s} \frac{i\xi_j}{(\xi_1\xi_3)}. \quad (17)$$

The pore fluid pressure p can be obtained easily by inverse transformation of Eq. (16) as

$$p = \frac{G/(\alpha\alpha_2)}{(2\pi)^2} \frac{\delta(y)}{2ct} e^{-(x^2+z^2)/(4ct)}, \quad (18)$$

which shows that the fluid supplied at the source diffuses in the radial direction only in the plane $y = 0$ because of the zero permeability in the y -direction.

To evaluate the infinite integrals associated with the Fourier inversions of Eq. (17), we must apply the following variable transforms to it:

$$x_1 = r \cos \theta, \quad x_2 = y, \quad x_3 = r \sin \theta, \quad (19)$$

$$\xi_1 = \rho \cos \phi, \quad \xi_2 = \xi, \quad \xi_3 = \rho \sin \phi, \quad (20)$$

$$u_r = u_1 \cos \theta + u_3 \sin \theta, \quad u_\theta = -u_1 \sin \theta + u_3 \cos \theta. \quad (21)$$

By these transforms and the inverse Laplace transform, we obtain the nonzero displacement components in the form of triple integrals:

$$\begin{aligned} u_r &= \frac{\alpha_0/\alpha_2}{(2\pi)^3} \int_0^{\infty} \rho^2 e^{-\rho^2 ct} d\rho \\ &\quad \times \int_{-\pi}^{\pi} \cos \phi e^{-i\rho r \cos \phi} d\phi \int_{-\infty}^{\infty} \frac{ie^{-iy\xi}}{\rho^2 + \xi^2} d\xi, \end{aligned} \quad (22)$$

$$\begin{aligned} u_y &= \frac{\alpha_0/\alpha_2}{(2\pi)^3} \int_0^{\infty} \rho e^{-\rho^2 ct} d\rho \\ &\quad \times \int_{-\pi}^{\pi} e^{-i\rho r \cos \phi} d\phi \int_{-\infty}^{\infty} \frac{i\xi e^{-iy\xi}}{\rho^2 + \xi^2} d\xi. \end{aligned} \quad (23)$$

In these equations, the last two integrals can be evaluated with the help of the formulae

$$\begin{aligned} \frac{1}{2\pi} \int_{-\pi}^{\pi} e^{-i\mu \cos \phi} d\phi &= J_0(\mu), \\ \frac{i}{2\pi} \int_{-\pi}^{\pi} \cos \phi e^{-i\mu \cos \phi} d\phi &= J_1(\mu), \end{aligned} \quad (24)$$

$$\begin{aligned} \int_{-\infty}^{\infty} \frac{e^{-iy\xi}}{\rho^2 + \xi^2} d\xi &= \frac{\pi}{\rho} e^{-\rho|y|}, \\ \int_{-\infty}^{\infty} \frac{ie^{-iy\xi}}{\rho^2 + \xi^2} d\xi &= -i \operatorname{sgn}(y) \pi e^{-\rho|y|}, \end{aligned} \quad (25)$$

where $\operatorname{sgn}(y) = -1, 0, 1$ for $y < 0, y = 0$, and $y > 0$, respectively. These formulae are found in references (Grad-

shteyn and Ryzhik, 1965; Sneddon, 1951) or derived from the formulae in them. The results of the evaluations are

$$u_r = \frac{\alpha_0/\alpha_2}{4\pi} \int_0^\infty \rho e^{-\rho^2 ct} e^{-\rho|y|} J_1(\rho r) d\rho, \quad (26)$$

$$u_y = \frac{(\alpha_0/\alpha_2) \operatorname{sgn}(y)}{4\pi} \int_0^\infty \rho e^{-\rho^2 ct} e^{-\rho|y|} J_0(\rho r) d\rho. \quad (27)$$

Because of the axial symmetry, $u_\theta = 0$. Note that u_y has a discontinuity at $y = 0$. This discontinuity comes from the assumption of zero permeability in the y -direction.

Fundamental Solution for an Instantaneous Point Force in the y -Direction

Consider an instantaneous point force with unit impulse acting in the y -direction at the origin, at $t = 0$. The forcing fields are

$$f_2 = \delta(x)\delta(y)\delta(z)\delta(t), \quad f_1 = f_3 = r^F = 0. \quad (28)$$

Since the manner in which one obtains the solutions is similar to that for the case of the point fluid source, we shall show only the results:

$$p = \frac{(\alpha_0/\alpha_2) \operatorname{sgn}(y)}{4\pi} \times \left[\frac{\delta(t)|y|}{(r^2 + y^2)^{3/2}} - c \int_0^\infty \rho^3 e^{-\rho^2 ct} e^{-\rho|y|} J_0(\rho r) d\rho \right], \quad (29)$$

$$u_r = \frac{y}{8\pi G} \left[\frac{\delta(t)r}{2(1 - \nu_u)(r^2 + y^2)^{3/2}} - \alpha_3 c \int_0^\infty \rho^3 e^{-\rho^2 ct} e^{-\rho|y|} J_1(\rho r) d\rho \right], \quad (30)$$

$$u_y = \frac{1}{8\pi G} \left[\frac{\delta(t)}{2(1 - \nu_u)(r^2 + y^2)^{1/2}} \left(3 - 4\nu_u + \frac{y^2}{r^2 + y^2} \right) + \alpha_3 c \int_0^\infty \rho^2 (1 - \rho|y|) e^{-\rho^2 ct} e^{-\rho|y|} J_0(\rho r) d\rho \right], \quad (31)$$

where use has been made of the following formulae:

$$\int_{-\infty}^{\infty} \frac{\xi e^{-i\mu\xi}}{(\rho^2 + \xi^2)^2} d\xi = -\frac{i\pi}{2\rho} y e^{-\rho|y|},$$

$$\int_{-\infty}^{\infty} \frac{\xi^2 e^{-i\mu\xi}}{(\rho^2 + \xi^2)^2} d\xi = \frac{\pi}{2\rho} (1 - \rho|y|) e^{-\rho|y|}, \quad (32)$$

$$\int_0^\infty \rho e^{-\rho|y|} J_0(\rho r) d\rho = \frac{|y|}{(r^2 + y^2)^{3/2}},$$

$$\int_0^\infty \rho e^{-\rho|y|} J_1(\rho r) d\rho = \frac{r}{(r^2 + y^2)^{3/2}}. \quad (33)$$

Note again that the pore fluid pressure given by Eq. (29) is discontinuous at $y = 0$.

Fundamental Solution for an Instantaneous Point Force in the z -Direction

Here, we consider the point force in the z -direction. The single principal axis of permeability falls on the y -axis, while the point force acts in the z -direction. Therefore, there is no axis of symmetry for the present problem, in contrast with the former two cases. However, there is no substantial difference

in the approach for obtaining the fundamental solutions, although some more tedious manipulations are required.

In this case, the forcing fields are given by

$$f_3 = \delta(x)\delta(y)\delta(z)\delta(t), \quad f_1 = f_2 = r^F = 0, \quad (34)$$

for which the solutions obtained are

$$p = \frac{\alpha_0/\alpha_2}{4\pi} \sin \theta \left[\frac{\delta(t)r}{(r^2 + y^2)^{3/2}} - c \int_0^\infty \rho^3 e^{-\rho^2 ct} e^{-\rho|y|} J_1(\rho r) d\rho \right], \quad (35)$$

$$u_x = \frac{1}{8\pi G} \sin \theta \cos \theta \left[\frac{\delta(t)r^2}{2(1 - \nu_u)(r^2 + y^2)^{3/2}} - \alpha_3 c \int_0^\infty \rho^2 (1 + \rho|y|) e^{-\rho^2 ct} e^{-\rho|y|} J_2(\rho r) d\rho \right], \quad (36)$$

$$u_y = \frac{1}{8\pi G} y \sin \theta \left[\frac{\delta(t)r}{2(1 - \nu_u)(r^2 + y^2)^{3/2}} - \alpha_3 c \int_0^\infty \rho^3 e^{-\rho^2 ct} e^{-\rho|y|} J_1(\rho r) d\rho \right], \quad (37)$$

$$u_z = \frac{1}{8\pi G} \left[\frac{\delta(t)}{2(1 - \nu_u)(r^2 + y^2)^{1/2}} \left(3 - 4\nu_u + \frac{r^2}{r^2 + y^2} \sin^2 \theta \right) + \frac{1}{2} \alpha_3 c \int_0^\infty \rho^2 (1 + \rho|y|) e^{-\rho^2 ct} e^{-\rho|y|} \times \{ J_0(\rho r) + \cos 2\theta J_2(\rho r) \} d\rho \right], \quad (38)$$

where we have used the following additional formulae:

$$\frac{1}{2\pi} \int_{-\pi}^{\pi} \cos 2\phi e^{-i\mu \cos \phi} d\phi = -J_2(\mu), \quad (39)$$

$$\int_0^\infty e^{-\rho|y|} J_2(\rho r) d\rho = \frac{[(r^2 + y^2)^{1/2} - |y|]^2}{r^2(r^2 + y^2)^{1/2}}, \quad (40)$$

$$\int_0^\infty \rho e^{-\rho|y|} J_2(\rho r) d\rho = \frac{2}{r^2} \left[1 - \frac{|y|}{(r^2 + y^2)^{1/2}} \right] - \frac{|y|}{(r^2 + y^2)^{3/2}}. \quad (41)$$

Fundamental solutions for an instantaneous point force acting in the x -direction are easily obtained from Eqs. (35) through (38) by a coordinate transformation. Explicit expressions for these solutions are omitted here.

Reciprocal Theorem

Equations (1) through (7), supplemented by appropriate initial and boundary conditions, constitute a complete system of equations for an elastically isotropic, homogeneous, fluid-saturated, poroelastic solid with zero permeability in the y -direction. Solutions of this linear system of equations satisfy a reciprocal relation (Cleary, 1977; Kurashige and Clifton, 1992). The assumption of zero permeability in one direction has no influence on this relation. If we define the total fluid displacement Q_i and the total volume of supplied fluid R^F by

$$q_i = \partial Q_i / \partial t, \quad r^F = \partial R^F / \partial t, \quad (42)$$

the reciprocal theorem relates two independent "deformation" fields $\{u_i^{(1)}, Q_i^{(1)}\}$ and $\{u_i^{(2)}, Q_i^{(2)}\}$ and associated "stress" fields $\{\sigma_{ij}^{(1)}, p^{(1)}\}$ and $\{\sigma_{ij}^{(2)}, p^{(2)}\}$ resulting from the "forcing" fields $\{f_i^{(1)}, R^{F(1)}\}$ and $\{f_i^{(2)}, R^{F(2)}\}$ by

$$\begin{aligned} & \int_S [\sigma_{ij}^{*(1)} u_j^{*(2)} - p^{*(1)} Q_i^{*(2)}] n_i dS \\ & + \int_V [f_i^{*(1)} u_i^{*(2)} - R_{f(1)}^{*} p^{*(2)}] dV \\ & = \int_S [\sigma_{ij}^{*(2)} u_j^{*(1)} - p^{*(2)} Q_i^{*(1)}] n_i dS \\ & + \int_V [f_i^{*(2)} u_i^{*(1)} - R^{F*(2)} p^{*(1)}] dV, \quad (43) \end{aligned}$$

where V and S are, respectively, the volume and the surface of the body under consideration. In this relation, we have neglected a body force acting on the pore fluid, because we do not need it to obtain the integral equations that we require.

Application of Reciprocal Theorem

The reciprocal theorem can be used to obtain a pair of boundary integral equations for the crack problem. To this end, consider three solutions of Eqs. (1) through (7). These solutions, designated by (d) , (f) , and (s) , are described below.

Solution (d) corresponds to the sudden appearance of a closed dislocation loop that bounds a surface S_c across which the jump in displacement is given by the Burgers vector

$$b_i = u_{i+}^{(d)} - u_{i-}^{(d)}, \quad (44)$$

and the jump in the fluid displacement is

$$\Delta Q_i = Q_{i+}^{(d)} - Q_{i-}^{(d)}, \quad (45)$$

where the subscripts $+$ and $-$ denote evaluation on the lower and upper surfaces of S_c , which has unit normal $n_i = n_{i+} = -n_{i-}$.

Solution (f) corresponds to the instantaneous appearance of a point body force at position $\mathbf{r} = \mathbf{r}'$, described by

$$f_i^{*(f)} = \mathcal{L}[P_i \delta(t) \delta(\mathbf{r} - \mathbf{r}')] = P_i \delta(\mathbf{r} - \mathbf{r}'), \quad (46)$$

$$P_j P_j = 1, \quad (46)$$

where the asterisk and \mathcal{L} mean the Laplace transform as defined by Eq. (13).

Solution (s) corresponds to the instantaneous appearance of a point fluid volume source at $\mathbf{r} = \mathbf{r}'$. From the second equation of (42), the instantaneous point source is given by

$$s R^{*F(s)} = \mathcal{L}[\delta(t) \delta(\mathbf{r} - \mathbf{r}')] = \delta(\mathbf{r} - \mathbf{r}'). \quad (47)$$

Using (d) and (f) , and (d) and (s) as two separate fields in the reciprocal theorem (Eq. (43)), one obtains

$$\begin{aligned} P_j u_j^{*}(\mathbf{r}') &= - \int_{S_c} [\sigma_{ij}^{*(1)}(\mathbf{r}, \mathbf{r}') b_j^{*}(\mathbf{r}) \\ & - p^{*(1)}(\mathbf{r}, \mathbf{r}') \Delta Q_i^{*(1)}(\mathbf{r})] n_i(\mathbf{r}) dS, \quad (48) \end{aligned}$$

$$\begin{aligned} p^{*}(\mathbf{r}') &= s \int_{S_c} [\sigma_{ij}^{*(1)}(\mathbf{r}', \mathbf{r}') b_j^{*}(\mathbf{r}) \\ & - p^{*(1)}(\mathbf{r}, \mathbf{r}') \Delta Q_i^{*(1)}(\mathbf{r})] n_i(\mathbf{r}) dS, \quad (49) \end{aligned}$$

where superscripts (d) have been omitted from the fields associated with the dislocation loop. Interchanging \mathbf{r} and \mathbf{r}' and using the fluid volume supply rate per unit fracture area, Δq_n , defined by (see the first equation of (42))

$$\Delta q_n^* = -s \Delta Q_i^* n_j, \quad (50)$$

one obtains

$$u_m^*(\mathbf{r}) = u_m^{*(b)}(\mathbf{r}) + u_m^{*(q)}(\mathbf{r}), \quad (51)$$

$$p^*(\mathbf{r}) = p^{*(b)}(\mathbf{r}) + p^{*(q)}(\mathbf{r}), \quad (52)$$

where

$$u_m^{*(b)}(\mathbf{r}) = - \int_{S_c} \sigma_{(m)ij}^*(\mathbf{r}', \mathbf{r}) b_j^*(\mathbf{r}') n_i' dS', \quad (53)$$

$$u_m^{*(q)}(\mathbf{r}) = - \frac{1}{s} \int_{S_c} p_{(m)}^*(\mathbf{r}', \mathbf{r}) \Delta q_n^*(\mathbf{r}') dS', \quad (54)$$

$$p^{*(b)}(\mathbf{r}) = s \int_{S_c} \sigma_{(0)ij}^*(\mathbf{r}', \mathbf{r}) b_j^*(\mathbf{r}') n_i' dS', \quad (55)$$

$$p^{*(q)}(\mathbf{r}) = \int_{S_c} p_{(0)}^*(\mathbf{r}', \mathbf{r}) \Delta q_n^*(\mathbf{r}') dS', \quad (56)$$

where $n_i' = n_i(\mathbf{r}')$. In Eq. (50), the minus sign is required because $\Delta Q_i n_j$ is fluid flow into the fracture, since n_{i+} and n_i point into the fracture, while Δq_n is fluid supply from the fracture into the porous solid. In the last four equations, $\sigma_{(m)ij}^*(\mathbf{r}', \mathbf{r})$ and $p_{(m)}^*(\mathbf{r}', \mathbf{r})$ are the stresses and pore fluid pressures at \mathbf{r}' caused by the instantaneous point force acting at \mathbf{r} in the x_m -direction, while $\sigma_{(0)ij}^*(\mathbf{r}', \mathbf{r})$ and $p_{(0)}^*(\mathbf{r}', \mathbf{r})$ are the stresses and pore fluid pressures at \mathbf{r}' caused by the instantaneous point fluid volume source at \mathbf{r} . Superscripts (b) and (q) indicate contributions from the Burgers vector of the displacement discontinuity and from the fluid supply, respectively.

Dislocation Segment Solutions

To obtain the stresses and pressure resulting from an infinitesimal dislocation segment, as required for a numerical method analogous to that used in the elastic and isotropic poroelastic cases (Clifton and Abou-Sayed, 1979; Clifton and Wang, 1991), consider $u_m^{*(b)}(\mathbf{r})$ and $p^{*(b)}(\mathbf{r})$ given by Eqs. (53) and (55). Differentiating these equations with respect to x_s , one obtains

$$\frac{\partial u_m^{*(b)}(\mathbf{r})}{\partial x_s} = \int_{S_c} b_i^*(\mathbf{r}') \frac{\partial}{\partial x_s} \sigma_{(m)ij}^*(\mathbf{r}', \mathbf{r}) n_j' dS', \quad (57)$$

$$\frac{\partial p^{*(b)}(\mathbf{r})}{\partial x_s} = -s \int_{S_c} b_i^*(\mathbf{r}') \frac{\partial}{\partial x_s} \sigma_{(0)ij}^*(\mathbf{r}', \mathbf{r}) n_j' dS', \quad (58)$$

where use has been made of

$$\frac{\partial}{\partial x_s} \sigma_{(\beta)ij}^*(\mathbf{r}', \mathbf{r}) = - \frac{\partial}{\partial x_s} \sigma_{(\beta)ij}^*(\mathbf{r}', \mathbf{r}) \quad (\beta = m, 0). \quad (59)$$

From equilibrium Eq. (5), except at $\mathbf{r}' = \mathbf{r}$,

$$b_i^*(\mathbf{r}') \frac{\partial}{\partial x_j'} \sigma_{(\beta)ij}^*(\mathbf{r}', \mathbf{r}) n_s' = 0 \quad (\beta = m, 0). \quad (60)$$

Use of this equation in Eqs. (57) and (58) and application of the Stokes theorem gives

$$\frac{\partial u_m^{*(b)}(\mathbf{r})}{\partial x_s} = \epsilon_{jsn} \oint b_i^* \sigma_{(m)ij}^*(\mathbf{r}', \mathbf{r}) dx_n', \quad (61)$$

$$\frac{\partial p^{*(b)}(\mathbf{r})}{\partial x_s} = -s \epsilon_{jsn} \oint b_i^* \sigma_{(0)ij}^*(\mathbf{r}', \mathbf{r}) dx_n', \quad (62)$$

where ϵ_{jsn} is the permutation symbol and, temporarily, the Burgers vectors b_i^* are assumed to be spatially constant. These are extensions of Mura's formulae (Hirth and Rothe, 1982) to the case of a fluid-saturated, poroelastic solid; they are valid for a material which is both elastically and hydraulically anisotropic. From Eqs. (61), (62), and (1), the stresses and pressure gradi-

ent caused by dislocations with Burgers vector b_i^* along line segment $\Delta x'_n$ are as follows:

$$\Delta\sigma_{pq}^{*(b)}(\mathbf{r}) + \alpha\delta_{pq}\Delta p^{*(b)}(\mathbf{r}) = L_{pqms}\epsilon_{jsn}b_i^*\sigma_{(m)ij}^*(\mathbf{r}', \mathbf{r})\Delta x'_n, \quad (63)$$

$$\frac{\partial}{\partial x_s}\Delta p^{*(b)}(\mathbf{r}) = -s\epsilon_{jsn}b_i^*\sigma_{(0)ij}^*(\mathbf{r}', \mathbf{r})\Delta x'_n, \quad (64)$$

where L_{pqms} are elastic moduli given by Eq. (1).

Equations (63) and (64) are the general dislocation segment solutions. For applications in hydraulic fracturing, our interest is in the stress $\Delta\sigma_{zz}^{(b)}$ and pore fluid pressure $\Delta p^{(b)}$ on the plane $z = 0$ caused by a dislocation segment on the plane $z' = 0$. For definiteness, consider a "horizontal" dislocation segment with Burgers vector b_z^h along the line segment $\Delta x' = \Delta x'_1$; later, a "vertical" dislocation segment with Burgers vector b_z^v along the line segment $\Delta y' = -\Delta x'_2$ will be included to allow representation of a general dislocation segment in the plane $z' = 0$. See Fig. 1 for the sign convention. The position vectors in the plane $z = 0$ will be denoted by \mathbf{R} and \mathbf{R}' , and the lengths of the relative position vectors by

$$r = |\mathbf{r}' - \mathbf{r}|, \quad R = |\mathbf{R}' - \mathbf{R}|. \quad (65)$$

With this notation, the inverse Laplace transforms of Eqs. (63) and (64) become

$$\Delta\sigma_{zz}^{(b)h}(\mathbf{R}, t) + \alpha\Delta p^{(b)h}(\mathbf{R}, t) = \frac{2G}{1-2\nu} \int_0^t b_z^h(\tau) [(1-\nu)\sigma_{(z)xy}(\mathbf{R}', \mathbf{R}, t-\tau) - \nu\sigma_{(y)zz}(\mathbf{R}', \mathbf{R}, t-\tau)] d\tau \Delta x', \quad (66)$$

$$\Delta p^{(b)h}(\mathbf{R}, t) = - \left[b_z^h(t) \int_{-\infty}^0 \sigma_{(0)xy}(\mathbf{R}', \mathbf{r}, 0) dz + \int_0^t b_z^h(\tau) \frac{\partial}{\partial t} \int_{-\infty}^0 \sigma_{(0)xy}(\mathbf{R}', \mathbf{r}, t-\tau) dz d\tau \right] \Delta x'. \quad (67)$$

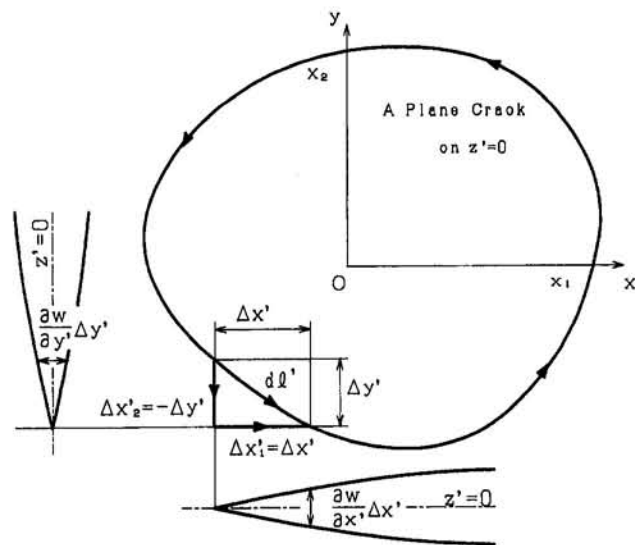


Fig. 1 Sign convention for dislocation segments $\Delta x'$ and $\Delta y'$ and crack opening $w(x', y')$; $\Delta x'_n$ in the extended Mura's formulae means the line segment along the dislocation loop in the three-dimensional body, whereas $\Delta x'$ and $\Delta y'$ are the line segments of "horizontal" and "vertical" dislocations on the plane $z' = 0$, respectively, so that $\Delta x' = \Delta x_1$ and $\Delta y' = -\Delta x_2$; the minus sign in Eqs. (68) is necessary because the Burgers vectors defined by Eq. (44) and the unit normals on the crack faces given by $n_i = n_{i+} = -n_{i-}$ mean that the crack surfaces overlap due to these Burgers vectors while $w(x', y')$ is the opening.

For the vertical dislocation segment, one can obtain expressions that are similar to Eqs. (66) and (67) by replacing h , x , and y by v , y , and x , respectively.

The crack opening $w(x', y')$ can be related to the Burgers vectors of the dislocation line segments (Clifton and Abousayed, 1979) by

$$b_z^h = -\frac{\partial w(x', y')}{\partial y'}, \quad b_z^v = -\frac{\partial w(x', y')}{\partial x'}, \quad (68)$$

where the minus sign is necessary because the Burgers vectors defined by Eq. (44) and the unit normals on the crack faces given by $n_i = n_{i+} = -n_{i-}$ mean that the crack surfaces overlap due to these Burgers vectors while $w(x', y')$ is the opening (see Fig. 1).

Substituting the above relations into Eqs. (66) and (67) for the horizontal dislocation segments and the similar ones for the vertical segments, combining the contributions from the both segments, and then integrating the resulting equations over the whole fracture area S_c with area element $dS' = \Delta x' \Delta y'$ yields

$$\begin{aligned} \sigma_{zz}^{(b)}(\mathbf{R}, t) + \alpha p^{(b)}(\mathbf{R}, t) &= -\frac{2G}{1-2\nu} \int_{S_c} \int_0^t \frac{\partial w(\mathbf{R}', \tau)}{\partial x'_\beta} [(1-\nu) \\ &\quad \times \sigma_{(z)z\beta}(\mathbf{R}', \mathbf{R}, t-\tau) - \nu\sigma_{(z)zz}(\mathbf{R}', \mathbf{R}, t-\tau)] d\tau dS', \quad (69) \end{aligned}$$

$$\begin{aligned} p^{(b)}(\mathbf{R}, t) &= \int_{S_c} \left[\frac{\partial w(\mathbf{R}', t)}{\partial x'_\beta} \int_{-\infty}^0 \sigma_{(0)z\beta}(\mathbf{R}', \mathbf{r}, 0) dz \right. \\ &\quad \left. + \int_0^t \frac{\partial w(\mathbf{R}', \tau)}{\partial x'_\beta} \right. \\ &\quad \left. \times \frac{\partial}{\partial t} \int_{-\infty}^0 \sigma_{(0)z\beta}(\mathbf{R}', \mathbf{r}, t-\tau) dz d\tau \right] dS', \quad (70) \end{aligned}$$

where repeated subscripts β mean the summation over $\beta = 1$ and 2 (or x and y).

Point Force and Source Solutions

To obtain explicit expressions of $\sigma_{zz}^{(b)}(\mathbf{R}, t)$ and $p^{(b)}(\mathbf{R}, t)$ from Eqs. (69) and (70), one needs stress components $\sigma_{(z)zx}$, $\sigma_{(z)zy}$, $\sigma_{(x)zy}$, $\sigma_{(y)zz}$ at $z = 0$, $\sigma_{(0)zx}$, $\sigma_{(0)zy}$ for arbitrary z , and integrals $\int_{-\infty}^0 \sigma_{(0)zx}(\mathbf{r}, t) dz$, $\int_{-\infty}^0 \sigma_{(0)zy}(\mathbf{r}, t) dz$. All the needed stress components (see Appendix) can be obtained from the fundamental solutions in the previous sections by easy but tedious manipulations. We show only the evaluation of the infinite integrals:

$$\begin{aligned} \int_{-\infty}^0 \sigma_{(0)zx}(\mathbf{r}, t) dz &= \frac{G\alpha_0}{2\pi\alpha_2} \operatorname{sgn}(x) \int_0^\infty \rho e^{-\rho^2 ct} e^{-\rho|y|} J_1(\rho|x|) d\rho, \quad (71) \end{aligned}$$

$$\begin{aligned} \int_{-\infty}^0 \sigma_{(0)zy}(\mathbf{r}, t) dz &= \frac{G\alpha_0}{2\pi\alpha_2} \operatorname{sgn}(y) \int_0^\infty \rho e^{-\rho^2 ct} e^{-\rho|x|} J_0(\rho|y|) d\rho, \quad (72) \end{aligned}$$

where use has been made of (Gradshteyn and Ryzhik, 1965)

$$\begin{aligned} \int_0^\infty \frac{z}{(x^2 + z^2)^{\beta/2}} J_\beta(\rho\sqrt{x^2 + z^2}) dz &= \frac{1}{\rho|x|^{\beta-1}} J_{\beta-1}(\rho|x|). (\beta=1,2) \quad (73) \end{aligned}$$

The infinite integrals in Eqs. (71) and (72) for $t = 0$, which appear in Eq. (70), can be easily carried out. Using these evaluations, Eqs. (71) and (72), and the equations given in the Appendix, one obtains

$$\begin{aligned} \sigma_{zz}^{(b)}(\mathbf{R}, t) + \alpha p^{(b)}(\mathbf{R}, t) &= \frac{2G}{1-2\nu} \frac{1}{4\pi} \\ &\times \int_{Sc} dS' \left\{ \frac{1-2\nu_u}{2(1-\nu_u)} \frac{(\mathbf{R}' - \mathbf{R}) \cdot \nabla' w(\mathbf{R}', t)}{R^3} \right. \\ &+ \alpha_3 c \int_0^t d\tau \int_0^\infty d\rho \rho^3 e^{-\rho^2 c(t-\tau)} e^{-\rho|y'-y|} \\ &\times \left[\frac{\partial w(\mathbf{R}', \tau)}{\partial x'} \left((1-2\nu) \frac{1+\rho|y'-y|}{\rho(x'-x)} J_2(\rho|x'-x|) \right. \right. \\ &+ 2\nu \operatorname{sgn}(x'-x) J_1(\rho|x'-x|) \\ &+ \frac{\partial w(\mathbf{R}', \tau)}{\partial y'} \left((1-2\nu) \frac{y'-y}{|x'-x|} J_1(\rho|x'-x|) \right. \\ &\left. \left. + 2\nu \operatorname{sgn}(y'-y) J_0(\rho|x'-x|) \right) \right] \left. \right\}, \quad (74) \end{aligned}$$

$$\begin{aligned} p^{(b)}(\mathbf{R}, t) &= -\frac{G\alpha_0}{2\pi\alpha_2} \int_{Sc} dS' \left[\frac{(\mathbf{R}' - \mathbf{R}) \cdot \nabla' w(\mathbf{R}', t)}{R^3} \right. \\ &- c \int_0^t d\tau \int_0^\infty d\rho \rho^3 e^{-\rho^2 c(t-\tau)} e^{-\rho|y'-y|} \cdot \left. \right\} \\ &\times \frac{\partial w(\mathbf{R}', \tau)}{\partial x'} \operatorname{sgn}(x'-x) J_1(\rho|x'-x|) \\ &+ \frac{\partial w(\mathbf{R}', \tau)}{\partial y'} \operatorname{sgn}(y'-y) J_0(\rho|x'-x|) \left. \right\}. \quad (75) \end{aligned}$$

Stress and Pressure Caused by Fluid Supply

Let us return to Eqs. (54) and (56) and seek stresses and pressure caused by the fluid volume supply through the crack surfaces. Employing Eqs. (1) and (7) to (54), one obtains

$$\begin{aligned} \sigma_{zz}^{*(q)}(\mathbf{r}) + \alpha p^{*(q)}(\mathbf{r}) &= \frac{2G}{s} \int_{Sc} \left[\frac{\partial p_{(z)}^*(\mathbf{r}', \mathbf{r})}{\partial z'} \right. \\ &+ \frac{\nu}{1-2\nu} \frac{\partial p_{(m)}^*(\mathbf{r}', \mathbf{r})}{\partial x'_m} \left. \right] \Delta q_n(\mathbf{r}') dS'. \quad (76) \end{aligned}$$

Pressures $p_{(m)}$ in the above equation and $p_{(0)}$ in Eq. (56) are the solutions for the instantaneously applied point force problem and the instantaneously appearing fluid volume source problem, given by Eqs. (29), (35), and (18), respectively. Using these solutions in Eqs. (76) and (56), applying the inverse Laplace transform to them, and carrying out one of the double integrals after interchanging the order of integrations, one obtains for $z = 0$

$$\begin{aligned} \sigma_{zz}^{(q)}(\mathbf{R}, t) + \alpha p^{(q)}(\mathbf{R}, t) &= \frac{G\alpha_0}{2\pi\alpha_2} \int_{Sc} dS' \int_0^t \int_0^\infty \rho e^{-\rho^2 c(t-\tau)} e^{-\rho|y'-y|} \\ &\times \frac{J_1(\rho|x'-x|)}{|x'-x|} d\rho \Delta q_n(\mathbf{R}', \tau) d\tau, \quad (77) \end{aligned}$$

$$\begin{aligned} p^{(q)}(\mathbf{R}, t) &= \frac{G}{8\pi^2\alpha\alpha_2} \int_{Sc} dS' \int_0^t \frac{\delta(y'-y)}{c(t-\tau)} \\ &\times e^{-(x'-x)^2/4c(t-\tau)} \Delta q_n(\mathbf{R}', \tau) d\tau. \quad (78) \end{aligned}$$

Integral Equations

Here, let us seek the integral equations for the case of the zero permeability in the y -direction. Combine Eqs. (74) and (75) and Eqs. (77) and (78), one obtains two coupled integral equations that relate the normal traction $\sigma_{zz}(\mathbf{R}, t)$ and pore fluid pressure $p(\mathbf{R}, t)$ at the crack surface to the crack opening $w(\mathbf{R}', \tau)$ and fluid supply rate per unit fracture area $\Delta q_n(\mathbf{R}', \tau)$:

$$\begin{aligned} \sigma_{zz}(\mathbf{R}, t) &= \frac{G}{4\pi(1-\nu_u)} \int_{Sc} \left\{ \frac{(\mathbf{R}' - \mathbf{R}) \cdot \nabla' w(\mathbf{R}', t)}{R^3} \right. \\ &+ \int_0^t \left[H_{11}(\mathbf{R}' - \mathbf{R}, t-\tau) \frac{\partial w(\mathbf{R}', \tau)}{\partial x'} \right. \\ &+ H_{12}(\mathbf{R}' - \mathbf{R}, t-\tau) \frac{\partial w(\mathbf{R}', \tau)}{\partial y'} \\ &\left. \left. + H_{13}(\mathbf{R}' - \mathbf{R}, t-\tau) \Delta q_n(\mathbf{R}', \tau) \right] d\tau \right\} dS', \quad (79) \end{aligned}$$

$$\begin{aligned} p(\mathbf{R}, t) &= \frac{GB(1+\nu_u)}{6\pi(1-\nu_u)} \int_{Sc} \left\{ \frac{(\mathbf{R}' - \mathbf{R}) \cdot \nabla' w(\mathbf{R}', t)}{R^3} \right. \\ &+ \int_0^t \left[H_{21}(\mathbf{R}' - \mathbf{R}, t-\tau) \frac{\partial w(\mathbf{R}', \tau)}{\partial x'} \right. \\ &+ H_{22}(\mathbf{R}' - \mathbf{R}, t-\tau) \frac{\partial w(\mathbf{R}', \tau)}{\partial y'} \\ &\left. \left. + H_{23}(\mathbf{R}' - \mathbf{R}, t-\tau) \Delta q_n(\mathbf{R}', \tau) \right] d\tau \right\} dS', \quad (80) \end{aligned}$$

where

$$\begin{aligned} H_{11}(\mathbf{R}, t) &= \frac{\nu_u - \nu}{1-\nu} c \int_0^\infty \rho^3 e^{-\rho^2 ct} e^{-\rho|y|} \\ &\times \left[\frac{1+\rho|y|}{\rho x} J_2(\rho|x|) - \operatorname{sgn}(x) J_1(\rho|x|) \right] d\rho, \quad (81) \end{aligned}$$

$$\begin{aligned} H_{12}(\mathbf{R}, t) &= \frac{\nu_u - \nu}{1-\nu} c \int_0^\infty \rho^3 e^{-\rho^2 ct} e^{-\rho|y|} \\ &\times \left[\frac{y}{|x|} J_1(\rho|x|) - \operatorname{sgn}(y) J_0(\rho|x|) \right] d\rho, \quad (82) \end{aligned}$$

$$\begin{aligned} H_{13}(\mathbf{R}, t) &= -\frac{2}{3} B(1+\nu_u) \left[\frac{1}{4\pi} \frac{2(1-\nu)}{1-2\nu} \frac{\delta(y)}{ct} e^{-x^2/(4ct)} \right. \\ &\left. - \int_0^\infty \rho e^{-\rho^2 ct} e^{-\rho|y|} \frac{J_1(\rho|x|)}{|x|} d\rho \right], \quad (83) \end{aligned}$$

$$H_{21}(\mathbf{R}, t) = -c \int_0^\infty \rho^3 e^{-\rho^2 ct} e^{-\rho|y|} \cdot \operatorname{sgn}(x) J_1(\rho|x|) d\rho, \quad (84)$$

$$H_{22}(\mathbf{R}, t) = -c \int_0^\infty \rho^3 e^{-\rho^2 ct} e^{-\rho|y|} \cdot \operatorname{sgn}(y) J_0(\rho|x|) d\rho, \quad (85)$$

$$H_{23}(\mathbf{R}, t) = \frac{1}{4\pi} \frac{2B(1+\nu_u)(1-\nu)}{3(\nu_u-\nu)} \frac{\delta(y)}{ct} e^{-x^2/(4ct)}. \quad (86)$$

Equations (79) and (80) are the required integral equations. For the nonporous case where $\nu_u = \nu$ and $B = 0$, Eq. (79) reduces to the integral equation for an elastic solid (Clifton and Abou-Sayed, 1979) and Eq. (80) vanishes.

Although evolutionary functions $H_{ij}(\mathbf{R}, t)$ involve infinite integrals with respect to ρ , except $H_{23}(\mathbf{R}, t)$, their integrands have no singularities and decay rapidly as $\rho \rightarrow \infty$; thus, the numerical evaluations of these integrals are not difficult.

Some insight into the relative magnitudes of the normal tractions in Eq. (79) and the pressure in Eq. (80) can be obtained by noting that the two factors on the right sides of Eqs. (79) and (80) satisfy the inequality

$$[G/4\pi(1 - \nu_u)] \geq [GB(1 + \nu_u)/6\pi(1 - \nu_u)], \quad (87)$$

since $B \leq 1$ and $\nu_u \leq \frac{1}{2}$. Equality holds only for $B = 1$ and $\nu_u = \frac{1}{2}$. Therefore, if, for example, the applied normal traction on the crack surface is stepwise (discontinuous) at $t = 0$, the induced pore fluid pressure $p(\mathbf{R}, 0+)$ is less than the applied traction for the case of compressible constituents. Further insight into the behavior described by Eqs. (79) and (80) will be obtained by solving Eq. (79) for hydraulic fracturing applications where $\Delta q_n(\mathbf{R}', \tau)$ is regarded as prescribed.

References

Cleary, M. P., 1977, "Fundamental Solutions for a Fluid-Saturated Porous Solid," *International Journal of Solids and Structures*, Vol. 13-9, pp. 785-806.
 Clifton, R. J., and Abou-Sayed, A. S., 1979, "On the Computation of the Three-Dimensional Geometry of Hydraulic Fractures," Paper SPE 7943 presented at the 1979 SPE symposium on low permeability gas reservoirs, Denver, May, pp. 20-22.
 Clifton, R. J., and Wang, J. J., 1991, "Modeling of Poroelastic Effects in Hydraulic Fracturing," Paper SPE 21871 presented at the 1991 SPE Rocky Mountain Regional Meeting/Low-Permeability Reservoirs Symposium, Denver, Apr., pp. 15-17.
 Gradshteyn, I. S., and Ryzhik, I. M., 1965, *Tables of Integrals, Series, and Products*, Academic Press, New York.
 Hirth, J. P., and Lothe, J., 1982, *Theory of Dislocations*, John Wiley and Sons, New York.
 Kurashige, M., and Clifton, R. J., 1992, "Integral Equations for the Problem of a 3D Crack in an Infinite, Fluid-Filled, Poroelastic Solid," *SPE Production Engineering*, Feb., pp. 34-38.
 Sneddon, I. N., 1951, *Fourier Transforms*, McGraw-Hill, New York.

APPENDIX

After some tedious manipulations, the stress components necessary to obtain explicit expressions of $\sigma_{zz}^{(b)}(\mathbf{R}, t)$ and $p^{(b)}(\mathbf{R}, t)$ from Eqs. (69) and (70) are obtained as follows:

$$\sigma_{(z)zx}(x, y, 0) = -\frac{1}{4\pi} \frac{1}{x} \left\{ \frac{1 - 2\nu_u}{2(1 - \nu_u)} \frac{x^2 \delta(t)}{(x^2 + y^2)^{3/2}} \right.$$

$$\left. + \alpha_3 c \int_0^\infty \rho^2 (1 + \rho|y|) e^{-\rho^2 c t} e^{-\rho|y|} J_2(\rho x) d\rho \right\}, \quad (A1)$$

$$\sigma_{(z)zy}(x, y, 0) = -\frac{1}{4\pi} \left\{ \frac{1 - 2\nu_u}{2(1 - \nu_u)} \frac{y \delta(t)}{(x^2 + y^2)^{3/2}} \right.$$

$$\left. + \alpha_3 c \int_0^\infty \rho^3 e^{-\rho^2 c t} e^{-\rho|y|} \frac{y}{x} J_1(\rho|x|) d\rho \right\}, \quad (A2)$$

$$\sigma_{(x)zx}(x, y, 0) = \frac{1}{4\pi} \left(\frac{1 - 2\nu_u}{2(1 - \nu_u)} \frac{x \delta(t)}{(x^2 + y^2)^{3/2}} \right.$$

$$\left. - \alpha_3 c \int_0^\infty \rho^3 e^{-\rho^2 c t} e^{-\rho|y|} \times \left\{ \frac{1 + \rho|y|}{\rho x} J_2(\rho x) - 2J_1(\rho x) \right\} d\rho \right\}, \quad (A3)$$

$$\sigma_{(y)zx}(x, y, 0) = \frac{1}{4\pi} \left(\frac{1 - 2\nu_u}{2(1 - \nu_u)} \frac{y \delta(t)}{(x^2 + y^2)^{3/2}} \right.$$

$$\left. + \alpha_3 c \int_0^\infty \rho^3 e^{-\rho^2 c t} \left\{ 2 \operatorname{sgn}(y) J_0(\rho x) \right.$$

$$\left. - \frac{y}{x} J_1(\rho x) \right\} d\rho \right\}, \quad (A4)$$

$$\sigma_{(0)zx}(x, y, z) = -\frac{G}{2\pi} \frac{\alpha_0}{\alpha_2} \frac{xz}{x^2 + z^2}$$

$$\times \int_0^\infty \rho^2 e^{-\rho^2 c t} e^{-\rho|y|} \cdot J_2(\rho \sqrt{x^2 + z^2}) d\rho, \quad (A5)$$

$$\sigma_{(0)zy}(x, y, z) = -\frac{G}{2\pi} \frac{\alpha_0}{\alpha_2} \frac{\operatorname{sgn}(y)z}{(x^2 + z^2)^{1/2}}$$

$$\times \int_0^\infty \rho^2 e^{-\rho^2 c t} e^{-\rho|y|} \cdot J_1(\rho \sqrt{x^2 + z^2}) d\rho. \quad (A6)$$

C. W. Fan

Ph.D. Student.

Chyanbin Hwu¹

Professor.

Institute of Aeronautics and Astronautics,
National Cheng Kung University,
Tainan, Taiwan 70101
Republic of China

Punch Problems for an Anisotropic Elastic Half-Plane

By combining Stroh's formalism and the method of analytical continuation, several mixed-typed boundary value problems of an anisotropic elastic half-plane are studied in this paper. First, we consider a set of rigid punches of arbitrary profiles indenting into the surface of an anisotropic elastic half-plane with no slip occurring. Illustrations are presented for the normal and rotary indentation by a flat-ended punch. A sliding punch with or without friction is then considered under the complete or incomplete indentation condition.

1 Introduction

The problem of plane punch indentation has been investigated for many years due to its broad application in engineering mechanics. This is one of the mixed boundary value problems and may be considered as a particular contact problem because of the line contact region. For the contact problems, most of the analytical formula can be found in the books written by Galin (1961), Gladwell (1980), and Johnson (1985). Muskhelishvili (1954) and England (1971) provided solutions for several types of punch problems in their books by using the method of analytical continuation. Gladwell and England (1977) and Gladwell (1978) have investigated the use of certain orthogonal polynomial expansions in the solutions of some mixed boundary value problems such as crack and punch problems. Frictional punch of flat-ended or wedge-shaped profile with crack initiating at one end of the contact region has been studied by Hasebe et al. (1989) and Okumura et al. (1990) who used a rational mapping function and complex stress function to carry out the analysis. Fabrikant (1986a, b) presented an integral equation based on the reciprocal distance established by himself to solve the problem for a punch of arbitrary shape on an elastic half-space. A similar case for an elliptical punch on an elastic half-space with friction was analyzed by Shibuya et al. (1989) who used the generalized Abel transform method.

The literature survey stated in the above paragraph is for the cases of isotropic materials. For anisotropic materials, Willis (1966) studied the Hertzian contact problem of anisotropic bodies by the Fourier transform method. Chen (1969) investigated stresses fields in anisotropic half-plane due to indentation and sliding by a frictionless punch with smooth end face. Tsiang and Mandell (1985) employed a two-dimensional assumed stress hybrid finite element to obtain the characteristic matrices of the bodies brought into contact. Shield (1987) provided the variational principles for some elastic problems involving smooth contact and crack problem. Jaffar and Savage (1988) investigated the contact problem in which an elastic strip is indented by a rigid punch of arbitrary shape by using a numerical method proposed by Gladwell (1976). Klintworth and Stronge (1990) used a potential function approach to construct solutions for planar punch problems in an anisotropic half-plane where there is no slip on the surface of a flat punch. In contrast to homogeneous materials, a multilayered medium bounded to an elastic half-space has also been examined by many researchers; for

example, Lin et al. (1991) applied the complex potential functions suggested by Green and Zerna (1954) and Pan and Chou (1976) to obtain the closed-form solution for a transversely isotropic half-space subjected to various distribution of normal and tangential contact stresses on its surface, and Kuo and Keer (1992) used the Hankel transform to numerically solve the contact problem of a layered transversely isotropic half-space.

Although there are many results obtained in the literature, to the authors' knowledge the analytical solutions for the general punch problems, such as a problem of arbitrary number of punches with arbitrary profiles, have not been found for the general anisotropic elastic half-plane. If such a general solution can be found analytically, the effects of material anisotropy and punch profiles can be studied easily, which is helpful for the physical applications to composite materials, road pavements, geotechnical engineering and tribology, etc. In the present paper, Stroh's formalism (Stroh, 1958, 1962) which has been proved to be elegant and powerful for anisotropic elasticity are combined with the method of analytical continuation (Muskhelishvili, 1954) to solve the problems of indentation of plane punches with arbitrary profiles into an anisotropic elastic half-plane. Explicit solutions expressed in complex matrix notation are obtained from the Hilbert problem of vector form (Muskhelishvili, 1954; Hwu, 1992). For the purpose of illustration, some special cases are deduced from this general solution, such as normal and rotary indentation by a flat-ended punch. Moreover, in order to verify our results, the solutions are simplified to the cases of isotropic materials and the results agree with those given by Muskhelishvili (1954). The other case which has also been studied in this paper is the problem of a sliding punch with friction. An example of incomplete indentation by a wedge-shaped punch under normal pressure is solved explicitly and the condition to have complete indentation is discussed.

2 Basic Formulation for Anisotropic Elastic Half-Plane

(a) **Stroh's Formalism and Analytical Continuation.** The basic equations for two-dimensional anisotropic elasticity are the strain-displacement equations, the stress-strain laws, and the equations of equilibrium. By applying the Stroh's formalism (Stroh, 1958, 1962), a general solution satisfying these equations may be expressed as

$$\mathbf{u} = \mathbf{A} \mathbf{f}(z) + \overline{\mathbf{A} \mathbf{f}(z)}, \quad \boldsymbol{\phi} = \mathbf{B} \mathbf{f}(z) + \overline{\mathbf{B} \mathbf{f}(z)}, \quad (2.1a)$$

where

$$\mathbf{A} = [\mathbf{a}_1 \quad \mathbf{a}_2 \quad \mathbf{a}_3], \quad \mathbf{B} = [\mathbf{b}_1 \quad \mathbf{b}_2 \quad \mathbf{b}_3],$$

$$\mathbf{f}(z) = [f_1(z_1) \quad f_2(z_2) \quad f_3(z_3)]^T, \quad z_\alpha = x + p_\alpha y,$$

$$\alpha = 1, 2, 3. \quad (2.1b)$$

¹ To whom all correspondence should be addressed.

Contributed by the Applied Mechanics Division of THE AMERICAN SOCIETY OF MECHANICAL ENGINEERS for publication in the ASME JOURNAL OF APPLIED MECHANICS.

Discussion on this paper should be addressed to the Technical Editor, Professor Lewis T. Wheeler, Department of Mechanical Engineering, University of Houston, Houston, TX 77204-4792, and will be accepted until four months after final publication of the paper itself in the ASME JOURNAL OF APPLIED MECHANICS.

Manuscript received by the ASME Applied Mechanics Division, June 2, 1994; final revision, Oct. 7, 1994. Associate Technical Editor: R. Abeyaratne.

In the above equation, (x, y) is a fixed rectangular coordinate system; \mathbf{u} and $\boldsymbol{\phi}$ represent, respectively, the displacements and stress functions; p_α , $(\mathbf{a}_\alpha, \mathbf{b}_\alpha)$, $\alpha = 1, 2, 3$, are the eigenvalues and eigenvectors of the materials; and $\mathbf{f}(z)$ is a holomorphic complex function vector to be determined by satisfying the boundary condition of the problems considered. The superscript T denotes the transpose and the overbar represents the conjugate of a complex number. Note that (Suo, 1990; Hwu, 1993) in the derivation throughout this paper, the argument of each component function of $\mathbf{f}(z)$ is written as $z = x + py$ without referring to the associated eigenvalues p_α . Once the solution of $\mathbf{f}(z)$ is obtained for a given boundary value problem, a replacement of z_1, z_2 , or z_3 should be made for each component function to calculate field quantities from (2.1).

The stresses σ_{ij} are related to the stress function $\boldsymbol{\phi}$ by

$$\sigma_{i1} = -\phi_{i,2}, \quad \sigma_{i2} = \phi_{i,1}. \quad (2.2a)$$

More generally, if \mathbf{t} is the surface traction vector, then

$$\mathbf{t} = \frac{d\boldsymbol{\phi}}{ds}, \quad (2.2b)$$

where s is the arc length measured along the curved boundary in the direction such that when one faces the direction of increasing s , the material is located on the right-hand side.

Through the use of the analytical continuation method, a Hilbert problem (Muskhelishvili, 1954) can be formulated for the half-plane problems. It will be assumed that the elastic body occupies the lower half-plane $y < 0$ which is denoted by S^- , so that the region S^- is to the right if one moves in the positive direction along the x -axis. The upper half-plane is denoted by S^+ (Fig. 1).

Since ds is equal to dz on $y = 0$, the traction on the surface $y = 0$ of the half-plane S^- can be represented as

$$\mathbf{t} = \lim_{y \rightarrow 0^-} \frac{d}{dz} \{ \mathbf{B} \mathbf{f}(z) + \overline{\mathbf{B} \mathbf{f}(z)} \}, \quad (2.3)$$

and the last term of (2.3) has the following relation:

$$\lim_{y \rightarrow 0^-} \frac{d}{dz} \overline{\mathbf{B} \mathbf{f}(z)} = \lim_{y \rightarrow 0^+} \frac{d}{dz} \overline{\mathbf{B} \mathbf{f}(z)}.$$

From the theory of functions of a complex variable, we know that if $\mathbf{f}(z)$ is holomorphic for $z \in S^-$, then $\mathbf{f}(\bar{z})$ is holomorphic for $z \in S^+$, and $(d/dz) \mathbf{f}(\bar{z}) = \mathbf{f}'(\bar{z})$ where prime $'$ denotes differentiation with respect to its argument. With this in mind, we introduce $\boldsymbol{\theta}'(z)$ such that

$$\boldsymbol{\theta}'(z) = \begin{cases} \mathbf{B} \mathbf{f}'(z), & z \in S^-, \\ -\overline{\mathbf{B} \mathbf{f}'(\bar{z})}, & z \in S^+. \end{cases} \quad (2.4)$$

Since $\mathbf{f}'(z)$ should be holomorphic in the elastic body S^- , $\boldsymbol{\theta}'(z)$ is now holomorphic in S^- and S^+ , i.e., $\boldsymbol{\theta}'(z)$ is sectionally holomorphic in the whole plane except possibly on some segments of x -axis.

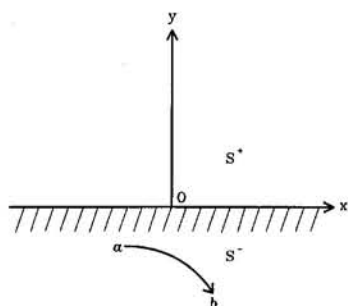


Fig. 1 Notation of the half-plane

By the above definition and the following notation,

$$\lim_{y \rightarrow 0^-} \boldsymbol{\theta}'(z) = \boldsymbol{\theta}'(x^-), \quad \lim_{y \rightarrow 0^+} \boldsymbol{\theta}'(z) = \boldsymbol{\theta}'(x^+),$$

(2.3) can be rewritten as

$$\begin{aligned} \mathbf{t}(x) &= \lim_{y \rightarrow 0^-} \mathbf{B} \mathbf{f}'(z) + \lim_{y \rightarrow 0^+} \overline{\mathbf{B} \mathbf{f}'(z)} \\ &= \boldsymbol{\theta}'(x^-) - \boldsymbol{\theta}'(x^+). \end{aligned} \quad (2.5)$$

In a similar way, the differentiation of displacement vector \mathbf{u} shown in (2.1a) for $y \rightarrow 0^-$ can be written as

$$i\bar{\mathbf{M}}\mathbf{u}'(x) = \boldsymbol{\theta}'(x^+) + \bar{\mathbf{M}}\mathbf{M}^{-1}\boldsymbol{\theta}'(x^-), \quad (2.6)$$

where $\mathbf{M} = -i\bar{\mathbf{B}}\mathbf{A}^{-1} = \mathbf{H}^{-1}(\mathbf{I} + i\mathbf{S}) = \mathbf{L}(\mathbf{I} - i\mathbf{S})^{-1}$ is the impedance matrix, and \mathbf{S} , \mathbf{H} , and \mathbf{L} are three real fundamental elasticity matrices (Ting, 1988).

(b) **Half-Plane Far-Field Condition.** Consider an arc ab in the body S^- having the direction from a to b as its positive direction (Fig. 1). By using (2.2b) and (2.1a)₂, the resultant force \mathbf{q} on the arc ab can be represented as

$$\mathbf{q} = \int_a^b \mathbf{t} ds = [\mathbf{B} \mathbf{f}(z) + \overline{\mathbf{B} \mathbf{f}(z)}]_a^b. \quad (2.7)$$

If we consider the case where the stresses and rotation tend to zero as $|z|$ tends to infinity, for large $|z|$ the complex function vector $\mathbf{f}(z)$ has the form

$$\mathbf{f}(z) = \langle \langle \log z_\alpha \rangle \rangle \mathbf{q}^* + O(1), \quad (2.8)$$

where the angular bracket $\langle \langle \dots \rangle \rangle$ stands for the diagonal matrix in which each component is varied according to the Greek index α , \mathbf{q}^* is a complex constant vector to be determined by the half-plane far-field condition. With the arc ab lying on the boundary of the half-plane, i.e., x -axis, we let $a = R_1 e^{i\pi}$, $b = R_2 e^{i2\pi}$. The resultant force \mathbf{q} applied on the surface of the half-plane can now be calculated by substituting (2.8) into (2.7). The result is

$$\mathbf{q} = (\mathbf{B} \mathbf{q}^* + \overline{\mathbf{B} \mathbf{q}^*}) \log \frac{R_2}{R_1} + \pi i (\mathbf{B} \mathbf{q}^* - \overline{\mathbf{B} \mathbf{q}^*}).$$

Since R_1, R_2 tend to infinity independently, we must conclude

$$\mathbf{B} \mathbf{q}^* + \overline{\mathbf{B} \mathbf{q}^*} = \mathbf{0}, \quad \mathbf{q} = \pi i (\mathbf{B} \mathbf{q}^* - \overline{\mathbf{B} \mathbf{q}^*}), \quad (2.9)$$

and hence

$$\mathbf{q}^* = \frac{1}{2\pi i} \mathbf{B}^{-1} \mathbf{q}. \quad (2.10)$$

By (2.4), (2.8), and (2.10), the half-plane far-field condition for $\boldsymbol{\theta}'(z)$ is

$$\boldsymbol{\theta}'(z) = \frac{1}{2\pi i} \mathbf{B} \left\langle \left\langle \frac{1}{z_\alpha} \right\rangle \right\rangle \mathbf{B}^{-1} \mathbf{q}, \quad \text{as } |z| \rightarrow \infty. \quad (2.11)$$

If $y \rightarrow 0^-$, the diagonal matrix $\langle \langle 1/z_\alpha \rangle \rangle$ approximates $(1/x)\mathbf{I}$ since the second part of $z_\alpha, p_\alpha y$, disappears. Therefore

$$\boldsymbol{\theta}'(x) = \frac{\mathbf{q}}{2\pi i} \frac{1}{x}, \quad \text{as } |x| \rightarrow \infty \quad \text{and } y \rightarrow 0^-. \quad (2.12)$$

In summary, instead of finding $\mathbf{f}(z)$ in S^- , we define a new function $\boldsymbol{\theta}'(z)$ which is sectionally holomorphic in the whole plane except on some segments of the boundary, and by solving (2.5) and/or (2.6) with the half-plane far-field condition derived in (2.12), $\boldsymbol{\theta}'(z)$, hence $\mathbf{f}(z)$, can be determined for the half-plane problem.

One thing that should be emphasized here is the applicability of $\mathbf{f}(z)$ in the full field of the half-plane. As we know, the general solution shown in (2.1) requires that each component

of the complex function vector $\mathbf{f}(z)$ be a holomorphic function with argument z_1 , z_2 , and z_3 , respectively. This means that each component of the new function $\boldsymbol{\theta}'(z)$ introduced in (2.4) may not be a function with only one argument z_1 or z_2 or z_3 . The question now is that $\mathbf{f}(z)$ is determined after $\boldsymbol{\theta}'(z)$ is found through a certain Hilbert problem and how can we know the argument of $\boldsymbol{\theta}'(z)$ is z_1 , z_2 , or z_3 or any combination of them. In solving the Hilbert problem, which is set through the method of analytical continuation for a specific boundary, the full-field solution may be expressed in terms of the complex variable $z = x + iy$. In the case of half-plane problem, this specific boundary is x -axis in which $y = 0$, hence the full-field solution may be expressed in terms of z or $z_\alpha (= x + p_\alpha y)$, $\alpha = 1, 2, 3$, depending on the requirement of $\mathbf{f}(z)$. Therefore, the most appropriate way to get the solution, which is valid for the full field including the boundary, is dropping the subscripts of z during the derivation of $\boldsymbol{\theta}'(z)$ and $\mathbf{f}(z)$. Once the solution of $\mathbf{f}(z)$ is obtained from a certain boundary value problem, a replacement of z_1 , z_2 , or z_3 should be made for each component function to calculate the full-field solution for the deformations and stresses. A translating technique for the above statement has been introduced by Hwu (1993) as follows.

If an implicit solution is written as

$$\mathbf{f}(z) = \mathbf{C} \langle \langle g_\alpha(z) \rangle \rangle \mathbf{q}, \quad (2.13a)$$

with the understanding that the subscript of z is dropped before the matrix product and a replacement of z_1 , z_2 , or z_3 should be made for each component function of $\mathbf{f}(z)$ after the multiplication of matrices, the explicit solution can be expressed as

$$\mathbf{f}(z) = \sum_{k=1}^3 \langle \langle g_k(z_\alpha) \rangle \rangle \mathbf{C} \mathbf{I}_k \mathbf{q}, \quad (2.13b)$$

where

$$\mathbf{I}_1 = \begin{bmatrix} 1 & 0 & 0 \\ 0 & 0 & 0 \\ 0 & 0 & 0 \end{bmatrix}, \quad \mathbf{I}_2 = \begin{bmatrix} 0 & 0 & 0 \\ 0 & 1 & 0 \\ 0 & 0 & 0 \end{bmatrix}, \quad \mathbf{I}_3 = \begin{bmatrix} 0 & 0 & 0 \\ 0 & 0 & 0 \\ 0 & 0 & 1 \end{bmatrix}. \quad (2.13c)$$

3 Punch Problems—A Type of Mixed Boundary Value Problems

In the following sections, a variety of mixed boundary value problems for the half-plane S^- will be considered. In all cases, the analytical continuation method described in Section 2 will be used to represent the stress and displacement fields in terms of a single complex function vector which may be determined by satisfying the Hilbert problem for a set of line intervals on $y = 0$.

In this section, we examine the case that a set of rigid punches of given profiles are brought into contact with the surface of the half-plane and are allowed to indent the surface in such a way that the punches completely adhere to the half-plane on initial contact and during the subsequent indentation no slip occurs and the contact region does not change. Let us suppose the contact region L is the union of a finite set of line segments $L_k = (a_k, b_k)$, $k = 1, 2, \dots, n$, where the ends of the segments are encountered in the order $a_1, b_1, a_2, b_2, \dots, a_n, b_n$ when moving in the positive x -direction. For this case the displacements of the surface of the half-plane are known at each point of the contact region, then the boundary conditions are

$$\begin{aligned} \mathbf{u}(x) &= (u_k(x), v_k(x) + c_k, 0)^T = \hat{\mathbf{u}}(x), \quad x \in L, \\ \mathbf{t}(x) &= (\sigma_{xy}, \sigma_{yy}, \sigma_{zz})^T = \mathbf{0}, \quad x \notin L, \end{aligned} \quad (3.1)$$

where $u_k(x)$ and $v_k(x)$ are related to the profile of the k th punch and c_k is the relative depth of indentation. From (2.5) and (2.6), the boundary conditions lead to the following Hilbert problem:

$$\boldsymbol{\theta}'(x^+) - \boldsymbol{\theta}'(x^-) = \mathbf{0}, \quad x \notin L,$$

$$\boldsymbol{\theta}'(x^+) + \bar{\mathbf{M}} \mathbf{M}^{-1} \boldsymbol{\theta}'(x^-) = i \bar{\mathbf{M}} \hat{\mathbf{u}}'(x), \quad x \in L. \quad (3.2)$$

The solution to this Hilbert problem of vector form is (Hwu, 1992)

$$\begin{aligned} \boldsymbol{\theta}'(z) &= \frac{1}{2\pi} \mathbf{X}_0(z) \int_L \frac{1}{t - z} [\mathbf{X}_0^+(t)]^{-1} \bar{\mathbf{M}} \hat{\mathbf{u}}'(t) dt \\ &\quad + \mathbf{X}_0(z) \mathbf{p}_n(z), \end{aligned} \quad (3.3a)$$

where $\mathbf{p}_n(z)$ is an arbitrary polynomial vector with degree not higher than n , and $\mathbf{X}_0(z)$ is the basic Plemelj function satisfying

$$\begin{aligned} \mathbf{X}_0^+(x) &= \mathbf{X}_0^-(x), \quad x \notin L, \\ \mathbf{X}_0^+(x) + \bar{\mathbf{M}} \mathbf{M}^{-1} \mathbf{X}_0^-(x) &= \mathbf{0}, \quad x \in L, \end{aligned} \quad (3.3b)$$

i.e.,

$$\mathbf{X}_0(z) = \boldsymbol{\Lambda} \boldsymbol{\Gamma}(z), \quad (3.3c)$$

where

$$\begin{aligned} \boldsymbol{\Lambda} &= [\boldsymbol{\lambda}_1, \boldsymbol{\lambda}_2, \boldsymbol{\lambda}_3], \\ \boldsymbol{\Gamma}(z) &= \langle \langle \prod_{j=1}^n (z - a_j)^{-(1+\delta_\alpha)} (z - b_j)^{\delta_\alpha} \rangle \rangle. \end{aligned} \quad (3.3d)$$

δ_α and $\boldsymbol{\lambda}_\alpha$, $\alpha = 1, 2, 3$ of (3.3d) are the eigenvalues and eigenvectors of

$$(\mathbf{M}^{-1} + e^{2\pi i \delta} \bar{\mathbf{M}}^{-1}) \boldsymbol{\lambda} = \mathbf{0}. \quad (3.4a)$$

The explicit solutions for the eigenvalues δ are (see Appendix A)

$$\delta_\alpha = -\frac{1}{2} + i\epsilon_\alpha, \quad \alpha = 1, 2, 3, \quad (3.4b)$$

where

$$\epsilon_1 = \epsilon = \frac{1}{2\pi} \ln \frac{1+\beta}{1-\beta}, \quad \epsilon_2 = -\epsilon, \quad \epsilon_3 = 0,$$

$$\beta = [-\frac{1}{2} \operatorname{tr}(\mathbf{S}^2)]^{1/2}, \quad \mathbf{S} = i(2\mathbf{A}\mathbf{B}^T - \mathbf{I}). \quad (3.4c)$$

tr stands for the trace of matrix. Moreover, for normalizing the eigenvector matrix $\boldsymbol{\Lambda}$, the normalization proposed by Hwu (1993) may be slightly changed to fit the present case, i.e.,

$$\frac{1}{2} \bar{\boldsymbol{\Lambda}}^T (\mathbf{M}^{-1} + \bar{\mathbf{M}}^{-1}) \boldsymbol{\Lambda} = \mathbf{I}. \quad (3.4d)$$

To determine $\mathbf{p}_n(z)$, we see that it is at most a polynomial of degree $n - 1$

$$\mathbf{p}_n(z) = \mathbf{d}_0 + \mathbf{d}_1 z + \dots + \mathbf{d}_{n-1} z^{n-1}, \quad (3.5)$$

and also from (2.12)

$$\mathbf{d}_{n-1} = \frac{1}{2\pi i} \boldsymbol{\Lambda}^{-1} \mathbf{q}. \quad (3.6)$$

As to the remaining $(n - 1)$ unknown coefficients of $\mathbf{p}_n(z)$, additional physical assumptions are required before the problem is solved completely. Let us suppose that the resultant forces applied to each punch are known. Then if \mathbf{q}_k is the known resultant force vector on L_k , we find from (2.4) and (2.7)

$$\mathbf{q}_k = - \int_{L_k} [\boldsymbol{\theta}'(x^+) - \boldsymbol{\theta}'(x^-)] dx, \quad (3.7)$$

for $k = 1, 2, \dots, n$. Substituting (3.3a) into (3.7) yields n equations for the determination of the n coefficient vectors \mathbf{d}_i . It is apparent that one of these equations is redundant as (3.6) ensures the overall equilibrium of the elastic body with

$$\mathbf{q} = \sum_{k=1}^n \mathbf{q}_k.$$

However, these n equations completely determine the solution (3.3a).

Now the problem is solved in principle. For illustrating the solutions derived above, some special cases will be investigated as follows.

(a) **Indentation by a Flat-Ended Punch.** We first examine the case of indentation by a single punch with a flat-ended profile which makes contact with S^- over the region $|x| \leq a$, and the force \mathbf{q} applied on the punch is given. Then

$$\hat{\mathbf{u}}'(x) = \mathbf{0}, \quad (3.8)$$

and from (3.3a), (3.3c), and (3.6) we find

$$\hat{\mathbf{t}}'(z) = \frac{1}{2\pi i} \mathbf{A} \Gamma(z) \mathbf{A}^{-1} \mathbf{q}, \quad (3.9)$$

where

$$\mathbf{t}(x) = \frac{1}{\pi\sqrt{a^2 - x^2} \sqrt{1 - \beta^2}} \begin{Bmatrix} \cos\left(\epsilon \ln \frac{a+x}{a-x}\right) q_x - \sqrt{-\frac{S_{21}}{S_{12}}} \sin\left(\epsilon \ln \frac{a+x}{a-x}\right) q_y \\ \sqrt{-\frac{S_{12}}{S_{21}}} \sin\left(\epsilon \ln \frac{a+x}{a-x}\right) q_x + \cos\left(\epsilon \ln \frac{a+x}{a-x}\right) q_y \\ q_z \end{Bmatrix}, \quad |x| \leq a, \quad (3.16)$$

$$\Gamma(z) = \left\langle \left\langle \frac{1}{\sqrt{z^2 - a^2}} \left(\frac{z+a}{z-a} \right)^{-i\epsilon_\alpha} \right\rangle \right\rangle.$$

The stresses under the punch can then be determined by using (2.5), (3.2)₂, and (3.8), i.e.,

$$\mathbf{t}(x) = (\mathbf{I} + \bar{\mathbf{M}} \mathbf{M}^{-1}) \hat{\mathbf{t}}'(x^-), \quad |x| \leq a. \quad (3.10)$$

Since the stresses $\mathbf{t}(x)$ are real, the result of the right-hand side of (3.10) manipulated by some complex matrices should be real. Therefore it is of interest to obtain the real form of the solution, because it should provide a better understanding of the physical behavior of the stress field under the punch. To this end, the following equalities derived in a way similar to that presented in the Hwu's paper (1993) are used for the simplification of (3.10), i.e.,

$$(\mathbf{I} + \bar{\mathbf{M}} \mathbf{M}^{-1}) \mathbf{A} = 2\mathbf{A} \langle \langle e^{-\pi\epsilon_\alpha} \cosh(\pi\epsilon_\alpha) \rangle \rangle, \quad (3.11)$$

and

$$\mathbf{A} \langle \langle c_\alpha \rangle \rangle \mathbf{A}^{-1} = \mathbf{I} + \frac{1 - c_R}{\beta^2} \mathbf{S}^{T2} + \frac{c_I}{\beta} \mathbf{S}^T, \quad (3.12)$$

where $c_1 = c$, $c_2 = \bar{c}$, $c_3 = 1$ and c_R, c_I are real and imaginary parts of c which is an arbitrary complex number. Also, for $y \rightarrow 0^-$ and $|x| \leq a$, it can be shown that

$$\Gamma(x^-) = \left\langle \left\langle \frac{ie^{\pi\epsilon_\alpha}}{\sqrt{a^2 - x^2}} e^{-\kappa_\alpha} \ln \frac{a+x}{a-x} \right\rangle \right\rangle. \quad (3.13)$$

By the use of (3.9) and (3.11)–(3.13), Eq. (3.10) can be written in real form as

$$\mathbf{t}(x) = \frac{1}{\pi\sqrt{a^2 - x^2}} \left[\mathbf{I} + \frac{1 - c_R}{\beta^2} \mathbf{S}^{T2} + \frac{c_I}{\beta} \mathbf{S}^T \right] \mathbf{q}, \quad |x| \leq a, \quad (3.14)$$

where

$$c_R + ic_I = \cosh(\pi\epsilon) e^{-i\epsilon} \ln \frac{a+x}{a-x}.$$

For orthotropic materials, (3.12) can be expressed as

$$\mathbf{A} \langle \langle c_\alpha \rangle \rangle \mathbf{A}^{-1} = \begin{bmatrix} c_R & c_I \sqrt{-\frac{S_{21}}{S_{12}}} & 0 \\ -c_I \sqrt{-\frac{S_{12}}{S_{21}}} & c_R & 0 \\ 0 & 0 & 1 \end{bmatrix}, \quad (3.15)$$

where S_{12}, S_{21} are the {12} and {21} components of \mathbf{S} . Then $\mathbf{t}(x)$ becomes

where q_x, q_y , and q_z are the components of the force vector \mathbf{q} .

It should be noted that the general solutions shown in Section 2 are valid only for the nondegenerate materials, that is the material eigenvalues $p_\alpha, \alpha = 1, 2, 3$, are distinct or three independent material eigenvectors $\mathbf{a}_\alpha, \mathbf{b}_\alpha, \alpha = 1, 2, 3$, can be found when p_α is repeated. Otherwise, the general solutions shown in Section 2 should be modified (Ting, 1982). However, if the final solutions do not contain any material eigenvalues p_α or eigenvectors \mathbf{A}, \mathbf{B} explicitly, and are composed of the real fundamental elasticity matrices such as $\mathbf{S}, \mathbf{H}, \mathbf{L}$, and \mathbf{N}_i (Ting, 1988), they may be applied to any kind of anisotropic materials including the degenerate materials such as the isotropic materials. Following is the presentation for the reduction to isotropic materials.

Consider that the special case of the isotropic body and the force \mathbf{q} applied on the punch is given as $(0, -q_0, 0)^T$. Knowing that for an isotropic body

$$\mathbf{S} = \frac{\kappa - 1}{\kappa + 1} \begin{bmatrix} 0 & -1 & 0 \\ 1 & 0 & 0 \\ 0 & 0 & 0 \end{bmatrix},$$

where $\kappa = 3 - 4\nu$ for plane-strain conditions and $\kappa = 3 - \nu / 1 + \nu$ for the generalized plane-stress condition, and ν is the Poisson's ratio, we have by (3.4c)

$$\beta = \frac{\kappa - 1}{\kappa + 1}, \quad \epsilon = \frac{1}{2\pi} \ln \kappa. \quad (3.17)$$

From (3.16) and (3.17), the stresses under the punch can then be found explicitly as

$$\mathbf{t}(x) = \begin{cases} \sigma_{xy} \\ \sigma_{yy} \\ \sigma_{zy} \end{cases}$$

$$= \frac{1+\kappa}{\sqrt{\kappa}} \frac{q_0}{2\pi\sqrt{a^2-x^2}} \begin{cases} \sin\left(\epsilon \ln \frac{a+x}{a-x}\right) \\ -\cos\left(\epsilon \ln \frac{a+x}{a-x}\right) \\ 0 \end{cases}, \quad (3.18)$$

which agree with those shown in Muskhelishvili (1954).

(b) **A Flat-Ended Punch Tilted by a Couple.** A second problem illustrating the above theory is the case of a flat-ended punch which adheres to the half-plane S^- and is then tilted by the application of a couple m . Let us suppose the punch is of width $2a$ and is tilted through a small angle ϵ measured in the counterclockwise direction. Then in (3.2)

$$\hat{\mathbf{u}}'(x) = \epsilon \begin{cases} 0 \\ 1 \\ 0 \end{cases} = \epsilon \mathbf{i}_2, \quad |x| \leq a, \quad (3.19)$$

and from (3.3a)

$$\boldsymbol{\theta}'(z) = \frac{\epsilon}{2\pi} \mathbf{X}_0(z) \int_{-a}^a \frac{1}{t-z} [\mathbf{X}_0^+(t)]^{-1} dt \bar{\mathbf{M}} \mathbf{i}_2. \quad (3.20)$$

Note that the last term in (3.3a) vanishes since the resultant forces are zero. In order to evaluate the above integral of vector form, a special technique similar to that presented in the book of England (1971) for line integrals of scalar form has been developed in Appendix B. Applying that technique we find

$$\boldsymbol{\theta}'(z) = i\epsilon \{ \mathbf{I} - \mathbf{X}_0(z) \langle \langle z + 2ia\epsilon_a \rangle \rangle \Lambda^{-1} \} (\mathbf{I} + \bar{\mathbf{M}} \mathbf{M}^{-1})^{-1} \bar{\mathbf{M}} \mathbf{i}_2. \quad (3.21)$$

This now enables us to calculate the stresses over the contact region in terms of the angle of tilt ϵ . However, in an alternative problem it may be assumed that the couple m acting on the punch is given and it is required to find the corresponding angle of tilt ϵ . Hence it is necessary to evaluate the relation between the applied couple m and the angle of tilt ϵ .

For this purpose, we first calculate the stresses under the punch, by (2.5), (3.2)₂, (3.19), and (3.4d), we have

$$\mathbf{t}(x) = -\frac{i}{2} \epsilon (\mathbf{I} + \bar{\mathbf{M}} \mathbf{M}^{-1}) \Lambda \Gamma(x^-) \langle \langle z + 2ia\epsilon_a \rangle \rangle \bar{\Lambda}^T \mathbf{i}_2, \quad |x| \leq a. \quad (3.22)$$

With this result, the couple m may now be calculated by

$$m = \int_{-a}^a x \sigma_{yy} dx = \int_{-a}^a x \mathbf{i}_2^T \mathbf{t} dx, \quad (3.23)$$

in which the integral may be evaluated by a way similar to that presented in Appendix B. The result is

$$m = \frac{\pi}{2} a^2 \epsilon \mathbf{i}_2^T \Lambda \langle \langle 1 + 4\epsilon_a^2 \rangle \rangle \bar{\Lambda}^T \mathbf{i}_2. \quad (3.24)$$

For a given couple m , the angle of tilt ϵ is determined by

$$\epsilon = \frac{2m}{\pi a^2 \mathbf{i}_2^T \Lambda \langle \langle 1 + 4\epsilon_a^2 \rangle \rangle \bar{\Lambda}^T \mathbf{i}_2}. \quad (3.25)$$

Substituting this value of ϵ into (3.22), one obtains the stresses under the punch tilted by a given couple m .

4 A Sliding Punch With Friction

Using the analytical continuation method in the preceding sections, we may also solve the problems of a sliding punch with or without friction. Since frictionless problems may be covered by setting the friction coefficient to be zero in the friction problems, in this section consideration will be limited to the case where friction exists and the punch is on the verge of equilibrium. The boundary conditions for this kind of problems may be expressed as

$$\begin{cases} T(x) = \tan \lambda P(x) \\ v(x) = g(x) + \text{constant} \end{cases}, \quad \text{on } x \in L, \quad (4.1)$$

$$T(x) = P(x) = 0, \quad \text{on } x \notin L, \quad (4.2)$$

where $P(x)$ and $T(x)$ are, respectively, the absolute values of pressure and tangential stress, λ is the angle of limiting friction for the punch and is a constant under the punch, and $g(x)$ is a given function for the profile of the punch. As before, if we suppose the elastic body occupies the lower half-plane $y < 0$, we have the relation $T(x) = \sigma_{xy}$ if the punch is propelled from left to right and $T(x) = -\sigma_{xy}$ if the punch is propelled from right to left. Moreover, to ensure contact $P(x) = -\sigma_{yy}$ and the first Eq. of (4.1) only holds provided $\sigma_{yy} < 0$, which must be checked when the solution is obtained.

By using (2.5), the relation between the pressure $P (= -\sigma_{yy})$ and the tangential stress $T (= \pm \sigma_{xy})$ shown in (4.1)₁ may be expressed as

$$\theta'_1(x^+) - \theta'_1(x^-) = \mp(\tan \lambda)[\theta'_2(x^+) - \theta'_2(x^-)], \quad x \in L, \quad (4.3)$$

where θ_1 and θ_2 are, respectively, the first and second components of $\boldsymbol{\theta}$. Rearrangement gives

$$\begin{aligned} \lim_{y \rightarrow 0^+} [\theta'_1(z) \pm (\tan \lambda) \theta'_2(z)] \\ = \lim_{y \rightarrow 0^-} [\theta'_1(z) \pm (\tan \lambda) \theta'_2(z)]. \end{aligned} \quad (4.4)$$

Thus the function $\theta'_1(z) \pm (\tan \lambda) \theta'_2(z)$ is holomorphic in the whole plane including the point at infinity and it tends to zero as $|z| \rightarrow \infty$ from (2.11), hence by Liouville's theorem one can conclude that

$$\theta'_1(z) \pm (\tan \lambda) \theta'_2(z) = 0. \quad (4.5)$$

The problem now reduces to determine a sectionally holomorphic scalar function $\theta_2(z)$ (or $\theta_1(z)$) satisfying the displacement boundary condition of (4.1)₂. This condition can be expressed in terms of θ_2 by employing (2.6) and (4.5) into (4.1)₂, as

$$\theta'_2(x^+) + \frac{d}{d} \theta'_2(x^-) = \frac{i}{d} g'(x), \quad (4.6)$$

where $d = \mp m_{12}^* \tan \lambda + \bar{m}_{22}^*$, m_{12}^* and m_{22}^* are the {12} and {22} components of the matrix \mathbf{M}^{-1} . Equation (4.6) is a standard Hilbert problem, the solution to it is (Muskhelishvili, 1954)

$$\theta'_2(z) = \frac{X(z)}{2\pi d} \int_L \frac{g'(t)}{X^+(t)(t-z)} dt + X(z) p_n(z), \quad (4.7)$$

where

$$X(z) = \prod_{k=1}^n (z - a_k)^{-\delta} (z - b_k)^{\delta-1},$$

$$\delta = \frac{1}{2\pi} \arg \left(-\frac{d}{i} \right), \quad 0 \leq \delta < 1. \quad (4.8)$$

$p_n(z)$ is an arbitrary polynomial with degree not higher than n and \arg stands for the argument of a complex number. Note

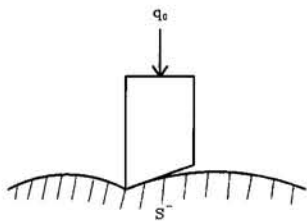


Fig. 2 A wedge-shaped punch under normal pressure

that δ is a real number and hence there are no oscillatory singularities in the solution.

The problem now is solved in principle. For the purpose of illustration, we examine an example of incomplete indentation where the region of contact is unknown and has to be determined by assuming the stresses are bounded at the ends of the contact region.

Consider a wedge-shaped punch under a total pressure q_0 which induces the contact with half-plane S^- and the motion of the punch is to the left as shown in Fig. 2. The profile of the punch can be expressed as $g(x) = ex$ where the origin is taken so that the contact region is $-a \leq x \leq a$. Then from (4.8), $X(z) = (z + a)^{-\delta}(z - a)^{\delta-1}$ and from (4.7) we see that the evaluation of $\theta'_2(z)$ depends on the integral

$$\int_{-a}^a \frac{dt}{X^+(t)(t - z)},$$

which has been evaluated by Muskhelishvili (1954) as

$$\int_{-a}^a \frac{dt}{X^+(t)(t - z)} = \frac{2\pi i d}{d + \bar{d}} \left\{ \frac{1}{X(z)} - [z + (2\delta - 1)a] \right\}. \quad (4.9)$$

To determine the polynomial $p_n(z)$, using the half-plane far-field condition (2.12) one obtains

$$p_n(z) = \frac{iq_0}{2\pi}. \quad (4.10)$$

Substituting (4.9), (4.10) with $g'(t) = e$ into (4.7), $\theta'_2(z)$ becomes

$$\theta'_2(z) = \frac{ie}{d + \bar{d}} \{1 - [z + (2\delta - 1)a]X(z)\} + \frac{iq_0}{2\pi} X(z). \quad (4.11)$$

The pressure $P(x)$ under the punch can now be calculated by

$$\begin{aligned} P(x) &= -\sigma_{yy} = \theta'_2(x^+) - \theta'_2(x^-) \\ &= -\frac{ie}{d + \bar{d}} [x + (2\delta - 1)a][X^+(x) - X^-(x)] \\ &\quad + \frac{iq_0}{2\pi} [X^+(x) - X^-(x)], \quad |x| \leq a. \end{aligned}$$

By using the bipolar coordinates $z + a = R_1 e^{i\varphi_1}$, $z - a = R_2 e^{i\varphi_2}$, it will be seen that

$$X^\pm(x) = -\frac{e^{\pm i\pi\delta}}{(a + x)^\delta(a - x)^{1-\delta}}, \quad |x| \leq a.$$

Hence the pressure $P(x)$ can be simplified as

$$\begin{aligned} P(x) &= \frac{\sin \pi\delta}{\pi(a + x)^\delta(a - x)^{1-\delta}} \\ &\quad \times \left\{ q_0 - \frac{2\pi e}{(d + \bar{d})} [x + (2\delta - 1)a] \right\}. \quad (4.12) \end{aligned}$$

The above expression is valid for general anisotropic half-plane. It can be shown that for isotropic bodies

$$m_{12}^* = \frac{i(\kappa - 1)}{4\mu}, \quad m_{22}^* = \frac{1 + \kappa}{4\mu}, \quad (4.13)$$

where μ is the shear modulus. By using these values for the calculation of d and δ , we have

$$d = \frac{1}{4\mu} \{1 + \kappa + i(\kappa - 1) \tan \lambda\},$$

$$\delta = 1 - \gamma, \quad \gamma = \frac{1}{2\pi} \arg \left\{ -\frac{1 + \kappa e^{2i\lambda}}{\kappa + e^{2i\lambda}} \right\},$$

and Eq. (4.12) can be proved to agree with that given in (England, 1971). If the motion of the punch is to the right, the same expression as (4.12) will be obtained except that

$$d = \frac{1}{4\mu} \{1 + \kappa - i(\kappa - 1) \tan \lambda\}, \quad \delta = \gamma.$$

As stated in the beginning of this section, to have a complete indentation, the applied force q_0 should be large enough that the end-face of the punch touches the half-plane, i.e., the pressure $P(x)$ should be positive under the punch. By letting $P(\pm a) > 0$, we may find the minimum requirement for the applied force q_0 to reach complete indentation;

$$q_0 \geq \frac{4\pi e \delta}{d + \bar{d}} a. \quad (4.14)$$

However, if q_0 is not sufficiently large to satisfy the above inequality, a state of incomplete indentation will result as illustrated in Fig. 2. In this case the length of the contact region will depend on q_0 and is determined from the condition that the stress is bounded at the point $x = a$ where the punch and the half-plane meet smoothly. For a bounded stress at $x = a$, from (4.12)

$$a = \frac{d + \bar{d}}{4\pi e \delta} q_0, \quad (4.15)$$

and hence

$$P(x) = \frac{2e \sin \pi\delta}{d + \bar{d}} \left(\frac{a - x}{a + x} \right)^\delta. \quad (4.16)$$

5 Conclusions

By applying Stroh's formalism and the method of analytical continuation, a general solution for the problems of punch indentation into an anisotropic elastic half-plane is derived in this paper. The generality of the present solution is shown as follows. (1) The half-plane is a general anisotropic medium. (2) The number of rigid punches indenting into the surface is arbitrary. (3) The location of each punch on the surface is arbitrary. (4) The profile of each punch is arbitrary but must be continuous, and in the case of sliding friction, the solution must be checked to ensure that the contact pressure is greater than zero. (5) The punches may completely adhere to the half-plane, or slide with or without friction. (6) The cases of normal, tangential, and rotary indentation are all included. For the purpose of verification and illustration, some special cases are deduced from this general solution, such as normal and rotary indentation by a flat-ended punch into anisotropic or isotropic half-plane. The results show that our solutions are simple, general, and exact.

Acknowledgment

The authors would like to thank the support of the National Science Council, Republic of China, through Grant No. 83-0424-E006-010.

References

Chen, W. T., 1969, "Stresses in Some Anisotropic Materials Due to Indentation and Sliding," *International Journal of Solids and Structures*, Vol. 5, pp. 191-214.

England, A. H., 1971, *Complex Variable Methods in Elasticity*, Wiley Interscience, London.

Fabrikant, V. I., 1986a, "Flat Punch of Arbitrary Shape on an Elastic Half-space," *International Journal of Engineering Science*, Vol. 24, pp. 1731-1740.

Fabrikant, V. I., 1986b, "Inclined Flat Punch of Arbitrary Shape on an Elastic Half-space," *ASME JOURNAL OF APPLIED MECHANICS*, Vol. 53, pp. 798-806.

Galin, L. A., 1961, *Contact Problems in the Theory of Elasticity*, translation by I. N. Sneddon, North Carolina State College, Raleigh, N.C.

Gladwell, G. M. L., 1976, "On Some Unbonded Problems in Plane Elasticity Theory," *ASME JOURNAL OF APPLIED MECHANICS*, Vol. 43, pp. 263-267.

Gladwell, G. M. L., and England, A. H., 1977, "Orthogonal Polynomial Solutions to Some Mixed Boundary Value Problems in Elasticity Theory," *Quarterly Journal of Mechanics and Applied Mathematics*, Vol. 30, pp. 175-185.

Gladwell, G. M. L., 1978, "Polynomial Solutions for an Ellipse on an Anisotropic Elastic Half-Space," *Quarterly Journal of Mechanics and Applied Mathematics*, Vol. 31, pp. 251-260.

Gladwell, G. M. L., 1980, *Contact Problems in the Classical Theory of Elasticity*, Sijhoff and Noordhoff.

Green, A. E., and Zerna, W., 1954, *Theoretical Elasticity*, Clarendon Press, Oxford, UK.

Hasebe, N., Okumura, M., and Nakamura, T., 1989, "Frictional Punch and Crack in Plane Elasticity," *ASCE Journal of Engineering Mechanics*, Vol. 115, pp. 1137-1149.

Hwu, C., 1992, "Thermoelastic Interface Crack Problems in Dissimilar Anisotropic Media," *International Journal of Solids and Structures*, Vol. 29, pp. 2077-2090.

Hwu, C., 1993, "Explicit Solutions for the Collinear Interface Crack Problems," *International Journal of Solids and Structures*, Vol. 30, pp. 301-312.

Jaffar, M. J., and Savage, M. D., 1988, "On the Numerical Solution of Line Contact Problems Involving Bonded and Unbonded Strips," *Journal of Strain Analysis*, Vol. 23, pp. 67-77.

Johnson, K. L., 1985, *Contact Mechanics*, Cambridge University Press, Cambridge, U.K.

Klintworth, J. W., and Stronge, W. L., 1990, "Plane Punch Indentation of Anisotropic Elastic Half-Space," *ASME JOURNAL OF APPLIED MECHANICS*, Vol. 57, pp. 84-90.

Kuo, C. H., and Keer, L. M., 1992, "Contact Stress Analysis of a Layered Transversely Isotropic Half-Space," *Journal of Tribology*, Vol. 114, pp. 253-262.

Lin, W., Kuo, C. H., and Keer, L. M., 1991, "Analysis of a Transversely Isotropic Half-Space Under Normal and Tangential Loadings," *Journal of Tribology*, Vol. 113, pp. 335-338.

Muskeshishvili, N. I., 1954, *Some Basic Problems of the Mathematical Theory of Elasticity*, Noordhoff, Groningen, The Netherlands.

Okumura, M., Hasebe, N., and Nakamura, T., 1990, "Crack Due to Wedge-shaped Punch with Friction," *ASCE Journal of Engineering Mechanics*, Vol. 116, pp. 2173-2185.

Pan, Y. C., and Chou, T. W., 1979, "Green's Function Solutions for Semi-infinite Transversely Isotropic Materials," *International Journal of Engineering Science*, Vol. 17, pp. 545-551.

Shibuya, T., Koizumi, T., Kawamura, N., and Gladwell, G. M. L., 1989, "The Contact Problem Between an Elliptical Punch and an Elastic Half-space with Friction," *JSME International Journal*, Series I, Vol. 32, pp. 192-198.

Shield, R. T., 1987, "Variational Principles for Some Nonstandard Elastic Problems," *ASME JOURNAL OF APPLIED MECHANICS*, Vol. 54, pp. 768-771.

Stroh, A. N., 1958, "Dislocations and Cracks in Anisotropic Elasticity," *Philosophical Magazine*, Vol. 7, pp. 625-646.

Stroh, A. N., 1962, "Steady State Problems in Anisotropic Elasticity," *Journal of Mathematics and Physics*, Vol. 41, pp. 77-103.

Suo, Z., 1990, "Singularities, Interfaces and Cracks in Dissimilar Anisotropic Media," *Proceedings of the Royal Society, London*, Vol. A427, pp. 331-358.

Ting, T. C. T., 1982, "Effects of Change of Reference Coordinates on the Stress Analysis of Anisotropic Elastic Materials," *International Journal of Solids and Structures*, Vol. 18, pp. 139-152.

Ting, T. C. T., 1986, "Explicit Solution and Invariance of the Singularities at an Interface Crack in Anisotropic Composites," *International Journal of Solids and Structures*, Vol. 22, pp. 965-983.

Ting, T. C. T., 1988, "Some Identities and the Structures of N_i in the Stroh Formalism of Anisotropic Elasticity," *Quarterly Journal of Applied Mathematics*, Vol. 46, pp. 109-120.

Tsiang, T. H., and Mandell, J. F., 1985, "Bearing/Contact for Anisotropic Materials," *AIAA Journal*, Vol. 23, pp. 1273-1277.

Willis, J. R., 1966, "Hertzian Contact of Anisotropic Bodies," *Journal of the Mechanics and Physics of Solids*, Vol. 14, pp. 163-176.

Appendix A

Consider the eigenproblem

$$(\mathbf{M}^{-1} + e^{2\pi i\delta} \mathbf{M}^{-1}) \boldsymbol{\lambda} = \mathbf{0}, \quad (A1)$$

where \mathbf{M} is the impedance matrix defined as $\mathbf{M} = -i\mathbf{B}\mathbf{A}^{-1}$. With the identities shown by Ting (1988), we have

$$\mathbf{M}^{-1} = i\mathbf{A}\mathbf{B}^{-1} = (\mathbf{I} - i\mathbf{S})\mathbf{L}^{-1}, \quad (A2)$$

where \mathbf{L} , \mathbf{S} are real matrices composed of elasticity constants. Moreover, it can be shown that $\mathbf{S}\mathbf{L}^{-1}$ is antisymmetric and \mathbf{L}^{-1} is symmetric and positive definite.

Substituting (A2) into (A1) and for a nontrivial solution of $\boldsymbol{\lambda}$, we obtain

$$\|(1 - e^{2\pi i\delta})\mathbf{S}\mathbf{L}^{-1} + i(1 + e^{2\pi i\delta})\mathbf{L}^{-1}\| = 0. \quad (A3)$$

Since \mathbf{L}^{-1} is positive definite, the determinant is nonzero if we set $\delta = 0$. Hence $(1 - e^{2\pi i\delta}) \neq 0$, and (A3) may be rewritten as

$$\|\mathbf{S}\mathbf{L}^{-1} + i\beta\mathbf{L}^{-1}\| = 0, \quad (A4)$$

where

$$\beta = \frac{1 + e^{2\pi i\delta}}{1 - e^{2\pi i\delta}}.$$

Rearranging the above relation, we have

$$e^{2\pi i\delta} = -\frac{1 - \beta}{1 + \beta}.$$

It can be shown that if δ is a root, so is $\delta + n$ where n is an integer. If only $-1 < \text{Re}(\delta) \leq 0$ are considered (Ting, 1986), we have

$$\delta = -\frac{1}{2} + \frac{i}{2\pi} \ln \frac{1 + \beta}{1 - \beta}.$$

The theorem proved by Ting (1986) states the following. Let β be a root of the 3×3 determinant

$$\|\mathbf{W} + i\beta\mathbf{D}\| = 0,$$

where \mathbf{D} is a real, symmetric, and positive definite matrix, while \mathbf{W} is a real antisymmetric matrix, then

$$-\frac{1}{2} \text{tr}(\mathbf{W}\mathbf{D}^{-1})^2 > 0,$$

and the three roots are all real given by

$$\beta = 0, \quad \beta = \pm[-\frac{1}{2} \text{tr}(\mathbf{W}\mathbf{D}^{-1})^2]^{1/2}.$$

By the above theorem, and replacing \mathbf{W} , \mathbf{D} by $\mathbf{S}\mathbf{L}^{-1}$, \mathbf{L}^{-1} , we have the solution for the eigenproblem (A1). The results are

$$\delta_\alpha = -\frac{1}{2} + i\epsilon_\alpha, \quad \alpha = 1, 2, 3, \quad (A5)$$

where

$$\epsilon_1 = \epsilon = \frac{1}{2\pi} \ln \frac{1 + \beta}{1 - \beta}, \quad \epsilon_2 = -\epsilon, \quad \epsilon_3 = 0,$$

$$\beta = \left[-\frac{1}{2} \text{tr}(\mathbf{S}^2) \right]^{1/2}. \quad (A6)$$

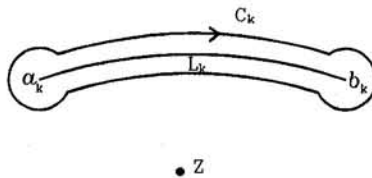


Fig. 3 A lacet integral contour

A p p e n d i x B

Consider the integral

$$\mathbf{j}(z) = \int_L \frac{1}{t-z} [\mathbf{X}_0(t)]^{-1} \mathbf{g}(t) dt, \quad (B1)$$

where L is the union of a finite number of arcs L_1, L_2, \dots, L_n and $\mathbf{X}_0(z)$ is the Plemelj function satisfying the relation

$$\mathbf{X}_0^+(t) + \bar{\mathbf{M}}\mathbf{M}^{-1}\mathbf{X}_0^-(t) = \mathbf{0}. \quad (B2)$$

Suppose that $\mathbf{g}(t)$ is a polynomial, a situation which often occurs in practice. Then the integral along each L_k may be expressed in terms of an integral along a lacet C_k surrounding L_k as shown in Fig. 3, and assume that z remains outside these lacets.

The contour integral around the lacet C_k may be represented as

$$\begin{aligned} & \int_{C_k} \frac{1}{\zeta-z} [\mathbf{X}_0(\zeta)]^{-1} \mathbf{g}(\zeta) d\zeta \\ &= \int_{L_k} \frac{1}{t-z} [\mathbf{X}_0^+(t)]^{-1} \mathbf{g}(t) dt - \int_{L_k} \frac{1}{t-z} [\mathbf{X}_0^-(t)]^{-1} \mathbf{g}(t) dt \\ &+ \lim_{\rho \rightarrow 0} \int_{|\zeta-a_k|=\rho} \frac{1}{\zeta-z} [\mathbf{X}_0(\zeta)]^{-1} \mathbf{g}(\zeta) d\zeta \\ &+ \lim_{\rho \rightarrow 0} \int_{|\zeta-b_k|=\rho} \frac{1}{\zeta-z} [\mathbf{X}_0(\zeta)]^{-1} \mathbf{g}(\zeta) d\zeta. \end{aligned}$$

It may be shown that the last two integrals above tend to zero as $\rho \rightarrow 0$. Hence from (B2)

$$\begin{aligned} & \int_{C_k} \frac{1}{\zeta-z} [\mathbf{X}_0(\zeta)]^{-1} \mathbf{g}(\zeta) d\zeta \\ &= \int_{L_k} \frac{1}{t-z} [\mathbf{X}_0^+(t)]^{-1} (\mathbf{I} + \bar{\mathbf{M}}\mathbf{M}^{-1}) \mathbf{g}(t) dt, \end{aligned}$$

then the integral $\mathbf{j}(z)$ may be expressed in the form

$$\mathbf{j}(z) = \int_C \frac{1}{\zeta-z} [\mathbf{X}_0(\zeta)]^{-1} (\mathbf{I} + \bar{\mathbf{M}}\mathbf{M}^{-1})^{-1} \mathbf{g}(\zeta) d\zeta, \quad (B3)$$

where C is the union of the lacets C_1, C_2, \dots, C_n .

Replacing C by a counterclockwise circle contour C_∞ at a large distance R , we can obtain that

$$\mathbf{j}(z) = 2\pi i S - \int_{C_\infty} \frac{1}{\zeta-z} [\mathbf{X}_0(\zeta)]^{-1} (\mathbf{I} + \bar{\mathbf{M}}\mathbf{M}^{-1})^{-1} \mathbf{g}(\zeta) d\zeta, \quad (B4)$$

where S is the sum of residues of the poles of the integrand in (B3) lying between C and C_∞ . The second term has the form

$$\lim_{R \rightarrow \infty} \int_0^{2\pi} \frac{Re^{i\theta}}{Re^{i\theta} - z} [\mathbf{X}_0(Re^{i\theta})]^{-1} (\mathbf{I} + \bar{\mathbf{M}}\mathbf{M}^{-1})^{-1} \mathbf{g}(Re^{i\theta}) id\theta, \quad (B5)$$

where R is the radius of the contour C_∞ . It can be shown that only terms independent of $Re^{i\theta}$ can contribute to the above integral. Then with a given function $\mathbf{g}(t)$, the integral $\mathbf{j}(z)$ can be explicitly evaluated from (B4) and (B5).

For example, consider an integral along a single line $L = (-a, a)$ and let $\mathbf{g}(t) = \mathbf{g}$, where \mathbf{g} is a given constant vector. The sum of the residues is

$$S = [\mathbf{X}_0(z)]^{-1} (\mathbf{I} + \bar{\mathbf{M}}\mathbf{M}^{-1})^{-1} \mathbf{g}. \quad (B6)$$

To calculate the integral shown in (B5), by (3.3d) we express $\Gamma_\alpha^{-1}(\zeta)$ for large $|\zeta|$ as

$$\begin{aligned} \Gamma_\alpha^{-1}(\zeta) &= (\zeta + a)^{1+\delta_\alpha} (\zeta - a)^{-\delta_\alpha} \\ &= \zeta + 2ia\epsilon_\alpha + O\left(\frac{1}{\zeta}\right), \quad \alpha = 1, 2, 3. \end{aligned}$$

Hence (B5) becomes

$$\lim_{R \rightarrow \infty} \int_0^{2\pi} \left(1 + \frac{z}{Re^{i\theta}} + \dots \right)$$

$$\begin{aligned} & \times \langle \langle Re^{i\theta} + 2ia\epsilon_\alpha + \dots \rangle \rangle id\theta \Lambda^{-1} (\mathbf{I} + \bar{\mathbf{M}}\mathbf{M}^{-1})^{-1} \mathbf{g} \\ &= 2\pi i \langle \langle z + 2ia\epsilon_\alpha \rangle \rangle \Lambda^{-1} (\mathbf{I} + \bar{\mathbf{M}}\mathbf{M}^{-1})^{-1} \mathbf{g}. \quad (B7) \end{aligned}$$

From (B4), (B6), and (B7) we obtain the final result of $\mathbf{j}(z)$ as

$$\begin{aligned} \mathbf{j}(z) &= 2\pi i \{ [\mathbf{X}_0(z)]^{-1} - \langle \langle z + 2ia\epsilon_\alpha \rangle \rangle \Lambda^{-1} \} \\ & \quad \times (\mathbf{I} + \bar{\mathbf{M}}\mathbf{M}^{-1})^{-1} \mathbf{g}. \quad (B8) \end{aligned}$$

S. D. Guest

S. Pellegrino

Engineering Department,
Cambridge University,
Trumpington Street,
Cambridge, CB2 1PZ U.K.

The Folding of Triangulated Cylinders, Part III: Experiments

This paper describes an experimental investigation of a type of foldable cylindrical structure, first presented in two earlier papers. Three cylinders of this type were designed and manufactured, and were then tested to find the force required to fold them. The results from these tests show some discrepancies with an earlier computational simulation, which was based on a pin-jointed truss model of the cylinders. Possible explanations for these discrepancies are explored, and are then verified by new simulations using computational models that include the effect of hinge stiffness, and the effect of geometric imperfections.

1 Introduction

Foldable structures are used for a variety of applications, ranging from umbrellas to solar arrays for spacecraft. This paper describes an experimental investigation of a type of foldable cylindrical structure, first presented in two earlier papers (Guest and Pellegrino, 1994a, b). These structures are formed by dividing up the surface of a cylinder into a series of identical triangles, the sides of which approximate to helices. The side-lengths of the triangles are chosen such that (i) the cylinder is bi-stable, having two strain-free configurations, one extended and one folded; (ii) the strains induced by the folding process are sufficiently small that the cylinder deforms purely elastically.

The first paper in this series (Guest and Pellegrino, 1994a), henceforth referred to as Part I, introduced this type of foldable cylinders, and described the four topological and geometric parameters that are required to identify a particular cylinder. The parameters are the number of starts of two of the helices on the surface of the cylinders, denoted by the letters a and b , and the ratios between the lengths of two sides of a triangle and the third. With the symbols introduced in Figs. 2 and 3 of Part I, the four parameters are m , n , l_b/l_a , and l_c/l_a , respectively. By considering a simplified, uniform folding mode, Part I obtained estimates of the strains induced by folding cylinders with $m = 1$, $n = 7$, and $m = 2$, $n = 7$, for a wide range of ratios l_b/l_a and l_c/l_a .

The second paper in this series (Guest and Pellegrino, 1994b), henceforth referred to as Part II, looked in more detail at the folding process of three particular cylinders, and described a computer simulation of that process. The simulation showed that the folding process is broadly similar in the three cylinders and consists of two distinct phases. During the first phase, the cylinder forms a strained shape-transition region under a steadily increasing folding force. When this force reaches a peak and starts to decrease, the second phase begins. Now, the shape transition region moves along the cylinder under a small force, leaving behind a fully folded part of the cylinder. This type of behavior is observed in the collapse of many structures, and is generally known as a *propagating instability* (Kyriakides, 1994). However, while propagating instabilities are usually destructive, for these cylinders this behavior is highly desirable.

This paper describes three foldable cylinders that have been designed, manufactured, and tested. The first two cylinders were

designed simply to validate the theoretical work in the previous papers. The third cylinder was aimed at a possible application, to produce a collapsible fuel tank for Hydrazine, a highly corrosive rocket fuel. As fuel is used, the tank would reduce its volume, thus preventing sloshing of the remaining fuel, and also reducing the amount of fuel which collects away from the supply pipe, and hence is left unused. A summary of the geometry of the cylinders that were manufactured is given in Table 1. The observed experimental behavior shows complexities that were not predicted in Part II. However, a re-analysis of the folding process which allows for two effects that had been neglected previously, hinge stiffness along the connections between panels, and the presence of manufacturing imperfections, predicts the kind of behavior that is observed in practice.

The layout of the paper is as follows. Section 2 describes the manufacture and compression testing of the models, and identifies the key discrepancies between the behavior predicted by the computer simulations in Part II and the actual behavior of the models. Possible explanations for these discrepancies are discussed in Section 3, and these explanations are investigated in detail, in Section 4, by modifying the computer model and producing new simulations. Section 5 discusses these simulations, and concludes the paper.

2 Experiments

Irathane and Aluminium-Alloy Cylinders. Two of the cylinders described in Part I have been made from sheets of 0.9 mm thick aluminium alloy plate, coated with a 0.7 mm thick layer of Irathane on both sides (Irathane is a flexible polyurethane). Hinges were made by forming a series of straight, parallel grooves, using a milling machine. Both one layer of the Irathane and the Al-alloy were removed, thus leaving only one layer of Irathane to form the hinge. Each sheet was milled to the correct fold pattern. The final cylinders were formed by joining together opposite edges of the sheets with small plates. The bases of both cylinders were fully restrained before testing.

Each cylinder was tested using a Howden testing machine in a displacement controlled mode. The top of the cylinder was loaded using a plate attached to the testing machine through a central ball joint, thus allowing the plate to change its orientation during folding. The total compressive load on the cylinder was obtained by adding the weight of the loading plate to the force measured by a load cell, at the top of the testing machine. Once the cylinder had been fully compressed the test was reversed, as further compression would have damaged the connection between the cylinder and the base plate.

The results of the compression test on cylinder no. 1 are shown in Fig. 1(a). This plot of force during folding shows a clear periodicity, where the period is approximately 20 mm.

Contributed by the Applied Mechanics Division of THE AMERICAN SOCIETY OF MECHANICAL ENGINEERS for publication in the ASME JOURNAL OF APPLIED MECHANICS.

Discussion on this paper should be addressed to the Technical Editor, Professor Lewis T. Wheeler, Department of Mechanical Engineering, University of Houston, Houston, TX 77204-4792, and will be accepted until four months after final publication of the paper itself in the ASME JOURNAL OF APPLIED MECHANICS.

Manuscript received by the ASME Applied Mechanics Division, Aug. 1, 1994; final revision, Dec. 23, 1994. Associate Technical Editor: S. Kyriakides.

Table 1 Geometric parameters

	<i>m</i>	<i>n</i>	<i>l_a</i> (mm)	<i>l_b</i> (mm)	<i>l_c</i> (mm)
Irathane and Al-alloy cylinder no. 1	1	8	50.0	50.0	90.1
Irathane and Al-alloy cylinder no. 2	1	7	50.0	50.0	86.6
Cu-Be and steel cylinder	1	7	124.8	104.7	205.3

For this cylinder, the change in the relative height coordinates of two nodes on the *a*-helix is 2.7 mm between the extended and folded configuration, while this difference is 22 mm for two nodes on the *b*-helix. Hence, it can be concluded that the basic periodicity of the force plot has a wavelength corresponding to the relative height of successive nodes on the *b*-helix.

The cylinder formed one transition zone at the top of the cylinder, which moved down the cylinder as the test proceeded. As displacement δ was increased, no triangles would fold while the force was increasing, but several triangles folded in quick succession while the force was decreasing.

The results of the compression test on cylinder no. 2 are shown in Fig. 1(b). For this case the change in the relative height coordinates of two successive nodes between the extended and folded configuration is 4.0 mm along the *a*-helix, and 28 mm on the *b*-helix. The behavior of cylinder no. 2 was similar to the previous cylinder, except that in this case there is no consistent periodicity in the results.

Cu-Be and Steel Cylinder. The third cylinder was manufactured using a copper beryllium alloy (Cu-Be) as a hinge material. Cu-Be was used because, when correctly heat-treated, it has a large elastic strain range and hence a thin strip of Cu-Be can be elastically bent around a small radius. The cylinder was made from a flat, 0.1 mm thick sheet of Cu-Be. A series of stiff triangular panels were formed by sandwiching the Cu-Be between triangles of 0.5 mm thick steel plate. These plates

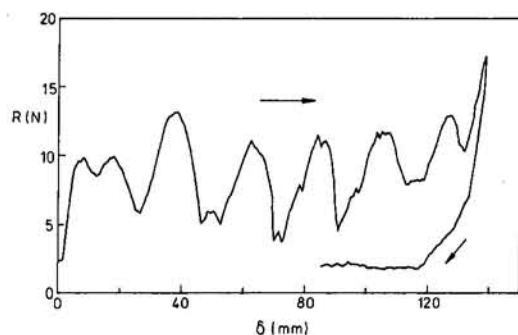


Fig. 1(a)

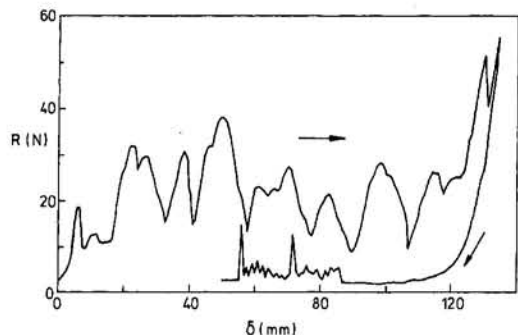


Fig. 1(b)

Fig. 1 Force required to compress the Irathane and Al-alloy cylinders: (a) Cylinder no. 1, (b) Cylinder no. 2

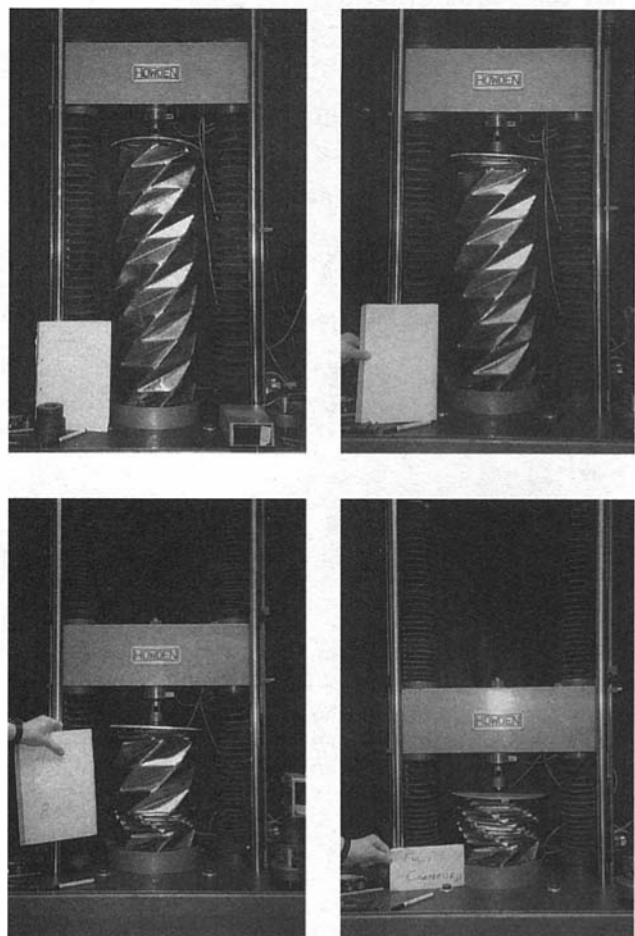


Fig. 2 Folding of the Cu-Be and steel cylinder: initial state, $\delta = 100$ mm; $\delta = 400$ mm; $\delta = 630$ mm, fully folded

were spot welded in place. Then, the two edges of the sheet were joined together, to form the cylinder. Note that steel plates could not be used for a Hydrazine tank, as the steel and the Hydrazine would react. A different stiffening material would have to be used.

The steel triangles were placed 6 mm apart on the Cu-Be sheet to allow an elastic hinge to form. Also, the corners of the steel plates were rounded, to increase the width of the unrestrained Cu-Be sheet near the intersection of hinge lines. One problem with this method of construction is the detail of folds around a node. Inevitably there is an incompatibility where concave and convex folds meet. At this point a crease forms in the Cu-Be sheet, causing plastic deformation. Thus the aim of purely elastic folding was not entirely achieved in this design. The base of the cylinder was fully fixed, by casting it into an epoxy base.

Four compression tests were performed, following the same procedure as for the Irathane and Al-alloy cylinders. Figure 2 shows four photographs taken during the first test. It can be seen from the first photograph that the cylinder had to be initially slightly folded to fit in the testing machine. A plot of the force required to fold the cylinder during this test, Fig. 3(a), shows a period of approximately 60 mm. The change in relative height coordinates of two successive nodes between the extended and the folded configuration is 9 mm along the *a*-helix, and 64 mm along the *b*-helix, and so clearly the periodicity of the plot corresponds to the folding of successive nodes on the *b*-helix.

One important effect shown in Fig. 2 is the formation of a second transition zone close to the base of the cylinder. This

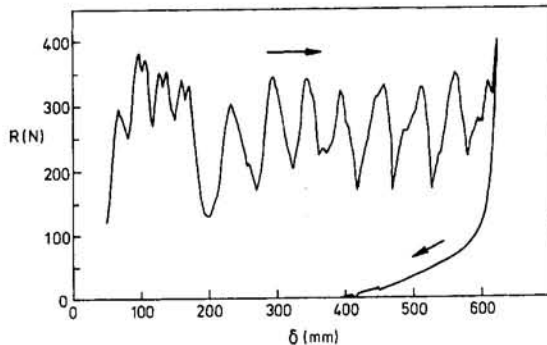


Fig. 3(a)

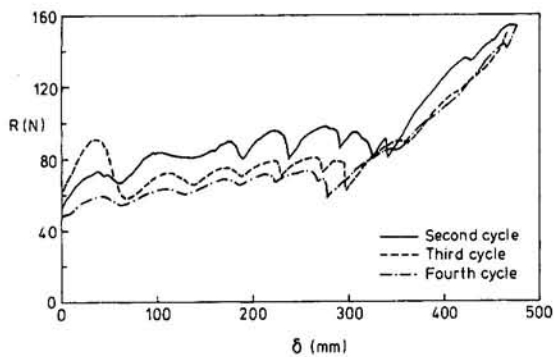


Fig. 3(b)

Fig. 3 Force required to compress the Cu-Be and steel cylinder: (a) first test, (b) second, third, and fourth tests

occurred when the cylinder had been compressed by 125 mm. For the rest of the test it was this transition zone which moved up through the cylinder. A likely reason for the formation of this second transition zone is the weight of the cylinder, which led to a compressive force approximately 55 N greater in the second transition zone than in the top transition zone.

As for the previous tests, during this test no new triangles folded while the force was rising, but many triangles folded in quick succession as the force dropped.

When fully folded, the cylinder had a height of 242 mm, compared with an original height of 872 mm. 150 mm of the compressed height was accounted for by the part of the cylinder fixed open at the base.

When the test was reversed, and the top plate moved up, the cylinder showed some spring-back, and regained a height of 540 mm. Closer inspection of the Cu-Be hinges, showed that the creases around the nodes had moved closer together by 1-2 mm. Stretching the cylinder caused these creases to move back towards their original position, and the cylinder to regain an extended configuration. The creases did not, however, return completely to their original position, and the cylinder only regained a height of 763 mm.

Three further tests were performed on this cylinder. After each test the cylinder was pulled back towards its original configuration. The force required to fold the cylinder in each case is plotted in Fig. 3(b). In each test the cylinder folded by forming a transition zone close to the base of the cylinder, which then moved up through the cylinder as the test proceeded. The force plotted is that in the transition zone, and so the original data has been modified to account for the steadily decreasing weight of the portion of the cylinder above the transition zone. Again during the test a number of triangles would fold each time the force decreased.

For each of the further three tests performed the change in the relative height coordinates of two successive nodes between

the extended and folded configuration is 7 mm along the *a*-helix, and 45 mm on the *b*-helix. Note that these values are smaller than for the original test, as the plastic deformation around the nodes has reduced the height of the cylinder. Again, the basic periodicity of these force plots has a wavelength corresponding to relative height of successive nodes on the *b*-helix.

3 Discussion of Experiments

All the cylinders tested initially formed a transition zone, which then moved through the cylinder. Generally the zone moved from the top down, but for the Cu-Be and steel cylinder it moved from the bottom up, due to the self-weight of the cylinder. The shapes of the corresponding force plots also have a number of similarities. They all show a periodic variation of the force. In two of the cylinders, the Cu-Be and steel cylinder, and the Irathane and Al-alloy cylinder no. 1, the wavelength of this variation corresponds to the folding of successive nodes along the *b*-helix, i.e., of *n* pairs of triangles on the *a*-helix. In the Irathane and Al-alloy cylinder no. 2 the period of variation shows no obvious pattern.

Comparing these results with the computer simulation in Part II, a number of similarities can be seen. In both the simulation and the tests the modes of deformation of the cylinder are similar. A transition zone forms, which then moves through the cylinder. Comparing the plots of force from the computations with the experimental results, both cases show the force varying around a constant value as the transition zone moves through the cylinder.

There are, however, also a number of discrepancies. One is that the force in the experimental results does not vary about zero, but about an average compressive force. This implies that some strain energy is being stored in the cylinder during the folding process. Another discrepancy is that the actual force variation does not correspond to the height difference between successive nodes on the *a*-helix. Indeed, for two of the cylinders tested it corresponded to the height difference between successive nodes on the *b*-helix. A third discrepancy is the absence in the experimental results of any sign of an initial force peak, as the transition zone forms.

There is a fairly obvious explanation for the first discrepancy. The computer model in Part II assumed momentless hinges between the triangles. With this model, stretching energy builds up in the transition zone, at the start of the folding process and—once a certain energy level has been reached—the transition zone moves along the cylinder while the energy stored in the system remains constant. There is no bending energy anywhere in the cylinder. In reality, some energy must be put into the hinges to cause them to fold. Thus, as the transition zone moves down the cylinder, energy must be put into the cylinder to fold more hinges, and so the average compressive force must be greater than zero. It will be seen later that the effect of hinge stiffness explains the third discrepancy, the absence of an initial force peak.

To explain the second discrepancy, it should be noted that the most critical part of the manufacturing technique described in the Section 2 is the final joining process between the two edges of the sheet containing all the triangles. It is difficult to keep the two edges perfectly aligned during this process, and hence it is reasonable to expect that only one of the *b*-helices contains a series of geometric imperfections. Thus, if these imperfections are sufficiently large, the periodicity of the force plot would correspond to the folding of complete turns of the *a*-helix, not to the folding of successive pairs of triangles. The more random periodicity shown by the Irathane and Al-alloy cylinder no. 2 could be due to more distributed errors, as this was an early attempt at making a cylinder, and it had already been damaged by a number of demonstrations prior to the test.

4 Computer Modeling

In order to validate the reasons suggested in the previous section for the discrepancies between experimental results and those predicted by the computer simulation, two changes were made to the computer model described in Part II. The first change was to modify the model so that it no longer assumed momentless hinges between the triangles, and the second was to modify the model to simulate the effect of a final misalignment during the manufacture of a cylinder.

Elastic Hinges. The aim of this section is to describe how elastic hinges were incorporated into the computational model described in Part II. The original model was a pin-jointed truss, with bars of equal cross section along the edges of the triangles. This model was analyzed using the Force Method of structural analysis, and hence by setting up and solving appropriate systems of equilibrium and compatibility equations. To include in this model a series of elastic hinges that oppose relative rotations between adjacent triangles, the equilibrium, compatibility and flexibility matrices for a general hinge element are needed. In analogy with Section 2 of Part II, these matrices are derived directly in the global coordinate system. The stiffness matrix of a similar element was derived in Chapter 5 of Phaal (1990), using a transformation from a local coordinate system.

Consider a typical elastic hinge, Fig. 4, between two triangles. The triangle $\mathbf{P}_1\mathbf{P}_2\mathbf{P}_3$, Fig. 4(a), has unit normal

$$\mathbf{u} = \frac{(\mathbf{P}_2 - \mathbf{P}_1) \times (\mathbf{P}_3 - \mathbf{P}_2)}{\|(\mathbf{P}_2 - \mathbf{P}_1) \times (\mathbf{P}_3 - \mathbf{P}_2)\|} \quad (1)$$

and triangle $\mathbf{P}_4\mathbf{P}_5\mathbf{P}_6$, Fig. 4(b), has unit normal

$$\mathbf{v} = \frac{(\mathbf{P}_5 - \mathbf{P}_4) \times (\mathbf{P}_6 - \mathbf{P}_5)}{\|(\mathbf{P}_5 - \mathbf{P}_4) \times (\mathbf{P}_6 - \mathbf{P}_5)\|}. \quad (2)$$

Let M be the moment exerted by the hinge, positive in the direction shown in Fig. 4(a, b). Equilibrium of each triangle is maintained by three corner forces, normal to the triangle. Any in-plane force component exerts no in-plane moment, and hence makes no contribution to the equilibrium equations that are derived below. These in-plane forces are carried by the original truss model.

Consider the triangle $\mathbf{P}_1\mathbf{P}_2\mathbf{P}_3$, shown in Fig. 4(a). The magnitude of the corner forces, r_1, r_2, r_3 , can be found by considering moment equilibrium along the three sides of the triangle.

Taking moments initially about $\mathbf{P}_1\mathbf{P}_2$,

$$(\mathbf{P}_3 - \mathbf{P}_2) \times r_3 \mathbf{u} \cdot \left(\frac{\mathbf{P}_2 - \mathbf{P}_1}{\|\mathbf{P}_2 - \mathbf{P}_1\|} \right) + M = 0, \quad (3)$$

rearranging the scalar triple product gives

$$\mathbf{u} \cdot (\mathbf{P}_2 - \mathbf{P}_1) \times (\mathbf{P}_3 - \mathbf{P}_2) \left(\frac{r_3}{\|\mathbf{P}_2 - \mathbf{P}_1\|} \right) + M = 0. \quad (4)$$

As \mathbf{u} is a unit vector, and is parallel to $(\mathbf{P}_2 - \mathbf{P}_1) \times (\mathbf{P}_3 - \mathbf{P}_2)$, this can be written

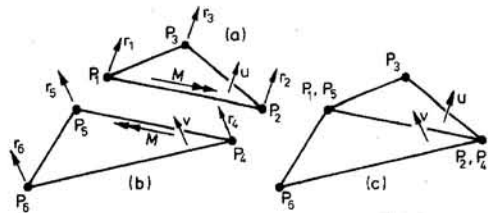


Fig. 4 Elastic hinge element

$$\|(\mathbf{P}_2 - \mathbf{P}_1) \times (\mathbf{P}_3 - \mathbf{P}_2)\| \left(\frac{r_3}{\|\mathbf{P}_2 - \mathbf{P}_1\|} \right) + M = 0 \quad (5)$$

and so

$$r_3 = - \frac{\|\mathbf{P}_2 - \mathbf{P}_1\|}{\|(\mathbf{P}_2 - \mathbf{P}_1) \times (\mathbf{P}_3 - \mathbf{P}_2)\|} M. \quad (6)$$

Similarly, taking moments about $\mathbf{P}_2\mathbf{P}_3$ gives

$$(\mathbf{P}_1 - \mathbf{P}_3) \times r_1 \mathbf{u} \cdot \left(\frac{\mathbf{P}_3 - \mathbf{P}_2}{\|\mathbf{P}_3 - \mathbf{P}_2\|} \right) + \left(\frac{\mathbf{P}_2 - \mathbf{P}_1}{\|\mathbf{P}_2 - \mathbf{P}_1\|} \right) \cdot \left(\frac{\mathbf{P}_3 - \mathbf{P}_2}{\|\mathbf{P}_3 - \mathbf{P}_2\|} \right) M = 0 \quad (7)$$

which can be reduced to

$$r_1 = - \frac{(\mathbf{P}_2 - \mathbf{P}_1) \cdot (\mathbf{P}_3 - \mathbf{P}_2)}{\|(\mathbf{P}_3 - \mathbf{P}_2) \times (\mathbf{P}_1 - \mathbf{P}_3)\| \|(\mathbf{P}_2 - \mathbf{P}_1)\|} M. \quad (8)$$

Also, taking moments about $\mathbf{P}_3\mathbf{P}_1$ gives

$$(\mathbf{P}_2 - \mathbf{P}_1) \times r_2 \mathbf{u} \cdot \left(\frac{\mathbf{P}_1 - \mathbf{P}_3}{\|\mathbf{P}_1 - \mathbf{P}_3\|} \right) + \left(\frac{\mathbf{P}_2 - \mathbf{P}_1}{\|\mathbf{P}_2 - \mathbf{P}_1\|} \right) \cdot \left(\frac{\mathbf{P}_1 - \mathbf{P}_3}{\|\mathbf{P}_1 - \mathbf{P}_3\|} \right) M = 0 \quad (9)$$

which can be reduced to

$$r_2 = - \frac{(\mathbf{P}_2 - \mathbf{P}_1) \cdot (\mathbf{P}_1 - \mathbf{P}_3)}{\|(\mathbf{P}_1 - \mathbf{P}_3) \times (\mathbf{P}_2 - \mathbf{P}_1)\| \|(\mathbf{P}_2 - \mathbf{P}_1)\|} M. \quad (10)$$

Similar relationships can be found for triangle $\mathbf{P}_4\mathbf{P}_5\mathbf{P}_6$

$$r_6 = - \frac{\|\mathbf{P}_5 - \mathbf{P}_4\|}{\|(\mathbf{P}_5 - \mathbf{P}_4) \times (\mathbf{P}_6 - \mathbf{P}_5)\|} M \quad (11)$$

$$r_4 = - \frac{(\mathbf{P}_5 - \mathbf{P}_4) \cdot (\mathbf{P}_6 - \mathbf{P}_5)}{\|(\mathbf{P}_6 - \mathbf{P}_5) \times (\mathbf{P}_4 - \mathbf{P}_6)\| \|(\mathbf{P}_5 - \mathbf{P}_4)\|} M \quad (12)$$

$$r_5 = - \frac{(\mathbf{P}_5 - \mathbf{P}_4) \cdot (\mathbf{P}_4 - \mathbf{P}_6)}{\|(\mathbf{P}_4 - \mathbf{P}_6) \times (\mathbf{P}_5 - \mathbf{P}_4)\| \|(\mathbf{P}_5 - \mathbf{P}_4)\|} M. \quad (13)$$

The equilibrium matrix for the general hinge element of Fig. 4(c) relates the moment M to all of the external forces in equilibrium with it. At $\mathbf{P}_1 = \mathbf{P}_5$, the total force is $r_1\mathbf{u} + r_5\mathbf{v}$, and similarly, at $\mathbf{P}_2 = \mathbf{P}_4$, the total force is $r_2\mathbf{u} + r_4\mathbf{v}$. At \mathbf{P}_3 and \mathbf{P}_6 the total forces are $r_3\mathbf{u}$ and $r_6\mathbf{v}$, respectively. Hence the 16×1 equilibrium matrix, \mathbf{A}_h , for this element is defined by the following system of equilibrium equations. For brevity, the notation $\mathbf{P}_{ij} = \mathbf{P}_j - \mathbf{P}_i$ has been adopted.

$$\left[\begin{array}{c} -\left(\frac{\mathbf{P}_{12} \cdot \mathbf{P}_{23}}{\|\mathbf{P}_{23} \times \mathbf{P}_{31}\| \|\mathbf{P}_{12}\|} \right) \mathbf{u} - \left(\frac{\mathbf{P}_{45} \cdot \mathbf{P}_{56}}{\|\mathbf{P}_{64} \times \mathbf{P}_{45}\| \|\mathbf{P}_{45}\|} \right) \mathbf{v} \\ -\left(\frac{\mathbf{P}_{12} \cdot \mathbf{P}_{31}}{\|\mathbf{P}_{31} \times \mathbf{P}_{12}\| \|\mathbf{P}_{12}\|} \right) \mathbf{u} - \left(\frac{\mathbf{P}_{45} \cdot \mathbf{P}_{56}}{\|\mathbf{P}_{56} \times \mathbf{P}_{64}\| \|\mathbf{P}_{45}\|} \right) \mathbf{v} \\ -\left(\frac{\|\mathbf{P}_{12}\|}{\|\mathbf{P}_{12} \times \mathbf{P}_{23}\|} \right) \mathbf{u} \\ -\left(\frac{\|\mathbf{P}_{45}\|}{\|\mathbf{P}_{45} \times \mathbf{P}_{56}\|} \right) \mathbf{v} \end{array} \right] \begin{bmatrix} M \\ r_1\mathbf{u} + r_5\mathbf{v} \\ r_2\mathbf{u} + r_4\mathbf{v} \\ r_3\mathbf{u} \\ r_6\mathbf{v} \end{bmatrix} \quad (14)$$

The transpose of \mathbf{A}_h is the compatibility matrix of the hinge element, relating the rotation of the hinge to the displacement of the nodes $\mathbf{P}_1 - \mathbf{P}_6$. It is assumed that the hinge element is unstrained; i.e., the hinge rotation is zero, when the element is flat, to simulate the behavior of a cylinder made from a flat sheet.

The flexibility matrix relates M to the hinge rotation. It is defined in terms of the axial flexibility of the bars in the truss model, the hinge length, and a dimensionless constant f , which can be varied to simulate different hinge properties. For the element of Fig. 4

$$\mathbf{F}_h = \left[\frac{f}{AE \|\mathbf{P}_2 - \mathbf{P}_1\|} \right]. \quad (15)$$

The hinge elements for the cylinder are incorporated into the truss model to give enlarged equilibrium, compatibility and flexibility matrices for the entire structure. For a cylinder with N nodes and B bars, there are now H hinge elements. Thus the vectors of generalized stresses and strains include, as well as all the terms defined in Part II, H additional components. Apart from these changes, the simulation algorithm is unchanged from Part II.

One of the cylinders analyzed in Part II has been reanalysed incorporating hinge elements along all internal bars. It has parameters $m = 1$, $n = 7$, $l_b/l_a = 1$ and $l_c/l_a = \sqrt{3}$. The particular model that has been analyzed has $N = 36$ nodes, $B = 86$ bars and $H = 76$ hinge elements. Each simulation of the folding process consists of approximately 300 compression steps of size $0.01l_a$. Simulations were performed using different values of the flexibility factor, f . The results for $f = 1 \times 10^6$, $f = 1 \times 10^5$ and $f = 1 \times 10^4$ are presented in Fig. 5. Note that decreasing f corresponds to making the hinges stiffer.

Figure 5(a) shows the force R required to compress the cylinder for the three different values of hinge stiffness. Each of the plots shows the force rising at the end, which is due to the interaction between the transition zone and the fully fixed base.

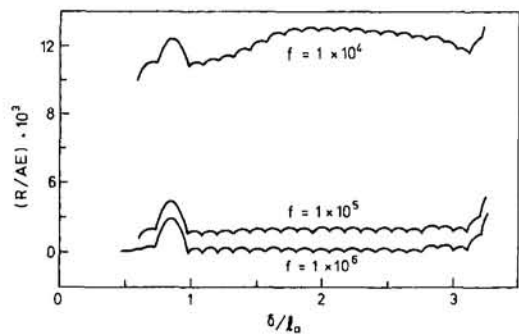


Fig. 5(a)

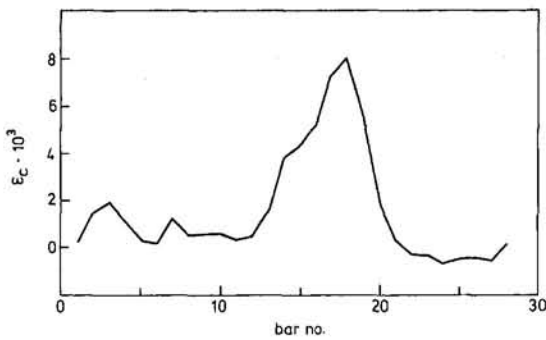


Fig. 5(b)

Fig. 5 Folding of cylinders with $m = 1$, $n = 7$, $l_b/l_a = 1$, $l_c/l_a = \sqrt{3}$: (a) force required to compress cylinders with different hinge flexibilities; (b) distribution of ϵ_c , when $\delta = 1.91l_a$ and $f = 1 \times 10^4$. Bars take the number of their bottom node, and nodes are numbered going up on the α -helix. Discrete values have been joined, for legibility.

When $f = 1 \times 10^6$ the force plot appears very similar to the results presented in Part II. The stiffness of the hinge has very little effect in this case.

When $f = 1 \times 10^5$ a larger peak force is required to form the transition zone at the top of the cylinder, and an approximately constant, nonzero force is required to move this zone down the cylinder.

When $f = 1 \times 10^4$, some clear changes in behaviour become evident, as the formation of the transition zone is now a two-stage process. During the first stage, the force R reaches a peak as the transition zone is initially formed at the top of the cylinder. This zone includes some bars which are also elastic hinges, and some which are not. The second stage occurs as this transition zone starts moving down the cylinder. R increases as the number of hinges in the transition zone increases. The transition zone is finally fully formed when *all* the bars within the zone are also elastic hinges. After this, there is a steady-state part of the plot as the fully formed transition zone moves down the cylinder. The steady-state part for this particular simulation is rather short, as the cylinder that is being simulated is small, and the effect of the base quickly becomes important. Note that there is an average compressive force in the cylinder during the steady-state phase, as energy must now be put into the cylinder to fold the hinges. Also note that the force required to form the initial transition zone is now seven times higher than for the case with momentless hinges. Finally note that the steady-state part of this plot involves compressive forces larger than those in the initial force peak.

Figure 5(b) shows the strain in the c -bars, defined in Fig. 2 of Part I when the cylinder has been compressed by $\delta = 1.91l_a$, for $f = 1 \times 10^4$. This value of δ corresponds to a peak in the force plot. The plots for $f = 1 \times 10^5$ and $f = 1 \times 10^6$ are similar, but with slightly lower strains. The plot is presented for $\delta = 1.91l_a$ rather than $\delta = 1.62l_a$, as used in Part 2, so that the transition zone has had time to fully form. The peak strain in the bars is only 2% higher when $f = 1 \times 10^4$ than for the case with momentless hinges.

Manufacturing Errors. The original computer model of the structure was also altered to assess the effect of misaligning the final seam of the cylinder during manufacture. These errors were simulated by imposing an initial strain e on the bars which cross the final join-line of the cylinder. Simulations were performed for cylinders with parameters $m = 1$, $n = 7$, $l_b/l_a = 1$ and $l_c/l_a = \sqrt{3}$ as before. The cylinders were compressed in approximately 300 steps of size $0.01l_a$ for three different values of e , 0.1 percent, 1 percent and 2.5 percent. The results are shown in Fig. 6.

When $e = 0.1$ percent, Fig. 6(a), the force plot is very similar to the case when the manufacturing error is zero.

When $e = 1$ percent, Fig. 6(b), however, the steady-state part of the plot becomes periodic with a wavelength corresponding to the folding of a set of $n =$ seven pairs of triangles, forming a complete turn of the α -helix. The manufacturing error prevents the folding from proceeding smoothly.

Similar results are obtained when $e = 2.5$ percent, Fig. 6(c). Again the results are periodic with a wavelength corresponding to the folding of $n =$ seven pairs of triangles. The variation in force is greater than for $e = 1$ percent as larger errors make it more difficult to fold parts of the cylinder.

Comparing the strain in the bars for the three cylinders containing manufacturing errors with a perfect cylinder, it is found that the peak strain is little changed. The largest increase occurs for $e = 2.5$ percent, when the peak strain is increased by 16 percent. However, because of the incompatibility introduced by making some bars longer, the manufacturing errors lead to generally higher levels of strain distributed throughout the cylinder.

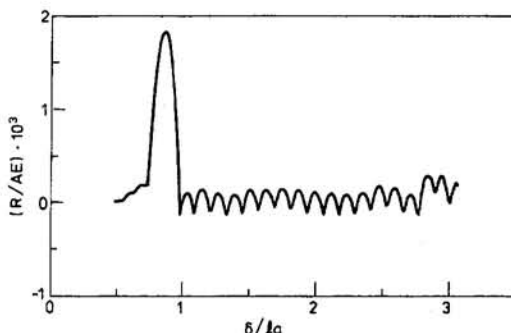


Fig. 6(a)

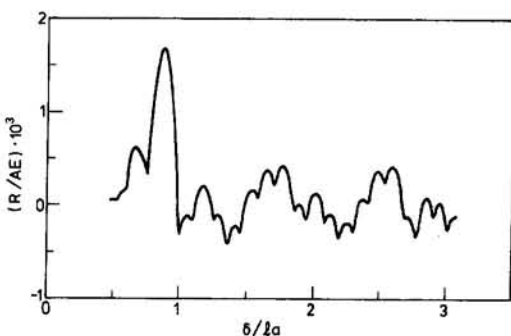


Fig. 6(b)

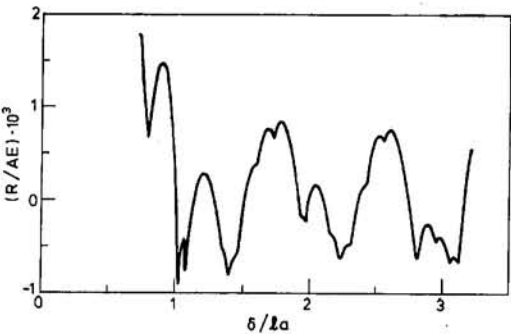


Fig. 6(c)

Fig. 6 Force required to compress initially strained cylinders with $m = 1$, $n = 7$, $l_b/l_a = 1$, $l_c/l_a = \sqrt{3}$: (a) $e = 0.1$ percent, (b) $e = 1$ percent, (c) $e = 2.5$ percent.

5 Discussion and Conclusions

This paper has shown the practical realization of the triangulated cylinders introduced in the previous two papers. In particular, it has explored two reasons why the experimental behaviour of these cylinders differs from the predictions obtained from the simple pin-jointed truss model analyzed in Part II.

The first effect that has been explored is the effect of hinge stiffness. It has been found that the effect of adding a series of elastic hinges to the truss model has the effect of raising the average compressive force to fold the models above zero, an effect seen in all of the cylinders tested. Indeed, sufficiently high hinge stiffnesses lead to the compressive force during steady-state folding being similar in size to the force required to form the initial transition zone. This explains why the initial force peak associated with the formation of the transition zone, predicted from the truss model in Part II, is not shown in the experimental results.

The second effect that has been explored is geometric misalignment during manufacturing. It has been found that the simple truss model predicts significant changes in behavior

when geometric errors are introduced. The force developed, while still oscillating about zero, no longer has a period corresponding to the folding of one pair of triangles, but corresponds to the folding of n pairs of triangles. Superimposed on this global behavior is the folding of individual pairs of triangles. This behavior is very similar to that seen in the experimental tests.

Some consideration must be given to the values of the parameters used during the simulations. The initial strains e used to simulate manufacturing errors can be easily justified. The maximum value of e , 2.5 percent, corresponds to a misalignment during final fabrication of 3 mm for the Cu-Be and steel cylinder, and of 1 mm for the Irathane and Al-alloy cylinder. Errors of this magnitude could certainly have been introduced.

It is less easy to justify the particular values of f used during the investigation of the effects of hinge stiffness. The reason for this is the generic nature of the original model. In particular, the deformation of the bars in the original truss model was not meant to directly simulate the deformation of the triangular plates, but to investigate the effect of distributed elasticity within the model. In the Irathane and Al-alloy cylinders, for example, this deformation in fact takes place by shearing of the hinges. Thus as no quantitative measure of the bar stiffnesses has yet been considered, the values of f must be seen as a qualitative exploration of the effects of hinge elasticity on the folding process.

To validate the proposed computational model, a simulation of the behavior of the Irathane and Al-alloy cylinder no. 1 (see Table 1) has been performed. The simulation included both hinge elasticity and manufacturing errors, and the following parameters were chosen to match the observed behavior of the cylinder: $AE = 6 \cdot 10^5 N$, $f = 1.25 \cdot 10^7$, $e = 0.15$ percent. The initial behavior of the cylinder has not been simulated, because in the experimental model, extra, partially cut triangles were added at the top of the cylinder to form a level edge.

A comparison of the experimental results (reproduced from Fig. 1), and the simulation results, is shown in Fig. 7. The agreement between the results is remarkably accurate; both the periodicity, and the magnitudes of peaks and troughs, of the actual behavior are reproduced by the simulation.

Finally, it is interesting to note how this paper fits in with the work described in the previous two papers. The two Irathane and Al-alloy cylinders were of the simple type described in Section 1 of Part I made from isosceles triangles that fold down to prismatic stacks of plates. The Cu-Be and steel cylinder is not of this simple type, and was the first to be designed using the more general geometric formulation presented in the remainder of Part I to limit the amount of deformation required during folding.

The computational modelling techniques of Part II have been shown to predict many of the characteristics seen in the folding process. Also, although the changes to the model described here have radically changed some aspects of the compressive

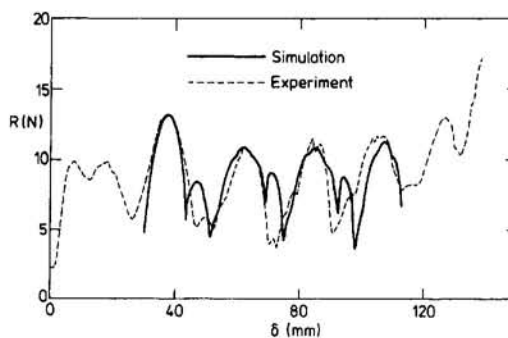


Fig. 7 Comparison of the force required to compress Irathane and Al-alloy cylinder no. 1, and a computer simulation

Table 2 Comparison of computational results for cylinders with $m = 1$, $n = 7$, $l_b/l_a = 1$, and $l_c/l_a = \sqrt{3}$

	$ \epsilon_a _{\max}$	$ \epsilon_b _{\max}$	$ \epsilon_c _{\max}$	R_{\max}/AE
$l/f = 0, e = 0$	$5.0 \cdot 10^{-3}$	$6.9 \cdot 10^{-3}$	$8.7 \cdot 10^{-3}$	$1.8 \cdot 10^{-3}$
$l/f = 1 \cdot 10^{-4}, e = 0$	$4.8 \cdot 10^{-3}$	$7.8 \cdot 10^{-3}$	$8.9 \cdot 10^{-3}$	$13.1 \cdot 10^{-3}$
$l/f = 0, e = 2.5 \text{ percent}$	$6.8 \cdot 10^{-3}$	$8.3 \cdot 10^{-3}$	$10.1 \cdot 10^{-3}$	$1.8 \cdot 10^{-3}$

behavior of the cylinder, the internal deformation of the cylinder during folding has not changed greatly. The maximum internal deformation, as measured by the strain in the c -bars of the model, has risen by no more than 16 percent in any simulation performed. A complete comparison of the computational results is made in Table 2. The original model remains a valid tool for predicting and comparing many aspects of the behavior of foldable cylinders, particularly the amount of deformation they undergo during folding. Also, the usefulness of having a simple computational model has been shown, as it can easily be modi-

fied to test the validity of different explanations for observed experimental behavior.

Acknowledgments

We would like to thank Mr. T. D. Wedgwood and Mr. K. Seffen for carrying out some of the experimental work described, and Mr. S. Vincer of Irathane International for supplying the Irathane coated plates. Financial support from British Aerospace (Space Systems) Ltd., and SERC is gratefully acknowledged.

References

Guest, S. D., and Pellegrino, S., 1994a, "The Folding of Triangulated Cylinders, Part I: Geometric Considerations," *ASME JOURNAL OF APPLIED MECHANICS*, Vol. 61, pp. 773-777.

Guest, S. D., and Pellegrino, S., 1994b, "The Folding of Triangulated Cylinders, Part II: The Folding Process," *ASME JOURNAL OF APPLIED MECHANICS*, Vol. 61, pp. 778-783.

Kyriakides, S., 1994, "Propagating Instabilities in Structures," *Advances in Applied Mechanics*, J. W. Hutchinson and T. W. Wu, eds., Academic Press, Boston, pp. 67-189.

Phaal, R., 1990, "A Two-Surface Computational Model for the Analysis of Thin Shell Structures," Ph.D. Dissertation, Cambridge University.

Dynamic Effects of Centrifugal Forces on Turbulence

L. S. Yao

S. Ghosh Moulic

Mechanical and Aerospace Engineering Department, Arizona State University, Tempe, AZ 85287

The dynamic effect of suddenly applied centrifugal forces on homogeneous and isotropic turbulence in the entrance region of a curved pipe is analyzed by a perturbation method. The model is for small-scale turbulence and is valid away from the pipe wall; hence is not restricted to a particular cross-sectional shape and can be applied even to external flows if the mean velocity profile is almost uniform, as in the region outside the turbulent boundary layer on a curved surface. The analysis indicates that the major effect of centrifugal forces is to generate pure turbulent shear and this effect is cumulative. Thus, an initially isotropic turbulence becomes anisotropic due to linear effects. This result is in contrast with the effect of solid-body rotation on isotropic turbulence, where rotation acts on an initially isotropic turbulence only through nonlinear interactions, and pure linear effects influence the double correlations only if the turbulence is initially anisotropic.

1 Introduction

Curved pipes and pipe bends are commonly found in pipe networks for engineering systems or human blood vessels. Therefore, an understanding of the flow through such devices is of paramount importance. Investigations of curved-pipe flows can be traced back as early as 1876 (Thomson, 1876). Since then, the problem has been extensively studied both theoretically and experimentally for more than a century. A comprehensive review of these studies can be found in Berger, Talbot, and Yao (1983). Taylor (1929) showed that the transition Reynolds number in curved-pipe flows is much larger than that found in straight pipes. Relaminarization has been observed by Sreenivasan and Strykowski (1983). They have shown that relaminarization starts to occur after about three turns in a helically coiled pipe, and the transition Reynolds number could be two to three times larger than that found in a straight pipe. The mechanism that causes relaminarization is probably due to the existence of low speed fluid near the inner bend as a consequence of the secondary flow induced by the centrifugal forces. The process takes a rather long distance to occur. In this paper, the turbulence structure near the entrance region of a curved pipe is examined.

For a laminar developing flow in the entry region of a curved pipe, three axial regions have been identified (Yao and Berger, 1975). At a distance of the order of the pipe radius from the entrance, the pressure gradient balances the centrifugal forces in the core region, and the secondary boundary layer flow near the pipe wall is gradually developed. This is a consequence of the fact that the centrifugal force effects are cumulative. Within this region, the magnitude of the secondary boundary layer is small compared to the axial boundary layer and the displacement effect of the boundary layer flow on the core flow is negligible (Singh, 1974). The second region is at a distance $(aR)^{1/2}$ from the entrance, where a is the radius of the pipe and R is the radius of the pipe curvature (see Fig. 1). Within this region, the boundary layer flow is further developed and becomes three dimensional. However, its displacement effect on

the core flow is still negligible. It has been shown (Yao and Berger, 1988) that the solution describing the flow in the first region is included in that of the second region. A comparison of two solutions shows that the size of the first region is $s < 0.1(aR)^{1/2}$, where s measures the axial distance along the centerline of the pipe. This has been experimentally verified by Olson and Snyder (1985). A substantial change of the core flow is developed at a much longer distance, $0(a \text{Re}/D^{1/2})$, from the entrance, where $\text{Re} = W_0 a / \nu$ is the Reynolds number, $D = (a \text{Re})^{1/2}$ is the Dean number, W_0 is the mean axial velocity, and $\alpha = a/R$ is the curvature ratio. As suggested by Pedley (1980), this is the required distance for the transport of secondary vorticity from the boundary layer to the core. Therefore, the interaction between the core flow and the boundary layer is small and can be ignored in the entry region of a curved pipe if $s \ll a \text{Re}/D^{1/2}$.

Even though centrifugal forces have a small direct effect on the development of the laminar core flow within a short distance from the entrance, their effects are much stronger for a turbulent flow because the redistribution of turbulent energy by the centrifugal forces are first-order effects. Moffatt (1981) has suggested that rapid distortion theory (RDT) could be used to analyze turbulent flow in a curved bend by relating the statistical properties of the turbulence immediately after the bend to those before the bend. The basis of RDT was originally suggested by Prandtl (1932) and Taylor (1935), and was used to estimate homogeneous turbulence behind a net of grid bars in a wind tunnel contraction. Since then, the theory was extensively developed by Batchelor (1953) and Batchelor and Proudman (1954). The theory provides a means of calculating the effect of a sudden change in mean velocity on a turbulent flow, and is only applicable when the time taken for a fluid particle to pass through the zone in which the mean velocity changes rapidly is much less than the time taken for the turbulence to change owing to viscous and nonlinear inertia forces. Therefore, it follows from these assumptions that the problem involving a random process is linear and is tractable by straightforward mathematical methods. More explicitly, the theory is applicable when turbulent diffusion and dissipation are negligible when compared with the rapid change of the mean flow and the pressure-redistribution effects. Townsend (1970, 1980) successfully used the theory to interpret experimental shear-flow data. Hunt (1973) applied the theory to nonhomogeneous distortions.

The turbulent flow in the entry region of a curved pipe shares some features with that in a solid-body rotation field, although they differ in many important aspects. Bradshaw (1969) pointed out the similarities between the effects of centrifugal forces due

Contributed by the Applied Mechanics Division of THE AMERICAN SOCIETY OF MECHANICAL ENGINEERS for publication in the ASME JOURNAL OF APPLIED MECHANICS.

Discussion on this paper should be addressed to the Technical Editor, Professor Lewis T. Wheeler, Department of Mechanical Engineering, University of Houston, Houston, TX 77204-4792, and will be accepted until four months after final publication of the paper itself in the ASME JOURNAL OF APPLIED MECHANICS.

Manuscript received by the ASME Applied Mechanics Division, June 8, 1994; final revision, Nov. 7, 1994. Associate Technical Editor: S. A. Berger.

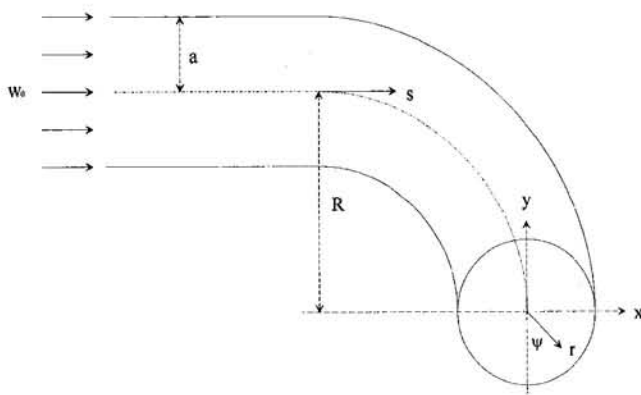


Fig. 1 Physical model and coordinates

to streamline curvature, the effects of Coriolis forces due to rotation, and the effects of buoyancy forces due to density stratification on turbulent shear flows. He showed that a formally exact analogy can be drawn between meteorological parameters such as the Richardson number and the parameters describing the effect on turbulent shear flows of streamline curvature in the plane of the principal rate of strain or rotation about an axis normal to that plane. Thus, it is of interest to us to review the literature on the effects of rotation on turbulent flows. Our analysis indicates that, contrary to popular belief, there are significant differences between the effects of centrifugal forces due to streamline curvature and the effects of Coriolis forces due to solid-body rotation on turbulent flows. As discussed in the Appendix, this difference is a consequence of the difference in the mean flow, which plays an important role in the production of Reynolds stresses. In order to compare and contrast the similarities and differences between the effects of centrifugal and Coriolis forces, we give a brief review of the literature on rotating turbulent flows.

The effects of rotation on turbulence has been studied experimentally by Traugott (1958), Ibbetson and Tritton (1975), Wigeland and Nagib (1978), and Hopfinger, Browand, and Gagne (1982). Traugott (1958) studied the effect of rotation on turbulence generated by passing air through several grids in the annular section between two rotating concentric cylinders. He found that rotation decreased the rate of decay of turbulence. Ibbetson and Tritton (1975) investigated the effect of rotation on turbulence generated in air by the sudden axial displacement of two grids in an annular container on a rotating table. They found that increasing the rotation rate produced a faster decay of the turbulence. Ibbetson and Tritton suggested that inertial waves carried energy to the boundaries of their apparatus, where it was dissipated in viscous boundary layers, thereby increasing the rate of decay of turbulence kinetic energy. They also observed that rotation produced a large increase in the integral scale parallel to the rotation axis, and a smaller increase in the integral scale perpendicular to the rotation axis. Wigeland and Nagib (1978) studied the decay of rotating grid-generated turbulence by passing a uniform flow through a rotating duct equipped with a honeycomb followed by a grid. Their experiments showed that in most cases, the turbulence decayed more slowly, and the time-integral scales increased more rapidly as the rate of rotation was increased. In a few cases they observed that the turbulence intensity decayed faster at small rotation rates but slower at larger rates of rotation. Hopfinger, Browand, and Gagne (1982) performed experiments in a deep rotating tank of water with an oscillating grid at the bottom. They observed that near the grid, where the Rossby number was large, the turbulence was locally unaffected by rotation. Away from the grid, the intensity of the turbulent velocity fluctuations decreased and the scales of the turbulence increased. At a local Rossby number of about 0.2, they observed a sudden transition,

which terminated the turbulent Ekman layer. Above the Ekman layer, the flow consisted of concentrated vortices having axes approximately parallel to the rotation axis and extending throughout the depth of the fluid above the Ekman layer. Hopfinger, Browand, and Gagne observed isolated propagating waves traveling along the axes of individual vortices. They used the phrase rotation-dominated rather than quasi-geostrophic to describe the turbulent velocity field.

The effects of rotation on turbulent shear flows have been analyzed by Bertoglio (1982) using rapid distortion theory. He found that Coriolis forces induced by rotation about an axis normal to the plane of the mean shear had a stabilizing or destabilizing influence on the turbulence, depending on the sense of rotation. Bardina, Ferziger, and Rogallo (1985) used large eddy and direct simulations to analyze the effects of uniform rotation on homogeneous turbulence. Their numerical simulations indicate that the predominant effect of rotation is to decrease the rate of dissipation of the turbulence, and to increase the length scales, especially those along the axis of rotation. They showed that it was possible to duplicate the phenomena observed in the experiments of Wigeland and Nagib (1978). They demonstrated that the increase in the decay of turbulence observed in some cases by Wigeland and Nagib is due to interactions between the rotation and the wakes of the turbulence-generating grid which modifies the initial conditions in the experiments. Cambon and Jacquin (1989) studied the anisotropic effects induced by solid-body rotation on homogeneous turbulence by applying an eddy-damped quasi-normal Markovian model to evaluate the triple correlations, which allows anisotropic effects to be taken into account. A direct numerical simulation of the decay of initially isotropic turbulence in a rapidly rotating frame shows that the turbulence remains essentially isotropic during the major part of the decay (Speziale et al., 1987). They found that the rapid rotation has the primary effect of shutting off the energy transfer; consequently, the turbulence dissipation is substantially reduced. The effects of uniform rotation is included in a single-point model for initially isotropic turbulence by Mansour et al. (1991). The effects of rotation on turbulence have been reviewed recently by Hopfinger and Linden (1990).

The effects of streamline curvature on turbulent shear flows has been studied by Castro and Bradshaw (1976), Townsend (1980), Muck, Hoffmann, and Bradshaw (1985), Hoffmann, Muck, and Bradshaw (1985), and Hunt, Leibovich, and Richards (1988). Castro and Bradshaw (1976) made extensive one-point measurements of the turbulence structure in a highly curved mixing layer bounding a normally impinging plane jet with an irrotational core. They found that the Reynolds stresses decreased in the region of high stabilizing curvature and then increased rapidly further downstream, overshooting the plane layer values before finally decreasing. Townsend (1980) demonstrated that the behavior of the ratio of the shear stress to the turbulence intensity observed by Castro and Bradshaw (1976) in a curved mixing layer could be reproduced qualitatively using rapid distortion theory without any difficulty. He suggested that the curious behaviour of the stress ratio was due to inertial waves that can propagate in rotationally stable flows. To illustrate this, he considered the effect of solid-body rotation on turbulence with an initial Reynolds shear stress. He obtained a closed-form solution of the rapid strain equations for this simplified model, and showed that the Reynolds shear stress goes through damped oscillations. Townsend (1980) also studied the irrotational distortion of turbulence for an axisymmetric constant-circulation mean flow along a curved path. Muck, Hoffmann, and Bradshaw (1985) studied the response of a well-developed turbulent boundary layer to suddenly applied convex surface curvature, using conditional sampling techniques. In a companion paper, Hoffmann, Muck, and Bradshaw (1985) studied the response of a turbulent boundary layer to suddenly applied concave surface curvature. Their main conclusion was

that the effects of convex (stabilizing) curvature and concave (destabilizing) curvature on turbulent boundary layers was totally different. Mild convex curvature tends to attenuate the pre-existing turbulence without producing large changes in statistical-average eddy shape. Concave curvature, on the other hand, results in the generation of longitudinal vortices, together with significant changes in the turbulence structure. Hunt, Leibovich, and Richards (1988) used an asymptotic analysis to study turbulent shear flows over hills with low slopes. They divided the flow into two regions, an outer and an inner region. The outer region was further divided into an upper and a middle layer, while the inner region was divided into a shear-stress layer and an inner surface layer. They derived analytical solutions for the inner region.

In this paper, the turbulence structure in the entry region of a curved pipe is examined. The turbulence is subjected to a rapid influence of the centrifugal forces instead of the mean-flow distortion. The turbulence is *inhomogeneous* along the mean flow direction. The physical model consists of a short straight pipe followed by a curved section so that the displacement effects of the boundary layer is negligible. A homogeneous and isotropic turbulence in the straight pipe is generated slightly upstream of the entrance of the curved pipe. The scalings revealed by the perturbation solutions show that turbulent diffusion and dissipation induced by the centrifugal forces are $0(\beta s)^2$, where β is the ratio of the convection time to the turbulent turnover time. This implies that the linearization is proper only when $\beta s \ll 1$, which agrees with the condition previously established for RDT (Batchelor, 1953; Hunt, 1973). Even though the analysis has not been carried out to include the distortion of the mean flow by the Reynolds stresses, which are treated as smaller-order terms, the model can be improved up to $0(\beta s)^2$ by following the expansion procedure outlined in the paper. Two curvature effects can influence the flow development. One is the geometric effects due to the variation of curvature on the cross section of the pipe. This is the factor which has been extensively used to correlate the turbulence data for curved flows. It is important to match the curvature ratio in order to satisfy the geometric similarity. Second is the direct effect of the centrifugal forces induced by the circular path of the mean flow. This effect on turbulence, which has so far been overlooked, is the focus of the present paper. As shown by Dean (1927, 1928), the effect of the centrifugal forces ensures the dynamic similarity of the flows along a curved path.

The mean flow analysed in Section 3 is for the model which consists of a short straight section before the curved pipe, as shown in Fig. 1. The velocity profile at the entrance to the straight pipe is taken to be uniform. The boundary layer displacement effect on the core flow is small in the entrance region of the pipe and is, therefore, not considered. Thus, the mean velocity profile in the core of the pipe remains uniform. In this respect, our model differs from the analysis of Townsend (1980) and Hunt et al. (1988), who considered a mean velocity gradient in their analysis. The impact of this difference in the mean flow is discussed in the Appendix, where the role played by the mean flow in the production of Reynolds stresses is analyzed. Two types of upstream influence on the turbulent flow exist because of the presence of the curved pipe: one is induced by the mean pressure field and the other is due to pressure fluctuations. Since the range of their influence is rather short and their magnitudes are exponentially small, these effects are indicated by "exp" so that the analysis can concentrate on the more profound effects of the centrifugal forces on the turbulence structure in the curved pipe. Consequently, the current analytical results are also valid for a curved pipe, connected to a large flow chamber, if the velocity profile at the pipe entrance is approximately uniform.

In Section 4, grid turbulence whose scale, 1, is smaller than the radius of the pipe is considered. The analysis is carried out for the core region of the pipe and is not valid at a distance

$O(1)$ from the pipe wall. Thus, our results cannot be compared with the turbulent boundary layer measurements of Muck, Hoffmann, and Bradshaw (1985) and Hoffmann, Muck, and Bradshaw (1985) for flow over slightly curved surfaces. The results of our analysis are not limited to circular pipe cross section, and can be applied to any cross-sectional shape or to external flows along a circular path if the mean velocity profile is uniform, as in the region outside the turbulent boundary layer on a curved surface. Higher-order rational expansions can be derived for the mean flow as well as the turbulent quantities as outlined in this section. This may extend the theory to a larger domain by including some nonlinear energy-cascade processes in the model. In this paper, however, only the leading-order terms of turbulence are obtained. Thus, the current model is identical to RDT. The key centrifugal force effect is to turn the principal Reynolds stresses 45 deg on the plane on which the centrifugal forces act and of the mean-flow direction. The implications of the present findings are then summarized and possible extension of the current results to a curved turbulent flow with variable curvature is discussed in Section 5.

Our analysis indicates that under the dynamic influence of centrifugal forces, an initially isotropic turbulence in the core region of a curved pipe becomes anisotropic due to *linear* effects. In this aspect, the effects of centrifugal forces differs from that of Coriolis forces due to solid-body rotation. Coriolis forces due to uniform rotation act on an initially isotropic turbulence only through *nonlinear* interactions, and pure linear effects influence the double correlations only if the turbulence is initially anisotropic (Bardina et al., 1985; Cambon and Jacquin, 1989). This difference between the effects of centrifugal and Coriolis forces may be traced to the difference in the mean velocity profiles in the two cases. The mean flow plays an important role in the production of Reynolds stresses. In the case of solid-body rotation, if the turbulence is initially isotropic, there is no *linear* mechanism to generate Reynolds stresses and the turbulence can become anisotropic only through *nonlinear* interactions. On the other hand, if the mean velocity profile is uniform, as in the core of a curved pipe, centrifugal forces can generate Reynolds shear stress through *linear* effects. This is discussed in detail in the Appendix.

2 Formulation

The flow through a pipe of circular cross section, radius a , that is straight for $s < 0$ but at $s = 0$ suddenly bends to form an arc of a circle of radius R (see Fig. 1) is considered. If the axial and the radial distances are measured by $a \cdot s$ and $a \cdot r$, respectively, and the velocity components are normalized by the mean axial velocity W_0 of the flow and the pressure by ρW_0^2 , then the Navier-Stokes equations in toroidal coordinates take the form (see Yao and Berger, 1975),

$$\frac{\partial u}{\partial r} + \frac{u}{r} + \frac{1}{r} \frac{\partial v}{\partial y} + J \left[\frac{\partial w}{\partial s} + a(u \sin \psi + v \cos \psi) \right] = 0,$$

$$\begin{aligned} \frac{\partial u}{\partial t} + u \frac{\partial u}{\partial r} + \frac{v}{r} \frac{\partial u}{\partial y} + J w \frac{\partial u}{\partial s} - \frac{v^2}{r} - a J w^2 \sin \psi \\ = - \frac{\partial p}{\partial r} + O(\text{Re}^{-1}), \end{aligned}$$

$$\begin{aligned} \frac{\partial v}{\partial t} + u \frac{\partial v}{\partial r} + \frac{v}{r} \frac{\partial v}{\partial y} + J w \frac{\partial v}{\partial s} + \frac{u v}{r} - a J w^2 \cos \psi \\ = - \frac{1}{r} \frac{\partial p}{\partial y} + O(\text{Re}^{-1}), \end{aligned}$$

$$\begin{aligned}\frac{\partial w}{\partial t} + u \frac{\partial w}{\partial r} + \frac{v}{r} \frac{\partial w}{\partial \psi} + J w \frac{\partial w}{\partial s} + a J w (u \sin \psi + v \cos \psi) \\ = -J \frac{\partial p}{\partial s} + O(\text{Re}^{-1}), \quad (2.1)\end{aligned}$$

where $J = 1/(1 + \alpha r \sin \psi)$, $\alpha = a/R$, $\text{Re} = W_0 a/v$, and ρ and v are the density and kinematic viscosity of the fluid, respectively. The Navier-Stokes equations in cylindrical polar coordinates for the upstream straight pipe ($s < 0$) can be obtained by setting $\alpha = 0$ in Eqs. (2.1).

The flow quantities in (2.1) are expressed in terms of their mean and fluctuating components, $\phi = \Phi + \beta \phi'$, where $\beta = q_0/W_0$. The turbulent kinetic energy of the straight-pipe flow is $q_0 = (k_0)^{1/2} = [u'^2 + v'^2 + w'^2]^{1/2}$ and (u', v', w') are the dimensional turbulent velocities. Since it will not cause confusion, the prime associated with the fluctuation quantities will be dropped in order to simplify the notations in the following analysis. The equations describing the mean flow, obtained from (2.1), are

$$\begin{aligned}\frac{\partial U}{\partial r} + \frac{U}{r} + \frac{1}{r} \frac{\partial V}{\partial \psi} + J \left[\frac{\partial W}{\partial s} + \alpha (U \sin \psi + V \cos \psi) \right] = 0, \\ U \frac{\partial U}{\partial r} + \frac{V}{r} \frac{\partial U}{\partial \psi} + J W \frac{\partial U}{\partial s} - \frac{V^2}{r} - a J W^2 \sin \psi \\ = -\frac{\partial P}{\partial r} + O(\text{Re}^{-1}, \beta^2), \\ U \frac{\partial V}{\partial r} + \frac{V}{r} \frac{\partial V}{\partial \psi} + J W \frac{\partial V}{\partial s} + \frac{U V}{r} - a J W^2 \cos \psi \\ = -\frac{1}{r} \frac{\partial P}{\partial \psi} + O(\text{Re}^{-1}, \beta^2), \\ U \frac{\partial W}{\partial r} + \frac{V}{r} \frac{\partial W}{\partial \psi} + J W \frac{\partial W}{\partial s} + \alpha J W (U \sin \psi + V \cos \psi) \\ = -J \frac{\partial P}{\partial s} + O(\text{Re}^{-1}, \beta^2). \quad (2.2)\end{aligned}$$

It can be concluded from the above equations that the straight-pipe flow forms the zeroth-order solution of (2.2) if $s \ll \text{Re}/D^{1/2}$, where $D = (\alpha \text{Re})^{1/2}$ is the Dean number (Dean, 1927, 1928). Within this region, the displacement effect of the boundary layer is small. In Section 4, the effects of the centrifugal forces are shown to be characterized by a set of linearized Navier-Stokes equations if $\beta s \ll 1$. Since the physical meaning of β is the ratio of the convection time to the turbulent "turn-over" time, the present analysis coincides with that of RDT. Equations (2.2) indicate that the influence of the Reynolds stresses on the mean flow is of $O(\beta s)^2$. It can also be shown that turbulent diffusion and dissipation induced by the centrifugal forces are small and are of $O(\beta s)$. Therefore, the solution for the problem can be expanded in a double series of α and β . The leading term is the solution for a straight-pipe flow and the dominant effects of the centrifugal forces are described by the rapid distortion theory in the entry region of a curved pipe for $s < 1/\beta$ and $s < \text{Re}/D^{1/2}$. Therefore, the primary concern of this paper is the analysis of the effects of centrifugal forces on turbulence.

Explicitly, the expansions are assumed to be

$$\begin{aligned}W &= 1 + \alpha W_1 \sin \psi + O(\alpha^2, \beta^2), \\ U &= \alpha U_1 \sin \psi + O(\alpha^2, \beta^2), \\ V &= \alpha V_1 \cos \psi + O(\alpha^2, \beta^2), \\ P &= P_s + \alpha P_1 \sin \psi + O(\alpha^2, \beta^2), \quad (2.3)\end{aligned}$$

for the mean flow and

$$\begin{aligned}w &= w_s + \alpha w_1 + O(\alpha^2, \beta), \\ u &= u_s + \alpha u_1 + O(\alpha^2, \beta), \\ v &= v_s + \alpha v_1 + O(\alpha^2, \beta), \\ p &= p_s + \alpha p_1 + O(\alpha^2, \beta), \quad (2.4)\end{aligned}$$

for the fluctuating components, where the subscript "s" is used to denote the quantities associated with straight-pipe flows. Both the mean-flow and the fluctuating components associated with the straight-pipe flows are known. Taylor's hypothesis is applicable to the fluctuating quantities in the straight pipe; therefore they are function of $(r, \psi, s-t)$. The quantities with the subscript "1" are due to the centrifugal forces and can be determined and expressed in terms of the known straight-pipe solutions.

The equations for the turbulent fluctuating components can now be obtained by subtracting (2.2) from (2.1). The equations of $O(\alpha)$, which are consistent with (2.3)-(2.4), are

$$\begin{aligned}\frac{\partial u_1}{\partial r} + \frac{u_1}{r} + \frac{1}{r} \frac{\partial v_1}{\partial \psi} + \frac{\partial w_1}{\partial s} \\ = \left\{ \left(r \sin \psi \frac{\partial w_s}{\partial s} - u_s \sin \psi - v_s \cos \psi \right) H(s) \right\}, \\ \frac{\partial u_1}{\partial t} + \frac{\partial u_1}{\partial s} - 2w_s \sin \psi H(s) = -\frac{\partial p_1}{\partial r} + \left\{ r \sin \psi \frac{\partial u_s}{\partial s} \right. \\ \left. - \left[\left(U_1 \frac{\partial u_s}{\partial r} + u_s \frac{\partial U_1}{\partial r} + W_1 \frac{\partial u_s}{\partial s} + w_s \frac{\partial U_1}{\partial s} \right) \sin \psi \right. \right. \\ \left. \left. + \frac{1}{r} \left(V_1 \frac{\partial u_s}{\partial \psi} + U_1 v_s - 2V_1 v_s \right) \cos \psi \right] \right\}, \\ \frac{\partial v_1}{\partial t} + \frac{\partial v_1}{\partial s} - 2w_s \cos \psi H(s) = -\frac{1}{r} \frac{\partial p_1}{\partial \psi} + \left\{ r \sin \psi \frac{\partial v_s}{\partial s} \right. \\ \left. - \left[\left(U_1 \frac{\partial v_s}{\partial r} + W_1 \frac{\partial v_s}{\partial s} + \frac{U_1 - V_1}{r} v_s \right) \sin \psi \right. \right. \\ \left. \left. + \left(u_s \frac{\partial V_1}{\partial r} + \frac{V_1}{r} \frac{\partial v_s}{\partial \psi} + w_s \frac{\partial V_1}{\partial s} + \frac{V_1 u_s}{r} \right) \cos \psi \right] \right\}, \\ \frac{\partial w_1}{\partial t} + \frac{\partial w_1}{\partial s} + (u_s \sin \psi + v_s \cos \psi) H(s) \\ = -\frac{\partial p_1}{\partial s} + \left\{ r \sin \psi \frac{\partial w_s}{\partial s} - \left[\left(U_1 \frac{\partial w_s}{\partial r} + u_s \frac{\partial W_1}{\partial r} \right. \right. \right. \\ \left. \left. \left. + W_1 \frac{\partial w_s}{\partial s} + w_s \frac{\partial W_1}{\partial s} \right) \sin \psi \right. \right. \\ \left. \left. + \frac{1}{r} \left(V_1 \frac{\partial w_s}{\partial \psi} + W_1 v_s \right) \cos \psi \right] \right\}, \quad (2.5)\end{aligned}$$

where $H(s)$ is the Heaviside step function. The above equations reveal that the turbulence field is distorted, to first order, by two elements: the centrifugal forces and the effect induced by variable curvatures. The terms within the curly brackets on the right-hand side of the above equations represent the effect of variable curvature. Among them, the most important curvature effect is the energy produced by induced mean flow motions (terms in square brackets). Turbulent diffusion and dissipation

are of $O(\beta)$ in the transport equations governing the fluctuating quantities. Therefore, they have no effects on the solutions which is larger than $O(\beta)$ (see Eqs. (2.4)). The variable-curvature effects ensure the geometric similarity and are negligible for small turbulent eddies or for slightly curved pipes. In the following analysis, we focus on the effect of the centrifugal forces to ensure the dynamic similarity of the flows. In Sections 3 and 4, it will be shown that the disturbances induced by the centrifugal forces can propagate upstream because of the "pressure" effect. Also, the energy production by the induced mean flow decays fast and is negligible compared with the effect of centrifugal forces.

3 Mean Flow

The equations describing the first-order mean flow can be obtained by substituting (2.3) into (2.2) and collecting terms of $O(\alpha)$. They are

$$\begin{aligned} \frac{\partial U_1}{\partial r} + \frac{U_1 - V_1}{r} + \frac{\partial W_1}{\partial s} &= 0, \\ \frac{\partial U_1}{\partial s} &= H(s) - \frac{\partial P_1}{\partial r}, \\ \frac{\partial V_1}{\partial s} &= H(s) - \frac{P_1}{r}, \\ \frac{\partial W_1}{\partial s} &= -\frac{\partial P_1}{\partial s}. \end{aligned} \quad (3.1)$$

Eliminating U_1 , V_1 , and W_1 among the above equations results in

$$\frac{\partial^2 P_1}{\partial r^2} + \frac{1}{r} \frac{\partial P_1}{\partial r} - \frac{P_1}{r^2} + \frac{\partial^2 P_1}{\partial s^2} = 0. \quad (3.2)$$

Since $(\partial U_1 / \partial s) = 0$ at $r = 1$ (slip condition) and $(\partial V_1 / \partial s) = 0$ at $r = 0$ (symmetry condition), the boundary conditions for P_1 can be determined from the second and third equations of (3.1) and are

$$\frac{\partial P_1}{\partial r} = H(s) \quad \text{at} \quad r = 1, \quad \text{and} \quad P_1 = 0 \quad \text{at} \quad r = 0. \quad (3.3)$$

It should be noted that the slip condition imposed at $r = 1$ is equivalent to setting $U_1 = 0$ at $r = 1$. Applying Fourier transform in the sense of generalized functions (Lighthill 1970), it can be shown that the solution of (3.2) satisfying (3.3) is

$$\begin{aligned} P_1 &= \frac{1}{2\pi} \int_{-\infty}^{\infty} \left[\pi \delta(\lambda) + \frac{i}{\lambda} \right] \\ &\quad \times \frac{I_1(\lambda r)}{\lambda I_0(\lambda) - I_1(\lambda)} \exp(-i\lambda s) d\lambda \end{aligned} \quad (3.4)$$

where the I 's are modified Bessel functions and δ is the Dirac delta function. U_1 , V_1 , and W_1 can then be calculated from (3.1) using (3.4). It is easier to interpret the physics of the flow by examining the asymptotic expansion of (3.4), which is

$$P_1 = rH(s) - \text{sgn}(s) \left(\frac{3}{32} \right)^{1/2} \left(r - \frac{r^3}{3} \right) \exp(-\sqrt{8/3}s), \quad (3.5)$$

where $\text{sgn}(s)$ denotes the sign of s . Equation (3.5) clearly shows that the first-order mean flow induced by the centrifugal forces consists of two parts. First, the pressure gradient is established in the curved pipe in order to balance the centrifugal forces. Secondly, the induced secondary flow (exponential decay term) exists within three radii both in the upstream ($s < 0$) and the downstream ($s > 0$) regions if one uses 1 percent

as the criterion to determine the penetration depth. The magnitude of the induced secondary flow drops below 5 percent when $s > 2$. This agrees very well with the measurements of Ito (1960) who shows that the secondary flow exists before the fluid enters the curved pipe. Since the induced secondary flow is only important within such a small region, it is ignored in the following analysis. This allows the discussion to concentrate on the more profound effects of the centrifugal forces on the turbulence structure in curved-pipe flows. Including the induced secondary flow in the analysis will not present any extra difficulty, but the algebra will be more tedious.

It is convenient to summarize the mean flow before solving (2.5) for the fluctuating components. The mean flow becomes

$$W = 1 + \alpha \exp + O(\alpha^2, \beta^2),$$

$$U = \alpha \exp + O(\alpha^2, \beta^2),$$

$$V = \alpha \exp + O(\alpha^2, \beta^2),$$

$$P = \text{constant} + \alpha[rH(s) + \exp] + O(\alpha^2, \beta^2), \quad (3.6)$$

where "exp" denotes the exponentially small terms. It is worthwhile to note that the turbulent flux terms in (2.2) are of $O(\beta^2)$. Therefore, the mean flow can be accurately calculated up to $O(\beta^2)$ by incorporating the Reynolds stresses determined in Section 4 into the mean flow analysis.

4 Turbulence

Substituting (3.6) into (2.5) and neglecting the exponentially small terms results in

$$\begin{aligned} \frac{\partial u_1}{\partial r} + \frac{u_1}{r} + \frac{1}{r} \frac{\partial v_1}{\partial \psi} + \frac{\partial w_1}{\partial s} &= 0, \\ \frac{\partial u_1}{\partial t} + \frac{\partial u_1}{\partial s} - 2w_s \sin \psi H(s) &= -\frac{\partial p_1}{\partial r}, \\ \frac{\partial v_1}{\partial t} + \frac{\partial v_1}{\partial s} - 2w_s \cos \psi H(s) &= -\frac{1}{r} \frac{\partial p_1}{\partial \psi}, \\ \frac{\partial w_1}{\partial t} + \frac{\partial w_1}{\partial s} + [u_s \sin \psi + v_s \cos \psi] H(s) &= -\frac{\partial p_1}{\partial s}. \end{aligned} \quad (4.1)$$

If the turbulence scale "1" is small relative to the radius of the pipe, the turbulence structure in the core of the pipe is not influenced by the boundary conditions at the wall. It is convenient to use Cartesian coordinates to describe the solution for this limiting case (see Fig. 1). This is because the turbulence in the core of the pipe is homogeneous in x and y . Accordingly, we introduce stretched coordinates \bar{x} , \bar{y} , \bar{s} , \bar{t} defined by

$$\begin{aligned} r \sin \psi &= r_0 \sin \psi_0 + \epsilon \bar{x}, & r \cos \psi &= r_0 \cos \psi_0 - \epsilon \bar{y}, \\ s &= \epsilon \bar{s}, & t &= \epsilon \bar{t}, \end{aligned} \quad (4.2)$$

where $\epsilon = 1/a$ is a small parameter, and (r_0, ψ_0) is a reference point in the cross-sectional plane of the pipe. The corresponding Cartesian components of velocity are related to the toroidal components by

$$\begin{aligned} \bar{u} &= u \sin \psi + v \cos \psi, \\ \bar{v} &= -u \cos \psi + v \sin \psi, \\ \bar{w} &= w. \end{aligned} \quad (4.3)$$

We assume that the turbulence upstream of the bend is statistically stationary and homogeneous. Thus, it can be Fourier analyzed in the sense of generalized functions as

$$\begin{aligned} \bar{u}_{s,i}(\mathbf{r}, t) &= \int_{-\infty}^{\infty} S_i(\mathbf{K}) \exp[i(\epsilon^{-1}K_r r_0 + K_s \bar{s} \\ &\quad + K_2 \bar{y} + K_3 \bar{s} - K_3 \bar{t})] d\mathbf{K}, \end{aligned} \quad (4.4)$$

where $K_r = K_1 \sin \psi_0 - K_2 \cos \psi_0$, \mathbf{K} denotes (K_1, K_2, K_3) and K_i is a dimensionless wave number defined in terms of the dimensional wave number k_i as $K_i = 1/k_i$. Here, we have used the index notation (x_1, x_2, x_3) to denote (x, y, s) and $(u_{s,1}, u_{s,2}, u_{s,3})$ to denote $(\bar{u}_s, \bar{v}_s, \bar{w}_s)$.

Since the turbulence is stationary in time, the turbulence becomes *inhomogeneous* in the streamwise direction due to the sudden application of centrifugal force at $s = 0$. The local turbulence can be expressed in terms of the spectra of the upstream turbulence through transfer functions $Q_1(\bar{s}, \mathbf{K})$, $Q_2(\bar{s}, \mathbf{K})$, $Q_3(\bar{s}, \mathbf{K})$, $Q_p(\bar{s}, \mathbf{K})$, $M_1(\bar{s}, \mathbf{K})$, $M_2(\bar{s}, \mathbf{K})$, $M_3(\bar{s}, \mathbf{K})$ and $M_p(\bar{s}, \mathbf{K})$ as

$$\begin{aligned} \begin{Bmatrix} \bar{u}_1(\mathbf{r}, t) \\ \bar{v}_1(\mathbf{r}, t) \\ \bar{w}_1(\mathbf{r}, t) \\ \bar{p}_1(\mathbf{r}, t) \end{Bmatrix} &= \epsilon \int_{-\infty}^{\infty} \begin{Bmatrix} Q_1(\bar{s}, \mathbf{K}) \\ Q_2(\bar{s}, \mathbf{K}) \\ Q_3(\bar{s}, \mathbf{K}) \\ Q_p(\bar{s}, \mathbf{K}) \end{Bmatrix} S_3(\mathbf{K}) \\ &\times \exp[i(\epsilon^{-1}K_r r_0 + K_1 \bar{x} + K_2 \bar{y} - K_3 \bar{t})] d\mathbf{K} \\ &+ \epsilon \int_{-\infty}^{\infty} \begin{Bmatrix} M_1(\bar{s}, \mathbf{K}) \\ M_2(\bar{s}, \mathbf{K}) \\ M_3(\bar{s}, \mathbf{K}) \\ M_p(\bar{s}, \mathbf{K}) \end{Bmatrix} S_1(\mathbf{K}) \\ &\times \exp[i(\epsilon^{-1}K_r r_0 + K_1 \bar{x} + K_2 \bar{y} - K_3 \bar{t})] d\mathbf{K}. \end{aligned} \quad (4.5)$$

The transfer function for pressure, $Q_p(\bar{s}, \mathbf{K})$, is obtained by solving

$$(D^2 - K_{12}^2) Q_p = 2iK_1 \exp(iK_3 \bar{s}) H(\bar{s}) \quad (4.6)$$

where

$$K_{12} = [K_1^2 + K_2^2]^{1/2}, \quad \text{and} \quad D^2 Q_p = \frac{d^2 Q_p}{d\bar{s}^2}.$$

Equation (4.6) is derived by the standard procedure of taking the divergence of the momentum equation and using the continuity equation in (4.1). The pressure perturbation must vanish far upstream of the bend. Thus, Eq. (4.6) has to be solved subject to the boundary condition $\bar{s} \rightarrow -\infty, Q_p \rightarrow 0$. The solution of (4.6) which remains bounded as $\bar{s} \rightarrow \infty$, may be expressed as

$$\begin{aligned} Q_p(\bar{s}, \mathbf{K}) &= -\frac{2iK_1}{K^2} \exp(iK_3 \bar{s}) H(\bar{s}) \\ &+ \frac{K_1 [K_3 + iK_{12} \operatorname{sgn}(\bar{s})]}{K_{12} K^2} \exp(-K_{12} |\bar{s}|), \end{aligned} \quad (4.7)$$

where $K = [K_1^2 + K_2^2 + K_3^2]^{1/2}$. Equation (4.7) indicates that the sudden change in curvature of the pipe at $\bar{s} = 0$ has an upstream influence on the fluctuating pressure, which decays exponentially upstream of the bend. The region of upstream influence is longer for the larger eddies, and is negligible for the smaller eddies.

Once Q_p has been determined, the transfer functions for the fluctuating velocity components may be obtained by solving the momentum equations:

$$\begin{aligned} (D - iK_3) Q_1 &= -iK_1 Q_p + 2 \exp(iK_3 \bar{s}) H(\bar{s}), \\ (D - iK_3) Q_2 &= -iK_2 Q_p, \\ (D - iK_3) Q_3 &= -D Q_p. \end{aligned} \quad (4.8)$$

The associated boundary conditions are, as $\bar{s} \rightarrow -\infty$, $Q_1 \rightarrow 0$, $Q_2 \rightarrow 0$, $Q_3 \rightarrow 0$. The solution is given by

$$\begin{aligned} Q_1(\bar{s}, \mathbf{K}) &= \left[2 \left(1 - \frac{K_1^2}{K^2} \right) \bar{s} - \frac{4iK_1^2 K_3}{K^4} \right] \exp(iK_3 \bar{s}) H(\bar{s}) + \exp, \\ &= \left[2 \left(1 - \frac{K_1^2}{K^2} \right) \bar{s} - \frac{4iK_1^2 K_3}{K^4} \right] \exp(iK_3 \bar{s}) H(\bar{s}) + \exp, \end{aligned}$$

$$\begin{aligned} Q_2(\bar{s}, \mathbf{K}) &= - \left[\frac{2K_1 K_2}{K^2} \bar{s} + \frac{4iK_1 K_2 K_3}{K^4} \right] \exp(iK_3 \bar{s}) H(\bar{s}) + \exp, \\ Q_3(\bar{s}, \mathbf{K}) &= - \left[\frac{2K_1 K_3}{K^2} \bar{s} + \frac{2iK_1 (K_3^2 - K_{12}^2)}{K^4} \right] \\ &\times \exp(iK_3 \bar{s}) H(\bar{s}) + \exp. \end{aligned} \quad (4.9)$$

The transfer function, $M_p(\bar{s}, \mathbf{K})$, is obtained by solving

$$(D^2 - K_{12}^2) M_p = -iK_3 \exp(iK_3 \bar{s}) H(\bar{s}), \quad (4.10)$$

subject to the boundary conditions $\bar{s} \rightarrow -\infty, M_p \rightarrow 0$. The solution of (4.10) which remains bounded as $\bar{s} \rightarrow \infty$ is given by

$$\begin{aligned} M_p(\bar{s}, \mathbf{K}) &= \frac{iK_3}{K^2} \exp(iK_3 \bar{s}) H(\bar{s}) \\ &- \frac{K_3 [K_3 + iK_{12} \operatorname{sgn}(\bar{s})]}{2K_{12} K^2} \exp(-K_{12} |\bar{s}|). \end{aligned} \quad (4.11)$$

The transfer functions, $M_i(\bar{s}, \mathbf{K})$, are then determined by solving the momentum equations:

$$\begin{aligned} (D - iK_3) M_1 &= -iK_1 M_p, \\ (D - iK_3) M_2 &= -iK_2 M_p, \\ (D - iK_3) M_3 &= -D M_p - \exp(iK_3 \bar{s}) H(\bar{s}). \end{aligned} \quad (4.12)$$

The solution of Eqs. (4.12), subject to the boundary conditions $\bar{s} \rightarrow -\infty, M_i \rightarrow 0$, may be expressed as

$$\begin{aligned} M_1(\bar{s}, \mathbf{K}) &= \left[\frac{K_1 K_3}{K^2} \bar{s} + \frac{2iK_1 K_3^2}{K^4} \right] \exp(iK_3 \bar{s}) H(\bar{s}) + \exp, \\ M_2(\bar{s}, \mathbf{K}) &= \left[\frac{K_2 K_3}{K^2} \bar{s} + \frac{2iK_2 K_3^2}{K^4} \right] \exp(iK_3 \bar{s}) H(\bar{s}) + \exp, \\ M_3(\bar{s}, \mathbf{K}) &= \left[\left(\frac{K_3^2}{K^2} - 1 \right) \bar{s} + \frac{iK_3 (K_3^2 - K_{12}^2)}{K^4} \right] \\ &\times \exp(iK_3 \bar{s}) H(\bar{s}) + \exp. \end{aligned} \quad (4.13)$$

4.1 Velocity Correlations. The transfer functions (4.9) and (4.13) are used to calculate the correlations in terms of upstream spectrum

$$\phi_{s,ij}(\mathbf{K}) = \frac{1}{(2\pi)^3} \int_{-\infty}^{\infty} R_{s,ij}(\mathbf{x}, 0) \exp(-i\mathbf{K} \cdot \mathbf{x}) d\mathbf{x},$$

where $R_{s,ij}(\mathbf{x}, \tau) = \bar{u}_{s,i}(\mathbf{r}, t) \bar{u}_{s,j}(\mathbf{r} + \mathbf{x}, t + \tau)$ is the velocity correlation in the straight pipe. In the following, only one-point correlations without time delay will be presented. The correlations may be expanded as a perturbation series in α :

$$R_{ij} = R_{s,ij} + \alpha R_{1,ij} + \dots,$$

where

$$R_{1,ij} = \overline{\bar{u}_{s,i}(\mathbf{r}, t) \bar{u}_{1,j}(\mathbf{r}, t)} + \overline{\bar{u}_{1,i}(\mathbf{r}, t) \bar{u}_{s,j}(\mathbf{r}, t)}, \quad (4.14)$$

is the correction due to centrifugal forces. Substituting Eqs. (4.4) and (4.5) into Eq. (4.14), and using the orthogonality relation of the Fourier modes

$$\overline{S_i(\mathbf{K}) S_i^*(\mathbf{K}')} = \phi_{s,ij}(\mathbf{K}) \delta(\mathbf{K} - \mathbf{K}') \quad (4.15)$$

where δ is the delta function of Dirac and the asterisk denotes the complex conjugate results in

$$\begin{aligned}
R_{1,ij} = & e \int_{-\infty}^{\infty} [Q_j(\bar{s}, \mathbf{K}) \exp(-iK_3\bar{s}) f_{s,i3}(\mathbf{K}) \\
& + Q_i^*(\bar{s}, \mathbf{K}) \exp(iK_3\bar{s}) f_{s,ij}(\mathbf{K})] d\mathbf{K} \\
& + e \int_{-\infty}^{\infty} [M_j(\bar{s}, \mathbf{K}) \exp(-iK_3\bar{s}) f_{s,i1}(\mathbf{K}) \\
& + M_i^*(\bar{s}, \mathbf{K}) \exp(iK_3\bar{s}) f_{s,ij}(\mathbf{K})] d\mathbf{K}.
\end{aligned}$$

In order to simplify the calculations and elucidate the physics of the problem we now assume that the upstream turbulence is isotropic, so that

$$\phi_{s,ij}(\mathbf{K}) = \frac{E(K)}{4\pi K^4} (K^2 \delta_{ij} - K_i K_j), \quad (4.16)$$

(Batchelor 1953), where $E(K)$ is the dimensionless form of the energy spectrum function. The velocity correlations become

$$\begin{aligned}
R_{1,xx} = R_{1,yy} = R_{1,ss} = R_{1,xy} = R_{1,ys} = 0, \\
R_{1,xs} = \frac{7}{30} \alpha \epsilon \bar{s} H(\bar{s}).
\end{aligned} \quad (4.17)$$

Equations (4.17) indicate that at order α , the only effect of the centrifugal force is to generate turbulent shear stress in the x - s plane. Since the mean flow through the pipe remains unchanged, there is no mechanism to stretch or squeeze the fluid elements. Thus, the turbulent normal stresses in the x , y , and s directions do not change. The trace of the velocity correlation tensor, $R_{xx} + R_{yy} + R_{ss}$, represents the kinetic energy of the turbulent fluctuations. At order α , there is no mechanism to transfer energy to the turbulent fluctuating velocity field. Hence, the turbulent kinetic energy remains unchanged. Since there is no component of the centrifugal force acting in the y -direction, the turbulent shear stresses in the x - y and y - s planes are zero. Thus, under the influence of centrifugal force, the principal axes of Reynolds stresses become inclined at an angle of 45 deg to the x and s axes.

It may be noted that although Eq. (4.17) predicts no change in the intensity of the turbulent velocity fluctuations in the x , y , and s directions, in a real flow situation, the turbulence intensity decays due to the dissipation of turbulence kinetic energy, as observed in experiments on the effects of rotation on turbulent flows (Ibbetson and Tritton, 1975; Wigeland and Nagib, 1978). However, Townsend (1970, 1980) and Maxey (1982) have demonstrated that RDT can predict the ratio of the Reynolds stresses to the local turbulence kinetic energy fairly well even in cases where the turbulence is decaying. Thus, the range of applicability of the RDT predictions (4.17) can be increased by taking the ratio of the Reynolds stresses to the turbulence kinetic energy.

Equations (4.17) reveal that an initially isotropic turbulence becomes anisotropic due to the linear effects of centrifugal forces. It is worthwhile to note that in the closely related problem of solid-body rotation, an initially isotropic turbulence becomes anisotropic only through nonlinear interactions, and pure linear effects influence the double correlations only if the turbulence is initially anisotropic (Bardina et al., 1985; Cambon and Jacquin, 1989). As discussed in the Appendix, this difference between the effects of centrifugal forces due to streamline curvature, and the effects of Coriolis forces due to solid-body rotation is due to the difference in the mean flow, which plays an important role in the production of Reynolds stresses.

The diagonal components of the Reynolds stress tensor along the principal directions are given by

$$\begin{aligned}
R_{\xi\xi} = & \frac{1}{3} [1 + \frac{7}{10} \alpha \epsilon \bar{s} H(\bar{s})], \\
R_{\eta\eta} = & \frac{1}{3} [1 - \frac{7}{10} \alpha \epsilon \bar{s} H(\bar{s})],
\end{aligned} \quad (4.18)$$

where ξ and η are the principal axes of Reynolds stress on the x - s plane, inclined at angles of 45 deg and 135 deg, respectively,

to the x -axis, $R_{\xi\xi} = \bar{u}_\xi^2$, $R_{\eta\eta} = \bar{u}_\eta^2$, and u_ξ and u_η are the components of the turbulent velocity fluctuations in the ξ and η directions, respectively. Equation (4.18) indicates that under the influence of centrifugal forces, the intensity of fluctuations of the turbulent velocity components is increased in the ξ direction, and reduced in the η direction. Downstream of the bend, the Reynolds stresses $R_{\xi\xi}$ and $R_{\eta\eta}$ increase linearly due to the continuing distortion of the turbulence structure under the influence of centrifugal force. The linear growth of the effect of centrifugal forces in (4.18) is a consequence of ignoring the nonlinear energy transfer and dissipation in RDT. As discussed before, this limits the model for $\beta s \ll 1$. Further downstream beyond the validity range of the current model, the nonlinear process will restrict the linear growth; then, turbulence will reach a new *equilibrium* state. The true range of validity of the current results can not be determined without comparing with experimental data, which are not available at present. Equation (4.18) indicates that the perturbation series breaks down when $\alpha \epsilon \bar{s} = \alpha s$ becomes $O(1)$, that is, when s becomes $O(\alpha^{-1})$, or in other words, when the distance in the streamwise direction is of the order of the radius of curvature of the pipe. For a slightly curved pipe, $\alpha \ll 1$, which implies that $\alpha^{-1} \gg 1$. Thus, this condition is not too restrictive. Equation (4.18) also indicates that the dynamic effect of centrifugal forces is independent of the radius of the pipe and the size of the turbulent eddies. It is worth noting that the model in the second region of the pipe entrance is identical to the current analysis as discussed in the Introduction. Thus, the perturbation results are limited by much less restriction and can be applied as long as $s \ll 1/\alpha^{1.5}$.

4.2 Pressure-Strain-Rate Correlations. The pressure-strain-rate correlation

$$\sigma_{ij} = p(\mathbf{r}, t) \left[\frac{\partial \bar{u}_i}{\partial x_j}(\mathbf{r}, t) + \frac{\partial \bar{u}_j}{\partial x_i}(\mathbf{r}, t) \right] \quad (4.19a)$$

may be written as a perturbation series in α :

$$\sigma_{ij} = \alpha \sigma_{1,ij} + \dots, \quad (4.19b)$$

where

$$\sigma_{1,ij} = p_1(\mathbf{r}, t) \left[\frac{\partial \bar{u}_{s,i}}{\partial x_j}(\mathbf{r}, t) + \frac{\partial \bar{u}_{s,j}}{\partial x_i}(\mathbf{r}, t) \right] \quad (4.19c)$$

is obtained by substituting (4.4) and (4.5) into (4.19c) and using (4.15). This gives

$$\begin{aligned}
\sigma_{1,ij} = & -e \int_{-\infty}^{\infty} Q_p(\bar{s}, \mathbf{K}) \exp(-iK_3\bar{s}) [iK_j f_{s,i3}(\mathbf{K}) \\
& + iK_i f_{s,ij}(\mathbf{K})] d\mathbf{K} - e \int_{-\infty}^{\infty} M_p(\bar{s}, \mathbf{K}) \exp(-iK_3\bar{s}) \\
& \times [iK_j f_{s,i1}(\mathbf{K}) + iK_i f_{s,ij}(\mathbf{K})] d\mathbf{K}.
\end{aligned}$$

For an isotropic upstream turbulent velocity field, the pressure-strain-rate correlations are given by

$$\begin{aligned}
\sigma_{1,xx} = \sigma_{1,yy} = \sigma_{1,ss} = \sigma_{1,xy} = \sigma_{1,ys} = 0, \\
\sigma_{1,xs} = -\frac{1}{10} H(\bar{s}).
\end{aligned} \quad (4.20)$$

Equation (4.20) indicates that σ_{xs} tends to reduce the magnitude of R_{xs} induced by the action of centrifugal force.

The pressure-strain-rate correlations, which can hardly be measured at present, play an important role in models of turbulence in which the Reynolds stresses are determined from the solution of transport equations for these variables (Lauder, Reece, and Rodi 1975; Lauder, 1975; Gibson and Rodi, 1981). Lauder et al. (1975), Lauder (1975), and Gibson and Rodi (1981) have approximated the pressure-strain-rate correlation tensor, σ_{ij} , as

$$\sigma_{ij} = \sigma_{ij}^{(1)} + \sigma_{ij}^{(2)}, \quad (4.21a)$$

where

$$\sigma_{ij}^{(1)} = -C_1 \frac{\epsilon_d}{2q^2} \left(\overline{u_i u_j} - \frac{1}{3} \overline{q^2} \delta_{ij} \right), \quad (4.21b)$$

and

$$\sigma_{ij}^{(2)} = -C_2 (P_{ij} - \frac{2}{3} P \delta_{ij}). \quad (4.21c)$$

Here $\overline{q^2} = \overline{u_i u_i}$ represents (twice) the turbulence kinetic energy, ϵ_d is the rate of dissipation of turbulence kinetic energy, P_{ij} and P are the rate of production of Reynolds stress, $\overline{u_i u_j}$, and turbulence kinetic energy, $(\frac{1}{2})q^2$, respectively, and the coefficients C_1 and C_2 are taken as constants in high Reynolds number turbulence. The term $\sigma_{ij}^{(1)}$ represents the contribution of nonlinear turbulence interactions to the pressure strain-rate correlations and is due to Rotta (1951). It is based on the hypothesis that the rate of return of anisotropic turbulence to isotropy is proportional to the local level of anisotropy. The ratio $(\frac{1}{2})q^2/\epsilon_d$ in Eq. (4.21b) represents a characteristic decay time of the turbulence. The term $\sigma_{ij}^{(2)}$ represents the contribution to the pressure strain of the linear interactions of the turbulence field with the strain rate of the mean flow, and was first proposed by Naot, Shavit, and Wolfshtein (1970), as a replacement for Rotta's term. Launder et al. (1975) identified $\sigma_{ij}^{(2)}$ as the dominant term in a more general expression and combined it with $\sigma_{ij}^{(1)}$ to obtain good results for a number of simple free shear flows. Launder et al. (1975) considered only the interactions of the turbulence with mean shear. Launder (1975) extended the model to include the additional effect of buoyancy forces due to mean density stratification in a gravitational field. He suggested that in the presence of body forces, the rate of production of Reynolds stress, P_{ij} , should be taken to stand for the total production of $u_i u_j$ due to the combined effects of shear and body forces. For small-scale turbulence in the core of a curved pipe, these production terms are given by

$$\begin{aligned} P_{11} &= 4\alpha \overline{u_1 u_3} + 2\alpha \overline{u_1 u_3^2}, \\ P_{22} &= 0, \\ P_{33} &= -2\alpha \overline{u_1 u_3} - 2\alpha \overline{u_1 u_3^2}, \\ P_{13} &= 2\alpha \overline{u_3^2} - \alpha \overline{u_1^2} + \alpha (\overline{u_3^2} - \overline{u_1^2} \overline{u_3}), \\ P_{12} &= 2\alpha \overline{u_2 u_3} + \alpha \overline{u_2 u_3^2}, \\ P_{23} &= -\alpha \overline{u_1 u_2} - \alpha \overline{u_1 u_2 u_3}, \\ P &= \alpha \overline{u_1 u_3}, \end{aligned} \quad (4.22)$$

where variable curvature effects have been neglected.

In the limit of rapid distortion, the approximate estimates of the linear (rapid) part of the pressure strain-rate correlation, $\sigma_{ij}^{(2)}$, may be compared with the results calculated directly using rapid distortion theory. Such a comparison has been done by Maxey (1982) for turbulent shear flows. Using the values of $u_i u_j$ predicted by rapid distortion theory for an initially isotropic turbulence to evaluate the production terms in Eq. (4.22), the values of $\sigma_{ij}^{(2)}$ are found to be

$$\begin{aligned} \sigma_{xx}^{(2)} &= O(\alpha^2), \\ \sigma_{yy}^{(2)} &= O(\alpha^2), \\ \sigma_{zz}^{(2)} &= O(\alpha^2), \\ \sigma_{xy}^{(2)} &= O(\alpha^2), \\ \sigma_{yz}^{(2)} &= O(\alpha^2), \\ \sigma_{xz}^{(2)} &= -\alpha \frac{C_2}{3} + O(\alpha^2). \end{aligned} \quad (4.23)$$

A comparison of Eqs. (4.20) and (4.23) reveals that in the limit of rapid distortion, the pressure-strain-rate correlations predicted by the turbulence closure model of Launder et al. (1975) have the same form as those predicted directly from rapid distortion theory. In particular, if $C_2 = 0.3$, the value of $\sigma_{xx}^{(2)}$ is identical to the value of σ_{xx} predicted by RDT.

4.3 Integral Length Scales. The transfer functions (4.9) and (4.13) are used to calculate the integral length scales for the distorted turbulence. The integral length scales $L_{ij,l}$ defined by

$$L_{ij,l} = \frac{1}{\overline{u_i u_j}} \int_0^\infty \overline{\overline{u_i(x) u_j(x + r e_l)}} dr, \quad (4.24a)$$

where e_l is the unit vector of the x_l coordinate axis, may be expressed as a perturbation series in α :

$$L_{ij,l} = L_{ij,l}^{(s)} + \alpha L_{ij,l}^{(1)} + \dots, \quad (4.24b)$$

where

$$L_{ij,l}^{(s)} = \frac{1}{\overline{u_{s,i} u_{s,j}}} \int_0^\infty \overline{\overline{u_{s,i}(x) u_{s,j}(x + r e_l)}} dr \quad (4.24c)$$

is the integral length scale of the upstream turbulence in the straight pipe, and

$$\begin{aligned} L_{ij,l}^{(1)} &= \frac{1}{\overline{u_{s,i} u_{s,j}}} \left[\int_0^\infty \overline{\overline{u_{1,l}(x) u_{s,j}(x + r e_l)}} dr \right. \\ &\quad \left. + \int_0^\infty \overline{\overline{u_{1,l}(x) u_{s,j}(x + r e_l)}} dr - L_{ij,l}^{(s)} R_{1,ij} \right], \end{aligned} \quad (4.24d)$$

is the change in the integral length scale due to the effect of centrifugal forces.

For an initially isotropic turbulence, the integral length scales are given by

$$\begin{aligned} L_{11,1}^{(1)} &= L_{22,1}^{(1)} = L_{33,1}^{(1)} = L_{11,2}^{(1)} = L_{22,2}^{(1)} \\ &= L_{33,2}^{(1)} = L_{11,3}^{(1)} = L_{22,3}^{(1)} = L_{33,3}^{(1)} = 0. \end{aligned} \quad (4.25)$$

Equation (4.25) indicates that at order α there is no change in the integral length scales in the directions parallel to the x , y , and s -axes due to the effect of centrifugal forces. The major effect of centrifugal forces is to generate pure turbulent shear in the x - s plane; this does not affect the integral length scales in the x , y , and s directions. On the other hand, one would expect the length scales in the directions parallel to the principal axes of Reynolds stresses to change due to the distortion of the eddy structure induced by the turbulent shear stress generated by the effect of the centrifugal forces. In order to investigate this, we consider a coordinate system $(\tilde{x}_1, \tilde{x}_2, \tilde{x}_3)$ where the \tilde{x}_2 -axis coincides with the x_2 -axis, and the axes \tilde{x}_1 and \tilde{x}_3 are inclined at angles of 45 and 135 deg, respectively, to the x_1 -axis, and calculate the integral length scales $\tilde{L}_{ij,l}$ defined by

$$\tilde{L}_{ij,l} = \frac{1}{\tilde{u}_i \tilde{u}_j} \int_0^\infty \tilde{R}_{ij}(r \tilde{e}_l) dr, \quad (4.26)$$

where

$$\tilde{R}_{ij}(\mathbf{r}) = \overline{\tilde{u}_i(\mathbf{x}, t) \tilde{u}_j(\mathbf{x} + \mathbf{r}, t)},$$

\tilde{u}_i is the component of the turbulent velocity fluctuation in the \tilde{x}_i direction, and \tilde{e}_l is the unit vector in the \tilde{x}_l direction. For an initially isotropic turbulence, these length scales are given by

$$\begin{aligned} \tilde{L}_{11,1} &= l_1 [1 + \frac{3}{10} \alpha \epsilon \tilde{H}(\tilde{s}) + O(\alpha^2)], \\ \tilde{L}_{22,1} &= l_2 [1 - \frac{1}{4} \alpha \epsilon \tilde{H}(\tilde{s}) + O(\alpha^2)], \\ \tilde{L}_{33,1} &= l_2 [1 - \frac{1}{20} \alpha \epsilon \tilde{H}(\tilde{s}) + O(\alpha^2)], \end{aligned}$$

$$\begin{aligned}
\tilde{L}_{11,2} &= l_2[1 - \frac{1}{3}\alpha\epsilon\bar{s}H(\bar{s}) + O(\alpha^2)], \\
\tilde{L}_{22,2} &= l_1[1 + O(\alpha^2)], \\
\tilde{L}_{33,2} &= l_2[1 + \frac{1}{3}\alpha\epsilon\bar{s}H(\bar{s}) + O(\alpha^2)], \\
\tilde{L}_{11,3} &= l_2[1 + \frac{1}{20}\alpha\epsilon\bar{s}H(\bar{s}) + O(\alpha^2)], \\
\tilde{L}_{22,3} &= l_2[1 + \frac{1}{4}\alpha\epsilon\bar{s}H(\bar{s}) + O(\alpha^2)], \\
\tilde{L}_{33,3} &= l_1[1 - \frac{3}{10}\alpha\epsilon\bar{s}H(\bar{s}) + O(\alpha^2)], \quad (4.27)
\end{aligned}$$

where l_1 is the longitudinal integral length scale for isotropic turbulence, and $l_2 = (\frac{1}{2})l_1$ is the transverse integral length scale for isotropic turbulence. Equation (4.27) indicates that under the dynamic influence of centrifugal forces, the longitudinal integral scale, $\tilde{L}_{11,1}$, in the \tilde{x}_1 direction increases and the longitudinal integral length scale, $\tilde{L}_{33,3}$, in the \tilde{x}_3 direction decreases by an equal amount, while the longitudinal integral length scale, $\tilde{L}_{22,2}$, in the \tilde{x}_2 direction remains unchanged at order α . Thus, an initially spherical eddy becomes elongated in the \tilde{x}_1 direction and flattened in the \tilde{x}_3 direction under the effect of centrifugal forces as it passes round the bend. The transverse integral length scales $\tilde{L}_{22,1}$ and $\tilde{L}_{33,1}$ in the \tilde{x}_1 direction decrease due to an increase in the negative loop in the correlation spaces of $\tilde{R}_{22}(r, 0, 0)$ and $\tilde{R}_{33}(r, 0, 0)$. Similarly, the transverse integral length scales $\tilde{L}_{11,3}$ and $\tilde{L}_{22,3}$ in the \tilde{x}_3 direction increase due to a decrease in the negative loop in the correlation space of $\tilde{R}_{11}(0, 0, r)$ and $\tilde{R}_{22}(0, 0, r)$. In the \tilde{x}_2 direction, the transverse length scale $\tilde{L}_{11,2}$ decreases, while $\tilde{L}_{33,2}$ increases by an equal amount. These results show that the effect of centrifugal forces on the integral scales of the turbulence differs from that of Coriolis forces due to solid-body rotation. Coriolis forces due to solid-body rotation tend to increase the length scales in all directions, especially those along the axis of rotation (Ibbetson and Tritton, 1975; Wigeland and Nagib, 1978; Bardina et al., 1985). Centrifugal forces, on the other hand, do not change the longitudinal integral scale in the y -direction, which is the direction normal to the plane of curvature; the integral scales increase in the direction of one of the principal axes of Reynolds stress in the x - s plane, and decrease in the direction of the other principal axis.

4.4 One-Dimensional Spectra. The transfer functions (4.9) and (4.13) are used to calculate the one-dimensional spectrum

$$\Theta_{ij}(\bar{s}, K_3) = \frac{1}{2\pi} \int_{-\infty}^{\infty} \overline{\bar{u}_i(x, y, s, t) \bar{u}_j(x, y, s, t + \tau)} \times \exp(iK_3\tau) d\tau, \quad (4.28a)$$

which may be expressed as a perturbation series in α :

$$\Theta_{ij}(\bar{s}, K_3) = \Theta_{s,ij}(K_3) + \alpha\Theta_{1,ij}(\bar{s}, K_3) + \dots, \quad (4.28b)$$

where

$$\Theta_{s,ij}(K_3) = \frac{1}{2\pi} \int_{-\infty}^{\infty} \overline{\bar{u}_{s,i}(x, y, s, t) \bar{u}_{s,j}(x, y, s, t + \tau)} \times \exp(iK_3\tau) d\tau \quad (4.28c)$$

is the one-dimensional spectrum of the turbulence in the upstream straight pipe, and

$$\begin{aligned}
\Theta_{1,ij}(\bar{s}, K_3) &= \frac{1}{2\pi} \left[\int_{-\infty}^{\infty} \overline{\bar{u}_{s,i}(x, y, s, t) \bar{u}_{1,j}(x, y, s, t + \tau)} \right. \\
&\quad \times \exp(iK_3\tau) d\tau \\
&\quad \left. + \int_{-\infty}^{\infty} \overline{\bar{u}_{1,i}(x, y, s, t) \bar{u}_{s,j}(x, y, s, t + \tau)} \right. \\
&\quad \left. \times \exp(iK_3\tau) d\tau \right] \quad (4.28d)
\end{aligned}$$

is the change in the spectrum due to the effect of centrifugal forces.

For an initially isotropic turbulence, the changes in the one-dimensional spectrum are given by

$$\begin{aligned}
\Theta_{1,xx} &= \Theta_{1,yy} = \Theta_{1,ss} = \Theta_{1,xy} = \Theta_{1,ys} = 0, \\
\Theta_{1,xf} &= F(K_3)\bar{s}H(\bar{s}), \quad (4.29)
\end{aligned}$$

where

$$F(K_3) = \frac{1}{4} \int_0^{\infty} \frac{K_{12}^3}{(K_{12}^2 + K_3^2)^2} E(\sqrt{K_{12}^2 + K_3^2}) dK_{12}, \quad (4.30)$$

and $E(K)$ is the dimensionless form of the energy spectrum function defined in Eq. (4.16). Equation (4.29) indicates that at order α , the only effect of the centrifugal forces is to produce a change in the spectrum $\Theta_{xs}(K_3)$. This result may be contrasted with the measurements of one-dimensional spectra obtained by Ibbetson and Tritton (1975) in experiments on turbulence in a rotating fluid. Ibbetson and Tritton (1975) found that the normalized distribution of the energy spectra of the azimuthal (streamwise) and vertical velocity components changed with time. Equation (4.29), on the other hand, shows that centrifugal forces do not induce changes in the energy spectra of the velocity components in the x , y , and s directions.

In order to evaluate the integral (4.30), it is necessary to know the form of the energy spectrum function $E(K)$ over the whole wave number range. Here, $E(K)$ has been taken to have the commonly observed form

$$E(K) = \frac{55}{27\pi} \frac{g_2^{5/6} K^4}{(g_2 + K^2)^{17/6}}, \quad (4.31)$$

where $g_2 = 0.558$ (von Karman, 1948), which reduces to the Kolmogorov spectrum in the inertial subrange. Figure 2 shows the variation of $F(K_3)$ with K_3 for the spectrum (4.31). For small wave numbers, $F(K_3)$ is nearly constant. In the large wave number range, the curve has a slope of $-\frac{5}{3}$, as expected. It may be noted that the changes in the power spectral density of the fluctuations u_{ξ}^2 and u_{η}^2 of the turbulent velocity fluctuations in the directions of the principal axes of Reynolds stress ξ and η are given by

$$\begin{aligned}
\Theta_{1,\xi\xi} &= F(K_3)\bar{s}H(\bar{s}), \\
\Theta_{1,\eta\eta} &= -F(K_3)\bar{s}H(\bar{s}). \quad (4.32)
\end{aligned}$$

Thus, the spectrum $\Theta_{1,\xi\xi}$ increases, while $\Theta_{1,\eta\eta}$ decreases. Since the integral of the one-dimensional spectra $\Theta_{1,\xi\xi}$ and $\Theta_{1,\eta\eta}$ over the entire wave number range represent the change in the mean-square turbulent velocity fluctuations u_{ξ}^2 and u_{η}^2 , respectively, the result (4.32) is consistent with an increase in u_{ξ}^2 and a decrease in u_{η}^2 .

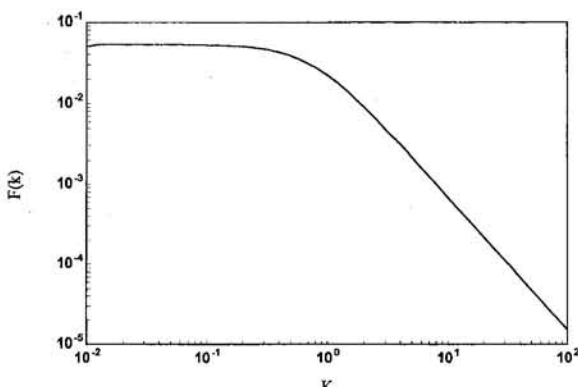


Fig. 2 Figure $F(K)$ versus K

5 Concluding Remarks

An asymptotic analysis of turbulent flows in the entry region of a curved pipe shows that the turbulent fluctuations can be described by the linearized Navier-Stokes equations if the convection time is much smaller than the turbulent turnover time. This condition coincides with the RDT assumption. The analysis neglects the small boundary layer displacement effect on the core flow near the entrance of a curved pipe and concentrates on the centrifugal force effects on the turbulence structure in the pipe core. Since the zeroth-order perturbation solutions are the turbulent flow in a straight pipe and are assumed known, the flow properties in the entry region of a curved pipe can be related to these solutions.

The pipe curvature influences the turbulence in two ways. One is contributed directly by the centrifugal forces and is of first-order magnitude. The other is due to the variation of curvature on the pipe cross section which ensures the geometric similarity of the flows. For small turbulent eddies or in slightly curved pipes, the variation of curvature is small and its effects can be neglected. The dynamic effect of the centrifugal forces is to generate a pure turbulent shear on the x - s and this effect is cumulative. Thus, the original isotropic turbulence becomes anisotropic due to linear effects. In this aspect, the effect of centrifugal forces on an initially isotropic turbulence in the core of the entry region of a curved pipe differs from the effect of Coriolis forces due to solid-body rotation. In the latter case, rotation acts on an initially isotropic turbulence only through nonlinear interactions, and pure linear effects influence the double correlations only if the turbulence is initially anisotropic.

For a flow path of variable radius of curvature, the superposition principle can be used to extend the current results. This is because that the transfer functions derived in Section 4 are governed by linear differential equations.

References

Bardina, J., Ferziger, J. H., and Rogallo, R. S., 1985, "Effects of Rotation on Isotropic Turbulence: Computation and Modelling," *Journal of Fluid Mechanics*, Vol. 154, pp. 321–336.

Batchelor, G. K., 1953, *The Theory of Homogeneous Turbulence*, Cambridge University Press, Cambridge, UK.

Batchelor, G. K., and Proudman, I., 1954, "The Effect of Rapid Distortion of a Fluid in Turbulent Motion," *Quarterly Journal for Mechanics and Applied Mathematics*, Vol. 1, pp. 83–103.

Berger, S. A., Talbot, L., and Yao, L. S., 1983, "Curved-Pipe Flows," *Annual Review of Fluid Mechanics*, Vol. 15, pp. 461–512.

Bertoglio, J. P., 1982, "Homogeneous Turbulence Field Within a Rotating Frame," *AIAA Journal*, Vol. 20, pp. 1175–1181.

Bradshaw, P., 1969, "The Analogy Between Streamline Curvature and Buoyancy in Turbulent Shear Flow," *Journal of Fluid Mechanics*, Vol. 36, pp. 177–191.

Cambon, C., and Jacquin, L., 1989, "Spectral Approach to Non-Isotropic Turbulence Subjected to Rotation," *Journal of Fluid Mechanics*, Vol. 202, pp. 295–317.

Castro, I. P., and Bradshaw, P., 1976, "The Turbulence Structure of a Highly Curved Mixing Layer," *Journal of Fluid Mechanics*, Vol. 73, pp. 265–304.

Dean, W. R., 1927, "Note on the Motion of Fluid in a Curved Pipe," *Philosophical Magazine*, Vol. 4, pp. 208–223.

Dean, W. R., 1928, "The Stream-Line Motion of Fluid in a Curved Pipe," *Philosophical Magazine*, Vol. 5, pp. 673–693.

Hoffmann, P. H., Muck, K. C., and Bradshaw, P., 1985, "The Effect of Concave Surface Curvature on Turbulent Boundary Layers," *Journal of Fluid Mechanics*, Vol. 161, pp. 371–403.

Hopfinger, E. J., Browand, F. K., and Gagne, Y., 1982, "Turbulence and Waves in a Rotating Tank," *Journal of Fluid Mechanics*, Vol. 125, pp. 505–534.

Hopfinger, E. J., and Linden, P. F., 1990, "The Effect of Background Rotation on Fluid Motions: A Report on Euromech 245," *Journal of Fluid Mechanics*, Vol. 211, pp. 417–435.

Hunt, J. C. R., 1973, "A Theory of Turbulent Flow Round Two-Dimensional Bluff Bodies," *Journal of Fluid Mechanics*, Vol. 61, pp. 625–706.

Hunt, J. C. R., Leibovich, S., and Richards, K. J., 1988, "Turbulent Shear Flows Over Low Hills," *Quarterly Journal of Royal Meteorological Society*, Vol. 114, pp. 1435–1470.

Ibbetson, A., and Tritton, D. J., 1975, "Experiments on Turbulence in a Rotating Fluid," *Journal of Fluid Mechanics*, Vol. 68, pp. 639–672.

Ito, H., 1960, "Pressure Losses in Smooth Pipe Bends," *Journal of Basic Engineering*, Vol. 82, pp. 131–143.

Lighthill, M. J., 1970, "Introduction to Fourier Analysis and Generalized Functions," Cambridge University Press, Cambridge, U.K.

Mansour, N. N., Cambon, C., and Speziale, C. G., 1991, "Single Point Modeling of Initially Isotropic Turbulence Under Uniform Rotation," *Annual Research Briefs*, Center for Turbulence Research, Stanford University/NASA Ames, pp. 159–167.

Maxey, M. R., 1982, "Distortion of Turbulence in Flows with Parallel Streamlines," *Journal of Fluid Mechanics*, Vol. 124, pp. 261–282.

Moffatt, H. K., 1981, "Some Developments in the Theory of Turbulence," *Journal of Fluid Mechanics*, Vol. 106, pp. 27–47.

Muck, K. C., Hoffmann, P. H., and Bradshaw, P., 1985, "The Effect of Convex Surface Curvature on Turbulent Boundary Layers," *Journal of Fluid Mechanics*, Vol. 161, pp. 347–369.

Olson, D. E., and Snyder, B., 1985, "The Upstream Scale of Flow Development in Curved Circular Pipes," *Journal of Fluid Mechanics*, Vol. 150, pp. 139–158.

Pedley, T. J., 1980, *The Fluid Mechanics of Large Blood Vessels*, Cambridge University Press, Cambridge, U.K., pp. 160–234.

Prandtl, L., 1932, "Herstellung einwandsfreier Luftströme (Windkanäle)," *Handbuch der Experimentalphysik* (Leipzig 1932), Vol. 4, Part 2, pp. 65–106.

Singh, M. P., 1974, "Entry Flow in a Curved Pipe," *Journal of Fluid Mechanics*, Vol. 87, pp. 517–539.

Speziale, C. G., Mansour, N. N., and Rogallo, R. S., 1987, "The Decay of Isotropic Turbulence in a Rapidly Rotating Frame," *Proceedings of the 1987 Summer Program of the Center for Turbulence Research*, Center for Turbulence Research, Stanford University/NASA Ames, pp. 205–211.

Sreenivasan, K. R., and Strykowski, P. J., 1983, "Stabilization Effects in Flow Through Helically Coiled Pipes," *Experiments in Fluids*, Vol. 1, pp. 31–36.

Taylor, G. I., 1929, "The Criterion for Turbulence in Curved Pipes," *Proceedings of Royal Society, London*, Vol. A124, pp. 243–249.

Taylor, G. I., 1935, "Turbulence in a Contracting Stream," *Zeitschrift für angewandte Mathematik*, Vol. 15, pp. 91–96.

Thomson, J., 1876, "On the Origin of Windings of Rivers in Alluvial Plains, with Remarks on the Flow of Water Round Bends in Pipes," *Proceedings of Royal Society, London*, Vol. A26, pp. 5–8.

Townsend, A. A., 1970, "Entrainment and the Structure of Turbulent Flow," *Journal of Fluid Mechanics*, Vol. 41, pp. 13–46.

Townsend, A. A., 1980, "The Response of Sheared Turbulence to Additional Distortion," *Journal of Fluid Mechanics*, Vol. 81, pp. 171–191.

Traugott, S. C., 1958, "Influence of Solid-Body Rotation on Screen-Produced Turbulence," *NACA Technical Note 4135*.

Von Karman, T., 1948, "Progress in the Statistical Theory of Turbulence," *Journal of Marine Research*, Vol. 7, pp. 252–264.

Wigeland, R. A., and Nagib, H. M., 1978, "Grid-Generated Turbulence With and Without Rotation About the Streamwise Direction," *IIT Fluids and Heat Transfer Rep. R78-1*, Illinois Institute of Technology, Chicago, Illinois.

Yao, L. S., and Berger, S. A., 1975, "Entry Flow in a Curved Pipe," *Journal of Fluid Mechanics*, Vol. 67, pp. 177–196.

Yao, L. S., and Berger, S. A., 1988, "The Three-Dimensional Boundary Layer in the Entry Region of Curved Pipes," *Physics of Fluids*, Vol. 31, pp. 486–494.

APPENDIX

In order to understand the difference between the effects of centrifugal forces due to streamline curvature and the effects of Coriolis forces due to rotation on homogeneous and isotropic turbulence from the standpoint of rapid distortion theory, it is instructive to consider the linearized equations for the turbulent velocity fluctuations in cylindrical polar coordinates. These equations, relative to a stationary frame of reference, are

$$\begin{aligned} \frac{\partial u_r}{\partial r} + \frac{u_r}{r} + \frac{1}{r} \frac{\partial u_\theta}{\partial \theta} + \frac{\partial u_z}{\partial z} &= 0, \\ \frac{\partial u_r}{\partial t} + \frac{U_\theta}{r} \frac{\partial u_r}{\partial \theta} - \frac{2U_\theta u_\theta}{r} &= -\frac{\partial p}{\partial r}, \\ \frac{\partial u_\theta}{\partial t} + \frac{U_\theta}{r} \frac{\partial u_\theta}{\partial \theta} + \left(\frac{U_\theta}{r} + \frac{\partial U_\theta}{\partial r} \right) u_r &= -\frac{1}{r} \frac{\partial p}{\partial \theta}, \\ \frac{\partial u_z}{\partial t} + \frac{U_\theta}{r} \frac{\partial u_z}{\partial \theta} &= -\frac{\partial p}{\partial z}, \end{aligned} \quad (A1)$$

where (r, θ, z) are coordinates in the radial, azimuthal, and axial directions, (u_r, u_θ, u_z) are the components of the turbulent velocity fluctuations in the r , θ and z directions, and the mean flow is given by $(0, U_\theta(r), 0)$, that is, the mean flow is in the azimuthal direction. The corresponding Reynolds stress equations are

$$\begin{aligned}
\overline{Du_r^2} &= -2u_r \overline{\frac{\partial p}{\partial r}} + P_{rr}, \\
\overline{Du_\theta^2} &= -2 \frac{u_\theta}{r} \overline{\frac{\partial p}{\partial \theta}} + P_{\theta\theta}, \\
\overline{Du_z^2} &= -2u_z \overline{\frac{\partial p}{\partial z}} + P_{zz}, \\
\overline{Du_r u_\theta} &= -\left(u_r \overline{\frac{\partial p}{\partial r}} + \frac{1}{r} u_r \overline{\frac{\partial p}{\partial \theta}} \right) + P_{r\theta}, \\
\overline{Du u} &= -u \overline{\frac{\partial p}{\partial r}} + u \overline{\frac{\partial p}{\partial z}} + P, \\
\overline{Du_\theta u_z} &= -\left(\frac{1}{r} u_z \overline{\frac{\partial p}{\partial \theta}} + u_\theta \overline{\frac{\partial p}{\partial z}} \right) + P_{\theta z}, \tag{A2}
\end{aligned}$$

where

$$\begin{aligned}
P_{rr} &= \frac{4U_\theta}{r} \overline{u_r u_\theta}, \\
P_{\theta\theta} &= -2 \left(\frac{U_\theta}{r} + \frac{\partial U_\theta}{\partial r} \right) \overline{u_r u_\theta}, \\
P_{zz} &= 0, \\
P_{r\theta} &= \frac{2U_\theta}{r} \overline{u_\theta^2} - \left(\frac{U_\theta}{r} + \frac{\partial U_\theta}{\partial r} \right) \overline{u_r^2}, \\
P_{rz} &= \frac{2U_\theta}{r} \overline{u_\theta u_z}, \\
P_{\theta z} &= -\left(\frac{U_\theta}{r} + \frac{\partial U_\theta}{\partial r} \right) \overline{u_r u_z}, \tag{A3}
\end{aligned}$$

represent the production of Reynolds stress, and D denotes differentiation with respect to time. We note that if the turbulence is isotropic, the production terms are given by

$$\begin{aligned}
P_{rr} &= P_{\theta\theta} = P_{zz} = P_{rz} = P_{\theta z} = 0, \\
P_{r\theta} &= \left(\frac{U_\theta}{r} - \frac{\partial U_\theta}{\partial r} \right) \frac{\overline{q^2}}{3}, \tag{A4}
\end{aligned}$$

where $\overline{q^2} = \overline{u_r^2} + \overline{u_\theta^2} + \overline{u_z^2}$ represents (twice) the turbulence kinetic energy.

If the mean flow is one of solid body rotation, then $U_\theta = r\Omega$, where Ω is the (constant) angular velocity, and the production term $P_{r\theta} = 0$. Thus, if the turbulence is initially isotropic, all the production terms in Eq. (A3) are zero at time $t = 0$. Furthermore, if the turbulence is isotropic, the pressure-strain-rate correlations are individually zero. Hence, all the terms on the right-hand side of Eq. (A2) are zero at time $t = 0$. Consequently, the Reynolds stresses do not change with time, that is, rapid distortion theory predicts that an initially isotropic turbulence will remain isotropic at all times, as there is no *linear* mechanism to produce anisotropy. This agrees with the direct numerical simulation by Speziale et al. (1987). This was noted by Bardina et al. (1985), who reached the same conclusion by considering the Reynolds stress equations in Cartesian coordinates relative to a rotating frame of reference.

On the other hand, if the mean flow is uniform, that is, if $U_\theta = C$, where C is a constant, as in the core of the entry region of a curved pipe with uniform inlet velocity conditions, the production term $P_{r\theta} = (C/r)(\overline{q^2}/3)$ is nonzero. Hence, the Reynolds stress $\overline{u_r u_\theta}$ will change with time, and the turbulence will become anisotropic due to *linear* effects.

It is worth noting that if the mean flow is irrotational, with constant circulation, that is, if $U_\theta = K/r$, where K is a constant, the production term $P_{r\theta}$ is given by $P_{r\theta} = (2K/r^2)(\overline{q^2}/3)$. In this case also, the Reynolds stress $\overline{u_r u_\theta}$ will change with time. However, since the production term $P_{r\theta}$ for a constant-circulation mean flow along a circular path is different from that for a uniform mean flow along a curved path, the magnitude of the Reynolds stress $\overline{u_r u_\theta}$ is different in the two cases.

The Freestream Matching Condition for Stagnation Point Turbulent Flows: An Alternative Formulation

R. Abid

Senior Scientist,
High Technology Corporation,
NASA Langley Research Center,
Hampton, VA 23681
Mem. ASME

C. G. Speziale

Professor,
Aerospace and Mechanical
Engineering Department,
Boston University,
Boston, MA 02215

The problem of plane stagnation point flow with freestream turbulence is examined from a basic theoretical standpoint. It is argued that the singularity which arises in the standard $K-\epsilon$ model results from the use of an inconsistent freestream boundary condition. The inconsistency lies in the implementation of a production-equals-dissipation equilibrium hypothesis in conjunction with a freestream mean velocity field that corresponds to homogeneous plane strain—a turbulent flow for which the standard $K-\epsilon$ model does not predict such a simple equilibrium. The ad hoc adjustment that has been made in the constants of the ϵ -transport equation to eliminate this singularity is shown to be inconsistent for homogeneous plane-strain turbulence as well as other benchmark turbulent flows. An alternative means to eliminate this singularity—without compromising model predictions in more basic turbulent flows—is proposed based on the incorporation of nonequilibrium vortex stretching effects in the turbulent dissipation rate equation.

1 Introduction

The calculation of stagnation point turbulent flows has a variety of important engineering applications in boiler tubes, gas turbines, and ramjet combustors. Most of the earlier analytical work on this subject (see Galloway (1973) and Gorla (1984)) was based on the use of algebraic eddy viscosity models that do not allow for the detailed calculation of the turbulence statistics which can play an important role in determining wall friction and heat-transfer coefficients. Consequently, more recent work on the subject has been based on the use of more sophisticated two-equation turbulence models of the $K-\epsilon$ type which have the advantage of allowing for the direct calculation of the turbulent kinetic energy and dissipation rate (see Strahle (1985) and Strahle, Sigman, and Meyer (1987)). Unfortunately, a problem with a singularity in the turbulent kinetic energy has arisen when the traditional dissipation rate transport equation of the $K-\epsilon$ model is applied to plane stagnation point turbulent flow. Strahle (1985) and Strahle, Sigman, and Meyer (1987) introduced an ad hoc modification of the constants in the ϵ -transport equation to eliminate the singularity. While this readjustment of constants did alleviate the problem, we find it to be rather unsettling since it yields an ϵ -transport equation which is incapable of collapsing most of the homogeneous turbulence data that is commonly used to benchmark turbulence models.

In this paper, it will be shown that the singularity in the turbulent kinetic energy that occurs when the standard $K-\epsilon$ model is applied to plane stagnation point flows arises from the use of an inconsistent freestream boundary condition. To be more specific, the commonly used formulation of plane stagnation point flow is ill-posed for the standard $K-\epsilon$ model since a production-equals-dissipation equilibrium hypothesis is im-

posed in the freestream in conjunction with a mean velocity field that corresponds to homogeneous plane strain—a turbulent flow for which this model does not possess such an equilibrium solution. In homogeneous plane-strain turbulence, the turbulent kinetic energy and dissipation rate obtained from the standard $K-\epsilon$ model grow exponentially with time. This is consistent with physical and numerical experiments on homogeneous plane-strain turbulence which indicate the same type of exponential growth (see Tucker and Reynolds (1968) and Lee and Reynolds (1985)). The ad hoc adjustment in the constants of the ϵ -transport equation which has been used to eliminate the singularity (Strahle (1985) and Strahle, Sigman, and Meyer (1987)) will be shown to be inconsistent for homogeneous turbulence since it erroneously predicts that plane-strain turbulence is stable with no exponential time growth of the turbulent kinetic energy. A more physically consistent means for eliminating the singularity in plane stagnation point flows—without yielding erroneous predictions for homogeneous turbulence or other benchmark turbulent flows—will be proposed based on the inclusion of nonequilibrium vortex stretching effects in the turbulent dissipation rate equation along the lines suggested by Bernard and Speziale (1992).

2 The Standard $K-\epsilon$ Model in Stagnation Point Flows

The problem to be considered is that of plane stagnation point flow with freestream turbulence as illustrated in Fig. 1. Outside of a boundary layer of thickness δ , the mean flow is assumed to be irrotational and incompressible with a background turbulence superimposed on it. This outer mean flow is taken to be of the form (see Strahle (1985) and Strahle, Sigman, and Meyer (1987))

$$\bar{u}_\infty = x, \quad \bar{v}_\infty = -y \quad (1)$$

where $\bar{\mathbf{v}}_\infty = \bar{u}_\infty \mathbf{i} + \bar{v}_\infty \mathbf{j}$ is the nondimensional mean velocity. The mean velocity ($\bar{\mathbf{v}} = \bar{u} \mathbf{i} + \bar{v} \mathbf{j}$) near the wall is a solution of the Reynolds-averaged continuity and Navier-Stokes equations which take the dimensionless form

Contributed by the Applied Mechanics Division of THE AMERICAN SOCIETY OF MECHANICAL ENGINEERS for publication in the ASME JOURNAL OF APPLIED MECHANICS.

Discussion on this paper should be addressed to the Technical Editor, Professor Lewis T. Wheeler, Department of Mechanical Engineering, University of Houston, Houston, TX 77204-4792, and will be accepted until four months after final publication of the paper itself in the ASME JOURNAL OF APPLIED MECHANICS.

Manuscript received by the ASME Applied Mechanics Division, June 30, 1994; final revision, Jan. 5, 1995. Associate Technical Editor: S. Lichter.

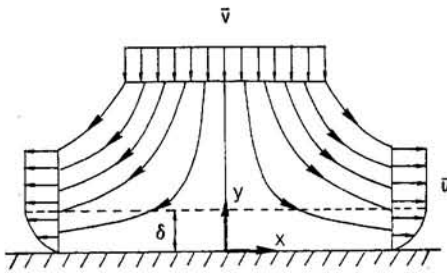


Fig. 1 Plane stagnation point flow

$$\frac{\partial \bar{u}}{\partial x} + \frac{\partial \bar{v}}{\partial y} = 0 \quad (2)$$

$$\bar{u} \frac{\partial \bar{u}}{\partial x} + \bar{v} \frac{\partial \bar{u}}{\partial y} = - \frac{\partial \bar{P}}{\partial x} + \frac{1}{Re} \nabla^2 \bar{u} + \frac{\partial \tau_{xx}}{\partial x} + \frac{\partial \tau_{xy}}{\partial y} \quad (3)$$

$$\bar{u} \frac{\partial \bar{v}}{\partial x} + \bar{v} \frac{\partial \bar{v}}{\partial y} = - \frac{\partial \bar{P}}{\partial y} + \frac{1}{Re} \nabla^2 \bar{v} + \frac{\partial \tau_{xy}}{\partial x} + \frac{\partial \tau_{yy}}{\partial y} \quad (4)$$

where \bar{P} is the mean pressure, Re is the Reynolds number, and τ_{ij} is the Reynolds stress tensor. For simplicity, since it will not alter the critical conclusions to be arrived at in this paper, we are considering the inner flow to be incompressible. The system of Eqs. (2)–(4) for the inner mean flow (\bar{u}, \bar{v}) are not closed and must be supplemented with a turbulence model. In the $K-\epsilon$ model, the Reynolds stress tensor is given by

$$\tau_{ij} = -\frac{2}{3}K\delta_{ij} + C_{\mu}f_{\mu} \frac{K^2}{\epsilon} \left(\frac{\partial \bar{v}_i}{\partial x_j} + \frac{\partial \bar{v}_j}{\partial x_i} \right) \quad (5)$$

where K is the turbulent kinetic energy, ϵ is the turbulent dissipation rate, C_{μ} is a dimensionless constant which is usually taken to be 0.09, and f_{μ} is a wall damping function that vanishes at the wall and approaches one sufficiently far from the wall. The turbulence quantities K and ϵ are determined from modeled versions of their transport equations which, for the Lam-Bremhorst (1981) model that was considered by Strahle and co-workers as well as for other near-wall models, take the general form

$$\bar{u} \frac{\partial K}{\partial x} + \bar{v} \frac{\partial K}{\partial y} = \frac{1}{Re} \nabla^2 K + \frac{\partial}{\partial x} \left(C_{\mu}f_{\mu} \frac{K^2}{\epsilon} \frac{\partial K}{\partial x} \right) + \frac{\partial}{\partial y} \left(C_{\mu}f_{\mu} \frac{K^2}{\epsilon} \frac{\partial K}{\partial y} \right) + \varphi - \epsilon \quad (6)$$

$$\bar{u} \frac{\partial \epsilon}{\partial x} + \bar{v} \frac{\partial \epsilon}{\partial y} = \frac{1}{Re} \nabla^2 \epsilon + \frac{\partial}{\partial x} \left(\frac{C_{\mu}f_{\mu} K^2}{\sigma_{\epsilon}} \frac{\partial \epsilon}{\partial x} \right) + \frac{\partial}{\partial y} \left(\frac{C_{\mu}f_{\mu} K^2}{\sigma_{\epsilon}} \frac{\partial \epsilon}{\partial y} \right) + C_{\epsilon 1}f_1 \frac{\epsilon}{K} \varphi - C_{\epsilon 2}f_2 \frac{\epsilon^2}{K} \quad (7)$$

where

$$\varphi = \tau_{ij} \frac{\partial \bar{v}_i}{\partial x_j} \quad (8)$$

is the turbulence production. In (6)–(7), σ_{ϵ} , $C_{\epsilon 1}$, and $C_{\epsilon 2}$ are dimensionless constants which typically assume the values of 1.3, 1.44, and 1.92, respectively; f_1 and f_2 are wall damping functions that vanish at the wall and approach unity sufficiently far from the wall (see Lam and Bremhorst (1981)). Sufficiently far from solid boundaries, at high Reynolds numbers where the molecular viscosity can be neglected, the modeled transport

equations (6)–(7) reduce to those of the standard $K-\epsilon$ model of Hanjalic and Launder (1972).

The equations of motion (2)–(7) for stagnation point turbulent flows are solved subject to the boundary conditions

$$\bar{u} = \bar{v} = K = \frac{\partial K}{\partial y} = 0, \quad \epsilon = \frac{1}{Re} \frac{\partial^2 K}{\partial y^2} \quad (9)$$

at the wall $y = 0$, along with the freestream boundary conditions (for $y \rightarrow \infty$)

$$\bar{u} = \bar{u}_{\infty}, \quad \bar{v} = \bar{v}_{\infty} \quad (10)$$

$$K_{\infty} = \frac{1}{2\sqrt{C_{\mu}}} \epsilon_{\infty}. \quad (11)$$

All of the boundary conditions except for (11) can be obtained as a rigorous consequence of the Navier-Stokes equations assuming that \bar{u} , \bar{v} , and K are Taylor expandable near the wall. Boundary condition (11) is obtained by a production-equals-dissipation hypothesis, i.e., by assuming that

$$\varphi = \epsilon \quad (12)$$

in the freestream based purely on an extrapolation of experimental observations for similar, although not identical, stagnation point turbulent flows (see Strahle (1985), Strahle, Sigman, and Meyer (1987), and Traci and Wilcox (1975)).

It will now be shown that the outer flow boundary condition (11) is inconsistent with the mean velocity field (1). This outer mean velocity has the following nonzero gradients:

$$\frac{\partial \bar{u}_{\infty}}{\partial x} = 1, \quad \frac{\partial \bar{v}_{\infty}}{\partial y} = -1 \quad (13)$$

and, hence, corresponds to the case of homogeneous plane-strain turbulence (see Tucker and Reynolds (1968) and Rogallo (1981)). It is now well established that homogeneous plane strain-turbulence is an unstable turbulent flow; the turbulent kinetic energy, dissipation rate, and length scales grow exponentially with time.¹

As an illustration, the time evolution of the turbulent kinetic energy (nondimensionalized by its initial value) taken from the direct numerical simulations of homogeneous plane-strain turbulence conducted by Lee and Reynolds (1985) is shown in Fig. 2. These results are suggestive of an exponential time growth of the turbulent kinetic energy which has been postulated based on alternative arguments (see Rogallo (1981)). The commonly used $K-\epsilon$ model (where $C_{\epsilon 1} = 1.44$ and $C_{\epsilon 2} = 1.92$) properly mimics this behavior as can be seen in Fig. 3. These computations, which were conducted using a fourth-order accurate Runge-Kutta numerical integration scheme, indicate that after an early decay (the turbulence was initially undergoing an isotropic decay), the turbulent kinetic energy then grows monotonically and becomes unbounded in the limit as $t \rightarrow \infty$. It can be shown analytically that the long-time growth of turbulent kinetic energy predicted by the traditional $K-\epsilon$ model is exponential (see Speziale and Mac Giolla Mhuiiris (1989)).

For general homogeneous plane-strain turbulence, with constant mean velocity gradients

$$\frac{\partial \bar{v}_i}{\partial x_j} = \begin{pmatrix} \Gamma & 0 \\ 0 & -\Gamma \end{pmatrix} \quad (14)$$

(where Γ is the strain rate), the standard $K-\epsilon$ model yields transport equations for K and ϵ that simplify to

¹ It is precisely this exponential growth of the length scales in numerical simulations of homogeneous plane strain turbulence that force a termination of such computations after relatively short elapsed times (see Rogallo 1981).

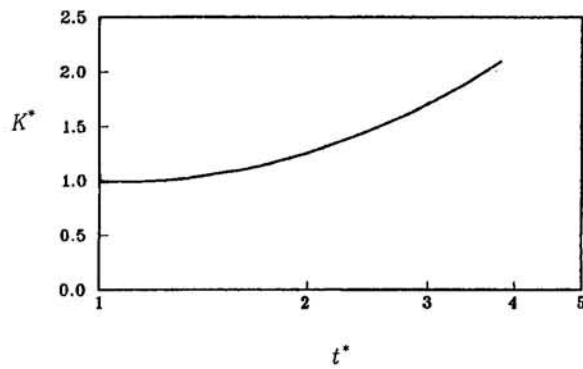


Fig. 2 Time evolution of the turbulent kinetic energy taken from the homogeneous plane-strain numerical experiments of Lee and Reynolds (1985) ($\Gamma K_0/\epsilon_0 = 10$)

$$\frac{dK}{dt} = 4C_\mu \frac{K^2}{\epsilon} \Gamma^2 - \epsilon \quad (15)$$

$$\frac{d\epsilon}{dt} = 4C_{\epsilon 1} C_\mu K \Gamma^2 - C_{\epsilon 2} \frac{\epsilon^2}{K}. \quad (16)$$

These equations can be manipulated into the alternative dimensionless form

$$\frac{dK^*}{dt^*} = \left(4C_\mu \frac{\Gamma K}{\epsilon} - \frac{\epsilon}{\Gamma K} \right) K^* \quad (17)$$

$$\frac{d}{dt^*} \left(\frac{\epsilon}{\Gamma K} \right) = 4C_\mu (C_{\epsilon 1} - 1) - (C_{\epsilon 2} - 1) \left(\frac{\epsilon}{\Gamma K} \right)^2 \quad (18)$$

where $t^* = \Gamma t$, $K^* = K/K_0$, and

$$\epsilon^* \equiv \frac{\epsilon}{\epsilon_0} = \left(\frac{\epsilon}{\Gamma K} \right) \left(\frac{\Gamma K_0}{\epsilon_0} \right) K^* \quad (19)$$

given that $(\cdot)_0$ denotes the initial value. Equation (18) has an equilibrium solution of the form

$$\left(\frac{\Gamma K}{\epsilon} \right)_0 = \frac{1}{2} \left(\frac{\alpha}{C_\mu} \right)^{1/2} \quad (20)$$

(in the limit as $t^* \rightarrow \infty$) where

$$\alpha = \frac{C_{\epsilon 2} - 1}{C_{\epsilon 1} - 1} \quad (21)$$

which is approximately two for the standard $K-\epsilon$ model.² Then, from Eqs. (17) and (19), it follows that for $t^* \gg 1$ we have

$$K^* \sim \exp \left[2 \sqrt{\frac{C_\mu}{\alpha}} (\alpha - 1) t^* \right] \quad (22)$$

$$\epsilon^* \sim \exp \left[2 \sqrt{\frac{C_\mu}{\alpha}} (\alpha - 1) t^* \right]. \quad (23)$$

It is therefore clear that the traditional $K-\epsilon$ model predicts an exponential time growth of the turbulent kinetic energy and dissipation rate where a structural equilibrium is reached with respect to their ratio—the turbulent time scale K/ϵ (in fact, $\Gamma K/\epsilon$ has a universal equilibrium value in the limit as $t \rightarrow \infty$).

² It is a simple matter to show that α is the equilibrium value of the ratio of production to dissipation and that the fixed point (20) is a stable node of the $K-\epsilon$ model (Speziale and Mac Giolla Mhuiris (1989)).

that is completely independent of the strain rate Γ as well as the initial conditions K_0 and ϵ_0 .

As shown above, the standard $K-\epsilon$ model (where $\alpha > 1$) predicts an exponential time growth of the turbulent kinetic energy and dissipation rate for plane strain turbulence which appears to be consistent with physical and numerical experiments. On the other hand, if we take $C_{\epsilon 1} = C_{\epsilon 2}$ as suggested by Strahle (1985) and Strahle, Sigman, and Meyer (1987), the $K-\epsilon$ model erroneously predicts a stable flow (with $\mathcal{P} = \epsilon$) where both K and ϵ approach a *finite asymptote* within a few eddy turnover times. This solution is of the form

$$K_\infty = \frac{1}{2\sqrt{C_\mu}} \epsilon_\infty \quad (24)$$

where ϵ_∞ is bounded and is determined by the initial conditions and the strain rate (it can be shown that $\epsilon_\infty/\epsilon_0 = (2\sqrt{C_\mu}\Gamma K_0/\epsilon_0)^\beta$ where $\beta = C_{\epsilon 1}/(C_{\epsilon 1} - 1)$). It is clear that if Eq. (24) is nondimensionalized it becomes identical to Eq. (11).

Now, we will return to the problem of stagnation point flow. By a Galilean transformation

$$y = U_0 t \quad (25)$$

(where U_0 is the characteristic mean velocity), the temporally evolving version of homogeneous plane-strain turbulence can be converted to a spatially evolving problem (in the coordinate y) governed by the equations

$$U_0 \frac{dK}{dy} = 4C_\mu \frac{K^2 \Gamma^2}{\epsilon} - \epsilon \quad (26)$$

$$U_0 \frac{d\epsilon}{dy} = 4C_{\epsilon 1} C_\mu K \Gamma^2 - C_{\epsilon 2} \frac{\epsilon^2}{K}. \quad (27)$$

This spatially evolving version of the problem (which is actually the way that the physical experiments are conducted; see Tucker and Reynolds 1968) has the *same* solution as the temporally evolving version if we set

$$t^* = \frac{y\Gamma}{U_0}. \quad (28)$$

As before, the standard $K-\epsilon$ model predicts an exponential growth of K and ϵ in y which properly mimics the experiments; the modified $K-\epsilon$ model where $C_{\epsilon 1} = C_{\epsilon 2}$ erroneously predicts a stable flow with $\mathcal{P} = \epsilon$ where K and ϵ approach *finite* asymptotes as $y \rightarrow \infty$ (see Fig. 4). These results have a direct bearing on the stagnation point flow problem. The boundary conditions (10)–(11) must be matched in the limit as $y \rightarrow \infty$. This is usually accomplished by marching in the y -direction from the wall starting at $y = 0$ (see Fig. 1). However, as can be seen from the previous analogy, if we march in the y direction from the wall with velocity U_0 , the standard $K-\epsilon$ model predicts an

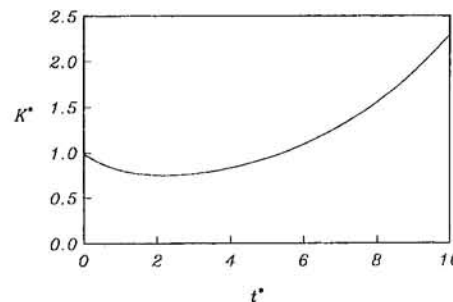


Fig. 3 Time evolution of the turbulent kinetic energy for homogeneous plane strain predicted by the standard $K-\epsilon$ model ($\Gamma K_0/\epsilon_0 = 1$)

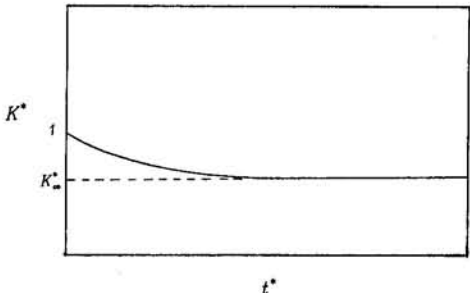


Fig. 4(a) $\Gamma K_0 / \epsilon_0 < \frac{1}{2} \sqrt{C_\mu}$

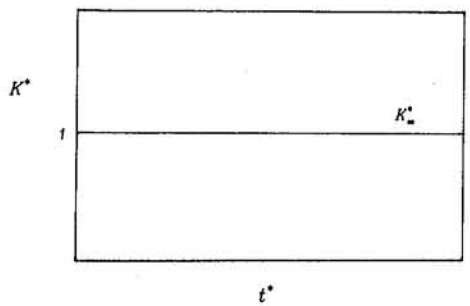


Fig. 4(b) $\Gamma K_0 / \epsilon_0 = \frac{1}{2} \sqrt{C_\mu}$

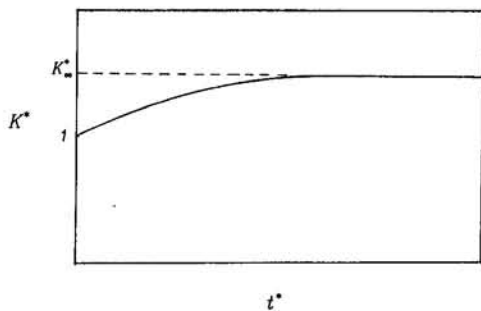


Fig. 4(c) $\Gamma K_0 / \epsilon_0 > \frac{1}{2} \sqrt{C_\mu}$

Fig. 4 Time evolution of the turbulent kinetic energy predicted by the modified $K-\epsilon$ model (where $C_{\epsilon 1} = C_{\epsilon 2}$) for homogeneous plane strain

exponential growth in the turbulent kinetic energy and dissipation rate:

$$K^* \sim \exp \left[2 \sqrt{\frac{C_\mu}{\alpha}} (\alpha - 1) \frac{y\Gamma}{U_0} \right] \quad (29)$$

$$\epsilon^* \sim \exp \left[2 \sqrt{\frac{C_\mu}{\alpha}} (\alpha - 1) \frac{y\Gamma}{U_0} \right] \quad (30)$$

for $y\Gamma/U_0 \gg 1$. If a freestream boundary condition is used where K_∞ and ϵ_∞ are bounded, an ill-posed problem results.

Although the singularity in the plane stagnation point flow problem can be eliminated by setting $C_{\epsilon 1} = C_{\epsilon 2}$, it is highly undesirable to do so since this results in a miscalibration of the $K-\epsilon$ model for homogeneous turbulence to the point where qualitatively incorrect results are predicted. Furthermore, this recalibration yields a reduction of α from approximately two to one which substantially degrades the predictions of the $K-\epsilon$ model for inhomogeneous benchmark turbulent flows such as free jets and the backstep problem (see Thangam (1991), Younis, Gatski, and Speziale, 1994). Consequently, the specific

quantitative results obtained from this alternatively calibrated $K-\epsilon$ model for stagnation point flows are likely to be questionable. Rather than rendering the problem well posed by an inconsistent recalibration of the model, it would appear to be preferable to consider an alternative formulation of the problem that is not intrinsically ill-posed. Such an alternative formulation would require an outer flow with a mean velocity field that is compatible with a bounded turbulent kinetic energy and dissipation rate that are statistically steady. One such example would be stagnation point flow that arises about a semi-infinite Rankine solid (see Fig. 5). For this problem, the outer mean velocity is obtained by the superposition of a uniform stream with a source located at point P (a velocity field that can be written in closed form). It is a simple matter to show that in the limit as $r \rightarrow \infty$

$$\bar{U}_\infty = U_\infty, \quad \bar{v}_\infty = 0 \quad (31)$$

for this flow. The mean velocity (31) has no spatial gradients, and hence no source for turbulence production; consequently, any background turbulence will decay yielding equilibrium values of

$$K_\infty = 0, \quad \epsilon_\infty = 0 \quad (32)$$

in the limit as $r \rightarrow \infty$. In addition, within the turbulent boundary layer there will be a region where production is approximately balanced by dissipation (the logarithmic region), so that (11) would be an appropriate boundary condition therein. No problems with singularities would arise with this alternative formulation of stagnation point flow that is more realistic from an aerodynamic standpoint.

3 An Alternative $K-\epsilon$ Model With Vortex Stretching

While the ill-posedness of the stagnation point flow problem can be overcome by considering more realistic aerodynamic configurations, it would nonetheless be useful to have the ability to compute idealized cases such as plane stagnation point flow with freestream turbulence. This would be worthwhile if a more physically consistent means were used to remove the singularity. One possible approach is to incorporate the effect of non-equilibrium vortex stretching in the dissipation rate transport equation, consistent with the theory of self-preservation (see Bernard and Speziale (1992) and Speziale and Abid (1993)). When this nonequilibrium vortex stretching effect is incorporated, a production-equals-dissipation equilibrium is obtained for plane-strain turbulence in the limit as $t \rightarrow \infty$; a feature that removes the singularity in the plane stagnation point flow problem since a bounded turbulent kinetic energy and dissipation rate are predicted.

For homogeneous plane strain turbulence, the dissipation rate equation with this nonequilibrium vortex stretching effect is given by (see Bernard and Speziale, 1992)

$$\frac{d\epsilon}{dt} = 4C_{\epsilon 1}C_\mu K\Gamma^2 + C_{\epsilon 3}R_i^{1/2} \frac{\epsilon^2}{K} - C_{\epsilon 2} \frac{\epsilon^2}{K} \quad (33)$$

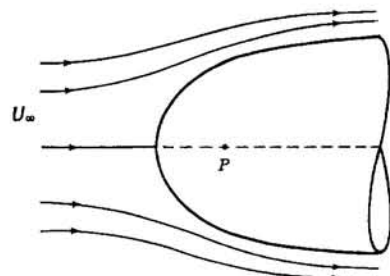


Fig. 5 Stagnation point flow for a semi-infinite Rankine solid

where $R_t \equiv K^2/\nu\epsilon$ is the turbulence Reynolds number and $C_{\epsilon 3}$ is a constant. The term containing $C_{\epsilon 3}$ arises when there is an imbalance between the production of dissipation by vortex stretching and the destruction of dissipation by viscous diffusion. When (33) is combined with (15), we obtain the transport equation

$$\frac{d}{dt^*} \left(\frac{\epsilon}{\Gamma K} \right) = 4C_\mu(C_{\epsilon 1} - 1) + C_{\epsilon 3} R_t^{1/2} \left(\frac{\epsilon}{\Gamma K} \right)^2 - (C_{\epsilon 2} - 1) \left(\frac{\epsilon}{\Gamma K} \right)^2 \quad (34)$$

from which the fixed point can be obtained.

Equations (15) and (33) were solved by using a Runge-Kutta numerical integration scheme. The initial conditions, which correspond to an isotropic turbulence, are taken to be $\Gamma K_0/\epsilon_0 = 1$ and $R_{t0} = 100$. Figures 6 and 7 show the time evolution of K^* and ϵ^* for a range of different values of $C_{\epsilon 3}$. The inclusion of vortex stretching has little effect on the short-time solution, but has a dramatic effect on the long-time behavior of K^* and ϵ^* . In fact, an equilibrium state is reached where the turbulent kinetic energy and dissipation rate saturate to bounded equilibrium values after a significant period of exponential growth. The saturation values are obtained by setting the right-hand sides of (17) and (34) to zero:

$$\frac{K_\infty}{K_0} = \frac{2\sqrt{C_\mu}}{R_{t0}} \left(\frac{C_{\epsilon 2} - C_{\epsilon 1}}{C_{\epsilon 3}} \right)^2 \left(\frac{\Gamma K_0}{\epsilon_0} \right) \quad (35)$$

$$\frac{\epsilon_\infty}{\epsilon_0} = \frac{4C_\mu}{R_{t0}} \left(\frac{C_{\epsilon 2} - C_{\epsilon 1}}{C_{\epsilon 3}} \right)^2 \left(\frac{\Gamma K_0}{\epsilon_0} \right)^2. \quad (36)$$

The relations (35) and (36) indicate that the value of $C_{\epsilon 3}$ determines the saturation level of K and ϵ .

Using (35) and (36), the following equilibrium values are obtained:

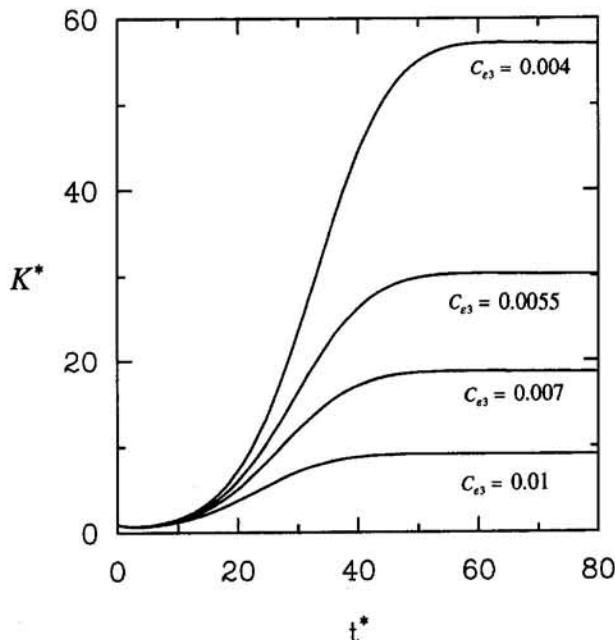


Fig. 6 Time evolution of the turbulent kinetic energy for homogeneous plane strain predicted by the $K-\epsilon$ model with vortex stretching ($\Gamma K_0/\epsilon_0 = 1$)

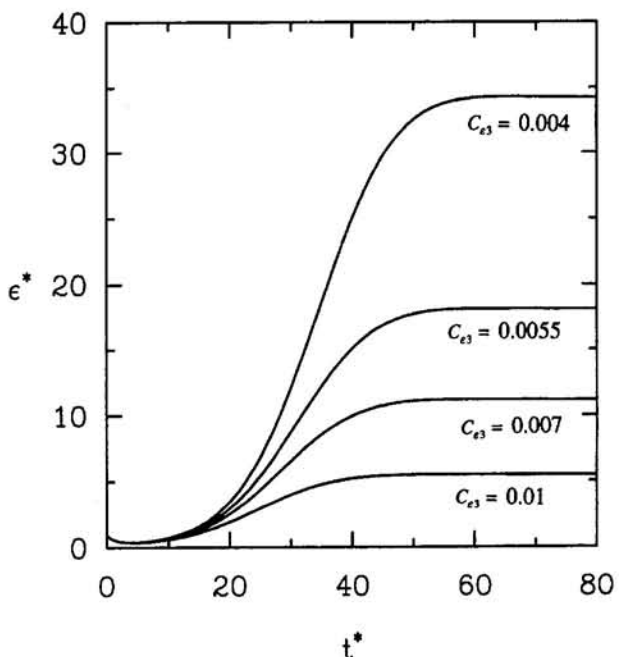


Fig. 7 Time evolution of the dissipation rate for homogeneous plane strain predicted by the $K-\epsilon$ model with vortex stretching ($\Gamma K_0/\epsilon_0 = 1$)

$$\left(\frac{\Gamma K}{\epsilon} \right)_\infty = \frac{1}{2\sqrt{C_\mu}} \quad (37)$$

$$\left(\frac{p}{\epsilon} \right)_\infty = 1 \quad (38)$$

$$R_{pe} = \left(\frac{C_{\epsilon 2} - C_{\epsilon 1}}{C_{\epsilon 3}} \right)^2. \quad (39)$$

These results demonstrate that a $K-\epsilon$ model with vortex stretching predicts an equilibrium state where production is equal to dissipation. Therefore, the singularity in the $K-\epsilon$ model for stagnation point flow would be eliminated by this modification. However, unlike the ad hoc change in the constants discussed above, this modification yields results that are completely consistent with physical and numerical experiments on homogeneous plane strain turbulence. K and ϵ grow exponentially until $\Gamma t = 30$ —an elapsed time that is far larger than any that have been considered in previous experiments. As discussed by Bernard and Speziale (1992), it remains an open question as to whether homogeneously strained turbulent flows ultimately saturate to a production-equals-dissipation equilibrium. The only thing that is beyond question is that they are unstable flows—where there is an exponential time growth of K and ϵ —for, at least, several eddy turnover times.

4 Concluding Remarks

It has been demonstrated in this paper that the problem of turbulent plane stagnation point flow, as it is usually formulated with two-equation models, constitutes an ill-posed problem. This ill-posed formulation arises since the outer mean flow corresponds to a homogeneous plane-strain turbulence for which the standard $K-\epsilon$ model predicts a turbulent kinetic energy and dissipation rate that grow exponentially with time. This precludes the application of a production-equals-dissipation equilibrium boundary condition in the freestream and renders the problem singular.

There is no doubt that the singularity in the standard $K-\epsilon$ model for plane stagnation point flow can be eliminated by setting $C_{\epsilon 1} = C_{\epsilon 2}$ in the dissipation rate transport equation as suggested by Strahle (1985) and Strahle, Sigman, and Meyer (1987). However, in the opinion of the authors, it is highly undesirable to do this since the recalibrated model yields completely incorrect results for most homogeneous and some inhomogeneous turbulent flows (e.g., the erroneous prediction that plane strain and plane shear flow turbulence are stable, in contradiction of the results of physical and numerical experiments, and the degradation of results for free jets as well as the backstep problem). An alternative formulation of the stagnation point flow problem based on a semi-infinite Rankine solid was discussed which is well posed for the standard $K-\epsilon$ model (i.e., no singularities would arise from the implementation of boundary conditions). Of course, other alternative formulations of turbulent stagnation point flows exist which are also well posed for two-equation models (for example, flow past a circular cylinder or the three-layer model of Traci and Wilcox (1975) for plane stagnation point flow). It is true that while these alternative formulations involve more realistic aerodynamic configurations, they are not quite as easy to compute since a similarity solution may not exist. Hence, an alternative means to remove the singularity in plane stagnation point flow was proposed based on a modification of the dissipation rate transport equation that includes nonequilibrium vortex stretching. Unlike the modified dissipation rate equation where $C_{\epsilon 1} = C_{\epsilon 2}$, this alternative proposal yields results that are not in contradiction of any existing results from physical and numerical experiments on homogeneous turbulence. If we are to obtain more reliable predictions of turbulent stagnation point flows, we must avoid making ad hoc adjustments in the constants of turbulence models which render incorrect predictions for basic benchmark turbulent flows.

Computations of plane stagnation point flow using the vortex stretching modification proposed herein were not presented since they are beyond the scope of the present paper for a variety of reasons. There are serious questions in regard to the near wall modeling that must first be addressed; this constitutes a nontrivial issue that can have a profound effect on the solution of wall bounded turbulent flows such as the plane stagnation point flow problem. Furthermore, state-of-the-art two-equation models should be used that have a more physically based representation for the Reynolds stress tensor than the isotropic eddy viscosity model that forms the basis for the standard $K-\epsilon$ model (the shortcomings of the standard $K-\epsilon$ model are well known in this regard; cf. Speziale 1991). Such models have an anisotropic eddy viscosity with strain-dependent coefficients that are sys-

tematically derived from a full second-order closure (see Gatski and Speziale, 1993). A computational study of the plane stagnation point flow problem that properly accounts for these important physical effects will form the basis of a future paper.

Acknowledgments

The first author (R.A.) would like to acknowledge the support of the National Aeronautics and Space Administration under NASA Contract NAS1-19299. CGS acknowledges the support of the Office of Naval Research through ARI Grant No. N00014-94-1-0088 on Nonequilibrium Turbulence (Dr. L. P. Purtell, Program Officer).

References

- Bernard, P. S., and Speziale, C. G., 1992, "Bounded Energy States in Homogeneous Turbulent Shear Flow—An Alternative View," *ASME Journal of Fluids Engineering*, Vol. 114, pp. 29–39.
- Galloway, T. R., 1973, "Enhancement of Stagnation Flow Heat and Mass Transfer through Interactions of Free Stream Turbulence," *A.I.Ch.E. Journal*, Vol. 19, pp. 608–617.
- Gatski, T. B., and Speziale, C. G., 1993, "On Explicit Algebraic Stress Models for Complex Turbulent Flows," *Journal of Fluid Mechanics*, Vol. 254, pp. 59–78.
- Gorla, S. R., 1984, "Effects of Unsteady Free Stream Velocity and Free Stream Turbulence on Stagnation Point Heat Transfer," *NASA CR-3804*.
- Hanjalic, K., and Launder, B. E., 1972, "A Reynolds Stress Model and its Application to Thin Shear Flows," *Journal of Fluid Mechanics*, Vol. 61, pp. 609–638.
- Lam, C. K. G., and Bremhorst, K., 1981, "A Modified Form of the $K-\epsilon$ Model for Predicting Wall Turbulence," *ASME Journal of Fluids Engineering*, Vol. 103, pp. 456–460.
- Lee, M. J., and Reynolds, W. C., 1985, "Numerical Experiments on the Structure of Homogeneous Turbulence," *Stanford University Technical Report TF-24*.
- Rogallo, R. S., 1981, "Numerical Experiments in Homogeneous Turbulence," *NASA TM 81315*.
- Speziale, C. G., 1991, "Analytical Methods for the Development of Reynolds Stress Closures in Turbulence," *Annual Review of Fluid Mechanics*, Vol. 23, pp. 107–157.
- Speziale, C. G., and Abid, R., 1993, "Reynolds Stress Calculations of Homogeneous Turbulent Shear Flow with Bounded Energy States," *International Journal of Non-Linear Mechanics*, Vol. 28, pp. 373–378.
- Speziale, C. G., and Mac Giolla Mhuiris N., 1989, "On the Prediction of Equilibrium States in Homogeneous Turbulence," *Journal of Fluid Mechanics*, Vol. 209, pp. 591–615.
- Strahle, W. C., 1985, "Stagnation Point Turbulent Flows with Freestream Turbulence—The Matching Condition," *AIAA Journal*, Vol. 23, pp. 1822–1824.
- Strahle, W. C., Sigman, R. K., and Meyer, W. L., 1987, "Stagnating Turbulent Flows," *AIAA Journal*, Vol. 25, pp. 1071–1077.
- Thangam, S., 1991, "Analysis of Two-Equation Turbulence Models for Recirculating Flows," *ICASE Report No. 91-61*, NASA Langley Research Center.
- Traci, R. M., and Wilcox, D. C., 1975, "Freestream Turbulence Effects on Stagnation Point Heat Transfer," *AIAA Journal*, Vol. 13, pp. 890–896.
- Tucker, H. J., and Reynolds, A. J., 1968, "The Distortion of Turbulence by Irrotational Plane Strain," *Journal of Fluid Mechanics*, Vol. 32, pp. 657–673.
- Younis, B. A., Gatski, T. B., and Speziale, C. G., 1994, "On the Prediction of Free Turbulent Jets with Swirl Using a Quadratic Pressure-Strain Model," *ICASE Report No. 94-70*, NASA Langley Research Center.

Wen Zhang

Professor,
Mem. ASME

Jiong Tang

Lecturer.

Mingde Tao

Associate Professor.

Department of Applied Mechanics,
Fudan University,
Shanghai 200433, P.R. China

Dynamic Stability of a Rotor Filled or Partially Filled With Liquid¹

The dynamic stability of a high-spinning liquid-filled rotor with both internal and external damping effects involved in is investigated in this paper. First, in the case of the rotor subjected to a transverse harmonic motion, the dynamic pressure of the liquid acting on the rotor is extracted through a planar flow analysis. Then the equation of perturbed motion for the liquid-filled rotor is derived. The analytical stability criteria as well as the stability boundaries are given. The results are extensions of those given by previous literature.

Introduction

In engineering, for various reasons liquid is often enclosed in rotors such as fluid-filled centrifuges, fluid-cooled turbines, and spin-stabilized satellites. When a liquid-filled rotor spins nonperturbedly, the free surface of the liquid forms a cylinder concentric with the rotor cavity and the liquid and the rotor rotate as one solid body. When the rotor is perturbed, a perturbation of the liquid will also be excited and in turn affect the perturbed motion of the rotor. Many experiments have shown that the liquid contained in a rotor not only changes the natural frequencies and critical speeds of the empty rotor, but also may lead to the instability of the system. Such a fluid-structure coupling problem is more complicated than others because the perturbed motion here is relative to a steady spinning.

The instability of a liquid-filled rotor was first noted experimentally by Schmidt (1958) and Kollman (1962). As the rotor they investigated was partially filled with liquid, they thought that it was the fluctuation of the free surface of the enclosed liquid that introduced the instability. Then, Wolf (1968) and Hendricks (1979, 1981, 1982) performed analytical investigations. Wolf regarded the condition for ruling out the translatory circular whirl as the instability condition, which is not strict in the mathematical sense. Hendricks and Lichtenberg (1982) improved Wolf's analysis by considering the liquid viscosity and the tilting of the rotor and dealt with three-dimensional problems.

The present work gives a complete analytical approach to a two-dimensional liquid-filled rotor.

1 The analytical expression of the dynamic pressure of the liquid acting on a rotor subjected to a transverse harmonic motion is given, then the general equation of perturbed motion for the liquid-filled rotor is derived.

2 Directly from the equation of motion, the exact criteria for stability and the stability boundaries are given analytically. The instability threshold speed, as well as the threshold internal and external damping, are obtained.

Equation of Perturbed Motion of the Enclosed Liquid

A rigid cylinder mounted symmetrically in the middle of a massless shaft is shown as Fig. 1. When the cylinder spins at

a constant rate Ω without perturbation, under the action of the centrifugal force the contained liquid is uniformly attached to the inner wall of the cylinder and spins synchronously as a rigid body. The dynamic stability of such a liquid-filled rotor is discussed in this paper.

In Fig. 2, a fixed Cartesian coordinate system $O\text{-}xyz$, a body-fixed Cartesian reference system $C\text{-}\xi\eta\zeta$, and a body-fixed cylindrical coordinate system $C\text{-}r\theta$ are established, where the z -axis coincides with the spinning direction and C is the center of the cylinder. The perturbed velocity of the flow at an arbitrary point (r, θ) is denoted as $u\mathbf{r}_0 + v\theta_0$. The flow pressure is P . Referred to the fixed system, the parallel perturbed motion of the cylinder is

$$\mathbf{r}_c = x(t)\mathbf{i} + y(t)\mathbf{j}. \quad (1)$$

The equation of motion for the inviscid incompressible liquid relative to the rotational system is such that

$$\frac{\partial \mathbf{V}_r}{\partial t} + (\mathbf{V}_r \cdot \nabla) \mathbf{V}_r + 2(\Omega \times \mathbf{V}_r) = -\frac{1}{\rho} \nabla P - \mathbf{a}_e \quad (2)$$

and the continuity equation is

$$\operatorname{div} \mathbf{V}_r = 0 \quad (3)$$

where \mathbf{V}_r is the relative perturbed velocity and \mathbf{a}_e is the convected acceleration given by

$$\mathbf{a}_e = \mathbf{a}_c + \Omega \times (\Omega \times \mathbf{r}) = \mathbf{a}_c - \Omega^2 \mathbf{r} \quad (4)$$

where \mathbf{a}_c is the translatory acceleration of the center

$$\mathbf{a}_c = \dot{x}(t)\mathbf{i} + \dot{y}(t)\mathbf{j}. \quad (5)$$

We set

$$P = \frac{\rho}{2} \Omega^2 (r^2 - b^2) + \bar{P} \quad (6)$$

here $(\rho/2)\Omega^2(r^2 - b^2)$ is the pressure of the liquid under steady spinning, whereas \bar{P} represents the perturbation pressure. In keeping with the hypothesis of small perturbation, both \mathbf{V}_r and \bar{P} are first-order small quantities. With higher order quantities neglected, Eq. (2) is linearized to

$$\frac{\partial \mathbf{V}_r}{\partial t} + 2(\Omega \times \mathbf{V}_r) = -\frac{1}{\rho} \nabla \bar{P} - \mathbf{a}_e. \quad (7)$$

Taking the vorticity of (7) leads to $(\partial/\partial t)(\operatorname{rot} \mathbf{V}_r) = 0$. As the

¹ The project was supported by the Foundation for Developing Chinese Education and Science and the Chinese National Science Foundation.

Contributed by the Applied Mechanics Division of THE AMERICAN SOCIETY OF MECHANICAL ENGINEERS for publication in the ASME JOURNAL OF APPLIED MECHANICS.

Discussion on this paper should be addressed to the Technical Editor, Prof. Lewis T. Wheeler, Department of Mechanical Engineering, University of Houston, Houston, TX 77204-4792, and will be accepted until four months after final publication of the paper itself in the ASME JOURNAL OF APPLIED MECHANICS.

Manuscript received by the ASME Applied Mechanics Division, Jan. 21, 1994; final revision, July 14, 1994. Associate Technical Editor: W. K. Liu.

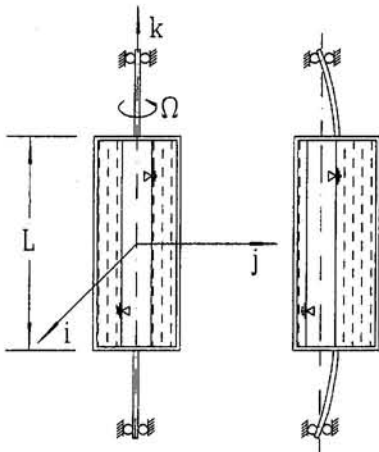


Fig. 1 Rotor system (side view)

system is initially nonperturbed, we then obtain $\text{rot } \mathbf{V}_r = \mathbf{0}$. Therefore, though the steady spinning flow of the liquid is rotational, the perturbed motion is irrotational. Taking the divergence of (7), we obtain

$$\Delta \bar{P} = 0 \quad (8)$$

where Δ is the Laplace operator.

The boundary conditions are next to be specified. On the solid surface, we have

$$u|_{r=a} = 0. \quad (9)$$

For the cylinder partially filled with liquid, during perturbed motion the free surface is defined by $r = b + \eta(\theta, t)$, here b is the radius of the nominal free surface for a nonperturbed rigid rotation and η is also a first-order small quantity. From the condition that the total pressure at the free surface must be zero, we obtain $\bar{P}|_{r=b} = -\rho\Omega^2 b\eta$. Then, from $u|_{r=b} = (\partial\eta/\partial t)$, the boundary condition on the free surface should be

$$\frac{\partial \bar{P}}{\partial t} \Big|_{r=b} = -\rho\Omega^2 b u|_{r=b}. \quad (10)$$

The perturbation flow is governed by (7)-(10).

Dynamic Pressure of the Liquid Under the Transverse Harmonic Motion of Rotor

Suppose that the rotor is subjected to a transverse perturbed motion given by

$$x(t) = Ae^{i\omega t}, \quad y(t) = Be^{i\omega t} \quad (11)$$

where A , B , and ω are all complex numbers. Physically, only the real parts of (11) are of sense. For convenience, we are first concerned with the transverse motion in the direction of x -axis ($A \neq 0, B = 0$). From (7) and (8) we have

$$\begin{cases} r \frac{\partial}{\partial r} \left(r \frac{\partial \bar{P}}{\partial r} \right) + \frac{\partial^2 \bar{P}}{\partial \theta^2} = 0 \\ \frac{\partial u}{\partial t} - 2\Omega v = -\frac{1}{\rho} \frac{\partial \bar{P}}{\partial r} + \frac{1}{2} A\omega^2 [e^{i(\omega t+\Omega t+\theta)} + e^{i(\omega t-\Omega t-\theta)}] \\ \frac{\partial v}{\partial t} + 2\Omega u = -\frac{1}{\rho} \frac{\partial \bar{P}}{\partial \theta} + \frac{i}{2} A\omega^2 [e^{i(\omega t+\Omega t+\theta)} - e^{i(\omega t-\Omega t-\theta)}] \end{cases} \quad (12)$$

Setting

$$\begin{cases} u = u_1(r)e^{i(\omega t+\Omega t+\theta)} + u_2(r)e^{i(\omega t-\Omega t-\theta)} \\ v = v_1(r)e^{i(\omega t+\Omega t+\theta)} + v_2(r)e^{i(\omega t-\Omega t-\theta)} \\ \bar{P} = P_1(r)e^{i(\omega t+\Omega t+\theta)} + P_2(r)e^{i(\omega t-\Omega t-\theta)} \end{cases} \quad (13)$$

and inserting them into (12), after a rather lengthy deduction (see Appendix), we have the perturbation pressure distribution on the inner wall of the cylinder as

$$\bar{P}(a, \theta) = \frac{A}{2} \rho a \omega^2 [M_1 e^{i(\omega t+\Omega t+\theta)} + M_2 e^{i(\omega t-\Omega t-\theta)}] \quad (14)$$

where

$$M_1 = \frac{2(\Omega + \omega)^2 - \omega^2}{(1 + \gamma)(\Omega + \omega)^2 - \omega^2},$$

$$M_2 = \frac{2(\Omega - \omega)^2 - \omega^2}{(1 + \gamma)(\Omega - \omega)^2 - \omega^2} \quad (15)$$

$$\gamma = \frac{a^2 + b^2}{a^2 - b^2}. \quad (16)$$

Similarly, when the cylinder is subjected to a transverse harmonic motion in the y direction ($A = 0, B \neq 0$), the pressure distribution on the inner wall of the cylinder can be obtained as

$$\bar{P}(a, \theta) = \frac{iB}{2} \rho a \omega^2 [-M_1 e^{i(\omega t+\Omega t+\theta)} + M_2 e^{i(\omega t-\Omega t-\theta)}]. \quad (17)$$

Therefore, the total perturbation pressure distribution under the general motion (11) is such that

$$\begin{aligned} \bar{P}(a, \theta) = & \frac{1}{2} \rho a \omega^2 [(A - iB)M_1 e^{i(\omega t+\Omega t+\theta)} \\ & + (A + iB)M_2 e^{i(\omega t-\Omega t-\theta)}]. \end{aligned} \quad (18)$$

The components of the total force of the liquid acting on the cylinder in the directions of the x and y -axes are, respectively,

$$F_x = La \int_0^{2\pi} \bar{P}(a, \theta) \cos(\Omega t + \theta) d\theta$$

$$F_y = La \int_0^{2\pi} \bar{P}(a, \theta) \sin(\Omega t + \theta) d\theta \quad (19)$$

where L denotes the length of the cylinder. Inserting (18) into the above expressions, we have

$$\begin{bmatrix} F_x \\ F_y \end{bmatrix} = \frac{1}{2} m_c \omega^2 \begin{bmatrix} M_1 + M_2 & -i(M_1 - M_2) \\ i(M_1 - M_2) & M_1 + M_2 \end{bmatrix} \begin{bmatrix} Ae^{i\omega t} \\ Be^{i\omega t} \end{bmatrix} \quad (20)$$

where

$$m_c = \rho \pi a^2 L \quad (21)$$

which denotes the mass of the liquid to fully fill the cavity.

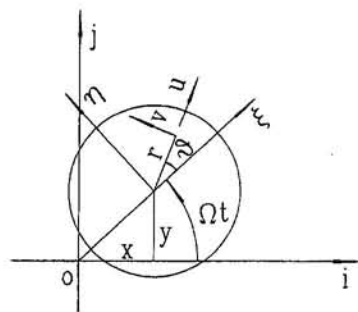


Fig. 2 Definition of coordinate systems (top view)

Formula (20) is the general representation of the liquid acting force. The formula shows that besides a force collinear with the displacement, a circulatory force is also excited. If the cylinder executes a circular whirl, i.e., $B = -iA$, we have

$$\begin{aligned} F_x &= m_c \omega^2 M_2 A \cos \omega t \\ F_y &= m_c \omega^2 M_2 A \sin \omega t \end{aligned} \quad (22)$$

then the liquid acting force is collinear with the displacement and no circulatory force appears. This special case has been solved by Wolf (1968) and Hendricks (1986).

Equation of Motion for Rotor and the Dynamic Stability

We consider the general case where both the internal and external damping effects are involved in. Referred to the fixed coordinate system, the equation of perturbed motion for the rotor is such that

$$\begin{bmatrix} m_r & \\ & m_r \end{bmatrix} \begin{bmatrix} \ddot{x} \\ \ddot{y} \end{bmatrix} + \begin{bmatrix} \bar{C}_e + \bar{C}_i & \\ & \bar{C}_e + \bar{C}_i \end{bmatrix} \begin{bmatrix} \dot{x} \\ \dot{y} \end{bmatrix} + \begin{bmatrix} k & \bar{C}_i \Omega \\ -\bar{C}_i \Omega & k \end{bmatrix} \begin{bmatrix} x \\ y \end{bmatrix} = \begin{bmatrix} F_x \\ F_y \end{bmatrix} \quad (23)$$

where m_r , k , \bar{C}_e , and \bar{C}_i are, respectively, the mass of the empty cylinder, the stiffness of the shaft and the internal and external damping coefficients. The internal damping force is assumed to be in direct proportion to the relative perturbed velocity

$$\begin{aligned} \mathbf{D}_i &= -\bar{C}_i (\mathbf{V}_c - \Omega \times \mathbf{r}_c) \\ &= -\bar{C}_i [(\dot{x} - \Omega y) \mathbf{i} + (\dot{y} + \Omega x) \mathbf{j}] \end{aligned} \quad (24)$$

which is a simple equivalent model for accounting for the fluid viscosity. When the center of the cylinder also rotates with angular velocity Ω , the cylinder and the contained liquid rotate synchronously around the z -axis and the viscosity of the liquid does not work. The right-hand side of (23) represents the force of the liquid acting on the cylinder. We are now concerned with the dynamic stability of (23). Set

$$x = Ae^{i\omega t}, \quad y = Be^{i\omega t} \quad (25)$$

where A , B , and ω are all complex numbers. From (23), recalling (20) we obtain the following eigenvalue problem

$$\begin{bmatrix} \alpha & -\beta \\ \beta & \alpha \end{bmatrix} \begin{bmatrix} A \\ B \end{bmatrix} = \mathbf{0} \quad (26)$$

where

$$\begin{cases} \alpha = \left[m_r + \frac{m_c}{2} (M_1 + M_2) \right] \omega^2 - i(\bar{C}_e + \bar{C}_i) \omega - k \\ \beta = \frac{i}{2} m_c (M_1 - M_2) \omega^2 + \bar{C}_i \Omega. \end{cases} \quad (27)$$

The corresponding characteristic equation of (26) is $\alpha^2 + \beta^2 = 0$, i.e.,

$$\alpha = \pm i\beta. \quad (28)$$

Inserting (27) and (15) into (28) and denoting

$$\begin{aligned} F &= \frac{\omega}{\omega_0}, \quad S = \frac{\Omega}{\omega_0}, \quad \omega_0^2 = \frac{k}{m_r}, \\ \mu &= \frac{m_c}{m_r}, \quad C_e = \frac{\bar{C}_e}{2m_r\omega_0}, \quad C_i = \frac{\bar{C}_i}{2m_r\omega_0} \end{aligned} \quad (29)$$

we have the nondimensional characteristic equation as

$$\begin{aligned} &(\gamma + \mu)F^4 + [\pm 2S(1 + \gamma + 2\mu) - 2i(C_e + C_i)\gamma]F^3 \\ &+ [S^2(1 + \gamma + 2\mu) - \gamma \mp 4iS(C_e + C_i)(1 + \gamma) \\ &\mp 2iC_i\gamma S]F^2 + [\mp 2(1 + \gamma)S - 2iS^2(C_e + C_i)(1 + \gamma) \\ &- 4iC_i(1 + \gamma)S^2]F + [-S^2(1 + \gamma) \\ &\mp 2iC_i(1 + \gamma)S^3] = 0. \end{aligned} \quad (30)$$

For an undamped system, (30) degenerates into the following characteristic equation with real coefficients as

$$\begin{aligned} &(\gamma + \mu)(\pm F)^4 + 2S(1 + \gamma + 2\mu)(\pm F)^3 \\ &+ [S^2(1 + \gamma + 2\mu) - \gamma](\pm F)^2 \\ &- 2(1 + \gamma)S(\pm F) - S^2(1 + \gamma) = 0. \end{aligned} \quad (31)$$

Taking the positive sign of F in the above equation leads to the characteristic equation given by Wolf (1968). Equation (31) shows that if one eigenroot F is a complex number, its conjugate number must also be an eigenroot, then one iF has positive real part and the system is unstable. So an undamped liquid-filled rotor cannot have the asymptotic stability. If all the eigenroots F extracted from (31) are real numbers, the system is stable and the whirl modes of the rotor can be obtained from (26) as

$$\begin{bmatrix} A \\ B \end{bmatrix} = \begin{bmatrix} 1 \\ \mp i \end{bmatrix}$$

which represent the forward and backward circular whirl, respectively (Zhang, 1990). Therefore, we have proved theoretically that it is reasonable for Wolf to regard the condition whether the circular whirl can exist or not as the criterion for stability. This criterion, however, is effective only for undamped systems. If damping occurs, we should directly discuss Eq. (30) by means of the generalized Routh-Hurwitz criterion (Porter, 1990). Denoting the coefficients of F^{n-j} as $b_j + ic_j$, we have

$$\begin{aligned} b_0 &= \gamma + \mu, \quad b_1 = \pm 2(1 + \gamma + 2\mu)S, \\ b_2 &= S^2(1 + \gamma + 2\mu) - \gamma \\ b_3 &= \mp 2(1 + \gamma)S, \quad b_4 = -S^2(1 + \gamma) \\ c_0 &= 0, \quad c_1 = -2(C_e + C_i)\gamma, \\ c_2 &= \mp 2S[2(C_e + C_i)(1 + \gamma) + C_i\gamma] \\ c_3 &= -2S^2(1 + \gamma)(C_e + 3C_i), \quad c_4 = \mp 2C_i(1 + \gamma)S^3. \end{aligned}$$

According to the generalized *R-H* criterion, the condition for stability is that all the even-order principle minors of the following Hurwitz matrix, Δ_{2k} ($k = 1, 2, 3, 4$), should be positive

$$H_8 = \begin{bmatrix} c_0 & c_1 & c_2 & c_3 & c_4 & 0 & 0 & 0 \\ b_0 & b_1 & b_2 & b_3 & b_4 & 0 & 0 & 0 \\ 0 & c_0 & c_1 & c_2 & c_3 & c_4 & 0 & 0 \\ 0 & b_0 & b_1 & b_2 & b_3 & b_4 & 0 & 0 \\ 0 & 0 & c_0 & c_1 & c_2 & c_3 & c_4 & 0 \\ 0 & 0 & b_0 & b_1 & b_2 & b_3 & b_4 & 0 \\ 0 & 0 & 0 & c_0 & c_1 & c_2 & c_3 & c_4 \\ 0 & 0 & 0 & b_0 & b_1 & b_2 & b_3 & b_4 \end{bmatrix}.$$

After some manipulations, we obtain

$$\begin{aligned} \Delta_2 &= 2(C_e + C_i)(\gamma + \mu)\gamma \\ \Delta_4 &= 4(\gamma + \mu)\{C_e^2[\gamma^3 + S^2\mu(\gamma - 1)(3\gamma + 4)] \\ &+ C_i^2[\gamma^3 - S^2(\gamma^3 + 4\mu + \gamma\mu - 4\gamma^2\mu)] \\ &+ 2C_e C_i[\gamma^3 + 4\mu S^2(\gamma^2 - 1)]\} \quad (32) \\ \Delta_6 &= -8S^4(\gamma^2 - 1)(\gamma + \mu)\mu\{C_e^3[S^2\mu(\gamma - 1) \\ &- (5\gamma^2 + 20\gamma + 16)] + C_e^2 C_i[5S^2\mu(\gamma - 1) - 11\gamma^2 \end{aligned}$$

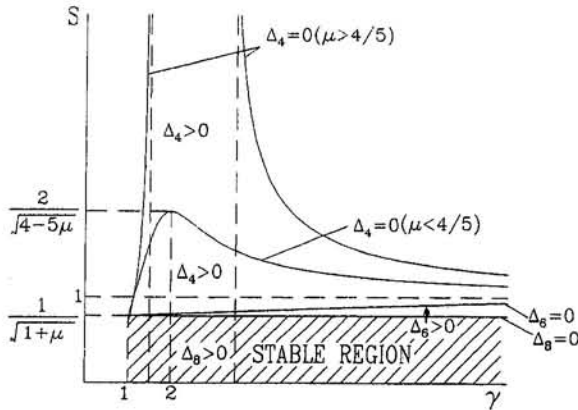


Fig. 3 Stability diagram (Case 3: $C_e = 0, C_i = 0$)

$$\begin{aligned}
 & + 52\gamma + 48)] + C_e C_i^2 [S^2(5\gamma^2 + 20\gamma \\
 & + 16 + 21\mu + 20\gamma\mu) - (7\gamma^2 + 44\gamma + 48)] \\
 & + C_i^3 [S^2(\gamma^2 + 12\gamma + 16 + 17\mu + 12\gamma\mu) \\
 & \quad - (\gamma^2 + 12\gamma + 16)] \\
 \Delta_8 = & 16(\gamma^2 - 1)^2\mu^2(\gamma + \mu)S^{10} \{ -C_e^4(1 + \gamma) \\
 & - 2C_e^3C_i(1 + \gamma) + C_e^2C_i^2[S^2(1 + \gamma + 2\mu) - \gamma] \\
 & \quad + 2C_eC_i^3 + C_i^4[1 - S^2(1 + \mu)] \}.
 \end{aligned}$$

The stability of the system is determined by $\Delta_i > 0$ ($i = 2, 4, 6, 8$).

We then consider the following cases:

Case 1. Only external damping occurs, $C_e \neq 0$ and $C_i = 0$. Equation (32) is reduced to

$$\begin{aligned}
 \Delta_2 &= 2C_e(\gamma + \mu)\gamma \\
 \Delta_4 &= 4C_e^2(\gamma + \mu)[\gamma^3 + S^2\mu(\gamma - 1)(3\gamma + 4)] \\
 \Delta_6 &= 8C_e^3S^4(\gamma^2 - 1)(\gamma + \mu) \\
 & \quad \times \mu[5\gamma^2 + 20\gamma + 16 - S^2\mu(\gamma - 1)] \\
 \Delta_8 &= -16C_e^4S^{10}\mu^2(\gamma + \mu)(\gamma + 1)(\gamma^2 - 1)^2.
 \end{aligned}$$

As $\Delta_8 < 0$, a liquid-filled rotor with external damping must be unstable. Such a conclusion has been obtained by Hendricks (1981).

Case 2. Only internal damping occurs, $C_e = 0$ and $C_i \neq 0$. Then (32) is reduced to

$$\begin{aligned}
 \Delta_2 &= 2C_i(\gamma + \mu)\gamma \\
 \Delta_4 &= 4C_i^2(\gamma + \mu)[\gamma^3 - S^2(\gamma^3 + 4\mu + \gamma\mu - 4\gamma^2\mu)] \\
 \Delta_6 &= -8C_i^3S^4(\gamma^2 - 1)(\gamma + \mu)\mu[S^2(\gamma^2 + 12\gamma + 16 \\
 & \quad + 17\mu + 12\gamma\mu) - (\gamma^2 + 12\gamma + 16)] \\
 \Delta_8 &= 16C_i^4S^{10}(\gamma^2 - 1)^2\mu^2(\gamma + \mu)[1 - S^2(1 + \mu)].
 \end{aligned}$$

From $\Delta_i > 0$, the condition for stability is given by

$$\Delta_4 > 0: S^2(\gamma^3 - 4\gamma^2\mu + \gamma\mu + 4\mu) < \gamma^3$$

$$\Delta_6 > 0: S^2 < \frac{1}{1 + \mu \frac{17 + 12\gamma}{\gamma^2 + 12\gamma + 16}}$$

$$\Delta_8 > 0: S^2 < \frac{1}{1 + \mu}.$$

In Fig. 3 the illustrative curves $\Delta_i = 0$ are plotted and the

region $\Delta_i > 0$ are indicated. The condition for stability, which satisfies all of the above three inequalities, is $\Delta_8 > 0$, i.e., $S^2 < 1/(1 + \mu)$, or alternatively

$$\Omega < \Omega^*, \quad \Omega^* = \frac{k}{m_r + m_c} \quad (33)$$

where Ω^* denotes the fundamental frequency of the rotor fully filled with liquid. Ω^* is the instability threshold speed for a liquid-filled rotor under the action of internal damping. Once $\Omega > \Omega^*$, the system loses stability. This conclusion is first obtained.

Case 3. Internal and external damping occurs simultaneously, $C_e \neq 0, C_i \neq 0$. We set

$$\eta = C_i/C_e. \quad (34)$$

From $\Delta_i > 0$ we obtain the condition for stability as

$$\begin{aligned}
 \Delta_4 > 0: & S^2[\eta^2(\gamma^3 - 4\gamma^2\mu + \gamma\mu + 4\mu) - 8\eta\mu(\gamma^2 - 1) \\
 & \quad - \mu(\gamma - 1)(3\gamma + 4)] < \gamma^3(1 + \eta)^2
 \end{aligned}$$

$$\begin{aligned}
 \Delta_6 > 0: & S^2 < \{ \eta^3(\gamma^2 + 12\gamma + 16) \\
 & \quad + \eta^2(7\gamma^3 + 44\gamma + 48) + \eta(11\gamma^2 + 52\gamma + 48) \\
 & \quad + (5\gamma^2 + 20\gamma + 16) \} / \{ \eta^3(\gamma^2 + 12\gamma + 16) \\
 & \quad + 17\mu + 12\gamma\mu \} + \eta^2(5\gamma^2 + 20\gamma + 16 + 21\mu \\
 & \quad + 20\gamma\mu) + (5\eta + 1)(\gamma - 1) \}
 \end{aligned}$$

$$\begin{aligned}
 \Delta_8 > 0: & S^2(1 + \mu)\eta^2 \left(\frac{1 + \gamma + 2\mu}{1 + \mu} - \eta^2 \right) \\
 & > (1 + \eta)^2(1 + \gamma - \eta^2).
 \end{aligned}$$

Figure 4 plots the curves $\Delta_i = 0$ and the regions $\Delta_i > 0$, where the parameters are taken from Wolf (1968), $\gamma = 2.6, \mu = 0.206$. The stability condition satisfying all above three inequalities is

$$\begin{cases} \eta^2 > 1 + \gamma \\ S^2 < f(\eta) = \frac{(1 + \eta)^2(\eta^2 - 1 - \gamma)}{(1 + \mu)\eta^2 \left(\eta^2 - \frac{1 + \gamma + 2\mu}{1 + \mu} \right)} \end{cases} \quad (35)$$

Therefore, only when the damping ratio $\eta > \sqrt{1 - r}$, there exists a stable region. For each η greater than $\sqrt{1 - r}$, there is a threshold speed $\Omega^* = \omega_0 \sqrt{f(\eta)}$. If $\Omega > \Omega^*$, the system must be unstable. From $(df(\eta)/d\eta) = 0$, we can extract the maximum threshold speed as

$$\begin{cases} \eta^{*4} + (\alpha - 1 - \gamma)\eta^{*3} - 2(1 + \gamma)\eta^{*2} \\ \quad + \alpha(1 + \gamma)\eta^* = 0 \quad (\eta^{*2} > 1 + \gamma) \\ \Omega^* = \omega_0 \sqrt{f(\eta^*)} \end{cases}$$

where $\alpha = (1 + \gamma + 2\mu)/(1 + \mu)$. For the aforementioned parameters, we have

$$\Omega^* = 1.2154\omega_0 \quad \eta^* = 2.40595.$$

The stable region (35) can be approximately represented by the following rectangular region:

$$\begin{cases} \eta^2 > 1 + \gamma \\ S^2 < \frac{1}{1 + \mu} \end{cases} \quad (36)$$

which is a sufficient condition for stability.

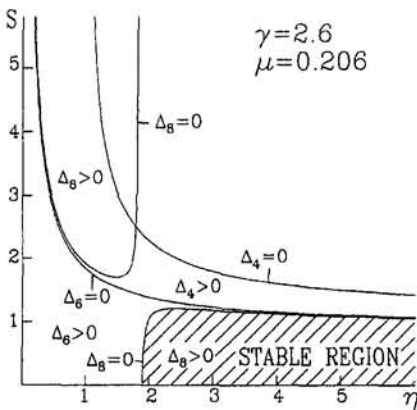


Fig. 4 Stability diagram (Case 4: $C = 0, C = 0$)

Conclusions

In this paper the dynamic stability of a two-dimensional liquid-filled rotor under the action of internal and external damping is analyzed. The cases that only external damping occurs, only internal damping occurs, and internal and external damping occurs simultaneously are discussed separately. For each case the analytical criterion for stability is derived. The analysis shows that the external damping is always a destabilizing factor and the internal damping, however, has certain stabilizing effect. For a general case there exists an instability threshold speed. Once the rotating speed exceeds the threshold speed, the system loses stability and can never be stabilized again by adjusting the parameters. Such an instability threshold can be approximately set as $1/(1 + \mu)$. All the above results can be regarded as the extensions of previous related conclusions.

References

Hendricks, S. L., and Morton, J. B., 1979, "Stability of a Rotor Partially Filled with Viscous Incompressible Fluid," *ASME JOURNAL OF APPLIED MECHANICS*, Vol. 46, pp. 913-918.
 Hendricks, S. L., 1981, "Instability of a Damped Rotor Partially Filled with an Inviscid Liquid," *ASME JOURNAL OF APPLIED MECHANICS*, Vol. 48, p. 674.
 Hendricks, S. L., 1986, "Stability of a Clamped-Free Rotor Partially Filled with Liquid," *ASME JOURNAL OF APPLIED MECHANICS*, Vol. 53, pp. 166-172.
 Kollmann, F. G., 1962, "Experimentelle und theoretische Untersuchungen Über die Kritischen Drehzahlen flüssigkeits gefüllter Hohlkörper," *Forschung auf dem Gebiete des Ingenieurwesens*, Vol. 28, pp. 115-123; 147-153.
 Lichtenberg, G., 1982, "Vibration of an Elastically Mounted Spinning Rotor Partially Filled with Liquid," *ASME Journal of Mechanical Design*, Vol. 104, pp. 389-396.
 Peter, B., 1990, *Stability Criteria for Linear Dynamic Systems*, Academic Press, New York.
 Schmidt, E., 1958, Das Gleichgewicht eines Wasserringes mit freier Oberfläche in einem rotierenden Hohlkörper, *Zeitschrift für angewandte Mathematik und Physik*, Vol. 96.
 Tao, M., and Zhang, W., 1993, "Exact Solution for a Partially Liquid-Filled Rotor Excited Laterally," *Acta Mechanica Sinica*, Vol. 25, No. 5, pp. 638-642 (in Chinese).
 Wolf, J. A., Jr., 1968, "Whirl Dynamic of a Rotor Partially Filled with Liquid," *ASME JOURNAL OF APPLIED MECHANICS*, Vol. 35, pp. 676-682.
 Zhang, W., 1990, *Theory of Rotordynamics*, Science Press, Beijing (in Chinese; to be translated into English).

APPENDIX

The Solving of (12)

According to the superposition principle for linear equations, we can solve the terms of $e^{i(\omega t + \Omega t + \theta)}$ and $e^{i(\omega t - \Omega t - \theta)}$ separately.

First, we seek the solutions u_1 , v_1 , and P_1 . Substituting (13) into (12), we have

$$r^2 \frac{d^2 P_1}{dr^2} + r \frac{dP_1}{dr} - P_1 = 0 \quad (37)$$

$$i\sigma u_1 - 2\Omega v_1 = -\frac{1}{\rho} \frac{dP_1}{dr} + \frac{1}{2} A\omega^2 \quad (38)$$

$$i\sigma u_1 + i\sigma v_1 = -\frac{i}{\rho} \frac{P_1}{2} + \frac{i}{2} A\omega^2 \quad (39)$$

where $\sigma = \omega + \Omega$. From (37) we have

$$P_1(r) = C_1 r + \frac{C_2}{r}. \quad (40)$$

Substitutions of the above expression into (38) and (39) lead to

$$u_1 = \frac{-i}{\rho(4\Omega^2 - \sigma^2)} \left[(\sigma + 2\Omega)C_1 + (2\Omega - \sigma) \frac{C_2}{r^2} - \frac{1}{2} \rho A\omega^2(\sigma + 2\Omega) \right]$$

$$v_1 = \frac{1}{\rho(4\Omega^2 - \sigma^2)} \left[(\sigma + 2\Omega)C_1 - (2\Omega - \sigma) \frac{C_2}{r^2} + \frac{1}{2} \rho A\omega^2(\sigma + 2\Omega) \right].$$

The boundary conditions (9) and (10) now become

$$i\sigma P_1(b) = -\rho\Omega^2 b u_1(b), \quad u_1(a) = 0,$$

i.e.,

$$\left\{ \begin{array}{l} \left(\sigma - \frac{\Omega^2}{2\Omega - \sigma} \right) C_1 + \left(\sigma - \frac{\Omega^2}{2\Omega + \sigma} \right) \frac{C_2}{b^2} = -\frac{\rho A\omega^2}{2} \frac{\Omega^2}{2\Omega - \sigma} \\ (\sigma + 2\Omega)C_1 + (2\Omega - \sigma) \frac{C_2}{a^2} = \frac{\rho A\omega^2}{2} (\sigma + 2\Omega) \end{array} \right.$$

which yields

$$C_1 = \frac{\rho A\omega^2}{2(2\Omega\sigma - \Omega^2 + \sigma^2\gamma)} \left[\frac{a^2}{a^2 - b^2} \sigma(2\Omega + \sigma) - \Omega^2 \right]$$

$$C_2 = -\frac{\rho A\omega^2}{2(2\Omega\sigma - \Omega^2 + \sigma^2\gamma)} \frac{a^2 b^2}{a^2 - b^2} \sigma(2\Omega + \sigma).$$

Inserting the above expressions into (40) leads to

$$P_1(a) = \frac{1}{2} \rho A\omega^2 a \frac{2(\Omega + \omega)^2 - \omega^2}{(1 + \gamma)(\Omega + \omega)^2 - \omega^2}.$$

Similarly, we have

$$P_2(a) = \frac{1}{2} \rho A\omega^2 a \frac{2(\Omega - \omega)^2 - \omega^2}{(1 + \gamma)(\Omega - \omega)^2 - \omega^2}.$$

Then (14) is obtained.

S. P. Lin

Department of Mechanical and
Aeronautical Engineering,
Clarkson University,
Potsdam, NY 13699
Mem. ASME.

Z. W. Zhou

Institute of Applied Mathematics,
and Mechanics,
Shanghai University of Technology,
Shanghai, China

The Hydrodynamic Stability of Pendent Drop Under a Liquid Column

The hydrodynamic stability of a liquid column resting on a gas in a vertical tube with its upper end closed is analyzed. The maximum height above which the interface is unstable is given as a function of the Bond number and the density ratio. The instability is shown to be monotonic, i.e., nonoscillatory.

Introduction

The stability of a column of liquid resting on a column of air in a vertical tube was investigated by Dussan (1975), Joseph (1976), and Huh (1969). The upper end of the tube is closed and the interface at the bottom of the liquid column is flat. The weight of the liquid column is supported by the air pressure which is greater than the pressure at the upper end of the tube by an amount equalling the hydrostatic pressure corresponding to the column height. It was deduced from energy analysis that the flat interface is conditionally stable if $0 < G < (3.83171)^2$, where $G = 4(\rho - \rho_a)a^2g/S$. In the definition of G , a is the tube radius, g is the gravitational acceleration, S is the surface tension, and ρ and ρ_a are, respectively, the densities of liquid and air. The static stability of a drop hanging from a tube was analyzed by Pitts (1973, 1974) by use of the energy method. Two cases were considered. The first case is that of constant drop volume and the second was that of constant pressure at the mouth of the tube. Numerical examples were used to demonstrate that stable drops on a tube can only be formed under constant pressure in the liquid if the radius is less than a certain critical value. However, no general criteria of stability are given. In this work we report the results of linear stability analysis of a pendent drop supporting the weight of a liquid column of finite height in a circular tube with its lower end open to air. The critical height of the liquid column below which the pendent drop is stable is given as a function of the Bond number in the form of a neutral stability curve. Measurements of liquid pendent shape have been used as a means of determining interfacial tension by Pitts (1973, 1974). Thus the stability of a liquid pendent in another fluid is of considerable practical importance. The stability of hanging drops is also of fundamental importance in understanding the regimes of jet breakup (Lin and Ibrahim, 1990).

Stability Analysis

Consider the stability of a drop hanging from a circular cylindrical tube as shown in Fig. 1. The shape of the pendent depends on the density of the liquid ρ and the ambient gas density ρ_a , the interfacial tension, and the liquid volume and the tube radius a . As the volume of the liquid is increased, it may reach a critical value beyond which the interfacial force is insufficient to maintain the pendent in equilibrium. Before this critical vol-

ume is reached, the shape of the interface is determined by the exact balance of the pressure difference across the interface and the interfacial force per unit area. We nondimensionalize the length with a , the pressure with $\rho g a$, where g is the gravitational acceleration. Then the dimensionless pressure exerted by the liquid is $p_1 = p_b + h$, where h is the distance between the upper solid lid, maintained at the pressure p_b , and the lower interface. The pressure exerted by the ambient gas is $p_2 = p_a + qh$, where $q = \rho_a/\rho$, and p_a is the gas pressure at the level of the upper lid. The force balance at the interface gives (see, for example, Joseph, 1976)

$$p_1 - p_2 - B^{-1} \nabla \cdot \mathbf{n} = 0$$

where \mathbf{n} is the unit normal vector pointing from the liquid to the ambient gas and B is the Bond number defined by

$$B = \rho g a^2/S.$$

In terms of the liquid column height and q , the equation of interfacial force balance can be written as

$$[p_b - p_a + h_1(1 - q)]$$

$$+ (h - h_1)(1 - q) - B^{-1} \nabla \cdot \mathbf{n} = 0, \quad (1)$$

where h_1 is so chosen that $h_1 = (p_a - p_b)/(1 - q)$, and thus the sum in the bracket vanishes. When $h = h_1$, $\nabla \cdot \mathbf{n} = 0$ and the interface is flat. Then the net weight of the liquid column of height $h = h_1$ and of unit cross-sectional area is exactly balanced by the pressure difference $p_a - p_b$. For an axisymmetric pendent $\nabla \cdot \mathbf{n}$ at the interface $z = h$ can be written in the cylindrical coordinates (r, θ, z) as

$$\nabla \cdot \mathbf{n} = -\bar{h}_{rr}(1 + \bar{h}_r^2)^{-3/2} - \bar{h}_r[r(1 + \bar{h}_r^2)^{1/2}]^{-1}, \quad (2)$$

where $\bar{h} = h - h_1$, h_1 being a constant. Strictly speaking, Eq. (1) with Eq. (2) applies only at the liquid-gas interface, but not at the solid-liquid-gas interline at the tube wall. Unfortunately, very little is known about the interline force. Usually, it is parameterized with contact angle θ . Nevertheless, Eq. (1) can be integrated with or without specifying θ . In this problem, the contact angle is not constant. The shapes of the pendants $z - h_1 = \bar{h}$ corresponding to three different volumes for given B and q are given in Fig. 2 for illustration. These shapes were determined from integration of Eq. (1) with given $\bar{h}(0)$ and $\bar{h}_r(0) = 0$ by use of the fourth-order Runge-Kutta method. The shapes so determined have different contact angles which depend on the liquid volume. Different solutions of (1) and (2) can be found for different contact angles specified at the wall. The specific contact angle depends on the interline force which in turn depends on the properties of pipe wall, liquid, and gas. The solutions we found are for the particular ones corresponding to zero interline force. Thus, the menisci we found can be held

Contributed by the Applied Mechanics Division of THE AMERICAN SOCIETY OF MECHANICAL ENGINEERS for publication in the ASME JOURNAL OF APPLIED MECHANICS.

Discussion on this paper should be addressed to the Technical Editor, Professor Lewis T. Wheeler, Department of Mechanical Engineering, University of Houston, Houston, TX 77204-4792, and will be accepted until four months after final publication of the paper itself in the ASME JOURNAL OF APPLIED MECHANICS.

Manuscript received by the ASME Applied Mechanics Division, July 5, 1994; final revision, Oct. 28, 1994. Associate Technical Editor: T. R. Akylas.

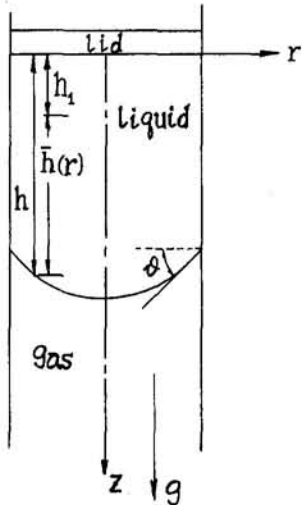


Fig. 1 Definition sketch

stationary without help from the interline force the physics of which is not yet understood.

To investigate the stability we introduce disturbances into the fluids, and determine the condition under which the disturbance will not grow in time. At the onset of instability the flow remains largely irrotational within the viscous diffusion time. Thus the velocity perturbation v_i is given by the gradient of the velocity potential ϕ , i.e.,

$$v_i = \nabla \phi_i, \quad (i = 1, 2) \quad (3)$$

where $i = 1$ stands for liquid and $i = 2$ stands for gas. ϕ_i satisfies the Laplace equation

$$\nabla^2 \phi_i = 0. \quad (4)$$

The solution of Eq. (4) for $i = 1$ which satisfies the no penetration conditions at the tube wall $r = 1$ and at the upper lid $z = 0$ is given by

$$\phi_1 = \sum_{n=1} B_n(t) J_o(k_n r) \cosh(k_n z) \quad (5)$$

where k_n are the roots of

$$[dJ_o(k_n r)/dr]_{r=1} = [-k_n J_1(k_n r)]_{r=1} = 0.$$

The solution of Eq. (4) for $i = 2$ which satisfies the condition of vanishing disturbances as $z \rightarrow \infty$, and the no penetration condition at $r = 1$ is given by

$$\phi_2 = \sum_{n=1} D_n(t) J_o(k_n r) \exp(-k_n z). \quad (6)$$

The perturbed interfacial position is given by

$$z = h(r) + d(r, t)$$

where $h(r)$ designates the unperturbed interfacial position, and the interfacial perturbation d is a function of r as well as time, t . It is assumed that $|d| \ll |h|$. The unknown function $B_n(t)$, $D_n(t)$ and $d(r, t)$ are to be determined by the three interfacial boundary conditions.

By definition the total time rate of change of the interfacial displacement is equal to the axial velocity of the fluid particle in each fluid, i.e.,

$$d_{,t} + \phi_{i,r} h_{,r} = \phi_{i,z} \quad (i = 1, 2). \quad (7)$$

Note that the nonlinear term $\phi_{i,r} d_{,r}$ is neglected in Eq. (7). This condition is assumed to be valid at the contact line. Thus the contact line is not fixed but moves with the fluids along the tube wall. This is possible either if the fluid is inviscid or if the

interline force vanishes. The perturbed pressure in the liquid and the gas at the interface can be obtained from the linearized Bernoulli equation, and are given, respectively, by

$$p_1 = p_b + (h + d) - (\phi_{1,t}) + (\phi_{1,z})_{z=0},$$

$$p_2 = p_a + q(h + d) - q[(\phi_{2,t}) - (\phi_{2,z})_{z=0}].$$

Note that $\phi_{i,t} \neq 0$ at $z = 0$. Hence p_1 is changed from the initial value of p_b to $p_b + (\phi_{1,t})_{z=0}$ when the basic state is perturbed. Substituting the expressions for the pressure and the interfacial position $H = h + d$ into the dynamic boundary condition Eq. (1) with Eq. (2), subtracting the basic state part, and linearizing the resulting equation, we have

$$(1 - q)d + \sum_{n=1} B_n J_o(k_n r) [1 - \cosh(k_n h)] + q \sum_{n=1} D_n J_o(k_n r) [\exp(-k_n h) - 1] + We Q^{-5/2} [Q d_{,r} - 3h_n h_r d_r + Q^2 d_{,r}/r - Q h_r^2 d_{,r}/r] = 0, \\ Q = 1 + h_r^2 \quad (8)$$

where the upper dot denotes time differentiation. The three interfacial boundary conditions admit solutions for the interfacial displacement of the form

$$d = \sum_{n=1} h_n J_o(k_n r) \exp(-i \omega t), \quad B_n = b_n \exp(-i \omega t), \\ D_n = d_n \exp(-i \omega t),$$

where ω is the complex eigenfrequency of disturbances. This particular form of d preserves the volume of the perturbed liquid column, since

$$\int_0^1 (2 \pi r d) dr = 2 \pi \sum_n (h_n/k_n) J_1(k_n) = 0$$

By virtue of the equation following (5). Substituting these expressions into the boundary conditions, and forming the Galerkin projection with $r J_o(k_m r)$, $m = 1$ to N , we obtain a system of $3N$ equations in $3N$ unknowns

$$\{[C] - i \omega [A]\} V = 0, \quad (9)$$

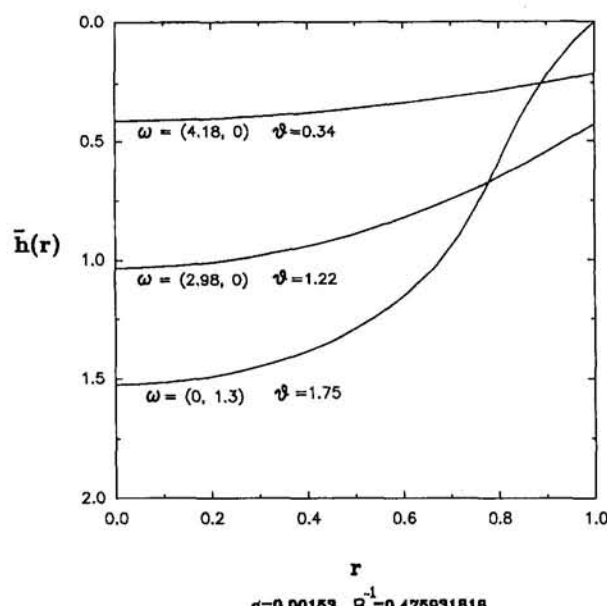


Fig. 2 Shapes of meniscus for three different liquid volumes

where V is the eigenvector

$$V = [h_1, \dots, h_N, b_1, \dots, b_N, d_1, \dots, d_N]^T,$$

and the elements of the matrices $[A]$ and $[C]$ are given by

$$\begin{aligned} a_{mn} &= \int_0^1 J_o(k_m r) J_o(k_n r) r dr = a_{N+m,n} \\ a_{2N+m,N+n} &= \int_0^1 J_o(k_m r) [1 - \cosh(k_n h)] J_o(k_n r) r dr, \\ a_{2N+m,2N+n} &= q \int_0^1 J_o(k_m r) J_o(k_n r) [\exp(-k_n h) - 1] r dr, \\ C_{m,N+n} &= -k_n \int_0^1 J_o(k_m r) \{ J_o(k_n r) \sinh(k_n h) \\ &\quad + h_r J_1(k_n r) \cosh(k_n h) \} r dr, \\ C_{N+m,2N+n} &= k_n \int_0^1 J_o(k_m r) \{ J_o(k_n r) \\ &\quad - h_r J_1(k_n r) \} \exp(-k_n h) r dr, \\ C_{2N+m,n} &= \int_0^1 J_o(k_m r) \{ (1 - q) J_o(k_n r) \\ &\quad + We[Q^{-3/2} k_n^2 J_o''(k_n r) \\ &\quad - (Q^{-1/2} r^{-1} - r^{-1} Q^{-3/2} h^2 \\ &\quad - 3 Q^{-5/2} h_r h_{rr}) k_n J_1(k_n r)] \} r dr, \\ &\quad (m = 1 \text{ to } N, n = 1 \text{ to } N); \end{aligned}$$

where J_o'' denotes second derivatives with respect to the argument of J_o . Note $h = h_1 + \bar{h}$ in the integrands. Thus the stability criteria will not only depend on B and q but also the pressure difference $(p_a - p_b)/(1 - q)$. Although h_1 is a constant for given p_a , p_b , and q . For numerical demonstration, we consider only the case of $p_a = p_b$, i.e., the case of a static liquid column supported solely by surface tension without help from the pressure difference $p_a - p_b$. For the case of $p_b < p_a$ the stable column is expected to be higher. For the case of $p_b > p_a$, the stable column is expected to be shorter. Hence the numerical results to be given are for the borderline case, but with some generic feature among all three cases. The eigenvalues of the system Eq. (9) have been solved with the values of N required for the accuracy up to the third decimal point. N was found to be ten over the parameter range considered here. The integrals

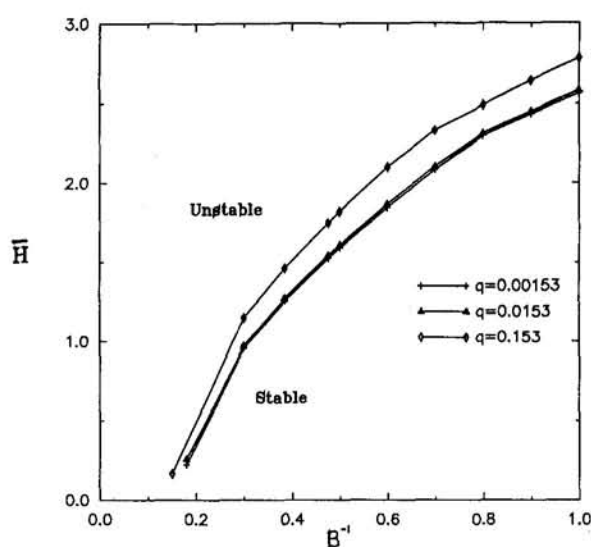


Fig. 3 Neutral curves for three different density ratios

Table 1 Unstable pendent with $q = 0.00153$

B^{-1}	0.30	0.39	0.48
ω^i	0.29	0.99	1.30
$h(o)$	0.90	1.19	1.44
$\theta(\text{rad})$	1.22	1.55	1.75

involving h are evaluated numerically by use of SLATEK subroutine dga458.

Results

There are two independent parameters in this problem, i.e., B and q , since we consider only the case of $p_b = p_a$. For each set of given (B, q) , static menisci are determined from Eq. (1) with Eq. (2) for different values of $h(o)$. Three such profiles are given in Fig. 2. The eigenvalue with the largest imaginary part corresponding to these three profiles are given in the figure. The real parts of the frequencies are given as the first numbers in the parentheses. The second numbers in the parentheses are the imaginary part of the frequencies. For the two basic states with smaller $h(o)$, the imaginary parts of ω are o . Thus, they are neutrally stable according to linear theory. The real parts of ω decrease as $h(o)$ is increased. Thus the frequency of oscillation decreases with increasing volume. However, the pendent drop with the largest $h(o)$ has a conjugate pair of frequency with zero real part. Hence this shape is hydrodynamically unstable. Moreover, the instability is nonoscillatory, i.e., monotonic. It appears that there exists a critical $h(o)$, beyond which the pendent drop is monotonically unstable for each pair of given (B, q) . The monotonic behavior of disturbance is probably due to the assumption that the interline is moveable. If the interline is held fixed and B is sufficiently small, the instability may be, on physical ground, conjectured to be oscillatory. The critical height $h_c(o) = \bar{H}$ is obtained for different pairs of (B, q) , and the results are given in Fig. 3. The interfacial tension and the ambient gas density are both stabilizing in a sense that the critical height can be increased by increasing their values. It is seen from Fig. 3 that there exists, for each given value of q , a critical Bond number, above which a flat interface, $\bar{H} = 0$, cannot be maintained. For $q = 0.00153$, B_c is approximately 6.897, and for $q = 0.153$ it is approximately 8.00. Our B is related to Dussan's surface tension parameter G by

$$G = 4(1 - q)B. \quad (10)$$

It was found from energy stability analysis that the flat interface of a liquid column over air is conditionally stable if

$$G < (3.83171)^2. \quad (11)$$

Substituting the critical Bond number for $q = 0.00153$ into Eq. (10), we find

$$G = 27.545,$$

which is larger than the critical value given in Eq. (11). Similarly for $q = 0.153$, we find the critical value of G to be 27.545 which is again larger than the critical value of G given by the energy theory. Thus the energy theory gives a rather conservative estimate. It should be pointed out that while the contact line is assumed to be immovable in the energy theory, it is assumed here to move with the fluids along the tube wall. However, the comparison is quite appropriate since the contact line motion is infinitesimal in the present theory, and the dynamic of contact line is not considered in both theories. It should be pointed out that for the case considered $p_b = p_a$, $q \neq 1$, we have $h_1 = 0$. Hence $h \rightarrow h_1 = 0$ for a flat interface. The liquid column is then reduced to a membrane. The comparison with the results of energy theory in this limiting case remains meaningful, because the energy stability results are valid for any h .

Table 1 gives the growth rates, the liquid pendent heights, and the contact angles for three different values of B , for the

Table 2 Unstable pendent with $q = 0.0153$

B^{-1}	0.30	0.39	0.48
ω_i	0.37	1.28	1.95
$h(o)$	0.97	1.27	1.54
$\theta(\text{rad})$	1.24	1.56	1.75

unstable pendent drop at $q = 0.00153$. This value of q corresponds to the case of an ethyl alcohol pendent in air under 1 atm at room temperature. Similar informations on the three characteristic quantities are given in Table 2 for the case of $q = 0.0153$. It is seen that all three characteristic quantities increase with B^{-1} and q . However, the change in contact angle is relatively insignificant, in view of the fact that the density of the gas is increased by tenfold from Table 1 to Table 2. It may be worth pointing out that the theory is still applicable when the ambient gas is replaced by liquid. Then the effect of the ambient liquid density will be more pronounced than that shown in this work.

The basic state is in static equilibrium. At the onset of instability the flow is largely irrotational within the viscous diffusion time. Hence the onset condition of instability predicted by the present theory is probably adequate. The subsequent nonlinear evolution of the unstable flow, however, will certainly be affected by viscosity. Physics of interline remains to be understood before a more complete theory can be advanced.

Conclusions

A liquid column resting above a gas in a vertical cylindrical pipe without suction at the closed upper end of the pipe, and

without help from interline force may be stably held against the action of gravity by virtue of the interfacial tension only if the height of the liquid column is sufficiently small. The critical height above which the column is unstable is shown to increase with the gas to liquid density ratio for a given Bond number. For a given density ratio, the critical height decreases with the Bond number. For the special case of a flat interface it is shown that the critical Bond number for the linear instability is larger than the known critical value predicted by the energy method, as expected. At the onset, the instability is monotonic without oscillation.

Acknowledgments

This work was supported in part by Grants No. DAAL 03-89-K-0179 of ARO, No. MSM-8817372 of NSF and a New York State Science Foundation Grant. The computation was carried out with the computer facility at Clarkson University and with the Cornell National Computer facility, which is funded by NSF, the State of New York and IBM Corporation.

References

- Dussan V., E. B., 1975, "Hydrodynamic stability and instability of fluid systems with interfaces," *Archives of Rational Mechanics and Analysis*, Vol. 57, p. 363.
- Huh, C., 1969, "Capillary Hydrodynamics-Interfacial instability and the solid-liquid-fluid contact line," Ph.D. thesis, University of Minnesota.
- Joseph, D. D., 1976, *Stability of Fluid Motion*, Springer-Verlag, New York.
- Lin, S. P., and Ibrahim, E. A., 1990, "Instability of a viscous liquid jet surrounded by a viscous gas in a pipe," *Journal of Fluid Mechanics*, Vol. 218, p. 641.
- Pitts, E., 1973, "The stability of pendent liquid drops, Part 1. Drops formed in a narrow gap," *Journal of Fluid Mechanics*, Vol. 59, p. 753.
- Pitts, E., 1974, "The stability of pendent liquid drops, Part 2. Axial symmetry," *Journal of Fluid Mechanics*, Vol. 63, p. 487.

Hydroelastic Vibration of Rectangular Plates

Moon K. Kwak

Department of Mechanical Engineering,
Dongguk University,
26, Pil-Dong 3-GA, Joong-Gu,
Seoul 100-715, Korea

This paper is concerned with the virtual mass effect on the natural frequencies and mode shapes of rectangular plates due to the presence of the water on one side of the plate. The approximate formula, which mainly depends on the so-called nondimensionalized added virtual mass incremental factor, can be used to estimate natural frequencies in water from natural frequencies in vacuo. However, the approximate formula is valid only when the wet mode shapes are almost the same as the one in vacuo. Moreover, the nondimensionalized added virtual mass incremental factor is in general a function of geometry, material properties of the plate and mostly boundary conditions of the plate and water domain. In this paper, the added virtual mass incremental factors for rectangular plates are obtained using the Rayleigh-Ritz method combined with the Green function method. Two cases of interfacing boundary conditions, which are free-surface and rigid-wall conditions, and two cases of plate boundary conditions, simply supported and clamped cases, are considered in this paper. It is found that the theoretical results match the experimental results. To investigate the validity of the approximate formula, the exact natural frequencies and mode shapes in water are calculated by means of the virtual added mass matrix. It is found that the approximate formula predicts lower natural frequencies in water with a very good accuracy.

1 Introduction

When the structure is in contact with water or immersed in water, the vibration of the structure is transferred to the water and give rise to water motion. As a result, there is a discernible increase in the kinetic energy due to the additional kinetic energy of the water. Because of increase in the kinetic energy, the natural frequencies of structures which are in contact with water, or immersed in water, decrease significantly compared to the natural frequencies in vacuo. This problem is referred to as the fluid-structure interaction problem or the hydroelastic vibration of structures. This kind of coupling problem does not permit the exact solution with ease. However, there have been theoretical approaches to the problem of circular and rectangular plates in contact with water based on the assumption that the mode shapes do not change under the influence of the water. This assumption leads to the following approximate formula

$$f_w = \frac{f_a}{\sqrt{1 + \beta \Gamma}} \quad (1)$$

where f_w is the natural frequency in water, f_a is the natural frequency in vacuo, $\beta = \rho_w a / \rho_p h$ is a nondimensional parameter called a thickness correction factor in which ρ_w and ρ_p are the mass densities of the water and the plate, a is the width for rectangular plates and the radius for circular plates, h is the thickness of plates, and Γ is a nondimensional parameter known as a nondimensionalized added virtual mass incremental (NAVMI) factor which mainly depends on the mode shape, respectively. The NAVMI factor, Γ , reflects the ratio of the kinetic energy of the water and the kinetic energy of the plate. This formula is very handy for the calculation of the natural frequency change since the natural frequency in water can be

calculated based on the natural frequency in vacuo and the NAVMI factor. Hence, the determination of the NAVMI factor is of prime interest in this case. However, currently the available NAVMI factors are limited to the special cases of circular and rectangular plates. If the structure and the water domain becomes complex, then we should seek the solution with the aid of the fluid finite element method (FFEM) (Zienkiewicz and Newman, 1969; Chowdhury, 1972; Marcus, 1978; Muthuverappan et al., 1978, 1979, 1980; Rao, 1985) or the Green function method (Fu and Price, 1987) for the water domain in conjunction with the structural finite element method. Due to the difficulty in the theoretical approach to the addressed problem, experiments have been also conducted (Carmichael, 1960, Lindholm et al., 1965; Morel, 1979).

Based on the assumption that the wet mode shapes are almost the same as the one in vacuo, Lamb (1920) calculated the change in natural frequencies of a thin clamped circular plate in an aperture of an infinite rigid plane wall in contact with water. By employing Lamb's approach, McLachlan (1932) extended Lamb's work to the free circular plate and Peak and Thurston (1954) generalized the work of Lamb and McLachlan. Powell and Roberts (1923) experimentally verified the theoretical results of Lamb's. Espinosa and Juarez (1984) calculated the pressure distribution of water numerically and compared theoretical results with Experimental results for the free-edge circular plate. Since these works are mostly related to the fundamental mode of the circular plate, Kwak (1994) generalized the approach by employing the Fourier-Bessel series and obtained the NAVMI factors for higher modes. He also studied the effect of water on the mode shape and found that the fundamental mode shape remains the same under the influence of water but higher mode shapes change. Since the Lamb's case is limited to the plate placed in the aperture of the rigid wall, his approach can not be applied to the case of the plate independently resting on the free surface or fully immersed in water. Thus, Kwak and Kim (1991) and Kwak (1991) solved the mixed boundary value problem and obtained NAVMI factors for circular plates independently resting on the free surface. All of these works are concerned with circular plates.

Compared to the theoretical achievement on the circular plates in contact with water, there are only few available theore-

Contributed by the Applied Mechanics Division of THE AMERICAN SOCIETY OF MECHANICAL ENGINEERS for publication in the ASME JOURNAL OF APPLIED MECHANICS.

Discussion on this paper should be addressed to the Technical Editor, Professor Lewis T. Wheeler, Department of Mechanical Engineering, University of Houston, Houston, TX 77204-4792, and will be accepted until four months after final publication of the paper itself in the ASME JOURNAL OF APPLIED MECHANICS.

Manuscript received by the ASME Applied Mechanics Division, July 11, 1994; final revision, Oct. 26, 1994. Associate Technical Editor: T. R. Akylas.

ical results on the vibration of rectangular plates in contact with water. Kito (1944) calculated the added virtual mass of rectangular plates by Fourier series method. He replaced the plate in an aperture of an infinite rigid wall by the equivalent problem consisting of many plates which are in opposite phase with the plate of interest. This approach enables the Fourier series expansion so that the plate can be regarded as being chordwisely semi-finite and lengthwisely semi-finite. Green-spon (1960) calculated the effect of water on the natural frequency by using the piston theory, which leads to the erroneous result that the added virtual mass effect is nullified in some modes. Kim (1978) for the first time derived the expression in terms of series for the added virtual mass of the simply supported rectangular plate which is chordwisely finite and lengthwisely semi-finite by using the Mathieu function. His work is the extended version of Kito's work. However, Kim's work is unique compared to the previous results since the rectangular plate is placed inside the water domain independently without any additional supporting structure. Considering the boundary condition that Kim considered in his paper, it becomes evident that the plate is pseudo independent. In later papers (Kim and Kim, 1978, Kim, Kim, and Lee, 1979), he studied the effect of supporting boundary conditions of plates and presented experimental results which verified his theoretical results. It should be noted here again that Kito (1944) and Kim (1978) fail to realize the exact boundary condition for either the plate in an infinite baffle or the plate independently resting on a free surface or fully immersed in water. This motivated the current research on the hydroelastic vibration of rectangular plates.

In this paper, an attempt is made to clarify the discrepancies found in theoretical and experimental works. To this end, the NAVMI factors are obtained for uniform rectangular plates having simply supported and clamped boundary conditions, and vibrating in contact with water. Two cases are considered for the outside boundary condition, i.e., the case of the plate placed in an aperture of an infinite rigid plane wall and the case of the plate independently resting on a free surface. The case of the plate fully immersed in water amounts to the case in which both sides of the plate are in contact with water, so that the NAVMI factor in this case is the twice the value of the one for the plate independently resting on a free surface.

Compared to the case of circular plates, the boundary value problem does not possess the closed-form expression. Thus, we should resort to the numerical approach. In this paper, the Green function is employed to solve the boundary value problem of the water domain. Since the resulting integral equation does not yield the exact form, we discretize the interfacing domain into a multitude of a small panel, which can be regarded as the Boundary Element Method (BEM). This method is then combined with the Rayleigh-Ritz method, leading to the equation of motion for rectangular plates in contact with water. As a result, the added virtual mass matrix is obtained instead of NAVMI factors which are in fact the diagonal terms of the added virtual mass matrix. The accuracy of the approximate formula is tested by calculating natural frequencies by solving the eigenvalue problem consisting of the plate mass and stiffness matrices and the virtual added mass matrix. Numerical results show that the approximate formula provide good accuracy for the first four modes. The theoretical results obtained in this paper are in good agreement with the experimental results.

2 Kinetic and Potential Energies of Rectangular Plates in Air

Let us consider a rectangular plate vibrating in vacuo and assume that the thickness, h , of the plate is very thin compared to the width, a , and the length, b . Introducing nondimensionalized variables, $\xi = x/a$ and $\eta = y/b$ and using the Rayleigh-Ritz method, we can expand the displacement vector in terms

of the admissible functions multiplied by the time-dependent generalized displacement vector.

$$w(\xi, \eta, t) = W(\xi, \eta) \mathbf{q}(t) \quad (2)$$

where $W = [X_1(\xi)Y_1(\eta) \ X_2(\xi)Y_2(\eta) \ \dots \ X_n(\xi)Y_n(\eta)]$ represent the vector of the admissible functions in which $X_i(\xi)$ and $Y_i(\eta)$ represent the admissible functions in x and y -directions and n is the number of the admissible functions, respectively, and $\mathbf{q}(t) = [q_1 \ q_2 \ \dots \ q_n]^T$ represents the generalized velocity. Then, the kinetic and potential energies can be expressed as

$$T_p = \frac{1}{2} \rho_p h a b \dot{\mathbf{q}}^T M_p^* \dot{\mathbf{q}}, \quad V_p = \frac{1}{2} \frac{D b}{a^3} \mathbf{q}^T K_p^* \mathbf{q} \quad (3a, b)$$

where ρ_p is the mass density of the plate, $D = Eh^3/12(1 - \nu^2)$, E is the Young's modulus, ν is the poisson's ratio, and the element of M_p^* and K_p^* are expressed as

$$(M_p^*)_{ij} = E_{ij}^x E_{ij}^y, \quad i, j = 1, 2, \dots, n \quad (4a)$$

and

$$(K_p^*)_{ij} = G_{ij}^x E_{ij}^y + \frac{1}{\delta^4} E_{ij}^x G_{ij}^y + \frac{2(1 - \nu)}{\delta^2} F_{ij}^x F_{ij}^y \\ + \frac{\nu}{\delta^2} (H_{ji}^x H_{ij}^y + H_{ij}^x H_{ji}^y), \quad i, j = 1, 2, \dots, n \quad (4b)$$

in which $\delta = b/a$ represents the aspect ratio of the rectangular plate and

$$E_{ij}^x = \int_0^1 X_i X_j d\xi, \quad E_{ij}^y = \int_0^1 Y_i Y_j d\eta, \\ F_{ij}^x = \int_0^1 X_i' X_j' d\xi, \quad F_{ij}^y = \int_0^1 Y_i' Y_j' d\eta \quad (5a-d) \\ G_{ij}^x = \int_0^1 X_i'' X_j'' d\xi, \quad G_{ij}^y = \int_0^1 Y_i'' Y_j'' d\eta, \\ H_{ij}^x = \int_0^1 X_i X_j'' d\xi, \quad H_{ij}^y = \int_0^1 Y_i Y_j'' d\eta \quad (5e-h)$$

where ' indicates the derivative. Eigenfunctions of the beam corresponding to the boundary condition of the plate are used as admissible functions for the evaluation of the integrals shown in Eqs. (5).

3 Added Virtual Mass

The boundary value problem of the plate in contact with water can be solved by using the Green function method. This implies that sources of unknown strength $\sigma(Q, t)$ are distributed on each panel over the water-vacuo or water-solid interface which includes the plate area. This approach is equivalent to the boundary element method. The velocity potential at a nominal position P in the water is then given by

$$\phi(P, t) = \frac{1}{4\pi} \iint_S \sigma(Q, t) G(P, Q) dS \quad (6)$$

where G is the Green function which satisfies the boundary conditions. In general, G has the form of

$$G(P, Q) = \frac{1}{|P - Q|} + G^*(P, Q) \quad (7)$$

where $G^*(P, Q)$ is introduced to compensate the boundary conditions such as bottom boundary condition, free-surface condition, etc. In this paper, the water is assumed to be unbounded so that $G^* = 0$. In addition,

$$|P - Q| = \sqrt{(x_p - x_q)^2 + (y_p - y_q)^2 + (z_p - z_q)^2}. \quad (8)$$

The unknown source strength σ can be determined from the integral equation

$$-\frac{1}{2} \sigma(P, t) + \frac{1}{4\pi} \iint_S \sigma(P, t) \frac{\partial G(P, Q)}{\partial n} dS = v(P, t) \quad (9)$$

where v is the normal velocity at the point of interest. In the case of flat surface, $(\partial G(P, Q)/\partial n)$ becomes zero. Hence, the source strength can be expressed in terms of the normal velocity given on the interfacing surface.

$$\sigma(x_p, y_p, t) = -2v(x_p, y_p, t) \quad (10)$$

Inserting Eq. (10) into Eq. (6), we can obtain the velocity potential at the interface

$$\phi(x_p, y_p, t) = -\frac{1}{2\pi} \iint_S \frac{v(x_p, y_p, t)}{\sqrt{(x_p - x_q)^2 + (y_p - y_q)^2}} dS. \quad (11)$$

Considering that beam eigenfunctions are used as admissible functions, it becomes evident that the exact integration is not available for such functions. Thus, we should resort to the numerical approach. Let us divide the interfacing surface into a multitude of a small panel and assume that the source strength and the velocity potential are uniform in each panel. This approach amounts to the collocated method used in the numerical evaluation of integral equations. Hence, the velocity potential in the i th panel can be written as

$$\begin{aligned} \phi_i(x_i, y_i, t) &= -\frac{1}{2\pi} \\ &\times \sum_{j=1}^m v_j \int_{x_j - (\Delta x/2)}^{x_j + (\Delta x/2)} \int_{y_j - (\Delta y/2)}^{y_j + (\Delta y/2)} \frac{dxdy}{\sqrt{(x - x_i)^2 + (y - y_i)^2}} \end{aligned} \quad (12)$$

where m is the number of square elements used to cover the interfacing area of interest. In matrix form, we may write

$$\phi = -\frac{\Delta y}{4\pi} \mathbf{A} \mathbf{v} \quad (13)$$

where $\phi = [\phi_1 \ \phi_2 \ \dots \ \phi_m]^T$ and $\mathbf{v} = [v_1 \ v_2 \ \dots \ v_m]^T$ and

$$A_{ij} = \frac{2}{\Delta y} \int_{x_j - (\Delta x/2)}^{x_j + (\Delta x/2)} \int_{y_j - (\Delta y/2)}^{y_j + (\Delta y/2)} \frac{dxdy}{\sqrt{(x - x_i)^2 + (y - y_i)^2}}. \quad (14)$$

For simplicity, let us consider a square panel, i.e., $\Delta x = \Delta y$. By introducing local variables,

$$x = x_j + \frac{\Delta x}{2} \xi, \quad y = y_j + \frac{\Delta y}{2} \eta, \quad (15a, b)$$

and nondimensionalized variables,

$$\xi_{ij} = \frac{2(x_i - x_j)}{\Delta x}, \quad \eta_{ij} = \frac{2(y_i - y_j)}{\Delta y}, \quad (16a, b)$$

we can derive

$$A_{ij} = \int_{-1}^1 \int_{-1}^1 \frac{d\xi d\eta}{\sqrt{(\xi - \xi_{ij})^2 + (\eta - \eta_{ij})^2}}. \quad (17)$$

The evaluation of the above integral was carried out using Mathematica (Wolfram, 1988) and the following were obtained:

$$A_{ij} = \begin{cases} 7.050989 & i = j \\ I(\xi_{ij}, \eta_{ij}) & i \neq j \end{cases} \quad (18)$$

in which

$$\begin{aligned} I(\xi_{ij}, \eta_{ij}) &= (1 - \eta_{ij}) \log \frac{1 - \xi_{ij} + \delta_1}{-1 - \xi_{ij} + \delta_2} \\ &+ \log (1 - \eta_{ij} + \delta_1)(1 - \eta_{ij} + \delta_2) \\ &+ \xi_{ij} \log \frac{-1 + \eta_{ij} + \delta_1}{-1 + \eta_{ij} + \delta_2} + (1 + \eta_{ij}) \log \frac{1 - \xi_{ij} + \delta_3}{-1 - \xi_{ij} + \delta_4} \\ &- \log (-1 - \eta_{ij} + \delta_3) - \log (-1 - \eta_{ij} + \delta_4) \\ &+ \xi_{ij} \log \frac{1 + \eta_{ij} + \delta_4}{1 + \eta_{ij} + \delta_3} \end{aligned}$$

where

$$\begin{aligned} \delta_1 &= \sqrt{(\xi_{ij} - 1)^2 + (\eta_{ij} - 1)^2}, \quad \delta_2 = \sqrt{(\xi_{ij} + 1)^2 + (\eta_{ij} - 1)^2} \\ \delta_3 &= \sqrt{(\xi_{ij} - 1)^2 + (\eta_{ij} + 1)^2}, \quad \delta_4 = \sqrt{(\xi_{ij} + 1)^2 + (\eta_{ij} + 1)^2}. \end{aligned}$$

We can decompose the matrix Eq. (13) into sub equations belonging to the plate area and the outside area of the plate. Hence, we may write

$$\begin{Bmatrix} \phi_p \\ \phi_o \end{Bmatrix} = -\frac{\Delta y}{4\pi} \begin{bmatrix} A_{pp} & A_{po} \\ A_{op} & A_{oo} \end{bmatrix} \begin{Bmatrix} \mathbf{v}_p \\ \mathbf{v}_o \end{Bmatrix} \quad (19)$$

where subscripts p and o denote the plate and the outside, A_{pp} is an $l \times l$ matrix, in which l is the number of elements belonging to the plate area, A_{po} is an $l \times (m - l)$ matrix, A_{op} is an $(m - l) \times l$ matrix, and A_{oo} is an $(m - l) \times (m - l)$ matrix, respectively. In the case that the plate is placed in an aperture of a rigid wall, then the outer boundary condition becomes $\mathbf{v}_o = 0$ and if the plate is resting independently on the free surface, then $\phi_o = 0$. Thus, we may write the following equation for both cases

$$\phi_p = -\frac{\Delta y}{4\pi} A^* \mathbf{v}_p \quad (20)$$

where

$$A^* = \begin{cases} A_{pp} & \text{for rigid wall} \\ A_{pp} - A_{po} A_{oo}^{-1} A_{op} & \text{for free surface.} \end{cases} \quad (21)$$

Using the same assumption used for the evaluation of the velocity potential, the kinetic energy of the water can be obtained by the summation of individual kinetic energy of each panel.

$$T_w = -\frac{1}{2} \rho_w \sum_{i=1}^m \iint_{S_i} \phi_i \mathbf{v}_i dS_i \quad (22)$$

The summation is carried out only for the plate domain since the product, $\phi_i \mathbf{v}_i$, becomes zero outside the plate in either case. Hence, we obtain

$$T_w = -\frac{1}{2} \rho_w \Delta x \Delta y \mathbf{v}_p^T \phi_p. \quad (23)$$

At the water-plate interface, we have the relation

$$\mathbf{v}_p = \Psi \mathbf{q} \quad (24)$$

where

$$\Psi = \begin{bmatrix} \Phi_1(x_1, y_1) & \Phi(x_1, y_1) & \dots & \Phi_n(x_1, y_1) \\ \Phi_1(x_2, y_2) & \Phi(x_2, y_2) & \dots & \Phi_n(x_2, y_2) \\ \vdots & \vdots & \ddots & \vdots \\ \Phi_1(x_l, y_l) & \Phi(x_l, y_l) & \dots & \Phi_n(x_l, y_l) \end{bmatrix}. \quad (25)$$

Inserting Eq. (20) into Eq. (23) and using Eq. (24), we obtain

$$T_w = \frac{1}{2} \dot{\mathbf{q}}^T M_w \dot{\mathbf{q}} \quad (26)$$

where

$$M_w = \frac{\rho_w \Delta x \Delta y^2}{4\pi} \Psi^T A^* \Psi \quad (27)$$

represents the added virtual mass matrix due to the presence of the water. As indicated by Eq. (27), the evaluation of the added virtual mass matrix depends on the evaluation of the matrix A^* , i.e., A given by Eq. (14). Since the square element is considered in the discretization process, $\Delta x = \Delta y = a/N$ where N is the number of divisions in x direction, we can rewrite Eq. (27) in the form

$$M_w = \rho_w a^2 b M_w^* \quad (28)$$

where

$$M_w^* = \frac{1}{4\pi N^3 \delta} \Psi^T A^* \Psi. \quad (29)$$

4 Equation of Motion

Using Hamilton's principle and Eq. (26), and considering Eqs. (3) and (28), we can obtain the equation of motion for the rectangular plate vibrating in contact with water.

$$[M_p^* + \beta M_w^*] \ddot{\mathbf{q}} + \frac{D}{\rho_p h a^4} K_p^* \mathbf{q} = 0. \quad (30)$$

Hence, the eigenvalue problem can be written as

$$|K_p^* - \lambda[M_p^* + \beta M_w^*]| = 0 \quad (31)$$

where $\lambda = \rho_p h a^4 \omega^2 / D$. It has been assumed in the previous research that the normal modes do not change when the water is present. In order to investigate the validity of this assumption, let us use the eigenvalue and eigenvector of the plate vibrating in vacuo. Using eigenvectors, eigenvalues, and the orthonormality relations, $U_p^T M_p^* U_p = I$ and $U_p^T K_p^* U_p = \Lambda_p$, we obtain

$$|\Lambda_p - \lambda[I + \beta \bar{M}_w^*]| = 0 \quad (32)$$

where $\bar{M}_w^* = U_p^T M_w^* U_p$. The assumption that mode shapes do not change under the presence of water amounts to saying that \bar{M}_w^* is a diagonal matrix. If this is true, then we may write

$$\lambda_{wi} = \lambda_{ai} / \sqrt{1 + \beta \Gamma_i} \quad (33)$$

where $\Gamma_i = (\bar{M}_w^*)_{ii}$ represents the nondimensionalized added virtual mass incremental factor for the i th mode. However, it is observed that \bar{M}_w^* is a diagonally dominant matrix but off-diagonal terms affect the mode shapes, so that the assumption is violated to some extent as shown in the numerical example.

5 Numerical Results

A question arising in the evaluation of the integral is how many elements are necessary for the convergence of the added virtual mass matrix. It was found from numerical experiments that 100 elements, which imply ten divisions in x and y -directions, are enough for the practical application.

Figure 1 shows the NAVMI factors for the first four modes of the simply supported rectangular plates resting on a free surface, where the numbers inside parenthesis represent the

number of nodal lines in x and y -directions. In Fig. 1, the dashed lines are the theoretical results obtained by Kim (1978) and symbols represent the experimental results obtained by Kim, Kim, and Lee (1979). The matrix A^* needs to be computed in order to evaluate the added virtual mass matrix. To this end, we need a fairly large water domain. Numerical experiments show that the area which is 4 times larger than the plate area is enough for practical applications. The calculation of A^* requires enormous CPU time and the inversion of the partial matrix shown in Eq. (21) also requires more CPU time. For instance, if we divide the square plate area into 100 elements, then we need at least 400 elements for the interfacing area and should invert a 300 by 300 matrix. This is not desirable from the viewpoint of computer floating point operations and the memory management. It should be mentioned that the numerical calculation performed for this research is very time-consuming and inefficient. As an alternative, one may consider the approach which shifts the pressure as the dependent variable within the Green's integral (Terai, 1980) for the case of plates independently resting on a free surface. However, as shown in the figure, the theoretical results obtained in this paper are very good agreement with experimental results and lower than those obtained by Kim (1978). This becomes evident since the rectangular plate considered by Kim is semi-finite in lengthwise.

Figure 2 shows the NAVMI factors for the first four modes of the simply supported rectangular plates placed in the aperture of the infinite rigid plane wall. It can be readily seen that the NAVMI factors of this case is larger than those for the plates resting on the free surface. This is due to the fact that the rigid wall constrains the motion of the water thus resulting in increase in the kinetic energy. The dashed line is the theoretical result for the fundamental mode obtained by Kito (1944). There is no experimental data for this case.

Figure 3 shows the NAVMI factors for the first 4 modes of the clamped rectangular plates resting independently on a free surface when $\nu = 0.3$. The same area of the water domain as the one used for the simply supported plates is considered. Symbols represent the experimental results obtained by Kim, Kim, and Lee (1979). As shown in the figure, the theoretical results obtained in this paper are good agreement with experimental results.

Figure 4 shows the NAVMI factors for the first 4 modes of the clamped rectangular plates placed in the aperture of the infinite rigid plane wall. It can be also seen as in the case of the simply supported plate that the NAVMI factors of this case is larger than those for the plates resting on the free surface. This can be explained by the same physical phenomena as in

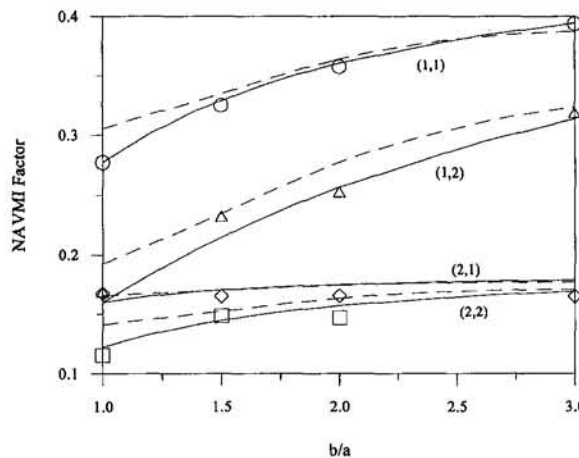


Fig. 1 NAVMI factor for the simply supported rectangular plates resting on a free surface (dashed lines: theoretical results by Kim (1978), symbols: experiments by Kim, Kim, and Lee (1979))

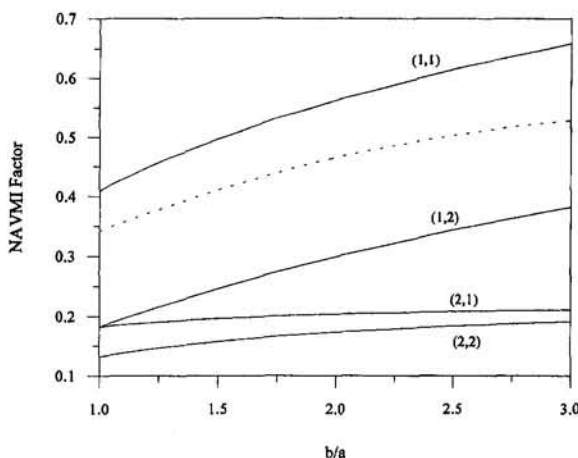


Fig. 2 NAVMI factor for the simply supported rectangular plates placed in an aperture of the rigid wall (dashed line: (1, 1) by Kito (1944))

the case of the simply-supported plates. There is no experimental data for this case.

It is found that the NAVMI factors of the simply supported plate is larger than those of the clamped plate. This can be explained by the fact that the vibration amplitude of the simply-supported plate is larger than that of the clamped plate due to the rotational freedom along its edge. This has also been observed in the case of circular plates (Kwak, 1991).

To answer the question regarding the accuracy of the approximate formula, the added virtual mass matrix was calculated by using 25 admissible functions for the case of simply-supported square plate vibrating in the aperture of an infinite plane rigid wall. As shown in Fig. 5, errors of natural frequencies for the first four modes remain very small even for large value of β which implies high water effect on the plate. Thus, it can be concluded that the approximate formula is valid for the first four modes of the plate. Although wet mode shapes for the lowest four modes do not change significantly from dry mode shapes, it was observed that the higher wet mode shapes change thus resulting in new breed of mode shapes among natural mode shapes.

6 Discussion and Conclusions

When the structure is in contact with water or immersed in water, there is a discernible increase in the kinetic energy due to the additional kinetic energy of the water. The problem associated with this phenomena is called the hydroelastic vibration.

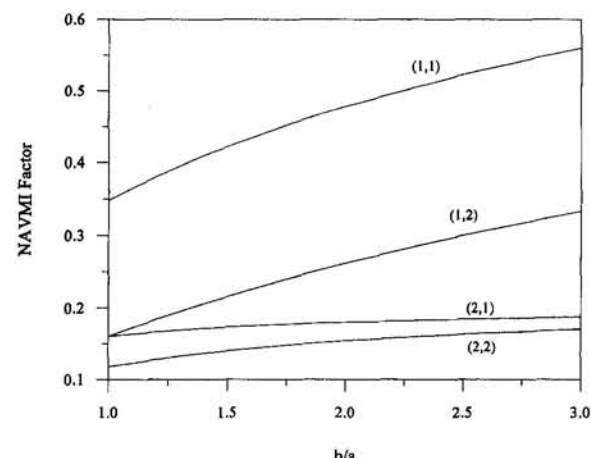


Fig. 4 NAVMI factor for the clamped rectangular plates placed in an aperture of the rigid wall

This paper is concerned with the hydroelastic vibration of rectangular plates.

Traditionally, the approximate formula has been used for the prediction of changes in natural frequencies of plates in contact with water, which mainly depends on the nondimensionalized added virtual mass incremental (NAVMI) factor. The NAVMI factor, Γ , reflects the ratio of the kinetic energy of the water and the kinetic energy of the plate. The validity of the approximate formula is governed by the assumption that mode shapes do not change under the influence of the water. However, this assumption has never been questioned for rectangular plates in contact with water even though it is found recently that mode shapes change in the case of circular plates (Kwak, 1994).

Compared to the theoretical achievement on the circular plates in contact with water, there are only few available theoretical results on the vibration of rectangular plates in contact with water. In this paper, an attempt is made to obtain the NAVMI factors for uniform rectangular plates having simply supported and clamped boundary conditions, and vibrating in contact with water. Two cases are considered for the outside boundary condition, i.e., the case of the plate placed in an aperture of the infinite rigid plane wall and the case of the plate independently resting on a free surface. Coupled boundary value problem was solved by employing the Green function. Since the boundary value problem addressed in this paper does not permit the closed-form expression, we should resort to the numerical approach. Hence, the interfacing area is discretized into a multi-

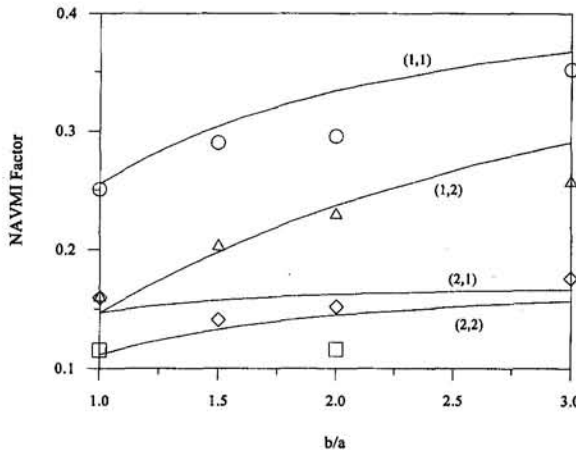


Fig. 3 NAVMI factor for the clamped rectangular plates resting on a free surface ($\nu = 0.3$, symbols: experiment by Kim, Kim, and Lee (1979))

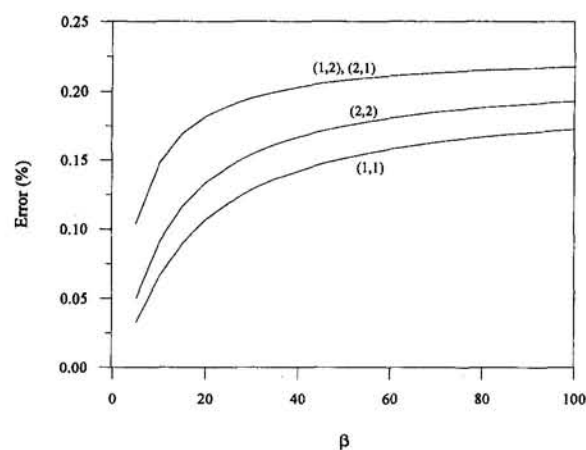


Fig. 5 Error in natural frequencies in water obtained by the approximate formula

tude of small elements, which is equivalent to the boundary element method. We then obtained the equation of motion by combining the kinetic and potential energies of the plate and the kinetic energy of the water. We solved the eigenvalue problem based on the mass and stiffness matrices and analyzed the effect of water on mode shapes as well as the accuracy of the approximate formula, where the mass matrix consists of the mass matrix of the plate and the virtual added mass matrix due to the presence of water.

It turns out that mode shapes change slightly for lower modes but change discernibly for some higher modes. Thus, we can conclude that the approximate formula guarantees very good accuracy for lower modes. The theoretical developments made in this paper were confirmed by comparing them to experimental results.

References

Carmichael, T. E., 1960, "Investigation into the Vibration of Ship's Plating: Part 3. The Effect of Entrained Water on the Vibration of Hull Plating below the Water-line," *The British Shipbuilding Research Association Report No. 305* (R.B. 1597).

Chowdhury, P. C., 1972, "Fluid Finite Elements for Added Mass Calculations," *International Shipbuilding Progress*, Vol. 19, pp. 302-309.

Espinosa, F. M., and Gallego-Juarez, J. A., 1984, "On the Resonance Frequencies of Water-Loaded Circular Plates," *Journal of Sound and Vibration*, Vol. 94, No. 2, pp. 217-222.

Fu, Y., and Price, W. G., 1987, "Interactions between a Partially or Totally Immersed Vibrating Cantilever Plate and the Surrounding Fluid," *Journal of Sound and Vibration*, Vol. 118, No. 3, pp. 495-513.

Greenspon, J. E., 1961, "Vibration of Cross-Stiffened and Sandwich Plates with Application to Underwater Sound Radiators," *Journal of Acoustical Society of America*, Vol. 33, No. 11, pp. 1485-1497.

Kim, K. C., 1977, "Calculation of Added Mass of a Rectangular Plate in Elastic Vibration," *PRADS*, Tokyo, Japan, Paper B-19.

Kim, K. C., and Kim, J. S., 1978, "The Effect of the Boundary Condition on the Added Mass of a Rectangular Plate," *Journal of the Society of Naval Architects of Korea*, Vol. 15, No. 2, pp. 1-11 (in Korean).

Kim, K. C., Kim, J. S., and Lee, H. Y., 1979, "An Experimental Study on the Elastic Vibration of Plates in Contact with Water," *Journal of the Society of Naval Architects of Korea*, Vol. 16, No. 2, pp. 1-7 (in Korean).

Kito, F., 1944, "On the Added Mass of Flat Plates Vibrating in Water," *Zotsan No. 266*, Zoxen Kyokai Japan, pp. 1-10 (in Japanese).

Kwak, M. K., and Kim, K. C., 1991, "Axisymmetric Vibration of Circular Plates in Contact with Fluid," *Journal of Sound and Vibration*, Vol. 146, No. 3, pp. 381-389.

Kwak, M. K., 1991, "Vibration of Circular Plates in Contact with Water," *ASME JOURNAL OF APPLIED MECHANICS*, Vol. 58, pp. 480-483.

Kwak, M. K., 1994, "Hydroelastic Vibration of Circular Plates," *ASME JOURNAL OF APPLIED MECHANICS*, submitted for publication.

Lamb, H., 1920, "On the Vibrations of an Elastic Plate in Contact with Water," *Proceedings of the Royal Society of London*, Vol. A98, pp. 205-216.

Lindholm, U. S., Kana, D. D., Chu, W. H., and Abramson, H. N., 1965, "Elastic Vibration Characteristics of Cantilever Plates in Water," *Journal of Ship Research*, Vol. 9, No. 1, pp. 11-22.

Marcus, M. S., 1978, "A Finite Element Method Applied to the Vibration of Submerged Plates," *Journal of Ship Research*, Vol. 22, No. 2, pp. 94-99.

McLachlan, N. W., 1932, "The Accession to Inertia of Flexible Discs Vibrating in a Fluid," *Proceedings of the Physical Society, London*, Vol. 44, pp. 546-555.

Morel, P., 1979, "Experimental Studies on the Subject of Virtual Intervenant in Vibrations of Naval Structures," *Bull. Tech. Bureau Veritas*, pp. 96-101 (in French).

Muthuverappan, G., et al., 1978, "Vibration of Square Cantilever Plate Immersed in Water," *Journal of Sound and Vibration*, Vol. 61, No. 3, pp. 467-470.

Muthuverappan, G., et al., 1979, "A Note on Vibration of a Cantilever Plate Immersed in Water," *Journal of Sound and Vibration*, Vol. 63, No. 3, pp. 385-391.

Muthuverappan, G., et al., 1980, "Influence of Fluid Added Mass on the Vibration Characteristics of Plate under Various Boundary Conditions," *Journal of Sound and Vibration*, Vol. 69, No. 4, pp. 612-615.

Peake, W. H., and Thurston, E. G., 1954, "The Lowest Resonant Frequency of a Water-Loaded Circular Plate," *Journal of the Acoustical Society of America*, Vol. 26, No. 7, pp. 166-168.

Powell, J. H., and Roberts, J. H. T., 1923, "On the Frequency of Vibration of Circular Diaphragms," *Proceedings of the Physical Society, London*, Vol. 35, pp. 170-182.

Rao, S. N., and Ganesan, N., 1985, "Vibration of Plates Immersed in Hot Fluids," *Computers & Structures*, Vol. 21, No. 4, pp. 777-787.

Tanida, K., 1981, "Elastic Vibration of Cantilever Plate Submerged in Water," *IHI Technical Report*.

Terai, T., 1980, "On Calculation of Sound Fields Around Three Dimensional Objects by Integral Equation Methods," *Journal of Sound and Vibration*, Vol. 69, No. 1, pp. 71-100.

Wolfram, S., 1988, *Mathematic: A System of Doing Mathematics by Computer*, Addison-Wesley, Redwood City, CA.

Zienkiewicz, O. C., and Newton, R. E., 1969, "Coupled Vibrations of a Structure Submerged in a Compressible Fluid," *Proceedings of Symposium on Finite Element Technique*, Stuttgart, West Germany, pp. 359-371.

Local Stability of Gyroscopic Systems Near Vanishing Eigenvalues

A. A. Renshaw

Department of Mechanical Engineering,
Columbia University,
500 W. 120th Street, 220 Mudd Building,
New York, NY 10027
Mem. ASME

C. D. Mote, Jr.

Department of Mechanical Engineering,
University of California,
Berkeley, CA 94720
Fellow ASME

Vanishing eigenvalues of a gyroscopic system are always repeated and, as a result of this degeneracy, their eigenfunctions represent a combination of constant displacements with zero velocity and the displacements derived from constant, nonzero velocity. In a second-order formulation of the equations of motion, the assumption of harmonic vibration is not sufficiently general to represent this motion as the displacements derived from constant, nonzero velocity are not included. In a first order formulation, however, the assumption of harmonic vibration is sufficient. Solvability criteria are required to determine the complete form of such eigenfunctions and in particular whether or not their velocities are identically zero. A conjecture for gyroscopic systems is proposed that predicts whether the eigenvalue locus is imaginary or complex in the neighborhood of a vanishing eigenvalue. If the velocities of all eigenfunctions with vanishing eigenvalues are identically zero, the eigenvalues are imaginary; if any eigenfunction exists whose eigenvalue is zero but whose velocity is nonzero, the corresponding eigenvalue locus is complex. The conjecture is shown to be true for many commonly studied gyroscopic systems; no counter examples have yet been found. The conjecture can be used to predict divergence instability in many cases without extensive computation.

1 Introduction

Gyroscopic systems include as examples translating and rotating strings, beams, membranes, and plates. These systems possess combinations of system parameters that produce vanishing eigenvalues. Such combinations of system parameters are designated herein as critical system parameters and their vanishing eigenvalues and the corresponding eigenfunctions as critical eigenvalues and critical eigenfunctions. For the examples listed above, critical eigenvalues occur at critical translation or rotation speeds.

The eigenvalue locus of a critical eigenfunction plotted as a function of a system parameter in the neighborhood of its critical value can be either imaginary, and therefore result in oscillatory solutions, or complex and indicate exponentially growing amplitudes. These two cases are normally distinguished by extensive computations. The goal of this paper is to provide an explanation for the different stabilities which can be applied without extensive computations. This explanation may also suggest techniques for controlling or improving the system's stability.

Stability criteria for gyroscopic systems have been formulated for both discrete and continuous systems. For discrete systems, the criteria usually relate the definiteness of a combination of the coefficient matrices in the equation of motion to the stability of the system (Huseyin et al., 1983; Inman, 1988; Huseyin, 1991). The extension of these criteria to continuous systems can only ensure stability when the system stiffness operator is positive definite (Shieh, 1971; Wickert and Mote, 1990). In the neighborhood of vanishing eigenvalues, the stiffness operator is not definite and these stability criteria do not apply. Other stability criteria have been developed to examine continuous

systems whose stiffness operator is not definite, but these criteria usually require knowledge of the system eigenfunctions (Shieh and Masur, 1968; Shieh, 1971), which is normally as difficult to obtain as the eigenvalues themselves.

The principal observation of this work is that, for both continuous and discrete gyroscopic systems at critical values of the system parameters, there may exist eigenfunctions describing the superposition of a constant displacement and the displacement derived from a constant, nonzero velocity. This form of eigenfunction is excluded from the solution space when harmonic vibration is assumed for the second order eigenvalue problem, but it is natural to the first-order eigenvalue problem (Wickert and Mote, 1990).

A stability conjecture is presented based on this observation that predicts whether the eigenvalue locus of a critical eigenfunction plotted as a function of a system parameter in the neighborhood of its critical value is imaginary or complex. Although no proof is furnished, the conjecture is shown to be true for many commonly studied gyroscopic systems, and no counter examples have yet been found. The conjecture can often be applied to predict divergence instability without computation if the shapes of the critical eigenfunctions are approximately known.

2 Equation of Motion

The equation of motion of a continuous (discrete) gyroscopic system is represented by

$$Mu_{,tt} + Gu_{,t} + Ku = f \quad (1)$$

where M , G , and K are linear differential (matrix) operators in the spatial domain, u is displacement, f is a forcing term, t is time, and a comma denotes partial differentiation. Symmetries of M , G , and K in the spatial domain give for all u and w satisfying appropriate boundary and continuity conditions

$$(Mu, w) = (u, Mw) \quad (Gu, w) = -(u, Gw) \quad (2)$$
$$(Ku, w) = (u, Kw)$$

Contributed by the Applied Mechanics Division of THE AMERICAN SOCIETY OF MECHANICAL ENGINEERS for publication in the ASME JOURNAL OF APPLIED MECHANICS.

Discussion on this paper should be addressed to the Technical Editor, Prof. Lewis T. Wheeler, Department of Mechanical Engineering, University of Houston, Houston, TX 77204-4792, and will be accepted until four months after final publication of the paper itself in the ASME JOURNAL OF APPLIED MECHANICS.

Manuscript received by the ASME Applied Mechanics Division, Aug. 6, 1993; final revision, May 19, 1994. Associate Technical Editor: F. Y. M. Wan.

where (\cdot, \cdot) is the inner product associated with (1). M is positive definite.

Equation (1) can be recast in first order form by defining the vectors

$$\mathbf{w} = [u, \dot{u}]^T \quad \mathbf{q} = [f, 0]^T \quad (3)$$

and the matrix differential operators

$$\mathbf{A} = \begin{bmatrix} M & 0 \\ 0 & K \end{bmatrix} \quad \mathbf{B} = \begin{bmatrix} G & K \\ -K & 0 \end{bmatrix}. \quad (4)$$

Equation (1) becomes

$$\mathbf{Aw}_t + \mathbf{Bw} = \mathbf{q}. \quad (5)$$

A system parameter, such as translation or rotation speed, is termed critical if nontrivial solutions exist to the homogeneous equation $Ku = 0$. The set of null solutions is S where

$$S = \{u : Ku = 0, u \neq 0, \text{ plus spatial boundary conditions}\}. \quad (6)$$

It is assumed that an orthogonal basis exists for S with respect to (\cdot, \cdot) which is denoted by $\{e_j\}$. The orthogonal complement of S is denoted by S^{orth} . S is divided into two classes depending on how G acts on S . If there exists a $u \in S$ such that $Gu \in S^{orth}$, then S is class I. Otherwise, S is class II.

3 Free Vibration Analysis

Initially consider the second-order system (1) with $f = 0$. Assume an admissible response of the form

$$u = \text{Re}\{\psi(x)e^{\lambda t}\} \quad (7)$$

where x is the spatial variable. The eigenvalue problem about the equilibrium $u = 0$ becomes

$$\lambda^2 M\psi + \lambda G\psi + K\psi = 0 \quad (8)$$

plus boundary conditions. At $\lambda = 0$, the solution of (8) is given by

$$\psi = \sum_{j=1}^N d_j e_j \quad (9)$$

for arbitrary d_j and $N \geq 1$.

The inner product of (8) with ψ gives a quadratic equation whose roots are (Shieh, 1971)

$$\lambda = \frac{1}{2}i(g \pm \sqrt{g^2 + 4k}) \quad (10)$$

ψ is normalized by $\langle M\psi, \psi \rangle = 1$, $g = \langle G\psi, \psi \rangle$, and $k = \langle K\psi, \psi \rangle$. The symmetries (2) ensure that g and k are real. Critical eigenfunctions exist when $k = 0$ and therefore $\lambda = 0$. (The other solution in (10), given by taking the + sign, gives $\lambda = ig$ which is not critical nor pertinent to the following discussion.) The existence of complex eigenvalues depends on the value of g and the sign of k . If $g = 0$ and $k < 0$, the eigenvalues are complex. If $g \neq 0$ and k is sufficiently small, the eigenvalues are imaginary. If the eigenfunctions are known, the values of k and g can be determined. However, if the eigenfunctions are known, so are the eigenvalues, and (10) does not provide new information.

Now consider the first order system (5) with $\mathbf{q} = 0$. For admissible response about $\mathbf{w} = 0$ assume

$$\mathbf{w} = \text{Re}\{[\phi_1(x) \quad \phi_2(x)]^T e^{\lambda t}\}. \quad (11)$$

This leads to the eigenvalue problem

$$\lambda \mathbf{A}\Phi + \mathbf{B}\Phi = 0 \quad (12)$$

plus boundary conditions where $\Phi = [\phi_1 \quad \phi_2]^T$. At $\lambda = 0$, (12) requires $\mathbf{B}\Phi = 0$, which is equivalent to the two scalar equations

$$K\phi_1 = 0 \quad K\phi_2 = -G\phi_1. \quad (13)$$

The assumption that $\lambda = 0$ ensures that S is nonempty. The solution for the first of equations (13) is therefore

$$\phi_1 = \sum_{j=1}^N c_j e_j \quad (14)$$

where the constants c_j are, for the moment, arbitrary and $N \geq 1$. ϕ_2 must satisfy

$$K\phi_2 = - \sum_{j=1}^N c_j G e_j. \quad (15)$$

Because K is symmetric, the solvability condition requires that the right-hand side of (15) be orthogonal to S (Stakgold, 1979)¹. Hence, the c_j are not all arbitrary in general. If $G e_j \in S^{orth}$, then c_j is arbitrary. If, however, $G e_j$ is not a member of S^{orth} , then solvability requires $c_j = 0$. With this understanding, the solution ϕ_2 is

$$\phi_2 = \phi_o + \sum_{j=1}^N d_j e_j \quad (16)$$

where ϕ_o is a particular solution of (15) when the c_j are selected to render (15) solvable and the d_j are arbitrary.

The eigenfunction Φ represents a time independent displacement, ϕ_2 , and a time-independent velocity, ϕ_1 . The magnitude of the velocity ϕ_1 is either identically zero if S belongs to class II, or arbitrary if S belongs to class I. The homogeneous form of problem (1) admits the solution

$$u = \phi_2 + \phi_1 t. \quad (17)$$

Although (17) is a solution of (1) with $f = 0$, it is not an eigenfunction of (8), derived from the assumed motion (7). Under (7) the eigenfunction with $\lambda = 0$ is given by (9) which is not identical to (16). Hence there is *not* a one to one correspondence between the critical eigenfunctions of the second order system using (7) and the critical eigenfunctions of the first-order system using (11). The consequences of this insufficiency to system stability are examined in the following section.

4 Eigenvalue Behavior and Stability

The possible forms of critical eigenfunctions lead to a conjecture on the behavior of the eigenvalue locus of a critical eigenfunction as a system parameter is varied from its critical value.

Conjecture: (1) If all critical eigenfunctions Φ have velocities ϕ_1 which are identically zero (class II), then the eigenvalue locus is imaginary for both increases and decreases in any critical system parameter.

(2) If any critical eigenfunction Φ has a nonzero velocity ϕ_1 (class I), then the eigenvalue locus is complex with nonzero real part for some change in any critical system parameter (either an increase, a decrease, or both).

For many commonly studied gyroscopic systems, the above conjecture is true and allows prediction of the behavior of the eigenvalue loci near a vanishing eigenvalue without extensive computation. Consider the following examples:

1 A tensioned string translates along its length and is pinned at its ends such that the transverse displacements at $x = 0$ and $x = 1$ are zero (Wickert and Mote, 1990). The dimensionless velocity is v , and M , G , and K are

¹ We assume the range of K is closed so that the solvability condition is both necessary and sufficient.

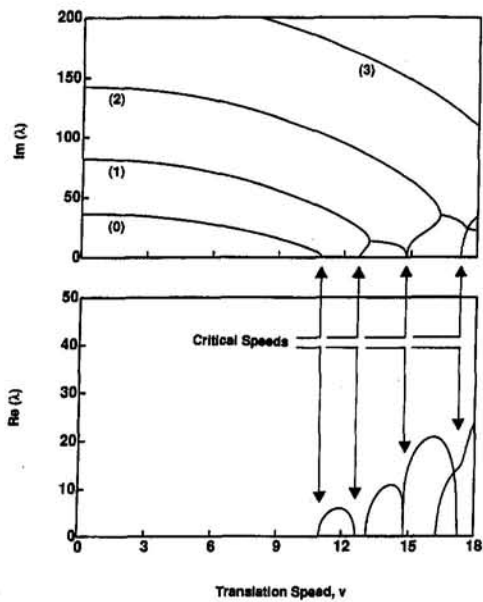


Fig. 1 Eigenvalues of a clamped-pinned, axially moving beam as a function of velocity. $\mu^2 = 100$. The critical translation speeds are marked by the arrows. The numbers in parentheses on the imaginary curves indicate the number of interior nodes in the corresponding eigenfunction.

$$M = I \quad G = 2v \frac{\partial}{\partial x} \quad K = (v^2 - 1) \frac{\partial^2}{\partial x^2} \quad (18)$$

where I is the identity operator. Critical speed is $v = 1$ where $K = 0$. Clearly when $K = 0$, the equation $K\phi_2 = -G\phi_1$ is insoluble for ϕ_2 . S is spanned by

$$e_j = \sin(j\pi x) \quad j = 1, 2, 3, \dots \quad (19)$$

S^{orth} is empty so G acting on S never returns members of S^{orth} . S is class II and the eigenvalues are imaginary for v in the neighborhood of $v = 1$.

2 A tensioned beam translates along its length at velocity v subject to either clamped or pinned boundary conditions at $x = 0$ and $x = 1$. With the dimensionless tension denoted by μ^2 , M , G , and K are (Wickert and Mote, 1990)

$$M = I \quad G = 2v \frac{\partial}{\partial x} \quad K = \frac{\partial^4}{\partial x^4} + (v^2 - \mu^2) \frac{\partial^2}{\partial x^2}. \quad (20)$$

S is nonempty only at specific velocities at which it contains one element satisfying $Ke_1 = 0$. It is assumed in all Examples that S^{orth} is spanned by all the noncritical eigenfunctions and that $S \cup S^{orth}$ is complete. The solvability condition reduces to

$$(Ge_1, e_1) = 2v \int_0^1 e_{1xx} e_1 dx = v(e_1)^2|_0^1 = 0. \quad (21)$$

Hence as long as the displacements at $x = 0$ and $x = 1$ vanish, S is class I, critical eigenfunctions exist with arbitrary velocity, and the eigenvalues are complex near critical speed. Figure 1 shows the frequency spectrum for a clamped-pinned beam with $\mu^2 = 100$ which confirms the prediction. Although both divergence and flutter instabilities exist above the first critical speed, the conjecture addresses only those instability regions which begin or end with vanishing eigenvalues (i.e., the divergence instabilities).

3 An axisymmetric disk rotating at speed Ω is described by the operators (Iwan and Moeller, 1976)

$$M = I \quad G = 2\Omega \frac{\partial}{\partial \theta}$$

$$K = \nabla^4 + \Omega^2 \frac{\partial^2}{\partial \theta^2} - \frac{1}{r} \frac{\partial}{\partial r} \left(r\sigma_r \frac{\partial}{\partial r} \right) - \frac{1}{r^2} \sigma_\theta \frac{\partial^2}{\partial \theta^2} \quad (22)$$

where ∇^4 is the biharmonic operator, σ_r and σ_θ are the axisymmetric radial and hoop stresses, and the disk domain is described by polar coordinates (r, θ) fixed in the nonrotating frame of reference. Under appropriate boundary conditions this system possesses critical speeds with a fixed number of nodal diameters, n , where n is greater than one (Iwan and Moeller, 1976; Renshaw and Mote, 1992). The elements of S can be written in alternative forms of which any two are linearly independent.

$$h(r) \cos(n\theta), \quad h(r) \sin(n\theta), \quad h(r)e^{in\theta}, \quad h(r)e^{-in\theta} \quad (23)$$

Note that the value of g at critical speed in (10) depends on which eigenfunction in (23) is used. However, regardless of the critical eigenfunction used, G operated on it never gives an element of S^{orth} . Hence S is class II and the eigenvalues are imaginary near critical speed. The eigenvalues of a disk clamped at inner radius $r = 0.1$ and free at $r = 1$ are shown in Fig. 2. As the eigenvalues exist in complex conjugate pairs, only the non-negative one of each pair is shown.

4 Consider predicting the eigenvalues of the disk in Example 3 using Galerkin's method and suppose the trial functions selected are proportional to $\cos(n\theta)$ only (i.e., the trial functions are not proportional to $\sin(n\theta)$). For $n \geq 1$, all members of G operating on S are elements of S^{orth} which makes S class I. According to the conjecture, the critical eigenvalue will be complex near critical speed. This is proved by noting that application of Galerkin's method with $\cos(n\theta)$ eliminates the contribution of G through the orthogonality $(Gw_m, w_n) = 0$ for all m and n where w_m is a trial function with m nodal diameters. The predicted eigenvalues are identical to those obtained when $G = 0$, which is a self-adjoint eigenvalue problem that exhibits divergence instability.

5 An axisymmetric rotating disk is subjected to a fixed, stationary, transverse spring of spring constant k' . The operators of this system are identical those of Example 3 if K is modified to

$$K = \nabla^4 + \Omega^2 \frac{\partial^2}{\partial \theta^2} - \frac{1}{r} \frac{\partial}{\partial r} \left(r\sigma_r \frac{\partial}{\partial r} \right) - \frac{1}{r^2} \sigma_\theta \frac{\partial^2}{\partial \theta^2} + k' \delta(r - r_o) \delta(\theta)/r \quad (24)$$

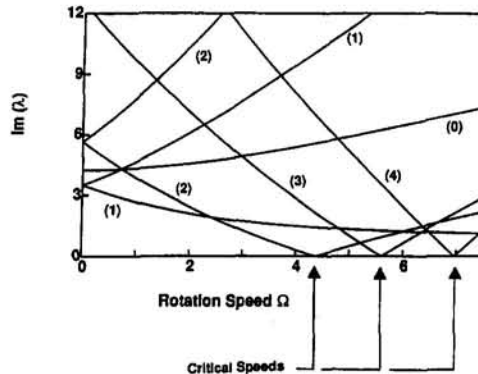


Fig. 2 Eigenvalues of an axisymmetric rotating disk clamped at $r = 0.1$ and free at $r = 1$. The eigenvalues are imaginary, complex conjugate pairs. Three critical speeds are indicated by the arrows. The numbers in parentheses indicate the number of nodal diameters in the corresponding eigenfunctions. For the eigenvalues shown, all corresponding eigenfunctions have zero nodal circles.

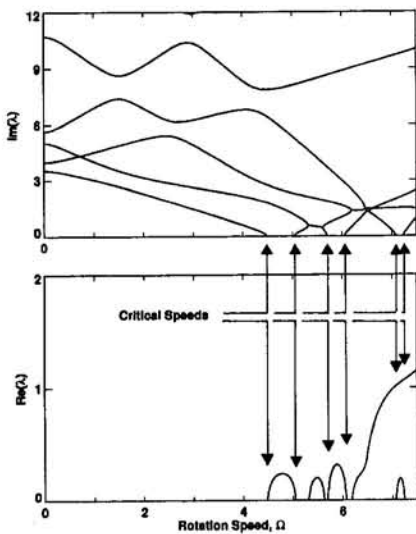


Fig. 3 Eigenvalues of the axisymmetric rotating disk of Fig. 2 loaded by a spring of stiffness 500 located at $r = 0.8, \theta = 0$

where $\delta(\cdot)$ is the delta function and the spring is located at $r = r_o, \theta = 0$. At any critical speed of the system in Example 3, the presence of the spring eliminates one of the two linearly independent critical speed modes (23). S is therefore spanned by

$$e_1 = h(r) \sin(n\theta). \quad (25)$$

Because $Ge_1 \in S^{\text{orth}}$, S is class I and the eigenvalues are complex near critical speed. This is illustrated in Fig. 4 for a system identical to Fig. 3 except that $k' = 500$ and $r_o = 0.8$. Galerkin's method was used to determine these eigenvalues with trial functions up to and including four nodal diameters. Both divergence and flutter instabilities are observed and the number of critical speeds is greater than in Fig. 2. However, each critical speed in Fig. 2 also appears in Fig. 3 as a complex eigenvalue locus near critical speed. This is consistent with the conjecture.

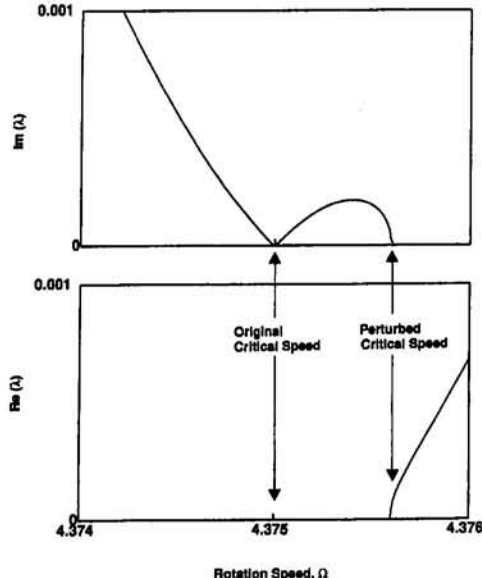


Fig. 4 Eigenvalues of Example 6, an axisymmetric rotating disk loaded by a stationary spring whose stiffness increases quadratically with rotation speed away from the first critical speed of the axisymmetric disk (see Fig. 2)

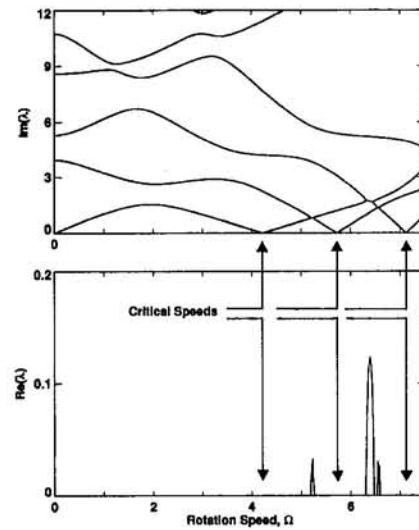


Fig. 5 Eigenvalues of an axisymmetric rotating disk that is loaded by a stationary spring and is allowed rigid-body translation and tilting

6 The following system is designed to partly test the robustness of the conjecture. Modify the system in Example 5 by tuning the spring stiffness to one of the critical speeds, Ω_{cr} .

$$k' = k'_o (\Omega - \Omega_{cr})^2. \quad (26)$$

At $\Omega = \Omega_{cr}$, the system is identical to that in Example 3 for which the eigenvalue locus is imaginary. However, away from $\Omega = \Omega_{cr}$ the system is that in Example 5 for which the eigenvalue locus is complex. Figure 4 shows a magnified view of the eigenvalue locus near the first critical speed of Example 3: $\Omega_{cr} = 4.37500$ and $k'_o = 500$. The stiffness k' perturbs the original critical speed solution into two critical speeds. The first remains at 4.37500 and the eigenvalue locus in the neighborhood of this speed is imaginary as predicted. The second critical speed is slightly greater than 4.37500 and the eigenvalue locus in its neighborhood is complex. Hence, within the accuracy of the Galerkin solution, the conjecture is satisfied.

7 Consider the system in Example 5 with the disk driven on a spindle by splines that allow it to freely slide along the spindle rather than being clamped rigidly at the inner radius. This system models a guided, free-center circular saw in common use (Mote, 1977). At any critical speed of the unclamped system, S is spanned by

$$e_1 = h(r) \sin(n\theta), \quad e_2 = h(r_o) - h(r) \cos(n\theta). \quad (27)$$

($h(r)$ is similar to the radial distribution of the critical speeds of Example 3, but not necessarily equal since it does not satisfy the same boundary conditions at $r = \kappa$.) G applied to S is not a member of S^{orth} and S is class II. Therefore the eigenvalues are imaginary as they pass through all critical speeds. Figure 5 shows the eigenvalues for the system in Fig. 3 with the disk allowed to translate and rotate rigidly. As predicted by the conjecture, the eigenvalues are imaginary across all critical speeds.

5 Discussion

The coalescence of an eigenvalue and its complex conjugate (which is not shown in the figures) occurs at critical speed. Hence, $\lambda = 0$ is always a repeated eigenvalue. The generalization of the admissible motion for m repeated eigenvalues is

$$u = [\psi_1(x) + t\psi_2(x) + \dots + t^{m-1}\psi_m(x)]e^{\lambda t} \quad (28)$$

(Shieh and Masur, 1968). With $\lambda = 0$, this generalization is analogous to the generalized eigenvectors obtained from a ma-

trix with repeated, vanishing eigenvalues. When the Jordan canonical form is diagonal (i.e., the null matrix), the matrix describes a class II problem since the exponential of the matrix is a constant. When the Jordan canonical form has unity on the off diagonal, the matrix describes a class I problem because the exponential of the matrix gives a solution similar to (17).

The conjecture may extend to merging eigenvalue loci which do not occur at $\lambda = 0$. However, the calculations involved in determining the eigenfunctions when $\lambda \neq 0$ appear to prohibit any useful insights. For example, at the onset of flutter instability the eigenfunctions have the generalized form described in (28) with $m = 2$. Substitution of (28) into the homogeneous form of (1) gives

$$\lambda^2 M\psi_2 + \lambda G\psi_2 + K\psi_2 = 0 \quad (29)$$

$$\lambda^2 M\psi_1 + \lambda G\psi_1 + K\psi_1 = -2\lambda M\psi_2 - G\psi_2. \quad (30)$$

Because the value of λ is not known, this problem is as complicated to solve as the original one. Further, the first-order representation of the equation of motion is not a simplified formulation. Numerical computation is required to find these solutions.

The conjecture does not distinguish whether the system parameter must be increased or decreased in order to produce complex eigenvalues when S is class I. However, when K is positive definite, the system eigenvalues are imaginary. For many systems such as rotating disks and translating strings and beams, K is positive definite until the first critical speed is reached. Consequently, complex eigenvalues and divergence instability can only occur above the first critical speed, not below. The conjecture, then, predicts whether or not this happens.

Perturbation methods do not offer a convenient method to establish conditions under which the conjecture is true. When the eigenvalue is considered as a function of the system parameters, the critical system parameters are branch points of that function (Bender and Orszag, 1978; Chen and Ginsberg, 1992). In fact, formal perturbation of a critical eigenvalue always predicts imaginary eigenvalues.

No counter examples to the conjecture have been found for which the system operators vary in a continuous manner. However, if discontinuous system operators are allowed, counter examples are easily constructed by juxtaposing different system operators at the critical values of system parameters. Any proof of the conjecture must therefore restrict the continuity of the system operators.

The results discussed are applicable to both continuous and discrete systems. For both systems, the conjecture is most useful when the approximate critical eigenfunctions are known. In these cases the influence of proposed modifications on the critical eigenvalues can often be assessed without extensive computation. For example, if the free-free disk of Example 7 is to be supported by multiple springs, the conjecture predicts that divergence instability is avoided whenever some combination of rigid translation and tilting of the disk produces two, linearly independent critical eigenfunctions involving no deflection of the springs. Accordingly, any disk supported by three or fewer springs, in any arrangement, avoids divergence instability because the three degrees-of-freedom represented by rigid-body translation and tilting permit two linearly independent critical eigenfunctions to exist. If four springs support the disk, divergence instability occurs except for critical eigenfunctions with 4, 8, 12, ... nodal diameters. If the disk is only allowed rigid translation without tilting, then divergence instability is avoided at the first critical speed only if the springs are located at intervals of $2\pi/n$, where n is the number of nodal diameters in the first critical eigenfunction. (The authors thank the anonymous reviewer for his comments on this example.)

6 Summary and Conclusions

1 Critical eigenfunctions have vanishing eigenvalues and describe both constant displacement and the displacement derived from a constant velocity. These eigenfunctions are excluded by the assumption of harmonic vibration in a second order formulation of the equation of motion of a gyroscopic system. However, these eigenfunctions arise naturally from the assumption of harmonic vibration in a first order formulation. It has long been recognized that the representation of eigenfunctions of repeated eigenvalues, such as critical eigenvalues, require more general formulations than simple harmonic vibration. The contribution of this study is to note that such a generalization is not required for a first-order formulation of gyroscopic systems and to relate the different kinds of eigenfunctions to the system stability.

2 The following conjecture is proposed to predict whether the eigenvalue locus of a critical eigenfunction is imaginary or complex in the neighborhood of critical system parameters:

If all critical eigenfunctions have velocities which are *identically zero*, then the eigenvalue locus is imaginary in the neighborhood of the critical values. If any critical eigenfunction has a *nonzero* velocity, then the eigenvalue locus is complex.

3 The conjecture is shown to be true for many commonly studied gyroscopic systems and no counter example with continuous system operators has yet been found. No proof is furnished although it is clear that a proof requires conditions on the continuity of the system operators. The positive test cases examined here suggest that the conjecture may be true for most gyroscopic systems derived from physical models.

4 The value of the conjecture for engineering purposes is its application to stability prediction. These predictions can often be based on an approximate knowledge of the shapes of the critical eigenfunctions. Not only does this reduce the numerical effort required to predict system stability, but it also can help guide system design to improve, control, or avoid degrading system stability.

Acknowledgment

The authors gratefully acknowledge the National Science Foundation, The Computer Mechanics Laboratory, and the authors' industrial sponsors for their support and interest in this work.

References

- Bender, C. M., and Orszag, S. A., 1978, *Advanced Mathematical Methods for Scientists and Engineers*, McGraw-Hill, New York.
- Chen, P., and Ginsberg, J. H., 1992, "On the Relationship Between Veering of Eigenvalue Loci and Parameter Sensitivity of Eigenfunctions," *Journal of Vibration and Acoustics*, Vol. 114, pp. 141-148.
- Huseyin, K., 1991, "On the Stability Criteria for Conservative Gyroscopic Systems," *Journal of Vibration and Acoustics*, Vol. 113, pp. 58-61.
- Huseyin, K., Hagedorn, P., and Teschner, W., 1983, "On the Stability of Linear Conservative Gyroscopic Systems," *Journal of Applied Mathematics and Physics (ZAMP)*, Vol. 34, pp. 807-815.
- Inman, D. J., 1988, "A Sufficient Condition for the Stability of Conservative Gyroscopic Systems," *ASME JOURNAL OF APPLIED MECHANICS*, Vol. 55, pp. 895-898.
- Iwan, W. D., and Moeller, T. L., 1976, "The Stability of a Spinning Elastic Disk with a Transverse Load System," *ASME JOURNAL OF APPLIED MECHANICS*, Vol. 43, pp. 485-490.
- Renshaw, A. A., and Mote, Jr., C. D., 1992, "Absence of One Nodal Diameter Critical Speed Modes in an Axisymmetric Rotating Disk," *ASME JOURNAL OF APPLIED MECHANICS*, Vol. 59, pp. 687-688.
- Shieh, R., and Masur, E., 1968, "Some General Principles of Dynamic Instability of Solid Bodies," *Journal of Applied Mathematics and Physics (ZAMP)*, Vol. 19, pp. 927-941.
- Shieh, R. C., 1971, "Energy and Variational Principles for Generalized (Gyroscopic) Conservative Problems," *International Journal of Non-Linear Mechanics*, Vol. 5, pp. 495-509.
- Stakgold, I., 1979, *Green's Functions and Boundary Value Problems*, John Wiley and Sons, New York.
- Wickert, J. A., and Mote, Jr., C. D., 1990, "Classical Vibration Analysis of Axially Moving Continua," *ASME JOURNAL OF APPLIED MECHANICS*, Vol. 57, pp. 738-744.

Stability and Vibration of a Rotating Circular Plate Subjected to Stationary In-Plane Edge Loads

I. Y. Shen

Assistant Professor,
Department of Mechanical Engineering,
University of Washington,
Seattle, WA 98195
Mem. ASME

Y. Song

Mechanical Engineer,
Centurion International, Inc.,
Lincoln, NE 68501

This paper predicts transverse vibration and stability of a rotating circular plate subjected to stationary, in-plane, concentrated edge loads. First of all, the equation of motion is discretized in a plate-based coordinate system resulting in a set of coupled Hill's equations. Through use of the method of multiple scales, stability of the rotating plate is predicted in closed form in terms of the rotational speed and the in-plane edge loads. The asymmetric membrane stresses resulting from the stationary in-plane edge loads will transversely excite the rotating plates to single-mode parametric resonances as well as combination resonances at supercritical speed. In addition, introduction of plate damping will suppress the parametric instability when normalized edge loads are small. Moreover, the radial in-plane edge load dominates the rotational speed at which the instability occurs, and the tangential in-plane edge load dominates the width of the instability zones.

1 Introduction

Vibration and stability of rotating, circular, Kirchhoff plates, subjected to various boundary conditions, loading and excitations, thermal environments, and asymmetry, have been analyzed extensively in the literature to predict response of computer disk drives, circular sawing rigs, and other rotating machine components.

In computer disk drives, rotating disks are sandwiched by a pair of read/write heads, which are often modeled as a stationary spring-mass-dashpot system. Vibration of disk drives, in general, are not desirable, because it will limit the area density of the disk drives and will increase the chance of the heads crash into the disks. On the other hand, the disk drive industry has been trying to increase the rotational speed of disk drives, because higher rotational speed implies higher data access rate. Existing literature, however, has shown that higher rotational speed results in larger vibration and possible instabilities of the disk drives, especially when the rotational speed exceeds a particular limit called critical speed. For example, Iwan and Stahl (1973) analyzed transverse vibration of a stationary Kirchhoff plate subjected to a rotating spring-mass-dashpot system. They found that the stiffness, inertia, and damping of the read/write head can excite the disk to instability of different natures at supercritical speed. Iwan and Moeller (1976) modified this model and included centrifugal in-plane stresses to predict vibration and stability of a rotating disk subjected to a stationary spring-mass-dashpot system. Shen and Mote (1991, 1992) used a coordinate system fixed to the rotating plate and concluded that the stiffness and the inertia of the read/write head parametrically excite the system to resonances, and the damping of the read/write head serves as negative damping at supercritical speed destabilizing the system. Ono et al. (1991)

and Chen and Bogy (1992a, 1992b) studied how the stiffness, inertia, and damping of the read/write head affect vibration and stability of a rotating circular plate from a coordinate system fixed in the space. To suppress these instabilities, Shen (1993) introduced damping treatments to circular plates and demonstrated that the plate damping can suppress parametric resonances caused by small stiffness of the read/write head.

Similar problems arise in circular sawing rigs. In sawing rigs, rotating circular saws are sandwiched either by a stationary fluid film bearing to position the saw or by the workpiece during cutting process. Such a system is also commonly modeled as a rotating circular plate subjected to a stationary spring-mass-dashpot system. Similar to disk drives, vibration of saw blades is not desirable, because it results in inaccurate machining, waste of raw materials, and excessive wear and early fracture of the saws. Although vibration of sawing rigs becomes severe as rotational speed increases, sawmills have been trying to operate their sawing rigs at increased rotational speed, because higher rotational speed implies higher productivity.

Compared with disk drives, sawing rigs have their unique factors to consider. For example, boundary conditions are a big concern in circular saws. Sawmills use circular saws whose inner rim is free and floating on the arbor, called floating collar saws. The semiconductor industry often uses a circular saw that is fixed at outer rim to cut silicon ingots through a central hole of the saw (Chonen et al., 1993). In addition, thermal membrane stresses resulting from cutting process can change natural frequencies and vibration mode shapes of the saws (Mote, 1967). Severe thermal environments can produce large in-plane thermal stresses that buckle a saw (Yu and Mote, 1987). Moreover, in-plane membrane stresses are often introduced purposely by rolling the plate to create plastic deformation (Mote, 1965). The purpose of rolling is to increase natural frequencies and the critical speed of the saws, so that the saws can be operated at increased rotational speed.

Though much research has been done in this area, vibration and stability of rotating saw blades under cutting conditions, however, remain open. In general, in-plane loading creates in-plane membrane stresses, which subsequently affect both in-plane and transverse vibration of the rotating plate. For example, Srinivasan and Ramamurti (1980) and Leung and Pinnington

Contributed by the Applied Mechanics Division of THE AMERICAN SOCIETY OF MECHANICAL ENGINEERS for publication in the ASME JOURNAL OF APPLIED MECHANICS.

Discussion on this paper should be addressed to the Technical Editor, Professor Lewis T. Wheeler, Department of Mechanical Engineering, University of Houston, Houston, TX 77204-4792, and will be accepted until four months after final publication of the paper itself in the ASME JOURNAL OF APPLIED MECHANICS.

Manuscript received by the ASME Applied Mechanics Division, May 18, 1994; final revision, Nov. 10, 1994. Associate Technical Editor: S. W. Shaw.

(1987) calculated free and forced in-plane vibration response of rotating disks subjected to in-plane edge loads. For lateral vibration, researchers have found that stationary in-plane edge loads create an asymmetric stress field in a nonrotating circular plate. The asymmetric stress field will change natural frequencies of the circular plate, and therefore the critical speed and buckling load (Carlin et al., 1975; Radcliffe and Mote, 1977). For rotating plates subjected to stationary in-plane loading, Chen and Bogy (1993) showed by sensitivity analysis and numerical computation that the asymmetric membrane stress field in a spinning disk by a stationary circumferential friction force has no effect on the stability of the transverse vibration of the disk except at specific rotational speeds. At or near those specific rotational speeds, the sensitivity analysis fails and no conclusions on the stability can be made. Also Chonen et al. (1993) showed by numerical simulation that in-plane slicing load, in general, has no noticeable effect on frequencies and stability. Later on, Chen (1994) showed that a rotating disk, subjected to a radial, in-plane, concentrated edge load, can undergo instability in transverse vibration at specific rotational speeds. If the radial in-plane load is a follower force, the instability results entirely from the asymmetric membrane stresses. If the radial in-plane load is conservative, the instability results partly from the asymmetric membrane stresses (<5 percent) and primarily from boundary effects. Chen (1994), however, did not predict analytically the rotational speed at which the instability occurs, nor did he explain the mechanism of the instability.

In light of Chen's work (1994), this paper presents research results independently performed by the authors (Song, 1993) to demonstrate that the asymmetric membrane stress field resulting from the stationary edge loads can excite a rotating circular plate transversely to parametric resonances at particular rotational speeds. In addition, this paper predicts analytically the rotational speed at which the instability occurs and the width of the instability zones through use of the method of multiple scales. Moreover, this paper suggests that plate damping will suppress the instability when normalized edge loads are small.

Existence of parametric resonances of a rotating plate subjected to stationary asymmetric membrane stresses can be demonstrated as follows. Consider a plate-based observer rotating with the circular plate. Because the plate is rotating and the in-plane edge loads are stationary, the plate-based observer will see a rotating asymmetric membrane stress field produced by the stationary in-plane edge loads. Therefore, the plate-based observer will experience a periodic change in plate stiffness. If the rotational speed is appropriate, small transverse disturbances will excite the plate to primary and combination resonances transversely.

It should be noted that the results reported in the existing literature (Chen and Bogy, 1993; Chonen et al., 1993) do not contradict the results presented in this paper. A quick review of the existing literature shows clearly that Chen and Bogy (1993) assumed the rotational speed being far away from parametric and combination resonances, and Chonen et al. (1993) used a too small normalized edge load in their simulations to find the instability zones numerically. Results from Chen and Bogy (1993) and Chonen et al. (1993) will be discussed in detail in this paper to reveal how the present paper complements their previously work in this area.

In this paper, the equation of motion from Chen and Bogy (1993) is discretized in a coordinate system fixed in the space resulting in a set of coupled, second-order ordinary differential equations with constant coefficients and gyroscopic terms. Through a transformation to a coordinate system fixed to the rotating circular plate, the gyroscopic equations become a set of coupled Hill's equations with periodic coefficients. Then the coupled Hill's equations are solved analytically through the method of multiple scales. Existence of secular terms determines the frequencies at which parametric resonances occur. Elimination of the secular terms then predicts how the width

of instability zones depends on the rotational speed and the magnitude of the in-plane edge loads. The frequencies and widths of parametric instabilities are determined for both undamped and damped circular plates. Finally, results obtained from the method of multiple scales are illustrated numerically. How normal and tangential edge loads and plate damping affect the parametric resonances are also discussed.

2 Formulation

Consider a linear, homogeneous, isotropic, elastic, axisymmetric, circular plate rotating at constant speed Ω and subjected to stationary in-plane edge forces P and T as shown in Fig. 1. Let (r, θ, z) be a stationary coordinate system fixed in the space and (r, ϕ, z) be a coordinate system fixed to the rotating plate. Also, let $w(r, \theta, t)$ be the plate deflection and let ρ and h be the density and the thickness of the plate, respectively. In addition, the plate may be fixed, free, or simply supported at inner boundary ($r = a$) or outer rim ($r = b$).

The equation of motion of a rotating plate subjected to a symmetric centrifugal stress field σ_r^* , σ_θ^* and an asymmetric membrane stress field σ_{rr} , $\sigma_{\theta\theta}$, and $\tau_{r\theta}$ is (Chen and Bogy, 1993)

$$\rho h \left(\frac{\partial^2 w}{\partial t^2} - 2\Omega \frac{\partial^2 w}{\partial t \partial \theta} + \Omega^2 \frac{\partial^2 w}{\partial \theta^2} \right) + D \nabla^4 w + \rho h L_1 w + L_2 w = 0 \quad (1)$$

where D is the flexural rigidity of the plate,

$$L_1 = -\frac{h}{r} \frac{\partial}{\partial r} \left(\sigma_r^* r \frac{\partial w}{\partial r} \right) - \frac{h \sigma_\theta^*}{r^2} \frac{\partial^2 w}{\partial \theta^2} \quad (2)$$

and

$$L_2 = -\frac{h}{r} \left[\frac{\partial}{\partial r} \left(r \sigma_{rr} \frac{\partial}{\partial r} + \tau_{r\theta} \frac{\partial}{\partial \theta} \right) + \frac{\partial}{\partial \theta} \left(\tau_{r\theta} \frac{\partial}{\partial r} + \frac{1}{r} \sigma_{\theta\theta} \frac{\partial}{\partial \theta} \right) \right]. \quad (3)$$

The explicit expressions of σ_{rr} , $\sigma_{\theta\theta}$, and $\tau_{r\theta}$ are given by Carlin et al. (1975) for the radial load P , and are shown in the Appendix for the tangential load T (Song, 1993). In addition, (1) has to satisfy boundary conditions at $r = a$ and $r = b$. The boundary conditions may take several different forms, depending on whether the in-plane edge loads are conservative or not (Chen, 1994).

The equation of motion can be discretized through an eigenfunction expansion

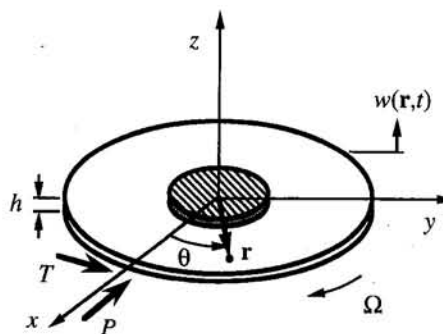


Fig. 1 A rotating circular plate subjected to in-plane edge loads

$$w(r, \theta, t) = \sum_{m=0}^{\infty} \sum_{n=-\infty}^{\infty} \psi_{mn}(r, \theta) A_{mn}(t). \quad (4)$$

Here $\psi_{mn}(r, \theta)$ is the (m, n) complex mode shape of the corresponding, stationary, axisymmetric elastic plate subjected to centrifugal membrane stresses σ_r^* and σ_θ^* , i.e., ψ_{mn} satisfies

$$D\nabla^4 \psi_{mn} + \rho h L_1 \psi_{mn} = \omega_{mn}^2 \rho h \psi_{mn} \quad (5)$$

where ω_{mn}^2 is the natural frequency of mode (m, n) . Notice that

$$\psi_{mn}(r, \theta) = \bar{\psi}_{m,-n}(r, \theta) = \frac{R_{mn}(r) e^{in\theta}}{\sqrt{\rho h b^2}} \quad (6)$$

where $R_{mn}(r)$ is a linear combination of Bessel's functions satisfying the boundary conditions at $r = a$ and $r = b$. Moreover, $R_{mn}(r)$ is normalized such that

$$\begin{aligned} \int_A \rho h \bar{\psi}_{mn}(\mathbf{r}) \psi_{pq}(\mathbf{r}) dA \\ = \int_A \rho h \bar{\psi}_{m,-n}(\mathbf{r}) \psi_{pq}(\mathbf{r}) dA = \delta_{mp} \delta_{nq} \end{aligned} \quad (7)$$

and

$$\int_A \bar{\psi}_{mn} [D \nabla^4 \psi_{pq} + \rho h L_1 \psi_{pq}] dA = \delta_{mp} \delta_{nq} \omega_{mn}^2 \quad (8)$$

where the integration is carried out over the disk domain A . Also notice that both $R_{mn}(r)$ and ω_{mn}^2 depend on the rotation speed Ω . Moreover, $A_{mn}(t)$ in (4) is the complex generalized coordinate associated with $\psi_{mn}(r, \theta)$ satisfying $A_{mn}(t) = \bar{A}_{m,-n}(t)$, where the overbar denotes the complex conjugation.

In discretizing Eq. (1), great care must be taken in handling the boundary conditions. If the edge loads are follower forces, then $\sum_{m=0}^{\infty} \sum_{n=-\infty}^{\infty} \psi_{mn}(r, \theta) A_{mn}(t)$ in (4) will satisfy the boundary conditions of (1) (Chen, 1994). Therefore, it is legitimate to substitute (4) into (1), premultiply (1) by $\bar{\psi}_{mn}$, integrate (1) over the disk domain A , and apply the orthogonality conditions (7) and (8) to obtain

$$\ddot{A}_{mn} - 2in\Omega \dot{A}_{mn} + (\omega_{mn}^2 - n^2 \Omega^2) A_{mn} + \sum_{p=0}^{\infty} \sum_{q=-\infty}^{\infty} C_{mnpq} A_{pq} = 0 \\ m = 0, 1, \dots, n = 0, \pm 1, \pm 2, \dots \quad (9)$$

where

$$\begin{aligned} C_{mnpq} = \bar{C}_{pqmn} = \int_A \bar{\psi}_{mn} L_2 \psi_{pq} dA \\ = h \int_A \left[\sigma_r \frac{\partial \bar{\psi}_{mn}}{\partial r} \frac{\partial \psi_{pq}}{\partial r} + \frac{\sigma_\theta}{r^2} \frac{\partial \bar{\psi}_{mn}}{\partial \theta} \frac{\partial \psi_{pq}}{\partial \theta} \right. \\ \left. + \frac{\tau_{r\theta}}{r} \left(\frac{\partial \bar{\psi}_{mn}}{\partial r} \frac{\partial \psi_{pq}}{\partial \theta} + \frac{\partial \bar{\psi}_{mn}}{\partial \theta} \frac{\partial \psi_{pq}}{\partial r} \right) \right] dA. \end{aligned} \quad (10)$$

Therefore, follower edge loads will affect the stability only through the asymmetric membrane stress field characterized by coefficient C_{mnpq} .

If the edge loads are conservative and do not change their directions during the transverse vibration, then $\sum_{m=0}^{\infty} \sum_{n=-\infty}^{\infty} \psi_{mn}(r, \theta) A_{mn}(t)$ in (4) will not satisfy the boundary conditions of (1) (Chen, 1994). In this case, one way to discretize (1) is to transform (1) and its boundary conditions into an integral equation. Then the integral equation is discretized through (4). The resulting equation will be identical to (9) with an additional term from the boundary conditions. Therefore, conservative edge loads affect plate stability through both the asymmetric membrane stresses and the boundary. Since the purpose of this

paper is to demonstrate the instability resulting from the asymmetric membrane stresses, only Eq. (9) will be addressed in the sequel.

Equation (9) is the governing equation in a stationary coordinate system (i.e., from a ground-based observer) and has constant coefficients. This governing equation, however, loses its positive definiteness at supercritical speed and makes closed-form predictions of instability regions very difficult. To facilitate analytical predictions, the governing equation (9) can be written in a coordinate system fixed to the rotating plate (i.e., from a plate-based observer) with the coordinate transformation $\theta = \phi - \Omega t$ and $q_{mn}(t) = e^{-int\Omega} A_{mn}(t)$, where $q_{mn}(t)$ is the generalized coordinates associated with the mode shape $\psi_{mn}(r, \phi)$ in the rotating coordinate system. Therefore, (9) becomes

$$\ddot{q}_{mn}(t) + \omega_{mn}^2 q_{mn}(t) + \sum_{p=0}^{\infty} \sum_{q=-\infty}^{\infty} C_{mnpq} e^{i(q-n)\Omega t} q_{pq}(t) = 0 \\ m = 0, 1, \dots; n = 0, \pm 1, \pm 2, \dots \quad (11)$$

for the plate-based observer. Moreover, the plate axisymmetry requires that

$$\begin{aligned} \omega_{mn} = \omega_{m,-n}, \quad R_{mn}(r) = R_{m,-n}(r), \\ q_{mn}(t) = \bar{q}_{m,-n}(t). \end{aligned} \quad (12)$$

To normalize (11), let ω_{cr} be the critical speed of a circular plate defined as

$$\omega_{cr} = \min \left\{ \Omega \text{ satisfying } \Omega = \frac{\omega_{mn}(\Omega)}{n}, \right. \\ \left. m = 0, 1, 2, \dots; n = 1, 2, \dots \right\}. \quad (13)$$

In addition, let

$$\tau = \omega_{cr} t, \quad \beta_{mn} \equiv \frac{\omega_{mn}}{\omega_{cr}}, \quad \omega \equiv \frac{\Omega}{\omega_{cr}}, \quad \epsilon \kappa C_{mnpq} \equiv \frac{C_{mnpq}}{\omega_{cr}^2} \quad (14)$$

where

$$\epsilon \kappa \equiv \frac{P}{\rho \pi h b^3 \omega_{cr}^2} \quad \text{or} \quad \frac{T}{\rho \pi h b^3 \omega_{cr}^2} \quad (15)$$

is a small load parameter associated with the normal or tangential edge loads.¹ Through the normalization above, the plate-based governing Eq. (11) is normalized as

$$\frac{d^2 q_{mn}}{d\tau^2} + \beta_{mn}^2 q_{mn} + \sum_{p=0}^{\infty} \sum_{q=-\infty}^{\infty} \epsilon \kappa C_{mnpq} e^{i(q-n)\omega \tau} q_{pq} = 0 \\ m = 0, 1, 2, \dots; n = \pm 1, \pm 2, \dots \quad (16)$$

When viscous plate damping is present, an additional term

$$\sum_{p=0}^{\infty} \sum_{q=-\infty}^{\infty} d_{mnpq} \frac{dq_{pq}}{d\tau} \quad (17)$$

will appear in (16), where d_{mnpq} is the modal damping coefficient. A simplified model is lightly damped Kelvin viscoelastic plate (Shen 1993). In this case,

¹ The assumption of small $\epsilon \kappa$ is made to facilitate analytical predictions of stability through the method of multiple scales. For large $\epsilon \kappa$, the method of multiple scales will only give the first-order approximation. The assumption of small $\epsilon \kappa$ is, in fact, reasonable for many applications. For example, Chonen et al. (1993) measured the radial slicing load $P = 36.18$ N and the tangential slicing load $T = 9.65$ N for a saw with $a = 12.0$ cm, $b = 31.25$ cm, $h = 0.15$ mm, $\nu = 0.28$, $\rho = 7.84 \times 10^3$ kg/m³, $E = 1.99 \times 10^{11}$ Pa, and $\omega_{cr} = 1550$ rpm. The resulting $\epsilon \kappa$ is 0.0122 for the radial slicing load P and 0.00325 for the tangential slicing load T .

$$d_{mnpq} = \epsilon\mu\delta_{mp}\delta_{nq}\beta_{mn}^2 \quad (18)$$

where $\epsilon\mu$ is a small damping parameter. Therefore, the equation of motion of the damped plate will be

$$\begin{aligned} \frac{d^2q_{mn}}{d\tau^2} + \epsilon\mu\beta_{mn}^2 \frac{dq_{mn}}{d\tau} + \beta_{mn}^2 q_{mn} \\ + \sum_{p=0}^{\infty} \sum_{q=-\infty}^{\infty} \kappa c_{mnpq} e^{i(q-n)\omega\tau} q_{pq} = 0 \\ m = 0, 1, 2, \dots; \quad n = \pm 1, \pm 2, \dots \quad (19) \end{aligned}$$

3 Stability Analysis

The method of multiple scales is used to predict the stability of (19). Assume that

$$q_{mn}(\tau) = q_{mn}^{(0)}(\tau, T_1) + \epsilon q_{mn}^{(1)}(\tau, T_1) + \dots \quad (20)$$

where $T_1 \equiv \epsilon\tau$. Substitute (20) into (19) to obtain

$$(D_0^2 + \beta_{mn}^2)q_{mn}^{(0)} = 0 \quad (21)$$

and

$$\begin{aligned} (D_0^2 + \beta_{mn}^2)q_{mn}^{(1)} = -D_0(2D_1 + \mu\beta_{mn}^2)q_{mn}^{(0)} \\ - \sum_{p=0}^{\infty} \sum_{q=-\infty}^{\infty} \kappa c_{mnpq} e^{i(q-n)\omega\tau} q_{pq}^{(0)} \quad (22) \end{aligned}$$

where $D_0 \equiv \partial/\partial\tau$ and $D_1 \equiv \partial/\partial T_1$. Solve (21) to obtain

$$q_{mn}^{(0)} = A_{mn}(T_1)e^{i\beta_{mn}\tau} + B_{mn}(T_1)e^{-i\beta_{mn}\tau}. \quad (23)$$

Notice that $q_{mn}(\tau) = \bar{q}_{m,-n}(\tau)$ resulting in

$$A_{m,-n}(\tau) = \bar{B}_{mn}(\tau), \quad B_{m,-n}(\tau) = \bar{A}_{mn}(\tau). \quad (24)$$

Substitute (23) into (22) to obtain

$$\begin{aligned} (D_0^2 + \beta_{mn}^2)q_{mn}^{(1)} = -i\beta_{mn}(2D_1 + \mu\beta_{mn}^2) \\ \times [A_{mn}(T_1)e^{i\beta_{mn}\tau} - B_{mn}(T_1)e^{-i\beta_{mn}\tau}] \\ - \sum_{p=0}^{\infty} \sum_{q=-\infty}^{\infty} \kappa c_{mnpq} e^{i(q-n)\omega\tau} \\ \times [A_{pq}(T_1)e^{i\beta_{pq}\tau} + B_{pq}(T_1)e^{-i\beta_{pq}\tau}]. \quad (25) \end{aligned}$$

Consider a vibration mode $q_{mn}(\tau)$, parametric resonances involving only a single-mode $q_{mn}(\tau)$ may occur at $2n\omega = 2\beta_{mn}$, $n > 0$. Combination resonances with mode (p, q) may occur at two different speeds: $(q - n)\omega = \beta_{mn} + \beta_{pq}$, $q > n \geq 0$ and $(q + n)\omega = \beta_{mn} + \beta_{pq}$, $q > 0$, $n \geq 0$, $n \neq q$. The stability of an undamped plate (i.e., $\mu = 0$) is derived as follows.

3.1 Single Mode Parametric Resonance at $2n\omega = 2\beta_{mn} + \epsilon\sigma$, $n > 0$. When $2n\omega \approx 2\beta_{mn}$, secular terms in equation (25) is

$$\begin{aligned} ST = -2i\beta_{mn}D_1(A_{mn}e^{i\beta_{mn}\tau} - B_{mn}e^{-i\beta_{mn}\tau}) \\ - \kappa c_{mnmn}(A_{mn}e^{i\beta_{mn}\tau} + B_{mn}e^{-i\beta_{mn}\tau}) \\ - \kappa c_{mnm,-n}A_{m,-n}e^{i\beta_{mn}\tau - i\sigma T_1}. \quad (26) \end{aligned}$$

To obtain bounded solutions $q_{mn}^{(1)}$, elimination of secular terms in (26) results in

$$-2i\beta_{mn}D_1A_{mn} - \kappa c_{mnmn}A_{mn} = 0 \quad (27)$$

$$2i\beta_{mn}D_1B_{mn} - \kappa c_{mnmn}B_{mn} - \kappa c_{mnm,-n}\bar{B}_{mn}e^{-i\sigma T_1} = 0 \quad (28)$$

where (24) has been used. From Eq. (27),

$$A_{mn}(T_1) = c_0 \exp\left\{i \frac{\kappa c_{mnmn}}{2\beta_{mn}} T_1\right\} \quad (29)$$

where c_0 is a constant of integration. Since c_{mnpq} is Hermitian, c_{mnmn} is real; therefore, $A_{mn}(T_1)$ is always oscillatory and bounded. To solve Eq. (28), assumed that (Nayfeh and Mook, 1987)

$$B_{mn}(T_1) = [x(T_1) + iy(T_1)]e^{-(i\sigma/2)T_1}. \quad (30)$$

Substitute (30) into Eq. (28) to obtain

$$\begin{cases} 2\beta_{mn}\dot{x} + (\sigma\beta_{mn} - \kappa c_{mnmn} + \kappa\Re[c_{mnm,-n}])y \\ \quad - \kappa\Im[c_{mnm,-n}]x = 0 \\ 2\beta_{mn}\dot{y} + (-\sigma\beta_{mn} + \kappa c_{mnmn} + \kappa\Re[c_{mnm,-n}])x \\ \quad - \kappa\Im[c_{mnm,-n}]y = 0. \end{cases} \quad (31)$$

Therefore, x and y have unbounded response when

$$\left| \sigma - \frac{\kappa c_{mnmn}}{\beta_{mn}} \right| \leq \frac{\kappa}{\beta_{mn}} |c_{mnm,-n}| \quad (32)$$

3.2 Combination Resonance at $(q - n)\omega = \beta_{mn} + \beta_{pq} + \epsilon\sigma$. When $(q - n)\omega \approx \beta_{mn} + \beta_{pq}$, the secular terms of (25) are

$$\begin{aligned} ST = -2i\beta_{mn}D_1[A_{mn}e^{i\beta_{mn}\tau} - B_{mn}e^{-i\beta_{mn}\tau}] \\ - \kappa c_{mnmn}(A_{mn}e^{i\beta_{mn}\tau} + B_{mn}e^{-i\beta_{mn}\tau}) \\ - \kappa c_{mnpq}B_{pq}e^{i(\beta_{mn} + \epsilon\sigma)\tau}. \end{aligned} \quad (33)$$

Existence of bounded $q_{mn}^{(1)}$ requires that

$$-2i\beta_{mn}D_1A_{mn} - \kappa c_{mnmn}A_{mn} - \kappa c_{mnpq}B_{pq}e^{i\sigma T_1} = 0 \quad (34)$$

and

$$2i\beta_{mn}D_1B_{mn} - \kappa c_{mnmn}B_{mn} = 0. \quad (35)$$

Similarly, existence of bounded $q_{pq}^{(1)}$ requires

$$-2i\beta_{pq}D_1A_{pq} - \kappa c_{pqpn}A_{pq} = 0 \quad (36)$$

and

$$2i\beta_{pq}D_1B_{pq} - \kappa c_{pqpn}B_{pq} - \kappa c_{pqmn}A_{mn}e^{-i\sigma T_1} = 0. \quad (37)$$

Equation (35) has the following solution:

$$B_{mn} = c_1 \exp\left\{i \frac{\kappa c_{mnmn}}{2\beta_{mn}} T_1\right\} \quad (38)$$

which is oscillatory and bounded. In addition, (36) has the following solution:

$$A_{pq} = c_2 \exp\left\{-i \frac{\kappa c_{pqpn}}{2\beta_{pq}} T_1\right\} \quad (39)$$

which is also oscillatory and bounded.

To solve (34) and (37), assume that

$$\begin{cases} A_{mn} = ae^{i\lambda T_1} \\ B_{pq} = be^{i(\lambda - \sigma)T_1}. \end{cases} \quad (40)$$

Substitute (40) into Eqs. (34) and (37), and nontrivial a and b require that

$$\begin{aligned} \left(\lambda - \frac{\kappa c_{mnmn}}{2\beta_{mn}}\right) \left[\lambda - \left(\sigma - \frac{\kappa c_{pqpn}}{2\beta_{pq}}\right)\right] \\ + \frac{\kappa^2 c_{mnpq} \bar{c}_{mnpq}}{4\beta_{mn}\beta_{pq}} = 0. \end{aligned} \quad (41)$$

Table 1 Normalized frequencies of the first five modes of a circular plate with $a/b = 0.5$

Modes (m, n)	$(0, 0)$	$(0, \pm 1)$	$(0, \pm 2)$
β_{mn}	1.77155	1.80766	2.00000

Notice that instability occurs when $\Im[\lambda] < 0$ implying that

$$\left| \sigma - \kappa \left(\frac{c_{mmmn}}{2\beta_{mn}} + \frac{c_{pqpq}}{2\beta_{pq}} \right) \right| = \frac{\beta_{mn}^2 + \beta_{pq}^2}{2} \sqrt{\frac{\kappa^2 |c_{mnpq}|^2}{\beta_{mn}^3 \beta_{pq}^3}}. \quad (42)$$

3.3 Combination Resonance at $(q + n)\omega = \beta_{mn} + \beta_{pq} + \epsilon\sigma$. Following the derivation in Section 3.2, one can show that instability occurs when

$$\left| \sigma - \kappa \left(\frac{c_{mmmn}}{2\beta_{mn}} + \frac{c_{pqpq}}{2\beta_{pq}} \right) \right| = \frac{\beta_{mn}^2 + \beta_{pq}^2}{2} \sqrt{\frac{\kappa^2 |c_{mnpq}|^2}{\beta_{mn}^3 \beta_{pq}^3}} \quad (43)$$

3.4 Parametric Instability of Damped Plates. The stability of a damped plate can be derived in a similar manner (Shen, 1993). It can be shown that the system response is unbounded, when

$$\left| \sigma - \frac{\kappa c_{mmmn}}{\beta_{mn}} \right| \leq \sqrt{\frac{\kappa^2}{\beta_{mn}^2} |c_{mmmn}|^2 - \mu^2 \beta_{mn}^4} \quad (44)$$

for single-mode parametric resonance at $2n\omega = 2\beta_{mn} + \epsilon\sigma$, when

$$\begin{aligned} \left| \sigma - \kappa \left(\frac{c_{mmmn}}{2\beta_{mn}} + \frac{c_{pqpq}}{2\beta_{pq}} \right) \right| \\ \leq \frac{\beta_{mn}^2 + \beta_{pq}^2}{2} \sqrt{\frac{\kappa^2 |c_{mnpq}|^2}{\beta_{mn}^3 \beta_{pq}^3} - \mu^2} \end{aligned} \quad (45)$$

for combination resonance at $(q - n)\omega = \beta_{mn} + \beta_{pq} + \epsilon\sigma$, and when

$$\begin{aligned} \left| \sigma - \kappa \left(\frac{c_{mmmn}}{2\beta_{mn}} + \frac{c_{pqpq}}{2\beta_{pq}} \right) \right| \\ \leq \frac{\beta_{mn}^2 + \beta_{pq}^2}{2} \sqrt{\frac{\kappa^2 |c_{mnpq}|^2}{\beta_{mn}^3 \beta_{pq}^3} - \mu^2} \end{aligned} \quad (46)$$

for combination resonance at $(q + n)\omega = \beta_{mn} + \beta_{pq} + \epsilon\sigma$.

4 Numerical Simulations

Five vibration modes are used in the numerical simulation. They are $(0, 0)$, $(0, \pm 1)$, and $(0, \pm 2)$ modes, where the first index is the number of nodal circles and the second index is the number of nodal diameters. As a first approximation, the centrifugal stress field is not included (Iwan and Stahl, 1973); therefore, both β_{mn} and $R_{mn}(r)$ are independent of the rotational speed ω . The normalized eigenvalues β_{mn} are shown in Table 1. The load parameter $\epsilon\kappa$ ranges from 0 to 0.12. The normalized damping coefficient $\epsilon\mu$ is 0.005 for the damped plate. The ratio of the inner to the outer rim is $a/b = 0.5$.

The stability of the plate/load system is predicted numerically through two different ways. One is the method of multiple scales described above, the other is an eigenvalue analysis to be described as follows.

Notice that (19) can be rewritten for a ground-based observer as

$$\begin{bmatrix} \mathbf{I} & \mathbf{0} \\ \mathbf{0} & -\mathbf{I} \end{bmatrix} \frac{d}{d\tau} \begin{pmatrix} \mathbf{p} \\ \mathbf{q} \end{pmatrix} + \begin{bmatrix} \mathbf{A} & \mathbf{B} \\ \mathbf{I} & \mathbf{0} \end{bmatrix} \begin{pmatrix} \mathbf{p} \\ \mathbf{q} \end{pmatrix} = \mathbf{0} \quad (47)$$

where \mathbf{I} is the identity matrix, \mathbf{p} , \mathbf{q} are column vectors with elements as $\mathbf{q} = [\dots, A_{mn}, \dots]^T$ and $\mathbf{p} = (d\mathbf{q}/d\tau)$. In addition,

$$\mathbf{A} = \text{diag}[\dots, -2in\omega + \epsilon\mu\beta_{mn}^2, \dots],$$

$$\mathbf{B} = \text{diag}[\dots, \beta_{mn}^2(1 - i\epsilon\mu n\omega) - n^2\omega^2, \dots] + \epsilon\kappa[c_{mnpq}]$$

$$m = 0, 1, 2, \dots; \quad n = \pm 1, \pm 2, \dots$$

The stability of the plate/load system is approximated by eigenvalues of (47), if finite equations of (47) are retained.

The stability diagrams of the plate/load system are shown in Figs. 2 to 5 on the $\epsilon\kappa$ - ω parameter plane. The discrete points within the shaded regions represent unstable systems predicted by the eigenvalue analysis and the solid lines are stability boundaries predicted by the method of multiple scales.

Figure 2 shows the instability of an undamped plate subjected to a normalized radial load $\epsilon\kappa$. Results from the eigenvalue analysis show four instability zones for $0.5 < \omega < 2$, which agree with those obtained from the method of multiple scales. According to the method of multiple scales, the first instability corresponds to the single-mode parametric resonance of $(0, 2)$ mode occurring at $\omega = \beta_{02}/2 = 1.0$. The second instability is the combination resonance of $(0, 1)$ and $(0, 2)$ modes occurring at $\omega = (\beta_{01} + \beta_{02})/(1 + 2) = 1.26922$. The third instability is the single-mode instability of $(0, 1)$ mode occurring at $\omega = \beta_{01}/1 = 1.80766$. The fourth instability is the combination resonance of $(0, 0)$ and $(0, 2)$ modes occurring at $\omega = (\beta_{00} + \beta_{02})/(0 + 2) = 1.88578$. Among the four instability zones, the $(0, 0) + (0, 2)$ combination resonance has small instability width and is difficult to detect numerically. Moreover, the results from the eigenvalue analysis show that the instability zones not only increase their width but also shift to a lower rotation speed, when the radial load $\epsilon\kappa$ is increased. The same result is predicted by the method of multiple scales, because c_{mmmn} and c_{pqpq} are both positive for a plate subjected to a radial edge load. According to (32), (42), and (43), the instability zones shift to lower rotation speed.

Figure 3 shows the instability of a damped plate subjected to a normalized radial edge load $\epsilon\kappa$. Introduction of damping avoids parametric resonances at least for the low load ranges. The results from the eigenvalue analysis and the method of multiple scales agree very well to each other.

Figure 4 shows the instability zones of an undamped plate subjected to a normalized tangential edge load $\epsilon\kappa$. Identical parametric resonances are obtained, except that the width of $(0, 0) + (0, 2)$ combination resonance is too small to detect numerically through the eigenvalue analysis. When the tangential load $\epsilon\kappa$ is increased, however, the rotation speed at which

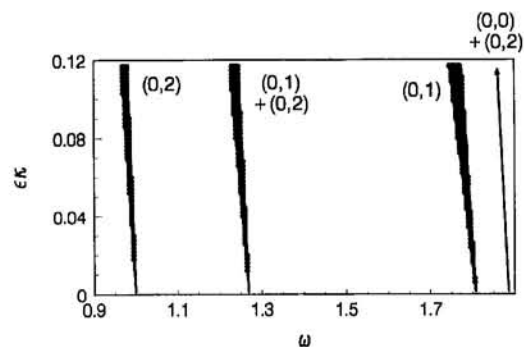


Fig. 2 Parametric instability of a rotating elastic plate subjected to a radial edge load P

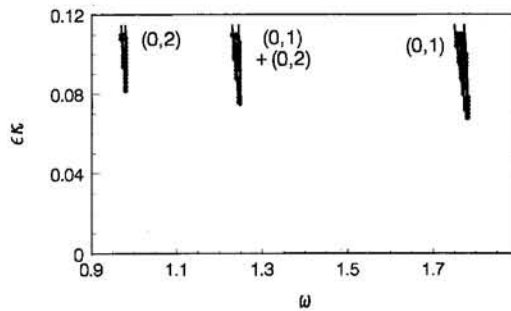


Fig. 3 Parametric instability of a rotating viscoelastic plate subjected to a radial edge load P

the instability occurs remains unchanged, as opposed to the decreasing rotational speed found in the radial edge load case. This is because c_{mmmn} and c_{pqpq} are both zero for a plate subjected to a tangential load. According to (32), (42), and (43), the instability zones will not shift their frequencies. Compared with Fig. 2, the instability zones caused by the radial load P are narrower than those caused by the tangential load T . In other words, the membrane stresses resulting from the tangential load T will dominate the destabilization of the plate.

Figure 5 shows the instability zones of a damped circular plate subjected to a normalized tangential load $\epsilon\kappa$. The damping suppresses the $(0, 2)$ parametric resonance for $0 < \epsilon\kappa < 0.01$ and the $(0, 1) + (0, 2)$ combination resonance for $0 < \epsilon\kappa < 0.3$. The plate damping completely suppresses the $(0, 1)$ mode parametric resonance. Compared with Fig. 3, the plate damping seems to be more effective in suppressing parametric resonances caused by the radial load P .

5 Discussions

The above analysis demonstrates the existence of parametric instability associated with a rotating plate subjected to stationary in-plane edge loads. Existing literature, at first glance, seems to report opposite findings. For example, Chen and Bogy (1993) wrote: "We have shown both by analysis and numerical computations that the in-plane membrane stress field induced in a spinning disk by a stationary circumferential force has no effect, at least to the first order, on the stability of transverse vibration of the disk." Also, Chonen et al. (1993) reported that "... the stresses from the in-plane slicing load and the centrifugal force have no noticeable effects on the frequencies." In fact, these existing results do not contradict what this paper concludes. An explanation is provided as follows.

Chen and Bogy's conclusion that the in-plane load has no effects on the disk stability was based on the following sensitivity analysis:

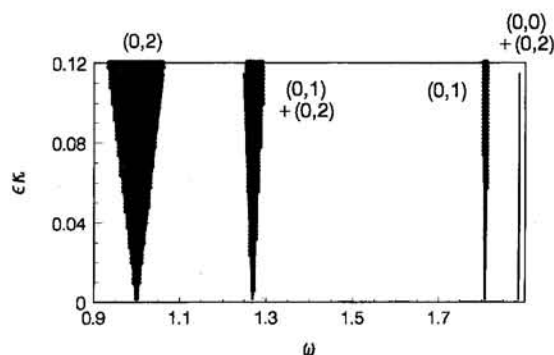


Fig. 4 Parametric instability of a rotating elastic plate subjected to a tangential edge load T

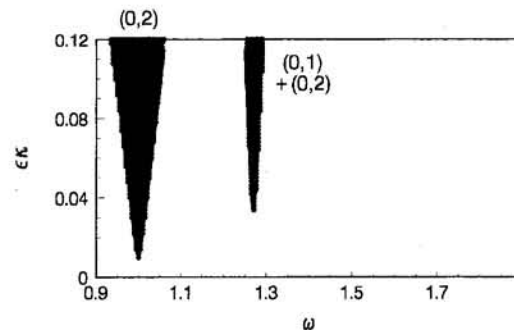


Fig. 5 Parametric instability of a rotating viscoelastic plate subjected to a tangential edge load T

$$\frac{\partial \lambda_{mn}}{\partial T} = \frac{1}{\rho h T \omega_{cr}} \frac{i C_{mmmn}}{4\pi(\beta_{mn} \pm n\omega) \int_a^b R_{mn}^2(r) r dr} \quad (48)$$

where λ_{mn} is the eigenvalue associated with mode (m, n) of a freely spinning circular plate. According to Chen and Bogy (1992a, b), Eq. (48) will break down when $\beta_{mn} = n\omega$ or $\beta_{mn} + \beta_{pq} = (n \pm q)\omega$, because the former will result in zero denominator in (48) and the latter will result in

$$\lambda_{mn} \approx \lambda_{pq} \quad (49)$$

which is called "degenerated systems." Notice that the rotational speed at which (48) breaks down is exactly the speed at which the parametric resonances occur.

Chonen et al. (1993) used numerical simulations to show that the in-plane slicing load has no noticeable effect on stability. According to their simulations, $a = 12.0$ cm, $b = 31.25$ cm, $h = 0.15$ mm, $\nu = 0.28$, $\rho = 7.84 \times 10^3$ kg/m³, $E = 1.99 \times 10^{11}$ Pa, and $\omega_{cr} = 1550$ rpm. In addition, the outer rim was fixed and inner rim was free. A combination of normal and tangential cutting loads was distributed at the inner rim spanning an angle of $2\phi_0 = 60$ deg, which corresponds to a normal slicing load $P = 36.18$ N and a tangential slicing load $T = 9.65$ N according to Fig. 2 of Chonen et al. (1993). From the normalization (15), $\epsilon\kappa = 0.0122$ for the radial slicing load P and $\epsilon\kappa = 0.00325$ for the tangential slicing load T . Because $\epsilon\kappa$ is very small, the instability zones might have been too tiny to be detected numerically.

As a closing remark, Srinivasan and Ramamurti (1980) and Leung and Pinnington (1987) do not result in parametric resonances in their papers, because they only consider in-plane vibration of circular plates. For in-plane vibration, the edge loads and in-plane stresses serve as periodic force excitations, as opposed to periodic stiffness excitations in the transverse vibration.

6 Conclusions

This paper concludes that the asymmetric membrane stresses resulting from stationary in-plane edge loads will transversely excite a rotating circular plate to parametric resonances at particular rotational speeds predicted by (32), (42), and (43). In addition, the radial edge load dominates the rotational speed at which the instability occurs, and the tangential edge load dominates the width of the instability zones. In addition, introduction of plate damping will suppress the parametric resonances when the normalized in-plane edge loads are small.

References

Carlin, J. F., Appl, F. C., Bridwell, H. C., and Dubois, R. P., 1975, "Effects of Tensioning on Buckling and Vibration of Circular Saw Blades," *ASME Journal of Engineering for Industry*, pp. 37-48.

Chen, J.-S., 1994, "Stability Analysis of a Spinning Elastic Disk under a Stationary Concentrated Edge Load," *ASME JOURNAL OF APPLIED MECHANICS*, in press.

Chen, J.-S., and Bogy, D. B., 1992a, "Mathematical Structure of Modal Interactions in a Spinning Disk-Stationary Load System," *ASME JOURNAL OF APPLIED MECHANICS*, Vol. 59, pp. 390-397.

Chen, J.-S., and Bogy, D. B., 1992b, "Effects of Load Parameters on the Natural Frequencies and Stability of a Flexible Spinning Disk with a Stationary Load System," *ASME JOURNAL OF APPLIED MECHANICS*, Vol. 59, pp. S230-S235.

Chen, J.-S., and Bogy, D. B., 1993, "The Effects of a Space-Fixed Friction Force on the In-Plane Stress and Stability of Transverse Vibrations of a Spinning Disk," *ASME JOURNAL OF APPLIED MECHANICS*, Vol. 60, pp. 646-648.

Chonens, S., Jiang, Z. W., and Yuki, Y., 1993, "Vibration and Deflection of a Silicon-Wafer Slicer Cutting the Crystal Ingot," *ASME Journal of Vibration and Acoustics*, Vol. 114, pp. 529-534.

Iwan, W. D., and Stahl, K. J., 1973, "The Response of an Elastic Disk with a Moving Mass System," *ASME JOURNAL OF APPLIED MECHANICS*, Vol. 40, pp. 445-451.

Iwan, W. D., and Moeller, T. L., 1976, "The Stability of a Spinning Elastic Disk with a Transverse Load System," *ASME JOURNAL OF APPLIED MECHANICS*, Vol. 43, pp. 485-490.

Leung, R. C. N., and Pinnington, R. J., 1987, "Vibration of a Rotating Disk Subjected to an In-Plane Force at Its Rim or at Its Center," *Journal of Sound and Vibration*, Vol. 114, pp. 281-295.

Mote, C. D., Jr., 1965, "Free Vibration of Initially Stressed Circular Disks," *Transactions of the ASME*, Vol. 87B, pp. 258-264.

Mote, C. D., Jr., 1967, "Natural Frequencies in Annuli with Induced Thermal Membrane Stresses," *Transactions of the ASME*, Vol. 89B, pp. 611-618.

Nayfeh, A. H., and Mook, D. T., 1979, *Nonlinear Oscillations*, John Wiley and Sons, New York.

Ono, K., Chen, J.-S., and Bogy, D. B., 1991, "Stability Analysis of the Head-Disk Interface in a Flexible Disk Drive," *ASME JOURNAL OF APPLIED MECHANICS*, Vol. 58, pp. 1005-1014.

Radcliffe, C. J., and Mote, C. D., Jr., 1977, "Stability of Stationary and Rotating Discs under Edge Load," *International Journal of Mechanical Science*, Vol. 19, pp. 567-574.

Shen, I. Y., 1993, "Response of a Stationary, Damped, Circular Plate Under a Rotating Slider Bearing System," *ASME Journal of Vibration and Acoustics*, Vol. 115, pp. 65-69.

Shen, I. Y., and Mote, C. D., Jr., 1991, "On the Mechanisms of Instability of a Circular Plate Under a Rotating Spring-Mass-Dashpot System," *Journal of Sound and Vibration*, Vol. 148, pp. 307-318.

Shen, I. Y., and Mote, C. D., Jr., 1992, "Parametric Resonances of an Axisymmetric, Circular Plate Subjected to a Rotating Mass," *Journal of Sound and Vibration*, Vol. 152, No. 3, pp. 573-576.

Song, Y., 1993, "Stability and Vibration of a Rotating Circular Plate Under Stationary In-Plane Edge Loads," Master Thesis, Department of Engineering Mechanics, University of Nebraska-Lincoln, Lincoln, NE.

Srinivasan, V., and Ramamurti, V., 1980, "Dynamic Response of an Annular Disk to a Moving Concentrated In-Plane Edge load," *Journal of Sound and Vibration*, Vol. 72, pp. 251-262.

Yu, R. C., and Mote, C. D., Jr., 1987, "Vibration of Circular Saws Containing Slots," *Holz als Roh- und Werkstoff*, Vol. 45, pp. 155-160.

Appendix

The asymmetric stress field of a circular plate subjected to a concentrated tangential edge load T is found as (Song, 1993)

$$\mathbf{C} = \begin{bmatrix} (n-n^2)b^{n-2} & -(n+n^2)b^{-n-2} & (2+n-n^2)b^n & (2-n-n^2)b^{-n} \\ (n^2-n)b^{n-2} & -(n^2+n)b^{-n-2} & (n+n^2)b^n & (n-n^2)b^{-n} \\ (1+\nu)na^{n-1} & (1+\nu)na^{-n-1} & [4+(1+\nu)n]a^{n+1} & -[4-(1+\nu)n]a^{-n+1} \\ -(1+\nu)na^{n-1} & (1+\nu)na^{-n-1} & [4-(1+\nu)(2+n)]a^{n+1} & [4-(1+\nu)(2-n)]a^{-n+1} \end{bmatrix} \quad \mathbf{x} = (a_n, b_n, c_n, d_n)^T$$

and

$$\mathbf{f} = \left(0, -\frac{T}{\pi b h}, 0, 0 \right)^T.$$

$$\sigma_r = \left[-\frac{2b_1}{r^3} + 2c_1r + \frac{d_1}{r} - \frac{2d_*}{r} \right] \sin \theta$$

$$+ \sum_{n=2}^{\infty} [a_n(n-n^2)r^{n-2} - b_n(n+n^2)r^{-n-2} \\ + c_n(2+n-n^2)r^n$$

$$+ d_n(2-n-n^2)r^{-n}] \sin n\theta \quad (50)$$

$$\tau_{r\theta} = \frac{a_*}{r^2} - \left[-\frac{2b_1}{r^3} + 2c_1r + \frac{d_1}{r} \right] \cos \theta$$

$$- \sum_{n=2}^{\infty} [a_n(n^2-n)r^{n-2} - b_n(n+n^2)r^{-n-2} \\ + c_n(n+n^2)r^n + d_n(n-n^2)r^{-n}] \cos n\theta \quad (51)$$

$$\sigma_\theta = \left[\frac{2b_1}{r^3} + 6c_1r + \frac{d_1}{r} \right] \sin \theta + \sum_{n=2}^{\infty} [a_n(n^2-n)r^{n-2} \\ + b_n(n+n^2)r^{-n-2} + c_n(2+3n+n^2)r^n$$

$$+ d_n(2-3n+n^2)r^{-n}] \sin n\theta \quad (52)$$

where

$$a_* = \frac{Tb}{2\pi h}$$

$$d_* = -\frac{T}{2\pi h}$$

$$b_1 = \frac{T}{8\pi h} \frac{(1+\nu)a^2 - (3+\nu)b^2}{(1+\nu)b^4 + (3-\nu)a^4} (1+\nu)b^4 + (3+\nu)b^2$$

$$c_1 = \frac{T}{8\pi h} \frac{(1+\nu)a^2 - (3+\nu)b^2}{(1+\nu)b^4 + (3-\nu)a^4} (1+\nu)$$

$$d_1 = -\frac{1-\nu}{4\pi h} T.$$

The coefficients a_n, b_n, c_n, d_n ($n = 2, 3, \dots$) can be obtained by the following linear equation:

$$\mathbf{C}\mathbf{x} = \mathbf{f} \quad (53)$$

where

Exact Boundary Condition Perturbation Solutions in Eigenvalue Problems

R. G. Parker

Department of Mechanical Engineering,
Ohio State University,
Columbus, OH
Assoc. Mem. ASME.

C. D. Mote, Jr.

Vice Chancellor—University Relations,
FAMUC Chair in Mechanical Systems,
Department of Mechanical Engineering,
University of California,
Berkeley, CA 94720
Fellow ASME.

A perturbation method is developed for linear, self-adjoint eigenvalue problems with perturbation operators confined to the boundary conditions. Results are derived through third order perturbation for distinct eigensolutions of the unperturbed problem and through second order perturbation for degenerate eigensolutions, where splitting of the degenerate eigensolutions from asymmetry is identified. A key feature, demonstrated for the plate vibration and Helmholtz equation problems on annular domains, is that the solutions of the perturbation problems are determined exactly in closed-form expressions. The approximation in the eigensolutions of the original problem results only from truncation of the asymptotic perturbation series; no approximation is made in the calculation of the eigensolution perturbations. Confinement of the perturbation terms to the boundary conditions ensures that the exact solutions can be calculated for any combination of unperturbed and perturbed boundary conditions that render the problem self-adjoint. The exact solution avoids the common expansion of the solution to the perturbation problems in infinite series of the unperturbed eigenfunctions. The compactness of solution in this formulation is convenient for modal analysis, system identification, design, and control applications. Examples of boundary asymmetries where the method applies include stiffness nonuniformities and geometric deviations from idealized boundary shapes such as annuli and rectangles.

Introduction

In many engineering problems, the boundary conditions are asymmetric and not known precisely. Examples include nonuniform, uncertain boundary fixity and geometric deviations from idealized boundary shapes such as annuli and rectangles. We present a perturbation method for self-adjoint eigenvalue problems having perturbation terms confined to the boundary conditions. The perturbed boundary conditions admit stiffness and geometric asymmetries, and the analytical expansions for the perturbed eigensolutions permit assessment of eigensolution sensitivity to ill-defined boundary conditions. General expressions for perturbations of unperturbed eigensolutions having distinct eigenvalues are derived through third order, and perturbations of unperturbed eigensolutions having degenerate eigenvalues are derived through second order. Degenerate eigenvalue splitting caused by asymmetry is identified, and the perturbed eigensolutions associated with the split eigenvalues are determined. Exact solutions for the perturbation problems are available provided that particular solutions to certain inhomogeneous differential equations can be found. The common expansion of the solutions to the perturbation problems in infinite series of the unperturbed eigenfunctions is then avoided, and the resulting simplicity allows extension of the solution to higher orders. The functional forms of the inhomogeneous differential equations and the associated particular solutions depend only on the operator and the shape of the domain, not on the boundary conditions. Once the particular solutions are known for a given operator and domain, exact solutions for the perturbations are available

for arbitrary self-adjoint boundary conditions. To illustrate the method, the eigensolution perturbations of the plate vibration and Helmholtz equation problems on annular domains with asymmetric boundary conditions are determined exactly. Extension to other operators and rectangular domains is straightforward. Applications of the method to plate vibration include, for example, elastic boundary restraints with varying stiffness, discontinuous boundary supports, variation of the domain boundary shape from annular or rectangular, and combinations of these. The eigensolutions for a solid, circular plate with asymmetric boundary stiffness are compared to a Ritz solution (Leissa et al., 1979).

Despite the common uncertainty in boundary conditions, general treatments of boundary condition asymmetries using perturbation methods are scarce. Selected references concerning perturbation of the boundary conditions are provided in (Pierre, 1987), where Pierre obtains expressions for the eigensolutions of a self-adjoint eigenvalue problem when the natural boundary conditions are perturbed; degenerate eigensolutions of the unperturbed problem are not addressed. In particular, exact solutions for the perturbation problems and the general boundary conditions for which they apply have not been previously discussed.

Eigenvalue Problem With Perturbed Boundary Conditions

Consider a linear, self-adjoint eigenvalue problem of order $2p$ defined on domain P bounded by ∂P . The boundary conditions are expanded in a power series in small $\epsilon \ll 1$

$$Ls - \bar{\lambda}^4 s = 0 \quad P \\ B_j s + \epsilon C_j s + \epsilon^2 D_j s + \epsilon^3 E_j s = 0 \quad \partial P \quad (1)$$

where $j = 1, 2, \dots, p$. The linear boundary operators B_j , C_j , D_j , and E_j involve derivatives normal and tangent to ∂P of at most order $2p - 1$. In general, the boundary operator coefficients vary along ∂P . All operators are independent of $\bar{\lambda}$.

Contributed by the Applied Mechanics Division of THE AMERICAN SOCIETY OF MECHANICAL ENGINEERS for publication in the ASME JOURNAL OF APPLIED MECHANICS.

Discussion on this paper should be addressed to the Technical Editor, Professor Lewis T. Wheeler, Department of Mechanical Engineering, University of Houston, Houston, TX 77204-4792, and will be accepted until four months after final publication of the paper itself in the ASME JOURNAL OF APPLIED MECHANICS.

Manuscript received by the ASME Applied Mechanics Division, May 27, 1994; final revision, Nov. 14, 1994. Associate Technical Editor: T. R. Akylas.

The eigenvalue problem for vibration of a circular plate with zero transverse displacement and a nonuniform, elastic, rotational stiffness along the outer boundary is described by (1). With the dimensionless variables

$$s = S/h \quad r = R/a \quad \bar{\lambda}^4 = (\rho h^4/D) \bar{\omega}^2 \quad K = (a^3/D) \bar{K}$$

where S is the transverse displacement, h the thickness, a the outer radius, D the flexural rigidity, ρ the volume density, \bar{K} the rotational stiffness per unit length, ν the Poisson's ratio, and $\bar{\omega}$ the natural frequency, and assuming $K(\theta) = K_0 + \epsilon k(\theta)$, the eigenvalue problem is

$$\begin{aligned} \nabla^4 s - \bar{\lambda}^4 s = 0 & \quad P: 0 \leq r < 1, \quad 0 \leq \theta < 2\pi \\ s = 0 \quad \nabla^2 s - \frac{1-\nu}{r} \left(s_{,r} + \frac{s_{,\theta\theta}}{r} \right) + K_0 s_{,r} + \epsilon k(\theta) s_{,r} & = 0 \\ \partial P: \quad r = 1. & \end{aligned} \quad (2)$$

The circumferentially varying component of the boundary stiffness, $\epsilon k(\theta)$, is small relative to K_0 . An approximate eigenvalue problem of the form (1) in which C_j , D_j , E_j are nontrivial operators can also result from perturbations of the domain boundaries from circular (Parker and Mote, 1996).

The eigensolutions are represented in asymptotic series in ϵ

$$\bar{\lambda}_{mn}^4 = \lambda_{mn}^4 + \epsilon \mu_{mn} + \epsilon^2 \eta_{mn} + \epsilon^3 \kappa_{mn} + O(\epsilon^4) \quad (3)$$

$$s_{mn} = u_{mn} + \epsilon v_{mn} + \epsilon^2 w_{mn} + \epsilon^3 z_{mn} + O(\epsilon^4). \quad (4)$$

Substitution of (3), (4) into (1) and collection of like powers of ϵ generates a sequence of boundary value problems on P and ∂P :

$$\epsilon^0: \quad Lu_{mn} - \lambda_{mn}^4 u_{mn} = 0 \quad B_j u_{mn} = 0 \quad (5)$$

$$\epsilon^1: \quad Lv_{mn} - \lambda_{mn}^4 v_{mn} = \mu_{mn} u_{mn} \quad B_j v_{mn} = -C_j u_{mn} \quad (6)$$

$$\begin{aligned} \epsilon^2: \quad Lw_{mn} - \lambda_{mn}^4 w_{mn} & = \mu_{mn} v_{mn} + \eta_{mn} u_{mn} \\ B_j w_{mn} & = -C_j v_{mn} - D_j u_{mn} \end{aligned} \quad (7)$$

$$\begin{aligned} \epsilon^3: \quad Lz_{mn} - \lambda_{mn}^4 z_{mn} & = \mu_{mn} w_{mn} + \eta_{mn} v_{mn} + \kappa_{mn} u_{mn} \\ B_j z_{mn} & = -C_j w_{mn} - D_j v_{mn} - E_j u_{mn}. \end{aligned} \quad (8)$$

The self-adjoint eigenvalue problem (1) ensures orthogonality of the eigenfunctions s_{mn} in the inner product $\langle f, g \rangle = \iint f g dA$. Furthermore, the unperturbed (ϵ^0) problem is specified as self-adjoint. With orthonormal u_{mn} , substitution of (4) into the normalization $\langle s_{mn}, s_{mn} \rangle = 1$ gives

$$\langle u_{mn}, v_{mn} \rangle = 0 \quad \langle u_{mn}, w_{mn} \rangle = -\frac{1}{2} \langle v_{mn}, v_{mn} \rangle. \quad (9)$$

The boundary conjunct $J(f, g)$ of L (Roach, 1982), required in the sequel, is defined by

$$J(f, g) = \langle Lf, g \rangle - \langle f, Lg \rangle. \quad (10)$$

$J(f, g)$ has the form of a boundary integral.

Solution of Perturbation Equations

The eigenvalue problem (5) yields an infinite set of unperturbed eigensolutions, which are assumed known. Subsequent solution of the perturbation problems (6)-(8) depends on the degeneracy of the unperturbed eigensolutions. Distinct and degenerate eigensolutions are addressed separately.

Distinct Eigensolution Perturbation. Consider perturbation of a distinct unperturbed eigenvalue λ_{m0}^4 with eigenfunction u_{m0} satisfying (5). (Though standard only for circular domains, we adopt the convention that subscripts $m0$ and mn refer to distinct and degenerate eigensolutions, respectively.) The homogeneous form of (6) has a nontrivial solution, u_{m0} . The inner

product of (6a) with u_{m0} and use of (9a) and (10) yields the solvability condition

$$\mu_{m0} = -J(u_{m0}, v_{m0}). \quad (11)$$

This necessary condition for solvability is sufficient if L has closed range (Stakgold, 1979). The second and third-order eigenvalue perturbations η_{m0} and κ_{m0} are derived formally from similar solvability conditions for (7) and (8)

$$\begin{aligned} \eta_{m0} & = -J(u_{m0}, w_{m0}) \\ \kappa_{m0} & = -J(u_{m0}, z_{m0}) - \mu_{m0} \langle u_{m0}, w_{m0} \rangle. \end{aligned} \quad (12)$$

Equation (11) can be evaluated without the solution for v_{m0} because only boundary values of v_{m0} are necessary. They are defined by the boundary conditions (6b). The higher order perturbations (12) cannot be evaluated until the preceding order eigenfunction is determined.

The common practice for solving (6) expands v_{m0} in an infinite series of the unperturbed eigenfunctions u_{mn} (Courant and Hilbert, 1989; Morse and Feshbach, 1953; Nayfeh et al., 1976; Pierre, 1987). Though sufficient for many purposes, this solution form has several limitations. Convergence of the solution is a potentially serious limitation that can arise when extending the solution to second order. For instance, when analyzing plate vibration on almost circular domains, a series for v_{m0} in the u_{mn} leads to a divergent series when (12a) is evaluated (Parker and Mote, 1996). Similar convergence difficulties occur when perturbing the boundary shape of the Helmholtz equation with either Dirichlet or Neumann boundary conditions (Morse and Feshbach, 1953). Series representations are also cumbersome when the eigenfunctions are required for response calculations or system identification. Additionally, as ϵ increases, higher order perturbations are necessary, and the series solutions are laborious to manipulate and program. Finally, eigenfunction expansions require many unperturbed eigensolutions, particularly if the series converges slowly.

Exact solutions of the perturbation problems (6) and (7) avoid the above difficulties. The eigenfunction perturbations v_{m0} and w_{m0} are decomposed as

$$\begin{aligned} v_{m0} & = c_{m0} u_{m0} + v_{m0}^h + v_{m0}^p \\ w_{m0} & = d_{m0} u_{m0} + w_{m0}^h + w_{m0}^p. \end{aligned} \quad (13)$$

The first terms are the nontrivial solutions to the homogeneous forms of (6) and (7); c_{m0} and d_{m0} are determined from the normalization conditions (9),

$$\begin{aligned} c_{m0} & = -\langle u_{m0}, v_{m0}^h + v_{m0}^p \rangle \\ d_{m0} & = -\langle u_{m0}, w_{m0}^h + w_{m0}^p \rangle - (1/2) \langle v_{m0}, v_{m0} \rangle. \end{aligned} \quad (14)$$

The terms v_{m0}^h and w_{m0}^h of (13) are the general solutions to the homogeneous forms of the field equations (6a) and (7a). They are known since (5) is solvable. The key to the decompositions (13) is the determination of v_{m0}^p and w_{m0}^p , the particular solutions of (6a) and (7a). (These are presented below for plate vibration and the Helmholtz equation on annuli.) With v_{m0}^h and w_{m0}^h known, the undetermined coefficients in v_{m0}^p and w_{m0}^p follow readily. Determination of v_{m0} and w_{m0} permits evaluation of (12). For specific problems, eigenfunction orthogonality reduces η_{m0} and κ_{m0} to compact expressions in the Fourier coefficients of the asymmetric perturbation. An example is presented later for nonuniformly restrained circular plates.

Particular solutions v_{m0}^p and w_{m0}^p are derived for annular plates, where $L = \nabla^4$ and the domain is $\gamma < r < 1, 0 \leq \theta \leq 2\pi$. The orthonormal unperturbed eigenfunctions are

$$\begin{aligned} u_{m0} & = f_{m0} J_0(\lambda_{m0} r) + g_{m0} I_0(\lambda_{m0} r) \\ & \quad + h_{m0} Y_0(\lambda_{m0} r) + i_{m0} K_0(\lambda_{m0} r) \end{aligned}$$

$$u_{mn}^{1,2} = [f_{mn}J_n(\lambda_{mn}r) + g_{mn}I_n(\lambda_{mn}r) + h_{mn}Y_n(\lambda_{mn}r) + i_{mn}K_n(\lambda_{mn}r)] \begin{cases} \cos n\theta & n \geq 1 \\ \sin n\theta & \end{cases} \quad (15)$$

where m and n indicate the number of nodal circles and nodal diameters, respectively, of the eigenfunction. For $n = 0$, the eigenvalues λ_{m0} are distinct; for $n > 0$, λ_{mn} is degenerate with $u_{mn}^{1,2}$ as corresponding independent eigenfunctions. The Bessel function coefficients are chosen to satisfy the boundary conditions in (5). (See McLachlan (1955) for a comprehensive list of Bessel function identities.) Equations (15) and (6a) lead to the particular and homogeneous solutions

$$v_{m0}^p = -\frac{\mu_{m0}r}{4\lambda_{m0}^3} [f_{m0}J_1(\lambda_{m0}r) - g_{m0}I_1(\lambda_{m0}r) + h_{m0}Y_1(\lambda_{m0}r) + i_{m0}K_1(\lambda_{m0}r)] \quad (16)$$

$$v_{m0}^h = \sum_{j=0}^{\infty} [P_jJ_j(\lambda_{m0}r) + Q_jI_j(\lambda_{m0}r) + \hat{P}_jY_j(\lambda_{m0}r) + \hat{Q}_jK_j(\lambda_{m0}r)] \cos j\theta + \sum_{j=1}^{\infty} [R_jJ_j(\lambda_{m0}r) + S_jI_j(\lambda_{m0}r) + \hat{R}_jY_j(\lambda_{m0}r) + \hat{S}_jK_j(\lambda_{m0}r)] \sin j\theta. \quad (17)$$

The coefficients in (17) are derived from the boundary conditions in (6),

$$B_j v_{m0}^h = -C_j u_{m0} - B_j v_{m0}^p \quad r = \gamma, 1; \quad j = 1, 2. \quad (18)$$

If the variable coefficients in C_j are represented by their Fourier series, the constants in (17) are obtained by equating coefficients of trigonometric terms on both sides of (18). Thus, perturbations of the boundary conditions having general circumferential dependence can be treated. The particular solution of (7a) is

$$w_{m0}^p = -\frac{\mu_{m0}r}{4\lambda_{m0}^3} \left\{ \frac{\mu_{m0}r}{8\lambda_{m0}^3} [f_{m0}J_0(\lambda_{m0}r) - g_{m0}I_0(\lambda_{m0}r) + h_{m0}Y_0(\lambda_{m0}r) - i_{m0}K_0(\lambda_{m0}r)] + \left(c_{m0} + \frac{\eta_{m0}}{\mu_{m0}} - \frac{\mu_{m0}}{2\lambda_{m0}^4} \right) [f_{m0}J_1(\lambda_{m0}r) - g_{m0}I_1(\lambda_{m0}r) + h_{m0}Y_1(\lambda_{m0}r) + i_{m0}K_1(\lambda_{m0}r)] + \sum_{j=0}^{\infty} [P_jJ_{j+1}(\lambda_{m0}r) - Q_jI_{j+1}(\lambda_{m0}r) + \hat{P}_jY_{j+1}(\lambda_{m0}r) + \hat{Q}_jK_{j+1}(\lambda_{m0}r)] \cos j\theta + \sum_{j=1}^{\infty} [R_jJ_{j+1}(\lambda_{m0}r) - S_jI_{j+1}(\lambda_{m0}r) + \hat{R}_jY_{j+1}(\lambda_{m0}r) + \hat{S}_jK_{j+1}(\lambda_{m0}r)] \sin j\theta \right\}. \quad (19)$$

The homogeneous solution w_{m0}^h has the form (17). The constants in w_{m0}^h are determined following the process for v_{m0}^h .

Exact solutions of the perturbation equations are also obtained for the operator $L = -\nabla^2$ on annular domains. The perturbed problem analogous to (1) is

$$-\nabla^2 s - \bar{\omega}^2 s = 0 \quad \gamma < r < 1$$

$$B_1 s + \epsilon C_1 s + \epsilon^2 D_1 s + \epsilon^3 E_1 s = 0 \quad r = \gamma, 1. \quad (20)$$

With the eigenvalue expansion $\bar{\omega}_{mn}^2 = \omega_{mn}^2 + \epsilon\mu_{mn} + \epsilon^2\eta_{mn} + \epsilon^3\kappa_{mn} + O(\epsilon^4)$ and the expansion (4), the results (11)-(14) apply. The perturbation problems (5)-(8) are obtained by letting $L = -\nabla^2$ and $\lambda_{mn}^4 = \omega_{mn}^2$. The results corresponding to (15)-(19) are

$$u_{m0} = f_{m0}J_0(\omega_{m0}r) + h_{m0}Y_0(\omega_{m0}r) \quad (21)$$

$$u_{mn}^{1,2} = [f_{mn}J_n(\omega_{mn}r) + h_{mn}Y_n(\omega_{mn}r)] \begin{cases} \cos n\theta & n \geq 1 \\ \sin n\theta & \end{cases} \quad (22)$$

$$v_{m0}^h = \sum_{j=0}^{\infty} [P_jJ_j(\omega_{m0}r) + \hat{P}_jY_j(\omega_{m0}r)] \cos j\theta + \sum_{j=1}^{\infty} [R_jJ_j(\omega_{m0}r) + \hat{R}_jY_j(\omega_{m0}r)] \sin j\theta \quad (23)$$

$$w_{m0}^p = -\frac{\mu_{m0}r}{2\omega_{m0}} \left\{ \frac{\mu_{m0}r}{4\omega_{m0}} [f_{m0}J_0(\omega_{m0}r) + h_{m0}Y_0(\omega_{m0}r)] + \left(c_{m0} + \frac{\eta_{m0}}{\mu_{m0}} - \frac{\mu_{m0}}{2\omega_{m0}^2} \right) [f_{m0}J_1(\omega_{m0}r) + h_{m0}Y_1(\omega_{m0}r)] + \sum_{j=0}^{\infty} [P_jJ_{j+1}(\omega_{m0}r) + \hat{P}_jY_{j+1}(\omega_{m0}r)] \cos j\theta + \sum_{j=1}^{\infty} [R_jJ_{j+1}(\omega_{m0}r) + \hat{R}_jY_{j+1}(\omega_{m0}r)] \sin j\theta \right\} \quad (24)$$

where the coefficients are different than those in (15)-(19) despite the identical notation. Thus, as for annular plates, eigen-solution expansions can be determined exactly through third order in ϵ for the eigenvalues $\bar{\omega}_{m0}^2$ and second order in ϵ for the eigenfunctions s_{m0} .

Degenerate Eigensolution Perturbation. Consider a degenerate unperturbed eigenvalue λ_{mn}^4 of multiplicity two with associated orthonormal eigenfunctions u_{mn}^1 and u_{mn}^2

$$\langle u_{mn}^i, u_{mn}^j \rangle = \delta_{ij}. \quad (25)$$

Asymmetries may split some repeated eigenvalues into two distinct ones, while others remain repeated (Tobias and Arnold, 1957; Yu and Mote, 1987). When asymmetry splits a repeated eigenvalue, the associated eigenfunctions, which in the unperturbed system lie arbitrarily in a two dimensional linear space spanned by u_{mn}^1 and u_{mn}^2 , become fixed in that space.

Eigensolution splitting can substantially alter dynamic response. Yu and Mote (1987) show that radial slots in rotating, circular plates split some degenerate eigensolutions. The split eigensolutions are subject to parametric instability below the critical speed. Tseng and Wickert (1994a) show that apparently slight boundary asymmetry in circular plate vibration can generate a beating response not present in the axisymmetric plate. The beating results from the participation of two closely spaced, split eigensolutions in the response. Previous works emphasize discrete asymmetries (Tobias and Arnold, 1957; Yu and Mote, 1987; Shen and Mote, 1993; Tseng and Wickert, 1994b). In this study, the boundary asymmetries are distributed and possibly discontinuous. Discrete asymmetries can be handled by the methods herein as a special case.

To ensure that the eigenfunctions $s_{mn}(x, y; \epsilon)$ vary continuously with perturbation amplitude ϵ , the eigenfunctions achieved in the limit of s_{mn} as $\epsilon \rightarrow 0$ are sought as the appropriate u_{mn} in the expansion (4). Two such unperturbed eigenfunctions must be determined, one for each of the degenerate unperturbed eigensolutions. These u_{mn} lie in the linear space spanned by u_{mn}^1 and u_{mn}^2 and are not known a priori. We take the linear combination

$$u_{mn} = a_{mn}^1 u_{mn}^1 + a_{mn}^2 u_{mn}^2 \quad (26)$$

and substitute this for u_{mn} in (4) and (6)-(8). a_{mn}^1 and a_{mn}^2 define the eigenfunctions u_{mn} from which the smooth s_{mn} loci originate; they are to be determined for each split eigensolution.

Solutions of the homogeneous form of (6) lie in the two-dimensional linear space spanned by u_{mn}^1 and u_{mn}^2 . Two solvability conditions are found from the inner products of (6a) with u_{mn}^1 and u_{mn}^2 and use of (10), (5a), and (25)

$$-J(u_{mn}^1, v_{mn}) = a_{mn}^1 \mu_{mn} \quad (27a)$$

$$-J(u_{mn}^2, v_{mn}) = a_{mn}^2 \mu_{mn}. \quad (27b)$$

Expansion of (27a, b) generates an algebraic eigenvalue problem for μ_{mn} and $\mathbf{a}_{mn} = (a_{mn}^1, a_{mn}^2)^T$

$$\mathbf{D}\mathbf{a}_{mn} = \mu_{mn}\mathbf{a}_{mn}. \quad (28)$$

\mathbf{D} is symmetric because (1) is self-adjoint (Appendix A). The two real eigenvalues $\mu_{mn}^{1,2}$ are the first-order eigenvalue perturbations of the split eigensolutions. The unit eigenvectors $\mathbf{a}_{mn}^{1,2}$ define the two unperturbed eigenfunctions (26). Symmetry of \mathbf{D} implies orthogonality of $\mathbf{a}_{mn}^{1,2}$ which, along with (25) and (26), guarantees that the unperturbed eigenfunctions associated with the split eigensolutions are orthogonal.

If the eigenvalues of \mathbf{D} are repeated, the eigensolution does not split at this order of perturbation. The eigenvectors $\mathbf{a}_{mn}^{1,2}$ of \mathbf{D} are arbitrary unit vectors, and the indeterminacy of the unperturbed eigenfunctions (26) is not removed at this order. If \mathbf{D} has distinct eigenvalues, the eigensolution splits, and the two unperturbed eigenfunctions are given by (26) and $\mathbf{a}_{mn}^{1,2}$.

The first-order eigenfunction perturbation v_{mn} is governed by (6) and (26). (Though there are two split eigensolutions, the notation μ_{mn} , a_{mn}^1 , a_{mn}^2 , v_{mn} represents a generic case.) The decomposition of v_{mn} is

$$v_{mn} = c_{mn}^1 u_{mn}^1 + c_{mn}^2 u_{mn}^2 + v_{mn}^h + v_{mn}^p. \quad (29)$$

The first two terms span the linear space of solutions to the homogeneous form of (6). The particular solution v_{mn}^p is again the critical term. For plate vibration and the Helmholtz equation on annular domains, v_{mn}^p is given at the close of this section. With v_{mn}^p known, the undetermined coefficients in v_{mn}^h follow easily as for distinct unperturbed eigenvalues. The normalization (9a) gives

$$a_{mn}^1 c_{mn}^1 + a_{mn}^2 c_{mn}^2 = -\langle a_{mn}^1 u_{mn}^1 + a_{mn}^2 u_{mn}^2, v_{mn}^h + v_{mn}^p \rangle. \quad (30)$$

Necessary additional equations to determine c_{mn}^1 and c_{mn}^2 are found at the next order of perturbation from the two solvability conditions for (7). Analogous to (27), these are

$$\begin{aligned} \mu_{mn} c_{mn}^1 + \mu_{mn} \langle u_{mn}^1, v_{mn}^h + v_{mn}^p \rangle + a_{mn}^1 \eta_{mn} \\ = -J(u_{mn}^1, w_{mn}) \end{aligned} \quad (31a)$$

$$\begin{aligned} \mu_{mn} c_{mn}^2 + \mu_{mn} \langle u_{mn}^2, v_{mn}^h + v_{mn}^p \rangle + a_{mn}^2 \eta_{mn} \\ = -J(u_{mn}^2, w_{mn}). \end{aligned} \quad (31b)$$

Equations (30) and (31) are solved simultaneously for c_{mn}^1 , c_{mn}^2 , and η_{mn} . Terms of $J(u_{mn}^{1,2}, w_{mn})$ that depend on c_{mn}^1 and c_{mn}^2 must first be separated (Appendix B)

$$J(u_{mn}^1, w_{mn}) = -D_{11}c_{mn}^1 - D_{12}c_{mn}^2 + \tilde{J}(u_{mn}^1, w_{mn}) \quad (32a)$$

$$J(u_{mn}^2, w_{mn}) = -D_{12}c_{mn}^1 - D_{22}c_{mn}^2 + \tilde{J}(u_{mn}^2, w_{mn}) \quad (32b)$$

where D_{ij} are components of \mathbf{D} and $\tilde{J}(u_{mn}^{1,2}, w_{mn}) = J(u_{mn}^{1,2}, w_{mn})|_{c_{mn}^{1,2}=0}$. The matrix form of (30) and (31) is

$$\begin{bmatrix} \mu_{mn} - D_{11} & -D_{12} & a_{mn}^1 \\ -D_{12} & \mu_{mn} - D_{22} & a_{mn}^2 \\ a_{mn}^1 & a_{mn}^2 & 0 \end{bmatrix} \begin{bmatrix} c_{mn}^1 \\ c_{mn}^2 \\ \eta_{mn} \end{bmatrix} = \begin{bmatrix} -\mu_{mn} \langle u_{mn}^1, v_{mn}^h + v_{mn}^p \rangle - \tilde{J}(u_{mn}^1, w_{mn}) \\ -\mu_{mn} \langle u_{mn}^2, v_{mn}^h + v_{mn}^p \rangle - \tilde{J}(u_{mn}^2, w_{mn}) \\ -a_{mn}^1 \langle u_{mn}^1, v_{mn}^h + v_{mn}^p \rangle - a_{mn}^2 \langle u_{mn}^2, v_{mn}^h + v_{mn}^p \rangle \end{bmatrix}. \quad (33)$$

Eigenfunction orthogonality frequently simplifies the integrals in (33) to closed-form expressions. If the eigenvalues $\mu_{mn}^{1,2}$ of \mathbf{D}

are distinct, the operator in (33) is invertible, and c_{mn}^1 , c_{mn}^2 , and η_{mn} are the solution of (33). This completes the solution for v_{mn} and gives the second order eigenvalue perturbation η_{mn} simultaneously.

When \mathbf{D} has repeated eigenvalues, the operator in (33) is singular. Furthermore, a_{mn}^1 and a_{mn}^2 are not yet determined. The first two equations in (33) reduce to

$$a_{mn}^1 \eta_{mn} = -\mu_{mn} \langle u_{mn}^1, v_{mn}^h + v_{mn}^p \rangle - \tilde{J}(u_{mn}^1, w_{mn}) \quad (34a)$$

$$a_{mn}^2 \eta_{mn} = -\mu_{mn} \langle u_{mn}^2, v_{mn}^h + v_{mn}^p \rangle - \tilde{J}(u_{mn}^2, w_{mn}). \quad (34b)$$

If the eigensolutions split in a second-order perturbation, equations (34) and $(a_{mn}^1)^2 + (a_{mn}^2)^2 = 1$ have two independent solutions for η_{mn} , a_{mn}^1 , and a_{mn}^2 . These solutions fix the unperturbed eigenfunctions (26) and determine the split second-order eigenvalue perturbations. If the eigensolutions do not split at second order, (34a, b) are satisfied for any unit vector \mathbf{a}_{mn} . In this case, the eigenvalues remain degenerate through second order in ϵ , and the unperturbed eigenfunctions (26) are still indeterminate. The degenerate second-order eigenvalue perturbation is calculable, however. For the perturbation considered by Parker and Mote (1996), the condition that (34a, b) have no unique solution for the unit vector \mathbf{a}_{mn} is exactly the condition that η_{mn} be independent of \mathbf{a}_{mn} . η_{mn} can then be evaluated at this order perturbation. \mathbf{a}_{mn} may be calculated with κ_{mn} at third order perturbation by a procedure similar to that described in this section.

For the annular plate, a particular solution satisfying (6a), (26), and (15b) is

$$\begin{aligned} v_{mn}^p = & -\frac{\mu_{mn} r}{4\lambda_{mn}^3} [f_{mn} J_{n+1}(\lambda_{mn} r) - g_{mn} I_{n+1}(\lambda_{mn} r) \\ & + h_{mn} Y_{n+1}(\lambda_{mn} r) + i_{mn} K_{n+1}(\lambda_{mn} r)] \\ & \times (a_{mn}^1 \cos n\theta + a_{mn}^2 \sin n\theta). \end{aligned} \quad (35)$$

The homogeneous solution v_{mn}^h has the form (17). Fourier expansion of the inhomogeneous boundary conditions (6b) allows closed-formed solution for the constants in v_{mn}^h . The analogous result for the Laplacian operator in (20) is

$$\begin{aligned} v_{mn}^h = & -\frac{\mu_{mn} r}{2\omega_{mn}} [f_{mn} J_{n+1}(\lambda_{mn} r) + h_{mn} Y_{n+1}(\lambda_{mn} r)] \\ & \times (a_{mn}^1 \cos n\theta + a_{mn}^2 \sin n\theta). \end{aligned} \quad (36)$$

Example: Nonuniformly Restrained Circular Plate

Consider the solid, circular plate described by (2) with its rim constrained by a linear rotational spring of stiffness $K(\theta)$. The only nontrivial boundary operators of (1) are B_1 , B_2 , and $C_2 = k(\theta)(\bullet)_{,r}|_{r=1}$.

The boundary conjunct of $L = \nabla^4$ (Meirovich, 1967) is manipulated into the form (A1), where

$$\begin{aligned} B_1^g u &= B_1 u = u|_{r=1} \\ B_1^n u &= \left[-(\nabla^2 u)_{,r} + \frac{1-\nu}{r^2} \left(\frac{u_{,\theta\theta}}{r} - u_{,r\theta\theta} \right) \right]_{r=1} \\ B_2^g u &= u_{,r}|_{r=1} \\ B_2^n u &= \left[\nabla^2 u - \frac{1-\nu}{r} \left(u_{,r} + \frac{u_{,\theta\theta}}{r} \right) + K_0 u_{,r} \right]_{r=1}. \end{aligned} \quad (37)$$

The variable component of the rotational stiffness has the Fourier representation

$$k(\theta) = \sum_{j=1}^{\infty} k_j^c \cos j\theta + \sum_{j=1}^{\infty} k_j^s \sin j\theta. \quad (38)$$

The unperturbed eigensolutions are given by (15), where λ_{mn} is the $(m+1)$ th positive root of

$$-x(1-\nu-K_0)[J_n(x)I_{n+1}(x) + J_{n+1}(x)I_n(x)] + 2x^2J_n(x)I_n(x) = 0. \quad (39)$$

The constants in (15) are

$$f_{mn} = \begin{cases} [2\pi Z_{mn} J_0^2(\lambda_{mn})]^{-1/2} & n = 0 \\ [\pi Z_{mn} J_{mn}^2(\lambda_{mn})]^{-1/2} & n > 0 \end{cases}$$

$$g_{mn} = \begin{cases} -[2\pi Z_{mn} I_0^2(\lambda_{mn})]^{-1/2} & n = 0 \\ -[\pi Z_{mn} I_n^2(\lambda_{mn})]^{-1/2} & n > 0 \end{cases}$$

$$h_{mn} = i_{mn} = 0$$

$$Z_{mn} = 1 - \frac{2n+2}{1-\nu-K_0} - \frac{2\lambda_{mn}^2}{(1-\nu-K_0)^2}$$

Distinct Eigensolutions. The distinct eigenvalue perturbations reduce from (11), (12), (A1), (37), and (5b)-(8b)

$$\mu_{m0} = (u_{m0,r}|_{r=1})^2 \int_0^{2\pi} k(\theta) d\theta = 0 \quad (40)$$

$$\eta_{m0} = (u_{m0,r}|_{r=1}) \int_0^{2\pi} (v_{m0,r}|_{r=1}) k(\theta) d\theta = -\left(\frac{2}{\pi Z_{m0}}\right)^{1/2} \times \frac{\lambda_{m0}^2}{1-\nu-K_0} \int_0^{2\pi} (v_{m0,r}|_{r=1}) k(\theta) d\theta \quad (41)$$

$$\kappa_{m0} = (u_{m0,r}|_{r=1}) \int_0^{2\pi} (w_{m0,r}|_{r=1}) k(\theta) d\theta = -\left(\frac{2}{\pi Z_{m0}}\right)^{1/2} \times \frac{\lambda_{m0}^2}{1-\nu-K_0} \int_0^{2\pi} (w_{m0,r}|_{r=1}) k(\theta) d\theta. \quad (42)$$

The solution for v_{m0} bounded at $r = 0$ and evaluation of (41) give

$$v_{m0} = -\left(\frac{2}{\pi Z_{m0}}\right)^{1/2} \frac{\lambda_{m0}^2}{1-\nu-K_0} \times \sum_{j=1}^{\infty} \frac{I_j(\lambda_{m0})J_j(\lambda_{m0}r) - J_j(\lambda_{m0})I_j(\lambda_{m0}r)}{\zeta_j} \times (k_j^c \cos j\theta + k_j^s \sin j\theta)$$

$$\eta_{m0} = -\frac{2\lambda_{m0}^5}{Z_{m0}(1-\nu-K_0)^2} \times \sum_{j=1}^{\infty} \frac{J_j(\lambda_{m0})I_{j+1}(\lambda_{m0}) + I_j(\lambda_{m0})J_{j+1}(\lambda_{m0})}{\zeta_j} \times [(k_j^c)^2 + (k_j^s)^2] \quad (43)$$

where ζ_j has the functional form of the characteristic Eq. (39)

$$\zeta_j = -\lambda_{m0}(1-\nu-K_0)[J_j(\lambda_{m0})I_{j+1}(\lambda_{m0}) + J_{j+1}(\lambda_{m0})I_j(\lambda_{m0})] + 2\lambda_{m0}^2J_j(\lambda_{m0})I_j(\lambda_{m0}).$$

The particular solution w_{m0}^p in (19) reduces substantially because $\mu_{m0} = 0$. To simplify notation in the solution for w_{m0}^h , (43) gives

$$v_{m0,r} = \sum_{j=1}^{\infty} T_j(k_j^c \cos j\theta + k_j^s \sin j\theta)$$

$$T_j = -\left(\frac{2}{\pi Z_{m0}}\right)^{1/2} \frac{\lambda_{m0}^3}{1-\nu-K_0} \times \frac{J_j(\lambda_{m0})I_{j+1}(\lambda_{m0}) + I_j(\lambda_{m0})J_{j+1}(\lambda_{m0})}{\zeta_j}.$$

The boundary conditions (7b) and solution for w_{m0}^h are

$$w_{m0}^h r = I = -w_{m0}^p r = I = \frac{\eta_{m0}}{(8\pi Z_{m0})^{1/2}(1-\nu-K_0)\lambda_{m0}^2} B_2 w_{m0}^h r = 1$$

$$w_{m0}^h = \sum_{j=0}^{\infty} [\bar{P}_j J_j(\lambda_{m0}r) + \bar{Q}_j I_j(\lambda_{m0}r)] \cos j\theta + \sum_{j=1}^{\infty} [\bar{R}_j J_j(\lambda_{m0}r) + \bar{S}_j I_j(\lambda_{m0}r)] \sin j\theta$$

$$\bar{P}_0 = \frac{\eta_{m0}}{(8\pi Z_{m0})^{1/2}(1-\nu-K_0)\lambda_{m0}^2 J_0(\lambda_{m0})} \bar{Q}_0 = 0$$

$$\left\{ \begin{array}{l} \bar{P}_j \\ \bar{Q}_j \end{array} \right\} = \frac{1}{2\zeta_j} \left\{ \begin{array}{l} I_j(\lambda_{m0}) \\ -J_j(\lambda_{m0}) \end{array} \right\} \left(\sum_{i=1}^{j-1} T_i (k_{j-i}^c k_i^c - k_{j-i}^s k_i^s) \right. \\ \left. + \sum_{i=j+1}^{\infty} T_i (k_{i-j}^c k_i^c + k_{i-j}^s k_i^s) + \sum_{i=1}^{\infty} T_i (k_{j+i}^c k_i^c + k_{j+i}^s k_i^s) \right) \\ \left\{ \begin{array}{l} \bar{R}_j \\ \bar{S}_j \end{array} \right\} = \frac{1}{2\zeta_j} \left\{ \begin{array}{l} I_j(\lambda_{m0}) \\ -J_j(\lambda_{m0}) \end{array} \right\} \left(\sum_{i=1}^{j-1} T_i (k_{j-i}^s k_i^c + k_{j-i}^c k_i^s) \right. \\ \left. + \sum_{i=j+1}^{\infty} T_i (-k_{i-j}^s k_i^c + k_{i-j}^c k_i^s) + \sum_{i=1}^{\infty} T_i (k_{j+i}^s k_i^c - k_{j+i}^c k_i^s) \right).$$

Equation (44b) completes the solution for w_{m0} . Expansion of (42) yields

$$\kappa_{m0} = -\left(\frac{2\pi}{Z_{m0}}\right)^{1/2} \frac{\lambda_{m0}^2}{1-\nu-K_0} \times \sum_{j=1}^{\infty} \left[\left(\bar{P}_j \frac{dJ_j(\lambda_{m0}r)}{dr} + \bar{Q}_j \frac{dI_j(\lambda_{m0}r)}{dr} \right)_{r=1} k_j^c \right. \\ \left. + \left(\bar{R}_j \frac{dJ_j(\lambda_{m0}r)}{dr} + \bar{S}_j \frac{dI_j(\lambda_{m0}r)}{dr} \right)_{r=1} k_j^s \right].$$

Notice that d_{m0} is not needed to extend the solution to third order in the eigenvalue. The results of this section apply for all m nodal circle, 0 nodal diameter unperturbed eigensolutions for a general Fourier stiffness representation. As $K_0 \rightarrow \infty$, all perturbation terms approach 0 independent of $k(\theta)$, and the clamped plate eigensolutions are obtained. Similarly, if $K_0 = k(\theta) = 0$, the perturbation terms vanish and we recover the simply supported plate eigensolutions.

To compare with Leissa et al. (1979), consider the case $K(\theta) = 1 + \epsilon \cos \theta$ and choose $\nu = \frac{1}{4}$. Thus, $K_0 = k_1^c = 1$ and all other Fourier coefficients in (38) vanish. The above equations reduce to

$$v_{m0} = \left(\frac{2}{\pi Z_{m0}}\right)^{1/2}$$

$$\times \frac{\lambda_{m0}^2}{\nu} \frac{I_1(\lambda_{m0})J_1(\lambda_{m0}r) - J_1(\lambda_{m0})I_1(\lambda_{m0}r)}{\zeta_1} \cos \theta$$

$$\eta_{m0} = -\frac{2\lambda_{m0}^5}{Z_{m0}\nu^2} \frac{J_1(\lambda_{m0})I_2(\lambda_{m0}) + I_1(\lambda_{m0})J_2(\lambda_{m0})}{\zeta_1} \quad \kappa_{m0} = 0.$$

The findings $\mu_{m0} = \kappa_{m0} = 0$ confirm the expectation, based on symmetry, that the eigenvalues are even in ϵ . The loci for the first three distinct eigenvalues are

$$\begin{aligned}\bar{\lambda}_{00}^4 &= 36.23 - 1.393\epsilon^2 + O(\epsilon^4) \\ \bar{\lambda}_{10}^4 &= 943.3 - 2.902\epsilon^2 + O(\epsilon^4) \\ \bar{\lambda}_{20}^4 &= 5645. - 4.461\epsilon^2 + O(\epsilon^4).\end{aligned}$$

They are monotonically decreasing functions of ϵ . For $\epsilon = 0$, the first three exact, axisymmetric eigenvalues of a plate supported by a uniform spring are recovered. Table 1 compares these results to the Ritz analysis of Leissa et al. (1979), where only values for the fundamental eigenvalue are presented. Over a large range in ϵ , the differences are less than 1 percent. The Ritz predictions bound the true eigenvalues from above and always exceed the perturbation solutions.

Degenerate Eigensolutions. Consider perturbation from a degenerate eigensolution with unperturbed eigenvalue λ_{mn} . The components of \mathbf{D} in (28) reduce from (27), (A1), and (37)

$$\begin{aligned}D_{ij} &= \int_{r=1} B_2^i u_{mn}^i C_2 u_{mn}^j ds = \int_0^{2\pi} u_{mn,r}^i u_{mn,r}^j k(\theta) d\theta \\ \mathbf{D} &= \frac{2\lambda_{mn}^4}{Z_{mn}(1 - \nu - K_0)^2} \begin{bmatrix} k_{2n}^c & k_{2n}^s \\ k_{2n}^s & -k_{2n}^c \end{bmatrix} \\ \mu_{mn}^{1,2} &= \pm \frac{2\lambda_{mn}^4}{Z_{mn}(1 - \nu - K_0)^2} [(k_{2n}^c)^2 + (k_{2n}^s)^2]^{1/2}.\end{aligned}$$

\mathbf{D} has repeated eigenvalues if and only if $k_{2n}^c = k_{2n}^s = 0$. Otherwise, the eigenvalues of \mathbf{D} are distinct and the eigensolutions split. Thus, to first order in ϵ , splitting of the eigensolutions is determined by the following rule: If the Fourier series for $k(\theta)$ has nonzero coefficients for either or both of $\cos 2n\theta$ and $\sin 2n\theta$, then the n nodal diameter eigensolutions split; otherwise they do not. This rule addresses distributed, possibly discontinuous, asymmetric boundary stiffness. Because splitting of the n nodal diameter eigensolutions depends solely on the $2n$ components of the Fourier series for $k(\theta)$, the odd components of the Fourier representation of stiffness do not influence splitting in first order perturbation. Additionally, the number of nodal circles m does not influence splitting. Rules for other boundary asymmetries are similarly obtained.

Discussion

A key feature of the method is that if particular solutions to the inhomogeneous Eqs. (6a) and (7a) can be found, exact perturbation solutions follow readily for any boundary operators B_j , C_j , D_j , E_j rendering (1) self-adjoint. Because the perturba-

tion terms of (1) are only present in the boundary conditions, they do not introduce inhomogeneities into the field Eqs. (6a) and (7a). The inhomogeneity of the field Eq. (6a) is proportional to the unperturbed eigenfunction u_{mn} . The functional form of u_{mn} depends on the operator L and domain P but is independent of the boundary conditions, which only fix constant coefficients. Consequently, the functional form of a calculated particular solution v_{mn}^p does not change for differing boundary conditions; only the constant coefficients of v_{mn}^p change. Because v_{mn}^p is the essential component of the exact solution, exact solutions are available for any boundary conditions once the functional form of v_{mn}^p is determined. Similarly, the functional forms of the inhomogeneities u_{mn} and v_{mn} in (7a) are also independent of the boundary conditions, so exact solutions of (7) are available for any combination of unperturbed and perturbed boundary conditions once the functional form of the particular solution w_{mn}^p is calculated. Thus, the particular solutions (16), (19), (22), (24), (35), and (36) derived for the biharmonic and Laplacian operators on annular domains allow exact calculation of eigensolution perturbations for all such problems with boundary conditions of the form (1b), including those mentioned in the Introduction. Derivation of particular solutions for rectangular domains should not pose significant difficulty, and many other operators, such as that occurring in vibration of plates with in-plane stress (Parker and Mote, 1991), can also be handled in this way. The eigenvalue perturbation expressions (11), (12), (28), and (33) apply for any operator L and domain P .

Boundary condition perturbation has features which make it an attractive alternative to finite element, Ritz, Galerkin, and other discretization methods. The perturbation does not rely on trial functions to estimate the eigenfunctions. This makes it particularly appropriate for analysis of higher eigensolutions for which the selection of trial functions is more difficult; the exact perturbation solutions apply for all eigensolutions. Boundary condition perturbation generates analytical expressions for the evolution of the eigensolutions from the normally well-understood unperturbed problem, thus explicitly identifying dependence on system parameters. Also, though discretized systems predict eigenvalue splitting, rules can not be stated in general terms; they must be inferred from numerical results. In contrast to perturbation analyses that expand higher order eigensolutions in series of the unperturbed eigenfunctions, the results presented here have the aesthetic and practical advantage of requiring the unperturbed eigensolutions for only those eigensolutions for which perturbations are sought.

Pierre (1988) determined that, for distinct eigenvalues of self-adjoint problems, first-order perturbation analysis and Rayleigh quotient analysis yield identical eigenvalue predictions provided the unperturbed eigenfunctions are chosen as the admissible functions for the Rayleigh quotient. Thus, second and third-order perturbations are expected to yield superior eigenvalue predictions compared to those obtained from the Rayleigh quotient using the unperturbed eigenfunctions.

Continuous system modal analysis for dynamic response is easily carried out for the perturbed system since orthogonality of the eigenfunctions s_{mn} is ensured. Physical understanding of the behavior, frequently lost through discretization, is thereby retained. The method also provides a useful means to identify boundary condition asymmetries using measured frequency spectra. In the example, an unknown boundary stiffness can be estimated by selecting a rotational stiffness Fourier series to predict eigenvalues that fit the measured data. The explicit expressions for the dependence of the perturbed eigenvalues on the stiffness simplify this iterative process. The physical system may suggest an initial selection, e.g., six equally spaced bolts in the plate inner boundary support suggests $\cos 6\theta$, $\sin 6\theta$ stiffness dependence might be expected. For design purposes, the eigenvalue formulae can be used to favorably affect the frequency spectrum by appropriate distribution of asymmetry.

Table 1 Comparison of third-order perturbation and Ritz (Leissa et al., 1979) solutions for the fundamental eigenvalue of a circular plate with zero transverse displacement and a rotational spring of stiffness $K(\theta) = 1 + \epsilon \cos \theta$ along the outer boundary. A superscript * indicates the exact value.

ϵ	$\bar{\lambda}_{00}^4$		Percent difference
	Perturbation	Ritz	
0	6.019*	6.04	-0.3
0.5	5.990	6.02	-0.5
0.6	5.977	6.01	-0.5
0.7	5.962	6.00	-0.6
0.8	5.944	5.99	-0.8
0.9	5.924	5.97	-0.8

Application of the method to particular problems is not difficult. For annular domain problems, Fourier series expansion of asymmetries and orthogonality of the trigonometric functions reduces the eigensolution perturbations to algebraic expressions. Symbolic mathematics software facilitates this reduction. Since the computations are exact, programming errors are avoided by verifying each calculation by direct substitution. The algebraic formulae are convenient to program when the eigensolutions are to be used for response analyses, system identification, or control.

Conclusions

(1) A boundary condition perturbation method is developed for linear, self-adjoint eigenvalue problems where the perturbation terms are restricted to the boundary conditions. Formal expressions for the eigenvalue perturbations are derived through third order in ϵ for distinct unperturbed eigensolutions and through second order for degenerate eigensolutions. This extends the magnitude of perturbation that can be treated accurately.

(2) For any boundary condition perturbation problem of plate vibration or the Helmholtz equation on annular domains, exact eigensolution perturbations are presented. The principal benefits are

- no approximation is introduced beyond truncation of the asymptotic series (3, 4);
- simpler forms of the exact solutions compared to traditional eigenfunction expansions allow higher order perturbations to be treated with relative ease;
- convenient form of the eigensolutions simplifies their use in modal analysis, system identification, design, and control applications;
- accuracy of the method is retained for all eigensolutions; and
- results are easily derived and verified using symbolic mathematics software.

Confinement of the perturbation terms to the boundary conditions ensures that, if particular solutions can be found for other operators and domains, exact solutions are readily obtained for arbitrary perturbed boundary conditions.

(3) Splitting of degenerate unperturbed eigensolutions is determined by the eigenvalues of a symmetric, algebraic eigenvalue problem. In contrast to previous works where splitting is studied, distributed, discontinuous asymmetries are treated by the method presented. Discrete asymmetries can be studied as a special case. Both of the split eigensolutions are calculated. For annular domains, Fourier series representation of the asymmetric boundary perturbations leads to simple rules that determine splitting by inspection of the Fourier coefficients.

(4) Natural applications of the method are to vibration and buckling problems, where many known unperturbed solutions exist. Buckling solutions are particularly sensitive to asymmetry. Geometric asymmetries such as noncircular boundaries (e.g., elliptical domains) or slightly skew rectangles can be cast as approximate eigenvalue problems of the form (1) and the presented results apply (Parker and Mote, 1996). Asymmetric boundary stiffness variations and partial boundary supports are readily handled for these regions.

References

Courant, R., and Hilbert, D., 1989, *Methods of Mathematical Physics*, John Wiley and Sons, New York.

Leissa, A. W., Laura, P. A. A., and Gutierrez, R. H., 1979, "Transverse Vibrations of Circular Plates having Nonuniform Edge Constraints," *Journal of the Acoustical Society of America*, Vol. 66, pp. 180-184.

McLachlan, N. W., 1955, *Bessel Functions for Engineers*, Clarendon Press, Oxford, pp. 190-206.

Meirovitch, L., 1967, *Analytical Methods in Vibration*, Macmillan, New York, p. 183.

Morse, P. M., and Feshbach, H., 1953, *Methods of Theoretical Physics*, McGraw-Hill, New York.

Nayfeh, A. H., Mook, D. T., Lobitz, D. W., and Sridhar, S., 1976, "Vibrations of Nearly Annular and Circular Plates," *Journal of Sound and Vibration*, Vol. 47, pp. 75-84.

Parker, R. G., and Mote, Jr., C. D., 1991, "Tuning of the Natural Frequency Spectrum of a Circular Plate by In-plane Stress," *Journal of Sound and Vibration*, Vol. 145, Feb., pp. 95-110.

Parker, R. G., and Mote, Jr., C. D., 1996, "Exact Perturbation for the Vibration of Almost Annular or Circular Plates," *Journal of Vibration and Acoustics*, Vol. 118.

Pierre, C., 1987, "Eigensolution Perturbation for Systems with Perturbed Boundary Conditions," *Journal of Sound and Vibration*, Vol. 112, No. 1, pp. 167-172.

Pierre, C., 1988, "Comments on Rayleigh's Quotient and Perturbation Theory for the Eigenvalue Problem," *ASME JOURNAL OF APPLIED MECHANICS*, Vol. 55, pp. 986-988.

Roach, G. F., 1982, *Green's Functions*, Cambridge University Press, Cambridge, UK, p. 156.

Shen, I. Y., and Mote, Jr., C. D., 1993, "On the Mode Splitting of Degenerate Mechanical Systems Containing Cracks," *ASME JOURNAL OF APPLIED MECHANICS*, Vol. 60, Dec., pp. 929-935.

Stakgold, I., 1979, *Green's Functions and Boundary Value Problems*, John Wiley and Sons, New York.

Tobias, S. A., and Arnold, R. N., 1957, "The Influence of Dynamical Imperfection on the Vibration of Rotating Disks," *Proc. of the Inst. of Mech. Engineers*, Vol. 171, pp. 669-690.

Tseng, J. G., and Wickert, J. A., 1994, "Vibration of an Eccentrically Clamped Annular Plate," *Journal of Vibration and Acoustics*, Vol. 116, pp. 155-160.

Tseng, J. G., and Wickert, J. A., 1994, "On the Vibration of Bolted Plate and Flange Assemblies," *Journal of Vibration and Acoustics*, Vol. 116, pp. 468-473.

Yu, R. C., and Mote, Jr., C. D., 1987, "Vibration and Parametric Excitation in Asymmetric Circular Plates Under Moving Loads," *Journal of Sound and Vibration*, Vol. 119, pp. 409-427.

APPENDIX A

Symmetry of D in (28)

The boundary conjunct defined in (10) takes the form of an integral over the boundary ∂P . Assuming a fourth-order operator L , it can be expressed in the form (Stakgold, 1979)

$$J(u, v) = \int_{\partial P} [B_1^g u B_1^n v + B_2^g u B_2^n v - B_1^n v B_1^g u - B_2^n v B_2^g u] d\hat{s} \quad (A1)$$

$B_{1,2}^g$ are boundary operators for the geometric boundary conditions and $B_{1,2}^n$ are the corresponding natural boundary conditions.

For concreteness, $J(u_{mn}^{1,2}, v_{mn})$ in (27) are evaluated for the case where B_1 and B_2 in (5b) are natural boundary operators, $B_1 = B_1^n$ and $B_2 = B_2^n$. Thus, using (5b), (6b), and (26),

$$\begin{aligned} B_1^n u_{mn}^{1,2} &= B_2^n u_{mn}^{1,2} = 0 \\ B_1^n v_{mn} &= -C_1 u_{mn} = -a_{mn}^1 C_1 u_{mn}^1 - a_{mn}^2 C_1 u_{mn}^2 \\ B_2^n v_{mn} &= -C_2 u_{mn} = -a_{mn}^1 C_2 u_{mn}^1 - a_{mn}^2 C_2 u_{mn}^2. \end{aligned}$$

Direct substitution into (A1) yields

$$\begin{aligned} -J(u_{mn}^1, v_{mn}) &= a_{mn}^1 \int_{\partial P} [B_1^g u_{mn}^1 C_1 u_{mn}^1 + B_2^g u_{mn}^1 C_2 u_{mn}^1] d\hat{s} \\ &\quad + a_{mn}^2 \int_{\partial P} [B_1^g u_{mn}^1 C_1 u_{mn}^2 + B_2^g u_{mn}^1 C_2 u_{mn}^2] d\hat{s} \\ &= D_{11} a_{mn}^1 + D_{12} a_{mn}^2 \end{aligned} \quad (A2a)$$

$$\begin{aligned} -J(u_{mn}^2, v_{mn}) &= a_{mn}^1 \int_{\partial P} [B_1^g u_{mn}^2 C_1 u_{mn}^1 + B_2^g u_{mn}^2 C_2 u_{mn}^1] d\hat{s} \\ &\quad + a_{mn}^2 \int_{\partial P} [B_1^g u_{mn}^2 C_1 u_{mn}^2 + B_2^g u_{mn}^2 C_2 u_{mn}^2] d\hat{s} \\ &= D_{21} a_{mn}^1 + D_{22} a_{mn}^2. \end{aligned} \quad (A2b)$$

Self-adjointness of the eigenvalue problem (1) requires that, for any two eigenfunctions \bar{g} and \bar{s} ,

$$J(\bar{s}, \tilde{s}) = 0 = \int_{\partial P} [B_1^g \bar{s} B_1^n \tilde{s} + B_2^g \bar{s} B_2^n \tilde{s} - B_1^g \tilde{s} B_1^n \bar{s} - B_2^g \tilde{s} B_2^n \bar{s}] d\hat{s}. \quad (\text{A3})$$

With $B_1 = B_1^n$ and $B_2 = B_2^n$ as above and with (4), (1b) gives

$$\begin{aligned} B_1^g \bar{s} &= -\epsilon C_1 \bar{u} + O(\epsilon^2) & B_1^g \tilde{s} &= B_1^g \bar{u} + O(\epsilon) \\ B_2^g \bar{s} &= -\epsilon C_2 \bar{u} + O(\epsilon^2) & B_2^g \tilde{s} &= B_2^g \bar{u} + O(\epsilon) \end{aligned} \quad (\text{A4})$$

with similar equations for \tilde{s} . Letting $\bar{s} = s_{mn}^1 = u_{mn}^1 + O(\epsilon)$ and $\tilde{s} = s_{mn}^2 = u_{mn}^2 + O(\epsilon)$, substitution of (A4) into (A3) yields

$$\begin{aligned} J(s_{mn}^1, s_{mn}^2) = 0 = \epsilon \int_{\partial P} &[-B_1^g u_{mn}^1 C_1 u_{mn}^2 - B_2^g u_{mn}^1 C_2 u_{mn}^2 \\ &+ B_1^g u_{mn}^2 C_1 u_{mn}^1 + B_2^g u_{mn}^2 C_2 u_{mn}^1] d\hat{s} + O(\epsilon^2) \end{aligned} \quad (\text{A5})$$

The condition (A5) for self-adjointness of the eigenvalue problem (1) requires that $D_{12} = D_{21}$ in (A2), and \mathbf{D} is symmetric.

APPENDIX B

Expansion of $J(u_{mn}^{1,2}, w_{mn})$ in (32)

For the boundary conjunct in the form (A1), expansion of $J(u_{mn}^i, w_{mn})$ for $u_{mn}^{1,2}$ satisfying the natural boundary conditions $B_1^n u_{mn}^{1,2} = 0$ and $B_2^n u_{mn}^{1,2} = 0$ yields

$$J(u_{mn}^i, w_{mn}) = \int_{\partial P} [B_1^g u_{mn}^i B_1^n w_{mn} + B_2^g u_{mn}^i B_2^n w_{mn}] d\hat{s} \quad i = 1, 2.$$

Substitution of the boundary conditions (7b) and use of the decomposition (29) gives

$$\begin{aligned} J(u_{mn}^i, w_{mn}) &= - \int_{\partial P} [B_1^g u_{mn}^i C_1 (c_{mn}^1 u_{mn}^1 + c_{mn}^2 u_{mn}^2 \\ &\quad + v_{mn}^h + v_{mn}^p) + B_1^g u_{mn}^i D_1 u_{mn}] d\hat{s} \\ &\quad - \int_{\partial P} [B_2^g u_{mn}^i C_2 (c_{mn}^1 u_{mn}^1 + c_{mn}^2 u_{mn}^2 \\ &\quad + v_{mn}^h + v_{mn}^p) + B_2^g u_{mn}^i D_2 u_{mn}] d\hat{s} \\ &= -c_{mn}^1 \int_{\partial P} [B_1^g u_{mn}^i C_1 u_{mn}^1 + B_2^g u_{mn}^i C_2 u_{mn}^1] d\hat{s} \\ &\quad + J(u_{mn}^i, w_{mn})|_{c_{mn}^{1,2}=0} \quad i = 1, 2 \end{aligned} \quad (\text{B1})$$

where the last term includes all terms independent of $c_{mn}^{1,2}$. Comparison of (B1) with the definitions of D_{ij} in (A2) yields (32).

Asymptotic Theory of Broadband Rotor Thrust, Part I: Manipulations of Flow Probabilities for a High Number of Blades

R. Martinez

Cambridge Acoustical Associates, Inc.
200 Boston Avenue, Suite 2500,
Medford, MA 02155-4243

Modern computer predictions of the frequency spectrum of net thrust for a rotor in turbulent flow display a number of features that call for interpretation. The success of the asymptotic development described here in providing the needed explanations lies in the relative generality of the model. The rotor is fully three dimensional. It is not a cutaway blade row. The theory's only requirement is that the number of blades be large (six is enough). The most practical aspect of the new work is that it supplies a highly accurate analytical solution for the broadband "haystacking" in a propulsor of high solidity. An important intermediate result is that the probabilistic amplitude of random gusts perceived by that propulsor climbs radially outwards along its blades, solely by virtue of the three-dimensional kinematics of the rotor's aerodynamic sampling of the turbulent flowfield: The behavior is r^3 for the normal-to-rotor flow statistics and r^4 for the cross correlation of normal and in-plane downwash components. The final effect is a spanwise distribution of sectional loads that is highly concentrated at the blade tips. The turbulence in the present study is homogeneous and isotropic but its integral scale may take on essentially any value and the asymptotic analysis still holds.

1 Introduction

This paper revisits the problem of predicting the frequency spectrum of broadband thrust experienced by a rotor ingesting homogeneous isotropic turbulence (Fig. 1). In Fig. 2, whose solid curve displays the output of a hypothetical example of the type treated exactly by Jiang et al. (1991), and independently by the present author (1990), one notes

- (1) a broad "haystack" hump roughly over the blade-rate frequency $\omega = B\Omega$, with
- (2) a small but still discernible first harmonic hump at $\omega/B\Omega \approx 2$, and
- (3) a slight right shift for the maximum response, which occurs just above $\omega/B\Omega = 1$.

The figure actually depicts a mild example for each of the three effects. It is nonetheless useful because it addresses a turbulence-scale case for which a simpler theory can also justifiably be brought to bear: Sevik's pioneering treatment (1971) of a rotor where by prescription a given turbulent "eddy" is struck no more than once. His model yields the broken monotonic curve and therefore fails to account for any of the three features noted in the solid one.

The first paper relevant to the work presented here seems to be Liepmann's 1952 analysis of a single airfoil cutting through a wave number spectrum of random isotropic downwash. Sev-

ik's later handling of the rotor problem differs in spirit from this, as well as from almost everything else both before and after 1971, in its attempt to keep the turbulence description in its original spatial domain. To cite but a few studies (beside Liepmann's) that have taken the alternate spectral approach: Mani (1971), for a two-dimensional cascade; Homicz and George (1974), Breit and Dickinson (1990), and Brown (1993), for a rotor; Blake (1984), for both cascades and rotors; Ventres et al. (1982) and Glegg (1993), for blade/blade correlated and uncorrelated flows, respectively, for a modern ducted propulsor at high subsonic speeds.

The present paper shows that not only can Sevik's spatial viewpoint be generalized readily to include the missing blade-to-blade temporal changes in flow statistics, i.e., the causes of the nonmonotonic haystack response, but that the resulting theory lends itself uniquely to an asymptotic analysis based on a single requirement: that the number of blades B in the rotor be large. The "closed-form" solution developed here for the frequency spectrum of net rotor thrust is uniformly valid for all frequencies $0 < \omega/B\Omega < \infty$ for any one practical value of the turbulence scale Λ/R , and, conversely, for an essentially unlimited range in Λ/R , at any one $\omega/B\Omega$. The new theory explains simply which of, and how, the flow and aerodynamic parameters affect all three of the features listed above for rigorously computed frequency spectra of rotor thrust. This paper addresses points 1 and 2 and defers 3 to a companion article.

The mathematical manipulations of the asymptotic theory will appear here to rely heavily on an assumed exponential form $\exp(-\bar{q}/\Lambda)$ for the fundamental correlation of in-line velocities " $f(q)$," for the isotropic flow impinging the rotor. However, yet another future paper will analytically continue the final results of this one to any form of $f(q)$. In doing so it will not only generalize f away from the exponential form, but will also dispense altogether with the somewhat artificial concept of an integral scale Λ in the context of rotor/turbulence interaction.

Contributed by the Applied Mechanics Division of THE AMERICAN SOCIETY OF MECHANICAL ENGINEERS for publication in the ASME JOURNAL OF APPLIED MECHANICS.

Discussion on this paper should be addressed to the Technical Editor, Professor Lewis T. Wheeler, Department of Mechanical Engineering, University of Houston, Houston, TX 77204-4792, and will be accepted until four months after final publication of the paper itself in the ASME JOURNAL OF APPLIED MECHANICS.

Manuscript received by the ASME Applied Mechanics Division, Sept. 23, 1994; final revision, Jan. 6, 1995. Associate Technical Editor: T. R. Akylas.

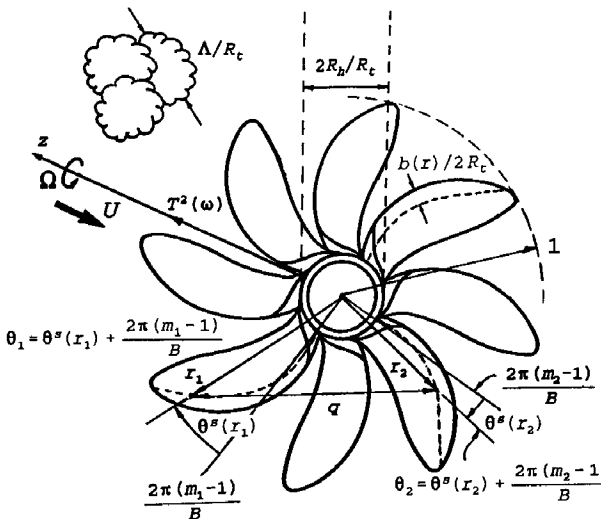


Fig. 1 NASA propfan normalized by its own radius R_t : The eddy size of the incident isotropic turbulence is Δ/R_t . The blades are twisted, swept, and of variable quarter chord $b(r)/2R_t$. The sketch defines the dimensionless coordinates r_1, r_2 (without tildes), and θ_1, θ_2 , of two general blade stations where turbulence velocities and random sectional loads are being correlated. Variable z runs along the fan's axis. The in-plane angle θ_2 has suppressed the convective effect of the turning speed Ω to make for a simpler picture. Variable q has similarly ignored the time-dependent axial distance Uz/R_t .

The new approximate analysis joins a growing class of mathematical treatments that make the same high- B assumption; see, for example, the acoustic theories by Crighton and Parry (1991), Peake and Crighton (1991), and Envia (1992). But in the tonal problem of those studies there is a single, definite relation connecting the high order νB of all the usual Bessel functions to their high-frequency argument $\nu B\Omega^* \text{const}$. The work described here, on the other hand, will be a high- B theory without restrictions regarding frequency range, essentially because in a nondeterministic problem a rotor's frequencies and circumferential modes exist independently of each other.

2 Summary of the Exact Fully Correlated Theory as the Launching Point for the New Work

Following Sevik (1971), $\tilde{T}^2(\omega)$ will be the frequency transform of the rotor's temporally correlated thrust $\tilde{T}^2(\tau)$, whose square power will therefore be strictly symbolic:

$$\tilde{T}^2(\tau) = \int_0^\infty d\omega \cos \omega \tau \tilde{T}^2(\omega);$$

$$\tilde{T}^2(\omega) = \int_{-\infty}^\infty \frac{d\tau}{\pi} e^{i\omega\tau} \tilde{T}^2(\tau). \quad (1a, b)$$

One defines the normalized thrust spectrum $T^2(\omega)$ related to $\tilde{T}^2(\omega)$ by

$$T^2(\omega) = \frac{\tilde{T}^2(\omega)}{\rho^2 U^3 R_t^5 (u/U)^2} = \frac{4\pi B^2}{\Gamma} \left(\frac{\Lambda}{R_t} \right) F, \quad (2)$$

where our new function F turns out to depend on eight nondimensional parameters:

$$B \quad \frac{b}{R_t} \quad \theta^s(r) \quad \frac{R_h}{R_t} \quad \frac{R_{\text{eff}}}{R_t} \quad \frac{B\Omega\Lambda}{U} \quad \frac{\Lambda}{R_t} \quad \Gamma = \frac{\omega\Lambda}{U}.$$

The first five and part of the sixth fix the rotor geometrically. The ratio $b/R_t = b(r)/R_t$ denotes the distribution of halfchords along the span "r" of each blade normalized by R_t (Fig. 1); $\theta^s(r)$ is the distribution of mean blade sweep from root to tip. The fourth parameter is the ratio of hub to tip radii. The fifth is an artifact of strip hydrodynamics: it introduces the radius R_{eff} to be that spanwise station past which one could arbitrarily cut off the integration of running loads to model "tip relief" crudely. Λ/R_t is the integral scale of the homogeneous isotropic turbulence normalized by the rotor's tip radius.

Embedded in the sixth parameter is the rotor's advance ratio J_t , since one may write it as

$$\frac{B\Omega\Lambda}{U} = \pi B \left(\frac{\Omega R_t}{\pi U} \right) \left(\frac{\Lambda}{R_t} \right) = \frac{\pi B}{J_t} \left(\frac{\Lambda}{R_t} \right); \quad J_t = \frac{\pi U}{\Omega R_t}. \quad (3a, b)$$

J_t is thus not independent of the others in the above roster and consequently does not show up in it. Ω and U are the rotor's turning and forward speeds, respectively. U normalizes the amplitude of the RMS turbulent fluctuations "u" in the denominator of the right-hand side of (2)'s first equality.

One finds after a fair amount of work that F may be put in a form that describes how the three-dimensional flow correlation tensors R^{zz} , $R^{z\theta, \theta z}$, and $R^{\theta\theta}$ are operated upon, in cylindrical coordinates, by a corresponding set of double $r_{1,2}$ integrals, a pair of $m_{1,2}$ summations over the B circumferential blade positions, and the τ transform of (1b). These operators will appear here compactly designated by the letters \mathcal{L}_{zz} , $\mathcal{L}_{z\theta}$, $\mathcal{L}_{\theta\theta}$:

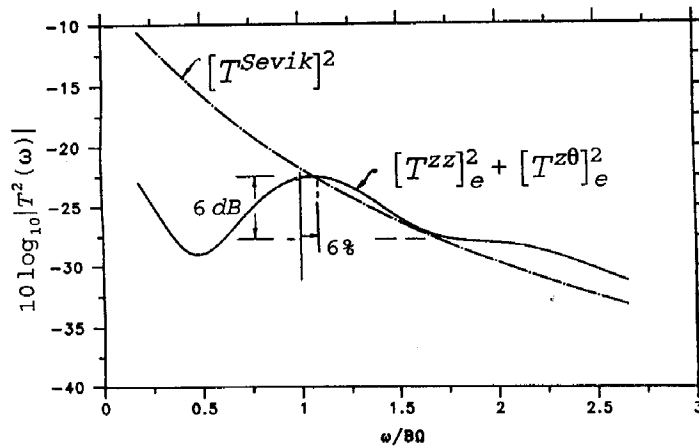


Fig. 2 Sample numerical experiment for the exact theory (solid curve), and for Sevik's model of effectively stationary blades: The exact calculation ("e" subscript) displays a broad, 6 dB hump over the blade-rate frequency and a six percent right shift for that maximum response.

$$F = \frac{\omega\pi}{B^2 R_t^2} \{ \mathcal{L}_{zz}[R^{zz}] + \mathcal{L}_{z\theta}[R^{z\theta} + R^{\theta z}] + \mathcal{L}_{\theta\theta}[R^{\theta\theta}] \}, \quad (4a)$$

$$\approx \frac{\omega\pi}{B^2 R_t^2} \{ \mathcal{L}_{zz}[R^{zz}] + \mathcal{L}_{z\theta}[R^{z\theta} + R^{\theta z}] \}. \quad (4b)$$

The second equality of (2) and (4b)'s first term together establish what we later shall refer to as the normal-to-rotor thrust correlation component $[T^{zz}(\omega)]^2$, etc. Blade pitch, and more generally, blade twist, is the cause of the three-element form of (4a). The $R^{zz, z\theta, \theta z}$ nomenclature in (4b) has adapted Hinze's equation (1-44) (1975); e.g., for R^{zz} his "i" = "j" indices have both become equal to our z in Fig. 1, and his points "A" and "B" have become our general correlation points 1 and 2. A rotor whose blade chords lie flat on their plane of rotation would contain only the R^{zz} component because the w^θ flow component would then only graze the blades' surfaces. Likewise, a rotor with similarly flat blades, but with chords now feathered into the freestream U , would be subject only to the flow's circumferential autocorrelation $R^{\theta\theta}$. And while $R^{\theta\theta}$ might be expected to contribute significantly to the net torque then, it would clearly have no impact on rotor thrust.

R^{zz} is given by

$$R^{zz} = \frac{1}{2} \left(q - \frac{\xi_z^2}{q} \right) \frac{\partial f}{\partial q} + f; \quad f = f(q) = e^{-(R/\Lambda)q}. \quad (5a, b)$$

Variable $q = \bar{q}/R_t$ is the normalized correlation distance between points 1 and 2:

$$q = \{ r_1^2 + r_2^2 - 2r_1 r_2 \cos [\theta^s(r_1) - \theta^s(r_2)] + 2\pi(m_1 - m_2)/B - \Omega\tau \} + (U\tau/R_t)^2 \}^{1/2}. \quad (6)$$

Quantity ξ_z in (5a) is the component of q normal to the rotor disk: $\xi_z = U\tau/R_t$, which embodies the frozenness hypothesis along with $\Omega\tau$, which appears in the angular argument of (6). Our modeled turbulence will therefore not undergo the type of distortion which Atassi and Grzedzinski (1989) analyze in their treatment of deterministic flow structures approaching a body.

The first step needed here to cast the exact spatial-domain theory in a form amenable to asymptotic analysis is to make use of the identity

$$\int_{-\infty}^{\infty} d\tau e^{i\omega\tau} \sum_{m_1=1}^B \sum_{m_2=1}^B e^{-q/\Lambda} = -\frac{2B^2}{U} \frac{\partial}{\partial \Lambda^{-1}} \times \sum_{\nu=-\infty}^{\infty} K_{\nu B}(\gamma r_1) I_{\nu B}(\gamma r_2) \cos [\nu B \{ \theta^s(r_1) - \theta^s(r_2) \}]. \quad (7)$$

The above holds for $r_2 < r_1$; a similar expression applies for $r_2 > r_1$. One therefore finds that the two parts of (4b)'s right-hand side are expressible as a series of circumferential modes ν , e.g.,

$$\frac{\omega\pi}{B^2 R_t^2} \mathcal{L}_{zz}[R^{zz}] = \sum_{\nu=-\infty}^{\infty} h_{\nu}^{zz}(\gamma), \quad (8a)$$

where it turns out that

$$h_{\nu}^{zz}(\gamma) = -4\Gamma\left(\frac{R_t}{\Lambda}\right)^2 \int_{R_t/R_t}^{R_{\text{eff}}/R_t} dr_1 g^z(r_1) \int_{R_t/R_t}^{r_1} dr_2 g^z(r_2) \times \cos [\alpha(r_1) - \alpha(r_2)] \cos [\nu B \{ \theta^s(r_1) - \theta^s(r_2) \}] \times \left\{ \frac{1}{2} \left[r_1^2 + r_2^2 + \frac{2(\nu B)^2}{\gamma^2} \right] K_{\nu B}(\gamma r_1) I_{\nu B}(\gamma r_2) \right.$$

$$+ r_1 r_2 K'_{\nu B}(\gamma r_1) I'_{\nu B}(\gamma r_2) + \frac{1}{\gamma} [r_1 K'_{\nu B}(\gamma r_1) I_{\nu B}(\gamma r_2) + r_2 K_{\nu B}(\gamma r_1) I'_{\nu B}(\gamma r_2)] \} . \quad (8b)$$

$K_{\nu B}$ and $I_{\nu B}$ are modified Bessel functions. The argument γ of h_{ν}^{zz} is the dimensionless radial "wave number"

$$\gamma = \sqrt{\left(\frac{\omega}{B\Omega} - \nu \right)^2 \left(\frac{B\Omega\Lambda}{U} \right)^2 + 1} \left(\frac{R_t}{\Lambda} \right). \quad (9)$$

The function $g^z(r)$ in (8b) is the z component of the deterministic aerodynamic transfer function for the blade section at radial station r :

$$g^z(r) = \frac{b(r)/R_t}{\sqrt{1 + J^2(r)/\pi^2}} \times \frac{\pi/J(r)}{\sqrt{1 + [2\pi\Gamma b(r)/\Lambda]/\sqrt{1 + \pi^2/J^2(r)}}}. \quad (10a)$$

$J(r)$ stands for J_r/r , which determines the twist distribution from root to tip by placing every blade section at zero angle of attack relative to the total local freestream $[U^2 + (\Omega R_t r)^2]^{1/2}$, with r dimensionless.

A related function $g^\theta(r)$ emerges in connection with the "z θ " problem in the second term of (4b)'s right-hand side. We state it now for purposes of comparison:

$$g^\theta(r) = g^z(r) \cdot J(r)/\pi = \frac{b(r)/R_t}{\sqrt{1 + J^2(r)/\pi^2}} \times \frac{1}{\sqrt{1 + [2\pi\Gamma b(r)/\Lambda]/\sqrt{1 + \pi^2/J^2(r)}}}. \quad (10b)$$

The second multiplicative factor of g^θ in (10b), i.e., $1/\sqrt{\dots}$, is the amplitude of a popular approximation of the Sears function (e.g., Goldstein, 1976) as the relevant transfer aerodynamic function for aero/hydroacoustically compact blade chords. Symbol α will denote the Sears phase for use in (8b) and others that will follow:

$$\alpha(r) = \frac{\Gamma b(r)}{\Lambda} \left[\frac{1}{\sqrt{1 + \pi^2/J^2(r)}} - \frac{\pi^2 \Lambda}{2[\Lambda \sqrt{1 + \pi^2/J^2(r)} + 2\pi\Gamma b(r)]} \right]. \quad (11)$$

The second term on (4b)'s right, which contains the effects of normal/in-plane cross correlation of turbulence velocities, is also expressible as a series of circumferential modes,

$$h_{\nu}^{\theta\theta}(\gamma) = 4 \frac{\omega}{\Omega} \left(\frac{R_t}{\Lambda} \right)^3 \left(\frac{B\Omega\Lambda}{U} \right)^2 \nu \left(\frac{\omega}{B\Omega} - \nu \right) \frac{1}{\gamma^2} \int_{R_t/R_t}^{R_{\text{eff}}/R_t} dr_1 \times \int_{R_t/R_t}^{r_1} dr_2 \cdot \left[\frac{g^z(r_2) g^\theta(r_2)}{r_2} + \frac{g^z(r_1) g^\theta(r_1)}{r_1} \right] \times \cos [\nu B \{ \theta^s(r_1) - \theta^s(r_2) \}] \cdot \cos [\alpha(r_1) - \alpha(r_2)] \times \left\{ \frac{1}{2} \left[r_1^2 + r_2^2 + \frac{2(\nu B)^2}{\gamma^2} \right] K_{\nu B}(\gamma r_1) I_{\nu B}(\gamma r_2) + r_1 r_2 K'_{\nu B}(\gamma r_1) I'_{\nu B}(\gamma r_2) - \frac{1}{\gamma} [r_1 K'_{\nu B}(\gamma r_1) I_{\nu B}(\gamma r_2) + r_2 K_{\nu B}(\gamma r_1) I'_{\nu B}(\gamma r_2)] \right\}. \quad (12)$$

3 The New Asymptotic Analysis for “ $B \gg 1$ ”

One takes γ in the arguments $\gamma r_1, \gamma r_2$ of the Bessel functions $K_{\nu B}, I_{\nu B}$ in (8b), (12) and writes it as $\gamma = \nu B(\gamma/\nu B)$ at least for $\nu \neq 0$. I.e., from (9) one defines

$$\begin{aligned}\hat{\gamma} &\equiv \frac{\gamma}{\nu B} = \sqrt{\left(\frac{\omega}{B\Omega} - \nu\right)^2 \left(\frac{\Omega\Lambda}{\nu U}\right)^2 + (\nu B)^{-2} \left(\frac{R_t}{\Lambda}\right)} \\ &= \sqrt{\left(\frac{\omega}{B\Omega} - \nu\right)^2 \left(\frac{\pi}{\nu J_t} \cdot \frac{\Lambda}{R_t}\right)^2 + (\nu B)^{-2} \left(\frac{R_t}{\Lambda}\right)}, \quad (13)\end{aligned}$$

and then expresses $K_{\nu B}(\nu B \hat{\gamma} r_1), I_{\nu B}(\nu B \hat{\gamma} r_2)$, etc., in terms of their turning-point expansions (cf., for example, Abramowitz and Stegun, 1968). After a great deal of mostly self-canceling algebra, the r_2 integral in (8b) filters down to

$$\begin{aligned}&\int_{R_h/R_t}^{r_1} dr_2 g^z(r_2) \cos [\alpha(r_1) - \alpha(r_2)] \\ &\times \cos \{ \nu B[\theta^s(r_1) - \theta^s(r_2)] \} \left\{ \frac{1}{2} \left[r_1^2 + r_2^2 + \frac{2(\nu B)^2}{\gamma^2} \right] \right. \\ &\times K_{\nu B}(\gamma r_1) I_{\nu B}(\gamma r_2) + r_1 r_2 K'_{\nu B}(\gamma r_1) I'_{\nu B}(\gamma r_2) \\ &+ \frac{1}{\gamma} [r_1 K'_{\nu B}(\gamma r_1) I_{\nu B}(\gamma r_2) + r_2 K_{\nu B}(\gamma r_1) I'_{\nu B}(\gamma r_2)] \left. \right\} \\ &\approx \frac{-2r_1^3 g^z(r_1)}{(\nu B)^4 [1 + (\hat{\gamma} r_1)^2]^3} = \frac{-2r_1^3 (\nu B)^2 g^z(r_1)}{[(\nu B)^2 + (\gamma r_1)^2]^3}. \quad (14a)\end{aligned}$$

For reasons that are beyond the scope of the present paper, but which appear documented in detail in Martinez (1993), this result holds regardless of the value of Λ/R_t so long as $B \gg 1$. The size of the largest error in the overall expansion is $4/(\nu B)$ (i.e., it is independent of Λ/R_t). That maximum “global” error occurs when Λ/R_t is large rather than small. The magnitude of the error decreases to $O(\nu B)^{-3/2}$ when Λ/R_t is small rather than large. One similarly finds that the r_2 integral in (12) becomes

$$\begin{aligned}&\int_{R_h/R_t}^{r_1} dr_2 \frac{g^z(r_2) g^\theta(r_2)}{r_2} \cos [\alpha(r_1) - \alpha(r_2)] \\ &\times \cos \{ \nu B[\theta^s(r_1) - \theta^s(r_2)] \} \left\{ \frac{1}{2} \left[r_1^2 + r_2^2 + \frac{2(\nu B)^2}{\gamma^2} \right] \right. \\ &\times K_{\nu B}(\gamma r_1) I_{\nu B}(\gamma r_2) + r_1 r_2 K'_{\nu B}(\gamma r_1) I'_{\nu B}(\gamma r_2) \left. \right\} \\ &- \frac{1}{\gamma} [r_1 K'_{\nu B}(\gamma r_1) I_{\nu B}(\gamma r_2) + r_2 K_{\nu B}(\gamma r_1) I'_{\nu B}(\gamma r_2)] \left. \right\} \\ &\approx \frac{2r_1^4 \hat{\gamma}^2 g^z(r_1) g^\theta(r_1)}{(\nu B)^4 [1 + (\hat{\gamma} r_1)^2]^3} = \frac{2r_1^4 \gamma^2 g^z(r_1) g^\theta(r_1)}{[(\nu B)^2 + (\gamma r_1)^2]^3}. \quad (14b)\end{aligned}$$

The final equalities in (14a, b) have reabsorbed νB into the original meaning of γ : $\gamma \equiv \nu B \hat{\gamma}$. These two expressions contain the two main analytical results of the paper. They explain how a B -bladed rotor perceives kinematically the field of homogeneous isotropic turbulence striking it. The result in (14a) states that the sampled subfield of normal-to-rotor statistics “zz” rises from hub to tip as r_1^3 , for eddy integral scales in the “large” range $\Lambda/R_t \gg 1/B$ and for frequencies in the neighborhood of the blade rate or its harmonics. Under both of these conditions the denominator in (14a)’s final right side becomes insensitive to r_1 as γ becomes much smaller than B (e.g., for $\nu = 1$), which is to say that $\hat{\gamma}$ becomes much smaller than 1. The effective rectilinear “gust” amplitudes of the “zz” field thus

climb radially as $r_1^{3/2}$, just by virtue of the acknowledgement by the rotor of the three-dimensionality of the turbulence field, i.e., by sampling it aerodynamically along a correct, *divergent* set of loaded quarter-chord curves. This novel finding is obviously beyond the reach of any two-dimensional cascade analysis such as Mani’s (1971), which focuses on a single slice around the rotor taken at some favorite radial position of that same three-dimensional field. Equation (14b) similarly deduces that the rotor-sampled “ $z\theta$ ” velocities coalesce at the rotor’s blade tips at the even higher rate of r_1^4 , and that their effective rectilinear gust amplitudes therefore do so as r_1^2 .

It is important to understand that these conclusions have nothing to do with the additional radially dependent “kinematics” of the aerodynamic transfer functions $g^z(r_1)$ and $g^\theta(r_1)$. The next step is to bring them in. One defines for convenience a new function $G(r)$ to be

$$G(r) = \frac{[b(r)/R_t]^2}{1 + J^2(r)/\pi^2} \times \frac{1}{1 + [2\pi\Gamma b(r)/\Lambda]/\sqrt{1 + \pi^2/J^2(r)}}, \quad (15)$$

which incidentally is $[g^\theta(r_1)]^2$ from (10b). Then

$$[g^z(r_1)]^2 = \frac{\pi^2}{J^2(r_1)} G(r_1) = \frac{\pi^2 r_1^2}{J_t^2} G(r_1). \quad (16a)$$

The first equality of (16a) follows from (10a) and its second equality from (18). The result in (10b) similarly leads to

$$g^z(r_1) g^\theta(r_1) = \frac{\pi r_1}{J_t} G(r_1). \quad (16b)$$

Inserting these results into (8) and (12), and these in turn into (18), etc., and finally into (4b) and (2), one obtains that

$$\begin{aligned}[T^{\text{total}}(\omega)]_a^2 &\approx [T^{zz}(\omega)]_a^2 + [T^{z\theta}(\omega)]_a^2 \\ &= \frac{147}{32} \frac{\pi^3}{J_t^2} \left(\frac{\Lambda}{R_t}\right)^4 \frac{B^2}{[1 + \Gamma^2]^{5/2}} \int_{R_h/R_t}^{R_{\text{eff}}/R_t} dr G(r) \\ &+ \frac{32\pi^3}{J_t^2} \left(\frac{R_t}{\Lambda}\right) B^4 \sum_{\nu=-\infty}^{\infty} \left[\nu^2 + 2\nu \left(\frac{\omega}{B\Omega} - \nu \right) \right] \\ &\times \int_{R_h/R_t}^{R_{\text{eff}}/R_t} dr \frac{r^5 G(r)}{[(\nu B)^2 + (\gamma r)^2]^3}, \quad (17a)\end{aligned}$$

with

$$\begin{aligned}[T^{z\theta}(\omega)]_a^2 &= \frac{64\pi^3}{J_t^2} \left(\frac{R_t}{\Lambda}\right) B^4 \\ &\times \sum_{\nu=-\infty}^{\infty} \nu \left(\frac{\omega}{B\Omega} - \nu \right) \int_{R_h/R_t}^{R_{\text{eff}}/R_t} dr \frac{r^5 G(r)}{[(\nu B)^2 + (\gamma r)^2]^3}. \quad (17b)\end{aligned}$$

The “*a*” subscript in the left-hand sides of (17a, b) denotes asymptotic. Three comments:

- (1) The order of all Bessel functions in (8b) and (12) became νB due to the double summation in m_1, m_2 , each from 1 to B . That sum obviously removed all blade-to-blade differences in the circumferential position of the points being correlated and left behind only the r_1, r_2 independent variables. It also left behind a single difference $\theta^s(r_1) - \theta^s(r_2)$ due to the relative sweep of the radial stations r_1 and r_2 for the rotor as a whole. That difference in sweep positions has now dropped out due to the high concentration at r_1 for all r_2 integrands. The relative phase of the loading $\alpha(r_1) - \alpha(r_2)$ among any two blade sections has similarly disappeared. And even though that

phase referred here only to the Sears function of strip aerodynamics, which outright ignores sweep effects as a transfer function, one is led nevertheless to the conclusion that all spanwise phase effects are globally irrelevant, at least for flows that are isotropic or nearly so. Put another way: spanwise cancellation effects due to sweep must be paradoxically local in a turbulence-ingesting rotor. The almost perfect agreement observed among rigorous computer runs with and without sweep for the points being correlated, but using the Sears transfer function in both cases, supports this expectation (this comment refers to comparative runs by Jiang et al. (1991) using a very detailed representation for a test geometry, i.e., including $\theta^*(r)$, and by the author, who applied the exact equations listed above with $\theta^*(r)$ set to zero. The two groups of runs agreed anyway).

(2) One of the analytical cancellation effects in (17a, b) is a fast decline of rotor thrust with an increasing value of the number of blades B , except for very low frequencies. The r integrand becomes proportional to B^{-6} for $\Lambda/R_t \gg 1/B$, which upon multiplication by B^4 —the constant outside the integral in (17b)—yields B^{-2} . The obvious conclusion is that the more blades the better, if one's goal is to reduce $T^2(\omega)$ with all else holding equal.

(3) One may interchange the ν sum and the r integral and evaluate the former analytically using standard complex-variables techniques. This has been done but the results are neither insightful nor compact looking. They are not insightful because the ν sum in (17a, b) already converges very quickly (as $1/\nu^4$), and thus hides no interesting secrets to be uncovered only by the analytical process of closed-form summation.

A By-Products of the Asymptotic Theory. The denominator of the r integrand in (17b) supplies an analytical expression for how much the blade-rate and higher-harmonic humps should protrude above their broadband “background.” That amount is

$$\begin{aligned}
 & \left[(\nu B)^2 + \gamma^2 \left(\frac{R_{\text{eff}}}{R_t} \right)^2 \right]_{\omega/B\Omega=\nu}^{-3} \\
 & \left[(\nu B)^2 + \gamma^2 \left(\frac{R_{\text{eff}}}{R_t} \right)^2 \right]_{\omega/B\Omega=\nu+1/2}^{-3} \\
 & = \left\{ \frac{\nu^2 + \left[\left(\frac{\pi}{2J_t} \right)^2 + \left(\frac{R_t/\Lambda}{B} \right)^2 \right] \left(\frac{R_{\text{eff}}}{R_t} \right)^2}{\nu^2 + \left(\frac{R_t/\Lambda}{B} \right)^2 \left(\frac{R_{\text{eff}}}{R_t} \right)^2} \right\}^3 \\
 & = \left\{ \frac{\nu^2 + \left(\frac{\pi}{J_t} \right)^2 \left[\frac{1}{4} + \left(\frac{B\Omega\Lambda}{U} \right)^{-2} \right] \left(\frac{R_{\text{eff}}}{R_t} \right)^2}{\nu^2 + \left(\frac{R_t/\Lambda}{B} \right)^2 \left(\frac{R_{\text{eff}}}{R_t} \right)^2} \right\}^3 \\
 & \approx \left\{ \frac{\nu^2 + \left(\frac{\pi}{2J_t} \right)^2 \left(\frac{R_{\text{eff}}}{R_t} \right)^2}{\nu^2 + \left(\frac{R_t/\Lambda}{B} \right)^2 \left(\frac{R_{\text{eff}}}{R_t} \right)^2} \right\}^3 \\
 & \approx \left\{ 1 + \left(\frac{\pi}{2\nu J_t} \right)^2 \left(\frac{R_{\text{eff}}}{R_t} \right)^2 \right\}^3. \quad (18)
 \end{aligned}$$

The first approximate equality holds for $B\Omega\Lambda/U \gg 1$; the second, under the simultaneous conditions $\Lambda/R_t \gg 1/B$ and $B\Omega\Lambda/U \gg 1$.

One recalls that $B\Omega\Lambda/U$ is one of the original eight parameters identified after (2). A small value for it causes the numerator on the right side of (18)'s second equality to match its denominator: there are no humps then. Homicz and George (1974) originally isolated $B\Omega\Lambda/U$ as the qualitative regulator of hump size for a rotor's acoustic signature. They deduced $B\Omega\Lambda/U$'s role from their version of (9) of this paper, and apparently from the behavior of their numerical experiments with respect to changes in this parameter. Thompson (1976) has made a similar observation regarding just B : that higher values for it should, and often do, bring sharper humps numerically. Blake (1984) states the $B\Omega\Lambda/U \gg 1$ criterion obliquely but equivalently: since $B\Omega\Lambda/U = (\pi B/J_t)(\Lambda/R_t)$, the inequality $B\Omega\Lambda/U \gg 1$ becomes $\Lambda/R_t \gg J_t/\pi B$, or, since J_t is a measure of the pitch at the tips (he implies), $\Lambda/R_t \gg \text{“pitch”}/B$.

Blake correctly reaches that important conclusion while regarding the haystacks as separate corrections to Sevik's broad monotonic base, though he (Blake) seems to overestimate the magnitude of the overtone humps at $\omega/B\Omega = 2, 3, \dots$. Expression (18) now predicts analytically and quantitatively how those haystacks should grow with increasing values of $B\Omega\Lambda/U$ as part of a *unified* result that approaches Sevik's monotonic response under special conditions. Moreover, the approximate equalities of (18) indicate for the first time that there is a limit to the degree of tonality thereby achieved: a true tonal limit is fundamentally unreachable for a fixed value of J_t . This is especially true of the higher harmonics $\nu > 1$ and for decreasing values of the tip relief parameter R_{eff}/R_t : either brings about a flattening effect within the curly brackets of (18)'s final right side. The expression produces an infinite ratio only for $J_t \rightarrow 0$, i.e., for $U \rightarrow 0$, when the rotor is made to churn the same flow statistics over and over again. That limit is understandably nonuniform: The tones are infinite in level but their coefficients are proportional to the vanishing freestream U raised to a positive power.

Additional Remark: Sevik cites an experiment in his paper that displays a large second hump at $\omega/B\Omega = 2$ that would appear to contradict (18). However, the consensus of the modern computational community is that the highest levels in that data are probably too high, and that the response measured near $\omega/B\Omega = 2$ is especially suspect.

B Corroboration of the Asymptotic Theory. The demonstration of the new asymptotic theory will proceed here as follows: (a) It will first explain the haystack features of these and other numerical experiments, i.e., it will show that the magnitude of the hump sizes, etc., are in fact accounted for parametrically by the spinoff asymptotic results of Section A, and then (b) it will compare the exact calculations in Fig. 2, and others, to new predictions by the asymptotic expressions for thrust spectra in (17a, b).

(a) Interpretation of Numerical Experiments. All of the calculations are for a rotor with blades of constant halfchord ratio $b/R_t = .1$. The ratio of hub and tip radii R_h/R_t is $.2$. The mean sweep $\theta^*(r)$ is zero. The advance ratio J_t is unity. R_{eff}/R_t will also be unity for simplicity's sake.

Figure 2 addresses a small turbulence scale case where $\Lambda/R_t = \frac{1}{16}$, $B = 6$. The rigorously computed blade-rate hump rises above its broadband base by roughly 6 dB and is hard to make out for twice the blade rate. The asymptotic hump size from (18) is 6.5 dB for $\nu = 1$ and 4 dB for $\nu = 2$. Figure 3 addresses a large scale case ($\Lambda/R_t = 2$) for 6 and 12-bladed rotors. The level of the blade rate hump for $B = 12$ is 6 dB below that of the $B = 6$ result [$6 = 10 \log_{10} (B_{\text{new}}/B_{\text{old}})^2 = 10 \log_{10} 4$]—consistent with the earlier discussion. Equation (18) performs similarly in its estimate of the size of the blade-rate hump: Its prediction is now 16 dB for $\nu = 1$ and so in good agreement with the figure's 14 dB, both for $B = 6$ and for $B = 12$. Either case is indeed more “tonal” than that of Fig. 2 because Λ/R_t

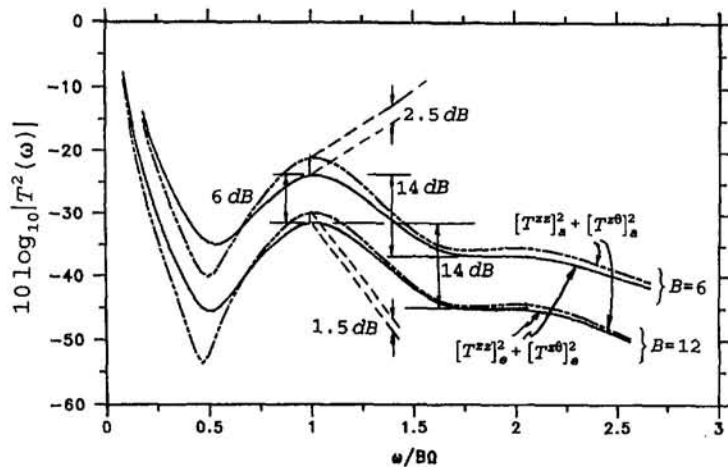


Fig. 3 Comparison of exact and asymptotic total spectra for the very large eddy case of $\Lambda/R_t = 2$, for $B = 6$ and $B = 12$, $R_{\text{eff}}/R_t = 1$. The largest differences between the exact and asymptotic curves are 2.5 dB for $B = 6$ and 1.5 dB for $B = 12$.

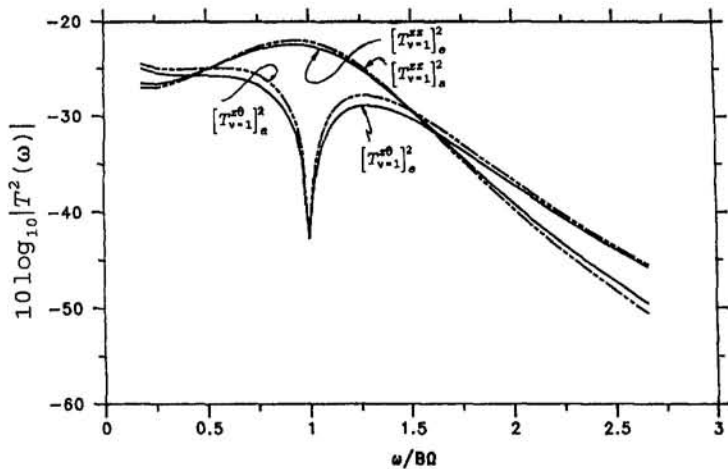


Fig. 4 Comparison of the new asymptotic spectra $[T_{v+1}^{xx}]_a^2$, $[T_{v+1}^{x0}]_a^2$ to their exact parents $[T_{v+1}^{xx}]_e^2$, $[T_{v+1}^{x0}]_e^2$. $B = 6$, $\Lambda/R_t = \frac{1}{10}$, and $R_{\text{eff}}/R_t = 1$.

R_t has increased, but by (18)'s second equality each is also essentially at its tonal limit: For $B = 6$, $B\Omega\Lambda/U$ is already "infinite" since $B\Omega\Lambda/U = (\pi B/J_t)(\Lambda/R_t)$ yields $12\pi \approx 38$ for this $J_t = 1$ rotor.

(b) *Direct Checks of the Asymptotic Theory.* Figure 4 plots the exact $\nu = 1$ component solutions from Fig. 2, where Λ/R_t was $\frac{1}{10}$, and the closed-form asymptotic results of (17a, b). The agreement is good. Returning now to Fig. 3, where the integral scale ratio Λ/R_t had the opposite extreme value of 2 (i.e., an eddy the size of the rotor diameter), one notes again good agreement. Exact and asymptotic results merge as they should when the rotor's number of blades B is doubled from 6 to 12. The indicated maximum gaps between the asymptotic and the exact solutions follow the $4/(\nu B)$ maximum error of the approximate expressions, as earlier discussed.

4 Conclusions

The paper's main objective was to produce a new asymptotic theory for the frequency spectrum of broadband thrust felt by a rotor chopping isotropic turbulence. The new solution was called upon to supply physical explanations for a number of features apparent in formally computed spectra:

(1) The height of these "humps" above their monotonic background;

(2) their relative size along the frequency abscissa, i.e., $\nu = 2$ versus $\nu = 1$.

A new asymptotic theory now exists based only on the requirement that the rotor's number of blades B be large. The analytical post-processing of its main solution (Eqs. (17a, b)) has generated a set of spinoff expressions that explain both of the above and others to be dealt with in future communications.

Acknowledgments

The author wishes to express his appreciation to ONR, with James A. Fein and Dr. Peter Majumdar as program managers, for supporting this study. Thanks are also due to the Carderock team of C.-W. Jiang, M. Chang, and Dr. Y.-N. Liu, for the many useful discussions that we have had on this general subject over the past several years.

References

- Abramowitz, M., and Stegun, I. E., 1968, *Handbook of Mathematical Functions*, Dover, Eqs. 9.7.7–10, p. 378.
- Atassi, H. M., and Grzadzinski, J., 1989, "Unsteady Disturbances of Streaming Motions Around Bodies," *Journal of Fluid Mechanics*, Vol. 109, pp. 385–403.
- Blake, W. K., 1984, *Aerohydroacoustics for Ships*, DTRC monograph series, 1181–1192; also published as (1986) *Mechanics of Flow-Induced Sound and Vibration*, Academic Press.

Breit, S. R., and Dickinson, A. L., 1990, "A Broadband Noise Analysis Code for Propellers and Appendages," BBN Report 7298.

Brown, N. A., 1993, "Aspects of the Noise of Propellers Operating in Turbulent Flows," NCA-Vol. 15/FED-Vol. 168, *Flow Noise Modeling and Control*, ASME, New York.

Crighton, D. G., and Parry, A. B., 1991, "Asymptotic Theory of Propeller Noise Part II: Supersonic Single-Rotation Propeller," *AIAA Journal*, Vol. 29, No. 12, pp. 2031-2037.

Envia, E., 1994, "Asymptotic Theory of Supersonic Propeller Noise," *AIAA Journal*, Vol. 32, No. 2, pp. 239-246.

Glegg, S. A. L., 1993, "Broadband Noise from Ducted Propfans," AIAA Paper 93-4402, 15th Aeroacoustics Conference, Long Beach, CA.

Goldstein, M. E., 1976, *Aeroacoustics*, McGraw-Hill, New York.

Hinze, H. O., 1975, *Turbulence*, McGraw-Hill, New York.

Homicz, G. F., and George, A. R., 1974, "Broadband and Discrete Frequency Radiation from Subsonic Rotors," *Journal of Sound and Vibration*, Vol. 36, No. 2, pp. 151-177.

Jiang, C.-W., Chang, M., and Liu, Y.-N., 1991, "The Effect of Turbulence Ingestion on Propeller Broadband Thrust," DTRC/SHD-1355 (report).

Liepmann, H. W., 1952, "On the Application of Statistical Concepts to the Buffeting Problem," *Journal of the Aeronautical Sciences*, Vol. 19, No. 12, pp. 793-800.

Mani, R., 1971, "Noise Due to Interaction of Inlet Turbulence With Isolated Stators and Rotors," *Journal of Sound and Vibration*, Vol. 17, No. 2, pp. 251-260.

Martinez, R., and Weissman, K., 1990, "Spatial-Domain Analysis of the Thrust on a Propeller Cutting Through Isotropic Turbulence," CAA Report U-1894-358.47.

Martinez, R., 1993, "Asymptotic Theory of Broadband Rotor Thrust," CAA Report U-2124-386.

Peake, N., and Crighton, D. G., 1991, "Lighthill Quadrupole Radiation in Supersonic Propeller Acoustics," *Journal of Fluid Mechanics*, Vol. 223, pp. 363-382.

Sevik, M., 1971, "Sound Radiation From a Subsonic Rotor Subjected to Turbulence," NASA SP 304, pp. 493-511.

Thompson, D., 1976, "Propeller Time-Dependent Forces Due to Nonuniform Flow," Pennsylvania State University, Applied Research Laboratory Report 76-48.

Ventres, C. S., Theobald, M. A., and Mark, W. D., 1982, "Turbofan Noise Generation, Volume 1: Analysis," NASA CR 167952.

Asymptotic Theory of Broadband Rotor Thrust, Part II: Analysis of the Right Frequency Shift of the Maximum Response

R. Martinez

Cambridge Acoustical Associates, Inc.
200 Boston Avenue, Suite 2500,
Medford, MA 02155-4243

One of the more intriguing features observed in rigorously computed frequency spectra of the random thrust on a turbulence-ingesting rotor is a shift of the broad peaks, or "haystacks," to frequencies slightly higher than blade passage and harmonics. This paper applies the final results of an earlier Part I article to uncover the rotor and flow parameters responsible for that shift. The new work is analytical and asymptotic rather than numerical. It relies on the sole requirement that the rotor have a reasonably high number of blades. The theory shows that the statistical mechanism that causes the shift is fundamentally antitonal, and that it therefore has no corresponding counterpart in deterministic systems of blade/flow interaction.

1. Introduction

This is the second in a series of three papers that attempt to explain analytically a number of features apparent in formal numerical "experiments" of rotor/turbulence interaction; cf., for example, Jiang et al. (1991) and Martinez (1991), for samples of such rigorous calculations, and Fig. 1 here for a sketch of the physical problem. Our focus this time will be the lean, or outright shift, often displayed by the maximum broadband response in the computed frequency spectrum of propulsor thrust. Figure 2's solid curve shows a typical case where the center of that broad peak occurs six percent above the rotor's blade-rate frequency.

The new development will demonstrate that the shift phenomenon is the simultaneous effect of (a) an interpretation of the impinging turbulent field that is strictly faithful to the flow's probabilistic character, for isotropic turbulence at least, and (b) of having a three-dimensional rotor as a "sampler" of the flow's statistics. The omission of either (a) or (b) from a theoretical analysis would make the capture of the observed right shift impossible.

The absence of (a), i.e., of a fully random flow model, enters Sevik's (1971) ground-breaking theory surreptitiously. The tacit assumption is that an "eddy" is struck no more than once during its crossing of the rotor disk: the rotor's turning speed Ω is zero throughout the flow model. Embedded in that viewpoint is a quasi-deterministic picture whereby the velocities of any two fluid particles within each eddy have a null joint probability for separations beyond a certain value (see Fig. 3 here). That implied distance becomes the interblade spacing for all three-dimensional combinations of flow and blade points from root to tip. Sevik's predicted frequency spectrum is accordingly monotonic, as indicated here by Fig. 2's broken curve, and so the issue of a right shift for broad peaks obviously does not come up.

Regarding now point (b), the sought-for explanation for a right shift also turns out to be beyond the reach of two-dimen-

sional analyses whether or not they account for a continuum of flow probabilities over the rotor. An example is Mani's (1971) otherwise powerful treatment of an airfoil cascade in globally correlated turbulence. His "slice" model would have failed to reproduce the spectral shifts for thrust in a true geometry, because it lacks from the beginning the three-dimensional kinematic mechanism that turns out to cause them: The statistical in-plane projected distances $\xi_b^{(1-2)}$, $\xi_b^{(2-1)}$ marked here in Fig. 1's three-dimensional propulsor (the first paper in our series has uncovered yet another effect of flow statistics sampled three-dimensionally that a cascade theory could also never explain: the high concentration of computed sectional lifts at the tips of the rotor's radially divergent blades).

2 Kinematics of the Velocity Correlation Tensors in the Rotor's Three-Dimensional Cylindrical Coordinate System

Mani's (1971) two-dimensional cascade analysis considers a row of blades pitched relative to a freestream aligned with the implied axis of rotation, z in the present nomenclature. What would have been our normal-to-blades correlation tensor $R^{n_1 n_2}$ becomes simply " R^{nn} " for him, because all of his blade-normal directions belong to the same radial station. He breaks up the R^{nn} function into its R^{zz} , $R^{\theta\theta}$, $R^{\theta\theta}$ component correlations.

Martinez (1991, 1996) did the same for the grazing "gust" correlated flow that defined $R^{n_1 n_2}$ for a three-dimensional rotor with blades that, unlike Mani's, were radially divergent and with normal directions that changed from root to tip (the second of these studies will be referred to as M1 throughout the discussion). The R^{zz} component of that blade-sampled flow had the following form by definition of isotropic turbulence:

$$R^{zz} = -\frac{\xi_z^2}{2q} \frac{\partial f(q)}{\partial q} + \left(f(q) + \frac{q}{2} \frac{\partial f(q)}{\partial q} \right). \quad (1)$$

R^{zz} has been normalized by the square of the fluctuation amplitudes, following the overall normalization of the thrust solution in M1's Eq. (2). The distance ξ_z becomes $U\tau/R_i$, the R_i -divided and differentially convected, or frozen, distance normal to the rotor disk, between an arbitrary blade-based point 1 and a fluid-borne point 2 elsewhere on the rotor. Variable q is the complete distance separating those two points, as given on M1's Eq. (6). The right side of (1) is structurally the same whether one

Contributed by the Applied Mechanics Division of THE AMERICAN SOCIETY OF MECHANICAL ENGINEERS for publication in the ASME JOURNAL OF APPLIED MECHANICS.

Discussion on this paper should be addressed to the Technical Editor, Professor Lewis T. Wheeler, Department of Mechanical Engineering, University of Houston, Houston, TX 77204-4792, and will be accepted until four months after final publication of the paper itself in the ASME JOURNAL OF APPLIED MECHANICS.

Manuscript received by the ASME Applied Mechanics Division, Sept. 23, 1994; final revision, Jan. 6, 1995. Associate Technical Editor: T. R. Akylas.

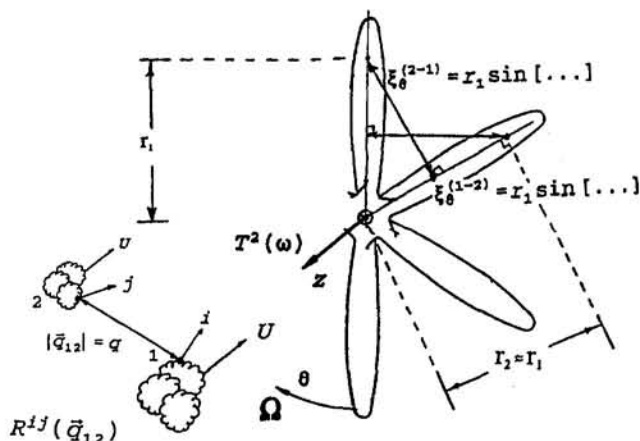


Fig. 1 In-plane projection distance ξ_θ for use in the rotor's interpretation of the three-dimensional components $R^{z\theta}$, $R^{\theta z}$ of the isotropic velocity correlation tensor. The value of r_2 has been put equal to r_1 , following the concentration of all r_2 -dependent functions at r_1 , found in M1.

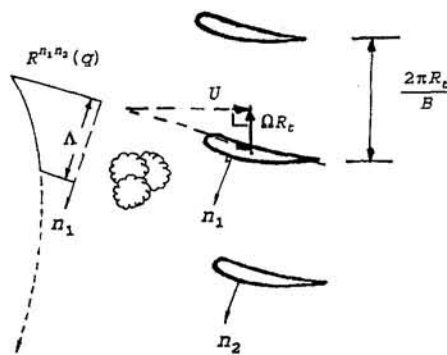


Fig. 3 Quasi-deterministic picture of the correlation of blade-normal incident flow velocities in globally uncorrelated models of turbulence ingestion. The sketch displays the tip sections of a three-dimensional propulsor. The infinite tail (dashed) of the probability function $R^{n_1 n_2}$ has been arbitrarily cut off past a distance " Λ ," which becomes the eddy "size." If the value of the combined rotor/turbulence parameter $B\Omega\Lambda/U$ were small enough, that nonprobabilistic discrete eddy could in fact affect only one blade as it passes through the rotor disk.

considers a three-dimensional rotor, as in Martinez (1991), or a two-dimensional circumferential cutaway of a rotor, as in Mani (1971).

The fundamental differences between two and three-dimensional theories emerge only through the process of writing down their specific forms of $R^{z\theta}$ and $R^{\theta\theta}$, e.g., for $R^{z\theta}$, which for isotropic turbulence becomes

$$R^{z\theta} = -\frac{\xi_z \xi_\theta}{2q} \frac{\partial f(q)}{\partial q}. \quad (2)$$

The shortness of (2) relative to (1) is the result of putting the Kronecker delta δ_{ij} that multiplies the missing terms in the general isotropic velocity tensor equal to zero, given that the in-plane coordinate θ is orthogonal to the rotor's axial coordinate z (cf. Hinze's (1975) Eqs. (3)-(11)).

The in-plane distance ξ_θ collapses to $\Omega\tau r$ in a two-dimensional theory. Here, as in M1, r appears normalized by R_c . In the full-fledged three-dimensional case in Fig. 1, however, ξ_θ becomes *cyclical* in the correlation time τ :

$$\xi_\theta^{(2 \rightarrow 1)} = r_2 \sin [2\pi(m_1 - m_2)/B + \Omega\tau], \quad (3a)$$

and

$$\xi_\theta^{(1 \rightarrow 2)} = r_1 \sin [2\pi(m_1 - m_2)/B + \Omega\tau]. \quad (3b)$$

The symbol $2 \rightarrow 1$ denotes the statistical "gust" influence of a fluid point 2 on a blade point 1 in the direction normal to the blade's local quarter-chord curve, following strip theory for low speed aerohydrodynamics. The symbol $1 \rightarrow 2$ describes a similar but converse relationship for a fluid point 1 and a blade point 2. Variables m_1 and m_2 are discrete circumferential blade counters, each ranging from 1 to B .

The cyclical in-plane projection distances in (3a, b) are the agents behind the right shifts that Jiang et al. (1991) originally found in numerical experiments based on elaborate expressions for direct $R^{n_1 n_2}$ correlations in space/time, without the benefit of a $zz + z\theta + \theta\theta$ breakup. The shifting role of ξ_θ , which does not appear as such in their code, remained hidden.

Expressions (3a, b) above now showcase that role. They "contain" our earlier comments regarding the shift phenomenon's simultaneous reliance on a globally correlated model where the mutual temporal separation among blades, $\Omega\tau$, is not ignored, and on a three-dimensional description of the statistics of the flow incident on the rotor: setting Ω to zero in (3a, b)

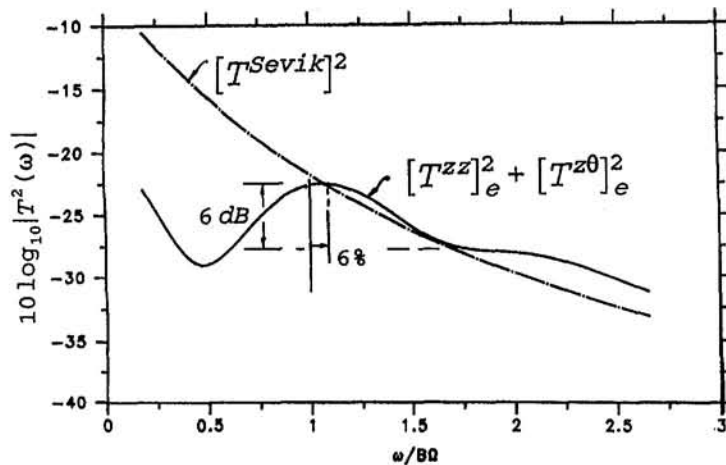


Fig. 2 Sample numerical experiment for the exact theory (solid curve), and for Sevik's model of effectively nonrotating blades: The exact calculation ("e" subscript) displays a broad hump over the blade-rate frequency and a six percent right shift for the maximum response.

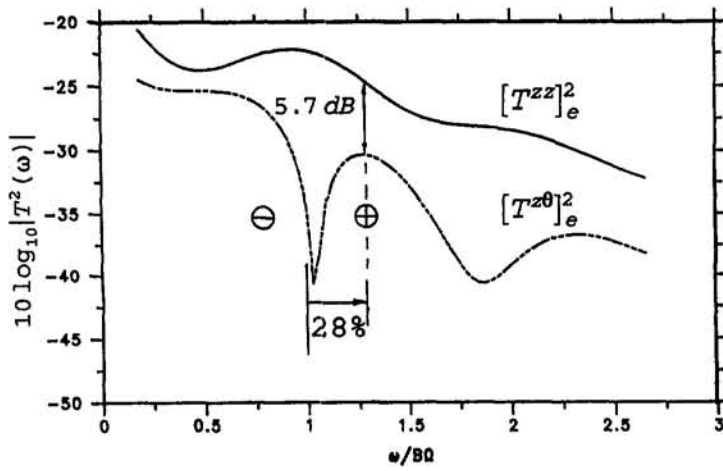


Fig. 4(a) Decomposition of Fig. 2's solid curve into its zz and $z\theta$ components: The $[T^z\theta]^2$ part is locally odd about $(\omega/B\Omega - 1)$; (+) and (-) mark the negative and positive "horns" of $[T^z\theta]^2$, both of which appear as positive only because the figure has taken their absolute values. Expressions (7) and (9) of the asymptotic analysis will explain $[T^z\theta]^2$'s 28 percent latent shift and $[T^zz]^2$'s 5.7 dB rise above $[T^z\theta]^2$.

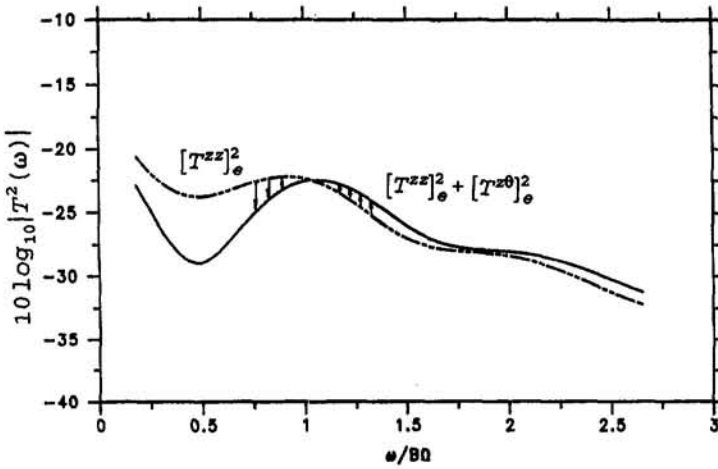


Fig. 4(b) Effect of $[T^z\theta]^2$ (from Fig. 4(a)) on $[T^zz]^2$: $[T^z\theta]^2$'s negative part pulls $[T^zz]^2$ down while its positive part pushes $[T^zz]^2$ up. The net effect is a right shift for the complete solution relative to $[T^zz]^2$ alone.

makes the double summation in m_1 and m_2 from 1 to B yield zero because the sine is odd in its remaining doubly variable argument. The requirement of three dimensionality is evident in Fig. 1's portrayed role for the sine function itself, which upon Fourier transformation in $R^z\theta$ in (2) produces the multiplicative factor $(\omega/B\Omega - \nu)$ in M1's Eq. (12) for the quantity h_ν^z . It was already therefore obvious from that earlier exact expression, which dates back to Martinez (1991), that the frequency spectrum of the cross-correlated thrust $[T^z\theta(\omega)]^2$ is locally odd about its $\omega/B\Omega = 1, 2, \dots$ points, and that it is zero there: $[T^z\theta(\omega)]^2$ is fundamentally antitonal and with no corresponding counterpart in the more familiar harmonic world of interactions among rotors and spatially nonuniform but time-invariant flow fields.

Figure 4(a) shows the decomposition of Fig. 2's solid curve into its zz and $z\theta$ exact thrust parts. Within the region marked (-), $[T^z\theta(\omega)]^2$ is in fact negative as per the $\omega/B\Omega - 1$ factor for $\omega < B\Omega$ (Fig. 2 plots the log of the absolute value of $[T^z\theta(\omega)]^2$). Figure 4(b) displays the effect of $[T^z\theta]^2$ on $[T^zz]^2$: $[T^z\theta]^2$ subtracts from the always positive $[T^zz]^2$ for frequencies below blade passage and adds to it otherwise. The result is the right shift whose analytical explanation motivated this paper. The exact treatment by the author (1991), confirmed independently later by Novak (1991), isolated $T^z\theta$'s role in causing that shift. The following section will now complete the work.

by supplying closed-form formulas for $T^z\theta$'s latent shift and for $[T^zz]^2 + [T^z\theta]^2$'s final shift as noted in Fig. 2. Those physically revealing formulas are now made possible for the first time by M1's closed-form results, summarized next.

3 Closed-Form Shift Analysis Based on Part I's Asymptotic Results for $B \gg 1$

The final product of M1's asymptotic analysis are a pair of expressions, the first for the frequency spectrum of the total thrust and the second for the contribution of the cross-correlated "zθ" flow components of the random flow striking the rotor. Respectively, they are

$$\begin{aligned}
 [T^{\text{total}}(\omega)]_a^2 &\approx [T^zz(\omega)]_a^2 + [T^z\theta(\omega)]_a^2 \\
 &= \frac{147}{32} \frac{\pi^3}{J_i^2} \left(\frac{\Lambda}{R_i} \right)^4 \frac{B^2}{[1 + \Gamma^2]^{5/2}} \int_{R_h/R_i}^{R_{\text{eff}}/R_i} dr G(r) \\
 &\quad + \frac{32\pi^3}{J_i^2} \left(\frac{R_i}{\Lambda} \right) B^4 \sum_{\nu=-\infty}^{\infty} \left[\nu^2 + 2\nu \left(\frac{\omega}{B\Omega} - \nu \right) \right] \\
 &\quad \times \int_{R_h/R_i}^{R_{\text{eff}}/R_i} dr \frac{r^5 G(r)}{[(\nu B)^2 + (\gamma r)^2]^3}, \quad (4a)
 \end{aligned}$$

and

$$[T^{z\theta}(\omega)]_a^2 = \frac{64\pi^3}{J_t^2} \left(\frac{R_t}{\Lambda} \right) B^4 \sum_{\nu=-\infty}^{\infty} \nu \left(\frac{\omega}{B\Omega} - \nu \right) \times \int_{R_h/R_t}^{R_{\text{eff}}/R_t} dr \frac{r^5 G(r)}{[(\nu B)^2 + (\gamma r)^2]^3}. \quad (4b)$$

The “*a*” subscript on the left-hand sides of (4*a*, *b*) stands again for asymptotic. *B* is the number of blades in the rotor; *J_t* is its advance ratio $\pi U/\Omega R_t$, whose spanwise running version is $J(r) = J_t/r$; Γ is short for $\omega\Lambda/U$; R_{eff}/R_t is a tip-relief parameter which strip aerodynamics injects into the rotor theory; and Λ/R_t is ratio of the integral scale to R_t .

The remaining two quantities in (4*a*, *b*) to be defined are the radial “wave number” γ that arises in spite of the fact that the analysis has been kept in the spatial domain, and $G(r)$, which is proportional to the square of the amplitude of the Sears function. Respectively, they are

$$\gamma = \sqrt{\left(\frac{\omega}{B\Omega} - \nu \right)^2 \left(\frac{B\Omega\Lambda}{U} \right)^2 + 1} \left(\frac{R_t}{\Lambda} \right), \quad (5)$$

$$G(r) = \frac{[b(r)/R_t]^2}{1 + J^2(r)/\pi^2} \times \frac{1}{1 + [2\pi\Gamma b(r)/\Lambda]/\sqrt{1 + \pi^2/J^2(r)}}. \quad (6)$$

Figure 4(*a*) remarked on the formally computed right “horn” of the $[T^{z\theta}]^2$ cross-correlated thrust. The frequency position where $[T^{z\theta}(\omega)]^2$ reaches that peak now follows readily from (4*b*). One simply passes the frequency-dependent constant $\omega/B\Omega - \nu$ from outside to inside the *r* integral, which then looks like

$$\int_{R_h/R_t}^{R_{\text{eff}}/R_t} dr r^5 G(r) \left\{ \frac{\omega}{B\Omega} - \nu \right\}.$$

The next step is to differentiate the contents of the curly brackets with respect to $\omega/B\Omega$. The roots of the resulting equation are

$$\left(\frac{\omega}{B\Omega} - \nu \right)_{T_{\max}^{z\theta}} = \pm \frac{1}{\sqrt{5}} \frac{J(R_{\text{eff}}/R_t)}{\pi} \sqrt{\nu^2 + \frac{(R_t/\Lambda)^2 (R_{\text{eff}}/R_t)^2}{B^2}} = \pm \frac{J_t}{\pi\sqrt{5}} \left(\frac{R_t}{R_{\text{eff}}} \right) \sqrt{\nu^2 + \frac{(R_t/\Lambda)^2 (R_{\text{eff}}/R_t)^2}{B^2}}. \quad (7)$$

The (−) solution in (7), with $\nu = 1$, marks the frequency point of the negative trough of $[T^{z\theta}]^2$ to the left of $\omega/B\Omega = 1$ observed in Fig. 4(*a*). The (+) frequency marks the positive peak of $[T^{z\theta}]^2$ to the right of $\omega/B\Omega = 1$. Together these account for the “latent” shift of the rotor/turbulence system.

There is one hidden assumption in (7), to be checked a posteriori: that the latent shifts predicted by it will be small. If the equation’s right-hand side is small, it follows from the left that $\omega/B\Omega \approx \nu$ (= 1 for blade rate), and so, that $\gamma \approx R_t/\Lambda$ for $\omega/B\Omega \approx \nu$ in M1’s Eq. (9). M1 established that for $\Lambda/R_t \gg 1/B$ the remaining r^5 integrand in the ν sum of (4*a*, *b*) here then becomes highly concentrated at its top value R_{eff}/R_t , which may then be substituted into the denominator of the term to be differentiated—hence (7)’s dependence on the end-point *r* value R_{eff}/R_t .

A similar operation applied to (4*a*) yields the theoretical shift of the complete signature:

$$\left(\frac{\omega}{B\Omega} - \nu \right)_{\left([T^{z\theta}]^2 + [T^{z\theta}]^2 \right)_{\max}} = \frac{3\nu}{10} \left\{ -1 + \sqrt{1 + \frac{20J^2(R_{\text{eff}}/R_t)}{9\pi^2\nu^2} \left[\nu^2 + \frac{(R_t/\Lambda)^2 (R_{\text{eff}}/R_t)^2}{B^2} \right]} \right\}. \quad (8a)$$

The constant $20J^2(R_{\text{eff}}/R_t)/(9\pi^2\nu^2) = 20(R_t/R_{\text{eff}})^2 J_t^2/(9\pi^2\nu^2)$ is roughly only $\frac{1}{5}$ for $\nu = 1$ when $R_{\text{eff}}/R_t \approx 1$, and for such cases one thus may approximate (8*a*) to read

$$\left(\frac{\omega}{B\Omega} - \nu \right)_{\left([T^{z\theta}]^2 + [T^{z\theta}]^2 \right)_{\max}} \approx \frac{J_t^2}{3\pi^2\nu} \left(\frac{R_t}{R_{\text{eff}}} \right)^2 \left[\nu^2 + \frac{(R_t/\Lambda)^2 (R_{\text{eff}}/R_t)^2}{B^2} \right]. \quad (8b)$$

The expressions in (7) and (8*a*, *b*) expose analytically the dependence of both the latent and actual shifts on the turbulence and rotor parameters Λ/R_t , B , R_{eff}/R_t , and J_t . The question naturally comes up as to whether it would be practical to use impeller-like devices to measure Λ by means of (8*b*). The actual shift is small mostly because the out-front constant in (8*b*), $1/3\pi^2$, is only about three percent. By comparison the constant in (7), $1/\pi 5^{1/2}$, is 14 percent. Latent and actual shifts both increase with decreasing eddy size and with a lower number of blades. Moreover, the latent shift of the $\nu = 2$ modal contribution of $[T^{z\theta}]^2$ is twice as great as that of $\nu = 1$ for turbulence scales satisfying $\Lambda/R_t \gg 1/B$, since the radical in (7) reduces then to ν . The same is true of the total shift as given in (8*b*): for $\Lambda/R_t \gg 1/B$ it is also “harmonic” in ν .

Returning to (7) with $\Lambda/R_t \gg 1/B$, one now notes that the latent shift becomes then proportional to R_t/R_{eff} , the inverse of the tip-relief parameter, whereas the total shift of (8*b*) depends on the square of that parameter.

The last of the shift questions put to the new asymptotic theory is: just how *latent* is *latent*?; i.e., by how much is $[T^{z\theta}]^2$ overwhelmed by $[T^{zz}]^2$ in a given rotor/turbulence interaction problem? The answer clearly lies with the following ratio, whose analytical right side now falls out from the new asymptotic equations (cf. M1’s Eq. (4*b*)):

$$\frac{\frac{\pi\omega}{B^2 R_t^2} \mathcal{L}_{z\theta}[R^{z\theta} + R^{\theta z}]}{\frac{\pi\omega}{B^2 R_t^2} \mathcal{L}_{zz}[R^{zz}]} \Big|_{T_{\max}^{z\theta}} = \frac{2}{\pi\sqrt{5}} J \left(\frac{R_{\text{eff}}}{R_t} \right) = \frac{2J_t}{\pi\sqrt{5}} \left(\frac{R_t}{R_{\text{eff}}} \right). \quad (9)$$

The “ $T_{\max}^{z\theta}$ ” designation at the bottom of the vertical marker on the left-hand side indicates evaluation at (7)’s (+) frequency solution.

It was intuitively clear from the beginning that the “differential shifting” of inboard sections had to be greater than that of outboard sections—the former are more feathered into the freestream and their chords are therefore more vulnerable to the “ θ ” part of the “ $z\theta$ ” cross statistics of the impinging turbulence. What is remarkable about the result in (9) is that that guess is essentially complete: Λ does not figure in it at all, and neither do the number of blades *B* nor the modal counter ν . Equation (9) led to the development of Section 5 below, a generalization of the present theory that considers spatially inhomogeneous flows concentrated at the hub.

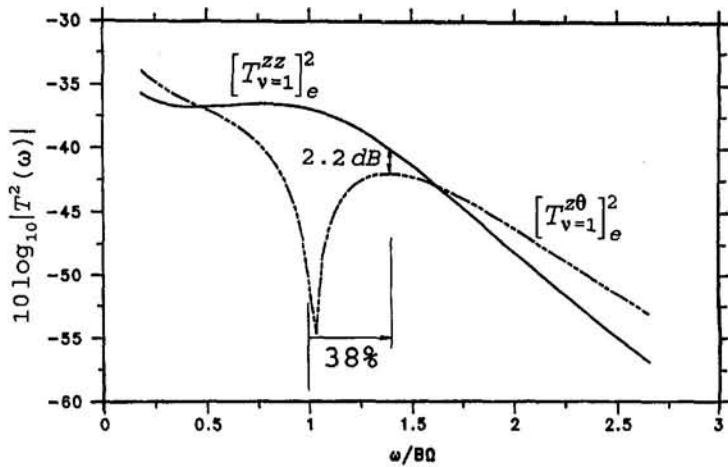


Fig. 5(a) Calculation of the exact $\nu = 1$ mode of $[T^{zz}]^2$ and $[T^{z\theta}]^2$ for the $R_{\text{eff}}/R_t = \frac{1}{2}$ case. $[T_{\nu=1}^{zz}]^2$ does not bottom out precisely at $\omega/B\Omega = 1$ because it contains also the results of the $\nu = -1$ calculation, which alters it slightly.

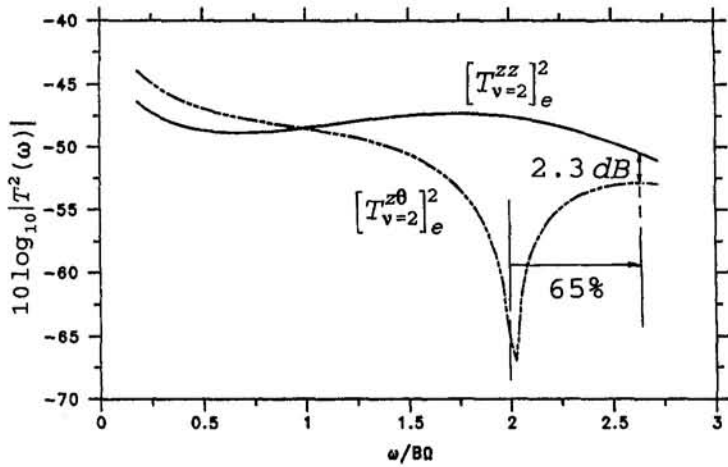


Fig. 5(b) Same as Fig. 5(a) but for $\nu = 2$

4 Demonstration of the Shift Formulas

Figure 4(b): The computed latent right shift for $[T_v^{z\theta}]^2$ is 28 percent. The (+) solution of (7) for $\nu = 1$ gives 28 percent again. At this value of frequency $[T_v^{zz}]^2$ is higher than $[T_v^{z\theta}]^2$ by 5.71 dB; whereas (9) predicts 5.46 dB. The total shift observed in Fig. 2 is six percent. Expression (8b) yields six percent.

The new set of exact calculations in Figs. 5(a, b) have a twofold mission upon comparison to Figs. 2 and 4(a): (1) to investigate the effects of the tip relief ratio R_{eff}/R_t , which will now be $\frac{1}{2}$ rather than 1 (all other parameters will remain the same); and (2) to show the ν breakup of the rigorously computed solution in order to bring out the so-far hidden workings of the hump at $\nu = 2$.

Figure 5(a) displays a latent right shift of 38 percent for $[T_v^{z\theta}]^2$ relative to $[T_v^{zz}]^2$. And (7) gives 37 percent. This establishes the correctness of (7) regarding R_{eff}/R_t . The total computed $\nu = 1$ shift $[T_v^{zz}]^2 + [T_v^{z\theta}]^2$ is 12.3 percent (total curve not shown). The prediction of (8a) is 17.6 percent [(8b)'s estimate is unfortunately worse; at any rate, the true total shift of the ν -added solution for this case is only nine percent, unfortunately almost half that predicted by (8a)]. Such is the effect of mode-to-mode "interference" for small values of R_{eff}/R_t . Equations (8a, b) seem to be breaking down only for this artificial case of extreme tip relief. The rigorously computed nine percent shift for $R_{\text{eff}}/R_t = .5$ proves in any case that

inboard sections do indeed contribute more efficiently to the shifting process than those closer to the tips.

Fig. 5(a) still: $[T_v^{zz}]^2$ lies above $[T_v^{z\theta}]^2$ by 2.17 dB. Expression (9) yields 2.44, i.e., 3.02 dB less than 5.46, which was the corresponding number in Fig. 4(a) when R_{eff}/R_t was 1. Fig. 5(b) considers $\nu = 2$. Equation (9) claims that the gap between $[T_v^{zz}]^2$ and $[T_v^{z\theta}]^2$ should be the same as that of Fig. 5(a) for $\nu = 1$; that the difference should be ν -invariant. Figure 5(b) confirms that conclusion: $[T_v^{zz}]^2$ passes above $[T_v^{z\theta}]^2$'s maximum by 2.31 dB. $[T_v^{z\theta}]^2$'s rigorously calculated latent shift occurs just off the plotted abscissa, at about 65 percent. Equation (7)'s prediction is 62 percent and this proves (7)'s correctness with respect to ν . The rigorously calculated total shift for $[T_v^{zz}]^2 + [T_v^{z\theta}]^2$ is 19 percent (total curve not shown). Equation (8a)'s result is 23 percent.

5 Hub-Strong Quasi-Isotropic Flow With a Constant Integral Scale Λ

The normalization constant of $T^2(\omega)$ in M1's Eq. (2) included the square of turbulence fluctuations u^2 . The purpose of this final section will be to construct an amplitude-modulated quasi-isotropic (or quasi anisotropic) flow by generalizing the meaning of that constant, which in what follows will undergo the following transformation:

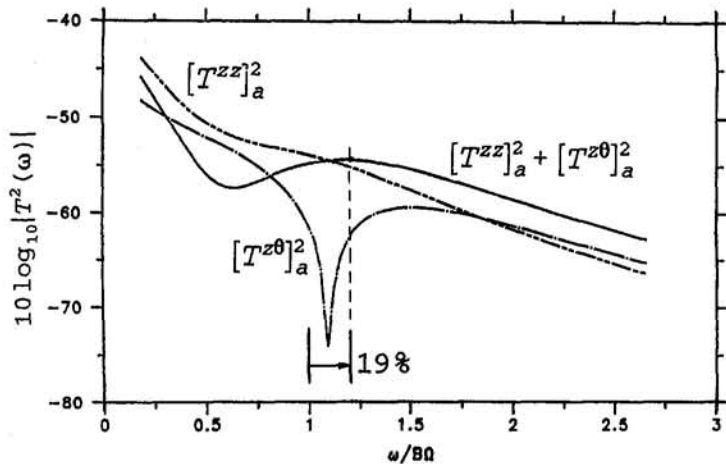


Fig. 6 Asymptotic predictions of frequency thrust spectra for a quasi-isotropic flow concentrated at the hub; $\sigma = 4$ in (10)

$$u^2 \rightarrow u(r_1)u(r_2) = u^2 \left(\frac{R_h/R_t}{r_1} \right)^\sigma \left(\frac{R_h/R_t}{r_2} \right)^\sigma. \quad (10)$$

There are two reasons for this change, as well as at least two experimental studies justifying it:

(1) Regarding the r_1, r_2 dependence of (10)'s right side: (9), which resulted for constant u^2 , has ferreted out the increased influence of near-hub blade stations ($R_{\text{eff}}/R_t \rightarrow R_h/R_t$) on the shifting process. It will be the purpose of these r_1, r_2 dependent factors to now model a radially inhomogeneous, "hub-strong" turbulent flow by choosing a power σ that will offset the combined effects of the kinematic sampling by the rotor and the r dependence of its aerodynamic transfer functions—the effects that produced the r^5 power in (4b)'s r integrand. It follows that σ must be greater than $\frac{5}{2}$ in order to achieve this, and to thereby provide for efficient shifting. The $\sigma > \frac{5}{2}$ hub-flow criterion is yet another spinoff result of the new asymptotic theory, which, incidentally, did not set out to find it. It will be interesting to note that even though (8a, b) and (9) inspired the generalization in (10), they no longer support it by accounting for (10)'s features: all three expressions grossly overestimate the shifting process when applied blindly with " $R_{\text{eff}}/R_t = R_h/R_t$ ".

The physical basis for the r_1, r_2 factors in (10) is twofold: (a) it is not hard to imagine real-life conditions that would promote high turbulence intensities near a rotor's hub, both for the incident and for the hub's own secondary "self" flows; and (b) turbulence that appears to be highly sheared could nonetheless behave isotropically from point to point; i.e., its "anisotropy" could be due only to its "globally" inhomogeneous character. Breit and Dickinson (1990) have demonstrated this for a relevant flow by properly scaling its local wave number spectra, and by properly including observed variations in the postulated integral scale Λ that are ignored here in Eq. 10's simple model. These two investigators processed data taken point by point across the flow's shear direction and found that the results collapsed to a single curve: the "Liepmann spectrum"—essentially the spatial Fourier transform of (1) here.

Figure 6 shows calculations based on (4a, b) with their r integrands changed to include (10)'s factor of $(R_h/R_t)^{2\sigma}$ for

$r_2 = r_1 = r$. The power σ is four in order to fulfill the $>5/2$ requirement. The purpose of the exercise is to demonstrate that this concocted example of an inhomogeneous turbulent flow may in fact turn $[T^{\theta\theta}]^2$'s large latent right shift into an actual one for the total thrust $[T^{zz}]^2 + [T^{z\theta}]^2$. $[T^{\theta\theta}]_a^2$'s right horn now crosses $[T^{zz}]_a^2$. The total calculated shift for $[T^{zz}]_a^2 + [T^{z\theta}]_a^2$ is now roughly 19 percent, a substantial increase from the homogeneous isotropic case of Fig. 2.

6. Conclusions

The right shift of the maximum broadband thrust observed in rigorous numerical calculations is "real." The main objective of this paper was to uncover its causes analytically. Equations (7), (8b), and (9) have achieved that goal by reproducing the formally generated data and by explaining it physically in terms of the problem's flow and aerohydrodynamic parameters. One such conclusion is that the right-shifting rises with the square of the rotor's advance ratio as the propulsor is increasingly made to "sample" statistical flow components parallel to its plane of rotation.

Acknowledgments

The author is grateful to ONR for funding this work, which was managed by James A. Fein and Dr. Peter Majumdar, and to Dr. C.-W. Jiang of DTRC/Carderock for his continuing interest in the research.

References

- Breit, S. R., and Dickinson, A. L., 1990, "A Broadband Noise Analysis Code for Propellers and Appendages," BBN Report 7298.
- Hinze, H. O., 1975, *Turbulence*, McGraw-Hill, New York.
- Jiang, C.-W., Chang, M., and Liu, Y.-N., 1991, "The Effect of Turbulence Ingestion on Propeller Broadband Thrust," DTRC/SHD-1355 (report).
- Martinez, R., 1991, "Analysis of the Right Shift of the Blade-Rate "Hump" in Broadband Spectra of Rotor Thrust," CAA Report U-1993-381.9.
- Martinez, R., 1996, "Asymptotic Theory of Broadband Rotor Thrust; Part I: Manipulations of Flow Probabilities for High Blade Number," (this paper is cited as M1 throughout the present text); ASME JOURNAL OF APPLIED MECHANICS, Vol. 63, pp. 136-142.
- Novak, S., 1991, personal communication. Excellent relevant work has also been conducted by Dr. J. L. Codona, also in Novak's organization.
- Sevik, M., 1971, "Sound Radiation from a Subsonic Rotor Subjected to Turbulence," NASA SP 304, pp. 493-511.

P. Tsiotras

Assistant Professor,
Department of Mechanical, Aerospace,
and Nuclear Engineering,
University of Virginia,
Charlottesville, VA 22903-2442

J. M. Longuski

Associate Professor,
School of Aeronautics and Astronautics,
Purdue University,
West Lafayette, IN 47907-1282

Analytic Solution of Euler's Equations of Motion for an Asymmetric Rigid Body

The problem of the time evolution of the angular velocity of a spinning rigid body, subject to torques about three axes, is considered. An analytic solution is derived that remains valid when no symmetry assumption can be made. The solution is expressed as a first-order correction to a previous solution, which required a symmetry or near-symmetry assumption. Another advantage of the new solution (over the former) is that it remains valid for large initial conditions of the transverse angular velocities.

1 Introduction

In recent years a considerable amount of effort has been devoted to the development of a comprehensive theory that will allow a better understanding of the complex dynamic behavior associated with the motion of rotating bodies. A cornerstone in this effort is the development of analytic solutions that can describe—at least qualitatively—the problem dynamics. The system of the associated equations, the celebrated Euler's equations of motion for a rigid body, consists of three nonlinear, coupled differential equations, the complete general solution of which is still unknown. Special cases for which solutions have been found include the torque-free rigid body and the forced symmetric case. Solutions for these two particular cases were known for some time and have been reported in the literature (Golubev, 1953; Leimanis, 1965; Greenwood, 1988). The discovery of complete solutions for those and other special cases, initially gave rise to optimism that a general solution was in sight; however, since then progress has been remarkably slow. The conjecture that studying several special cases would eventually lead to a comprehensive theory of the problem proved to be false. In fact, a complete characterization of the motion of a rotating solid body quickly turned out to be a formidable task, eluding the wit of some of the most prominent mathematicians of our time; see, for example, Leimanis (1965) and Golubev (1953) and the references therein. Even today, it is still not clear that a complete solution even exists. (It is well known, however, that for the closely related problem of a heavy rigid body rotating about a fixed point, integrability is possible for only four special cases (Golubev, 1953).)

Most attempts to generalize the previous results were confined to some kind of perturbation approach of the known and well understood integrable, torque-free, and/or symmetry cases (Kraige and Junkins, 1976; van der Ha, 1984; Kane and Levinson, 1987; Or, 1992). Recently, significant results made it possible to extend the existing theory to include the attitude motion of a *near-symmetric spinning* rigid body under the influence of *constant* (Longuski, 1991; Tsiotras and Longuski, 1991a) and *time-varying torques* (Tsiotras and Longuski, 1991b, 1993; Longuski and Tsiotras, 1993). The purpose of the present work

Contributed by the Applied Mechanics Division of THE AMERICAN SOCIETY OF MECHANICAL ENGINEERS for publication in the ASME JOURNAL OF APPLIED MECHANICS.

Discussion on this paper should be addressed to the Technical Editor, Professor Lewis T. Wheeler, Department of Mechanical Engineering, University of Houston, Houston, TX 77204-4792, and will be accepted until four months after final publication of the paper itself in the ASME JOURNAL OF APPLIED MECHANICS.

Manuscript received by the ASME Applied Mechanics Division, Jan. 7, 1994; final revision, Feb. 15, 1995. Associate Technical Editor: E. J. Haug, Jr.

is to extend these results to a spinning body with *large asymmetries*, subject to large initial angular velocities.

2 Equations and Assumptions

We are mainly interested in the problem of spin-up maneuvers of a non-symmetric spinning body in space, subject to constant torques and nonzero initial conditions. To this end, let M_1 , M_2 , and M_3 denote the torques (in the body-fixed frame) acting on a rigid body, and let ω_1 , ω_2 , and ω_3 denote the angular velocity components in the same frame. Then Euler's equations of motion for a rotating rigid body with principal axes at the center of mass are written as

$$\dot{\omega}_1 = \frac{M_1}{I_1} + \frac{I_2 - I_3}{I_1} \omega_2 \omega_3 \quad (1a)$$

$$\dot{\omega}_2 = \frac{M_2}{I_2} + \frac{I_3 - I_1}{I_2} \omega_3 \omega_1 \quad (1b)$$

$$\dot{\omega}_3 = \frac{M_3}{I_3} + \frac{I_1 - I_2}{I_3} \omega_1 \omega_2. \quad (1c)$$

These equations describe the evolution in time of the angular velocity components ω_1 , ω_2 , ω_3 in the body-fixed frame. For consistency we will assume that the spin axis is the 3-axis, corresponding to the maximum moment of inertia, and also that the ordering of the other principal moments of inertia is given by the inequalities $I_3 > I_1 \geq I_2$.

We henceforth define the *spin-up problem* of a rigid body rotating about its 3-axis, when the following conditions are satisfied:

$$M_1^2 + M_2^2 \leq M_3^2 \quad \text{and} \quad I_1^2 \omega_1^2(0) + I_2^2 \omega_2^2(0) \leq I_3^2 \omega_3^2(0) \quad (2)$$

along with the condition that $\text{sgn}(M_3) = \text{sgn}(\omega_3(0))$. (Here sgn denotes the signum function defined as usual by $\text{sgn}(x) = +1$ for $x > 0$ and $\text{sgn}(x) = -1$ for $x < 0$.) This last condition simply states the requirement for spin-up, whereas the inequalities in (2) restrict the angles of the torque vector and the angular momentum vector at time $t = 0$ to be less than or equal to 45 deg from the body 3-axis. This, according to the previous discussion, implies that the transverse torques M_1 , M_2 , as well as the initial conditions $\omega_1(0)$, $\omega_2(0)$, are considered as undesired deviations or perturbations from the *pure spin case*, namely when $M_1 = M_2 = \omega_1 = \omega_2 \equiv 0$. In practical problems these unwanted deviations tend to remain indeed small throughout the maneuver.

One more parameter needs to be introduced in order to describe the “relative effect” of the two inequalities (2) in the solution. This parameter, defined by

$$\rho_0 \triangleq \frac{\sqrt{M_1^2 + M_2^2}}{I_3 \omega_3^2(0)}$$

describes the angle of departure of the angular momentum vector from its initial state (the angular momentum vector bias). During a spin-up maneuver (Longuski et al., 1989), the angular momentum vector traces out a spiral path about a line in inertial space having an angle ρ_0 from the inertial 3-axis (see Fig. 1). The angle ρ_0 is small for cases where the transverse torques are "small" compared with the quantity $I_3 \omega_3^2(0)$. The formula for ρ_0 applies even for asymmetric bodies as long as the angle of departure is small and the body is spinning about a stable principal axis. Throughout this work we assume that ρ_0 is relatively small, an assumption that is usually true for most satellite applications.

3 Analytic Solution

3.1 Assumptions. If we assume a near-symmetric (or symmetric) spinning rigid body with the spin axis being its axis of near-symmetry (or symmetry), then the near-symmetry assumption ($I_1 \approx I_2$) allows one to neglect the second term on the right-hand side of (1c) and therefore safely assume that the solution of ω_3 is approximated very closely by

$$\omega_3^0(t) = (M_3/I_3)t + \omega_3(0). \quad (3)$$

This allows the decoupling and complete integration of Eqs. (1). The use of complex notation facilitates the analysis (Tsiortras and Longuski, 1991a, 1991b, 1993; Longuski and Tsiortras, 1993). Also introducing, for convenience, the new independent variable $\tau \triangleq \omega_3^0(t)$, one then writes the differential equation for the transverse angular velocities ω_1 and ω_2 as

$$\Omega' + i\rho\tau\Omega = F \quad (4)$$

where prime denotes differentiation with respect to τ , $i = \sqrt{-1}$ and where (Tsiortras and Longuski, 1993)

$$\Omega \triangleq \omega_1\sqrt{k_2} + i\omega_2\sqrt{k_1} \quad (5a)$$

$$F \triangleq (M_1/I_1)(I_3/M_3)\sqrt{k_2} + i(M_2/I_2)(I_3/M_3)\sqrt{k_1} \quad (5b)$$

$$\rho \triangleq k(I_3/M_3), \quad k_1 \triangleq (I_3 - I_2)/I_1,$$

$$k_2 \triangleq (I_3 - I_1)/I_2, \quad k \triangleq \sqrt{k_1 k_2}. \quad (5c)$$

Integrating (4) one obtains the solution for ω_1 and ω_2 from

$$\begin{aligned} \Omega(\tau) &= \Omega_0 \exp\left(i\frac{\rho}{2}\tau^2\right) \\ &+ \exp\left(i\frac{\rho}{2}\tau^2\right) F \int_{\tau_0}^{\tau} \exp\left(-i\frac{\rho}{2}u^2\right) du \\ &= \Omega_0 \exp\left(i\frac{\rho}{2}\tau^2\right) + \exp\left(i\frac{\rho}{2}\tau^2\right) F \\ &\times \sqrt{\frac{\pi}{\rho}} \{ \operatorname{sgn}(\tau) E(\sigma) - \operatorname{sgn}(\tau_0) E(\sigma_0) \} \quad (6) \end{aligned}$$

where $\tau_0 = \omega_3^0(0)$ and $\Omega_0 \triangleq \Omega(\tau_0) \exp(-i(\rho/2)\tau_0^2)$ and where $\Omega(\tau_0)$ is the initial condition at $\tau = \tau_0$ ($t = 0$). The function $E(\cdot)$ in (6) represents the complex Fresnel integral of the first kind (Abramowitz and Stegun, 1972; Tsiortras and Longuski, 1993), defined by

$$E(x) \triangleq \int_0^x \exp\left(-i\frac{\pi}{2}u^2\right) du.$$

The parameter σ is defined by $\sigma \triangleq \tau\sqrt{\rho/\pi}$. (Here we obviously assume $M_3 > 0$, so that $\rho > 0$; the case when $\rho < 0$ can be treated similarly (Tsiortras and Longuski, 1993). Equation (6) gives the complete solution for the transverse components of

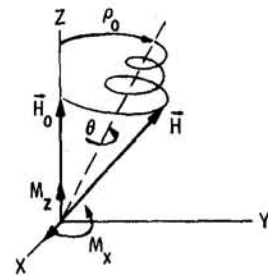


Fig. 1 Angular momentum behavior during spin-up (Longuski et al., 1989)

the angular velocity ω_1 and ω_2 in the body-fixed frame, and for the symmetric case it provides the *exact* solution. For the nonsymmetric case, the accuracy of solution (6) depends on the "smallness" of the product $\omega_1\omega_2$, which will be discussed next.

3.2 The Effect of Asymmetry. In order to have a measure of the body asymmetry, we introduce the following *asymmetry parameter*:

$$e \triangleq \frac{I_1 - I_2}{I_3}.$$

Because of the well-known relationship $I_2 + I_3 \geq I_1$ between the moments of inertia (Greenwood, 1988)—for the assumed ordering of the principal axes—the parameter e takes values in the range $0 \leq e \leq 1$. The case of $e = 0$ corresponds to complete symmetry (about the 3-axis), whereas the extreme case of $e = 1$ (not considered here) corresponds to complete asymmetry (about the 3-axis). For the latter case one has $I_3 = I_1$ and $I_2 = 0$, i.e., the body resembles a thin rod along the 2-axis. (In the current work when we discuss a nonsymmetric problem we have in mind values of e greater than 0.1 and perhaps as high as about 0.7.)

We note in passing, that the validity of solution (6) is not confined to near-symmetry cases. To understand this point, notice that the neglected term

$$g(t) = \frac{I_1 - I_2}{I_3} \omega_1(t) \omega_2(t) \quad (7)$$

in Eq. (1c) is small not only for the near-symmetry case, i.e., when $I_1 \approx I_2$, but also when the transverse angular velocity components ω_1 and ω_2 are small. This is indeed the case, for example, for a spin-stabilized vehicle (spinning about its 3-axis), when ω_1 and ω_2 tend to remain small for all times. For the pure spin case of a symmetric body we have of course that $\omega_1 = \omega_2 \equiv 0$. This fact justifies the often used terminology in the spacecraft dynamics literature which refers to ω_1 and ω_2 as *the angular velocity error components*. The previous assumption about the smallness of the term in Eq. (7) however does not incorporate the case where the initial conditions $\omega_1(0)$ and $\omega_2(0)$ are large (compared to the initial spin rate $\omega_3(0)$). As can be easily verified in such cases, the initial error

$$g(0) = \frac{I_1 - I_2}{I_3} \omega_1(0) \omega_2(0)$$

propagates quickly and renders the analytic solution inaccurate after a short time interval. On the other hand, as can also be easily verified through numerical simulations, analytic solutions based on the near-symmetry assumption remain insensitive to large inertia differences, as long as the initial conditions for ω_1 and ω_2 are zero. Therefore, the intent of this paper is to extend the analytic solutions for a near-symmetric rigid body subject to constant torques (Tsiortras and Longuski, 1991a), when both large asymmetries and nonzero initial conditions for the trans-

verse angular velocities are considered at the same time. In such a case, the neglected term (7) may not be negligible and the exact solution for ω_3 may depart significantly from the linear solution (3) for ω_3 .

3.3 General Theory. A first correction to the linear zero-order solution $\omega_3^0(\cdot)$ is obtained as follows. Using solution (6), the differential equation for ω_3 can be approximated by

$$\omega_3 = M_3/I_3 + e \omega_1^0 \omega_2^0 \quad (8)$$

where the superscript zero denotes the zero-order solution of (1) (i.e., the solution with the term (7) in (1c) neglected). From (6) we can equivalently replace equation (8) with

$$\omega_3' = 1 + \epsilon \operatorname{Im}[(\Omega^0)^2] \quad (9)$$

where $\epsilon \triangleq (I_1 - I_2)/2M_3k$ and $\Omega^0 = \omega_1^0 \sqrt{k_2} + i \omega_2^0 \sqrt{k_1}$, prime again denotes differentiation with respect to the independent variable $\tau = \omega_3^0$ and $\operatorname{Im}(\cdot)$ denotes the imaginary part of a complex number. Under these assumptions and integrating (9) with respect to τ , one gets for the first-order correction for ω_3 :

$$\omega_3(\tau) = \tau + \epsilon \operatorname{Im} \int_{\tau_0}^{\tau} [\Omega^0(u)]^2 du \quad (10)$$

The first-order solution for ω_1 and ω_2 is then given by the solution of the differential equation

$$\Omega' + i\rho \omega_3(\tau) \Omega = F. \quad (11)$$

Integrating, one obtains

$$\begin{aligned} \Omega(\tau) &= \Omega(\tau_0) \exp \left[i\rho \int_{\tau_0}^{\tau} \omega_3(u) du \right] \\ &+ \exp \left[i\rho \int_{\tau_0}^{\tau} \omega_3(u) du \right] F \\ &\times \int_{\tau_0}^{\tau} \exp \left[-i\rho \int_{\tau_0}^u \omega_3(v) dv \right] du. \quad (12) \end{aligned}$$

Notice that this expression provides the general exact solution for $\Omega(\cdot)$ if knowledge of the time history of ω_3 is available a priori. Of course, this is not possible, in general, because of the coupled character of Eqs. (1). However, we will assume that Eq. (10) gives a very accurate approximation of the exact ω_3 , which can be used in (12).

The zero-order solution $\Omega^0(\cdot)$ required in (10) is given in (6). From the asymptotic expansion of the complex Fresnel integral one has that (Abramowitz and Stegun, 1972)

$$\begin{aligned} E(x) &= \frac{1-i}{2} - \frac{\exp(-ix^2/2)}{i\pi x} \\ &\times \left\{ 1 - \frac{1}{i\pi x^2} + \frac{1 \cdot 3}{(i\pi x^2)^2} - \dots \right\}. \quad (13) \end{aligned}$$

Thus, the Fresnel integral appearing in (6) can be approximated by

$$\begin{aligned} \int_{\tau_0}^{\tau} \exp \left(-i \frac{\rho}{2} u^2 \right) du &\approx \frac{i}{\rho} \left[\frac{\exp(-i(\rho/2)\tau^2)}{\tau} \right. \\ &\left. - \frac{\exp(-i(\rho/2)\tau_0^2)}{\tau_0} \right]. \end{aligned}$$

Substituting this expression in (6) and carrying out the algebraic manipulations, one approximates $[\Omega^0(\cdot)]^2$ by

$$[\Omega^0(\tau)]^2 = r_0 \exp(i\rho\tau^2) + \frac{r_1}{\tau^2} + r_2 \frac{\exp(i(\rho/2)\tau^2)}{\tau}$$

where r_j ($j = 0, 1, 2$) are complex constants given by

$$r_0 \triangleq \left[\Omega_0 - i \frac{F}{\rho\tau_0} \exp \left(-i \frac{\rho}{2} \tau_0^2 \right) \right]^2$$

$$r_1 \triangleq -\frac{F^2}{\rho^2}$$

$$r_2 \triangleq 2i \frac{F}{\rho} \left[\Omega_0 - i \frac{F}{\rho\tau_0} \exp \left(-i \frac{\rho}{2} \tau_0^2 \right) \right].$$

The integral of $[\Omega^0(\cdot)]^2$ is then given by

$$\begin{aligned} \int_{\tau_0}^{\tau} [\Omega^0(u)]^2 du &= r_0 h_0(\tau_0, \tau; \rho) + r_1 h_1(\tau_0, \tau) + r_2 h_2(\tau_0, \tau; \rho) \end{aligned}$$

where

$$\begin{aligned} h_0(\tau_0, \tau; \rho) &\triangleq \int_{\tau_0}^{\tau} \exp(i\rho u^2) du \\ &= \sqrt{\frac{\pi}{2\rho}} [\operatorname{sgn}(\tau) \bar{E}(\tau\sqrt{2\rho/\pi}) - \operatorname{sgn}(\tau_0) \bar{E}(\tau_0\sqrt{2\rho/\pi})] \\ h_1(\tau_0, \tau) &\triangleq \int_{\tau_0}^{\tau} \frac{\exp(i(\rho/2)u^2)}{u} du \\ h_2(\tau_0, \tau; \rho) &\triangleq \int_{\tau_0}^{\tau} \frac{\exp(i(\rho/2)u^2)}{u} du \\ &= \frac{1}{2} \left[Ei\left(\frac{\rho}{2} \tau_0^2\right) - Ei\left(\frac{\rho}{2} \tau^2\right) \right] \end{aligned}$$

where bar denotes the complex conjugate and where

$$Ei(x) \triangleq \int_x^{\infty} \frac{e^{iu}}{u} du$$

is called the exponential integral (Abramowitz and Stegun, 1972). The integrals of h_j ($j = 0, 1, 2$) can be then computed as follows:

$$H_0(\tau_0, \tau; \rho)$$

$$\begin{aligned} &\triangleq \int_{\tau_0}^{\tau} h_0(\tau_0, u; \rho) du \\ &= -\sqrt{\frac{\pi}{2\rho}} \operatorname{sgn}(\tau_0) \bar{E}(\tau_0\sqrt{2\rho/\pi})(\tau - \tau_0) \\ &+ \sqrt{\frac{\pi}{2\rho}} \operatorname{sgn}(\tau_0) \int_{\tau_0}^{\tau} \bar{E}(u\sqrt{2\rho/\pi}) du \quad (14) \end{aligned}$$

where the last integral is given by

$$\int \bar{E}(\tau\sqrt{2\rho/\pi}) d\tau = \tau \bar{E}(\tau\sqrt{2\rho/\pi}) + \frac{i}{\sqrt{2\rho\pi}} \exp(i\rho\tau^2). \quad (15)$$

Similarly,

$$H_1(\tau_0, \tau) \triangleq \int_{\tau_0}^{\tau} h_1(\tau_0, u) du = \frac{\tau - \tau_0}{\tau_0} - \ln\left(\frac{\tau}{\tau_0}\right)$$

and

$$\begin{aligned} H_2(\tau_0, \tau; \rho) &\triangleq \int_{\tau_0}^{\tau} h_2(\tau_0, u; \rho) du \\ &= \frac{1}{2} Ei\left(\frac{\rho}{2} \tau_0^2\right)(\tau - \tau_0) - \frac{1}{2} \int_{\tau_0}^{\tau} Ei\left(\frac{\rho}{2} u^2\right) du \quad (16) \end{aligned}$$

where the last integral can be evaluated using

$$\int Ei\left(\frac{\rho}{2} \tau^2\right) d\tau = \tau Ei\left(\frac{\rho}{2} \tau^2\right) + 2 \int \exp\left(i \frac{\rho}{2} u^2\right) du. \quad (17)$$

We therefore have that the integral of $\omega_3(\cdot)$ required in (12) is given by

$$\int_{\tau_0}^{\tau} \omega_3(u) du = \frac{\tau^2}{2} - \frac{\tau_0^2}{2} + \epsilon \operatorname{Im}\left(\sum_{j=0}^2 r_j H_j\right). \quad (18)$$

Equation (18) gives the final expression for the integral of $\omega_3(\cdot)$ required in (12).

In order to proceed with our analysis, we need to calculate the last integral in (12). Any attempt to evaluate this integral by direct substitution of (18) into

$$I_{\omega}(\tau_0, \tau; \rho) = \int_{\tau_0}^{\tau} \exp\left[-i\rho \int_{\tau_0}^u \omega_3(v) dv\right] du \quad (19)$$

is futile. Notice however, that because of the oscillatory behavior of the kernel of the integral (19) one needs to know only the secular behavior of (18) in order to capture the essential contribution of (19). Thus, we next compute the secular effect due to the integrals $H_0(\tau_0, \tau; \rho)$ and $H_2(\tau_0, \tau; \rho)$. The integral $H_1(\tau_0, \tau)$ already has the required form.

From (14) and (15) and the asymptotic approximation of the Fresnel integral (13) one can immediately verify that, within a first-order approximation, the integral $H_0(\tau_0, \tau; \rho)$ behaves as

$$H_0(\tau_0, \tau; \rho) \sim A_0^0 + A_0^1 \tau \quad (20)$$

where

$$\begin{aligned} A_0^0 &\triangleq -\frac{i}{2\rho} \exp(i\rho\tau_0^2), \\ A_0^1 &\triangleq \sqrt{\frac{\pi}{2\rho}} \left[\frac{1+i}{2} - \operatorname{sgn}(\tau_0) \bar{E}(\tau_0 \sqrt{2\rho/\pi}) \right]. \end{aligned}$$

Similarly, using (16) and (17) and the fact that $\lim_{x \rightarrow \infty} Ei(x) = 0$, one can show that the integral $H_2(\tau_0, \tau; \rho)$ behaves, to a first-order approximation, as

$$H_2(\tau_0, \tau; \rho) \sim A_2^0 + A_2^1 \tau$$

where

$$\begin{aligned} A_2^0 &\triangleq -\sqrt{\frac{\pi}{\rho}} \left[\frac{1+i}{2} - \operatorname{sgn}(\tau_0) \bar{E}(\tau_0 \sqrt{\rho/\pi}) \right], \\ A_2^1 &\triangleq \frac{1}{2} Ei\left(\frac{\rho}{2} \tau_0^2\right). \end{aligned}$$

Also writing the integral $H_1(\tau_0, \tau)$ in the form

$$H_1(\tau_0, \tau) = A_1^0 + A_1^1 \tau - \ln(\tau) \quad (21)$$

where

$$A_1^0 \triangleq \ln(\tau_0) - 1, \quad A_1^1 \triangleq \frac{1}{\tau_0}$$

we have for the secular part of (18)

$$\int_{\tau_0}^{\tau} \omega_3(u) du = \frac{\tau^2}{2} - \frac{\tau_0^2}{2} + b_0 + b_1 \tau + b_2 \ln(\tau) \quad (22)$$

where

$$\begin{aligned} b_0 &\triangleq \epsilon \operatorname{Im}(r_0 A_0^0 + r_1 A_1^0 + r_2 A_2^0) \\ b_1 &\triangleq \epsilon \operatorname{Im}(r_0 A_0^1 + r_1 A_1^1 + r_2 A_2^1) \\ b_2 &\triangleq -\epsilon \operatorname{Im}(r_1). \end{aligned}$$

Unfortunately, the logarithmic term in (22) leads to an intractable form when substituted into (19) and we therefore approximate the former expression by

$$\int_{\tau_0}^{\tau} \omega_3(u) du \approx \frac{\tau^2}{2} - \frac{\tau_0^2}{2} + b_3 + b_1 \tau \quad (23)$$

where $b_3 = \epsilon \operatorname{Im}(r_0 A_0^0 - r_1 + r_2 A_2^0)$. This approximation amounts to the assumption that $\ln(\tau/\tau_0) \approx 0$ in Eq. (21). Since the logarithmic function is dominated everywhere by any polynomial, we expect the error committed in passing from (22) to (23) to be relatively small, at least as $\tau \rightarrow \infty$. Using (23) in (19) we can finally write

$$\begin{aligned} &\int_{\tau_0}^{\tau} \exp\left[-i\rho \int_{\tau_0}^u \omega_3(v) dv\right] du \\ &\approx \exp\left(i \frac{\rho}{2} \gamma_0\right) \int_{\tau_0}^{\tau} \exp\left[-i \frac{\rho}{2} (u + b_1)^2\right] du \\ &= \exp\left(i \frac{\rho}{2} \gamma_0\right) \sqrt{\frac{\pi}{\rho}} [\operatorname{sgn}(\tilde{\tau}) E(\tilde{\sigma}) - \operatorname{sgn}(\tilde{\tau}_0) E(\tilde{\sigma}_0)] \end{aligned}$$

where $\gamma_0 \triangleq \tau_0^2 + b_1^2 - 2b_3$, $\tilde{\tau} = \tau + b_1$ and $\tilde{\sigma} = \tilde{\tau} \sqrt{\rho/\pi}$.

3.4 Simplified Analysis. The analysis of the previous subsection allows for a direct calculation of the solution $\Omega(\cdot)$ from (12). In most cases encountered in practice, however, a simplified version of the previous procedure is often adequate. For example, for the case when $\rho_0 \ll 1$ (see Fig. 1) the initial conditions have a more profound effect than the acting torques in solution (6), and we can take just the asymptotic contribution of the nonhomogeneous part of (6) to approximate the zero-order solution $\Omega^0(\cdot)$. Writing

$$\begin{aligned} \Omega^0(\tau) &\approx \left\{ \Omega_0^0 + F \sqrt{\frac{\pi}{\rho}} \operatorname{sgn}(\tau_0) [(1-i)/2 - E(\sigma_0)] \right\} \\ &\quad \times \exp\left(i \frac{\rho}{2} \tau^2\right) \triangleq B_0 \exp\left(i \frac{\rho}{2} \tau^2\right), \end{aligned}$$

substituting this expression into (10), and approximating $E(\cdot)$ by its asymptotic limit $E(\infty) = (1-i)/2$, as $x \rightarrow \infty$, we get for $\omega_3(\cdot)$ that

$$\omega_3(\tau) = \tau + \alpha_0$$

where α_0 is the constant

$$\alpha_0 \triangleq \epsilon \sqrt{\pi/2\rho} \operatorname{sgn}(\tau_0) \operatorname{Im}\{B_0^2 [\frac{1}{2}(1+i) - \bar{E}(\tau_0 \sqrt{2\rho/\pi})]\}.$$

We can therefore write for the first-order solution (11) of the transverse angular velocities

$$\Omega(\tau) = \hat{\Omega}_0^0 \exp[i\varphi(\tau)] + \exp[i\varphi(\tau)] F \int_{\tau_0}^{\tau} \exp[-i\varphi(u)] du \quad (24)$$

where

$$\varphi(\tau) \triangleq \frac{\tau^2}{2} + \alpha_0 \tau$$

and $\hat{\Omega}_0^0 \triangleq \Omega(\tau_0) \exp[-i\varphi(\tau_0)]$. From Eqs. (6), (12), and (24) it is seen that the first-order solution for the transverse angular velocities ω_1 and ω_2 may be obtained in the same form as the zero-order solution; the initial condition of τ , however, has to be modified to include α_0 . In other words, (24) can also be written in the more explicit form

$$\Omega(\tau) = \hat{\Omega}_0^0 \exp\left(i\frac{\rho}{2}\tilde{\tau}^2\right) + \exp\left(i\frac{\rho}{2}\tilde{\tau}^2\right) F \sqrt{\frac{\pi}{\rho}} \{ \operatorname{sgn}(\tilde{\tau}) E(\tilde{\sigma}) - \operatorname{sgn}(\tilde{\tau}_0) E(\tilde{\sigma}_0) \} \quad (25)$$

where now $\hat{\Omega}_0^0 \triangleq \Omega(\tau_0) \exp(-i(\rho/2)\tilde{\tau}_0^2)$, $\tilde{\tau} = \tau + \alpha_0$ and $\tilde{\sigma} \triangleq \tilde{\tau}\sqrt{\rho/\pi}$. It is interesting to compare Eq. (25) with (6). We see that the two equations have exactly the same form, but that Eq. (25) has a frequency shift which depends directly on ϵ .

4 A Formula for the Error

In this section we derive an error formula for the zeroth-order solution derived in (6), that is, we seek an expression for the difference between the exact solution and the approximate solution for the angular velocities, obtained by omitting the term $(I_1 - I_2)\omega_1\omega_2/I_3$ in Eq. (1c). Throughout this section, for notational convenience, we rewrite Eq. (1) in the form

$$\dot{x}_1 = a_1 x_2 x_3 + u_1 \quad (26a)$$

$$\dot{x}_2 = a_2 x_3 x_1 + u_2 \quad (26b)$$

$$\dot{x}_3 = a_3 x_1 x_2 + u_3 \quad (26c)$$

where a_j , x_j and u_j ($j = 1, 2, 3$) are defined by

$$x_1 \triangleq I_1 \omega_1, \quad x_2 \triangleq I_2 \omega_2, \quad x_3 \triangleq I_3 \omega_3 \quad (27a)$$

$$u_1 \triangleq M_1, \quad u_2 \triangleq M_2, \quad u_3 \triangleq M_3 \quad (27b)$$

$$a_1 \triangleq \frac{I_2 - I_3}{I_2 I_3}, \quad a_2 \triangleq \frac{I_3 - I_1}{I_3 I_1}, \quad a_3 \triangleq \frac{I_1 - I_2}{I_1 I_2}. \quad (27c)$$

We also rewrite the equations that describe the reduced (zeroth-order) system in the form

$$\dot{x}_1^0 = a_1 x_2^0 x_3^0 + u_1 \quad (28a)$$

$$\dot{x}_2^0 = a_2 x_3^0 x_1^0 + u_2 \quad (28b)$$

$$\dot{x}_3^0 = u_3. \quad (28c)$$

Given any positive number $T \in [0, \infty)$, our aim is to compute the error between the solutions of (26) and (28) over the time interval $0 \leq t \leq T$. We can rewrite equations (26) and (28) in the compact form

$$\dot{x} = f(x) + g(x) \quad (29)$$

$$\dot{x}^0 = f(x^0) \quad (30)$$

where $x = (x_1, x_2, x_3)$, $x^0 = (x_1^0, x_2^0, x_3^0)$ and $f: \mathbb{R}^3 \rightarrow \mathbb{R}^3$ and $g: \mathbb{R}^3 \rightarrow \mathbb{R}^3$ are the functions defined by

$$f(x) \triangleq \begin{bmatrix} a_1 x_2 x_3 + u_1 \\ a_2 x_3 x_1 + u_2 \\ u_3 \end{bmatrix}, \quad g(x) \triangleq \begin{bmatrix} 0 \\ 0 \\ a_3 x_1 x_2 \end{bmatrix}. \quad (31)$$

We also assume that (29) and (30) are subject to the same initial conditions, that is, $x(0) = x^0(0)$. Throughout the following discussion $\|\cdot\|$ will denote the usual Euclidean norm (or 2-norm) on \mathbb{R}^3 , namely, $\|x\| \triangleq (x_1^2 + x_2^2 + x_3^2)^{1/2}$.

Lemma 4.1. *The solution of the exact system (26), satisfies the inequality*

$$\|x(t)\| \leq \|u\|T + \|x(0)\| \triangleq B$$

for all $0 \leq t \leq T$, where $u = (u_1, u_2, u_3)$.

Proof. Multiplying Eq. (26a) by x_1 , Eq. (26b) by x_2 and Eq. (26c) by x_3 and adding, and since $a_1 + a_2 + a_3 = 0$, one gets that

$$\dot{x}_1 x_1 + \dot{x}_2 x_2 + \dot{x}_3 x_3 = u_1 x_1 + u_2 x_2 + u_3 x_3.$$

In other words,

$$\frac{1}{2} \frac{d}{dt} \|x\|^2 = \langle u, x \rangle \quad (32)$$

where $\langle \cdot, \cdot \rangle$ denotes the usual inner product on \mathbb{R}^3 , namely $\langle x, y \rangle \triangleq \sum_{j=1}^3 x_j y_j$. Using the Cauchy-Schwarz inequality (32) gives

$$\frac{1}{2} \frac{d}{dt} \|x\|^2 \leq \|u\| \cdot \|x\|. \quad (33)$$

The 2-norm $\|\cdot\|$ is a differentiable function on \mathbb{R}^3 , so the differential inequality (33) can be solved for $\|x(\cdot)\|$ (here u is constant) to obtain

$$\|x(t)\| \leq \|u\|t + \|x(0)\|, \quad 0 \leq t \leq T \quad (34)$$

In particular, $\|x(t)\| \leq \sup_{0 \leq t \leq T} \|u\|t + \|x(0)\| = B$, as claimed. \square

This result should not be surprising. If one looks carefully, ones sees that the vector x defined in Eq. (27a) is the angular momentum vector \mathbf{H} , which obeys the equation $d\mathbf{H}/dt = \mathbf{M}$. This differential equation for \mathbf{H} requires that both \mathbf{H} and \mathbf{M} be expressed in the same coordinate system and that differentiation be carried out with respect to an inertial reference frame. In general, given the components M_1, M_2, M_3 of \mathbf{M} in the body-fixed system, does not provide any immediate information about the components of \mathbf{M} with respect to another (inertial) coordinate system. However, the *magnitude* of \mathbf{M} is independent of the coordinate system. Equation (34) simply states the relationship between the magnitude of the acting torques and the time history of the magnitude of the angular momentum vector \mathbf{H} . With this observation in mind, one can easily re-derive (34) starting from Euler's equation $d\mathbf{H}/dt = \mathbf{M}$.

Lemma 4.2. *Given a fixed positive number T , there exist positive constants M and L , such that the following conditions hold for all $0 \leq t \leq T$.*

$$\|g(x(t))\| \leq M \quad (35a)$$

$$\|f(x(t)) - f(x^0(t))\| \leq L \|x(t) - x^0(t)\| \quad (35b)$$

Proof. From Lemma 4.1 we have that for $t \in [0, T]$ all solutions of (26) satisfy $\|x(t)\| \leq B$. In particular, $|x_j(t)| \leq B$, $j = 1, 2, 3$, for all $t \in [0, T]$, where $|\cdot|$ denotes absolute value. Clearly,

$$\|g(x(t))\| = |a_3| |x_1(t)| |x_2(t)| \leq |a_3| B^2 \triangleq M.$$

Now let $B_1 \triangleq \max_{0 \leq t \leq T} \{ |x_1^0(t)|, |x_2^0(t)|, |x_3^0(t)| \}$. This number can be computed immediately, since the solution $x^0(\cdot)$ of the system (28) is known. If we define $B_0 \triangleq \max\{B, B_1\}$, then we have that all solutions of (29) and (30) are confined inside the region $\{x \in \mathbb{R}^3 : \|x\| \leq B_0\}$ for all $0 \leq t \leq T$. The partial derivatives of f are then bounded by

$$|\partial f_i / \partial x_j| \leq R, \quad 1 \leq i, j \leq 3, \quad 0 \leq t \leq T, \quad \|x\| \leq B_0$$

where $R \triangleq \max\{|a_1|, |a_2|\} B_0$ and by the Mean Value Theorem (Boothby, 1986), we have

$$\|f(x(t)) - f(x^0(t))\| \leq 3R \|x(t) - x^0(t)\|$$

for all $0 \leq t \leq T$, and therefore (35b) is satisfied with $L \triangleq 3R$. This completes the proof. \square

Lemma 4.2 implies that over the time interval $0 \leq t \leq T$ the function g is bounded by M and the function f is Lipschitz continuous with Lipschitz constant L . These two results allow us, as the next theorem states, to find an *explicit* bound for the error of the approximate solution.

Theorem 4.1. *Let T be a given positive number and let M , L as in Lemma 4.2. Then, for $x(0) = x^0(0)$, the error between the solutions $x(\cdot)$ and $x^0(\cdot)$ over the time interval $0 \leq t \leq T$ is given by*

$$\|x(t) - x^0(t)\| \leq \frac{M}{L} e^{Lt}, \quad 0 \leq t \leq T.$$

Proof. Subtract (30) from (29) to obtain

$$\dot{x} - \dot{x}^0 = f(x) - f(x^0) + g(x). \quad (36)$$

By integrating (36) and considering norms, we obtain the following estimate:

$$\begin{aligned} \|x(t) - x^0(t)\| &\leq \int_0^t \|f(x(s)) - f(x^0(s))\| ds \\ &\quad + \int_0^t \|g(x(s))\| ds. \end{aligned}$$

Now, use of Lemma 4.2 implies that

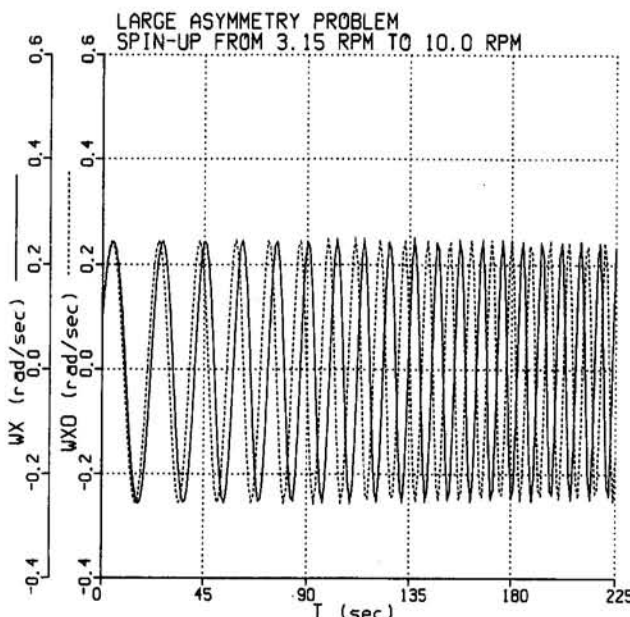


Fig. 2 Zero-order versus exact solutions for ω_1

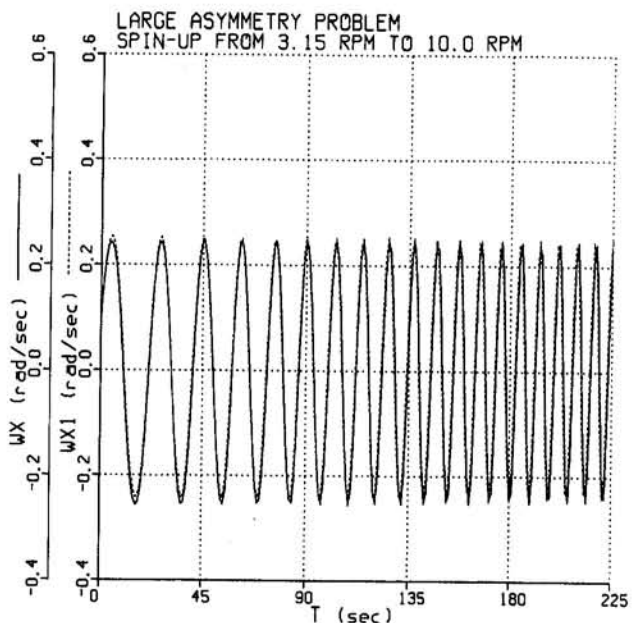


Fig. 3 First-order versus exact solutions for ω_1

$$\|x(t) - x^0(t)\| \leq L \int_0^t \|x(s) - x^0(s)\| ds + Mt. \quad (37)$$

Now, applying Gronwall's Lemma (Hille, 1969) to (37) gives finally that

$$\|x(t) - x^0(t)\| \leq \frac{M}{L} e^{Lt}. \quad (38)$$

This completes the proof. \square

This error formula, involves only known quantities of the problem (time duration T of the maneuver, inertias I_1, I_2, I_3 , acting torques M_1, M_2, M_3 , and initial conditions $x_1(0), x_2(0)$, and $x_3(0)$) and can be computed immediately once these data are given. For most of the applications encountered in spacecraft problems it turns out, however, that (38) provides a very conservative estimate of the true error, but usually this is the most one can expect, without resorting to the numerical solution of (1).

Having established an error formula for the angular momentum, it is an easy exercise to find a corresponding error formula for the angular velocity vector, using the simple relation between the two. Thus, the following corollary holds.

Corollary 4.1. *Let $K \triangleq \max\{1/I_1, 1/I_2, 1/I_3\}$. The error between the exact and the zeroth order solutions of the angular velocities over the time interval $0 \leq t \leq T$ is given by*

$$\|\omega(t) - \omega^0(t)\| \leq \frac{KM}{L} e^{Lt}. \quad (39)$$

Proof. It follows immediately from the fact that

$$\begin{bmatrix} \omega_1 \\ \omega_2 \\ \omega_3 \end{bmatrix} = \begin{bmatrix} 1/I_1 & 0 & 0 \\ 0 & 1/I_2 & 0 \\ 0 & 0 & 1/I_3 \end{bmatrix} \begin{bmatrix} x_1 \\ x_2 \\ x_3 \end{bmatrix}$$

and therefore that

$$\|\omega(t)\| \leq \max\{1/I_1, 1/I_2, 1/I_3\} \|x(t)\| = K \|x(t)\|$$

for all $0 \leq t \leq T$. \square

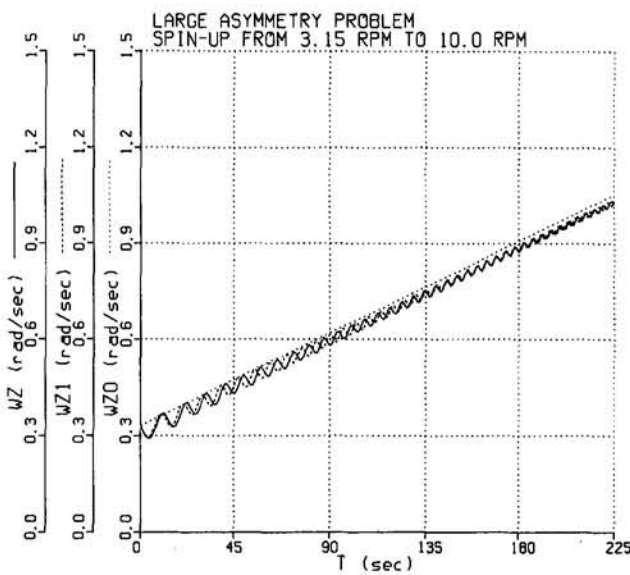


Fig. 4 Zero-order and first-order versus exact solutions for ω_3

5 Numerical Example

The analytic solution of Euler's equations of motion for an asymmetric rigid body is applied to a numerical example. The mass properties of the spinning body are chosen as $I_1 = 3500 \text{ kg} \cdot \text{m}^2$, $I_2 = 1000 \text{ kg} \cdot \text{m}^2$ and $I_3 = 4200 \text{ kg} \cdot \text{m}^2$. The constant torques are assumed to be $M_1 = -1.2 \text{ N} \cdot \text{m}$, $M_2 = 1.5 \text{ N} \cdot \text{m}$, $M_3 = 13.5 \text{ N} \cdot \text{m}$ and the initial conditions are set to $\omega_1(0) = 0.1 \text{ r/s}$, $\omega_2(0) = -0.2 \text{ r/s}$ and $\omega_3(0) = 0.33 \text{ r/s}$. Figure 2 shows the zero-order solution versus the exact solution for ω_1 . Figure 3 shows the first-order solution versus the exact solution for ω_1 . Notice the dramatic improvement of the first-order solution over the zero-order solution for this problem, where the asymmetry parameter, e , is 60 percent. The results for the ω_2 component of the angular velocity are similar. Finally, Fig. 4 presents the zero-order and the first-order solutions (given by (3) and (10), respectively) versus the exact solution for ω_3 . Note the bias between the zero-order and the first-order secular terms (which is responsible for the frequency shift between Fig. 2 and Fig. 3). We mention at this point, although not demonstrated here, that the solution also remains valid for spin-down maneuvers, as long as the initial conditions $\omega_1(0)$ and $\omega_2(0)$ are small and as long as the spin rate ω_3 does not pass through zero. These observations are in agreement with the previous results of Tsotras and Longuski (1991a).

6 Conclusions

Analytic solutions are derived for the angular velocity of a nonsymmetric spinning body subject to external torques about three axes. The solution is developed as a first-order correction

to previously reported solutions for a near-symmetric rigid body. The near-symmetric solution provides accurate results even when the asymmetry is large, provided the initial condition for the transverse angular velocity is near zero. The problem of the asymmetry becomes apparent when the initial transverse angular velocities are not small. It is shown that the first-order solution for the angular velocity takes a simple form and is very accurate, at least for the cases when the effect of the transverse torques is not too large compared with the effect of the initial conditions. The formulation of the problem therefore allows for nonzero initial conditions in the transverse angular velocities, in conjunction with large asymmetries. Finally, an explicit formula for the bound of the error of the approximate solution is derived and a numerical example demonstrates the accuracy of the proposed analytic solution.

Acknowledgment

This research has been supported by the National Science Foundation under Grant No. MSS-9114388.

References

- Abramowitz, M., and Stegun, I. A., 1972, *A Handbook of Mathematical Functions*, Dover Publications Inc., New York.
- Boothby, W. M., 1986, *An Introduction to Differential Manifolds and Riemannian Geometry*, Academic Press, San Diego.
- Golubev, V. V., 1953, *Lectures on Integration of the Equations of Motion of a Rigid Body about a Fixed Point*, State Publishing House of Theoretical Literature, Moscow.
- Greenwood, D. T., 1988, *Principles of Dynamics*, 2nd ed., Prentice-Hall, Englewood Cliffs, NJ.
- Hille, E., 1969, *Lectures on Ordinary Differential Equations*, Addison-Wesley, London.
- Kane, T. R., and Levinson, D. A., 1987, "Approximate Description of Attitude Motions of a Torque-Free, Nearly Axisymmetric Rigid Body," *Journal of the Astronautical Sciences*, Vol. 35, pp. 435-446.
- Kraige, L. G., and Junkins, J. L., 1976, "Perturbation Formulations for Satellite Attitude Dynamics," *Celestial Mechanics*, Vol. 13, pp. 39-64.
- Leimanis, E., 1965, *The General Problem of the Motion of Coupled Rigid Bodies About a Fixed Point*, Springer-Verlag, New York.
- Longuski, J. M., 1991, "Real Solutions for the Attitude Motion of a Self-Excited Rigid Body," *Acta Astronautica*, Vol. 25, No. 3, pp. 131-140.
- Longuski, J. M., Kia, T., and Breckenridge, W. G., 1989, "Annihilation of Angular Momentum Bias During Thrusting and Spinning-Up Maneuvers," *Journal of the Astronautical Sciences*, Vol. 37, No. 4, pp. 433-450.
- Longuski, J. M., and Tsotras, P., 1993, "Analytic Solutions for a Spinning Rigid Body Subject to Time-Varying Body-Fixed Torques. Part I: Constant Axial Torque," *ASME JOURNAL OF APPLIED MECHANICS*, Vol. 60, pp. 970-975.
- Or, A. C., 1992, "Injection Errors of a Rapidly Spinning Spacecraft with Asymmetries and Imbalances," *Journal of the Astronautical Sciences*, Vol. 40, No. 3, pp. 419-427.
- Tsotras, P., and Longuski, J. M., 1991a, "A Complex Analytic Solution for the Attitude Motion of a Near-Symmetric Rigid Body Under Body-Fixed Torques," *Celestial Mechanics and Dynamical Astronomy*, Vol. 51, pp. 281-301.
- Tsotras, P., and Longuski, J. M., 1991b, "Analytic Solutions for the Attitude Motion of Spinning Rigid Bodies Subject to Periodic Torques," *Advances in the Astronautical Sciences*, Vol. 76, pp. 661-678; also, AAS Paper 91-404, AAS/AIAA Astrodynamics Conference, Durango, CO, Aug. 19-22.
- Tsotras, P., and Longuski, J. M., 1993, "Analytic Solutions for a Spinning Rigid Body Subject to Time-Varying Body-Fixed Torques, Part II: Time-Varying Axial Torque," *ASME JOURNAL OF APPLIED MECHANICS*, Vol. 60, pp. 976-981.
- Van der Ha, J. F., 1984, "Perturbation Solution of Attitude Motion Under Body-Fixed Torques," *35th Congress of the International Astronautical Federation*, Paper IAF 84-357, Lausanne, Switzerland, Oct. 7-13.

C. E. Brennen

Professor of Mechanical Engineering,
Mem. ASME.

S. Ghosh

Undergraduate Student.

C. R. Wassgren

Graduate Research Assistant.

California Institute of Technology,
Pasadena, CA 91125

Vertical Oscillation of a Bed of Granular Material

A bed of granular material which is subjected to vertical vibration will exhibit at least one sudden expansion at a critical acceleration amplitude. This sudden expansion corresponds to a bifurcation similar to that exhibited by a single ball bouncing on a vibrating plate. Theoretical analysis based on this model yields results which are in accord with the experimental observations. Other bifurcations may occur at higher vibration levels.

1 Introduction

The vibration of granular materials is of interest for a number of reasons. First, vibration is sometimes used instead of an upward flow of gas to fluidize a particle bed reactor and in such devices it is clearly important to know the state of the bed. Secondly, vibration is often used to induce flow in recalcitrant bulk flow transport devices such as hoppers and chutes. It is also used to induce segregation of different density and different size particles. Clearly, knowledge of how vibration affects these granular materials provides important design information. As a third incentive we note that there has been a growing recognition of and interest in the granular state. In a recent review, Jaeger and Nagel (1992) have summarized some of the important issues, questions, and applications of knowledge of the granular state and highlight the need for understanding the response to vibration. The analogy to molecular dynamics is often drawn but an important difference is that the particles in a granular material are inelastic and therefore only sustain random motions when either (a) the material is flowing (more specifically, undergoing continuous deformation) in which case the random motions are produced by the collisions or (b) externally imposed vibrations generate particle motions. Consequently, research on the flow of granular materials and on the vibrational excitation of granular material would seem complementary and knowledge gained from one should provide insights to the other.

Several investigators have previously examined the response of a bed of particles subjected to vertical vibrations and identified a number of states and transitions between those states. Observations have been made for fine powders in which the interstitial fluid plays an important role in the response (see, for example Gutman, 1976a, 1976b) and for larger particles (typically > 0.1 mm diameter) in which the effects of the interstitial fluid are small. In this paper we shall focus on the latter case because, even in the absence of the interstitial fluid effects, phenomena occur which have yet to be adequately explained. The important variables are the radian frequency of vibration, Ω , vibration amplitude, a , particle diameter, d , and bed height at rest, h_0 , as well as material properties such as the coefficient of restitution, ϵ_p , for collisions between the individual particles and the base plate. Clearly two appropriate dimensionless parameters which will influence the state of the material

are the dimensionless acceleration amplitude, $\Gamma = a\Omega^2/g$, where g is the acceleration due to gravity, and the number of layers in the bed, h_0/d .

Most investigators agree that within the range of frequencies usually explored ($5 \rightarrow 100$ Hz) the phenomena are relatively independent of frequency but depend strongly on the acceleration level, Γ , and the bed thickness, h_0/d . We describe the phenomena which have been reported to occur as Γ is increased from zero. As long as $\Gamma < 1$, the visual appearance of the bed changes little; however Chlenov and Mikhailov (1965, 1972) report an increase in mobility and this manifests itself as a decrease in the angle of repose (Rajchenbach and Evesque, 1988). When Γ exceeds unity by a small amount, the bulk of the particles separate from the base plate each cycle of oscillation when the downward acceleration exceeds $1g$. We note, parenthetically, that one of the effects of the resistance to air flow in fine powders is to delay the inception of separation to values of Γ greater than unity (Thomas et al., 1989). For the larger particles (typically > 0.1 mm diameter), when Γ is just a little larger than unity the flight time of the particles, Δt (the time between separation and subsequent recontact), is short compared with the period, $T = 2\pi/\Omega$, of the oscillations. In these circumstances the material essentially comes to rest relative to the plate prior to the next flight.

A number of phenomena are observed to occur when the acceleration level, Γ , is increased to higher levels so that the flight time, Δt , approaches the period, T . It is clear that the events depend upon the layer thickness, h_0/d . Douady, Fauve, and Laroche (1989) examined fairly thick layers with h_0/d in the $10 \rightarrow 100$ range and observed that when the flight time becomes slightly greater than the period, a period doubling bifurcation occurred. This resulted in two different flights which alternated to produce a 2Ω component in the motion. The critical Γ at which this occurred increased from 4.5 for $h_0/d = 7$ to 5.3 for $h_0/d = 25$.

Thomas et al. (1989) examined much thinner layers including very dilute systems consisting of much less than a single layer of particles. They describe four identifiable states which can occur at large Γ (typically $2.5 \rightarrow 6.0$) and are primarily distinguished by different layer thicknesses, h_0/d . For very small h_0/d (of order 0.17) they describe a "Newtonian-I" state in which the particles are bouncing so randomly that the vertical concentration profile changes little during a cycle. At somewhat larger h_0/d (at 0.273 for example) there is a transition to a "Newtonian-II" state in which a dense layer of particles accumulates on the surface during one part of each cycle. Thicker layers of particles (for example $h_0/d = 1.7$) lead to a "coherent-expanded" state in which the particles all oscillate as a coherent mass. This mass does, however, expand and contract during each cycle. Bachmann (1940) had earlier observed the transi-

Contributed by the Applied Mechanics Division of THE AMERICAN SOCIETY OF MECHANICAL ENGINEERS for publication in the ASME JOURNAL OF APPLIED MECHANICS.

Discussion on this paper should be addressed to the Technical Editor, Professor Lewis T. Wheeler, Department of Mechanical Engineering, University of Houston, Houston, TX 77204-4792, and will be accepted until four months after final publication of the paper itself in the ASME JOURNAL OF APPLIED MECHANICS.

Manuscript received by the ASME Applied Mechanics Division, Jan. 24, 1994; final revision, Nov. 21, 1994. Associate Technical Editor: W. N. Sharpe, Jr.

Table 1 Bead and lid masses for the various experiments

Experiment No.	Bead Mass [gm.]	Lid Mass [gm.]
1	250	3.44
2	125	3.44
3	125	7.17
4	375	3.44
5	125	17.06
6	625	3.44
7	45	3.51
8	125	28.14

tion to coherent motion and reported that this occurred when $h_0/d = 6$.

Finally, Thomas et al. (1989) identify a "coherent-condensed" state at larger values of h_0/d on the order of 4. In this state the particles move as a mass but the mass remains compact throughout the cycle. They report that the transition from the "coherent-expanded" state to the "coherent-condensed" state is sudden and repeatable.

In the present paper we describe the phenomena which were observed to occur as the vertical acceleration of a bed of material is increased and identify a transition or bifurcation similar to that which occurs with a single bouncing ball on a vertically vibrating plate (Wood and Byrne, 1981; Holmes, 1982).

2 Experiments

Experiments were carried out to investigate the behavior of a bed of granular material subjected to vertical vibration. The materials used were A-285 glass beads with a mean diameter of 2.85 mm. Various quantities of these beads were placed in a rectangular box with cross-sectional dimensions of 11 cm by 13.2 cm which was in turn mounted on an electro-mechanical shaker and subjected to vertical vibration at frequencies between 4 and 10 Hz with amplitudes up to about 2.5 g. A Statham A73TC-4-350 accelerometer was used to measure the acceleration level accurately.

The box had a thick aluminum base and back but the other three sides were made of lucite so that the behavior of the beads could be observed. Paper lids of various thickness were placed on top of the beads leaving a clearance of about 1 mm between the edge of the lid and the walls of the box. When the box was vibrated vertically the bed of beads would expand and the lid would float on the beads. Fortunately, the lid proved to be quite stable and under all of the conditions used in the present experiments would remain horizontal and centralized with a roughly equal spacing all around the periphery. Because this spacing was smaller than the diameter of the beads, all of the beads would remain under the lid. A stroboscope was used to examine the motion of the lid and the beads during various parts of the oscillation cycle. By this means we were able to observe that the spacing, h , between the base and the lid did not vary greatly during the oscillations. The beads would bounce around below the lid but because of the resistance to the flow of air around the sides of the lid, the volume of beads and air would remain almost constant during a cycle of oscillation. Thus, using the strobe and a scale attached to the exterior of the box, it was possible to measure the height, h , for each operating condition.

Experiments were conducted by observing the evolution of the bed of beads as the vibration amplitude, a , was increased from zero to the maximum of which the shaker was capable. Such experiments were conducted over a range of frequencies (4 → 10 Hz) for various quantities of beads and for lids with different weights as listed in Table 1.

It should be noted that a single packed layer of beads resting on the base of the box would weigh approximately 62 gm. Consequently the masses of beads range from less than a single layer to about ten layers. The 45 gm of experiment 7 was close to the minimum at which the lid would remain horizontal for the duration of the experiment.

3 Experimental Results

The results for the base-to-lid spacing, h , as a function of vibration amplitude will be presented in various ways but we focus here on the expansion of the bed, $h^* = h - h_0$, where h_0 is the spacing at rest. For reasons which will become clear, h^* will be presented both as a function of the non-dimensional acceleration amplitude $\Gamma = a\Omega^2/g$ where g is the acceleration due to gravity, and as a function of the vibration velocity, $a\Omega$. The typical behavior of the bed is best illustrated by the results from experiment 7 which are presented in Fig. 1.

The bed would begin to expand at an acceleration amplitude of about 1 g and this expansion would gradually increase until one reached a certain critical value of the acceleration amplitude, Γ_c , which appeared to be independent of frequency but to vary with both the mass of beads and the mass of the lid. At this critical acceleration amplitude the lid would rise quite abruptly and then settle down at a substantially larger spacing, h . As illustrated in Fig. 1, further increase in the acceleration would result in further bed expansion but this was more gradual than the expansion encountered during transition. The top graph in Fig. 1 illustrates the fact that the critical conditions appear to occur at a given acceleration amplitude regardless of the frequency. On the other hand, the bottom graph in Fig. 1 illustrates the fact that the supercritical conditions correlate with the velocity amplitude, $a\Omega$, rather than the acceleration amplitude.

Using the strobe, one could observe that prior to the transition the motions of the particles were fairly uncoordinated. However, above the transition the beads began to move as a mass which collided once per cycle with the base and with the lid. The collision with the base seemed quite inelastic and it appeared

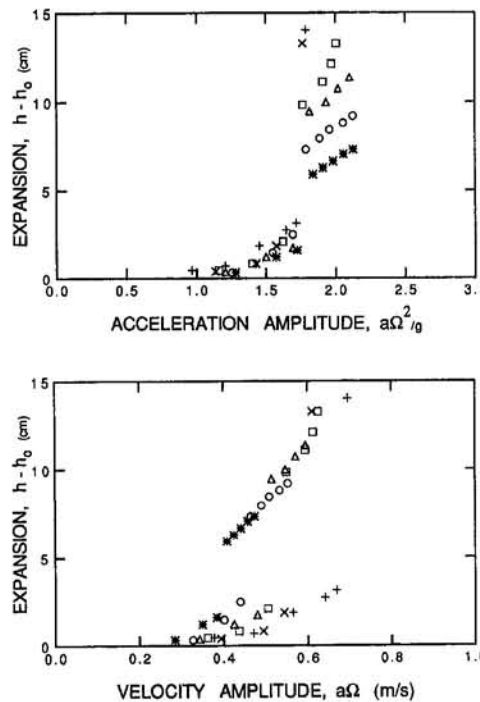


Fig. 1 The dependence of the bed expansion, $h - h_0$, on the acceleration amplitude, $\Gamma = a\Omega^2/g$, and the velocity amplitude, $a\Omega$ (in m/s), for experiment 7. Various frequencies as follows: $+$ = 4 Hz, x = 4.5 Hz, \square = 5 Hz, \triangle = 5.5 Hz, \circ = 6 Hz, and $*$ = 7 Hz.

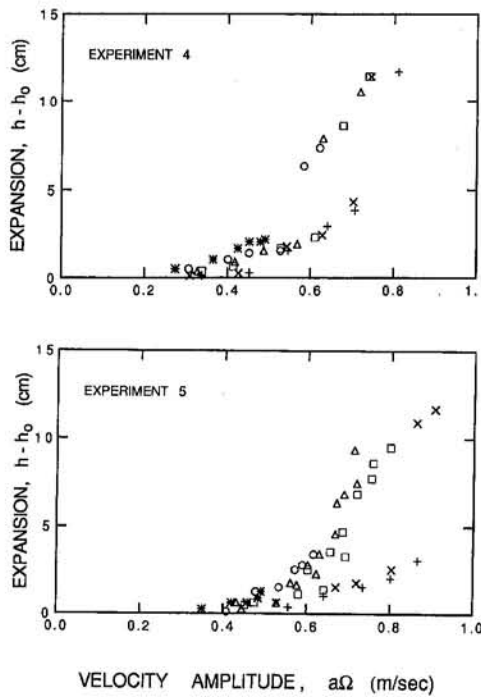


Fig. 2 Data from experiments 4 (top) and 5 (bottom) with frequency key as in Fig. 1

that the mass only left the base again when the acceleration of the base exceeded some critical value. However, it is also important to emphasize that the mass expands and contracts substantially during each cycle being quite concentrated while it is in contact with the base but quite dilute while it is in flight.

Experiment 7 was chosen to illustrate the transition because it does so most clearly. This is because it used the smallest mass of beads. As the mass of beads was increased (for the same lid weight) the critical transition became less distinct in the sense that the expansion at the critical acceleration became somewhat less abrupt and somewhat smaller. The same trend was manifest as one increased the weight of the lid. Both effects are illustrated in Fig. 2 which presents data from experiments 4 and 5.

The critical acceleration, Γ_c , also increases with both the mass of the beads and the mass of the lid. These trends are shown in Fig. 3.

In order to understand the fundamental dynamics behind the above phenomena it is valuable to present the data non-dimensionally. This is accomplished by nondimensionalizing the expansion as $(h - h_0)\Omega^2/g$ and plotting this versus the nondimensional acceleration amplitude, $\Gamma = a\Omega^2/g$. Examples from experiments 2 and 3 are shown in Fig. 4 in which the subcritical and supercritical data clearly form two distinct groups of points. Indeed the two groups of points both appear to lie close to quadratic curves which imply that each group of points correspond to a roughly constant value of the inverse Froude number,

$$\text{Fr}^{-1} = \frac{[g(h - h_0)]^{1/2}}{a\Omega}. \quad (1)$$

To examine this further, the inverse Froude number is plotted versus the acceleration, Γ , in Fig. 5 for the typical data of experiments 2 and 3.

It seems particularly noteworthy that the subcritical data corresponds roughly to an inverse Froude number, Fr^{-1} , of between 0.5 and 1.0 and that the supercritical corresponds quite closely to $\text{Fr}^{-1} = 1.5$ (recall that the values of $(h - h_0)$ and a for some of the subcritical data are quite small and this may account for the larger scatter in that group of points). The specific values

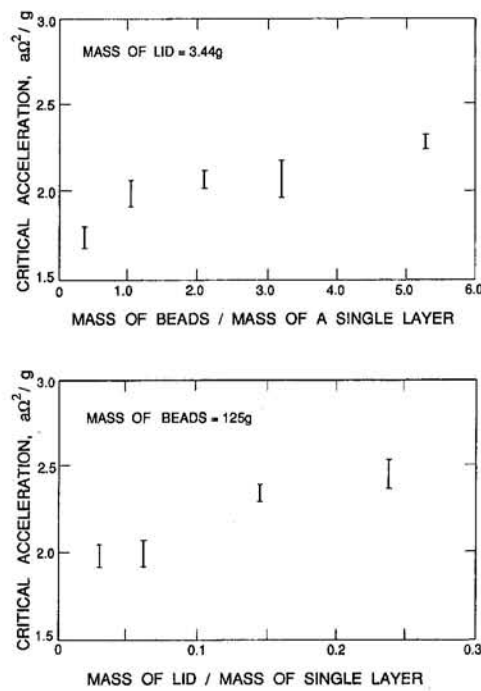


Fig. 3 The critical acceleration, $\Gamma_c = (a\Omega^2/g)_c$, as a function of the mass of beads (top graph for 3.44 gm lid) and as a function of the mass of the lid (bottom graph for 125 gm of beads)

for Fr^{-1} decrease significantly as the mass of beads increases and as the mass of the lid is increased. The subcritical data shows similar trends though they are less distinct due to greater scatter in the data.

4 Theoretical Analyses

The analytical solutions to the problem of a ball bouncing on a horizontal flat plate performing vertical oscillations (ampli-

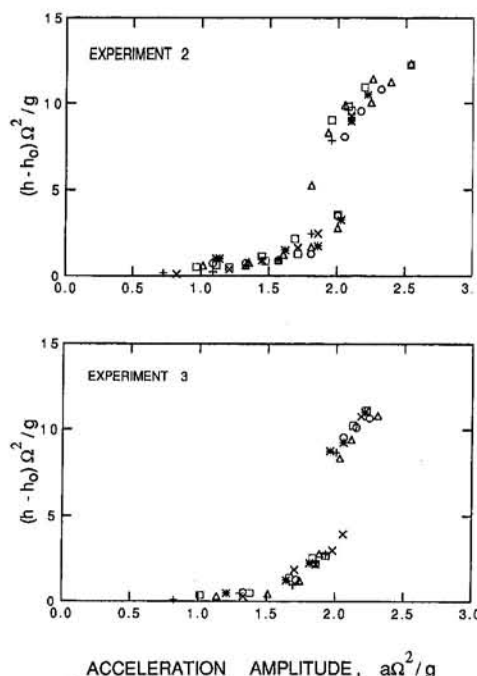


Fig. 4 Dimensionless expansion, $(h - h_0)\Omega^2/g$, plotted against dimensionless acceleration, $\Gamma = a\Omega^2/g$, for experiments 2 and 3. Frequency key as in Fig. 1.

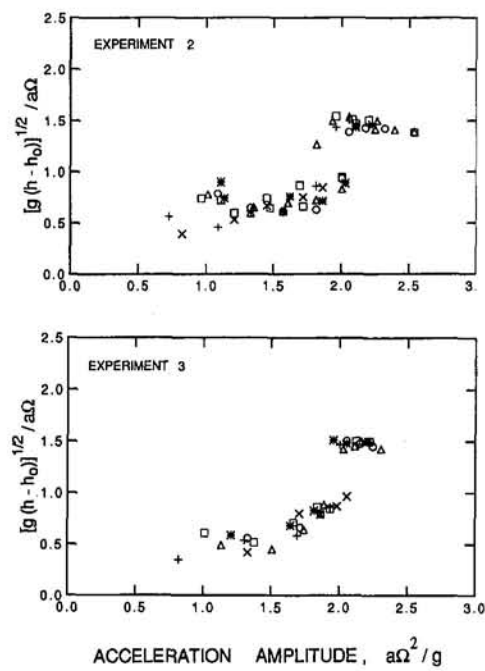


Fig. 5 Inverse Froude number, $[g(h - h_0)]^{1/2}/a\Omega$, plotted against dimensionless acceleration, $\Gamma = a\Omega^2/g$, for experiments 2 and 3. Frequency key as in Fig. 1.

tude, a , and radian frequency, Ω) are of interest for several reasons. First, the model could be considered appropriate for individual particles when particle/particle collisions are relatively rare, as, for example, in the case where less than a single layer of particles was used. Alternatively, in the case of a larger mass of particles, the solution might be considered applicable to the whole mass when it performs a coherent periodic motion. In either case, we shall consider that the particles bounce off a lid which, by some unspecified damping mechanism, is maintained at a constant height above the oscillating plate. The lid is, however, entirely supported in the mean by the impulses imparted by the particles; thus solutions will be sought for various ratios of the lid mass to the particle mass, f . The problem also requires specification of the coefficients of restitution, ϵ_p and ϵ_l for collisions with the plate and lid, respectively.

The dynamics of the ball bouncing problem without a lid have now become a classic example of the occurrence of bifurcations (see, for example, Wood and Byrne, 1981; Holmes, 1982) and we shall see that this seems the probable explanation for the experimentally observed transition.

The first, simple solution which is useful is that for no lid and for $\epsilon_p = 0$. The ball remains in contact with the plate until the latter is accelerating downward at an acceleration equal to g . The maximum height, h_s , to which the ball rises above the plate can readily be identified parametrically as

$$\frac{h_s \Omega^2}{g} = \Gamma[(x_2 - x_1) \cos x_1 + \sin x_1 - \sin x_2] \quad (2)$$

where

$$\sin x_1 = 1/\Gamma; x_2 - x_1 = \Gamma(\cos x_1 - \cos x_2). \quad (3)$$

This relationship between the dimensionless "expansion," $h_s \Omega^2/g$ and the acceleration amplitude was obtained numerically and is identified in Fig. 6 as the "no bounce" solution. Note that it corresponds quite closely with the subcritical experimental data (in Fig. 6 we have used the data of experiment 2 as typical).

When one examines the specifics of this solution for the range of Γ values of interest here (less than about 2) one finds that

after becoming airborne the particle (or particle mass) will return to impact the plate after less than about 0.6 of a cycle. Even if ϵ_p were nonzero and there were several small bounces following this impact there is more than sufficient time left in the cycle for the particle (or particle mass) to effectively come to rest on the plate before the next occurrence of a downward acceleration of $1g$. Thus the solution is valid for a range of ϵ_p .

The second benchmark which is of interest here is the periodic solution in which the particle (or particle mass) bounces off the plate and off the lid once per cycle of plate oscillation. In order for such a periodic solution to exist the relative velocity of departure from the lid collision, u_4 , the relative velocity of incidence on the plate, u_1 (both u_4 and u_1 considered positive downward), the relative velocity of departure from the plate, u_2 , and the relative velocity of incidence on the lid, u_3 , (u_2 and u_3 considered positive upward) must be given by

$$\begin{aligned} \frac{u_1 \Omega}{g} &= \frac{2\pi(1+f)}{(1+\epsilon_p)}; & \frac{u_2 \Omega}{g} &= \frac{2\pi\epsilon_p(1+f)}{(1+\epsilon_p)} \\ \frac{u_3 \Omega}{g} &= \frac{2\pi f}{(1+\epsilon_l)}; & \frac{u_4 \Omega}{g} &= \frac{2\pi\epsilon_l f}{(1+\epsilon_l)}. \end{aligned} \quad (4)$$

The solution is most readily obtained parametrically by selecting the times t_1 and t_2 during a cycle when collision with the plate and the lid, respectively, occur. It then follows that

$$\Gamma = \frac{\left[\Omega(t_1 - t_2) \right] \left[\frac{u_2 \Omega}{g} + \frac{u_3 \Omega}{g} \right] + \left[\Omega(t_1 + t_2) + 2\pi \right] \left[\frac{u_1 \Omega}{g} + \frac{u_4 \Omega}{g} \right]}{2\pi(\cos \Omega t_1 + \cos \Omega t_2)} \quad (5)$$

and that the expansion, h , defined as the increase in the spacing between the plate and the lid is given by

$$\frac{h}{a} = \sin \Omega t_1 - \sin \Omega t_2 + \frac{\Omega(t_2 - t_1)}{2} \left[\frac{u_2}{a\Omega} + \frac{u_3}{a\Omega} + \cos \Omega t_1 + \cos \Omega t_2 \right]. \quad (6)$$

Thus the choice of two arbitrary values of Ωt_1 and Ωt_2 corresponds to a solution for specific values of f and Γ and yields a specific value for h/a . In addition one must check to ensure that there are no unforeseen overlaps between the particle and the lid or plate during the oscillation cycle. Typical results for this analysis are included in Fig. 6 (identified as "with bounce" solution) for $\epsilon_p = 0.25$, $\epsilon_l = 0$, and $f = 0.01, 0.1, 0.2$. Note that for a given lid and given coefficients of restitution there

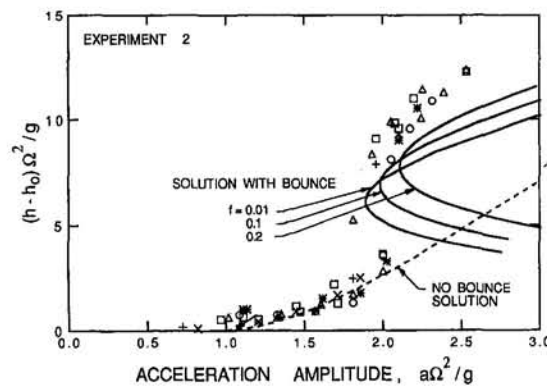


Fig. 6 Typical data (from experiment 2) compared with the analytical solutions described in the text

exist no periodic solutions of this type for accelerations below a certain critical level.

It should be noted in passing that there is a large variety of other possible periodic solutions. For example there exist the possibilities of one bounce for every two or more plate cycles and of two or more bounces in a single plate cycle. Alternatively the ball might cycle through two or more types of bounce before repeating itself. It is important to point out that studies of the dynamics of the much simpler system of a single particle on a vibrating plate (Wood and Byrne, 1981 and Holmes, 1982) have revealed a system of bifurcations at different critical values of the acceleration, Γ .

As the acceleration amplitude is increased the dynamics of the single ball exhibits the first bifurcation from the "no bounce" solution to the "with bounce" state at

$$\Gamma_c = \frac{\pi(1 - \epsilon_p)}{(1 + \epsilon_p)}. \quad (7)$$

The present experimental data clearly indicates that such a bifurcation also occurs with the granular mass. Though the analogy may only be of qualitative value, it is nevertheless of interest to observe that Eq. 7 yields $\Gamma_c = 1.88$ when $\epsilon_p = 0.25$, a value we have arbitrarily chosen to demonstrate the results of the analytical calculation. This analysis is qualitatively consistent with the current experimental data since the effective ϵ_p for the mass of particles may be as low as 0.25.

Thus the analysis is consistent with the following explanation of the observed experimental behavior. At small values of the acceleration just above $1g$, the data is consistent with the simple, no-bounce solution. However, when the acceleration approaches the critical or bifurcation value of Γ , a sudden expansion of the bed occurs as the particle mass begins to move as a fairly coherent whole, bouncing off the plate once each oscillation cycle.

A computer simulation was developed in order to determine if a column of inelastic particles vibrating on an oscillating plate and bouncing off one another would behave in a manner similar to a single particle. A hard sphere model was used to simulate a column of up to ten particles with zero radius, constrained to move vertically, supported by a sinusoidally vibrating plate. The separation height, h , between the top particle and the oscillating plate was averaged over many cycles for values of the parameter Γ between 1.0 and 5.0. It was found that a series of "jumps" in the bed expansion existed for combinations of N , the number of particles, and ϵ , the coefficient of restitution between particles and between the bottom particle and the plate. Figure 7 presents the results of a typical simulation where the dimensionless expansion $h\Omega^2/g$, is plotted against the acceleration amplitude $a\Omega^2/g$. For cases where N was small and ϵ was large, the effective coefficient of restitution of the column of particles is nonzero and sudden increases in the column expansion occurred. However, when N was large and ϵ was small, the effective restitution coefficient was zero and the column of particles remained grouped together. In this regime the characteristic sudden expansion was not observed for the range of acceleration amplitudes examined.

Clément et al. (1993) found similar results both experimentally and numerically for a column of spherical particles vibrating on a sinusoidally oscillating base. They plotted the separation height of the center of mass of a column of ten particles vibrating on a sinusoidally oscillating base as a function of acceleration amplitude and also found sudden jumps at particular values of Γ . They, however, did not discuss the cause of these jumps. Clément et al. also describe regimes where particles cluster together and move as a coherent mass. Here the column of particles behaves in a manner similar to a single particle with a coefficient of restitution equal to zero. Clearly the same phenomena are being observed in the present simulations.

As a last note, it is interesting to consider the possible role of the present bifurcations in the onset of the heaping phenome-

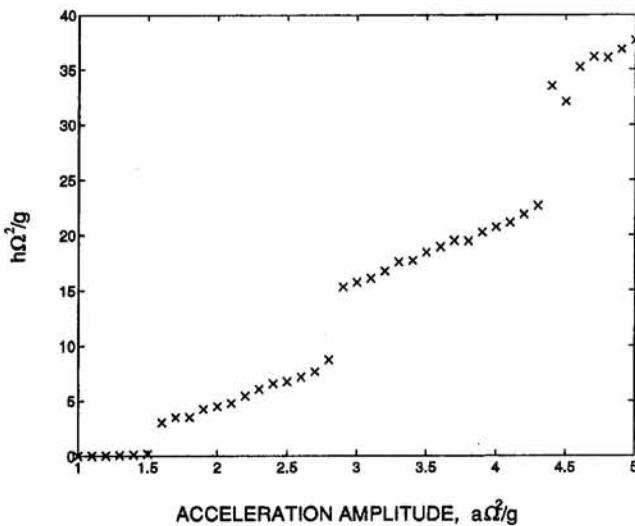


Fig. 7 Results from the computer simulation of a column of ten particles with zero radius. In the simulation, $\epsilon = 0.90$, and the separation height, $h\Omega^2/g$ was averaged over 400 oscillations.

non (and its convection pattern) observed in the experiments of Evesque and Rajchenbach (1989), Laroche et al. (1989), and others. Since the bifurcations observed here occur at nearly the same value of Γ as the onset value for heaping ($\Gamma_H = 1.2$) it is worth considering how the two phenomena might be related. The authors suggest that the two are in fact not related. The sudden bed expansion which occurs for the shallow beds examined here are due to a bifurcation in the dynamics of a bed that has an effective restitution coefficient which is greater than zero, $\epsilon_{eff} > 0$. Heaping, however, is observed for deeper beds where $\epsilon_{eff} = 0$ and the first bifurcation occurs when $\Gamma \approx 3.3$. Furthermore, when $\epsilon_{eff} = 0$, the bed does not exhibit the sudden expansion described in this paper but instead displays a period doubling bifurcation.

5 Conclusions

A bed of granular material which is subjected to vertical vibration will exhibit at least one sudden expansion at a critical acceleration amplitude. This sudden expansion corresponds to a bifurcation similar to that exhibited by a single ball bouncing on a vibrating plate. Theoretical analysis based on this model yields results which are in accord with the experimental observations. Other bifurcations may occur at higher vibration levels.

Acknowledgments

The authors would like to thank Prof. Rolf Sabersky for his always helpful encouragement and advice. The work described herein was partly carried out during the summer of 1984 while one of the authors (S. Ghosh) was supported by a Summer Undergraduate Research Fellowship (SURF) at the California Institute of Technology. This paper was prepared with the support of the National Science Foundation under grant number CTS 9300665.

References

- Bachmann, D., 1940, *Verfahrenstechnik Z.V.D.I. Beiheft*, No. 2, p. 43 (cited by Gutman, 1976a).
- Chlenov, V. A., and Mikhailov, N. V., 1965, "Some Properties of Vibrating Fluidized Bed," *Inzh.-Fiz. Zh.*, Vol. 9, No. 2, pp. 196-200.
- Chlenov, V. A., and Mikhailov, N. V., 1972, *Vibrofluidized beds*, Izdatel'stvo Nauka, Moscow.
- Clément, E., Luding, S., Blumen, A., Rajchenbach, J., and Duran, J., 1993, "Fluidization, Condensation, and Clusterization of a Vibrating Column of Beads," *International J. of Mod. Phys. B*, Vol. 7, Nos. 9 and 10, pp. 1807-1827.

Douady, S., Fauve, S., and Laroche, C., 1989, "Subharmonic Instabilities and Defects in a Granular Layer Under Vertical Vibrations," *Europhys. Lett.*, Vol. 8, No. 7, pp. 621-627.

Evesque, P., and Rajchenbach, J., 1989, "Instability in a Sand Heap," *Phys. Rev. Lett.*, Vol. 62, No. 1, pp. 44-46.

Gutman, R. G., 1976a, "Vibrated Beds of Powders Part I: A Theoretical Model for the Vibrated Ved," *Trans. Instn. Chem. Engrs.*, Vol. 54, pp. 174-183.

Gutman, R. G., 1976b, "Vibrated Beds of Powders Part II: Heat Transfer in and Energy Dissipation of a Vibrated Bed," *Trans. Instn. Chem. Engrs.*, Vol. 54, pp. 251-257.

Holmes, P. J., 1982, "The Dynamics of Repeated Impacts with a Sinusoidally Vibrating Table," *J. of Sound and Vibration*, Vol. 84, No. 2, pp. 173-189.

Jaeger, H. M., and Nagel, S. R., 1992, "Physics of the Granular State," *Science*, Vol. 255, No. 5051, pp. 1523-1531.

Laroche, C., Douady, S., and Fauve, S., 1989, "Convective Flow of Granular Masses Under Vertical Vibrations," *J. Phys. France*, Vol. 50, No. 7, pp. 699-706.

Rajchenbach, J., and Evesque, P., 1988, "Instabilité Convective Dans un tas de Sable," *C.R. Acad. Sci. Ser. II (Paris)*, Vol. 307, pp. 1-4.

Thomas, B., Mason, M. O., Liu, Y. A., and Squires, A. M., 1989, "Identifying States in Shallow Vibrated Beds," *Powder Tech.*, Vol. 57, pp. 267-280.

Wood, L. A., and Byrne, K. P., 1981, "Analysis of a Random Repeated Impact Process," *J. of Sound and Vibration*, Vol. 78, No. 3, pp. 329-345.

A Comparison Between the Tiersten Model and $O(H)$ Boundary Conditions for Elastic Surface Waves Guided by Thin Layers

P. Bövik

Division of Mechanics,
Chalmers University of Technology,
S-412 96 Göteborg, Sweden

In this paper we make a comparison between the boundary conditions (BCs) derived by Tiersten and the so-called $O(h)$ BCs for elastic surface waves guided by thin films. By a thin layer we here mean a layer for which the thickness is much smaller than the wavelengths involved. The advantage of the $O(h)$ model is that it starts with the general three-dimensional equation of motion and derives the boundary conditions in a rational manner keeping all terms linear in the layer thickness. The Tiersten model is obtained from the approximate equations for low frequency and flexure of thin plates by neglecting the flexural stiffness. We consider straight-crested surface waves under plane-strain conditions, so-called Rayleigh-type waves (P-SV), and Love waves (SH). It is shown that for the Rayleigh type waves the $O(h)$ BCs gives a much better approximation of the exact case than the Tiersten BCs. Even for the Tiersten model including flexural stiffness, the $O(h)$ BCs yields more accurate results. Concerning Love waves both the Tiersten model and $O(h)$ model reduces to the same dispersion relation which quite well approximates the exact solution.

Introduction

It is well known that thin layers of finite width coated on an isotropic half-space can be used to guide elastic surface waves in the substrate. The first one to study this problem seems to be Bromwich (1899) who considered long waves. For a half-space of incompressible materials, the work was extended by Love (1911), who considered short wavelengths compared to the thickness of the layer. Over the past decades there has been a renewed interest in the problem of effective modeling thin layers for application in wave propagation problems. Important technical applications are flaw detection and nondestructive testing of components which, due to manufacturing or surface conditioning, have been covered with thin films of different materials. Other areas where effective modeling of thin layers are important include signal processing and microwave theory where surface acoustic waves (SAW) and so-called SAW-filters are of great interest. Also in piezoelectric media, in which a deformation produces an electric field, thus giving rise to a coupling of mechanical and electric phenomena, we find important technical applications of electromechanical surface waves, Parker and Maugin (1988).

Probably the most commonly used approach to model thin elastic layers is the so-called "spring contact model." This model employs boundary conditions which are linear and relate the discontinuity of the displacement to the surface traction. With this model it is also possible to model, not only the open and closed crack, but also perfectly lubricated cracks and partially closed cracks (Wickham and Boström, 1991).

Contributed by the Applied Mechanics Division of THE AMERICAN SOCIETY OF MECHANICAL ENGINEERS for publication in the ASME JOURNAL OF APPLIED MECHANICS.

Discussion on this paper should be addressed to the Technical Editor, Professor Lewis T. Wheeler, Department of Mechanical Engineering, University of Houston, Houston, TX 77204-4792, and will be accepted until four months after final publication of the paper itself in the ASME JOURNAL OF APPLIED MECHANICS.

Manuscript received by the ASME Applied Mechanics Division, May 12, 1994; final revision, Sept. 16, 1994. Associate Technical Editor: X. Markenscoff.

In some recent investigations of scattering properties of thin interface layers surrounding certain elastic inclusions, Olsson et al. (1990) and Boström et al. (1992) showed that the spring contact boundary conditions are in fact inadequate to describe the scattering from a thin elastic layer. Regarding quantities like the scattering cross sections of coated elastic inclusions, the use of spring contact boundary conditions, in some situations lead to a prediction of a *decrease* in the scattering cross section when in fact both exact solutions (when available) and a more careful approximate analysis predict an *increase*. There is also one rather obvious and somewhat absurd consequence of the spring contact boundary conditions: They predict a scattering from the layer itself even when the layer is of the same material as the matrix.

In Bövik and Olsson (1992) effective boundary conditions for SH waves were derived for almost arbitrarily curved elastic isotropic layers imbedded in a different elastic isotropic material. These boundary conditions are exact up to and including the first order in the layer thickness. The method was extended in Bövik (1994) to cover the full three-dimensional vector case and with more material configurations though the configuration in this paper were not included. In a paper by Tiersten (1969), elastic surface waves guided by thin films are considered by using the approximate equations of low frequency extension and flexure of thin plates. These approximate equations enable the effect of the plating to be treated as a boundary condition at the surface of the substrate. The model by Tiersten have been widely used in many different contexts concerning wave propagation in thin layers, and in this paper we will numerically compare the dispersion relations for the two models which will be referred to as the $O(h)$ boundary conditions and the approximate model by Tiersten.

In Section 1 we review the solution of elastic surface waves guided by a thin elastic layer coated on a semi-infinite elastic half-space of a different material. In Section 2 we review the model derived by Tiersten and derive the dispersion relation for Rayleigh-type waves and in Section 3 we use the perturba-

tion method to obtain the $O(h)$ boundary conditions and derive a similar dispersion relation. In Section 4 we show that both the Tiersten model and the $O(h)$ model give identical dispersion relations for Love waves in a layer on a semi infinite half-space. This results corrects an error in Wickham (1992) where different dispersion curves were obtained for the two models. Finally in Section 5 we give some numerical results showing comparisons between the different models.

1 Preliminary Considerations

In this section we briefly review the solution of elastic surface waves guided by a thin coating bonded to its surface, the coating being of a different material than the substrate. The Lamé parameters in the half-space are λ , and μ , respectively, and the density is denoted by ρ . The corresponding parameters in the coating are denoted by λ' , μ' and ρ' (see Fig. 1).

The elastodynamic equation of motion for a linear isotropic elastic material (without any body forces) can be written in terms of the displacement field as

$$\mu u_{i,jj} + (\lambda + \mu) u_{j,ji} = \rho \ddot{u}_i. \quad (1)$$

The stress tensor is given by

$$\tau_{ij} = \lambda u_{k,k} \delta_{ij} + \mu (u_{i,j} + u_{j,i}). \quad (2)$$

$$\begin{vmatrix} -(2\alpha' \theta_s + \alpha t \sigma_c) & (2\alpha' \beta \theta_s + t \sigma_c) & \alpha' (2\theta_c - t \sigma_c) & (2\alpha' \beta' \theta_s - t \sigma_s) \\ (t \theta_c + 2\alpha' \beta' \sigma_s) & -(2\beta t \theta_c + 2\beta' \sigma_s) & (2\alpha' \beta' \sigma_s - t \theta_s) & \beta' (2\sigma_c - t \theta_c) \\ \alpha (2 - r_\mu t) & (r_\mu t - 2 + q^2) & \alpha' r_\mu r_v^2 q^2 & 0 \\ (r_\mu t - 2 + q^2) & \beta (2 - r_\mu t) & 0 & \beta' r_\mu r_v^2 q^2 \end{vmatrix} = 0 \quad (6)$$

The traction vector on surfaces with a normal vector pointing in the x_2 -direction is given by the components τ_{2j} .

Let us now consider the problem of Rayleigh-type surface waves propagating along a plated surface and confined to the vicinity of the surface of the substrate shown in Fig. 1. Equations (1) and (2) are valid in the half-space and the same equations but with the material parameters primed are valid within the coating. The boundary conditions for a surface wave are

$$\begin{aligned} \tau'_{2j} &= 0 \quad \text{at} \quad x_2 = -2h' \\ u'_j &= u_j \quad \text{and} \quad \tau'_{2j} = \tau_{2j} \quad \text{at} \quad x_2 = 0 \\ u_j &\rightarrow 0 \quad \text{as} \quad x_2 \rightarrow \infty. \end{aligned} \quad (3)$$

A general solution to this problem is given by

$$\begin{aligned} u_1 &= k [C e^{-\alpha k x_2} - \beta D e^{-\beta k x_2}] e^{i k (x_1 - c t)} \\ u_2 &= i k [\alpha C e^{-\alpha k x_2} - \beta D e^{-\beta k x_2}] e^{i k (x_1 - c t)} \\ u_3 &= 0 \end{aligned} \quad (4)$$

valid for $x_2 > 0$, where $\alpha^2 = 1 - (c/c_p)^2 = 1 - (c_s/c_p)^2$, $\beta^2 = 1 - q^2$, and

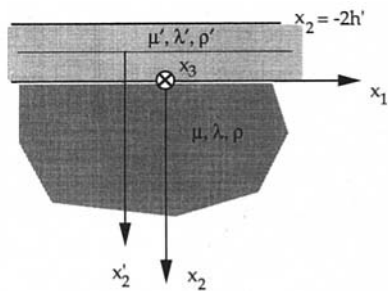


Fig. 1 A thin layer of thickness $2h'$ over a semi-infinite half-space

$$\begin{aligned} u'_1 &= k [A e^{-\alpha' k x_2} + B e^{\alpha' k x_2} - \beta' E e^{-\beta' k x_2} + \beta' F e^{\beta' k x_2}] e^{i k (x_1 - c t)} \\ u'_2 &= i k [\alpha' A e^{-\alpha' k x_2} - \alpha' B e^{\alpha' k x_2} + E e^{-\beta' k x_2} + F e^{\beta' k x_2}] e^{i k (x_1 - c t)} \\ u'_3 &= 0 \end{aligned} \quad (5)$$

for $-2h' < x_2 < 0$, and where

$$(\alpha')^2 = 1 - r_v^2 (d')^2 q^2$$

$$(\beta')^2 = 1 - r_v^2 q^2$$

$$r_v = c_s/c_s'$$

$$d' = c_s'/c_p'.$$

Equations (4) and (5) inserted into (2) gives the stress components, which together with the boundary conditions (3) yields six linear algebraic equations in A , B , C , D , E , F . Nontrivial solutions are given by the vanishing of the determinant of the coefficients. This 6×6 determinant can be reduced to a 4×4 determinant, so the dispersion relation can be written as (here we adopt the same notation as in Tiersten (1969))

where

$$\theta_s = \sinh (\alpha' \gamma) \quad \theta_c = \cosh (\alpha' \gamma)$$

$$\sigma_s = \sinh (\beta' \gamma) \quad \sigma_c = \cosh (\beta' \gamma)$$

$$r_\mu = \mu'/\mu \quad t = 2 - r_v^2 q^2$$

$$\gamma = 2kh'. \quad (7)$$

This is the exact dispersion relation which governs the propagation of all Rayleigh-type waves in a coated isotropic semi-infinite solid. When the coating is very thin compared with the wavelengths involved it is possible to derive an approximation to this exact theory, and in the next two sections we briefly review a model derived by Tiersten, and a more rational approach to derive boundary conditions which are exact up to $O(h)$.

2 The Tiersten Model

In a paper by Tiersten (1969) the propagation of elastic waves guided by thin films are considered by using the approximate equations for low-frequency extension and flexure of thin plates. He shows that it is possible to treat the entire effect of the plating as a nonzero homogeneous boundary condition at the surface of the substrate, and by omitting also the flexural stiffness the resulting dispersion relation becomes a polynomial in the wave number which is much more readily informative than the transcendental equation of the three-dimensional solution. The same technique, using higher order plate equations that include shearing deformation and rotary inertia has been employed by Achenbach and Keshava (1967) in a similar situation.

The two-dimensional equations governing the low-frequency extensional motion of thin plates may be written

$$\frac{1}{2}(1-v')u_{b,aa}^{(0)} + \frac{1}{2}(1+v')u_{a,ab}^{(0)} + \frac{F_b^{(0)}(1-v'^2)}{2E'h'} = \frac{\rho'}{E'}(1-v'^2)\ddot{u}_b^{(0)} \quad (8)$$

and for the flexural motion we have

$$-D'u_{2,abb}^{(0)} + F_{a,2a}^{(0)} + F_2^{(0)} = 2\rho'h'\ddot{u}_2^{(0)} \quad (9)$$

where v' is the Poisson's ratio and the flexural stiffness D' and Young's modulus E' are

$$D' = \frac{4h'^3\mu'}{3(1-v')}$$

$$E' = 2\mu'(1+v').$$

In the following we will use the convention that the indices a, b, c, d range over the numbers 1, 3 and skip 2 whereas i, j, k, l range over 1, 2, 3. $u_a^{(0)} = u_a^{(0)}(x_1, x_3, t)$ are the components of the extensional motion in the midplane of the plate. By making the assumption that $\tau_{22}^{(0)} = 0$ and also neglecting the shear strain components $\epsilon_{2a}^{(0)} = 0$, we find

$$u_{2,2}^{(0)} = -\frac{\lambda'}{\lambda' + 2\mu'} u_{a,a}^{(0)} \quad (10)$$

$$u_{a,2}^{(0)} = -u_{2,a}^{(0)}. \quad (11)$$

where $x_2' = x_2 + h'$. The total displacements at $x_2 = 0$, are obtained from (16) together with (10)–(12) as

$$\begin{aligned} u_a &= u_a^{(0)} - h'u_{2,a}^{(0)} \\ u_2 &= u_2^{(0)} - h'\kappa'u_{a,a}^{(0)} + \frac{1}{2}h'^2\kappa'u_{2,aa}^{(0)} \end{aligned} \quad (17)$$

where $\kappa' = \lambda'/(2\mu') = v'/(1-v')$.

Equations (14) and (15) determine the approximate form taken by the traction boundary condition at the coated surface of the substrate with $\tau_{2j}(0)$ given by (2). The relation between the plating displacements $u_j^{(0)}$ and the substrate displacements u_j at the surface of the substrate are given by (17). Hence, Eqs. (14), (15), and (17) yield the boundary conditions at the surface of the substrate and the displacement field at the substrate is given by (4).

The motion of the surface of the substrate does not coincide with the motion of the centerplane of the plating, which are given by

$$\begin{aligned} u_1^{(0)} &= kGe^{ik(x_1-ct)} \\ u_2^{(0)} &= ikLe^{ik(x_1-ct)} \\ u_3^{(0)} &= 0. \end{aligned} \quad (18)$$

Substituting the Eqs. (4) and (18) into the boundary conditions (14), (15), and (17) yields a fourth-order system of linear algebraic equations and the dispersion relation is obtained through the condition of nontrivial solutions as

$$\begin{vmatrix} 1 & -\beta & -1 & \frac{\gamma}{2} \\ -\alpha & 1 & -\frac{\gamma\kappa'}{2} & \left(\frac{\gamma^2\kappa'}{8} - 1\right) \\ -2\alpha & 2 - q^2 & -\gamma r_\mu(c'^2 - r_v^2 q^2) & 0 \\ 2 - q^2 + \gamma\alpha & -\left(2\beta + \frac{\gamma}{2}(2 - q^2)\right) & 0 & \gamma r_\mu\left(r_v^2 q^2 - \frac{\gamma^2}{6(1-v')}\right) \end{vmatrix} = 0 \quad (19)$$

From the condition that $\tau_{2,22}^{(0)} = 0$, and by using (11), we also find

$$u_{2,22}^{(0)} = \frac{\lambda'}{\lambda' + 2\mu'} u_{2,aa}^{(0)}. \quad (12)$$

The applied forces and couples at the midplane of the plate and perpendicular to the plate are given by

$$\begin{aligned} F_j^{(0)} &= \tau_{2j}(0) \\ F_{a,2}^{(0)} &= h'\tau_{2a}(0) \\ F_{2,2}^{(0)} &= 0. \end{aligned} \quad (13)$$

Inserting Eqs. (10)–(13) into the equations of motion of the plate, i.e., (8), (9) gives the traction components at $x_2 = 0$ as

$$\tau_{2b}(0) = -2\mu'h'\left[u_{b,aa}^{(0)} + \frac{(1+v')}{(1-v')} u_{a,ab}^{(0)}\right] + \rho'h'\ddot{u}_b^{(0)} \quad (14)$$

$$\tau_{22}(0) + h'\tau_{2a,a}(0) = D'u_{2,abb}^{(0)} + 2\rho'h'u_2^{(0)}. \quad (15)$$

The total displacement components u_j' at any point in a plate undergoing both flexural and extensional motion are given by

$$\begin{aligned} u_a' &= u_a^{(0)} + x_2'u_{a,2}^{(0)} \\ u_2' &= u_2^{(0)} + x_2'u_{2,2}^{(0)} + x_2'^2u_{2,22}^{(0)} \end{aligned} \quad (16)$$

where $c' = 2[(\lambda' + \mu')/(\lambda' + 2\mu')]^{1/2}$. Expanding the determinant (19) results in a fourth-order polynomial in γ . In the following we will call Eq. (19) the dispersion relation of the Tiersten model including flexural stiffness.

Tiersten simplifies this dispersion relation further by neglecting the flexural stiffness D' and the surface couples $h'T_{2a}^{(0)}$ in Eqs. (14) and (15) while still retaining the vertical inertia and the extensional stiffness and inertia. Moreover, in the plate displacement continuity conditions (17) he neglects all $O(h')$ and $O(h'^2)$ terms keeping only the lowest order terms so Equation (17) reduces to $u_j = u_j^{(0)}$. In this respect the boundary conditions (14), (15) reduce to

$$\tau_{2b}(0) = -2\mu'h'\left[u_{b,aa} + \frac{(1+v')}{(1-v')} u_{a,ab}\right] + 2\rho'h'\ddot{u}_b \quad (20)$$

$$\tau_{22}(0) = 2\rho'h'\ddot{u}_2 \quad (21)$$

where $\tau_{2j}(0)$ are given by (2). Equations (20) and (21) are Tiersten's approximate boundary conditions which replace the vanishing of the traction in the Rayleigh problem. By this we have removed the layer and applied nonhomogeneous BCs at the surface $x_2 = 0$. Equations (2) and (4) inserted into (20) and (21) and the condition for a nontrivial solution gives Tiersten's dispersion relation as

$$\begin{vmatrix} 2\alpha + r_\mu(c'^2 - r_v^2 q^2) & q^2 - 2 + r_\mu(r_v^2 q^2 - c'^2) \\ 2 - q^2 - r_\mu r_v^2 q^2 \alpha \gamma & r_\mu r_v^2 q^2 \gamma - 2\beta \end{vmatrix} = 0. \quad (22)$$

Expansion of (22) gives

$$A_0 + A_1\gamma + A_2\gamma^2 = 0 \quad (23)$$

where

$$A_0 = (2 - q^2)^2 - 4\alpha\beta \quad (24)$$

$$A_1 = r_\mu q^2[(r_v^2 q^2 - c'^2)\beta + r_v^2 q^2 \alpha] \quad (25)$$

$$A_2 = r_\mu^2 r_v^2 q^2 (c'^2 - r_v^2 q^2)(1 - \alpha\beta). \quad (26)$$

It is noted that the equation $A_0 = 0$ is the well-known Rayleigh dispersion equation for Rayleigh waves on a free surface.

Equation (23) is a quadratic in the dimensionless wave number γ and the coefficients are functions of the dimensionless phase velocity q . Hence, for a given real q , any real positive root γ gives a point on the dispersion curves. Complex and real negative values of γ are inadmissible as points on the dispersion curves since h' is positive and we have restricted ourselves to real positive wavelengths. Equation (23) will be compared numerically with the dispersion relation obtained through the use of the $O(h)$ boundary conditions for the layer which will be derived in the next section.

3 The $O(h)$ Boundary Conditions

In this section we will use a different approach in deriving an approximation to the dispersion relation for Rayleigh-type waves on a layered half-space. In Bövik and Olsson (1992), boundary conditions for scattering of SH waves from a thin elastic layer were derived by using a perturbation technique in which the field variables were expanded in the layer thickness in the normal direction. An extension to cover the full three-dimensional case, and to other material combinations was given in Bövik (1994). The advantage of this method is that it takes into account all terms which are of the first order in the layer thickness.

The boundary conditions at the two surfaces $x_2 = 0$ and $x_2 = -2h'$ in Fig. 1 can be written

$$\begin{vmatrix} [2\alpha + \gamma r_\mu(c'^2 - r_v^2 q^2) - \gamma\kappa'(2 - q^2)] & -[2 - q^2 - \gamma r_\mu\beta(r_v^2 q^2 - c'^2) - \gamma\kappa'2\beta] \\ [2 - q^2 - \gamma\alpha r_\mu r_v^2 q^2 + 2\alpha\gamma] & -[2\beta - \gamma r_\mu r_v^2 q^2 + (2 - q^2)\gamma] \end{vmatrix} = 0 \quad (37)$$

$$u'_j|_0 = u_j|_0 \quad (27)$$

$$\tau'_{2j}|_0 = \tau_{2j}|_0 \quad (28)$$

$$\tau'_{2j}|_{-2h'} = 0 \quad (29)$$

where τ'_{2j} and u'_j are the traction field and the displacement field inside the layer, respectively. If we subtract Eq. (29) from (28) and expand the field at the surface $x_2 = -2h'$ around $x_2 = 0$ inside the layer in the normal direction we find

$$\begin{aligned} \tau_{2j}|_0 &= \tau'_{2j}|_0 - \tau'_{2j}|_{-2h'} = \tau'_{2j}|_0 \\ &- \{\tau'_{2j}|_0 + \tau'_{2j,2}|_0(-2h' - 0) \\ &+ \frac{1}{2}\tau'_{2j,22}|_0(-2h' - 0)^2 + O(h'^3)\} \\ &= 2h'\tau'_{2j,2}|_0 - 2h'^2\tau'_{2j,22}|_0 + O(h'^3). \quad (30) \end{aligned}$$

To first order in h' we find

$$\tau_{2j}|_0 = 2h'\tau'_{2j,2}|_0 + O(h'^2). \quad (31)$$

Combining Eqs. (1) and (2) we can separate the equations of motion into one tangential part and one normal part as

$$\tau'_{2a,2} = \rho' \ddot{u}'_a - \tau'_{ba,b}$$

$$\tau'_{22,2} = \rho' \ddot{u}'_2 - \tau'_{2a,a}. \quad (32)$$

By summing the two equations in (32) we can write the normal derivative of the traction in terms of the tangential derivatives as

$$\tau'_{2j,2} = \rho' \ddot{u}'_j - \delta_{bj} \tau'_{ab,a} - \delta_{2j} \tau'_{2a,a}. \quad (33)$$

From the expression for the traction vector τ'_{2j} we can write the normal derivative of the displacement components in terms of tangential derivatives as

$$u'_{j,2} = \delta_{aj} \left[\frac{1}{\mu'} \tau'_{2a} - u'_{2,a} \right] + \frac{1}{\lambda' + 2\mu'} \delta_{2j} [\tau'_{22} - \lambda' u'_{b,b}]. \quad (34)$$

Combining Eqs. (33) and (34) and using the boundary conditions (27) and (28) to replace the primed fields in the tangential derivatives by the fields in the substrate (see Bövik and Olsson (1992) for more information), the approximate boundary condition (31) can be written (where we omit the $O(h'^2)$ -terms) as

$$\begin{aligned} \tau_{2b} &= -2h'\mu' \left[u_{b,aa} + \frac{(1 + v')}{(1 - v')} u_{a,ab} \right] \\ &\quad - 2h'\kappa' \tau_{22,b} + 2h'\rho' \ddot{u}_b \quad (35) \end{aligned}$$

$$\tau_{22} = -2h'[\tau_{2a,a} - \rho' \ddot{u}_2] \quad (36)$$

where $\kappa' = \lambda' / (\lambda' + 2\mu') = v' / (1 - v')$.

These equations (35) and (36) should now be compared with Tiersten's approximate boundary conditions (20) and (21). We note that there are some terms missing in (20) and (21) which are of first order in magnitude. The advantage of the perturbation method is that it starts with the general three-dimensional equation of motion and derives the boundary conditions in a rational manner keeping all terms linear in h' . For the Rayleigh-type waves, i.e., Eq. (4) and the expressions for the traction components in the substrate (2), the boundary conditions (35) and (36) result in a dispersion relation similar to (22) as

Expanding the determinant we obtain a quadratic polynomial in γ as

$$P_2\gamma^2 + A_1\gamma + A_0 = 0 \quad (38)$$

where the coefficients A_0 and A_1 are the same as in Tiersten's dispersion relation, i.e., (24) and (25), and P_2 is given by

$$P_2 = A_2 + r_\mu(2\alpha\beta - 2 + q^2)(c'^2 + r_v^2 q^2(\kappa' - 1)) \quad (39)$$

where A_2 is given by (26).

4 Love Waves

It is well known that for $c'_s < c < c_s$, there exist guided SH-waves, known as Love waves which can propagate along a layer overlaying a semi-infinite half-space. In our coordinate system the only nonzero component of the displacement field is u_3 which is independent of x_3 . For a layer with thickness $2h'$ the exact dispersion relation is given by

$$\sqrt{q^2 r_v^2 - 1} \tan(\gamma \sqrt{q^2 r_v^2 - 1}) - \frac{1}{r_\mu} \sqrt{1 - q^2} = 0. \quad (51)$$

For the approximate models it is straightforward to show that both the Tiersten model, i.e., equations (20), (21) and the $O(h)$ -boundary conditions, i.e., Eqs. (35), (36) reduce to iden-

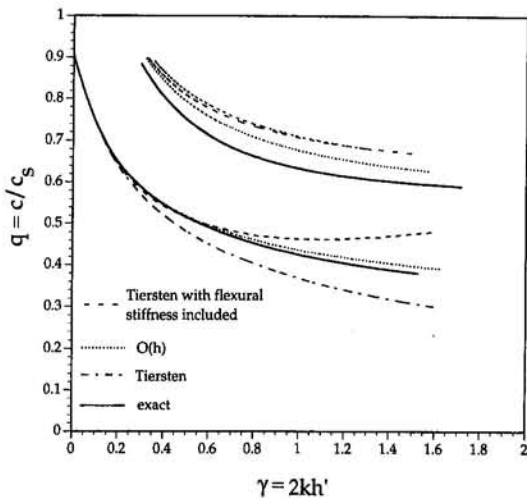


Fig. 2 Roots of dispersion relations for Rayleigh-type waves in a gold layer over a fused silica substrate

tical boundary conditions, hence the only nonvanishing component of the BCs for both models is

$$\tau_{23} = -2h' \mu' u_{3,11} + 2h' \rho' \ddot{u}_3. \quad (52)$$

With the ansatz for u_3 like

$$u_3 = Pe^{-\beta kx_2} e^{ik(x_1 - ct)}, \quad (53)$$

we obtain the approximate dispersion relation as

$$\gamma(q^2 r_v^2 - 1) - \frac{1}{r_\mu} \sqrt{1 - q^2} = 0 \quad (54)$$

which to first order agree with the exact dispersion relation.

In the paper by Wickham (1992) a comparison was made for Love waves by comparing the dispersion relations (Fig. 4, p. 208) for the Tiersten model (curve *d*), O(*h*)-BCs (curve *c*) and the so-called PIE (Polarized Integral Equation) technique (curve *b*). The material configuration was a copper layer over a steel or glass substrate. There obviously are some errors in his Fig. 4. As have just been shown both the Tiersten model and the O(*h*)-BCs yield identical dispersion relations for Love waves in layers over a semi-infinite half-space, hence the curves *c* and *d* should be identical.

5 Numerical Results

In this section we numerically compare the approximate models against the exact solution for some different material configurations. We have used the same materials as those used in Tiersten (1969). In Fig. 2, the roots of the dispersion relation for Rayleigh-type waves (P-SV waves) are plotted for the Tiersten model including flexural stiffness, the Tiersten model, and the O(*h*) BCs against the exact solution. The first branch is the fundamental Rayleigh-type branch and the second is the higher M_2 -mode (or Sezawa-branch, see Sezawa and Kanai (1935)). The materials are a gold layer on a fused silica substrate, hence the material parameters are $\mu' = 2.85 \cdot 10^{-10} \text{ N/m}^2$, $\lambda' = 15 \cdot 10^{-10} \text{ N/m}^2$, $c_s' = 1200 \text{ m/s}$, $c_p' = 3240 \text{ m/s}$, $\mu = 3.12 \cdot 10^{-10} \text{ N/m}^2$, $\lambda = 1.61 \cdot 10^{-10} \text{ N/m}^2$, $c_s = 3764 \text{ m/s}$, $c_p = 5968 \text{ m/s}$. It is seen that the O(*h*)-boundary conditions yield more accurate results than both the model by Tiersten and the Tiersten model including flexural stiffness.

In Fig. 3, where the layer is faster than the half-space, we likewise find good agreement with the O(*h*) BCs and the exact solution. The Tiersten model gives qualitative poor results. The dispersion curve consists of two roots which becomes complex at the maximum point. For the Tiersten's model including flex-

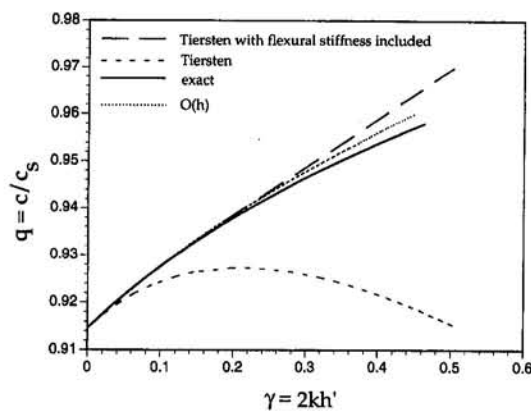


Fig. 3 Roots of dispersion relations for Rayleigh-type waves in an aluminium layer over a heavy silica substrate

ural stiffness, qualitative correct results obtained though the O(*h*) BCs yield better results. The materials are an aluminium layer over a heavy silica (flint glass) substrate with material parameters, $\mu' = 2.5 \cdot 10^{-10} \text{ N/m}^2$, $\lambda' = 6.1 \cdot 10^{-10} \text{ N/m}^2$, $c_s' = 3040 \text{ m/s}$, $c_p' = 6420 \text{ m/s}$, $\mu = 2.18 \cdot 10^{-10} \text{ N/m}^2$, $\lambda = 1.77 \cdot 10^{-10} \text{ N/m}^2$, $c_s = 2380 \text{ m/s}$, $c_p = 3980 \text{ m/s}$.

In Figs. 4, 5, and 6 we compare the roots of the exact and approximate dispersion relations (i.e., both O(*h*)- and the Tiersten model) for Love waves in a gold and copper layer over a fused silica substrate and a copper layer over a stainless steel substrate. As is seen the approximate dispersion relation gives quite good results. Love waves only exist when the layer loads the substrate, hence no Love wave exists for an aluminium layer over a heavy silica substrate.

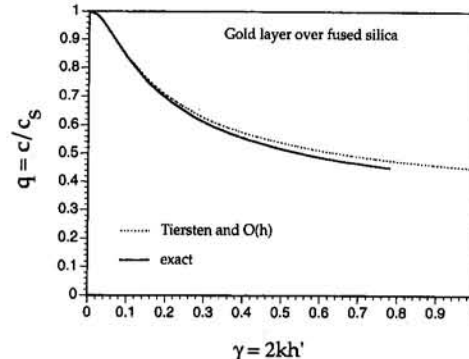


Fig. 4 Roots of dispersion relations for Love waves in a gold layer over a fused silica substrate

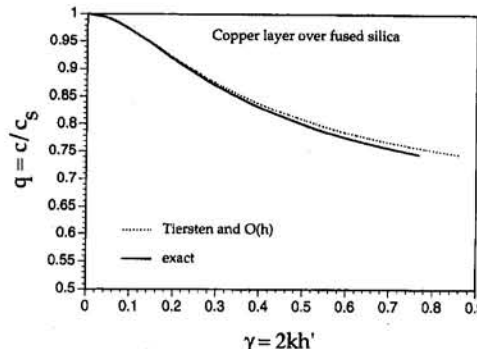


Fig. 5 Roots of dispersion relations for Love waves in a copper layer over a fused silica substrate

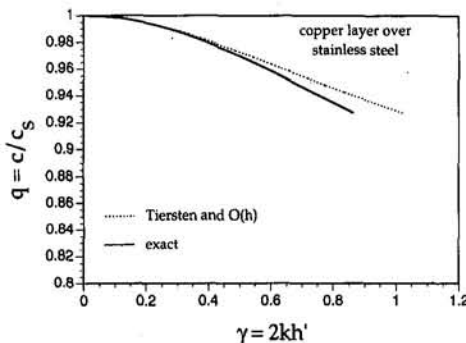


Fig. 6 Roots of dispersion relations for Love waves in a copper layer over a stainless steel substrate

7 Concluding Remarks

In this paper we have compared two different models of approximating thin layers in elastic and acoustic wave propagation, the model by Tiersten and the $O(h)$ BCs. Both models actually replace the layer by a mathematical surface at the substrate and specify a nonzero expression of the traction as an equivalent boundary condition. The advantage of this is that it clearly simplifies the mathematical treatment of wave propagation problems in thin layers. The $O(h)$ BCs can be used for almost arbitrarily curved layers (Bövik, 1994), and even for anisotropic layers (Bövik and Olsson, 1991) whereas the model by Tiersten only works for planar layers.

Both models yield accurate results when the layer is slower than the substrate, though the $O(h)$ BCs give better results. But for layers that are faster than the substrate the Tiersten model gives results that are not even qualitatively comparable to the exact solution.

In conclusion it can be stated that since the $O(h)$ BCs are far more general in nature (they work with other material configurations and for curved layers as well) than the BCs by Tiersten and give better results, they should be the more versatile and useful ones.

Acknowledgment

The author would like to acknowledge the referees for their comments which made it possible to correct an error in the computer program, which in turn totally changed the appearance of Fig. 3.

References

Achenbach, J. D., and Keshava, S. P., 1967, "Free Waves in a Plate Supported by a Semi-Infinite Continuum," *ASME JOURNAL OF APPLIED MECHANICS*, Vol. 34, pp. 397-404.

Boström, A., Bövik, P., and Olsson, P., 1992, "A Comparison of Exact First Order and Spring Boundary Conditions for Scattering by Thin Layers," *Journal of Nondestructive Evaluation*, Vol. 11, No. 3-4, pp. 175-184.

Bromwich, T. J. I., 1899, "On the Influence of Gravity on Elastic Waves and in Particular, on the Vibrations on an Elastic Globe," *Proceedings of the London Mathematical Society*, Vol. 30, pp. 98-120.

Bövik, P., 1994, "On the Modelling of Thin Interface Layers in Elastic and Acoustic Scattering Problems," *Quarterly Journal of Mechanics and Applied Mathematics*, Vol. 47, No. 1, pp. 16-42.

Bövik, P., and Olsson, P., 1991, "Diffraction of Horizontally Polarised Shear Waves by a Crack Extending From a Thin Anisotropic Layer," Division of Mechanics, Report CTH 1991:11, Chalmers University of Technology, S-412 96 Göteborg, Sweden.

Bövik, P., and Olsson, P., 1992, "Effective Boundary Conditions for the Scattering of Two-Dimensional SH Waves From a Curved Thin Elastic Layer," *Proceedings of the Royal Society of London*, Vol. A439, pp. 257-269.

Love, A. E. H., 1911, *Some Problems of Geodynamics*, Cambridge University Press, Cambridge, U.K.

Olsson, P., Datta, S. K., and Boström, A., 1990, "Elastodynamic Scattering From Inclusions Surrounded by Thin Interface Layers," *ASME JOURNAL OF APPLIED MECHANICS*, Vol. 57, pp. 672-676.

Parker, D. F., and Maugin, G. A., eds., 1988, *Recent Developments in Surface Acoustic Waves: Proceedings of the European Mechanics Colloquium 226*, University of Nottingham, U.K., Sept. 2-5. Springer-Verlag, New York.

Sezawa, K., and Kanai, K., 1935, "The M_2 Seismic Waves," *Bulletin of the Earthquake Institute of Tokyo*, Vol. 13, pp. 740-749.

Tiersten, H. F., 1969, "Elastic Surface Waves Guided by Thin Films," *Journal of Applied Physics*, Vol. 40, No. 2, pp. 770-789.

Wickham, G., 1992, "A Polarization Theory for the Scattering of Sound at Imperfect Interfaces," *Journal of Nondestructive Evaluation*, Vol. 11, No. 3-4, pp. 199-210.

Wickham, G., and Boström, A., 1991, "On the Boundary Conditions for Ultrasonic Transmission by Partially Closed Cracks," *Journal of Nondestructive Evaluation*, Vol. 10, No. 4, pp. 139-149.

Rough Balanced Collisions

J. A. Batlle

Department of Mechanical Engineering,
Polytechnical University of Catalunya,
Av. Diagonal, 647,
08028 Barcelona, Spain

In multibody systems, balanced collisions—in which the sliding velocity would not change if friction was negligible—are a generalization of central collisions. For them Newton's and Poisson's rules are energetically consistent, but even though they are applied an “all linear solution” does not exist if the sliding varies its direction and does not stop. The properties of these collisions are reviewed, the hodographs of the sliding velocity are calculated and used to develop a systematic method to integrate the equations of motion that relies on a single integration from which the remaining unknowns are calculated by means of algebraic expressions.

1 Introduction

For smooth single-point collisions in multibody systems with perfect constraints, the percussive rigid-body dynamics leads always to an “all linear” solution relating the velocities at the end of the collision to the initial ones. This is not so if friction is considered at the collision point because, in the general case, the friction laws for forces cannot be extended to the friction impulses calculated over the collision interval, and Newton's and Poisson's rules (with coefficient of restitution e , $0 \leq e \leq 1$, independent from initial conditions) are, in general, energetically inconsistent (Batlle, 1993; Smith and Liu, 1992; Smith, 1991; Stronge, 1990, 1991a, 1991b). Consequently the equations of motion for rough collisions must be integrated over the collision interval, (Routh, 1905; Beghin, 1951; Batlle and Condomines, 1991). Beghin developed a geometry-based method to solve three-dimensional rough collisions. Batlle and Condomines (1991) extended Routh's and Beghin's approach to multibody systems by means of the Lagrangian formulation.

Balanced collisions are a particular kind of single-point collisions in which there is no inertial coupling between the normal and tangential directions—and consequently the sliding velocity would not change if friction was negligible. They have been referred to for nonplanar collisions in multibody systems by several authors (Smith and Liu, 1992; Batlle, 1993) who have shown the energetical consistency of Newton's and Poisson's rules for them. However, this energetical consistency does not guarantee an “all linear” solution in all cases. Such a solution does not exist when there is sliding that varies its direction and does not stop.

In this article the properties of the balanced collisions are reviewed and a method for integrating their equations of motion when there is not an “all linear” solution is developed. This method requires a single analytical or numerical integration that relates the normal velocity to one of the components of the sliding velocity at the collision point. From the result of this integration, the remaining unknowns are calculated by means of algebraic expressions. Two illustrative examples are presented.

2 The Lagrangian Formulation of Rough Balanced Collisions

If the n -degrees-of-freedom of the system are described by means of the generalized velocities $\{u\}^T = \{u_1, u_2, \dots, u_n\}$,

Contributed by the Applied Mechanics Division of THE AMERICAN SOCIETY OF MECHANICAL ENGINEERS for publication in the ASME JOURNAL OF APPLIED MECHANICS.

Discussion on this paper should be addressed to the Technical Editor, Professor Lewis T. Wheeler, Department of Mechanical Engineering, University of Houston, Houston, TX 77204-4792, and will be accepted until four months after final publication of the paper itself in the ASME JOURNAL OF APPLIED MECHANICS.

Manuscript received by the ASME Applied Mechanics Division, Jan. 11, 1994; final revision, Dec. 2, 1994. Associate Technical Editor: E. J. Haug, Jr.

the differential Lagrangian equations of motion can be written in matrix form as

$$[M]\{du\} = \{d\Pi_n\} + \{d\Pi_t\} \equiv \{d\Pi\}, \quad (1)$$

where $[M]$ is the $n \times n$ inertia matrix of the system for the impact configuration and $\{d\Pi_n\}$ and $\{d\Pi_t\}$ are the generalized normal and tangential differential impulses, respectively. The n -vector $\{d\Pi\}$ is related to differential normal and tangential impulses dP_n and dP_t by means of the equation

$$\{d\Pi\} = [k] \begin{Bmatrix} dP_n \\ dP_t \end{Bmatrix} \equiv [k]\{dP\}, \quad (2)$$

where $[k]$ is a $n \times 3$ matrix of coefficients relating the normal velocity v_n and the sliding velocity \mathbf{v}_t at the collision point to the generalized velocities

$$\{v\} = \begin{Bmatrix} v_n \\ \mathbf{v}_t \end{Bmatrix} = [\{\alpha\} \{\beta\}]^T \{u\} = [k]^T \{u\}. \quad (3)$$

From (1), (2), and (3),

$$\{du\} = [M]^{-1}[k]\{dP\}, \quad (4)$$

$$\{dv\} = [k]^T [M]^{-1}[k]\{dP\} \equiv [N]\{dP\}, \quad (5)$$

where $[N]$ is a symmetrical positive definite matrix that is conveniently written in the form

$$[N] = \begin{bmatrix} \alpha^T M^{-1} \alpha & \alpha^T M^{-1} \beta \\ \beta^T M^{-1} \alpha & \beta^T M^{-1} \beta \end{bmatrix} = \begin{bmatrix} a & \mathbf{h}^T \\ \mathbf{h} & [b] \end{bmatrix}. \quad (6)$$

It coincides with matrix $[N]$ used by Smith and Liu (1992).

Condition for Balanced Collisions. The lack of inertial coupling between the normal and tangential directions requires $\mathbf{h} = 0$, and this condition reduces (5) to

$$dv_n = adP_n; \quad \text{or} \quad \Delta v_n = a\Delta P_n \quad (7)$$

$$d\mathbf{v}_t = [b]dP_t; \quad \text{or} \quad \Delta \mathbf{v}_t = [b]\Delta P_t \quad (8)$$

If Coulomb's friction and infinite tangential stiffness are assumed at the collision point, when sliding occurs dP_t^s can be expressed in terms of dP_n , the friction coefficient μ and the unit vector $\boldsymbol{\sigma} = \mathbf{v}_t / |\mathbf{v}_t|$ along the sliding direction, $dP_t^s = -\mu \boldsymbol{\sigma} dP_n$. Substitution into (8) and (4) leads to

$$d\mathbf{v}_t = -\mu [b]\boldsymbol{\sigma} dP_n \quad (9)$$

$$\{du\} = [M]^{-1}[k] \begin{Bmatrix} 1 \\ -\mu \boldsymbol{\sigma} \end{Bmatrix} dP_n \equiv \{C^s\} dP_n \quad (10)$$

when there is no sliding, according to (8), $dP_t^s = 0$, and substitution on (4) leads to

$$\{du\} = [M]^{-1}[k] \begin{cases} 1 \\ 0 \end{cases} dP_n \equiv \{C^{ns}\} dP_n \quad (11)$$

Equations (7)–(9) lead to interesting properties.

Autonomous Evolution of v_n . Usually the evolution of v_n is linked to that of v_t by means of the term $\mathbf{h}^T d\mathbf{P}_t$ of (5) in which $d\mathbf{P}_t$ depends upon v_t through the friction law considered. However, for balanced collisions its evolution is autonomous as shown by (7). The relationship $dv_n/dP_n = a$ is independent of the sliding or nonsliding conditions and keeps a constant value over the collision interval. Consequently balanced collisions verify the sufficiency condition for energetical consistency of Newton's and Poisson's rules (Battile, 1993).

The Origin of the Hodograph Plane of v_t is a Sink Point. According to (9), the projection of dv_t/dP_n (9) over σ is opposite to σ ,

$$\sigma^T d\mathbf{v}_t = -\mu \sigma^T [b] \sigma < 0, \quad (12)$$

because $[b]$, defined in (6), is positive definite.

Consequently the hodographs of v_t are centripetal in all their points and the origin $\mathbf{v}_t = 0$ of the hodograph plane is a *sink* point. Hence once the sliding has stopped it does not restart.

The Tangential Impulse \mathbf{P}_t . When there is no sliding, according to (8), $d\mathbf{P}_t^{ns} = 0$ and consequently when sliding stops the normal force at the collision point vanishes to zero. So the tangential impulse comes only from tangential force during the sliding, and according to (8)

$$\mathbf{P}_t = [b]^{-1} \Delta \mathbf{v}_t. \quad (13)$$

In cases where the sliding stops (13) leads to $\mathbf{P}_t = -[b]^{-1} \mathbf{v}_t^{(0)}$, because $\Delta \mathbf{v}_t = -\mathbf{v}_t^{(0)}$, being $\mathbf{v}_t^{(0)}$ the initial sliding velocity.

Energy Dissipation. The energy dissipated by the normal force is readily calculated from $dW_n = v_n dP_n = a^{-1} v_n dv_n$, where $v_n = -ev_a$ if Newton's rule is applied. Integration over the collision interval leads to

$$W_n = \frac{1}{2} a^{-1} (v_n^2 - v_n^{(0)2}) = \frac{-1}{2} a^{-1} v_a^2 (1 - e^2). \quad (14)$$

The energy dissipated by friction can be analytically calculated by integrating $dW_f = \mathbf{v}_t d\mathbf{P}_t = \mathbf{v}_t [b]^{-1} d\mathbf{v}_t$ over the collision interval, which leads to

$$W_f = \Delta T_t = T_t - T_t^{(0)}, \quad (15)$$

where

$$T_t = \frac{1}{2} \mathbf{v}_t^T [b]^{-1} \mathbf{v}_t. \quad (16)$$

According to (16), T_t could be given the meaning of "kinetic energy associated with sliding." Equation (15) equals the reduction of this kinetic energy to the energy dissipated by friction.

3 The Hodographs Sliding Velocity

The set of hodographs for the sliding velocity \mathbf{v}_t give a detailed picture of the evolution of \mathbf{v}_t for the collision configuration considered and arbitrary initial conditions.

If the eigendirections of matrix $[b]$ are taken as the axes 1 and 2 for \mathbf{v}_t on the tangential plane, (8) leads to

$$\frac{dv_{t2}}{dv_{t1}} = \frac{b_2}{b_1} \frac{v_{t2}}{v_{t1}}, \quad (17)$$

where b_1 and b_2 are the eigenvalues of $[b]$. The hodograph

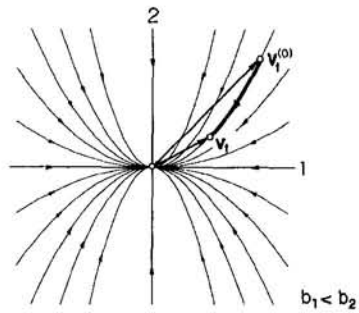


Fig. 1 Hodograph plane for balanced collisions

equation is obtained by integration of (17) from an initial sliding velocity $\mathbf{v}_t^{(0)}$,

$$v_{t2} = v_{t2}^{(0)} (v_{t1}/v_{t1}^{(0)})^{b_2/b_1}. \quad (18)$$

Figure 1 depicts the hodograph plane where $b_2 > b_1$ (axis 1 is associated with the smaller eigenvalue of $[b]$). Axes 1 and 2—which are the eigendirections of $[b]$ —are the only asymptotes in the hodograph plane. From $\mathbf{v}_t^{(0)}$ the sliding velocity evolves towards the origin along the hodograph containing the initial sliding velocity $\mathbf{v}_t^{(0)}$, until the end of the collision.

The end point $\mathbf{v}_t^{(e)}$ depends upon the value of the initial normal approaching velocity, $v_a = -v_a^{(0)}$. For increasing values of v_a the end point approaches the origin, reaching it for a certain threshold value v_a^{\square} . For greater values of v_a^{\square} a phase without sliding follows the initial sliding phase until the collision is over.

For $b_1 = b_2$ the hodographs degenerate to straight lines through the origin, (Fig. 2).

4 "All Linear" Solution

Newton's and Poisson's rules (with coefficient of restitution e , $0 \leq e \leq 1$, independent from initial conditions) are energetically consistent for balanced collisions. If any of them is used, an "all linear" solution exists provided that an explicit expression for \mathbf{P}_t can be found.

This happens if the sliding keeps a constant direction and does not stop (or stops just when the collision ends), as in this case $\mathbf{P}_t = -\mu \sigma \mathbf{P}_n$, or if the sliding stops during the collision, regardless of its direction being constant or not, as in this case the constraint condition $\mathbf{v}_t = 0$ leads to $\mathbf{P}_t = -[b]^{-1} \mathbf{v}_t^{(0)}$, according to (13).

If Newton's rule is used,

$$\begin{aligned} \Delta v_n &= +(1 + e)v_a = -(1 + e)v_a^{(0)} \\ &= -(1 + e)\{\alpha\}^T \{u^{(0)}\}, \end{aligned} \quad (19)$$

where the value "e" is the restitution coefficient relating the

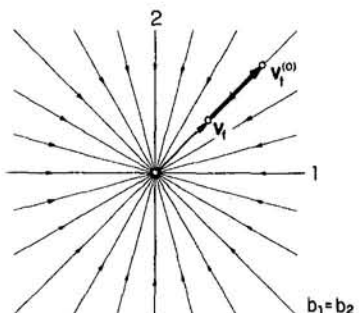


Fig. 2 Hodograph plane for balanced collisions with $b_1 = b_2$

normal separating velocity to the normal approaching one, at the collision point, $v_s = ev_a$.

In the case of constant σ (the hodograph is one of the asymptotes), as C^s in (10) is constant this equation can be integrated over the collision interval leading to

$$\{\Delta u\} = \{C^s\} P_n, \quad (20)$$

but from (7),

$$P_n = a^{-1} \Delta v_n. \quad (21)$$

Substitution of (18) and (20) into (19) leads to

$$\{\Delta u\} = [P]\{u^{(0)}\}, \quad \text{or} \quad \{u^{(e)}\} = ([I] + [P])\{u^{(0)}\}, \quad (22)$$

where $[I]$ is the unit matrix of dimension n and

$$[P] = -(1 + e)a^{-1}\{C^s\}\{\alpha\}^T. \quad (23)$$

If the sliding stops during the collision, the substitution of (13) with $\Delta v_t = -\mathbf{v}_t^{(0)} = -[\beta]^T\{u^{(0)}\}$, (19) and (21) into (4) integrated over the collision interval leads to

$$\{\Delta u\} = [P']\{u^{(0)}\}; \quad \text{or} \quad \{u^{(e)}\} = ([I] + [P'])\{u^{(0)}\}, \quad (24)$$

with

$$\begin{aligned} [P'] = -[M]^{-1}(a^{-1}(1 + e)\{\alpha\}\{\alpha\}^T \\ + [\beta][b]^{-1}[\beta]^T). \end{aligned} \quad (25)$$

5 Non "All Linear" Solution

If sliding does not stop and its direction varies there is not an "all linear" solution because, even if applying Newton's (or Poisson's) rule, the two equations concerning \mathbf{P}_t would be lacking. In this case the equations of motion must be (analytically or numerically) integrated over the collision interval.

If the hodograph equation is used, this integration needs to be extended only to the calculation of $v_n(v_{t1})$.

From (8)

$$dv_{t1} = -\mu b_1 a^{-1} \frac{v_{t1}}{\sqrt{v_{t1}^2 + v_{t2}^2}} dv_n, \quad (26)$$

and by substitution of v_{t2} from (18)

$$-\frac{a}{\mu b_1} \sqrt{1 + v_{t2}^{(0)2} v_{t1}^{2[\nu-1]}} dv'_{t1} = dv_n, \quad (27)$$

where $\nu \equiv b_2/b_1 > 1$ and adimensional velocities $v' \equiv v/v_{t1}^{(0)}$ are used.

Integration of (27) leads to

$$-\frac{a}{\mu b_1} \int_1^{v'_{t1}^{(e)}} \sqrt{1 + v_{t2}^{(0)2} v_{t1}^{2[\nu-1]}} dv'_{t1} = \Delta v_n, \quad (28)$$

with $0 \leq v'_{t1}^{(e)} \leq 1$.

For practical purposes this result is better expressed by means of the adimensional velocities $\tilde{v}_n \equiv v_n/v_a$ and $\tilde{v}'_{t1} \equiv v'_{t1}^{(0)}/v_a$ in spite of working out the integral by means of adimensional velocities v' ,

$$-\frac{a}{\mu b_1} \tilde{v}'_{t1} \int_1^{v'_{t1}^{(e)}} \sqrt{1 + v_{t2}^{(0)2} v_{t1}^{2[\nu-1]}} dv'_{t1} = \Delta \tilde{v}_n. \quad (29)$$

The integration over v'_{t1} converges better because axis 1 corresponds to the smallest eigenvalue of $[b]$.

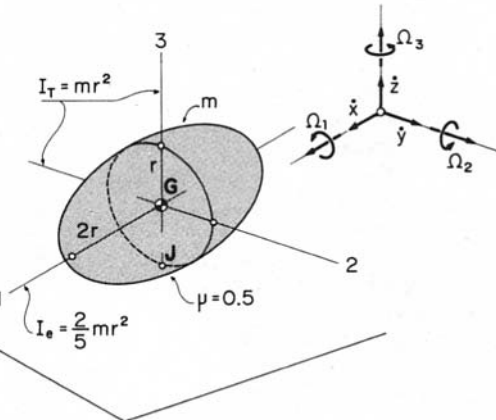


Fig. 3 Diametral collision of an homogeneous ellipsoid of revolution. Notation.

If Newton's rule is applied, the end value $v'_{t1}^{(e)}$ corresponds to

$$\Delta \tilde{v}_n = 1 + e. \quad (30)$$

From (29) and (30) the threshold value v_a^\square above which sliding stops during the collision is given by

$$v_a^\square = \frac{a}{\mu b_1 (1 + e)} v_{t1}^{(0)} \int_0^1 \sqrt{1 + v_{t2}^{(0)2} v_{t1}^{2[\nu-1]}} dv'_{t1}. \quad (31)$$

Once the end value $v'_{t1}^{(e)} = v_{t1}^{(0)} v_{t1}^{(0)}$ has been found by means of (28) or (29), v_{t2} is obtained from the hodograph equation, (18), the impulse $\{P\}$ is obtained from (7)-(8),

$$\begin{aligned} P_n = a^{-1} \Delta v_n &= a^{-1} (1 + e) v_a \\ \mathbf{P}_t = [b]^{-1} \Delta \mathbf{v}_t & \end{aligned} \quad (32)$$

and substitution into (4), integrated over the collision interval, leads to the increments of the generalized velocities:

$$\begin{aligned} \{\Delta u\} &= (1 + e) a^{-1} v_a [M]^{-1} \{\alpha\} \\ &+ [M]^{-1} [\beta] [b]^{-1} \{\Delta \mathbf{v}_t\}. \end{aligned} \quad (33)$$

6 Application Example 1: Balanced Collision of an Homogeneous Ellipsoid of Revolution With a Fixed Surface

The bounding of an homogeneous ellipsoid of revolution with a rough fixed surface is a balanced one provided that the collision point belongs to the equator, as it is assumed in this example, or coincides with one of the poles, because in such cases \mathbf{P}_n goes through the mass center, and consequently \mathbf{v}_t is unchanged if friction is neglected. The sliding direction will change if $\mathbf{v}_t^{(0)}$ is not directed along one of the ellipsoid axes, and in this case there is not an "all linear" solution if sliding does not stop.

Let's assume the case depicted in Fig. 3 with friction coefficient $\mu = 0.5$. The degrees-of-freedom $\{u\}$ and initial velocities $\{u^{(0)}\}$ are described by

$$\{u\} = \begin{Bmatrix} \dot{x} \\ \dot{y} \\ \dot{z} \\ \Omega_1 \\ \Omega_2 \\ \Omega_3 \end{Bmatrix}; \quad \{u^{(0)}\} = \begin{Bmatrix} (5/\sqrt{2})v_a \\ (5/\sqrt{2})v_a \\ -v_a \\ 0 \\ 0 \\ 0 \end{Bmatrix}. \quad (34)$$

Table 1 End sliding velocity $\tilde{v}_t^{(e)}$ and $\tilde{v}_t^{(e)} - v_t^{(0)}$ for different values of e

e	$\tilde{v}_{t1}^{(e)}$	$\tilde{v}_{t2}^{(e)}$	$\Delta\tilde{v}_{t1}$	$\Delta\tilde{v}_{t2}$
0	1.000	0.652	-0.768	-1.116
0.2	0.829	0.470	-0.939	-1.298
0.4	0.652	0.308	-1.116	-1.460
0.6	0.467	0.172	-1.300	-1.595
0.8	0.276	0.069	-1.491	-1.699
1.0	0.088	0.008	-1.688	-1.760

The basic matrices, vectors, and parameters are

$$[M] = m \begin{bmatrix} 1 & & & & \\ & 1 & & & \\ & & 1 & & \\ & & & (2/5)r^2 & \\ & & & & r^2 \\ & & & & r^2 \end{bmatrix};$$

$$\{\alpha\} = \begin{bmatrix} 0 \\ 0 \\ 1 \\ 0 \\ 0 \\ 0 \end{bmatrix}; \quad [\beta] = \begin{bmatrix} 1 & 0 \\ 0 & 1 \\ 0 & 0 \\ 0 & r \\ -r & 0 \\ 0 & 0 \end{bmatrix}, \quad (35)$$

$$a = \frac{1}{m}; \quad [b] = \frac{1}{m} \begin{bmatrix} 2 & 0 \\ 0 & \frac{7}{2} \end{bmatrix}; \quad \nu = \frac{7}{4}. \quad (36)$$

According to (36), axes 1 and 2 are the eigenvectors of $[b]$ and axis 1 is associated with the smaller eigenvalue as assumed in the presented integration method.

The hodograph followed by $\tilde{v}_t = v_t/v_a$ is defined by

$$\tilde{v}_{t2} = \left(\frac{\sqrt{2}}{5}\right)^{3/4} \tilde{v}_{t1}^{7/4}. \quad (37)$$

The integration of (29) with $\Delta\tilde{v}_n = 1 + e$ leads to the end sliding velocities $\tilde{v}_t^{(e)}$, shown in Table 1 and depicted in Fig. 4 for several values of e . The incremental values $\Delta\tilde{v}_t$ in Table 1 are used to calculate the incremental values of the generalized velocities, according to (33),

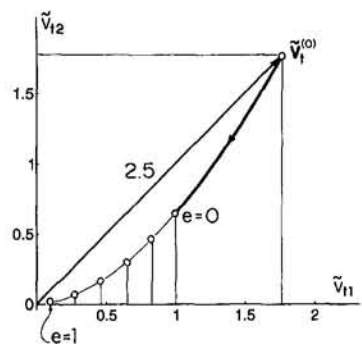


Fig. 4 Evolution of the normalized sliding velocity $\tilde{v}_t = v_t/v_a$

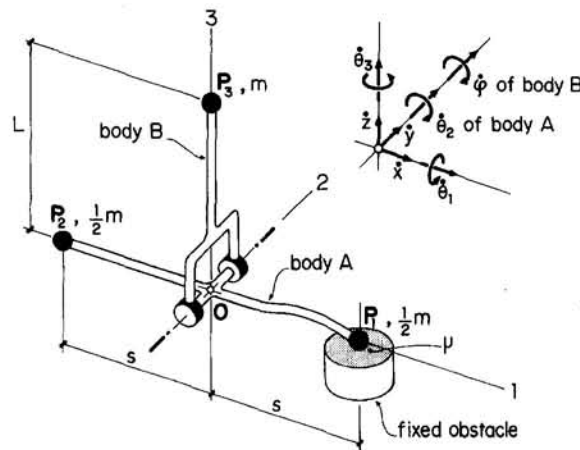


Fig. 5 Bounding of two articulated bodies on a rough fixed plane. Notation.

$$\{\Delta\tilde{u}\} = \begin{bmatrix} \Delta\tilde{v}_{t1}/2 \\ (2/7)\Delta\tilde{v}_{t2} \\ 1 + e \\ (5/7)\Delta\tilde{v}_{t2}/r \\ -\Delta\tilde{v}_{t1}/2r \\ 0 \end{bmatrix}. \quad (38)$$

The energy dissipated by the normal force is given by (14)

$$W_n = -\frac{1}{2}mv_a^2(1 - e^2), \quad (39)$$

while that dissipated by friction is defined by (15)

$$W_f = -\frac{1}{2}mv_a^2[\frac{1}{2}(\frac{25}{2} - \tilde{v}_{t1}^2) + \frac{2}{7}(\frac{25}{2} - \tilde{v}_{t2}^2)]. \quad (40)$$

The threshold normal approaching velocity v_a^\square above which sliding stops during collision is, for $v_{t1}^{(0)} = v_{t2}^{(0)}$, and according to (31)

$$v_a^\square = \frac{1}{2\mu(1 + e)} v_{t1}^{(0)} \int_0^1 \sqrt{1 + v_{t1}^{\prime,3/2}} dv_{t1}' = \frac{1,174}{2\mu(1 + e)} v_{t1}^{(0)}. \quad (41)$$

7 Application Example 2: Bounding of Two Articulate Bodies on a Rough Fixed Plane

The balanced collision considered in this example is no longer a central or a colinear one. Let's assume the mechanism shown in Fig. 5. The mass is concentrated at points P_1 , P_2 , and P_3 . The articulation is free from friction. At the configuration shown and with a translational initial movement defined by $x^{(0)}$, $y^{(0)}$ and, a negative $z^{(0)}$, $z^{(0)} < 0$, the system collides at P_1 with a rough fixed surface which is horizontal at that point.

The degrees-of-freedom $\{u\}$ and initial velocities $\{u^{(0)}\}$ are described by

$$\{u\} = \begin{bmatrix} \dot{x} \\ \dot{y} \\ \dot{z} \\ \dot{\theta}_1 \\ \dot{\theta}_2 \\ \dot{\theta}_3 \\ \dot{\phi} \end{bmatrix}; \quad \{u^{(0)}\} = \begin{bmatrix} \lambda v_0 \\ \lambda v_0 \\ -v_0 \\ 0 \\ 0 \\ 0 \\ 0 \end{bmatrix}. \quad (42)$$

The basic matrices, vectors, and parameters are

$$[M] = m \begin{bmatrix} 2 & & & & & \\ 0 & 2 & & & & \\ 0 & 0 & 2 & & & \\ 0 & -L & 0 & L^2 & & \\ 0 & 0 & 0 & 0 & S^2 & \\ 0 & 0 & 0 & 0 & 0 & S^2 \\ L & 0 & 0 & 0 & 0 & 0 & L^2 \end{bmatrix};$$

$$\{\alpha\} = \begin{Bmatrix} 0 \\ 0 \\ 1 \\ 0 \\ S^2 \\ 0 \\ 0 \end{Bmatrix}; \quad [\beta] = \begin{bmatrix} 1 & 0 \\ 0 & 1 \\ 0 & 0 \\ 0 & 0 \\ 0 & 0 \\ 0 & 5 \\ 0 & 0 \end{bmatrix}, \quad (43)$$

$$a = \frac{3}{2m}; \quad [b] = \frac{1}{m} \begin{bmatrix} 1 & 0 \\ 0 & 2 \end{bmatrix}; \quad \mathbf{h} = \begin{Bmatrix} 0 \\ 0 \end{Bmatrix}. \quad (44)$$

The value $\mathbf{h} = 0$ confirms that the collision is balanced. In this case $\nu = b_2/b_1 = 2$, and consequently the hodographs of \mathbf{v}_t are parabolas

$$v_{t2} = (v_{t2}^{(0)}/v_{t1}^{(0)2})v_{t1}^2. \quad (45)$$

At the collision point, the initial velocities lead to

$$v_a = v_0; \quad v_{t1}^{(0)} = v_{t2}^{(0)} = \lambda v_0. \quad (46)$$

The particular value of ν allows the analytical integration of (29) defining the reduced normal velocity $\tilde{v}_n \equiv v_n/v_a$

$$\tilde{v}_n = -1 + \frac{3}{4\mu} \tilde{v}_{t1}^{(0)} [\sqrt{2} + \ln(1 + \sqrt{2})] - v_{t1}' \sqrt{1 + v_{t1}'^2} - \ln(v_{t1}' + \sqrt{1 + v_{t1}'^2}), \quad (47)$$

where $v_{t1}' \equiv v_{t1}/v_{t1}^{(0)}$.

If Newton's rule is applied, the end values of v_{t1}' correspond to $\tilde{v}_n^{(e)} = e$. For both of them, $e = 1$ and $e = 0$, the end values $v_{t1}'^{(e)}$ and their corresponding $(\tilde{v}_{t1}^{(e)}, \tilde{v}_{t2}^{(e)})$, for different values of $\tilde{v}_{t1}^{(0)}$ are shown in Table 2, and depicted in Fig. 6 for $\mu = 0.75$. From these values the incremental values of the generalized velocities can be calculated by means of (33),

$$\{\Delta \tilde{v}\} = \begin{Bmatrix} \Delta \tilde{v}_{t1} \\ \Delta \tilde{v}_{t2}/2 \\ (1+e)/3 \\ \Delta \tilde{v}_{t2}/2L \\ -(1+e)2/35 \\ \Delta \tilde{v}_{t2}/25 \\ -\Delta \tilde{v}_{t1}/L \end{Bmatrix} \quad (48)$$

where $\Delta \tilde{v}_{t1} = -\lambda(1 - v_{t1}'^{(e)})$ and $\Delta \tilde{v}_{t2} = -\lambda(1 - v_{t1}'^{(e)2})$.

8 Conclusions

Lack of inertial coupling between normal and tangential directions in balanced collisions leads to direct proportionality between normal velocity and normal impulse at the collision point and to interesting specific properties concerning the tangential impulse and the energy dissipated by friction.

Table 2 End sliding velocity $\tilde{v}_t^{(e)}$ for $e = 1, e = 0$ and several values of $v_{t1}^{(0)} = \tilde{v}_{t2}^{(0)}$

e	$\tilde{v}_{t1}^{(0)} = \lambda$	$v_{t1}^{(e)}$	$v_{t1}^{(e)} = \lambda v_{t1}^{(e)}$	$\tilde{v}_{t2}^{(e)} = \lambda v_{t1}^{(e)}$
1	$4\mu/3$	0.14725	0.1963μ	0.0289μ
1	2μ	0.46490	0.9298μ	0.4323μ
1	$8\mu/3$	0.61156	1.6308μ	0.9973μ
0	$4\mu/3$	0.61156	0.8154μ	0.4987μ
0	2μ	0.74930	1.4986μ	1.1229μ
0	$8\mu/3$	0.81494	2.1732μ	1.7710μ

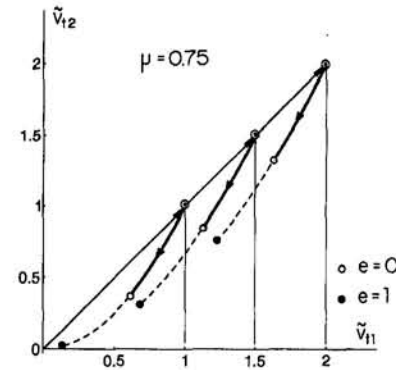


Fig. 6 Evolution of the normalized sliding velocity $\tilde{v}_t = v_t/v_a$

The analytical expression $v_{t2}(v_{t1})$ of the hodographs of \mathbf{v}_t has been obtained and used to develop a general and systematic method to integrate the equations of motion when there is not an "all linear" solution—which is the case if sliding varies its direction and doesn't stop—has been presented. This method is based upon a single integration relating the normal separating velocity v_n to one of the components of the tangential velocity at the collision point. A convenient choice of this component is made in order to improve the convergence of the integral. From the result of this integration the remaining unknowns are calculated by means of algebraic expressions.

Acknowledgment

The author expresses his thanks to the referees, whose advice has been of great value to improve the final version of the article.

References

- Battle, J. A., 1993, "On Newton's and Poisson's Rules of Percussive Dynamics," *ASME JOURNAL OF APPLIED MECHANICS*, Vol. 60, pp. 376–381.
- Battle, J. A., and Condomines, A. B., 1991, "Rough Collisions in Multibody Systems," *Mechanisms and Machine Theory*, Vol. 26, No. 6, pp. 565–577.
- Beghin, H., 1967, *Cours de Mécanique Théorique et Appliquée*, Vol. 1, Gauthier-Villars, Paris.
- Routh, E. J., 1905, *Dynamics of a System of Rigid Bodies*, Vol. 1, Macmillan and Co., London.
- Smith, C. E., 1991, "Predicting Rebounds Using Rigid-Body Dynamics," *ASME JOURNAL OF APPLIED MECHANICS*, Vol. 58, pp. 754–758.
- Smith, C. E., and Liu, P., 1992, "Coefficients of Restitution," *ASME JOURNAL OF APPLIED MECHANICS*, Vol. 59, pp. 963–968.
- Stronge, W. J., 1991a, "Unraveling Paradoxical Theories for Rigid Body Collisions," *ASME JOURNAL OF APPLIED MECHANICS*, Vol. 58, pp. 1049–1055.
- Stronge, W. J., 1991b, "Friction in Collisions: Resolution of a Paradox," *Journal of Applied Physics*, Vol. 69, No. 2, pp. 610–612.
- Stronge, W. J., 1990, "Rigid Body Collisions with Friction," *Proc. Royal Society London*, Vol. A431, pp. 169–181.

The Effect of Water on Thermal Stresses in Polymer Composites

R. M. Sullivan

Structures and Dynamics Laboratory,
George C. Marshall Space Flight Center
Marshall Space Flight Center, AL 35812

The fundamentals of the thermodynamic theory of mixtures and continuum thermochemistry are reviewed for a mixture of water and polymer. A specific mixture which is mechanically elastic, where the strain states remain infinitesimal and where water concentration gradients are possible is considered. An expression for the partial pressure of water in the mixture is obtained from Gibbs relation based on certain assumptions regarding the thermodynamic state of the water in the mixture. Along with a simple diffusion equation, this partial pressure expression may be used to simulate the thermostructural behavior of polymer composite materials due to water in the free volumes of the polymer. These equations are applied to a specific polymer composite material during isothermal heating conditions. The thermal stresses obtained by the application of the theory are compared to measured results to verify the accuracy of the approach.

Introduction

In their application as thermal protection barriers, polymer composite materials are subjected to severe heating conditions. The success of these materials as thermal protectants is contingent upon a thorough understanding of the thermostructural behavior so that sound design practices may be employed. Water and other volatiles may be entrapped in the polymer during curing or they may be adsorbed from the surroundings prior to their use. Since it is common for these volatiles to be present in the polymer, it is also essential to characterize how they will alter the thermostructural response of polymer composite materials.

Over the past few years, there have been many attempts to model, in an explicit manner, the thermostructural response of phenolic resin composites as they are heated to high temperatures¹. These attempts have been based on and derived from the porous media theory. Although some have included the effect of water on the thermomechanical response, the primary emphasis has been to simulate the effect of thermal decomposition of the polymer on the structural behavior of the composite. These attempts have been successful in the sense that they have demonstrated the direct dependence of the transient thermomechanical response on the diffusion process. The shortcoming with the porous media approach is the inability to accurately relate the stresses in the polymer chains to the chemical state of the volatile species.

The present effort approaches this problem from the perspective that the polymer and the water in its free volumes constitute a miscible mixture. In this study, we will review the principles of the thermodynamic theory of mixtures as discussed in the works by deGroot (1963), Guggenheim (1933), Katchalsky and Curran (1965), and Prigogine (1955) and apply these principles to a specific binary mixture of polymer and water. We restrict our attention to a mixture which is mechanically elastic, where the deformation states are assumed to remain infinitesimal and where no chemical reactions occur which would cause

the generation or consumption of any of the chemical species. Furthermore, only the water constituent is considered volatile.

It is well established that the mechanical response of glassy polymers is viscoelastic at temperatures near and above the glass transition temperature. Therefore, an accurate high temperature mechanical model for the polymer should include viscous terms. However, our main goal here is to establish the contribution from water residing in the free volumes of the polymer to the total stress expression. For simplicity sake, we will assume that the polymer behaves as an elastic solid and develop the total stress expression accordingly. We will leave the task of incorporating a viscoelastic constitutive theory into the present formulation as the subject of a future study.

Through the application of mixtures principles to this specific problem, an expression for the partial pressure of water is developed based upon certain assumptions regarding the thermodynamic state of water as it resides in the polymer free volumes. This partial pressure expression is a function of the partial density of water in the mixture and the entropy of water in the polymer. In the final section, a simple diffusion equation and the partial pressure expression are employed to model the thermal stress response of carbon phenolic composite specimens under uniform heating conditions. The diffusion equation is used to determine the local partial density of water in the specimen as a function of spatial location and temperature. From these results, the volume average partial density in the specimens is determined for each temperature. Using the volume average partial density and the expression for the partial stress, the volume average partial stress of water is calculated. Comparisons are made between the calculated thermal stresses and measured stresses in order to exercise the theory and determine its accuracy.

Review of Thermochemistry and Formulation of the Theory

Description of the Mixture. Figure 1 illustrates the architecture of a reinforced polymer composite. The sketch shows the reinforcing fiber bundles embedded in the polymeric resin, the polymer free volumes and the polymer network crosslink junctions². The enlarged view illustrates the relation between polymer free volumes and occupied volumes. The volume

Contributed by the Applied Mechanics Division of THE AMERICAN SOCIETY OF MECHANICAL ENGINEERS for publication in the ASME JOURNAL OF APPLIED MECHANICS.

Discussion on this paper should be addressed to the Technical Editor, Professor Lewis T. Wheeler, Department of Mechanical Engineering, University of Houston, Houston, TX 77204-4792, and will be accepted until four months after final publication of the paper itself in the ASME JOURNAL OF APPLIED MECHANICS.

Manuscript received by the ASME Applied Mechanics Division, May 31, 1994; final revision, Oct. 24, 1994. Associate Technical Editor: J. N. Reddy.

¹ These works are too numerous to list all the important contributions. For a fairly comprehensive list see Sullivan (1993).

² It should be noted that the polymer chains are not drawn to scale with respect to the reinforcing fibers. The polymer chains have been exaggerated for illustrative purposes.

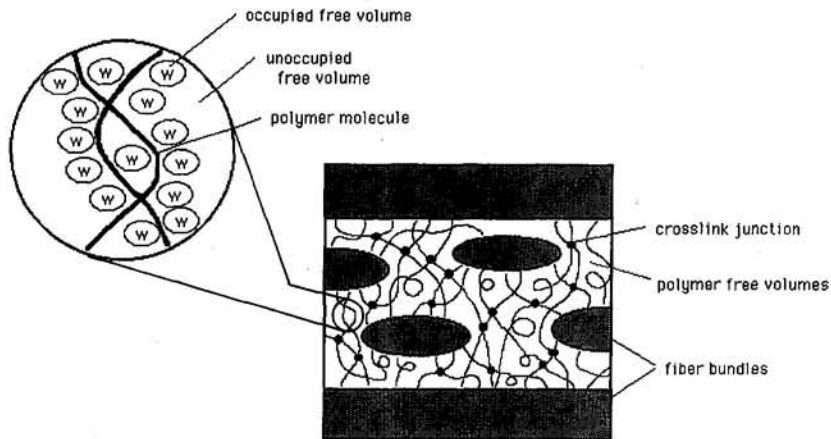


Fig. 1 Sketch showing the architecture of a polymer composite material

which the water occupies is only a fraction of the total polymer free volume. The occupied volume fraction may be defined as

$$\varphi^{oc} = \frac{V^{oc}}{V} \quad (1)$$

where V^{oc} is the volume occupied by water molecules and V is the total volume which is the sum of the volume occupied by polymer, that which is occupied by water and that which is unoccupied.

Treating the polymer and water in the free volumes as a mixture, the density of this mixture ρ is the sum of the partial densities of the individual constituents, namely

$$\rho = \rho_w + \rho_p \quad (2)$$

where ρ_w and ρ_p represent the partial density of water and polymer, respectively. Since only the water constituent is volatile and since no chemical reactions occur which would cause the generation or consumption of either of the chemical species, then the mass of the polymer within the mixture must remain constant. Furthermore, since the deformation states remain infinitesimal, the density of the polymer ρ_p remains constant. Thus, the density of the mixture varies only with the partial density of water in the mixture ρ_w .

The partial density of water in the mixture may be written as

$$\rho_w = \varphi^{oc} \rho_w^{oc} \quad (3)$$

where ρ_w^{oc} is the density of water inside the occupied volume which we shall refer to as the *occupational density* of the water. Since the mass of each water molecule remains constant, the *occupational density* depends upon the volume that each water molecule will effectively occupy. This effective volume will depend primarily upon the forces which exist between the water molecules and the polymer molecule since these forces restrict the motion of the water molecules in the free volumes³.

We will assume as a primary postulate that the forces which exist between the polymer molecules and the water molecules are such that the occupational density of water may be approximated by the density of pure, condensed water which we denote by ρ_w^o . Equation (3) may now be rewritten as $\varphi^{oc} = \rho_w / \rho_w^o$ and it becomes obvious that the occupied volume fraction represents the ratio of the density of water in the mixture to the density of pure, condensed water. We may now think of the occupied volume fraction as defining the mass concentration of water in the mixture in addition to being a volume ratio.

³Other factors which may determine this volume include the space available in the free volumes, the temperature and the forces which exist between the water molecules themselves as they reside in the free volumes.

Since condensed water is nearly incompressible and doesn't vary considerably upon heating, variations in the partial density of water in the mixture are due only to variations in φ^{oc} . For homogeneous mixtures, φ^{oc} is a function of the affinity for storage of water in the polymer, the relative humidity of the surroundings and the temperature of the system. For nonequilibrium or transient conditions, the occupied volume fraction is a function of the spatial coordinates as well as the time coordinate. The variation of the local occupied volume fraction within the mixture is dependent upon the process of diffusion of water molecules through the polymer.

Conservation Laws for a Binary Mixture in a Continuous System. Let us consider a miscible mixture of polymer and water occupying some arbitrary volume. Within this volume, the temperature, stress and partial density of the water may be continuous functions of the spatial coordinates X_i and the time variable t . The conservation laws which govern the variation of the temperature, stress and partial density inside this mixture are the conservation of energy, force equilibrium and the conservation of water mass, respectively. Following the usual approach in continuum mechanics, the conservation laws are written for the entire volume in the form of volume integrals using Gauss' theorem (Chung, 1988 and Fung, 1965). The local form of these laws are then extracted from the volume integrals.

For the binary mixture of polymer and water with water concentration and temperature gradients present, the local form of the conservation laws are written

Conservation of Water Mass:

$$\dot{\rho}_w + \operatorname{div} \mathbf{J}_w = 0; \quad (4)$$

Force Equilibrium:

$$\operatorname{div} \boldsymbol{\sigma} = 0; \quad (5)$$

Conservation of Energy:

$$\rho \dot{u} = \operatorname{tr} (\boldsymbol{\sigma} \cdot \dot{\boldsymbol{\epsilon}}) - \operatorname{div} \mathbf{J}_q + pr; \quad (6)$$

where $\dot{\rho}_w$ is the local time derivative of the partial density of water, $\boldsymbol{\sigma}$ is the Cauchy stress tensor for the mixture, \dot{u} is the time derivative of the specific internal energy, $\dot{\boldsymbol{\epsilon}}$ is the time derivative of the infinitesimal strain tensor, and r is the heat supplied per unit mass. The vectors \mathbf{J}_w and \mathbf{J}_q are the water mass flux and heat flux vectors, respectively. In Eq. (5), body forces have been ignored.

The local entropy balance equation is (Coleman and Gurtin, 1967; Katchalsky and Curran, 1965)

$$\rho \dot{s} + \operatorname{div} \mathbf{J}_s = \sigma + \frac{\rho r}{T} \quad (7)$$

where \dot{s} is the local time derivative of the entropy of the mixture per unit mass, \mathbf{J}_s is the entropy flux vector, σ is the local rate of entropy production, and T is the absolute temperature.

Since we have assumed an elastic mixture, there are no irreversible effects due to the viscosity of the polymer; the entropy flow and entropy production are due only to the heat and mass flows. The entropy flow vector \mathbf{J}_s is

$$\mathbf{J}_s = \frac{\mathbf{J}_q - \mu_w \mathbf{J}_w}{T} \quad (8a)$$

and the local entropy production rate σ is given by (Katchalsky and Curran, 1965)

$$\sigma = \mathbf{J}_q \cdot \mathbf{X}_q + \mathbf{J}_w \cdot \mathbf{X}_w. \quad (8b)$$

In Eq. (8a), μ_w is the chemical potential of the water in the mixture. The vectors \mathbf{X}_q and \mathbf{X}_w are the forces responsible for the heat and mass fluxes, respectively. Mathematically, they are written $\mathbf{X}_q = \operatorname{grad} (1/T)$ and $\mathbf{X}_w = \operatorname{grad} (-\mu_w/T)$.

Claussius-Duhem Inequality. The local form of the second law of thermodynamics is known as the Claussius-Duhem inequality and it states that the local rate of entropy production for any admissible thermodynamic process must be non-negative (Coleman and Gurtin, 1967). Therefore, for the two simultaneous irreversible processes, there is the restriction that

$$\mathbf{J}_q \cdot \mathbf{X}_q + \mathbf{J}_w \cdot \mathbf{X}_w \geq 0. \quad (9)$$

For a continuous system where heat and mass fluxes occur simultaneously, the simplest relation between the flux vectors \mathbf{J}_q and \mathbf{J}_w and their corresponding force vectors \mathbf{X}_q and \mathbf{X}_w are the linear relations

$$\mathbf{J}_q = L_{qq} \mathbf{X}_q + L_{qw} \mathbf{X}_w \quad \mathbf{J}_w = L_{wq} \mathbf{X}_q + L_{ww} \mathbf{X}_w \quad (10)$$

where L_{ij} is the set of arbitrary constitutive coefficients known as the phenomenological coefficients. The Claussius-Duhem inequality imposes the restriction on the matrix of constitutive coefficients L_{ij} that the determinant must be non-negative, $|L_{ij}| \geq 0$. Furthermore, Onsager (1931) established that $L_{ij} = L_{ji}$, $i \neq j$, giving for the present case that $L_{qq} L_{ww} \geq L_{qw}^2$.

Isothermal Conditions. Under isothermal conditions, the second expression in Eq. (10) reduces to

$$\mathbf{J}_w = -\frac{L_{ww}}{T} \operatorname{grad} \mu_w. \quad (11)$$

Choosing the variables $\mathbf{\tilde{e}}$, T and ρ_w as independent, the chemical potential may be written as a function of these variables, namely $\mu_w = \mu_w(\mathbf{\tilde{e}}, T, \rho_w)$. However, if the strain tensor has a negligible effect on the chemical potential, then, for an isothermal body, Eq. (11) takes a form similar to Fick's law which is

$$\mathbf{J}_w = -D \operatorname{grad} \rho_w. \quad (12)$$

In (12), D is the diffusivity coefficient and is a function of temperature.

Substituting Eq. (12) into Eq. (4), we obtain the familiar equation for the diffusion of moisture through an isothermal body which is nondeformable or one where the deformation states do not affect the chemical state. This is

$$\rho_w - \operatorname{div} (D \operatorname{grad} \rho_w) = 0. \quad (13)$$

The choice of (13) as the equation which governs the diffusion of water through the polymer implies that the diffusion process is independent of the pressure. This is not strictly so as a general rule. However, we will show in what follows that this simplifying assumption is sufficient for the present application.

The partial density of water is therefore assumed to be independent of pressure and the forces which drive the diffusion of water are due solely to the concentration gradients which exist within the polymer/water mixture.

A Simple Thermomechanical Model. In order to develop an expression for the total stress at each spatial location in the mixture, we consider the mechanical analog shown in Fig. 2 which consists of a spring in a parallel arrangement with a piston and cylinder device. The spring represents the collective stiffness of the polymer network as well as any additional stiffness provided by reinforcing fibers. The cylinder contains a mixture of water and the nonvolatile polymer with a mass concentration of water defined by ρ_w .

Since we have assumed a miscible mixture, the force in the piston and the force in the spring act over the same area⁴. The total stress of the mixture is therefore the sum of these forces divided by the infinitesimal area. Mathematically, this is simply

$$\tilde{\sigma} = \tilde{\sigma}^p + \tilde{\sigma}^w \quad (14)$$

where $\tilde{\sigma}^p$ is the partial stress tensor of the polymer and $\tilde{\sigma}^w$ is the partial stress tensor for the water.

In the most general sense, the partial stresses are functions of the independent variables $\mathbf{\tilde{e}}$, T and ρ_w . The differential of the partial stress of the polymer can be expanded in terms of these independent variables as

$$d\tilde{\sigma}^p = \left\{ \frac{\partial \tilde{\sigma}^p}{\partial \mathbf{\tilde{e}}} \right\}_{T, \rho_w} d\mathbf{\tilde{e}} + \left\{ \frac{\partial \tilde{\sigma}^p}{\partial T} \right\}_{\mathbf{\tilde{e}}, \rho_w} dT + \left\{ \frac{\partial \tilde{\sigma}^p}{\partial \rho_w} \right\}_{T, \mathbf{\tilde{e}}} d\rho_w \quad (15)$$

where the subscripts on the brackets indicate differentiation with those variables held constant. In the model of Fig. 2, the force in the spring is independent of the density of water in the cylinder when temperature and strain are held constant. Thus, the expression for the polymer partial stress increment, Eq. (15), reduces to

$$d\tilde{\sigma}^p = \left\{ \frac{\partial \tilde{\sigma}^p}{\partial \mathbf{\tilde{e}}} \right\}_{T, \rho_w} d\mathbf{\tilde{e}} + \left\{ \frac{\partial \tilde{\sigma}^p}{\partial T} \right\}_{\mathbf{\tilde{e}}, \rho_w} dT. \quad (16)$$

Recognizing the first term in brackets as the fourth-order stiffness tensor $\tilde{\mathbf{C}}^p$ and the second term as the negative product of the stiffness tensor and the tensor of thermal expansion coefficients $\tilde{\mathbf{B}}^p$, Eq. (16) may be written

$$d\tilde{\sigma}^p = \tilde{\mathbf{C}}^p d\mathbf{\tilde{e}} - \tilde{\mathbf{C}}^p \tilde{\mathbf{B}}^p dT. \quad (17)$$

An Expression for the Partial Pressure of Water in the Mixture. In arriving at Eq. (13), we assumed that the chemical state of the water in the mixture is independent of the strain state. Similarly, we now neglect the effect of strain on the partial stress of water. Therefore, in general terms, $\tilde{\sigma}^w = \tilde{\sigma}^w(T, \rho_w)$. The partial stress of water is related to the partial pressure of water P_w by $\tilde{\sigma}^w = -\tilde{\mathbf{I}} P_w$ where $\tilde{\mathbf{I}}$ is the identity tensor. In view of these relations, the differential increment in the partial pressure of the water may be written as

$$dP_w = \left\{ \frac{\partial P_w}{\partial T} \right\}_{\rho_w} dT + \left\{ \frac{\partial P_w}{\partial \rho_w} \right\}_T d\rho_w. \quad (18)$$

In order to determine the first term on the right-hand side of Eq. (18), we will assume that processes that occur under con-

⁴We follow the traditional approach in solid mechanics where the Cauchy stresses are defined as the internal forces acting over an infinitesimal area. This area is assumed much larger than the atomic dimensions, so the forces in the lattice network are assumed to be evenly distributed over the infinitesimal area. Therefore, in the present case, the partial stress of the polymer is the force in the polymer network evenly distributed over the total or bulk area of the mixture and the partial stress of the water is the force exerted by the water in the free volumes evenly distributed over the bulk area.

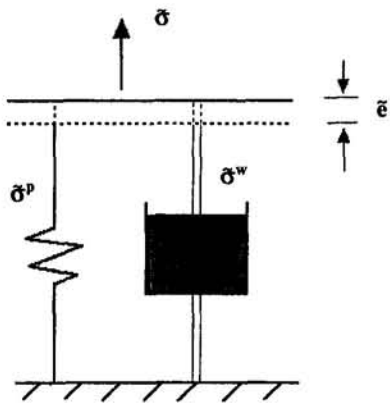


Fig. 2 Sketch of the mechanical analog

stant composition conditions also occur under the condition that the chemical potential of the water in the mixture remains constant. Gibbs expression for constant composition conditions is (Guggenheim, 1933)

$$d\mu_w = V_w dP - S_w dT \quad (19)$$

where V_w is the partial volume of water in the mixture and S_w is the partial entropy. Setting the differential increment in the chemical potential equal to zero and noting that the partial volume is the inverse of the partial density, we obtain

$$\left\{ \frac{\partial P_w}{\partial T} \right\}_{\rho_w} = \rho_w S_w. \quad (20)$$

The differential in the second term in (18) will be a function of temperature. In order to determine its variation with temperature we invoke Maxwell's reciprocal relation between the partial pressure and the variables T and ρ_w . That is

$$\frac{\partial^2 P_w}{\partial T \partial \rho_w} = \frac{\partial^2 P_w}{\partial \rho_w \partial T}. \quad (21)$$

Substituting (20) into (21), we obtain

$$\frac{\partial^2 P_w}{\partial T \partial \rho_w} = \frac{\partial}{\partial \rho_w} (\rho_w S_w) = S_w. \quad (22)$$

Integrating (22) with respect to temperature yields

$$\left\{ \frac{\partial P_w}{\partial \rho_w} \right\}_T = \int_{T_o}^T S_w dT + R_o \quad (23)$$

where R_o relates variations in the partial pressure to variations in the partial density at constant temperature T_o .

Substituting (20) and (23) into (18) and upon performing the integration, we obtain

$$P_w = P_w^o + \int_{T_o}^T \rho_w S_w dT + \int_{\rho_w^o}^{\rho_w} \left\{ \int_{T_o}^T S_w dT \right\} d\rho_w + \int_{\rho_w^o}^{\rho_w} R_o d\rho_w \quad (24)$$

where P_w^o is the partial pressure at temperature T_o and water concentration ρ_w^o . Integrating the first integral term in (24) by parts yields two terms one of which cancels with the second integral in (24). Equation (24) then reduces to

$$P_w = P_w^o + \rho_w \int_{T_o}^T S_w dT + \int_{\rho_w^o}^{\rho_w} R_o d\rho_w. \quad (25)$$

Substituting the partial entropy of water in the mixture with the specific entropy of pure, condensed water s_w and neglecting the term involving R_o , Eq. (25) becomes

$$P_w = P_w^o + \rho_w \int_{T_o}^T s_w dT. \quad (26)$$

The partial entropy of water in the mixture is replaced by the specific entropy of pure, condensed water for the same reason that the occupational density was replaced by the density of pure, condensed water.

Using (26), the expression for the partial stress tensor of water is

$$\tilde{\sigma}^w = \tilde{\sigma}_o^w - \tilde{\mathbf{I}} \rho_w \int_{T_o}^T s_w dT \quad (27)$$

where $\tilde{\sigma}_o^w = -\tilde{\mathbf{I}} P_w^o$.

Integrating Eq. (17) and combining with (27), the total stress expression is

$$\tilde{\sigma} = \tilde{\sigma}_o + \int_{\tilde{\epsilon}_o}^{\tilde{\epsilon}} \tilde{\mathbf{C}}^p d\tilde{\epsilon} - \int_{T_o}^T \tilde{\mathbf{C}}^p \tilde{\beta}^p dT - \tilde{\mathbf{I}} \rho_w \int_{T_o}^T s_w dT \quad (28)$$

where $\tilde{\sigma}_o$ is the initial total stress at temperature T_o and strain state $\tilde{\epsilon}_o$.

Demonstration and Verification of the Theory

Test Description. We will now apply the principles and equations which have been established in the previous section to simulate the effect of water in the free volumes on the thermo-mechanical response of a specific polymer composite material under a specific set of heating conditions. The material which is chosen for this simulation is carbon phenolic. Carbon phenolic is a general class of laminated, composite materials which are constructed with carbon fabric which has been impregnated with a phenolic resin.

We will simulate the conditions imposed during the tests reported in Hubbert (1989) where cylindrical specimens made of FM5055 carbon phenolic were heated uniformly at a constant rate of 5.5 °C/sec. The specimens were 1.27 cm in diameter and 2.54 cm in length and were fabricated such that the direction transverse to the fabric plane was aligned with the axial direction of the specimen (Fig. 3). As the specimens were heated, the stress required to maintain zero strain in the axial direction was measured as a function of temperature. The oven chamber in which the specimens were heated was maintained at zero percent relative humidity.

In Fig. 4, the measured restraining stress is plotted versus temperature. The results are shown for specimens with three different initial moisture contents. The amount of water in the specimens has two effects on the measured thermal stresses. The most obvious effect is that the magnitude of the restraining stress is proportional to the initial moisture content in the speci-

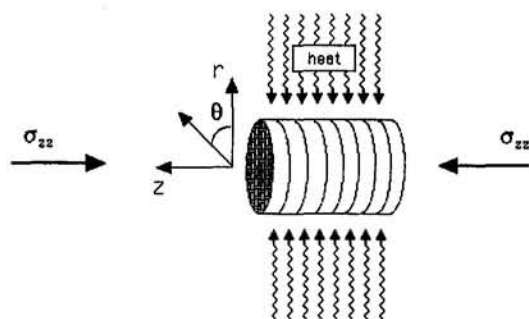


Fig. 3 Sketch of the carbon phenolic specimens and heating conditions imposed during the tests by Hubbert (1989)

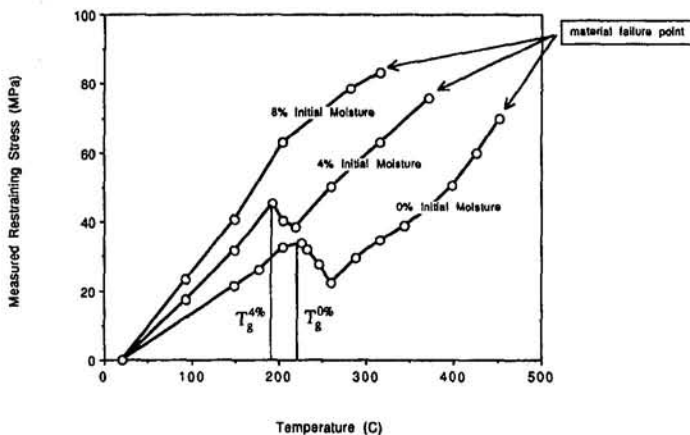


Fig. 4 Plot of the measured restraining stresses versus temperature for three different initial moisture conditions

men. In addition, water is known to lower the glass transition temperature in glassy polymers (Meares, 1965). For carbon phenolic, this effect is illustrated in Fig. 4 where we have identified the approximate glass transition temperatures for the zero percent and four percent moisture conditions. The glass transition temperature for the eight percent initial moisture specimen is more difficult to identify since, in this case, the partial stress of water becomes more significant and obscures the glass transition effect on the measured stress.

Analysis Approach. Since the specimens were heated uniformly, the temperature is independent of the spatial coordinates. Furthermore, we will assume that the response of the specimens is axisymmetric with symmetry about the r - z plane and that the diffusion of water occurs only in the radial direction (Fig. 3). The variables σ and ρ_w are therefore independent of θ . We will also assume that these variables are independent of z so that $\sigma = \sigma(r, t)$ and $\rho_w = \rho_w(r, t)$.

The axisymmetric, one-dimensional form of Eq. (13), with diffusion in only the radial direction, is

$$\frac{\partial \rho_w}{\partial r} - \frac{1}{r} \left\{ \frac{\partial}{\partial r} \left(r D_r \frac{\partial \rho_w}{\partial r} \right) \right\} = 0 \quad (29)$$

where D_r is the diffusivity of water in the radial direction. The boundary and initial conditions which are imposed are

$$\rho_w(a, t) = 0 \quad \text{and} \quad \rho_w(r, 0) = \rho_{w0},$$

respectively, where a is the radial dimension of the specimen and ρ_{w0} is the initial partial density of water in the specimen. The initial partial density is estimated as the product of the initial moisture content and the dry density of the composite. In the case of carbon phenolic, we'll approximate the dry density as 1.5 g/cc.

In Fig. 5, the diffusivity of FM5055 carbon phenolic in the direction parallel to the fabric plane is plotted versus temperature. The hollow circles represent measurements made by Stokes (1990). The solid line represents the diffusivity versus temperature description which will be used for this simulation. It was obtained by a linear fit through the measured data points.

The diffusion equation is solved numerically under the imposed boundary and initial conditions using the finite element method. The Galerkin weighted residual method was used to cast the diffusion equation into a matrix equation which is necessary for the numerical solution⁵. Linear one-dimensional ele-

ments were used to discretize the domain of the problem and to implement the finite element method.

Results. Figures 6(a) and 6(b) are plots of the calculated partial density of water versus radial location at various temperatures obtained from the numerical solution of Eq. (29). Figure 6(a) shows the partial density for the four percent moisture specimen and 6(b) shows the values for the eight percent moisture specimen. In both cases, the partial density is initially uniform. As time and temperature increase, the diffusivity increases according to the model in Fig. 5. Driven by the density gradient, the radial diffusion of water begins to occur to a noticeable extent at temperatures above 350°C when the diffusivity has reached a sufficient value. Diffusion continues until approximately 475°C when, as the numerical results indicate, there is very little water left in the specimens and therefore the density gradients at all spatial locations approach zero.

The volume average partial density of water is given by $\bar{\rho}_w = \int \rho_w dV/V$. For this specific problem, where the partial density is only a function of time and the radial coordinate and where the time variable is related to the temperature variable by a constant, the volume average partial density may be written specifically as

$$\bar{\rho}_w(T) = \frac{1}{a^2} \int \rho_w(r, T) r dr. \quad (30)$$

The volume average partial density in the specimen was calculated using Eq. (30) and the numerical results of Figs. 6. The

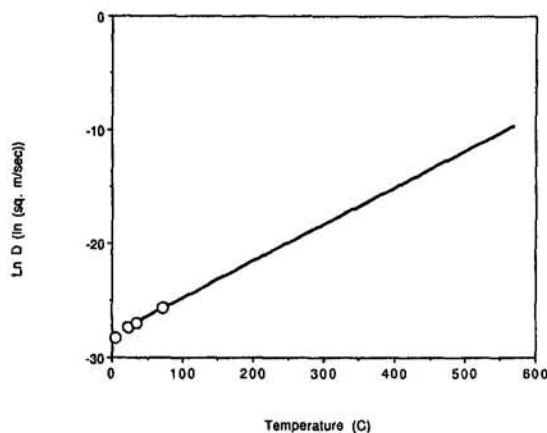


Fig. 5 Plot of the moisture diffusivity versus temperature in the direction parallel to the fabric plane

⁵ A detailed discussion of the method is given in Zienkiewicz (1977) and Segerlind (1984).

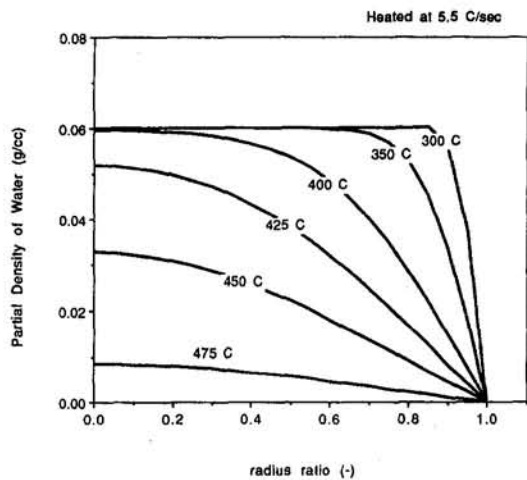


Fig. 6(a) Four percent initial moisture condition

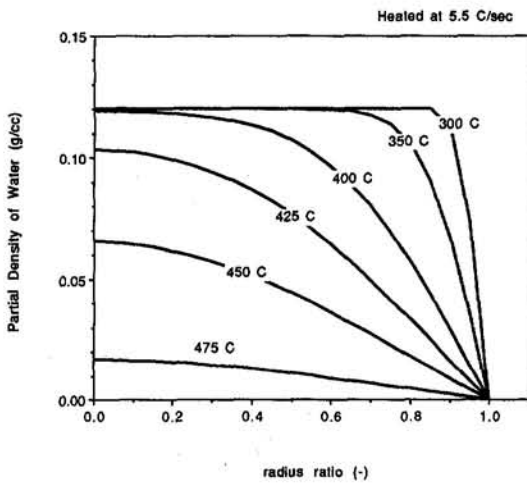


Fig. 6(b) Eight percent initial moisture condition

Fig. 6 Partial density of water as a function of radial location for various temperatures

average densities are plotted for the two initial moisture conditions in Fig. 7.

We may approximate the volume average partial pressure of water in the specimen using the volume average densities of

Fig. 7 and the expression for the partial pressure given in Eq. (26). The numerical values for s_w are obtained from Keenan, et al. (1969). The variation of s_w with temperature is specified by the path along the liquid portion of the saturation curve (Kestin, 1966). In Fig. 8, the average partial pressure is plotted versus temperature for the two initial moisture conditions. From room temperature to 350°C, the partial pressure increases with temperature since the partial density remains constant and since the specific entropy is a positive function of the temperature. The increase in the partial pressure with temperature is governed by the integral term in Eq. (26). As the diffusion of water occurs above 350°C, the partial pressure drops with the drop in partial density and falls to zero when the partial density falls to zero. At all temperatures, the partial pressure of water for the eight percent initial moisture case is twice that of the four percent initial moisture case.

The present approach may be verified by comparing the total stress given by Eq. (28) to the total stress measured by Hubbert for both the four percent and eight percent conditions. We may rewrite Eq. (28) as

$$\tilde{\sigma} = \tilde{\sigma}^p + \tilde{\sigma}_o^w - \tilde{I} \rho_w \int_{T_o}^T s_w dT \quad (31)$$

where

$$\tilde{\sigma}^p = \tilde{\sigma}_o^p + \int_{T_o}^T \tilde{C}^p dT - \int_{T_o}^T \tilde{C}^p \tilde{\beta}^p dT \quad (32)$$

and where $\tilde{\sigma}_o^p$ is the initial partial stress of the polymer. Setting $\tilde{\sigma}_o^w$ equal to zero, the total stress component in the axial direction, according to equation (31), is

$$\sigma_{zz} = \sigma_{zz}^p - \overline{\rho_w} \int_{T_o}^T s_w dT \quad (33)$$

where we have replaced the partial density with the volume average partial density.

The measured restraining stress for the zero percent water condition shown in Fig. 4 is a direct measurement of the polymer partial stress component σ_{zz}^p . The second term on the right-hand side of Eq. (33) is the volume average partial pressure which has been plotted in Fig. 8 for the two moisture conditions. Superimposing the measured restraining stress profile for the zero percent condition with the two pressure profiles of Fig. 8, the total stress profiles for the four percent and eight percent moisture conditions may be determined. These are plotted in Fig. 9 along with the measured values.

There are slight discrepancies between the calculated and the measured total stresses near the glass transition temperature. This results from simply superimposing the two profiles to-

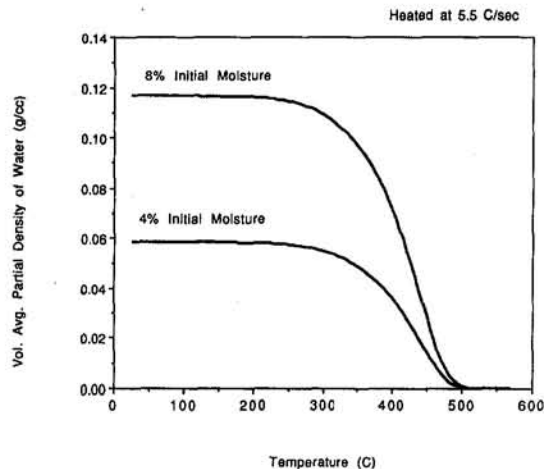


Fig. 7 Volume average partial density of water as a function of temperature for the two initial moisture conditions

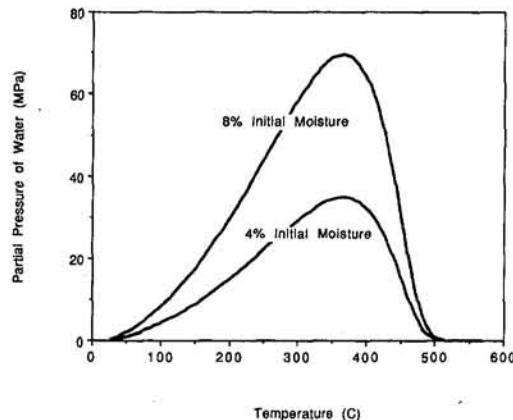


Fig. 8 Volume average partial pressure of water as a function of temperature for the two initial moisture conditions

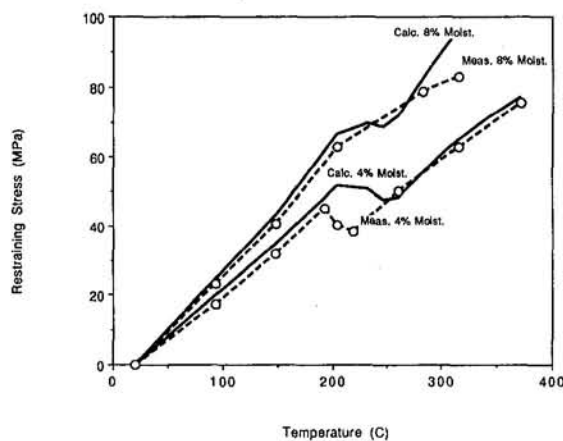


Fig. 9 Measured and calculated restraining stress in the axial direction plotted versus temperature for the two initial moisture conditions

gether. The polymer partial stress profiles have not been adjusted to account for the effect of moisture content on the glass transition behavior of the polymer. In spite of these slight discrepancies, the measured and calculated total stress profiles compare quite well for both moisture conditions.

Discussion and Conclusions

From the framework of continuum thermochemistry and the thermodynamics of mixtures, we have developed an analytical approach for modeling the transient thermomechanical response of polymer composite materials which are influenced by the presence of water in the free volumes of the polymer. An equation for the partial pressure of water has been obtained and has been applied along with a diffusion equation to model the time and temperature-dependent thermal stresses in carbon phenolic composite specimens under isothermal heating conditions. The numerical results obtained from this method compare quite well with the measured response.

In calculating the partial pressure of water in the mixture, we assumed that the thermodynamic state of the water in the free volumes of the polymer could be approximated by the thermodynamic state of condensed water. The fact that the numerical results were consistent with the measured effect of water validates this assumption. This approach is in contrast to previous analytical techniques which treat the escaping volatiles as being in the gaseous state.

The diffusivity model which was used for this simulation has been extrapolated from measurements made at lower temperatures. The accuracy of the diffusivity model at higher temperatures cannot be fully verified in this problem since the specimens failed before the total stress measurements could indicate when the exodus of moisture occurs. The diffusivity model is verified, in part, since the exodus of moisture must occur at temperatures higher than the failure point and since the partial pressures calculated with this diffusivity model are consistent with this observation.

Acknowledgments

The author is grateful for financial support from the National Aeronautics and Space Administration. The author is also grateful to Mr. Scott Brown, Mr. Tony Day, and Prof. N. J. Salamon for their contributions.

References

- Chung, T. J., 1988, *Continuum Mechanics*, Prentice-Hall, Englewood Cliffs, NJ.
- Coleman, B. D., and Gurtin, M. E., 1967, "Thermodynamics with Internal State Variables," *J. Chem. Phys.*, Vol. 47, No. 2, pp. 597-613.
- deGroot, S. R., 1963, *Thermodynamics of Irreversible Processes*, North-Holland Publishing Company, Amsterdam.
- Fung, Y. C., 1965, *Foundations of Solid Mechanics*, Prentice-Hall, Englewood Cliffs, NJ.
- Guggenheim, 1933, *Modern Thermodynamics by the Methods of Willard Gibbs*, Methuen and Company, Ltd., London.
- Hubbert, T. E., 1989, "Mechanical Properties of FM5055 Baseline Carbon Phenolic," Southern Research Institute Report No. SRI-MME-89-1149-6071-23, Southern Research Institute, Birmingham, AL.
- Katchalsky, A., and Curran, P. F., 1965, *Nonequilibrium Thermodynamics in Biophysics*, Harvard University Press, Cambridge, MA.
- Keenan, J. H., Keyes, F. G., Hill, P. G., and Moore, J. G., 1969, *Steam Tables: Thermodynamic Properties of Water Including Vapor, Liquid and Solid Phases*, John Wiley and Sons, New York.
- Kestin, J., 1966, *A Course in Thermodynamics*, Blaisdell Publishing Company, Waltham, MA.
- Meares, P., 1965, *Polymers: Structure and Bulk Properties*, D. Van Nostrand, London.
- Onsager, L., 1931, *Phys. Rev.*, Vol. 37, pp. 405-426.
- Prigogine, I., 1955, *Introduction to Thermodynamics of Irreversible Processes*, Interscience Publishers (division of John Wiley and Sons, London).
- Segerlind, L. J., 1984, *Applied Finite Element Analysis*, John Wiley and Sons, New York.
- Stokes, E. H., 1990, "Equilibrated Moisture Contents of Several Carbon Phenolics as a Function of the Relative Humidity of the Conditioning Environment," Southern Research Institute Report No. SRI-MME-90-291-6526-7, Southern Research Institute, Birmingham, AL.
- Sullivan, R. M., 1993, "A Coupled Solution Method for Predicting the Thermostructural Response of Decomposing, Expanding Polymeric Composites," *Journal of Composite Materials*, Vol. 27, No. 4, pp. 408-434.
- Zienkiewicz, O. C., 1977, *The Finite Element Method*, McGraw-Hill, London.

O. M. O'Reilly

Assistant Professor,
Department of Mechanical Engineering,
University of California at Berkeley,
Berkeley, CA 94720-1740
Assoc. Mem. ASME

Steady Motions of a Drawn Cable

The steady motions of nonlinearly elastic and inextensible strings which are being drawn between two fixed points and are subject to a gravitational load are examined. It is shown that, dependent on the boundary conditions, constitutive equations and a reference drawing speed, multiple co-existent steady motions are possible in certain situations. Using a variational method, stability criteria are also established for some of these motions.

1 Introduction

This paper examines the steady motions of a string which is being drawn between two fixed points. While undergoing these motions the string is assumed to be under the influence of a gravitational force (cf. Fig. 1(c)). This system forms an important component of many industrial processes, in particular in the textile industry. To accommodate as large a variety of materials as possible, both nonlinearly elastic and inextensible strings will be considered. For certain boundary conditions, a reference drawing speed c and the constitutive relations for the string, the existence of multiple steady motions will be established. These steady motions are conveniently classified as *convex* and *concave*. The former are similar in appearance to the classical catenary, while the latter are similar to the inverted catenary. Nonlinear stability results are also established for certain *convex* steady motions.

Before presenting an outline of this paper, it is appropriate to discuss a selection of recent work on this system. Briefly, this work has focused primarily on an examination of the linear stability of steady motions of elastic and inextensible strings. It was necessary to obtain an explicit analytical expression for the configuration of the string undergoing the steady motion of interest. The difficulty of this endeavor has necessitated the introduction of various simplifying assumptions. For inextensible strings under symmetric boundary conditions, Simpson (1972, cf. Section 6 in particular) established the surprising result that the *convex* steady motion is (linearly) stable for all c . Perkins and Mote (1987, cf. Section 5.3 in particular) established a similar result for a particular class of elastic cables. In a subsequent paper, Perkins and Mote (1989) demonstrated experimentally the existence of a *concave* steady motion and the manner by which this steady motion stabilizes. O'Reilly and Varadi (1995) examined certain qualitative features of the steady motions for various nonlinearly elastic strings as c was varied. All of these works assume a unique *convex* and (where appropriate) a unique *concave* steady motion. The present work significantly extends certain aspects of these earlier works by demonstrating a far larger variety of possible steady motions and in some cases establishing their stability. The latter results rely only on easily obtained estimates and not on a precise expression for the deformed shape of the string. Our analysis is also trivially applicable to the threadline problem—where the gravitational force is neglected.

Contributed by the Applied Mechanics Division of THE AMERICAN SOCIETY OF MECHANICAL ENGINEERS for publication in the ASME JOURNAL OF APPLIED MECHANICS.

Discussion on this paper should be addressed to the Technical Editor, Professor Lewis T. Wheeler, Department of Mechanical Engineering, University of Houston, Houston, TX 77204-4792, and will be accepted until four months after final publication of the paper itself in the ASME JOURNAL OF APPLIED MECHANICS.

Manuscript received by the ASME Applied Mechanics Division, Dec. 9, 1993; final revision, Nov. 23, 1994. Associate Technical Editor: F. Y. M. Wan.

The following section of this paper discuss the convenient formulation of the equations governing the motion of the string with respect to a suitably chosen intermediate configuration. The various constitutive equations are also discussed there. Section 3 discusses two functionals which are used later to establish the stability results. The stability criteria for elastic and inextensible strings are developed in Section 4 using a variational method and rely on the conservation of the two aforementioned functionals. The required restrictions limit the applicability of the stability results obtained. Variants of the method we employ may be found in the fluids literature (cf. Abarbanel, Holm, Marsden, and Ratiu (1986) for further references) and in a paper by Healey (1990) where it was used to investigate the stability of rotating circular loops of string. It should be noted that our stability criteria lack the validation of existence results for dynamic solutions of the partial differential equations governing the motion of the string. Unfortunately, these results appear to be currently unavailable.

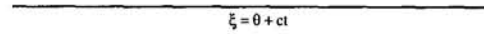
A method for determining the steady motions of the string is presented in Section 5. This section exploits an observation dating to Routh (1882, Section 524) that the boundary value problem for steady motions, when formulated with respect to the variables of an appropriately chosen intermediate configuration, correspond to the equilibrium conditions for the stationary string under a vertical gravitational load. This allows us, after some modifications, to use earlier work by Antman (1979) and Dickey (1969 and 1976) on the stationary string subject to a gravitational load. Their results, and Antman's in particular, are used extensively in preparation for the remaining two sections of this paper.

In Section 6 it will be shown how to determine all the steady motions of the string. As will become apparent, the task of determining all of these motions is nontrivial and will not be attempted here. Instead, results pertaining to the qualitative nature of these motions will be obtained. These results show that the nature of the deformation present in some of these steady motions are quite distinct from those recorded in the literature. In addition, several specific cases will be given additional consideration. These include *convex* steady motions of *stiff* nonlinearly elastic strings. It will be established for this case that such motions are unique, exist for all c and, provided symmetric boundary conditions are considered, are always nonlinearly stable. The case of a linearly elastic string is also considered. However, for *stiff* strings the stretch will become unbounded for sufficiently large c and the validity of their assumed stiffness becomes questionable. A brief discussion of the more physically reasonable *soft* string is included to address this issue. The concluding section (Section 7) of the paper addresses inextensible strings. For these types of strings the existence and uniqueness result for both *convex* and *concave* steady motions is established. After suitably restricting the boundary conditions, nonlinear stability of the *convex* motion is also established. It remains to remark that the stability criteria developed here are

(a)



(b)



(c)

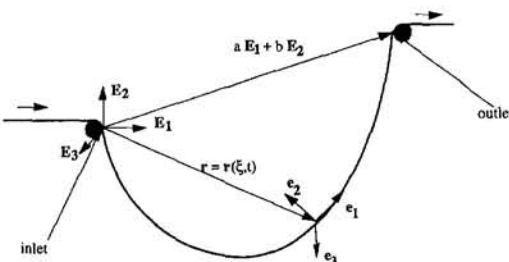


Fig. 1 The configurations of the string: (a) reference, (b) intermediate, and (c) deformed

inconclusive for all the *concave* steady motions. As a consequence, the results developed there cannot be used to demonstrate the stabilization of any *concave* steady motion.

2 Configurations and Balance Laws of the String

The string in this paper is modeled as a one-dimensional material curve \mathcal{L} which is embedded in \mathbb{E}^3 , and whose material points are uniquely specified by a (convected) coordinate θ . The reference configuration of \mathcal{L} is assumed to be undeformed and to occupy a straight curve ℓ . We denote the space curve occupied by \mathcal{L} in the deformed configuration by σ . The location of a material point in the reference and deformed configurations of the string are determined by the vector valued functions $\mathbf{R} = \mathbf{R}(\theta)$ and $\mathbf{r} = \mathbf{r}(\theta, t)$, respectively. In the later sections of this paper interest is focused on steady motions of strings and it is convenient to reformulate the boundary value problem in terms of an intermediate configuration. We provide a rapid summary of this configuration here and refer the reader to O'Reilly and Varadi (1995) for further details (cf. also Antman and Reeken, 1987).

The motion $\mathbf{r} = \mathbf{r}(\theta, t)$ is decomposed into two motions: $\mathbf{r}(\theta, t) = \mathbf{r}_1(\theta, t) + \mathbf{r}_2(\theta, t)$, where $\mathbf{r}_1(\theta, t)$ represents a rigid translational motion of speed c of the (undeformed) reference configuration along the θ coordinate direction: $\mathbf{r}_1(\theta, t) = (\theta + ct)\partial\mathbf{R}/\partial\theta$. The resulting configuration of \mathcal{L} is known as the intermediate configuration (cf. Fig. 1). The material points of this configuration are identified by the coordinate $\xi = \theta + ct$. Consequently the intermediate formulation of the motion \mathbf{r}_2 is given by $\mathbf{r}_2(\xi, t)$. The steady motions of the string which are of interest in this paper then correspond to $\mathbf{r}(\theta, t) = \mathbf{r}_2(\xi)$. In the sequel the string will be assumed to be drawn between an inlet and an outlet. The position vectors of these two points are denoted Ψ_{in} and Ψ_{out} , respectively, and the parameter Ξ represents the constant length of the intermediate configuration between these two points.

The local form of the balance laws which are assumed to hold at any point θ of \mathcal{L} are now provided. These may be obtained from the directed theory of rods after suitable restrictions have been employed (cf. Naghdi (1982) and references

therein). The referential formulation of mass conservation for \mathcal{L} is

$$\rho_o(\theta) = \lambda(\theta, t)\rho(\theta, t), \quad (1)$$

where the stretch $\lambda(\theta, t) = \sqrt{(\partial\mathbf{r}/\partial\theta) \cdot (\partial\mathbf{r}/\partial\theta)}$ and $\rho(\theta, t)$ is the mass per unit length of σ . This balance law is supplemented by the referential formulations of balance of linear momentum,

$$\frac{\partial \mathbf{n}}{\partial \theta} + \rho_o \mathbf{f} = \rho_o \dot{\mathbf{v}}, \quad (2)$$

and balance of angular momentum,

$$\frac{\partial \mathbf{r}}{\partial \theta} \times \mathbf{n} = \mathbf{0}, \quad (3)$$

$\mathbf{v} = \dot{\mathbf{r}} = \mathbf{v}(\theta, t)$ is the velocity vector, $\mathbf{f} = \mathbf{f}(\theta, t)$ is the body force per unit mass, $\mathbf{n} = \mathbf{n}(\theta, t)$ is the (contact) force and the superposed dot denotes material time derivative. It is convenient at this point to record the conservation law of energy in the form

$$\frac{d}{dt} \int_{\theta_1}^{\theta_2} \left(\frac{1}{2} \mathbf{v} \cdot \mathbf{v} + \epsilon \right) \rho d\bar{s} = \int_{\theta_1}^{\theta_2} \mathbf{f} \cdot \mathbf{v} \rho d\bar{s} + (\mathbf{n} \cdot \mathbf{v})_{\theta_1}^{\theta_2}, \quad (4)$$

where $d\bar{s} = \lambda d\theta$, $\epsilon = \epsilon(\theta, t)$ is the internal energy per unit mass and the symbol $(g(\theta, t))_{\theta_1}^{\theta_2}$ is used to denote $g(\theta_2, t) - g(\theta_1, t)$.

The constitutive relations for \mathbf{n} are determined using standard methods. A discussion of these methods may be found in Naghdi (1982, Sections 10-12). For elastic strings, $\epsilon = A = A(\lambda, \theta)$, where A is the free energy, and consequently,

$$\mathbf{n} = \rho_o \frac{1}{\lambda} \frac{\partial A}{\partial \lambda} \frac{\partial \mathbf{r}}{\partial \theta}. \quad (5)$$

For inextensible strings, the constraint of inextensibility (i.e., $\lambda(\theta, t) = 1$) is imposed and ϵ is assumed to be 0. For this case \mathbf{n} is specified by the constitutive relation

$$\mathbf{n} = m \frac{\partial \mathbf{r}}{\partial \theta} \quad (6)$$

where $m = m(\theta, t)$ is often identified as a Lagrange multiplier. We note that the constitutive relations (5) or (6) identically satisfy balance of angular momentum (3), and this balance law is not considered further.

For future purposes the Helmholtz free energy $A = A(\lambda, \theta)$, is assumed to have the following functional behavior (cf. Figs. 2, 3),

$$\frac{\partial A}{\partial \lambda} \Big|_{\lambda=1} = 0, \quad \frac{\partial A}{\partial \lambda} \rightarrow \begin{cases} -\infty \\ \infty \end{cases} \quad \text{as} \quad \lambda \rightarrow \begin{cases} 0 \\ \infty \end{cases}$$

$$\text{and} \quad \frac{\partial^2 A}{\partial \lambda^2} > 0, \quad (7)$$

and $A(\cdot, \theta) \in C^2((0, \infty), \mathbb{E})$. In preparation for the discussion of Sections 4 and 6, it is convenient to define certain classifications of the constitutive relation $A(\lambda)$. A string is *locally stiff* if

$$\frac{\partial^2 A}{\partial \lambda^2} > \frac{1}{\lambda} \frac{\partial A}{\partial \lambda} \quad \forall \lambda \in (\lambda_1, \lambda_2), \quad (8)$$

otherwise the string is *locally soft*. If $(\lambda_1, \lambda_2) = (0, \infty)$ then, following Healey (1990, Defn. 4.2) and with the assistance of (7)_{2,3} the string is said to be *stiff*, otherwise it is *soft*. Further classifications of strings are possible by relaxing (7)₃; however, this is beyond the needs of the present purposes.

The intermediate formulation of the balance and conservation laws can be obtained from their respective referential formulations (1)–(4) by changing the functional dependence of the

variables and by suitable modification of the integration limits of (4). These transformations are greatly facilitated by noting the equivalence of the partial derivatives, $\partial g(\theta, t)/\partial\theta = \partial g(\xi - ct, t)/\partial\xi = \partial\hat{g}(\xi, t)/\partial\xi$ and by the undeformed state of the intermediate configuration. In the sequel, the intermediate formulation will be used exclusively. For convenience the $\hat{\cdot}$'s employed earlier will be dropped and $\hat{\mathbf{r}}_2(\xi, t)$ will be denoted by $\mathbf{r}(\xi, t)$. The remaining nontrivial balance law is the intermediate formulation of the balance of linear momentum (from (2)):

$$\rho_o \mathbf{f} + \frac{\partial \mathbf{n}}{\partial \xi} = \rho_o \left(\frac{\partial^2 \mathbf{r}(\xi, t)}{\partial \xi^2} c^2 + 2 \frac{\partial^2 \mathbf{r}(\xi, t)}{\partial \xi \partial t} c + \frac{\partial^2 \mathbf{r}(\xi, t)}{\partial t^2} \right). \quad (9)$$

This equation is supplemented by the boundary conditions,

$$\begin{aligned} \mathbf{r}(\xi = 0, t) &= \Psi_{\text{in}} = \mathbf{0}, \\ \mathbf{r}(\xi = \Xi, t) &= \Psi_{\text{out}} = a\mathbf{E}_1 + b\mathbf{E}_2, \end{aligned} \quad (10)$$

the appropriate constitutive relations (5) or (6), and possibly the constraint $\lambda = 1$.

Henceforth it is assumed that ρ_o and A are independent of θ , and \mathbf{f} is constant (i.e., the string is homogeneous). The steady motions of the string of interest are of the functional form $\mathbf{r} = \mathbf{r}(\xi, t) = \mathbf{r}(\xi)$. For these motions, (9) simplifies considerably:

$$\rho_o \mathbf{f} + \frac{\partial}{\partial \xi} (\mathbf{n} - \rho_o c \mathbf{v}) = \mathbf{0}, \quad (11)$$

where $\mathbf{v} = \mathbf{v}(\xi) = c(\partial \mathbf{r} / \partial \xi)$. As remarked by Routh (1882, Section 524), for inextensible strings the equations for the boundary value problem (10)–(11) are identical to those for a stationary string, provided one considers $\mathbf{n} - \rho_o c \mathbf{v}$ as an *effective force* (cf. also Love (1897, Sections 270–271), and Lamb (1929, Section 50)). This observation has recently been used by Healey and Papadopoulos (1990) to construct steady axial motions of both nonlinearly elastic and inextensible strings

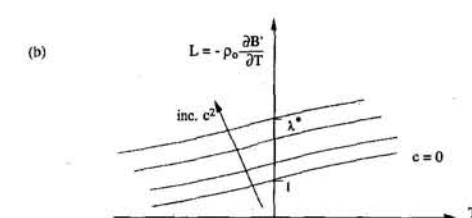
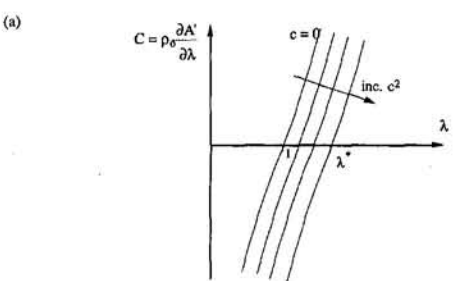


Fig. 2 The dependence of the functions (a) $C(\lambda, c)$ and (b) $L(T, c)$ for a stiff string on c . Note that $\partial A / \partial \lambda = C(\lambda, c = 0)$.

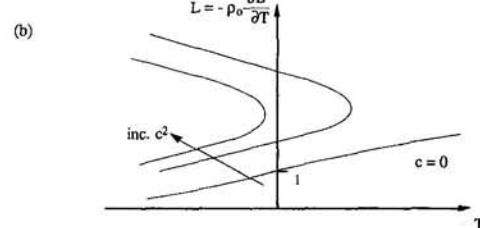
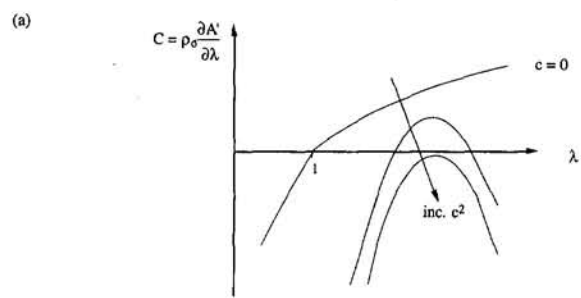


Fig. 3 The dependence of the functions (a) $C(\lambda, c)$ and (b) $L(T, c)$ for a soft string on c . Note that $\partial A / \partial \lambda = C(\lambda, c = 0)$.

when $\mathbf{f} = \mathbf{0}$. In Section 5 of this paper Routh's observation will also prove to be valuable.

3 Conserved Quantities

Using the energy conservation law (4), a Lagrangian \mathcal{L} and its Lagrangian density $\tilde{\mathcal{L}}$ may be defined

$$\mathcal{L} = \int_0^{\Xi} \tilde{\mathcal{L}} d\xi = \int_0^{\Xi} \left(\frac{1}{2} \mathbf{v} \cdot \mathbf{v} - \epsilon + \mathbf{f} \cdot \mathbf{r} \right) \rho_o d\xi. \quad (12)$$

With the assistance of a Legendre transformation, the corresponding Hamiltonian \mathcal{H} and its density $\tilde{\mathcal{H}}$ are obtained from (12):

$$\mathcal{H} = \int_0^{\Xi} \tilde{\mathcal{H}} d\xi = \int_0^{\Xi} \rho_o \left(\frac{1}{2} \mathbf{v} \cdot \mathbf{v} + \epsilon - \mathbf{f} \cdot \mathbf{r} \right) d\xi, \quad (13)$$

where the canonical variables are $(\mathbf{r}, \mathbf{p} = \rho_o \mathbf{v})$. We refrain from writing the variable \mathbf{p} explicitly in what follows as it does not form an essential part of the work.

The kinematical quantity Γ and its density $\tilde{\Gamma}$ which play a crucial role in the subsequent analysis are defined as

$$\Gamma = \int_0^{\Xi} \tilde{\Gamma} d\xi = \int_0^{\Xi} \mathbf{v} \cdot \frac{\partial \mathbf{r}}{\partial \xi} \rho_o d\xi. \quad (14)$$

The quantity Γ / ρ_o is related to a quantity which is known in fluid dynamics, after Kelvin, as the *flow* (cf. Lamb (1932, Section 31) and Casey and Naghdi (1991)).¹

The conditions under which \mathcal{H} and Γ are conserved are of interest in the next section of this paper. For elastic and inextensible strings, from (4) and (13) it follows that

$$\frac{d\mathcal{H}}{dt} = (\mathbf{n} \cdot \mathbf{v})_0^{\Xi}. \quad (15)$$

¹ Note added (21 Nov. 1994): After an earlier version of this paper was submitted for publication, Prof. T. J. Healey informed me that he and Prof. J. H. Maddocks had obtained a conservation law for the quantity described by (14). However, I had not seen their work, which has since appeared in J. H. Maddocks and D. J. Dichmann, 1994, "Conservation Laws in the Dynamics of Rods," *Journal of Elasticity*, Vol. 34, pp. 83–96. The latter paper references a forthcoming related paper by Healey (which I have not yet seen).

The material derivative of Γ for homogeneous elastic strings under a constant body force is

$$\frac{d\Gamma}{dt} = \rho_o \left(\frac{1}{2} \mathbf{v} \cdot \mathbf{v} + \mathbf{f} \cdot \mathbf{r} + \lambda \frac{\partial A}{\partial \lambda} - A \right) \Big|_0^{\Xi}, \quad (16)$$

where (2), (5) and an integration by parts were used in the calculation. The corresponding result for inextensible strings (cf. (6) and (7)) is

$$\frac{d\Gamma}{dt} = (\frac{1}{2} \rho_o \mathbf{v} \cdot \mathbf{v} + \rho_o \mathbf{f} \cdot \mathbf{r} + m(\xi)) \Big|_0^{\Xi}. \quad (17)$$

The relations (15)–(17) provide the boundary restrictions which are sufficient for the conservation of \mathcal{H} and Γ . We also summarize them here for future reference,

$$\begin{aligned} (\mathbf{v} \cdot \mathbf{v}) \Big|_0^{\Xi} &= 0, (\mathbf{n} \cdot \mathbf{v}) \Big|_0^{\Xi} = 0, \\ (\mathbf{f} \cdot \mathbf{r}) \Big|_0^{\Xi} &= 0, \lambda(0, t) = \lambda(\Xi, t). \end{aligned} \quad (18)$$

These conditions will severely restrict the steady motions whose stability can be determined using the methods described in the next section of this paper. Anticipating the results of Sections 6 and 7, they imply that the stability criteria can only be applied when the inlet and outlet have the same height (i.e., $b = 0$). The steady motions in this case are symmetric.

4 Stability Criteria for Elastic and Inextensible Strings

We now address the establishment of stability criteria. In the interests of brevity only the elastic case will be completely discussed. The corresponding result for inextensible strings will be presented at the end of this section, along with a brief description of how the result may be obtained. For elastic strings, using (13) and (14) the following functional is defined:

$$\begin{aligned} \mathcal{H}_{CE}(\mathbf{r}, \mathbf{v}, \mu) &= \int_0^{\Xi} \rho_o \left[\frac{1}{2} \mathbf{v} \cdot \mathbf{v} + A - \mathbf{f} \cdot \mathbf{r} \right] d\xi \\ &\quad - \mu \left(\int_0^{\Xi} \rho_o \mathbf{v} \cdot \frac{\partial \mathbf{r}}{\partial \xi} d\xi - \Gamma_o \right), \end{aligned} \quad (19)$$

where μ is a constant Lagrange multiplier and Γ_o represents the value of Γ for the steady motion of interest. The following norm is defined for the linear space (\mathbf{r}, \mathbf{v}) :

$$\begin{aligned} \|\mathbf{r}, \mathbf{v}\|_{ME} &= \max_{\xi \in I} \|\mathbf{r}(\xi, t)\| \\ &\quad + \max_{\xi \in I} \left\| \frac{\partial \mathbf{r}(\xi, t)}{\partial \xi} \right\| + \max_{\xi \in I} \|\mathbf{v}(\xi, t)\|, \end{aligned} \quad (20)$$

where $I = [0, \Xi]$. From the differentiability of A , it may be shown using standard methods that \mathcal{H}_{CE} is a continuous function of (\mathbf{r}, \mathbf{v}) with respect to this norm (cf. e.g., Troutman (1983, Chapter 5)). Admissible variations of \mathbf{r} and \mathbf{v} will be considered, i.e., $\mathbf{r} \rightarrow \mathbf{r} + \alpha \mathbf{a}$, $\mathbf{v} \rightarrow \mathbf{v} + \alpha \mathbf{b}$, where $(\mathbf{a}, \mathbf{b}) \in \mathcal{D}$:

$$\mathcal{D} = \left\{ (\mathbf{a}(\cdot, t), \mathbf{b}(\cdot, t)) \in (C^1([0, \Xi], \mathcal{E}^3), C^0([0, \Xi], \mathcal{E}^3)), \mathbf{a}(0, t) = \mathbf{a}(\Xi, t) = \mathbf{b}(0, t) = \mathbf{b}(\Xi, t) = \mathbf{0} \right\}. \quad (21)$$

It should be noted that there will be additional restrictions on the boundary values of $\mathbf{a}(\xi, t)$ which arise from the need to preserve \mathcal{H} and Γ (cf. (18)). These additional restrictions play no role in what follows and are not discussed any further.

To proceed the first Gâteaux variation² of \mathcal{H}_{CE} with respect to α is calculated and evaluated at $\alpha = 0$:

$$\begin{aligned} \delta \mathcal{H}_{CE} &= \frac{d \mathcal{H}_{CE}}{d \alpha} \Big|_{\alpha=0} = \int_0^{\Xi} \left[\frac{\partial}{\partial \xi} \left(\frac{1}{\lambda} \frac{\partial A}{\partial \lambda} - \mu \mathbf{v} \right) + \mathbf{f} \right] \cdot \mathbf{a} \\ &\quad + \left[\mathbf{v} - \mu \frac{\partial \mathbf{r}}{\partial \xi} \right] \cdot \mathbf{b} \rho_o d\xi. \end{aligned} \quad (22)$$

We note that in calculating (22) a standard integration by parts has been performed. From (22) and with the assistance of (5) and (11), it follows after setting $\mu = c$ that if (\mathbf{r}, \mathbf{v}) corresponds to a steady motion of the string then \mathcal{H}_{CE} has an extremum (i.e., $\delta \mathcal{H}_{CE} = 0$). The extremum $(\mathbf{r}(\xi), \mathbf{v}(\xi), \mu = c)$ of \mathcal{H}_{CE} is henceforth denoted $(\mathbf{r}_s, \mathbf{v}_s, \mu_s)$.

To establish the stability result, consider $\mathcal{H}_{CE}(\mathbf{r}_s + \mathbf{a}(\xi, t), \mathbf{v}_s + \mathbf{b}(\xi, t)) - \mathcal{H}_{CE}(\mathbf{r}_s, \mathbf{v}_s)$ where $(\mathbf{a}, \mathbf{b}) \in \mathcal{D}$ and $(\mathbf{r}, \mathbf{v}) = (\mathbf{r}_s + \mathbf{a}, \mathbf{v}_s + \mathbf{b})$ is a solution of the boundary value problem. Using Taylor's theorem, (21)–(22) and provided $\|\mathbf{a}, \mathbf{b}\|_{ME}$ is sufficiently small, then there exists a real number ω ($0 < \omega < 1$) such that

$$|\mathcal{H}_{CE}(\mathbf{r}_s + \mathbf{a}(\xi, t), \mathbf{v}_s + \mathbf{b}(\xi, t)) - \mathcal{H}_{CE}(\mathbf{r}_s, \mathbf{v}_s)| = \frac{1}{2} |\delta^2 \mathcal{H}_{CE}(\mathbf{r}_s + \omega \mathbf{a}(\xi, t), \mathbf{v}_s + \omega \mathbf{b}(\xi, t))|, \quad (23)$$

where $\delta^2 \mathcal{H}_{CE}$ is the second Gâteaux variation of \mathcal{H}_{CE} :

$$\delta^2 \mathcal{H}_{CE}(\mathbf{r}_s + \omega \mathbf{a}, \mathbf{v}_s + \omega \mathbf{b})$$

$$\begin{aligned} &= \frac{d^2 \mathcal{H}_{CE}(\mathbf{r}_s + \alpha \mathbf{a}, \mathbf{v}_s + \alpha \mathbf{b})}{d\alpha^2} \Big|_{\alpha=\omega} \\ &= \int_0^{\Xi} \left(\mathbf{b} - c \frac{\partial \mathbf{a}}{\partial \xi} \right) \cdot \left(\mathbf{b} - c \frac{\partial \mathbf{a}}{\partial \xi} \right) + (f_1) \frac{\partial \mathbf{a}}{\partial \xi} \cdot \frac{\partial \mathbf{a}}{\partial \xi} \\ &\quad + (f_2) \left(\frac{\partial \mathbf{r}_s}{\partial \xi} \cdot \frac{\partial \mathbf{a}}{\partial \xi} + \omega \frac{\partial \mathbf{a}}{\partial \xi} \cdot \frac{\partial \mathbf{a}}{\partial \xi} \right)^2 \rho_o d\xi, \end{aligned} \quad (24)$$

where

$$f_1 = \frac{1}{\lambda_\omega} \frac{\partial A}{\partial \lambda} (\lambda_\omega) - c^2, \quad f_2 = \frac{1}{\lambda_\omega^2} \left(\frac{\partial^2 A}{\partial \lambda^2} (\lambda_\omega) - \frac{1}{\lambda_\omega} \frac{\partial A}{\partial \lambda} (\lambda_\omega) \right),$$

$$\lambda_\omega^2 = \left(\frac{\partial \mathbf{r}_s}{\partial \xi} + \omega \frac{\partial \mathbf{a}}{\partial \xi} \right) \cdot \left(\frac{\partial \mathbf{r}_s}{\partial \xi} + \omega \frac{\partial \mathbf{a}}{\partial \xi} \right). \quad (25)$$

Assuming that the string is *locally stiff*, i.e., $f_2 > 0$ (cf. (8)) in a sufficiently large neighborhood of $\lambda = \lambda_s(\xi) = \sqrt{(\partial \mathbf{r}_s / \partial \xi) \cdot (\partial \mathbf{r}_s / \partial \xi)}$ $\forall \xi \in [0, \Xi]$, then (from (23)–(25))

$$|\mathcal{H}_{CE}(\mathbf{r}_s + \mathbf{a}(\xi, t), \mathbf{v}_s + \mathbf{b}(\xi, t)) - \mathcal{H}_{CE}(\mathbf{r}_s, \mathbf{v}_s)|$$

² Our terminology here follows Nashed (1966).

$$\begin{aligned} &> \frac{\sigma}{2} \int_0^{\Xi} \left(\mathbf{b} - c \frac{\partial \mathbf{a}}{\partial \xi} \right) \cdot \left(\mathbf{b} - c \frac{\partial \mathbf{a}}{\partial \xi} \right) \\ &+ \left(\frac{1}{\lambda_s} \frac{\partial A}{\partial \lambda} (\lambda_s) - c^2 \right) \frac{\partial \mathbf{a}}{\partial \xi} \cdot \frac{\partial \mathbf{a}}{\partial \xi} \rho_o d\xi, \quad (26) \end{aligned}$$

for some real valued positive constant σ . Tacitly assuming that $n(\xi) - \rho_o \lambda_s(\xi) c^2 > 0$, $\forall \xi \in [0, \Xi]$, the term on the right-hand side of (26) may be used to define a semi-norm for $(\mathbf{a}, \mathbf{b}) \in \mathcal{D}$:

$$\begin{aligned} \|\mathbf{F}, \mathbf{v}\|_E^2 &= \int_0^{\Xi} \left(\mathbf{v} - c \frac{\partial \mathbf{F}}{\partial \xi} \right) \cdot \left(\mathbf{v} - c \frac{\partial \mathbf{F}}{\partial \xi} \right) \\ &+ \left(\frac{1}{\lambda_s} \frac{\partial A}{\partial \lambda} (\lambda_s) - c^2 \right) \frac{\partial \mathbf{F}}{\partial \xi} \cdot \frac{\partial \mathbf{F}}{\partial \xi} \rho_o d\xi, \quad (27) \end{aligned}$$

where $\mathbf{F} = \mathbf{F}(\xi, t) = \mathbf{r}(\xi, t) - \mathbf{r}_s(\xi)$, $\mathbf{v} = \mathbf{v}(\xi, t) = \mathbf{v}(\xi, t) - \mathbf{v}_s(\xi)$. It should be noted that this semi-norm may also be used to define a norm for \mathcal{D} using some standard inequalities (cf. Knops and Wilkes (1966, Section 4.4), for instance). We are now in a position to state the stability criterion:

Theorem 4.1 If $n(\xi) - \rho_o \lambda_s(\xi) c^2 > 0 \forall \xi \in [0, \Xi]$ where

$$n_s(\xi) = \frac{\rho_o}{\lambda(\xi)} \frac{\partial A}{\partial \lambda} (\lambda_s(\xi)), \quad (28)$$

and the string is *locally stiff* in a sufficiently large neighborhood of $\lambda = \lambda_s(\xi)$, then the steady motion $(\mathbf{r}_s, \mathbf{v}_s)$ is nonlinearly stable.

Proof: From the continuity of $\mathcal{H}_{CE}(\mathbf{r}, \mathbf{v}, \mu)$ with respect to the norm $\|\mathbf{r}, \mathbf{v}\|_{ME}$, it follows that given $\epsilon > 0$, $\exists \delta > 0$ such that if $\|\mathbf{a}(\xi, 0), \mathbf{b}(\xi, 0)\|_{ME} < \delta$, then

$$|\mathcal{H}_{CE}(\mathbf{r}_s + \mathbf{a}(\xi, 0), \mathbf{v}_s + \mathbf{b}(\xi, 0)) - \mathcal{H}_{CE}(\mathbf{r}_s, \mathbf{v}_s)| < \epsilon. \quad (29)$$

Recalling the conservation of $\mathcal{H}_{CE}(\mathbf{r}, \mathbf{v})$, (6), (26)–(27), it follows from (29) that

$$\frac{\sigma}{2} \|\mathbf{a}(\xi, t), \mathbf{b}(\xi, t)\|_E^2$$

$$< |\mathcal{H}_{CE}(\mathbf{r}_s + \mathbf{a}(\xi, t), \mathbf{v}_s + \mathbf{b}(\xi, t)) - \mathcal{H}_{CE}(\mathbf{r}_s, \mathbf{v}_s)| < \epsilon \quad (30)$$

and nonlinear stability is concluded. ♦

The method of proof used in theorem 4.1 closely followed the work of Healey (1990). As a particular case of this theorem, a linearly elastic string is now considered. For strings of this type,

$$A(\lambda) = \frac{\hat{E}}{2} (\lambda - 1)^2, \quad (31)$$

where $\hat{E} > 0$ and Young's modulus $E = \rho_o \hat{E}$. It may be shown using (8) and (31) that strings of this type are always *stiff*. With the assistance of (5) and (31), the stability result of theorem 4.1 when interest is restricted to linearly elastic strings reads

Corollary 4.2: For linearly elastic strings if $\lambda_s(\xi) > \hat{E}/(\hat{E} - c^2) \forall \xi \in [0, \Xi]$ then the steady motion $(\mathbf{r}_s, \mathbf{v}_s)$ is nonlinearly stable.

We remark that $c^2 = \hat{E}$ corresponds to a well-known resonant instability (the translational speed c equals the longitudinal wave speed).

For inextensible strings, a stability theorem whose statement and proof are similar to theorem 4.1 may also be established. Among the principal differences is that the functional \mathcal{H}_{CE} is replaced by the functional

$$\begin{aligned} \mathcal{H}_{CI}(\mathbf{r}, \mathbf{v}, \mu_1, \mu_2) &= \int_0^{\Xi} \left[\frac{1}{2} \mathbf{v} \cdot \mathbf{v} - \mathbf{f} \cdot \mathbf{r} \right] \rho_o d\xi \\ &- \mu_1 \left(\int_0^{\Xi} \mathbf{v} \cdot \frac{\partial \mathbf{r}}{\partial \xi} \rho_o d\xi - \Gamma_o \right) \\ &+ \int_0^{\Xi} \frac{\mu_2}{2} \left(\frac{\partial \mathbf{r}}{\partial \xi} \cdot \frac{\partial \mathbf{r}}{\partial \xi} - 1 \right) \rho_o d\xi, \quad (32) \end{aligned}$$

where $\mu_2 = \mu_2(\xi, t)$ is an additional Lagrange multiplier. As in the discussion following (22), $\delta \mathcal{H}_{CI} = 0$ for a steady motion of the string if $\mu_1 = c$ and $\rho_o \mu_2 = m_s(\xi)$, where $m_s(\xi)$ is the tension in the string during the steady motion.

After noting that variations of $\mathbf{r}_s(\xi)$ are considered which satisfy the linearized inextensibility constraint $((\partial \mathbf{r}_s / \partial \xi) \cdot (\partial \mathbf{a} / \partial \xi) = 0)$ it is easily shown that \mathcal{H}_{CI} is quadratic in \mathbf{a} . Consequently, for inextensible strings the relation corresponding to (26) is

$$\begin{aligned} &|\mathcal{H}_{CI}(\mathbf{r}_s + \mathbf{a}(\xi, t), \mathbf{v}_s + \mathbf{b}(\xi, t)) - \mathcal{H}_{CI}(\mathbf{r}_s, \mathbf{v}_s)| \\ &= \frac{1}{2} \int_0^{\Xi} \rho_o \left(\mathbf{b} - c \frac{\partial \mathbf{a}}{\partial \xi} \right) \cdot \left(\mathbf{b} - c \frac{\partial \mathbf{a}}{\partial \xi} \right) \\ &+ (m_s(\xi) - \rho_o c^2) \frac{\partial \mathbf{a}}{\partial \xi} \cdot \frac{\partial \mathbf{a}}{\partial \xi} d\xi. \quad (33) \end{aligned}$$

With some obvious differences, the proof of the following theorem is similar to that used in obtaining theorem 4.1 and we merely quote its statement:

Theorem 4.3. For an inextensible string if $m(\xi) - \rho_o c^2 > 0 \forall \xi \in [0, \Xi]$, then the steady motion $(\mathbf{r}_s, \mathbf{v}_s)$ is nonlinearly stable.

For further details on methods which are similar to those used in establishing this result, the reader is referred to Abarbanel and Holm (1987) and Healey (1990). We shall concern ourselves exclusively with steady motions in the forthcoming sections and the subscript s accompanying \mathbf{r}_s , \mathbf{v}_s , m_s , n_s , etc., will be dropped.

5 Determination of the Steady Motions

To determine the steady motions of the string it is convenient to reorganize (11) as

$$\rho_o \mathbf{f} + \frac{d}{d\xi} (T(\xi) \mathbf{e}_1(\xi)) = 0, \quad (34)$$

where $T(\xi) = n(\xi) - \rho_o \lambda(\xi) c^2$ and $\mathbf{e}_1(\xi)$ is the unit tangent vector to σ at $\mathbf{r}(\xi)$. T is the tangential component of the *effective force* we referred to earlier (following (11)). It is also convenient to adapt the following form for the external body force term $\rho_o \mathbf{f}$ (due to Antman, 1979):

$$\rho_o \mathbf{f} = - \frac{\partial G(\xi)}{\partial \xi} \mathbf{E}_2,$$

$$\text{where } G(\xi = 0) = 0 \text{ and } \frac{\partial G(\xi)}{\partial \xi} > 0. \quad (35)$$

$G(\xi) \in C^1([0, \Xi], \mathcal{E})$ and for a vertical gravitational force $G(\xi) = \rho_o g \xi$ ($g = 9.81 \text{ m/s}^2$). In the sequel, the solution of (10), (34) and (35) with appropriate constitutive relations and possibly subject to the constraint $\lambda = 1$, is referred to as the boundary value problem for steady motions. The present formulation of the boundary value problem for steady motions permits the results of Antman (1979) and Dickey (1969 and 1974) analyses of the stationary string to be readily applied in order to solve for the steady motions of the string. There will be some

complications which are consequences of the drawing, but these will be accommodated.

From the previous discussion, the following four restrictions on the nature of steady motions follow from Antman's work by trivial extension and are provided here without proof. (I) Any solution $\{\mathbf{r}(\xi), \mathbf{n}(\xi)\} \in \{C^2([0, \Xi], \mathcal{E}^3), C^1([0, \Xi], \mathcal{E}^3)\}$ of (10), (34)–(35) where $\lambda(\xi) > 0$ and $\mathbf{x}(\xi)$ lies entirely in the \mathbf{E}_1 – \mathbf{E}_2 plane. As a consequence of (I) it is convenient to define the variable $\vartheta(\xi)$:

$$\mathbf{e}_1(\xi) = \cos(\vartheta(\xi))\mathbf{E}_1 + \sin(\vartheta(\xi))\mathbf{E}_2, \quad (36)$$

and to specify $\mathbf{T}(\xi)$ as

$$\mathbf{T}(\xi) = T(\xi)\mathbf{e}_1(\xi) = T_1(\xi)\mathbf{E}_1 + T_2(\xi)\mathbf{E}_2. \quad (37)$$

Integrating (34) and then using (35)–(37), the following relations are obtained (using the \mathbf{E}_1 , \mathbf{E}_2 and $\mathbf{e}_1(\xi)$ vectors, respectively),

$$\begin{aligned} T(\xi) \cos(\vartheta(\xi)) &= T_1(\xi) = T_1(0), \\ T(\xi) \sin(\vartheta(\xi)) &= T_2(\xi) = T_2(0) + G(\xi), \\ T(\xi) &= T_1(0) \cos(\vartheta(\xi)) \\ &\quad + (T_2(0) + G(\xi)) \sin(\vartheta(\xi)). \end{aligned} \quad (38)$$

The second result which follows trivially from Antman (1979) is; (II) if there exists a point $\bar{\xi} \in [0, \Xi]$ where either $T(\bar{\xi})$ or $\cos(\vartheta(\bar{\xi}))$ vanish then $T(\xi)$ and $\cos(\vartheta(\xi))$ vanish, and the string is vertical (i.e., $\mathbf{e}_1(\xi) = \mathbf{E}_2$ and $a = 0$). For every other solution either $n(\xi) > \rho_o \lambda(\xi) c^2$ or $n(\xi) < \rho_o \lambda(\xi) c^2$. In the sequel the vertical solution will not be considered and consequently the following Cartesian parameterization for the steady motion $\mathbf{r}(\xi)$ of the deformed space curve \mathcal{C} is allowed (III):

$$\mathbf{r} \cdot \mathbf{E}_1 = x \text{ and } \mathbf{r} \cdot \mathbf{E}_2 = y(x), \quad (39)$$

where $y(x)$ is a strictly convex or concave function of x . The fourth result which follows from Antman's work is (IV): for convex (concave) steady motions of both elastic and inextensible strings if $a > 0$, then $T_1(0) > 0$ (< 0) and $y(x)$ is a convex (concave) function of x . We remark that the deformed configuration shown in Fig. 1 is an example of a convex steady motion. Its inverted form is an example of a concave steady motion. It should be noted that the force $n(\xi)$ in a convex steady motion is always tensile. However, the force $n(\xi)$ in a concave steady motion may be tensile, compressive or both.

The results presented in the last two paragraphs are independent of the constitutive relations for the string. Prior to establishing the method for solving the boundary value problem, it is necessary to address further details concerning constitutive relations. The functional assumptions on the free energy A (cf. (7)–(8)) permits the definition of a complimentary energy $B(n)$ where

$$\lambda(n) = \rho_o \frac{\partial B(n)}{\partial n}, \quad (40)$$

using a Legendre transformation:³

$$B(n) = n\lambda(n) - A(\lambda(n)) = \mathbf{n} \cdot \frac{\partial \mathbf{r}}{\partial \xi} - A(\lambda(n)). \quad (41)$$

Motivated by (34), an augmented free energy is defined:

$$A'(\lambda, c) = A(\lambda) - \frac{1}{2}\lambda^2 c^2, \quad (42)$$

³ It should be noted that if A is a convex (concave) function of λ , then its dual B defined by the Legendre transformation is a convex (concave) function of n .

where

$$T = \rho_o \frac{\partial A'(\lambda, c)}{\partial \lambda} \equiv C(\lambda, c). \quad (43)$$

Finally, from (40)–(43) and after using another Legendre transformation:

$$B'(T, c) = \mathbf{T} \cdot \frac{\partial \mathbf{r}}{\partial \xi} - A'(L, c), \quad (44)$$

where

$$\lambda = \rho_o \frac{\partial B'(T, c)}{\partial T} \equiv L(T, c). \quad (45)$$

Representative examples of the functions C and L are shown in Figs. 2 and 3.

We are now in a position to expand upon an observation of Clebsch (1860), who noted that the solution $\mathbf{r}(\xi)$ of (34) for inextensible and linearly elastic strings may be determined using Hamilton-Jacobi theory. We will first consider elastic strings. Setting $\mathbf{v} = c(\partial \mathbf{r} / \partial \xi)$ in (12) and using (40)–(45), it follows that we may define a Hamiltonian system whose canonical variables are $(\mathbf{r}(\xi), \mathbf{T}(\xi))$ which is equivalent to (34):

$$\begin{aligned} \mathcal{H} &= \mathcal{H}(\mathbf{T}, \mathbf{r}, \xi) = \rho_o \mathbf{T} \cdot \frac{\partial \mathbf{r}}{\partial \xi} - \rho_o A' + \rho_o \mathbf{f} \cdot \mathbf{r} \\ &= \rho_o B' + \rho_o \mathbf{f} \cdot \mathbf{r}, \\ \frac{\partial \mathcal{H}}{\partial \mathbf{T}} &= \rho_o \frac{\partial \mathbf{r}}{\partial \xi}, \quad -\frac{\partial \mathcal{H}}{\partial \mathbf{r}} = \frac{\partial \mathbf{T}}{\partial \xi}. \end{aligned} \quad (46)$$

We now make use of the results summarized by (36)–(38) to reduce the three differential equations in (46)₂ to two algebraic equations. First, we use (46)₂ to write

$$\int_0^{\Xi} \frac{\partial}{\partial \mathbf{T}} \left(\rho_o \mathbf{T} \cdot \frac{\partial \mathbf{r}}{\partial \xi} - \mathcal{H} \right) d\xi = \mathbf{0}. \quad (47)$$

Then with the successive assistance of (38), (i.e., $\mathbf{T} = \mathbf{T}_o + G(\xi)\mathbf{E}_2 = T_1(0)\mathbf{E}_1 + T_2(0)\mathbf{E}_2 + G(\xi)\mathbf{E}_2$), (46), (34) and an integration by parts, (46)₂ may be rewritten as two algebraic equations

$$\frac{\partial}{\partial \mathbf{T}_o} \left[(\mathbf{T} \cdot \mathbf{r})_0^{\Xi} - \int_0^{\Xi} \rho_o B' d\xi \right] = \mathbf{0}. \quad (48)$$

For inextensible strings, algebraic equations similar to (48) may be established by appending a constraint equation similar to that used in defining \mathcal{H}_{Cl} (cf. (32)) to (12) and then setting $\epsilon = A = \text{constant}$ and $\mathbf{v} = c(\partial \mathbf{r} / \partial \xi)$ in (12). The resulting equations corresponding to (48) are

$$\frac{\partial}{\partial \mathbf{T}_o} \left[(\mathbf{T} \cdot \mathbf{r})_0^{\Xi} - \int_0^{\Xi} T d\xi \right] = \mathbf{0}. \quad (49)$$

The final development is to define two other Hamiltonian systems. For elastic strings this (canonical) Hamiltonian system is defined using (48),

$$\begin{aligned} \mathcal{H}^* &= \mathcal{H}^*(q, p, \kappa) = pb + qa - \int_0^{\Xi} \rho_o B'(T_{qp}(\xi, \tau), c^2) d\xi \\ \frac{dq}{d\tau} &= \frac{\partial \mathcal{H}^*}{\partial p} = b - \int_0^{\Xi} \frac{L(T_{qp}(\xi, \tau), c^2)}{T_{qp}(\xi, \tau)} (p(\tau) + G(\xi)) d\xi, \\ \frac{dp}{d\tau} &= -\frac{\partial \mathcal{H}^*}{\partial q} = -a + \int_0^{\Xi} \frac{L(T_{qp}(\xi, \tau), c^2)}{T_{qp}(\xi, \tau)} q(\tau) d\xi, \end{aligned} \quad (50)$$

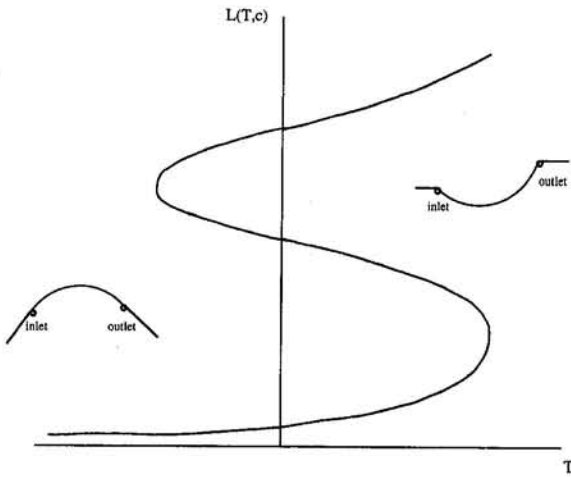


Fig. 4 A possible $L(T, c)$ for a fixed value of c . Also shown are possible convex ($T > 0$) and concave ($T < 0$) steady motions of the string.

where κ denotes the parameter set (a, b, c, Ξ, G) ,

$$T_{qp}(\xi, \tau) = \pm \sqrt{q^2(\tau) + (p(\tau) + G(\xi))^2}, \quad (51)$$

and we have used the boundary conditions (10). We emphasize that the equilibria $(q, p) = (\bar{q}, \bar{p})$ of the Hamiltonian system (50) may be identified with $(T_1(0), T_2(0))$. Consequently the equilibria of (50) provide the solutions of (48). The corresponding Hamiltonian for inextensible strings is obtained by setting $\rho_o B' = T$ in (50)₁ and $L = 1$ in (50)_{2,3}. It remains to note that the "time" parameter τ in both of these Hamiltonian systems has no physical relation to the dynamics of the string.

Once the equilibria of (50)_{2,3} have been determined then (following Antman, 1979) by using (37) with (38)_{1,2} and

$$\tan(\vartheta(\xi)) = \frac{T_2(0) + G(\xi)}{T_1(0)}, \quad (52)$$

$T(\xi)$ and $\vartheta(\xi)$ can be determined. Finally, $\mathbf{r}(\xi)$ may be calculated by integrating (46)₂ and these results then specify $n(\xi)$ (or $m(\xi)$ for inextensible strings) (cf. (34)).

In the work of Antman (1979) (cf. also Dickey, 1969 and 1974) on the stationary string ($c = 0$), a system of equations similar to (50)_{2,3} with $dq/d\tau = dp/d\tau = 0$ and $\tau = \text{constant}$ is obtained by integrating $d\mathbf{r}/d\xi$, using (36)–(38) and finally using (41). Our alternative development of (50)_{2,3} suggested itself to us by Antman's (1979) use of topological degree theory to examine the equilibria of his version of (50)_{2,3}.

6 Qualitative Features and Stability of the Steady Motions for Elastic Strings

Recall that for *convex* steady motions of the string $T(\xi) > 0$ (i.e., $n(\xi) > \rho_o \lambda(\xi) c^2$), and for *concave* steady motions of the string $T(\xi) < 0$ (i.e., $n(\xi) < \rho_o \lambda(\xi) c^2$). In this section, existence and uniqueness of these steady motions are examined for nonlinearly elastic strings. Consider the relation $(T, L(T, c))$ shown in Fig. 4. It may be subdivided into a series of branches based on the following criteria:

$$T, \frac{L}{T} \leq 0, \quad \text{and} \quad \frac{\partial L}{\partial T} \leq 0, \quad (53)$$

where (53)₂ is an alternative statement of the convexity (>0) or concavity (<0) of B' ⁴ (cf. (44)). It should be noted that

⁴The nongeneric cases of (53)₂ (i.e., $c^2 = \partial^2 A / \partial \lambda^2$) are not considered here. As may be seen from (42) strict convexity or concavity of A' does not hold and consequently the Legendre transformation (cf. (44)–(45)) is degenerate for these cases.

(53)₁ > 0 (<0) applies for *convex* (*concave*) steady motions. Referring again to Fig. 4, a constitutive relation of this form if it were presented as a constitutive equation for $\lambda(n)$ would be dismissed as physically unreasonable. It is a consequence of the dependence of L on c that it arises.

The principal motivation for distinguishing the various intervals of the relation $(T, L(T, c))$ using (53)₂ is provided by the following proposition:

Proposition 6.1: For *convex* steady motions of the string, either $\partial L / \partial T > 0$ or $\partial L / \partial T < 0$ for $\forall \xi \in [0, \Xi]$. A similar result holds for *concave* steady motions.

Proof: Suppose a *convex* steady motion exists where $T(\xi) \in (C^2([0, \Xi]), \mathcal{E})$. Without loss of generality, assume that for an interval $\xi \in [\xi_1, \bar{\xi}]$, $\partial L / \partial T > 0$, while for $\xi \in (\bar{\xi}, \xi_2]$, $\partial L / \partial T < 0$. From continuity $L(T(\bar{\xi}), c^2) = \bar{\lambda}$. For the interval where $\partial L / \partial T > 0$, (denoted branch I); $\bar{\lambda} > \lambda \forall \lambda = L(T, c)$. Similarly, for the interval where $\partial L / \partial T < 0$, (denoted branch II); $\bar{\lambda} < \lambda \forall \lambda = L(T, c)$. It should be noted that $\partial L / \partial T$ is not defined at $L(T(\bar{\xi}), c^2) = \bar{\lambda}$. It is evident after differentiating (45) with respect to ξ (after using (38)):

$$\frac{\partial \lambda}{\partial \xi} = \rho_o \frac{\partial^2 B'}{\partial T^2} \frac{\partial G}{\partial \xi} \sin(\vartheta), \quad (54)$$

that for continuity of T and consequently λ , it is necessary that $\sin(\vartheta(\bar{\xi})) = 0$. From (II) (i.e., the result following (38)) $\vartheta(\xi)$ is a strict monotonically increasing function of ξ , which implies that $\xi_1 = 0$ and $\xi_2 = \Xi$. By examining (54), for various cases the desired contradictions are obtained. For example, consider the case where $\sin(\vartheta(\xi)) < 0$ on branch I and >0 for branch II. For branch I, $\partial \lambda / \partial \xi < 0$ implying $\lambda(\xi = 0) > \bar{\lambda}$, which is the desired contradiction.

The result is similarly established for *concave* steady motions. ◆

The previous proposition can also be considered a consequence of our tacit neglect of shock-like solutions. As a consequence of Proposition 6.1, in order to examine the existence of steady motions it suffices to construct separate Hamiltonian dynamical systems (50) for the various intervals of the relation $(T, L(T, c))$ using (53) and for given values of the parameter set κ . For the case shown in Fig. 4, six dynamical systems need to be constructed (three for the *convex* steady motions alone). There is also the added difficulty that the states (q, p) of the appropriate Hamiltonian dynamical system are in some cases bounded. In order to establish the existence of an equilibrium on such intervals it is necessary to examine whether or not the appropriate Hamiltonian system (50) has an equilibrium for the given value of the parameters κ .

There are several interesting differences between the steady motions of these strings and previously reported steady motions of strings. These are reflected in the following two propositions:

Proposition 6.2: For convex steady motions of elastic strings where B' is convex (concave), if $\vartheta(\bar{\xi}) = 0$, for some $\bar{\xi} \in [0, \Xi]$, then the point of minimum (maximum) $\lambda(\xi)$ occurs when $\xi = \bar{\xi}$. Otherwise, if $\vartheta(\xi) < 0$, $\forall \xi \in [0, \Xi]$, then the point of minimum (maximum) $\lambda(\xi)$ occurs when $\xi = \Xi$, and if $\vartheta(\xi) > 0$, $\forall \xi \in [0, \Xi]$, then the point of minimum (maximum) $\lambda(\xi)$ occurs when $\xi = 0$.

Proof: To establish the point of minimum (maximum) stretch λ (54) is used. If at some point $\vartheta(\bar{\xi}) = 0$, for some $\bar{\xi} \in [0, \Xi]$, the first statement can be readily established by taking the second partial derivative of (54) with respect to ξ and then using the convexity (concavity) of B' and the definition of G (cf. (35)). The remaining statements where $\vartheta(\xi) \neq 0$, $\forall \xi \in [0, \Xi]$, follow from (54) and monotonicity of $\vartheta(\xi)$. ◆

A similar result can also be established for *concave* steady motions:

Proposition 6.3: For *concave* steady motions of elastic strings where B' is convex (concave), if $\vartheta(\bar{\xi}) = 0$ for some $\bar{\xi} \in [0, \Xi]$, then the point of maximum (minimum) $\lambda(\xi)$ occurs when $\xi = \bar{\xi}$. Otherwise, if $\vartheta(\xi) < 0 \forall \xi \in [0, \Xi]$ then the point of maximum (minimum) $\lambda(\xi)$ occurs when $\xi = \Xi$ and if $\vartheta(\xi) > 0 \forall \xi \in [0, \Xi]$ then the point of maximum (minimum) $\lambda(\xi)$ occurs when $\xi = 0$.

In words, Propositions 6.2–3 state that it is possible to have a convex steady motion of a string where the maximum stretch occurs at its lowest point. Furthermore, it is possible to have a concave steady motion where the minimum stretch in the string occurs at its highest point.

Dependent on the nature of the interval of (L, T) of interest, a uniqueness result can be established without recourse to a detailed examination of the Hamiltonian vector field. The method of proof follows the earlier cited work of Antman and Dickey.

Theorem 6.4: For *convex* (*concave*) steady motions of an elastic string, if B' is convex (concave) and the Hamiltonian system defined by (50) has an equilibrium, then it is unique. Consequently there is a unique solution to the boundary value problem and there are no other solutions on this particular interval of $(T, L(T, c))$.

Proof: Standard analysis shows that for a *convex* (*concave*) steady motion, the Hessian of \mathcal{H}^* with respect to (q, p) is negative (positive) definite (i.e., \mathcal{H}^* is strictly concave (*convex*)). Consequently the equilibrium (\bar{q}, \bar{p}) is unique. The remainder of the result follows from the construction of \mathcal{H}^* and its vector field. ♦

For intervals of (L, T) when B' is not strictly convex (concave), the definiteness of \mathcal{H}^* for *convex* (*concave*) steady motions is questionable and necessitates an examination of the integral terms on the right-hand sides of (50)_{2,3} for each $L(T, c)$ separately. A similar situation is encountered when examining *concave* equilibria of the stationary string (cf. Antman (1979, Section 3) and Dickey (1969 and 1974) where they are known as compressive solutions). After incorporating the results of Section 5, their analyses can be used to conclude the possible existence of multiple *concave* steady motions of the string. For *convex* steady motions the analysis is similar and nonuniqueness of *convex* steady motions are also to be expected.

There are two cases for elastic strings where results can be established without recourse to the estimates alluded to in the previous paragraph. The first of these is for *convex* steady motions and the second is for *concave* steady motions.

Theorem 6.5: For *convex* steady motions of *stiff* (nonlinearly elastic) strings, A' is a strictly convex function of λ , $\forall c$, and λ has a unique lower bound λ^* :

$$\lambda^* \rho_o c^2 = n(\lambda^*), \quad (55)$$

which is a monotonically increasing function of c^2 . If $a > 0$, then there is a unique steady solution of the boundary value problem $\forall c$ where $n(\xi) > \rho_o \lambda c^2$ and if $b = 0$, then this solution is nonlinearly stable $\forall c$.

Proof: For *convex* steady motions $n(\lambda) - \rho_o \lambda c^2 > 0$ and from the definition of a *stiff* string (cf. (8)) $\partial^2 A / \partial \lambda^2 > n / \rho_o \lambda$, consequently $\partial^2 A / \partial \lambda^2 > c^2$, and the strict convexity of A' follows. This implies that $n(\lambda) - \rho_o \lambda c^2$ is a strict monotonically increasing function of λ , and it is readily seen that (55) has a unique solution λ^* , which is a lower bound for λ (cf. (II) and Fig. 2). The monotonicity of λ^* as a function of c^2 is established by differentiating (55):

$$\left(\frac{\partial n(\lambda)}{\partial \lambda} - \rho_o c^2 \right) \frac{\partial \lambda^*}{\partial c^2} = \rho_o \lambda^*, \quad (56)$$

and using the convexity of A' . For *stiff* strings (53)₁ holds $\forall \lambda$

$> \lambda^*$ and $\forall T > T(\lambda^*) = 0$. Uniqueness then follows from theorem 6.4.

When $b = 0$, then from (35), (50)₂ and a mean value theorem, $T_2(0) = \rho_o \lambda \Xi / 2$. From (52) and Proposition 6.2, the steady motion is symmetric about $\xi = \Xi/2$ and the boundary restrictions placed on the use of the stability criteria are satisfied (cf. (18)). Referring to theorem 4.1, the steady motion can be concluded to be nonlinearly stable. ♦

Apart from the case $b = 0$, the previous theorem implies that even if the *convex* steady motion loses stability, there will be no other additional neighboring *convex* steady motions of this type present after the loss of stability.

Corollary 6.6: For *convex* steady motions of linearly elastic strings, A' is a strictly convex function of λ , $\forall c^2 < E / \rho_o$, and λ has a unique lower bound $\lambda^* = E / (E - \rho_o c^2)$ where E is Young's modulus of elasticity. If $a > 0$, then there is a unique *convex* steady motion and furthermore if $b = 0$, then this steady solution is nonlinearly stable $\forall c^2 < E / \rho_o$.

Proof: The proof follows from theorem 6.5 and corollary 4.2. ♦

The physical reasonableness of the results of theorem 6.5 and corollary 6.6 should be questioned. In particular, these results imply that the stretch λ must become unbounded for sufficiently large c . Consequently the string will have an indefinite length. To investigate this situation further it is appropriate to consider *convex* steady motions of *soft* strings. From a result of Healey (1990, Lemma 4.3) that all *soft* strings are initially (*locally*) *stiff* for $\lambda \in (1, \lambda_1)$, it follows that given $A(\lambda)$ as shown in Fig. 3, a sufficiently small c and appropriately chosen (a, b, Ξ, G) , a *convex* steady motion where $\lambda(\xi) \in (1, \lambda_1)$ will exist. As c increases from 0, $\lambda(\xi)$ necessarily increases and the string will eventually become *locally soft* at a particular $\xi = \bar{\xi} \in [0, \Xi]$ (i.e., from (8), (42) and (44): $\partial L / \partial T(T(\bar{\xi})) > L(T(\bar{\xi}))/T(\bar{\xi}) > 0$). As c increases further, the interval of $(T, L(T, c))$ where $\lambda(\xi) \in L(T, c)$, $T > 0$ and $(1 = L(T = 0, c = 0))$ will diminish and eventually disappear (cf. Fig. 3). In conclusion, the *convex* steady motion ceases to exist for a finite value of c . If $b = 0$, then this steady motion will initially be stable (from theorem 4.1). However, when the string described above becomes *locally soft* the functional \mathcal{H}_{CE} (cf. (24)) becomes indefinite and stability can no longer be concluded using the methods of Section 4.

The proof of the result for *concave* steady motions is similar to the latter part of the theorem 6.5. A particular interval of $(T, L(T, c))$ which corresponds to that which is about to be described may be seen in Fig. 3. Such an interval will not arise in *stiff* strings.

Theorem 6.7: For *concave* steady motions of *stiff* strings, if B' is a strictly convex function of λ , $\forall c > c_o$, $\forall \lambda > \lambda^*(c)$, and $a > 0$, then there is a unique steady solution of the boundary value problem $\forall c > c_o$ where $n(\xi) < \rho_o \lambda c^2$.

It remains to note that for the stability criteria developed here, the functional \mathcal{H}_{CE} loses definiteness for all *concave* steady motions. This indefiniteness holds even when the heuristic criterion for stabilization of the *concave* steady motions, $n(\xi) (= \mathbf{n}(\xi) \cdot \mathbf{e}_1(\xi)) > 0$, applies.

7 Qualitative Features and Stability of the Steady Motions for Inextensible Strings

Before establishing existence and uniqueness results for inextensible strings, the following well known restriction on the boundary parameters (a, b) is noted. For any solutions of (9) and (10) of an inextensible string, (a, b) must satisfy the inequality,

$$a^2 + b^2 < \Xi^2. \quad (57)$$

For inextensible strings it is possible to explicitly calculate the

equations describing the Hamiltonian vector field (50) which are valid for both $T_{qp} \leq 0$:

$$\begin{aligned} \frac{dq}{d\tau} &= b - \frac{1}{\rho_0 g} [\sqrt{q^2 + (p + \rho_0 g \Xi)^2} - \sqrt{q^2 + p^2}], \\ \frac{dp}{d\tau} &= -a + \frac{|q|}{\rho_0 g} \\ &\quad \times \log \left[\frac{p + \rho_0 g \Xi + \sqrt{q^2 + (p + \rho_0 g \Xi)^2}}{p + \sqrt{q^2 + p^2}} \right], \quad (58) \end{aligned}$$

where $G(\xi) = \rho_0 g \xi$ was used in evaluating the integrals.

For given values of a and b which satisfy (57), numerical simulations of (58) show that this system has two equilibria (\bar{q}_1, \bar{p}_1) and (\bar{q}_2, \bar{p}_2) , where $\bar{q}_1 > 0$ and $\bar{q}_2 < 0$ (cf. Fig. 5). From the earlier discussion in Section 5, the former corresponds to a *convex* steady motion and the latter to a *concave* steady motion. These equilibrium values also provide $(T_1(0), T_2(0))$. To establish the existence of these equilibria is not convenient to use (58) directly. Instead the Hamiltonian \mathcal{H}^* shall be used, for the two cases of $T_{qp} > 0$ and < 0 . Using (50)₁, with $\rho_0 B = T$ as the string is inextensible, it can be shown that for $T_{qp} > 0$, \mathcal{H}^* is a strictly concave function of (q, p) and for $T_{qp} < 0$ it is strictly convex. Furthermore it can be shown that $\infty > b - \partial \mathcal{H}^*/\partial p > 0$ and $\infty > a - \partial \mathcal{H}^*/\partial q > -\infty$. For the particular case $b = 0$, then the steady motion satisfies the boundary restrictions required to use the stability theorem established in Section 4. Referring there to theorem 4.3, the *convex* steady motion will be nonlinearly stable for all c . This last statement is in agreement with a related result of Simpson (1972). However the tension in the string $m(\xi)$ will necessarily become unbounded as c is increased indefinitely. In summary:

Theorem 7.1: For an inextensible string if $a^2 + b^2 < \Xi^2$ and $a > 0$, then there is a unique *convex* steady motion for all c where $T(\xi) > 0$ (i.e., $m(\xi) > \rho_0 c^2$). Similarly there is a unique *concave* steady motion where $T(\xi) > 0$ (i.e., $m(\xi) < \rho_0 c^2$). If, in addition, $b = 0$, then the *convex* motion is nonlinearly stable for all c .

The uniqueness results of theorem 7.1 may also be obtained by deriving a second-order differential equation for $y(x)$ using Eq. (52).⁵ The solution of this differential equation is identical to the classical catenary solution which satisfies the boundary condition $y(x = 0) = 0$:

$$y(x) = \frac{T_1(0)}{\rho_0 g} \left[\cosh \left(\frac{\rho_0 g}{T_1(0)} (x - \bar{x}) \right) - \cosh \left(\frac{\rho_0 g}{T_1(0)} \bar{x} \right) \right], \quad (59)$$

where $T_1(0) = \pm(m(0) - \rho_0 c^2) \cos(\vartheta(0))$, \bar{x} is specified by the remaining boundary condition $y(x = a) = b$, and $T_1(0)$ is as yet unknown. Provided the boundary parameters (a, b) satisfy (57), the existence of a unique $T_1(0) > 0$ (i.e., a *convex* steady motion) and a unique $T_1(0) < 0$ (i.e., a *concave* steady motion) can be readily shown by using the integral of $d\xi/dx$ with respect to x . The solution $y(x)$ is in agreement with the observation of Routh (1882, Section 524) and the calculation of Love (1897, Section 270). It also agrees with those of Perkins and Mote (1989, Eqs. (7)–(8)) and Simpson (1972, Eq. (14)) upon taking the appropriate limits of their results.

⁵ For elastic strings a differential equation for $y(x)$ may also be obtained. The reader is referred to Antman (1979) from which it may be readily derived after some suitable modifications.

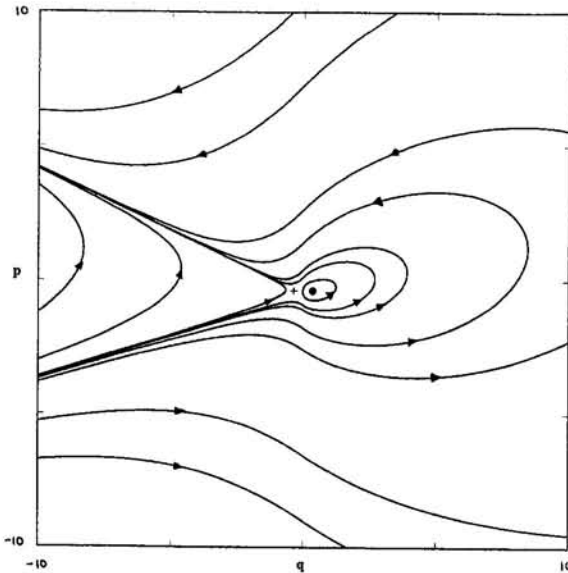


Fig. 5 Phase portraits of the dynamical system (58) ($\rho_0 g = 1$, $\Xi = 1$, $a = 0.8$, $b = 0.2$). The equilibria \bullet ($= (\bar{q}_1, \bar{p}_1) = (.3552, .3764)$) and $+$ ($= (\bar{q}_2, \bar{p}_2) = (.3552, -.3764)$) correspond to the *convex* and *concave* motions, respectively. For other values of the parameters which satisfy (57) the phase portraits are qualitatively similar.

Acknowledgments

Figure 5 was obtained using the dynamical systems package *dstool* from the Center of Applied Mathematics, Cornell University, Ithaca, NY. The author is also grateful to three anonymous reviewers for their helpful criticisms and suggestions.

References

- Abarbanel, H. D. I., Holm, D. D., Marsden, J. E., and Ratiu, T. S., 1986, "Nonlinear Stability Analysis of Stratified Fluid Equilibria," *Philosophical Transactions of the Royal Society of London*, Vol. A318, pp. 349–409.
- Abarbanel, H. D. I., and Holm, D. D., 1987, "Nonlinear Stability Analysis of Inviscid Flows in Three Dimensions: Incompressible Fluids and Barotropic Fluids," *Physics of Fluids*, Vol. 30, pp. 3369–3382.
- Antman, S. S., 1979, "Multiple Equilibrium States of Nonlinearly Elastic Strings," *SIAM Journal of Applied Mathematics*, Vol. 37, pp. 588–604.
- Antman, S. S., and Reeken, M., 1987, "The Drawing and Whirling of Strings: Singular Global Multiparameter Bifurcation Problems," *SIAM Journal on Mathematical Analysis*, Vol. 18, pp. 337–365.
- Casey, J., and Naghdi, P. M., 1991, "A Lagrangian Description of Vorticity," *Archive for Rational Analysis and Mechanics*, Vol. 115, pp. 1–15.
- Clebsch, A., 1860, "Ueber die Gleichgewichtsfigur eines biegsamen Fadens," *Crelle Journal für die reine und angewandte Mathematik*, Vol. 57, pp. 93–110.
- Dickey, R. W., 1969, "The Nonlinear String under a Vertical Load," *SIAM Journal of Applied Mathematics*, Vol. 17, pp. 172–178.
- Dickey, R. W., 1976, *Bifurcation Problems in Nonlinear Elasticity*, Pitman, London.
- Healey, T. J., 1990, "Stability and Bifurcation of Rotating Nonlinearly Elastic Loops," *Quarterly of Applied Mathematics*, Vol. 48, pp. 679–698.
- Healey, T. J., and Papadopoulos, J. N., 1990, "Steady Axial Motions of Strings," *ASME JOURNAL OF APPLIED MECHANICS*, Vol. 57, pp. 785–787.
- Knops, R. J., and Wilkes, E. W., 1966, "On Movchan's Theorems for Stability of Continuous Systems," *International Journal of Engineering Science*, Vol. 4, pp. 303–329.
- Lamb, H., 1929, *Dynamics*, 2nd reprinted ed., Cambridge University Press, Cambridge, U.K.
- Lamb, H., 1945, *Hydrodynamics*, 6th ed., Dover, New York.
- Love, A. E. H., 1897, *Theoretical Mechanics. An Introductory Treatise on the Principles of Dynamics*, Cambridge University Press, Cambridge, U.K.
- Naghdi, P. M., 1982, "Finite Deformation of Rods and Shells," *Proceedings of the IUTAM Symposium on Finite Elasticity*, D. E. Carlson, and R. T. Shield, eds., Martinus Nijhoff, The Hague, pp. 47–103.
- Nashed, M. Z., 1966, "Some Remarks on Variations and Differentials," *American Mathematical Monthly*, Vol. 73, No. 4, pp. 63–76.
- O'Reilly, O. M., and Varadi, P., 1995, "Elastic Equilibria of Translating Cables," *Acta Mechanica*, Vol. 118, pp. 189–206.

Perkins, N. C., and Mote, C. D., 1987, "Three Dimensional Vibration of Travelling Elastic Cables," *Journal of Sound and Vibration*, Vol. 114, pp. 325–340.

Perkins, N. C., and Mote, C. D., 1989, "Theoretical and Experimental Stability of Two Translating Cable Equilibria," *Journal of Sound and Vibration*, Vol. 128, pp. 397–410.

Rowth, E. J., 1882, *The Advanced Part of a Treatise on the Dynamics of Rigid Bodies*, 4th ed., Macmillan, London.

Simpson, A., 1972, "On the Oscillatory Motions of Translating Elastic Cables," *Journal of Sound and Vibration*, Vol. 20, pp. 177–189.

Troutman, J. L., 1983, *Variational Calculus with Elementary Convexity*, Springer-Verlag, New York.

Some Phenomena of Cracks Perpendicular to an Interface Between Dissimilar Orthotropic Materials

J. C. Sung
Professor.

J. Y. Liou
Graduate Student.

Y. Y. Lin
Graduate Student.

Department of Civil Engineering,
National Cheng Kung University,
Tainan, Taiwan 70101, R.O.C.

The problem of two aligned orthotropic materials bonded perfectly along the interface with cracks embedded in either one or both of the materials while their directions being perpendicular to the interface is considered. A system of singular integral equations for general anisotropic materials is derived. Employing four effective material parameters proposed by Krenk and introducing four generalized Dundurs' constants, the kernel functions appearing in the integrals are converted into real forms for the present problem which are keys to the present study. The kernel functions for isotropic dissimilar materials can be deduced from the present results directly, no any limiting process is needed. These kernel functions are then employed to investigate the singular behaviors for stresses at the point on the interface. Characteristic equation which determines the power of singularity for stresses is given in real forms for the case of cracks that are going through the interface. Studies of the characteristic equation reveal that the singular nature for the stresses could vanish for some material combinations and the singular nature for the stresses is found to be independent of the replacement of the material parameter Δ by Δ^{-1} . The kernel functions developed are further used to explore analytically some interesting phenomena for the stress intensity factors, which are discussed in detail in the present context. Some numerical results for the stress intensity factors for a typical dissimilar materials are also given.

1 Introduction

The problems of a crack or cracks near an interface between dissimilar materials have long interest in fracture mechanics. A considerable progress has been made for isotropic materials (Cook and Erdogan, 1972; Erdogan and Biricikoglu, 1973; Erdogan, 1972; Hutchinson et al., 1987; etc.). As to anisotropic materials, the problem of a crack with arbitrary size and orientation near the interface has been considered by Miller (1989) in which the stress intensity factors are computed numerically for mismatch materials. For the problem of two aligned orthotropic materials with a semi-infinite crack perpendicular to the interface has been investigated recently by Gupta et al. (1992). The importance of such an analysis in predicting the overall performance of a composite material has also been addressed in Gupta et al. (1992).

In this paper, the problem of two aligned orthotropic materials bonded perfectly along the interface with cracks embedded in either one or both of the materials while their directions being perpendicular to the interface is considered. A system of singular integral equations is derived by means of distribution of dislocations along the crack faces, wherein the fundamental solution of point dislocation acting in a general anisotropic bimaterials, obtained by Ting (1992) and Suo (1990), is used. By introducing four generalized Dundurs' constants and employing four effective material parameters proposed by Krenk (1979), the kernel functions, originally in complex forms, are

then converted into real forms that are useful for the present study. These kernel functions can be reduced directly to those for isotropic bimaterials so long as the actual material parameters corresponding to the isotropic bimaterials are substituted in, contrast to the common analysis of orthotropic materials from which the isotropic results usually can not be deduced directly. The kernel functions can also be reduced to those for a half-plane solid with traction-free boundary, which has been studied by the present authors (Sung and Liou, 1994) for more general material alignments, by letting one of the materials being very soft. The kernel functions are then used to investigate the singular behaviors at the point on the interface for the case when crack is through the interface. The characteristic equation which determines the power of singularity for stresses is given in real forms and the singular nature for the stresses is found to be independent of the replacement of the material parameter Δ by Δ^{-1} . Furthermore, there exists some material compositions such that the stresses at the point of interface would be finite. Analysis of this type of singularities for isotropic bimaterial problems has been given, e.g., by Erdogan and Biricikoglu (1973), their characteristic equations can be recovered from the present analysis. It is noted that analysis of the singular behaviors for the problem of one of the crack's tip terminating at the interface has been given by Sung and Liou (1994). Their results are for more general material alignments and some features about the singular behaviors for the stresses have been discussed in detail in that paper. Interested readers please refer to that paper (Sung and Liou, 1994). The kernel functions developed are further employed to investigate the behaviors of the stress intensity factors for cracks subjected to self-equilibrating loadings. Many interesting phenomena, which will be discussed in the present context, can be observed directly from the explicit expressions for the kernel functions. Finally, some numerical results for the problem of a cracked isotropic material jointed perfectly to a crack-free orthotropic material are given.

Contributed by the Applied Mechanics Division of THE AMERICAN SOCIETY OF MECHANICAL ENGINEERS for publication in the ASME JOURNAL OF APPLIED MECHANICS.

Discussion on this paper should be addressed to the Technical Editor, Professor Lewis T. Wheeler, Department of Mechanical Engineering, University of Houston, Houston, TX 77204-4792, and will be accepted until four months after final publication of the paper itself in the ASME JOURNAL OF APPLIED MECHANICS.

Manuscript received by the ASME Applied Mechanics Division, Mar. 16, 1994; final revision, Dec. 20, 1994. Associate Technical Editor: C. F. Shih.

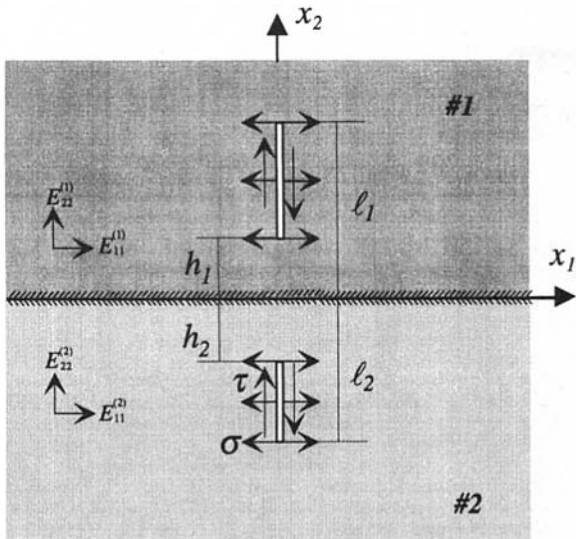


Fig. 1 Geometry of the problem

2 Singular Integral Equations

The problem considered here is shown in Fig. 1. Two aligned orthotropic materials are bonded perfectly along the interface while cracks may exist in either one or both of the materials, their directions being perpendicular to the interface. The faces of cracks are subjected to self-equilibrating loadings. It is known that the above problem can be formulated by distributing dislocation densities on the crack faces. By summing up the tractions induced by these dislocation densities, and then enforcing, on the crack faces, the satisfactions of the tractions induced by these dislocation densities, one leads to a system of singular integral equations from which the unknown dislocation densities can be determined. Although the singular integral equations can be derived for general anisotropic bimaterial problems, the kernel functions involve certain complex vector functions multiplied by matrices whose elements are determined by solving a sextic eigenvalue problem. Due to this fact, the results will be usually in complex form which are difficult to interpret. We will see in this section that for the present problem under consideration, by introducing four new generalized Dundurs' constants and by using the effective material constants proposed by Krenk (1979), the derived singular integral equations turn out to be in a real form from which many interesting phenomena can be observed.

To formulate the singular integral equations, the basic solution due to a point dislocation \mathbf{b} acting in a crack-free bimaterial problem has to be determined. This solution has been considered by Ting (1992) and Suo (1990). Results are valid for any two general anisotropic materials and are expressed in complex forms due to the fact that is mentioned above. For further details, please refer to the paper, e.g., by Ting (1992) (or Eshelby et al., 1953; Stroh, 1958). The result of Ting's (1992) is given by

$$\phi = 2 \operatorname{Re} \{ \mathbf{B}^{(\alpha)} f(z) \} \quad (1)$$

where ϕ is the stress function and function $f(z)$ is given in Appendix A (only those items that are relevant to the present discussions are listed). Superscript α in Eq. (1) is 1 (or 2) when point dislocation is acting at material #1 (or #2). Besides, superscript α with parenthesis in matrix \mathbf{B} and in what follows will denote quantity that is associated with material α ($\alpha = 1, 2$). Matrix $\mathbf{B}^{(\alpha)}$ in Eq. (1) is defined by

$$\mathbf{B}^{(\alpha)} = \mathbf{R}^{(\alpha)T} \mathbf{A}^{(\alpha)} + \mathbf{T}^{(\alpha)} \mathbf{A}^{(\alpha)} \mathbf{P}^{(\alpha)} \quad (2)$$

where $\mathbf{A}^{(\alpha)} = [\mathbf{a}_1^{(\alpha)}, \mathbf{a}_2^{(\alpha)}]$ and $\mathbf{P}^{(\alpha)} = \operatorname{diag} \{ p_1^{(\alpha)}, p_2^{(\alpha)} \}$ are formed

by the eigenvectors $\mathbf{a}_k^{(\alpha)}$, $k = 1, 2$ and eigenvalues $p_k^{(\alpha)}$, with $\operatorname{Im} \{ p_k^{(\alpha)} \} > 0$, $k = 1, 2$, respectively. The pair $(p_k^{(\alpha)}, \mathbf{a}_k^{(\alpha)})$, $k = 1, 2$ satisfied the following eigenvalue problem:

$$\begin{bmatrix} C_{11}^{(\alpha)} + p_k^{(\alpha)2} C_{66}^{(\alpha)} & p_k^{(\alpha)} (C_{12}^{(\alpha)} + C_{66}^{(\alpha)}) \\ p_k^{(\alpha)} (C_{12}^{(\alpha)} + C_{66}^{(\alpha)}) & C_{66}^{(\alpha)} + p_k^{(\alpha)2} C_{22}^{(\alpha)} \end{bmatrix} \mathbf{a}_k^{(\alpha)} = \mathbf{0}, \quad (k = 1, 2) \quad (3)$$

where $C_{nl}^{(\alpha)}$, ($n, l = 1, 2$ or 6) are the elastic moduli which relates the stress components to the strain components by

$$\begin{Bmatrix} \sigma_{11} \\ \sigma_{22} \\ \sigma_{12} \end{Bmatrix} = \begin{bmatrix} C_{11}^{(\alpha)} & C_{12}^{(\alpha)} & 0 \\ C_{12}^{(\alpha)} & C_{22}^{(\alpha)} & 0 \\ 0 & 0 & C_{66}^{(\alpha)} \end{bmatrix} \begin{Bmatrix} \epsilon_{11} \\ \epsilon_{22} \\ 2\epsilon_{12} \end{Bmatrix}. \quad (4)$$

The matrices $\mathbf{R}^{(\alpha)}$ and $\mathbf{T}^{(\alpha)}$ in (2) are defined by

$$\mathbf{R}^{(\alpha)} = \begin{bmatrix} 0 & C_{12}^{(\alpha)} \\ C_{66}^{(\alpha)} & 0 \end{bmatrix} \quad (5)$$

and

$$\mathbf{T}^{(\alpha)} = \begin{bmatrix} C_{66}^{(\alpha)} & 0 \\ 0 & C_{22}^{(\alpha)} \end{bmatrix}, \quad (6)$$

respectively. In Eq. (1), $z_k = x_1 + p_k^{(\alpha)} x_2$, ($k = 1, 2$). The traction at any point on a plane curve whose unit outward normal vector is \mathbf{n} can be computed from the stress function by

$$t_n = \frac{\partial \phi}{\partial s} \quad (7)$$

where s is the arc length measured along the curve. Positive direction of \mathbf{n} is on the left-hand side when one faces the direction of increasing s while the material is located on the right-hand side. With the known stress function given by Eq. (1) and the tractions evaluated by Eq. (7), one can follow the procedures described above to obtain the following system of singular integral equations:

$$\begin{aligned} -\frac{1}{2\pi} \left\{ \int_{h_1}^{l_1} \frac{\mathbf{b}^{(1)}(t)}{t - \xi} dt + \int_{h_1}^{l_1} \mathbf{K}^{11}(\xi, t) \mathbf{b}^{(1)}(t) dt \right. \\ \left. + \int_{h_2}^{l_2} \mathbf{K}^{12}(\xi, t) \mathbf{b}^{(2)}(t) dt \right\} = t_\eta(\xi), \quad h_1 \leq \xi \leq l_1 \\ -\frac{1}{2\pi} \left\{ \int_{h_2}^{l_2} \frac{\mathbf{b}^{(2)}(t)}{t - \xi} dt + \int_{h_2}^{l_2} \mathbf{K}^{22}(\xi, t) \mathbf{b}^{(2)}(t) dt \right. \\ \left. + \int_{h_1}^{l_1} \mathbf{K}^{21}(\xi, t) \mathbf{b}^{(1)}(t) dt \right\} = t_\eta(\xi), \quad h_2 \leq \xi \leq l_2 \quad (8) \end{aligned}$$

with auxiliary conditions

$$\int_{h_1}^{l_1} \mathbf{b}^{(1)}(t) dt = \mathbf{0}, \quad \int_{h_2}^{l_2} \mathbf{b}^{(2)}(t) dt = \mathbf{0} \quad (9)$$

which have to be satisfied for single displacements around a closed contour surrounding each crack. In the above equation, t_η is the traction applied on the crack faces. $\mathbf{b}^{(\alpha)}(t)$ ($\alpha = 1, 2$) is defined by

$$\begin{aligned} \mathbf{b}^{(1)}(t) &= \mathbf{L}^{(1)} \mathbf{b}_1(t), \quad h_1 \leq t \leq l_1 \\ \mathbf{b}^{(2)}(t) &= -\mathbf{L}^{(2)} \mathbf{b}_2(t), \quad h_2 \leq t \leq l_2 \quad (10) \end{aligned}$$

while $b_1(t)$ and $b_2(t)$ are dislocation densities each defined on different crack faces. $\mathbf{L}^{(\alpha)}$ is the matrix defined by (Ting, 1986)

$$\mathbf{L}^{(\alpha)} = -2i\mathbf{B}^{(\alpha)}\mathbf{B}^{(\alpha)T} \quad (11)$$

which is real, symmetric, and positive definite (Chadwick and Smith, 1977), $i = \sqrt{-1}$. The kernel functions in Eq. (8) are given by

$$\begin{aligned} \mathbf{K}^{11}(\xi, t) &= -\sum_{k=1}^2 \sum_{j=1}^2 \operatorname{Re}\{F_{kj}^{11}(\xi, t)\mathbf{E}_k^{(1)}\mathbf{M}^{11}\overline{\mathbf{E}_j^{(1)}}\} \\ \mathbf{K}^{12}(\xi, t) &= \sum_{k=1}^2 \sum_{j=1}^2 \operatorname{Re}\{F_{kj}^{12}(\xi, t)\mathbf{E}_k^{(1)}\mathbf{M}^{12}\mathbf{E}_j^{(2)}\} \\ \mathbf{K}^{22}(\xi, t) &= -\sum_{k=1}^2 \sum_{j=1}^2 \operatorname{Re}\{F_{kj}^{22}(\xi, t)\mathbf{E}_k^{(2)}\mathbf{M}^{22}\overline{\mathbf{E}_j^{(2)}}\} \\ \mathbf{K}^{21}(\xi, t) &= \sum_{k=1}^2 \sum_{j=1}^2 \operatorname{Re}\{F_{kj}^{21}(\xi, t)\mathbf{E}_k^{(2)}\mathbf{M}^{21}\mathbf{E}_j^{(1)}\} \end{aligned} \quad (12)$$

where $\mathbf{E}_j^{(\alpha)} = \mathbf{B}^{(\alpha)}\mathbf{I}_1\mathbf{B}^{(\alpha)T}$, $\mathbf{I}_1 = \operatorname{diag}\langle 1, 0 \rangle$, $\mathbf{I}_2 = \operatorname{diag}\langle 0, 1 \rangle$ and

$$\begin{aligned} F_{kj}^{11} &= \frac{p_k^{(1)}}{p_k^{(1)}\xi - \bar{p}_j^{(1)}t} \\ F_{kj}^{12} &= \frac{p_k^{(1)}}{p_k^{(1)}\xi + p_j^{(2)}t} \\ F_{kj}^{22} &= \frac{p_k^{(2)}}{p_k^{(2)}\xi - \bar{p}_j^{(2)}t} \\ F_{kj}^{21} &= \frac{p_k^{(2)}}{p_k^{(2)}\xi + p_j^{(1)}t}. \end{aligned} \quad (13)$$

Matrices $\mathbf{M}^{\alpha\beta}$ ($\alpha, \beta = 1, 2$) in Eq. (12) are given by

$$\begin{aligned} \mathbf{M}^{11} &= \mathbf{H}^{-1}\bar{\mathbf{G}}, \quad \mathbf{M}^{22} = -\overline{\mathbf{H}^{-1}\mathbf{G}}, \\ \mathbf{M}^{21} &= \mathbf{I} + \overline{\mathbf{M}^{11}}, \quad \mathbf{M}^{12} = \mathbf{I} + \overline{\mathbf{M}^{22}} \\ & \quad (\mathbf{I} \text{ is a } 2 \times 2 \text{ unit matrix}). \end{aligned} \quad (14)$$

where \mathbf{H} and \mathbf{G} are expressed as

$$\mathbf{H} = (i\mathbf{A}^{(1)}\mathbf{B}^{(1)T}) + \overline{(i\mathbf{A}^{(2)}\mathbf{B}^{(2)T})} \quad (15)$$

and

$$\mathbf{G} = (i\mathbf{A}^{(1)}\mathbf{B}^{(1)T}) - (i\mathbf{A}^{(2)}\mathbf{B}^{(2)T}), \quad (16)$$

$$\mathbf{B}^{(\alpha)} = \begin{cases} \sqrt{\frac{E^{(\alpha)}}{8\omega_+^{(\alpha)}\omega_-^{(\alpha)}}} \begin{bmatrix} -[\delta^{(\alpha)}(\omega_+^{(\alpha)} + \omega_-^{(\alpha)})]^{1/2}e^{i\pi/4} & [\delta^{(\alpha)}(\omega_+^{(\alpha)} - \omega_-^{(\alpha)})]^{1/2}e^{-i\pi/4} \\ [\delta^{(\alpha)}(\omega_+^{(\alpha)} + \omega_-^{(\alpha)})]^{-1/2}e^{-i\pi/4} & [\delta^{(\alpha)}(\omega_+^{(\alpha)} - \omega_-^{(\alpha)})]^{-1/2}e^{i\pi/4} \end{bmatrix}, & \kappa^{(\alpha)} > 1 \\ \sqrt{\frac{E^{(\alpha)}}{8\omega_+^{(\alpha)}\omega_-^{(\alpha)}}} \begin{bmatrix} [\delta^{(\alpha)}(\omega_-^{(\alpha)} - i\omega_+^{(\alpha)})]^{1/2}e^{i\pi/4} & -[\delta^{(\alpha)}(\omega_-^{(\alpha)} + i\omega_+^{(\alpha)})]^{1/2}e^{i\pi/4} \\ [\delta^{(\alpha)}(\omega_-^{(\alpha)} - i\omega_+^{(\alpha)})]^{-1/2}e^{i\pi/4} & [\delta^{(\alpha)}(\omega_-^{(\alpha)} + i\omega_+^{(\alpha)})]^{-1/2}e^{i\pi/4} \end{bmatrix}, & |\kappa^{(\alpha)}| < 1 \end{cases} \quad (23)$$

respectively. Here we have to mention that matrices $(i\mathbf{A}^{(1)}\mathbf{B}^{(1)T})$ and $(i\mathbf{A}^{(2)}\mathbf{B}^{(2)T})$ are both positive definite Hermitian, hence matrix \mathbf{H} will have this property too and its inverse will exist. For later reference, matrices \mathbf{H} and \mathbf{G} are further written in the following form:

$$\mathbf{H} = \mathbf{D} + i\mathbf{W} \quad (17)$$

and

$$\mathbf{G} = \mathbf{U} + i\mathbf{W} \quad (18)$$

where

$$\begin{aligned} \mathbf{D} &= \operatorname{Re}\{\mathbf{H}\} = (\mathbf{L}^{(1)T} + \mathbf{L}^{(2)T}) \\ \mathbf{W} &= \operatorname{Im}\{\mathbf{H}\} = (-\mathbf{S}^{(1)}\mathbf{L}^{(1)T} + \mathbf{S}^{(2)}\mathbf{L}^{(2)T}) \\ \mathbf{U} &= \operatorname{Re}\{\mathbf{G}\} = \mathbf{L}^{(1)T} - \mathbf{L}^{(2)T} \end{aligned} \quad (19)$$

and $\mathbf{S}^{(\alpha)} = i(2\mathbf{A}^{(\alpha)}\mathbf{B}^{(\alpha)T} - \mathbf{I})$ is a real matrix (Ting, 1986).

The kernel functions shown in Eq. (12) will now be rewritten in real forms that are more suitable for further investigations. To this end, first let's introduce the following four generalized Dundurs' constants as follows:

$$\begin{aligned} \alpha_1 &= \frac{-U_{11}}{D_{11}}, \quad \alpha_2 = \frac{-U_{22}}{D_{22}}, \\ \beta_1 &= \frac{-W_{12}}{D_{11}}, \quad \beta_2 = \frac{-W_{12}}{D_{22}} \end{aligned} \quad (20)$$

where $D_{\alpha\alpha}$ and $U_{\alpha\alpha}$ (no sum) are the diagonal components of the matrices \mathbf{D} and \mathbf{U} , respectively. W_{12} is the element of first row and second column of \mathbf{W} . Next, instead of expressing the kernel functions in terms of the elastic moduli $C_{nl}^{(\alpha)}$, ($n, l = 1, 2$ or 6), we will employ four effective parameters proposed by Krenk (1979), the usefulness of this adoption will be seen in the following. These parameters are related to the elastic moduli by

$$\begin{aligned} C_{11}^{(\alpha)} &= \frac{\delta^{(\alpha)2}E^{(\alpha)}}{1 - \nu^{(\alpha)2}}, \quad C_{12}^{(\alpha)} = \frac{\nu^{(\alpha)}E^{(\alpha)}}{1 - \nu^{(\alpha)2}}, \\ C_{22}^{(\alpha)} &= \frac{E^{(\alpha)}}{\delta^{(\alpha)2}(1 - \nu^{(\alpha)2})}, \quad C_{66}^{(\alpha)} = \frac{E^{(\alpha)}}{2(\kappa^{(\alpha)} + \nu^{(\alpha)})} \end{aligned} \quad (21)$$

where $E^{(\alpha)}$ is the plane strain effective stiffness, $\nu^{(\alpha)}$ is the effective Poisson ratio, $\delta^{(\alpha)}$ is the stiffness ratio and $\kappa^{(\alpha)}$ is the shear parameter. The positive definiteness of the strain energy density requires that

$$|\nu^{(\alpha)}| < 1, \quad \kappa^{(\alpha)} > -1, \quad \delta^{(\alpha)} > 0, \quad E^{(\alpha)} > 0. \quad (22)$$

Note that for isotropic material, $\delta^{(\alpha)} = \kappa^{(\alpha)} = 1$ and $E^{(\alpha)}, \nu^{(\alpha)}$ are reduced to $E_i^{(\alpha)}/(1 - \nu_i^{(\alpha)2})$ and $\nu_i^{(\alpha)}/(1 - \nu_i^{(\alpha)})$, respectively, where $E_i^{(\alpha)}$ is the Young's modulus and $\nu_i^{(\alpha)}$ is the Poisson ratio for isotropic material. Note also that the parameters $\kappa^{(\alpha)}$ and $\delta^{(\alpha)}$ are similar to those ρ and λ defined by Suo (1990). With the Krenk's parameters, the matrices $\mathbf{B}^{(\alpha)}, \mathbf{L}^{(\alpha)}, \mathbf{S}^{(\alpha)}$, and the eigenvalues $p^{(\alpha)}$ take the following forms (Sung and Liou, 1994; Dongye and Ting, 1989):

$$\mathbf{L}^{(\alpha)} = \frac{E^{(\alpha)}}{2\omega_+^{(\alpha)}} \begin{bmatrix} \delta^{(\alpha)} & 0 \\ 0 & \delta^{(\alpha)-1} \end{bmatrix},$$

$$\mathbf{S}^{(\alpha)} = \frac{1 - \nu^{(\alpha)}}{2\omega_+^{(\alpha)}} \begin{bmatrix} 0 & -\delta^{(\alpha)-1} \\ \delta^{(\alpha)} & 0 \end{bmatrix} \quad (24)$$

$$\mathbf{E}_1^{(\alpha)} = \begin{cases} \frac{1}{2\omega_-^{(\alpha)}} \begin{bmatrix} \omega_-^{(\alpha)} + \omega_+^{(\alpha)} & i\delta^{(\alpha)} \\ i\delta^{(\alpha)-1} & \omega_-^{(\alpha)} - \omega_+^{(\alpha)} \end{bmatrix}, & \kappa^{(\alpha)} > 1 \\ \frac{1}{2\omega_-^{(\alpha)}} \begin{bmatrix} \omega_-^{(\alpha)} - i\omega_+^{(\alpha)} & \delta^{(\alpha)} \\ \delta^{(\alpha)-1} & \omega_-^{(\alpha)} + i\omega_+^{(\alpha)} \end{bmatrix}, & |\kappa^{(\alpha)}| < 1 \end{cases}$$

$$\mathbf{E}_2^{(\alpha)} = \begin{cases} \frac{1}{2\omega_-^{(\alpha)}} \begin{bmatrix} \omega_-^{(\alpha)} - \omega_+^{(\alpha)} & -i\delta^{(\alpha)} \\ -i\delta^{(\alpha)-1} & \omega_-^{(\alpha)} + \omega_+^{(\alpha)} \end{bmatrix}, & \kappa^{(\alpha)} > 1 \\ \frac{1}{2\omega_-^{(\alpha)}} \begin{bmatrix} \omega_-^{(\alpha)} + i\omega_+^{(\alpha)} & -\delta^{(\alpha)} \\ -\delta^{(\alpha)-1} & \omega_-^{(\alpha)} - i\omega_+^{(\alpha)} \end{bmatrix}, & |\kappa^{(\alpha)}| < 1 \end{cases}$$

(25)

$$p_1^{(\alpha)} = \begin{cases} i\delta^{(\alpha)}(\omega_+^{(\alpha)} + \omega_-^{(\alpha)}), & \kappa^{(\alpha)} > 1 \\ \delta^{(\alpha)}(i\omega_+^{(\alpha)} - \omega_-^{(\alpha)}), & |\kappa^{(\alpha)}| < 1 \end{cases}$$

$$p_2^{(\alpha)} = \begin{cases} i\delta^{(\alpha)}(\omega_+^{(\alpha)} - \omega_-^{(\alpha)}), & \kappa^{(\alpha)} > 1 \\ \delta^{(\alpha)}(i\omega_+^{(\alpha)} + \omega_-^{(\alpha)}), & |\kappa^{(\alpha)}| < 1 \end{cases}$$

where

$$\omega_+^{(\alpha)} = \sqrt{(1 + \kappa^{(\alpha)})/2}, \quad \omega_-^{(\alpha)} = \sqrt{|1 - \kappa^{(\alpha)}|/2}. \quad (27)$$

Matrices \mathbf{D} , \mathbf{U} , and \mathbf{W} defined in Eq. (19) can also be expressed in terms of Krenk's parameters. The results are

$$\mathbf{D} = \begin{bmatrix} 2\omega_+^{(1)}(\delta^{(1)}E^{(1)})^{-1} + 2\omega_+^{(2)}(\delta^{(2)}E^{(2)})^{-1} & 0 \\ 0 & 2\omega_+^{(1)}\delta^{(1)}E^{(1)-1} + 2\omega_+^{(2)}\delta^{(2)}E^{(2)-1} \end{bmatrix}$$

$$\mathbf{U} = \begin{bmatrix} 2\omega_+^{(1)}(\delta^{(1)}E^{(1)})^{-1} - 2\omega_+^{(2)}(\delta^{(2)}E^{(2)})^{-1} & 0 \\ 0 & 2\omega_+^{(1)}\delta^{(1)}E^{(1)-1} - 2\omega_+^{(2)}\delta^{(2)}E^{(2)-1} \end{bmatrix}$$

$$\mathbf{W} = \begin{bmatrix} 0 & (1 - \nu^{(1)})E^{(1)-1} - (1 - \nu^{(2)})E^{(2)-1} \\ -(1 - \nu^{(1)})E^{(1)-1} + (1 - \nu^{(2)})E^{(2)-1} & 0 \end{bmatrix}. \quad (28)$$

Substitute the components of the matrices \mathbf{U} and \mathbf{W} into Eq. (20), one obtains

$$\alpha_1 = \frac{(1 + \alpha_0) - (1 - \alpha_0)\Delta^{-1}}{(1 + \alpha_0) + (1 - \alpha_0)\Delta^{-1}}$$

$$\alpha_2 = \frac{(1 + \alpha_0) - (1 - \alpha_0)\Delta}{(1 + \alpha_0) + (1 - \alpha_0)\Delta}$$

$$\beta_1 = \delta^{(2)} \frac{2\beta_0}{(1 + \alpha_0) + (1 - \alpha_0)\Delta^{-1}}$$

$$\beta_2 = \delta^{(2)-1} \frac{2\beta_0}{(1 + \alpha_0) + (1 - \alpha_0)\Delta} \quad (29)$$

where

$$\alpha_0 = \frac{\omega_+^{(2)} - \omega_+^{(1)}}{\frac{E^{(2)}}{E^{(1)}} - \frac{E^{(1)}}{E^{(2)}}} \quad \beta_0 = \frac{1 - \nu^{(2)} - 1 - \nu^{(1)}}{\frac{E^{(2)}}{E^{(1)}} - \frac{E^{(1)}}{E^{(2)}}} \quad (30a)$$

and

$$\Delta = \delta^{(1)}/\delta^{(2)}. \quad (30b)$$

It has been observed by the present authors (Sung and Liou, 1994) that the degenerate materials occur when $\kappa^{(\alpha)} = 1$ since the eigenvalues $p_1^{(\alpha)}$ and $p_2^{(\alpha)}$ are the same. In the degenerate case the matrix $\mathbf{B}^{(\alpha)}$ will be singular. Note also that matrices $\mathbf{B}^{(\alpha)}$, $\mathbf{L}^{(\alpha)}$, $\mathbf{D}^{(\alpha)}$, and $\mathbf{U}^{(\alpha)}$ are independent of $\nu^{(\alpha)}$. It is interesting at this stage to consider the isotropic bimaterial problems, i.e., consider both orthotropic materials being reduced to (different) isotropic materials. In this case, $\kappa^{(1)} = \kappa^{(2)} = 1$, $\delta^{(1)} = \delta^{(2)} = 1$ so that

$$\mathbf{D} = 2(E^{(1)-1} + E^{(2)-1})\mathbf{I}$$

$$\mathbf{U} = 2(E^{(1)-1} - E^{(2)-1})\mathbf{I}.$$

With these results, one can easily verify that four generalized Dundurs' constants defined in Eq. (20) are reduced to

$$\alpha_1 = \alpha_2 = \alpha_0 = \alpha, \quad \beta_1 = \beta_2 = \beta_0 = \beta \quad (31)$$

where α and β are Dundurs' constants (1968). Matrices $\mathbf{M}^{\alpha\beta}$ shown in Eq. (14) can be written in forms that completely depend on four generalized Dundurs' constants, i.e.,

$$\mathbf{M}^{11} = \frac{1}{1 - \beta_1\beta_2} \begin{bmatrix} -\alpha_1 + \beta_1\beta_2 & i\beta_1(1 - \alpha_2) \\ -i\beta_2(1 - \alpha_1) & -\alpha_2 + \beta_1\beta_2 \end{bmatrix}$$

$$\mathbf{M}^{12} = \frac{1}{1 - \beta_1\beta_2} \begin{bmatrix} 1 + \alpha_1 & i\beta_1(1 + \alpha_2) \\ -i\beta_2(1 + \alpha_1) & 1 + \alpha_2 \end{bmatrix}$$

$$\mathbf{M}^{22} = \frac{1}{1 - \beta_1\beta_2} \begin{bmatrix} \alpha_1 + \beta_1\beta_2 & -i\beta_1(1 + \alpha_2) \\ i\beta_2(1 + \alpha_1) & \alpha_2 + \beta_1\beta_2 \end{bmatrix}$$

$$\mathbf{M}^{21} = \frac{1}{1 - \beta_1\beta_2} \begin{bmatrix} 1 - \alpha_1 & -i\beta_1(1 - \alpha_2) \\ i\beta_2(1 - \alpha_1) & 1 - \alpha_2 \end{bmatrix}. \quad (32)$$

Substitution from Eqs. (23)-(26) and Eq. (32) to Eq. (12), one leads to the kernel functions which are expressed in real forms:

$$\begin{aligned}
\mathbf{K}^{11} &= \frac{1}{d_{11}(\xi, t)} \begin{bmatrix} c_1 \xi^2 + c_2 \xi t + c_3 t^2 & 0 \\ 0 & c_1^* \xi^2 + c_2^* \xi t + c_3^* t^2 \end{bmatrix} \\
\mathbf{K}^{12} &= \frac{1}{d_{12}(\xi, t)} \begin{bmatrix} c_4 \xi^3 + c_5 \xi^2 t + c_6 \xi t^2 + c_7 t^3 & 0 \\ 0 & c_4^* \xi^3 + c_5^* \xi^2 t + c_6^* \xi t^2 + c_7^* t^3 \end{bmatrix} \\
\mathbf{K}^{22} &= \frac{1}{d_{22}(\xi, t)} \begin{bmatrix} c_8 \xi^2 + c_9 \xi t + c_{10} t^2 & 0 \\ 0 & c_8^* \xi^2 + c_9^* \xi t + c_{10}^* t^2 \end{bmatrix} \\
\mathbf{K}^{21} &= \frac{1}{d_{21}(\xi, t)} \begin{bmatrix} c_{11} \xi^3 + c_{12} \xi^2 t + c_{13} \xi t^2 + c_{14} t^3 & 0 \\ 0 & c_{11}^* \xi^3 + c_{12}^* \xi^2 t + c_{13}^* \xi t^2 + c_{14}^* t^3 \end{bmatrix} \quad (33)
\end{aligned}$$

where the coefficients appearing in the diagonal terms are

$$\begin{aligned}
c_1 &= -N_{11}^{11} & c_1^* &= -N_{22}^{11} \\
c_2 &= 2\omega_+^{(1)} N_{21}^{11} - N_{22}^{11} - (4\omega_+^{(1)^2} - 1) N_{11}^{11} \\
c_2^* &= 2\omega_+^{(1)} N_{21}^{11} - N_{11}^{11} - (4\omega_+^{(1)^2} - 1) N_{22}^{11} \\
c_3 &= N_{22}^{11} - 2\omega_+^{(1)} N_{12}^{11} & c_3^* &= N_{11}^{11} - 2\omega_+^{(1)} N_{12}^{11} \\
c_4 &= N_{11}^{12} & c_4^* &= N_{22}^{12} \\
c_5 &= (4\omega_+^{(1)} \omega_+^{(2)} N_{11}^{12} - \Delta N_{22}^{12} - 2\omega_+^{(2)} N_{21}^{12}) \Delta^{-1} \\
c_5^* &= (4\omega_+^{(1)} \omega_+^{(2)} N_{22}^{12} + 2\omega_+^{(1)} \Delta^{-1} N_{21}^{12} - \Delta^{-1} N_{11}^{12}) \Delta^{-1} \\
c_6 &= ((4\omega_+^{(2)^2} - 1) N_{11}^{12} - 2\omega_+^{(1)} N_{21}^{12} - 2\omega_+^{(2)} \Delta N_{12}^{12}) \Delta^{-2} \\
c_6^* &= (2\omega_+^{(1)} N_{12}^{12} + 2\omega_+^{(2)} \Delta^{-1} N_{21}^{12} + (4\omega_+^{(2)^2} - 1) N_{22}^{12}) \Delta^{-2} \\
c_7 &= (N_{22}^{12} - 2\omega_+^{(1)} N_{12}^{12}) \Delta^{-2} \\
c_7^* &= (\Delta^{-1} N_{11}^{12} + 2\omega_+^{(2)} N_{12}^{12}) \Delta^{-3} \\
c_8 &= -N_{11}^{22} & c_8^* &= -N_{22}^{22} \\
c_9 &= 2\omega_+^{(2)} N_{21}^{22} - N_{22}^{22} - (4\omega_+^{(2)^2} - 1) N_{11}^{22} \\
c_9^* &= 2\omega_+^{(2)} N_{21}^{22} - N_{11}^{22} - (4\omega_+^{(2)^2} - 1) N_{22}^{22} \\
c_{10} &= N_{22}^{22} - 2\omega_+^{(2)} N_{12}^{22} & c_{10}^* &= N_{11}^{22} - 2\omega_+^{(2)} N_{12}^{22} \\
c_{11} &= N_{11}^{21} & c_{11}^* &= N_{22}^{21} \\
c_{12} &= (4\omega_+^{(1)} \omega_+^{(2)} N_{11}^{21} - \Delta^{-1} N_{22}^{21} - 2\omega_+^{(1)} N_{21}^{21}) \Delta \\
c_{12}^* &= (4\omega_+^{(1)} \omega_+^{(2)} N_{21}^{21} + 2\omega_+^{(2)} \Delta N_{21}^{21} - \Delta N_{11}^{21}) \Delta \\
c_{13} &= ((4\omega_+^{(2)^2} - 1) N_{11}^{21} - 2\omega_+^{(2)} N_{21}^{21} - 2\omega_+^{(1)} \Delta^{-1} N_{12}^{21}) \Delta^2 \\
c_{13}^* &= (2\omega_+^{(2)} N_{12}^{21} + 2\omega_+^{(1)} \Delta N_{21}^{21} + (4\omega_+^{(1)^2} - 1) N_{22}^{21}) \Delta^2 \\
c_{14} &= (N_{22}^{21} - 2\omega_+^{(2)} N_{12}^{21}) \Delta^2 \\
c_{14}^* &= (\Delta N_{11}^{21} + 2\omega_+^{(1)} N_{12}^{21}) \Delta^3 \quad (34)
\end{aligned}$$

and $d_{\alpha\beta}(\xi, t)$ ($\alpha, \beta = 1, 2$) are given by

$$\begin{aligned}
d_{11}(\xi, t) &= (\xi + t)(\xi^2 + (4\omega_+^{(1)^2} - 2)\xi t + t^2) \\
d_{12}(\xi, t) &= \xi^4 + 4\omega_+^{(1)} \omega_+^{(2)} \Delta^{-1} t \xi^2 \\
&\quad + (4\omega_+^{(1)^2} + 4\omega_+^{(2)^2} - 2)\Delta^{-2} t^2 \xi^2 \\
&\quad + 4\omega_+^{(1)} \omega_+^{(2)} \Delta^{-3} t^3 \xi + \Delta^{-4} t^4 \\
d_{22}(\xi, t) &= (\xi + t)(\xi^2 + (4\omega_+^{(2)^2} - 2)\xi t + t^2) \\
d_{21}(\xi, t) &= \xi^4 + 4\omega_+^{(1)} \omega_+^{(2)} \Delta t \xi^3
\end{aligned}$$

$$\begin{aligned}
&\quad + (4\omega_+^{(1)^2} + 4\omega_+^{(2)^2} - 2)\Delta^2 t^2 \xi^2 \\
&\quad + 4\omega_+^{(1)} \omega_+^{(2)} \Delta^3 t^3 \xi + \Delta^4 t^4. \quad (35)
\end{aligned}$$

In Eqs. (34) and (35), Δ and $N_{kj}^{\alpha\beta}$ ($\alpha, \beta, k, j = 1, 2$) are defined by

$$\begin{bmatrix} N_{11}^{11} & N_{12}^{11} \\ N_{21}^{11} & N_{22}^{11} \end{bmatrix} = \frac{1}{1 - \tilde{\beta}_1 \tilde{\beta}_2} \begin{bmatrix} -\alpha_1 + \tilde{\beta}_1 \tilde{\beta}_2 & \tilde{\beta}_1(1 - \alpha_2) \\ \tilde{\beta}_2(1 - \alpha_1) & -\alpha_2 + \tilde{\beta}_1 \tilde{\beta}_2 \end{bmatrix} \quad (36a)$$

$$\begin{bmatrix} N_{12}^{12} & N_{12}^{12} \\ N_{21}^{12} & N_{22}^{12} \end{bmatrix} = \frac{1}{1 - \tilde{\beta}_1 \tilde{\beta}_2} \begin{bmatrix} 1 + \alpha_1 & \tilde{\beta}_1(1 + \alpha_2) \\ \tilde{\beta}_2(1 + \alpha_1) & 1 + \alpha_2 \end{bmatrix} \quad (36b)$$

$$\begin{bmatrix} N_{11}^{22} & N_{12}^{22} \\ N_{21}^{22} & N_{22}^{22} \end{bmatrix} = \frac{1}{1 - \tilde{\beta}_1 \tilde{\beta}_2} \begin{bmatrix} \alpha_1 + \tilde{\beta}_1 \tilde{\beta}_2 & \tilde{\beta}_1(1 + \alpha_2) \\ \tilde{\beta}_2(1 + \alpha_1) & \alpha_2 + \tilde{\beta}_1 \tilde{\beta}_2 \end{bmatrix} \quad (36c)$$

$$\begin{bmatrix} N_{11}^{21} & N_{12}^{21} \\ N_{21}^{21} & N_{22}^{21} \end{bmatrix} = \frac{1}{1 - \tilde{\beta}_1 \tilde{\beta}_2} \begin{bmatrix} 1 - \alpha_1 & \tilde{\beta}_1(1 - \alpha_2) \\ \tilde{\beta}_2(1 - \alpha_1) & 1 - \alpha_2 \end{bmatrix} \quad (36d)$$

$$\begin{aligned}
\tilde{\beta}_1 &= -\delta^{(1)^{-1}} \beta_1, & \tilde{\beta}_2 &= -\delta^{(1)} \beta_2, \\
\beta_1 &= \delta^{(2)^{-1}} \beta_1, & \beta_2 &= \delta^{(2)} \beta_2.
\end{aligned}$$

Note that the kernel functions for many special cases can be obtained from the above results. For example, the kernel functions for the problem of a half-plane solid (say, only material #2 exists) with traction-free boundary can be obtained by letting the material parameter $E^{(1)}$ of material #1 being small (i.e., $E^{(1)} \ll E^{(2)}$). The results are found to be the same as those obtained by the present authors (Sung and Liou, 1994). Another example is the problem of a half-plane solid (say, material #2) with clamped conditions. For this case the matrix given by Eq. (36c) will take the following simple form:

$$\begin{bmatrix} N_{11}^{22} & N_{12}^{22} \\ N_{21}^{22} & N_{22}^{22} \end{bmatrix} = \frac{1}{4\omega_+^{(2)^2} - (1 - \nu^{(2)})^2} \times \begin{bmatrix} 4\omega_+^{(2)^2} + (1 - \nu^{(2)})^2 & 4\omega_+^{(2)}(1 - \nu^{(2)}) \\ 4\omega_+^{(2)}(1 - \nu^{(2)}) & 4\omega_+^{(2)^2} + (1 - \nu^{(2)})^2 \end{bmatrix} \quad (37)$$

if the condition of $E^{(2)} \ll E^{(1)}$ is enforced. With this results, one can obtain the kernel function \mathbf{K}^{22} for clamped problem

which shows that it is independent of $\delta^{(2)}$ and $E^{(2)}$ and its diagonal terms are exactly the same. There are still more special cases, e.g., when one of the orthotropic materials becomes degenerate (say, material #1 is degenerate, $\kappa^{(1)} = 1$), or when both of materials are degenerate (i.e., $\kappa^{(1)} = 1$ and $\kappa^{(2)} = 1$), etc. No matter how the special case is, the corresponding kernel functions can be obtained directly from the general expressions shown above, no special considerations are needed. This is contrast to the common analysis of orthotropic materials which usually requires limiting processes to obtain isotropic results. One final remark to be mentioned is that the kernel functions developed by Erdogan and Biricikoglu (1973), who considered the isotropic bimaterial problems, can be obtained from the present results.

3 Singular Behaviors at the Point on the Interface

When cracks go through the interface or one of the cracks terminates at the interface, the singular behavior near the interface is different from that for a crack in a homogeneous medium, which is the well-known square root singular for stresses. According to the analysis of Zwiers et al. (1982), only one singularity of the type $r^{-\gamma}$ ($0 < \gamma < 1$) will occur near the interface for cracks through the interface for the present problem under consideration. For the case of a crack terminating at the interface the stresses will exhibit two different singular behaviors, i.e., $r^{-\gamma_1}$ and $r^{-\gamma_2}$ (γ_1 and $\gamma_2 > 0$) for in-plane problem. The more general case of two anisotropic elastic media which accounts for the effect of the anti-plane deformation has been investigated by Ting and Hoang (1984). Their results show that the stresses will in general have three different powers of singularity. The analysis done by Zwiers, et al. (1982) and Ting and Hoang (1984) employs essentially the techniques of eigenfunction expansions around the crack tip. A characteristic equation is set up by which the powers of singularity can be determined. Great effort and care for locating the roots are usually needed (Ting and Hoang, 1984) due to the fact that the characteristic equation involved is complicated. For the present problem we will develop the characteristic equation directly from the singular equations by considering the singular behavior of the equations at the points near the interface for the case when crack is going through the interface. The obtained characteristic equation is given in a real form and can be reduced to those for isotropic media. Furthermore, we found that the singular behaviors for stresses may vanish for some material combinations for cracks going through the interface. The problem of a crack-tip terminating at the interface has been investigated by Sung and Liou (1994). In that paper, the two powers γ_1 and γ_2 stated above can be identified to which mode is associated with, which can not be told from the results given by Ting and Hoang (1984). There are more features for the singular behavior of stresses discussed in that paper. Interested readers please refer to that paper (Sung and Liou, 1994). In the following, we will discuss only the case for cracks through the interface:

Following Muskhelishvili (1953) and Erdogan and Biricikoglu (1973), the unknown functions in equation (8) may be expressed as

$$\mathbf{b}^{(\alpha)}(t) = \frac{\hat{\mathbf{b}}^{(\alpha)}(t)}{t^{\gamma}(l_a - t)^{1/2}}, \quad 0 < \operatorname{Re}(\gamma) < 1, \quad \alpha = 1, 2 \quad (38)$$

near the irregular points (i.e., $t = l_a$, $\alpha = 1, 2$ and $t = 0$). Square root singular has been assumed at points, $t = l_a$, $\alpha = 1, 2$ in the above equation. With the results of Eq. (38), the terms with the Cauchy singularity in Eq. (8) may be expressed as

$$\frac{1}{\pi} \int_0^{l_a} \frac{\mathbf{b}^{(\alpha)}(t)}{t - \xi} dt \approx \frac{\hat{\mathbf{b}}^{(\alpha)}(0)}{\sqrt{l_a}} \cot(\pi\gamma) \xi^{-\gamma},$$

$$(0 < \xi < l_a, \quad \alpha = 1, 2) \quad (39)$$

while the remaining terms in Eq. (8) may be expressed, with some manipulations, as

$$\frac{1}{\pi} \int_0^{l_a} \mathbf{K}^{\alpha\beta}(\xi, t) \mathbf{b}^{(\beta)}(t) dt \approx \begin{bmatrix} Q_{11}^{\alpha\beta}(\gamma) & 0 \\ 0 & Q_{22}^{\alpha\beta}(\gamma) \end{bmatrix} \frac{\hat{\mathbf{b}}^{(\beta)}(0)}{\sin(\pi\gamma)\sqrt{l_a}} \xi^{-\gamma} \quad (40)$$

where

$$\begin{aligned} Q_{11}^{\alpha\beta}(\gamma) &= \sum_{k=1}^2 \sum_{j=1}^2 n_{kj}^{\alpha\beta}(\gamma) N_{kj}^{\alpha\beta} \\ Q_{22}^{\alpha\beta}(\gamma) &= \sum_{k=1}^2 \sum_{j=1}^2 \tilde{n}_{kj}^{\alpha\beta}(\gamma) N_{kj}^{\alpha\beta} \end{aligned} \quad (41)$$

and the functions of $n_{kj}^{\alpha\beta}(\gamma)$ and $\tilde{n}_{kj}^{\alpha\beta}(\gamma)$ are given in Appendix B. Substitute Eqs. (38) and (39) into (8), and multiply both sides by ξ^γ and let $\xi \rightarrow 0$, one obtains the system of equations

$$\begin{bmatrix} \cos(\pi\gamma) + Q_{11}^{11}(\gamma) & 0 \\ 0 & \cos(\pi\gamma) + Q_{22}^{11}(\gamma) \end{bmatrix} \frac{\hat{\mathbf{b}}^{(1)}(0)}{\sqrt{l_1}} + \begin{bmatrix} Q_{11}^{12}(\gamma) & 0 \\ 0 & Q_{22}^{12}(\gamma) \end{bmatrix} \frac{\hat{\mathbf{b}}^{(2)}(0)}{\sqrt{l_2}} = \mathbf{0} \quad (42a)$$

$$\begin{bmatrix} Q_{11}^{21}(\gamma) & 0 \\ 0 & Q_{22}^{21}(\gamma) \end{bmatrix} \frac{\hat{\mathbf{b}}^{(1)}(0)}{\sqrt{l_1}} + \begin{bmatrix} \cos(\pi\gamma) + Q_{11}^{22}(\gamma) & 0 \\ 0 & \cos(\pi\gamma) + Q_{22}^{22}(\gamma) \end{bmatrix} \times \frac{\hat{\mathbf{b}}^{(2)}(0)}{\sqrt{l_2}} = \mathbf{0}. \quad (42b)$$

Express the components $\hat{\mathbf{b}}^{(1)}(0)$ and $\hat{\mathbf{b}}^{(2)}(0)$ explicitly by $\hat{\mathbf{b}}^{(1)}(0) = [\hat{b}_x^{(1)}(0), \hat{b}_y^{(1)}(0)]^T$ and $\hat{\mathbf{b}}^{(2)}(0) = [\hat{b}_x^{(2)}(0), \hat{b}_y^{(2)}(0)]^T$, respectively, then the above equations can be rearranged in the following form:

$$\begin{bmatrix} \cos(\pi\gamma) + Q_{11}^{11}(\gamma) & Q_{11}^{12}(\gamma) \\ Q_{11}^{21}(\gamma) & \cos(\pi\gamma) + Q_{11}^{22}(\gamma) \end{bmatrix} \times \begin{Bmatrix} \hat{b}_x^{(1)}(0)/\sqrt{l_1} \\ \hat{b}_x^{(2)}(0)/\sqrt{l_2} \end{Bmatrix} = \mathbf{0} \quad (43a)$$

$$\begin{bmatrix} \cos(\pi\gamma) + Q_{22}^{11}(\gamma) & Q_{22}^{12}(\gamma) \\ Q_{22}^{21}(\gamma) & \cos(\pi\gamma) + Q_{22}^{22}(\gamma) \end{bmatrix} \times \begin{Bmatrix} \hat{b}_y^{(1)}(0)/\sqrt{l_1} \\ \hat{b}_y^{(2)}(0)/\sqrt{l_2} \end{Bmatrix} = \mathbf{0}. \quad (43b)$$

It is noted that the deformation due to pressure loadings is totally decoupled from that due to shear loadings for the present problem, hence, Eq. (43a) will represent the singular behavior due to pressure loadings while Eq. (43b) is due to shear loadings. For nontrivial solutions of Eqs. (43a) and (43b), one leads to the characteristic equations for γ as follows:

$$\begin{aligned} \cos^2(\pi\gamma) + (Q_{11}^{11} + Q_{11}^{22}) \cos(\pi\gamma) \\ + (Q_{11}^{11} Q_{11}^{22} - Q_{11}^{12} Q_{11}^{21}) = 0 \end{aligned} \quad (44a)$$

(due to pressure loadings)

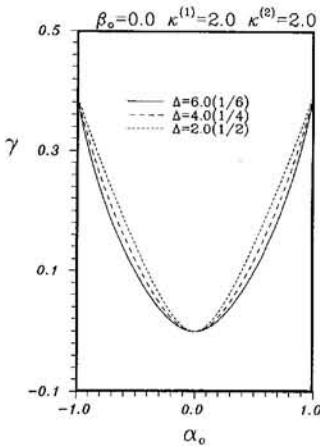


Fig. 2 Dependence of the root γ on α_0 for various Δ ($\beta_0 = 0$, $\kappa^{(1)} = \kappa^{(2)} = 2.0$)

and

$$\cos^2(\pi\gamma) + (Q_{22}^{11} + Q_{22}^{22}) \cos(\pi\gamma) + (Q_{22}^{11}Q_{22}^{22} - Q_{22}^{12}Q_{22}^{21}) = 0$$

(due to shear loadings). (44b)

Note that these two equations in the present forms are exactly the same because

$$Q_{11}^{11} + Q_{11}^{22} = Q_{22}^{11} + Q_{22}^{22} \quad (45a)$$

$$Q_{11}^{11}Q_{11}^{22} - Q_{11}^{12}Q_{11}^{21} = Q_{22}^{11}Q_{22}^{22} - Q_{22}^{12}Q_{22}^{21}. \quad (45b)$$

Hence, only one of them has to be considered for a crack going through the interface. One can verify that the characteristic equation shown in Eq. (44a) (or (44b)) will give the same equation as that obtained by Erdogan and Bircikoglu (1973) if the appropriate values of $Q_{11}^{\alpha\beta}$ (or $Q_{22}^{\alpha\beta}$) for isotropic materials are substituted in. The characteristic Eq. (44a) has the property that

$$\gamma(\Delta) = \gamma(\Delta^{-1}), \quad (46)$$

since the coefficients of the characteristic equation are both invariant when Δ is replaced by Δ^{-1} , i.e.,

$$(Q_{11}^{11} + Q_{11}^{22})(\Delta) = (Q_{11}^{11} + Q_{11}^{22})(\Delta^{-1}) \quad (47a)$$

$$(Q_{11}^{11}Q_{11}^{22} - Q_{11}^{12}Q_{11}^{21})(\Delta) = (Q_{11}^{11}Q_{11}^{22} - Q_{11}^{12}Q_{11}^{21})(\Delta^{-1}). \quad (47b)$$

In the following, we will investigate the effect of some material's parameters on the behavior of the root. Before doing so, we note again that the possible values of Krenk's parameters are $-1 < \nu^{(\alpha)} < 1$, $\kappa^{(\alpha)} > -1$, $E^{(\alpha)} > 0$, and $\delta^{(\alpha)} > 0$ if strain energy is positive definite. Hence, if one considers only the cases for $\nu^{(\alpha)} \geq 0$, then,

$$-1 < \alpha_0 < 1 \quad (48)$$

while β_0 is related to α_0 by

$$\beta_0 = \frac{1}{4} \left\{ \left(\frac{1 - \nu^{(2)}}{\omega_+^{(2)}} + \frac{1 - \nu^{(1)}}{\omega_+^{(1)}} \right) \alpha_0 + \left(\frac{1 - \nu^{(2)}}{\omega_+^{(2)}} - \frac{1 - \nu^{(1)}}{\omega_+^{(1)}} \right) \right\}. \quad (49)$$

In the numerical investigations, we choose $\beta_0 = m\alpha_0$ for simplicity where m is a constant. This choice of β_0 in part implies not only $\nu^{(\alpha)} \geq 0$ but also from Eq. (49)

$$\frac{1 - \nu^{(2)}}{\omega_+^{(2)}} = \frac{1 - \nu^{(1)}}{\omega_+^{(1)}} \quad (50)$$

is hold. Let's now consider the effect of the parameters Δ , α_0 , and β_0 in the following. Figures 2 to 4 are the results of the

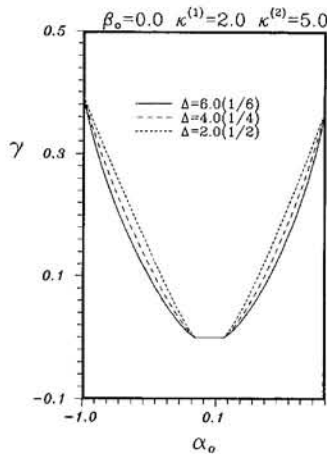


Fig. 3 Dependence of the root γ on α_0 for various Δ ($\beta_0 = 0$, $\kappa^{(1)} = 2.0$, $\kappa^{(2)} = 5.0$)

roots γ versus α_0 for various values of Δ with $\kappa^{(1)}$ and $\kappa^{(2)}$ both being kept constants. The property of $\gamma(\Delta) = \gamma(\Delta^{-1})$ is reflected in the numerical results, consistent with our previous study. Furthermore, the symmetric property of γ with respect to α_0 is observed in Fig. 2, i.e., $\gamma(\alpha_0) = \gamma(-\alpha_0)$, for the case of $\kappa^{(1)} = \kappa^{(2)} = 2.0$. In fact, this property can be verified directly from the characteristic equation for any values of $\kappa^{(1)}$ and $\kappa^{(2)}$, as long as $\kappa^{(1)} = \kappa^{(2)}$ is hold. It is also observed from these figures that the effect of Δ on the root γ is in general small. It is also observed that for most values of α_0 , a root of γ in $0 < \gamma < 1$ can be found. This means that one singularity of the type $r^{-\gamma}$ ($0 < \gamma < 1$) usually occurs for cracks going through the interface. However, more interesting thing is that we do find for some material combinations in which the singularity for stresses will disappear, i.e., no root is found in $0 < \gamma < 1$, only $\gamma = 0$ occurred for some material combinations. For instance, results plotted in Fig. 3 show that $\gamma = 0$ occurs when α_0 falls approximately in the range $-0.068 < \alpha_0 < 0.17$ for the case of $\beta_0 = 0.0$ ($\kappa^{(1)} = 2.0$, $\kappa^{(2)} = 5.0$) while the range for α_0 is longer for the case of $\beta_0 = 0.25\alpha_0$ ($\kappa^{(1)} = 2.0$, $\kappa^{(2)} = 5.0$) (see Fig. 4) comparing to that for $\beta_0 = 0.0$ (Fig. 3). The fact that stresses will be finite for some material combinations has also been observed by Bogy (1970) in the study of isotropic bimaterial problems, where the region for the material combinations to give finite stresses is given explicitly in terms of Dundurs' parameters.

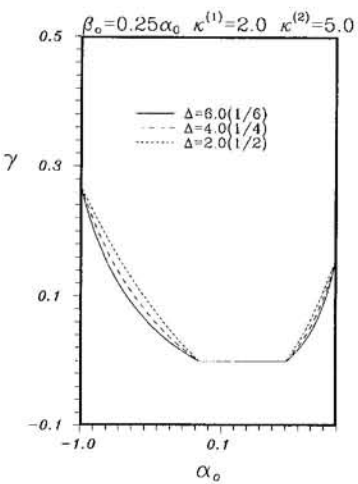


Fig. 4 Dependence of the root γ on α_0 for various Δ ($\beta_0 = 0.25\alpha_0$, $\kappa^{(1)} = 2.0$, $\kappa^{(2)} = 5.0$)

For the present problem, it seems that to investigate analytically the regions of all possible material combinations in which the stresses will be finite is not so straightforward, since the characteristic equation contains many material parameters. Hence, we investigate numerically only the cases that are related to the results presented in Fig. 3 and Fig. 4. The results of the regions for which the material combinations to give the stress finite, i.e., $\gamma = 0$, are shown, respectively, in Fig. 5 and Fig. 6. The shaded regions shown in Fig. 5 and Fig. 6 are both plotted with $\kappa^{(1)} = 2.0$ being kept constant. The difference in plotting these two figures is the choice of m ($m = 0$ for Fig. 5 while $m = 0.25$ for Fig. 6). It is worth to mention that in studying these shaded regions, numerical results tend to show that each shaded region plotted in Fig. 5 and Fig. 6 is independent of the parameter Δ . In fact this phenomenon has already been revealed in the results of Fig. 3 and Fig. 4, since it is seen that all curves corresponding to different values of Δ collapse to one point whenever $\gamma = 0$. One more finding is that for orthotropic bimaterials with property $\alpha_0 = \beta_0 = 0$ will always fall in the shaded regions.

Before ending this section, one final remark to be noted is that $\hat{b}_x^{(1)}(0)$ and $\hat{b}_x^{(2)}(0)$ (or $\hat{b}_y^{(1)}(0)$ and $\hat{b}_y^{(2)}(0)$) are related to each other by Eq. (43a) (or Eq. (43b)) which should be incorporated, besides the auxiliary condition

$$\int_0^{l_1} \mathbf{L}^{(1)-1} \mathbf{b}^{(1)}(t) dt = \int_0^{l_2} \mathbf{L}^{(2)-1} \mathbf{b}^{(2)}(t) dt, \quad (51)$$

into the solutions of the singular integral equations in order to have a unique solution for the problem.

4 Some Observations

The singular integral equations obtained in Section 2 which are given in real forms are now employed to explore in this section some interesting phenomena for the stress intensity factors for cases when crack faces are subjected to self-equilibrating loadings. Crack (or cracks) may be embedded in one of the materials (case I) or may be embedded in both (case II). The results are described below.

CASE I: (Only one vertical crack embedded in one of the materials (say material #2)).

For convenient discussion, we will assume that the crack is embedded in material #2 while material #1 is crack-free. Under this assumption, one can drop the coupled terms in the singular integral equations shown in Eq. (8) and only one of the singular integral equations with kernel function \mathbf{K}^{22} has to be considered.

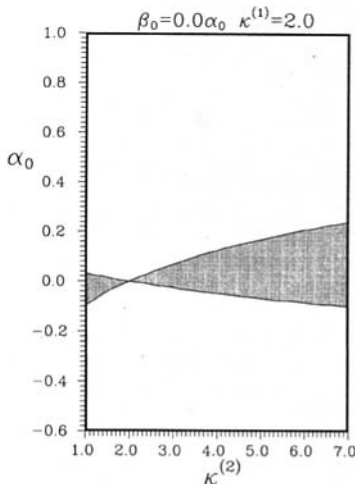


Fig. 5 Material combinations fallen in the shaded region will produce $\gamma = 0$ ($\beta_0 = 0$, $\kappa^{(1)} = 2.0$)

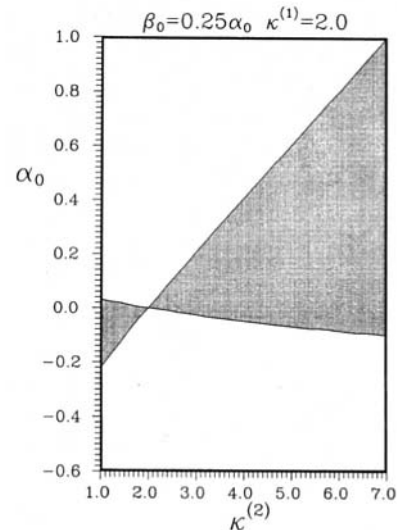


Fig. 6 Material combinations fallen in the shaded region will produce $\gamma = 0$ ($\beta_0 = 0.25\alpha_0$, $\kappa^{(1)} = 2.0$)

In the following two special orthotropic bimaterial compositions are considered.

(A) $\Delta = \delta^{(1)}/\delta^{(2)} = 1$. Suppose that the stiffness ratio $\delta^{(a)}$ of each orthotropic material has the same value, i.e., $\delta^{(1)} = \delta^{(2)}$, then one can easily find that the previous defined four generalized Dundurs' constants are reduced to two only, i.e.,

$$\begin{aligned} \alpha_1 &= \alpha_2 = \alpha_0 \\ \hat{\beta}_1 &= \hat{\beta}_2 = \beta_0. \end{aligned} \quad (52)$$

With these special results, matrix defined in Eq. (36c) becomes

$$\begin{bmatrix} N_{11}^{22} & N_{12}^{22} \\ N_{21}^{22} & N_{22}^{22} \end{bmatrix} = \frac{1}{1 - \beta_0^2} \begin{bmatrix} \alpha_0 + \beta_0^2 & \beta_0(1 + \alpha_0) \\ \beta_0(1 + \alpha_0) & \alpha_0 + \beta_0^2 \end{bmatrix} \quad (53)$$

and the coefficients defined in Eq. (34) will be

$$\begin{aligned} c_8 &= c_8^* \\ c_9 &= c_9^* \\ c_{10} &= c_{10}^*, \end{aligned}$$

which implies that diagonal terms of the kernel function \mathbf{K}^{22} are exactly the same, so that one can conclude from this fact that the stress intensity factors due to pressure loadings would be the same as those due to shear loadings, as long as the magnitude of both loadings is the same. This phenomenon is plotted schematically in Fig. 7.

Now suppose that the material alignments of both materials are rotated by 90 deg (see Fig. 3). Since the ratio of $\delta^{(1)}/\delta^{(2)}$ will remain the same value (i.e., equal to 1) and the kernel function \mathbf{K}^{22} is related to $\delta^{(a)}$ ($a = 1, 2$) only through the ratio of these two quantities so that the kernel function will be invariant under the rotations of 90 deg of both materials, so long as the condition $\delta^{(1)} = \delta^{(2)}$ is satisfied for the orthotropic bimaterial compositions. Based on this fact, one can conclude that the stress intensity factors will be invariant as well, obviously the tractions applied on the crack surface be kept the same magnitude under rotations. This fact is shown schematically in Fig. 8.

Let's further investigate the features of the kernel functions. Suppose that the material #2 is degenerated, i.e., $\kappa^{(2)} = 1$ while the condition $\delta^{(1)} = \delta^{(2)}$ is still held, then the kernel function \mathbf{K}^{22} will be reduced to that for isotropic bimaterial problems if

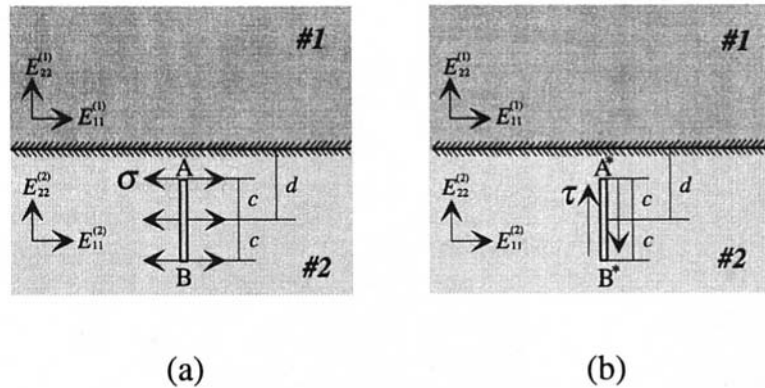


Fig. 7 If the compositions of dissimilar orthotropic materials are such that $\delta^{(1)} = \delta^{(2)}$, then $(K_I)_A = (K_{II})_{A^*}$, $(K_I)_B = (K_{II})_{B^*}$. (under the same magnitude of the applied load, i.e., $\sigma = \tau$)

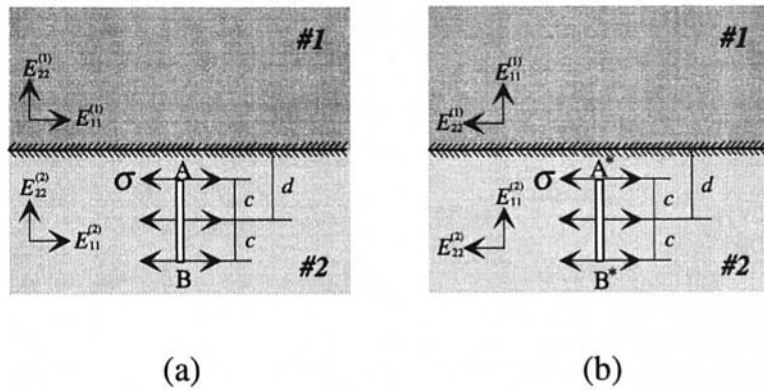


Fig. 8 If the compositions of dissimilar orthotropic materials are such that $\delta^{(1)} = \delta^{(2)}$ and if material axes of (b) are obtained by rotating 90 deg of material axes of (a), then $(K_I)_{A,B} = (K_{II})_{A^*,B^*}$. (This conclusion also holds for shear loadings.)

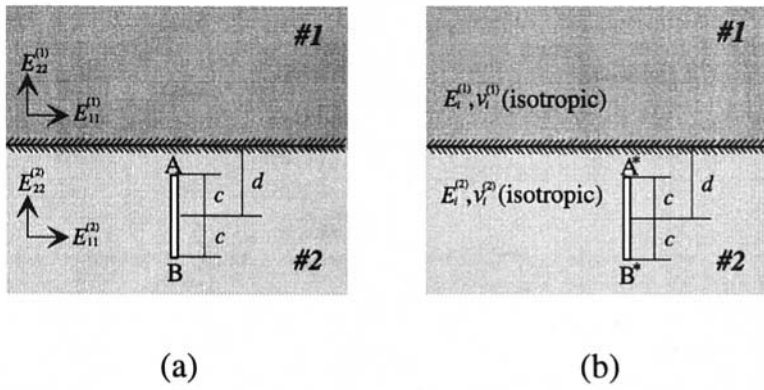


Fig. 9 If the compositions of dissimilar orthotropic materials are such that $\delta^{(1)} = \delta^{(2)}$ and furthermore if $\kappa^{(2)} = 1$ and $\alpha_0 = \alpha$, $\beta_0 = \beta$ (α , β : Dundurs' constants for isotropic bimaterials of (b); α_0 , β_0 : generalized Dundurs' constants for orthotropic bimaterials of (a)), then $(K_I)_{A,B} = (K_{II})_{A^*,B^*}$, $(K_{II})_{A,B} = (K_{II})_{A^*,B^*}$. (This is the feature of correspondence.)

the orthotropic bimaterial compositions are chosen such that the following conditions are satisfied

$$\alpha_0 = \alpha$$

$$\beta_0 = \beta$$

where α , β are Dundurs' constants for isotropic bimaterial problems. This implies that stress intensity factors of Fig. 9(a) can be obtained by the corresponding isotropic bimaterial problems as long as the conditions mentioned above are satisfied. This

establishes the correspondence between dissimilar orthotropic materials and isotropic bimaterials, at least for the problem of a crack perpendicular to the interface.

(B) $\mathbf{W} = \mathbf{0}$. Suppose that the compositions of the dissimilar orthotropic materials are chosen such that the matrix \mathbf{W} defined in Eq. (28) vanishes, then the generalized Dundurs' constants of β_1 and β_2 vanish too. With the property of $\mathbf{W} = \mathbf{0}$, one can find that the stress intensity factors due to pressure loadings (Fig. 10(a)) will be the same as those due to shear loadings ($\tau = \sigma$) (Fig. 10(b)), if the material axes of Fig.

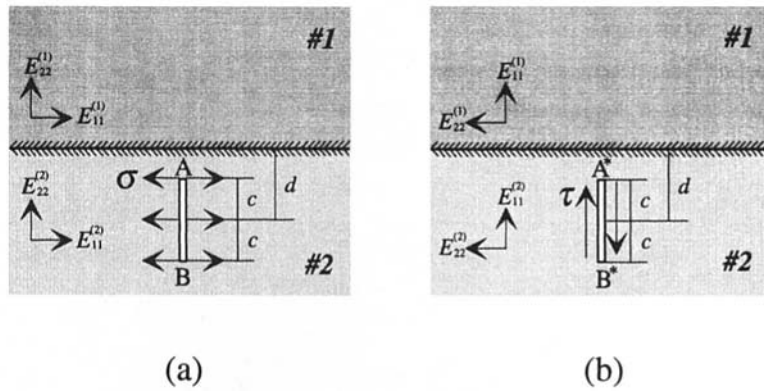


Fig. 10 If the material axes of (b) are obtained by rotating 90 deg of material axes of (a) and if the magnitude of the applied load is the same, i.e., $\sigma = \tau$, then $(K_I)_{A,B} = (K_I)_{A^*,B^*}$

10(b) are obtained by rotating 90 deg of the material axes of Fig. 10(a) for both materials. This is apparent due to the fact that the following parameters' changes according to the following ways when material axes are rotated by 90 deg:

$$\begin{aligned} \delta^{(1)}/\delta^{(2)} &\rightarrow \delta^{(2)}/\delta^{(1)} \\ \alpha_1 &\rightarrow \alpha_2 \\ \alpha_2 &\rightarrow \alpha_1. \end{aligned} \quad (54)$$

Substituting these new parameters into the kernel function \mathbf{K}^{22} one would find that the new kernel function is the same as before, the only difference is that the position of the diagonal terms of the kernel function is interchanged. The above phenomenon is plotted schematically in Fig. 10.

In addition to the condition $\mathbf{W} = \mathbf{0}$, let's further assume that the orthotropic bimaterial compositions have the properties, i.e., $\Delta = \delta^{(1)}/\delta^{(2)} = 1$ and $\alpha_1 = \alpha_2 = 0$, then the stress intensity factors for dissimilar orthotropic materials (Fig. 11(a)) would be the same as those for a homogeneous medium (Fig. 11(b)). This means that the stress intensity factors of this special kind of dissimilar orthotropic materials would be independent of the material constants. The conclusion stated above can be verified by noting that the kernel function \mathbf{K}^{22} vanishes if the above conditions are satisfied.

CASE II: (Two cracks each embedded in one of the materials).

For case II, the coupled singular integral Eqs. (8) have to be considered simultaneously. Hence, we will discuss only the phenomenon for $\Delta = \delta^{(1)}/\delta^{(2)} = 1$. Suppose that both of the materials, whose compositions are such that $\delta^{(1)} = \delta^{(2)}$, are

rotated by 90 deg, then the stress intensity factors will remain the same (Fig. 12). Let's further assume that $\kappa^{(1)} = \kappa^{(2)} = 1$, i.e., both orthotropic materials are degenerated, then one would find that the stress intensity factors for dissimilar orthotropic materials can be obtained from those for dissimilar isotropic materials if the dissimilar orthotropic materials are chosen such that the conditions of

$$\begin{aligned} \alpha_1 &= \alpha_2 = \alpha \\ \hat{\beta}_1 &= \hat{\beta}_2 = \beta \end{aligned}$$

are satisfied, here α, β are Dundurs' constants for isotropic bimaterial problems (Fig. 13).

5 Some Numerical Results

In this section, we will give some numerical results pertaining to the problem of an isotropic material (material #2) joined perfectly to an orthotropic material (material #1). The coupled singular integral equations developed in Section 3 are discretized according to the method suggested by Gerasoulis (1982). In the following, only the problem of one crack embedded in material #2 is investigated. For problems of cracks going through the interface, the numerical approach is essentially the same with the exception that if the singular behavior for stresses at the point of interface does exist, the singular behavior has to be taken care of in the numerical scheme.

Before presenting the results for the problem described above, it is better to compare our results with those available for isotropic bimaterial problems in order to ensure the accuracy of the present numerical approach. Figures 14 and 15 are the results for

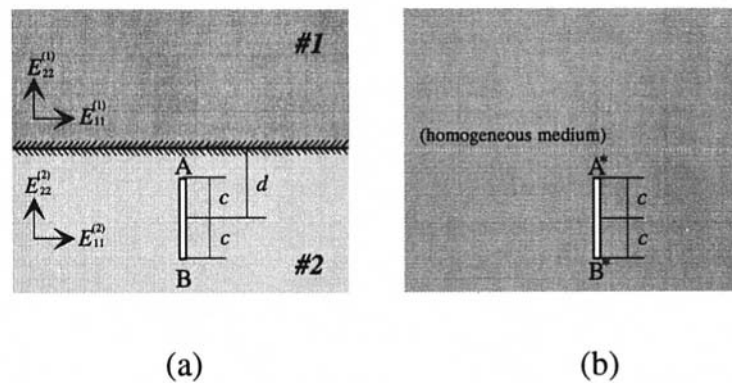


Fig. 11 The stress intensity factors of (a) are independent of the dissimilar orthotropic materials' constants, if $\mathbf{W} = \mathbf{0}$ and $\delta^{(1)} = \delta^{(2)}$ are satisfied

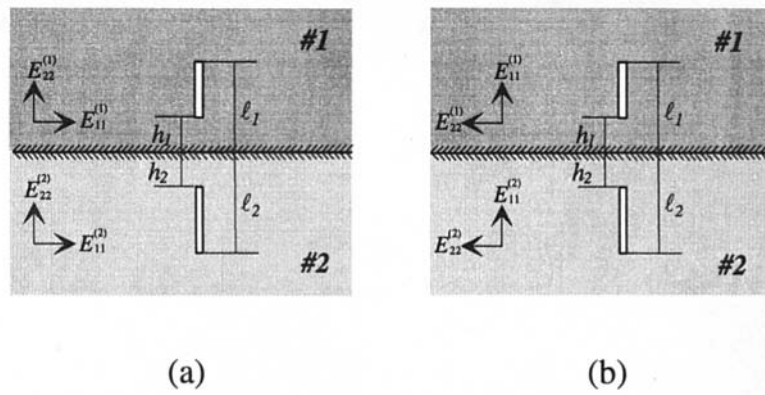


Fig. 12 If the compositions of dissimilar orthotropic materials are such that $\delta^{(1)} = \delta^{(2)}$, then the stress intensity factors of (a) and (b) are the same

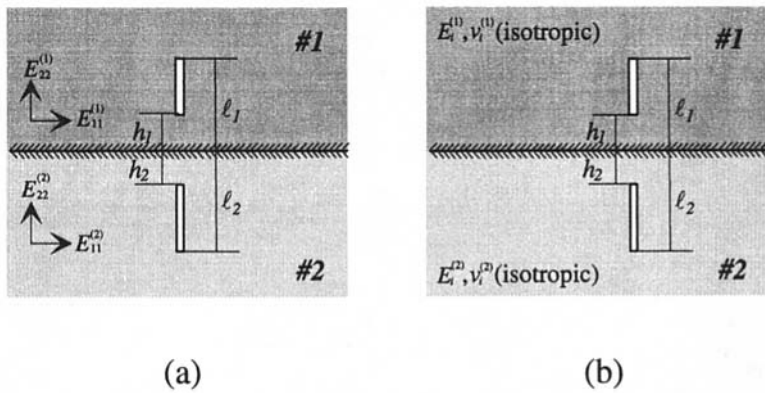


Fig. 13 If the compositions of dissimilar orthotropic materials are such that $\delta^{(1)} = \delta^{(2)}$ and furthermore if $\kappa^{(1)} = \kappa^{(2)} = 1$ and $\alpha_0 = \alpha$, $\beta_0 = \beta$ (α , β : Dundurs' constants for isotropic bimaterials of (b); α_0 , β_0 : generalized Dundurs' constants for orthotropic bimaterials of (a)), then the stress intensity factors of (a) can be obtained from (b). (This is the feature of correspondence.)

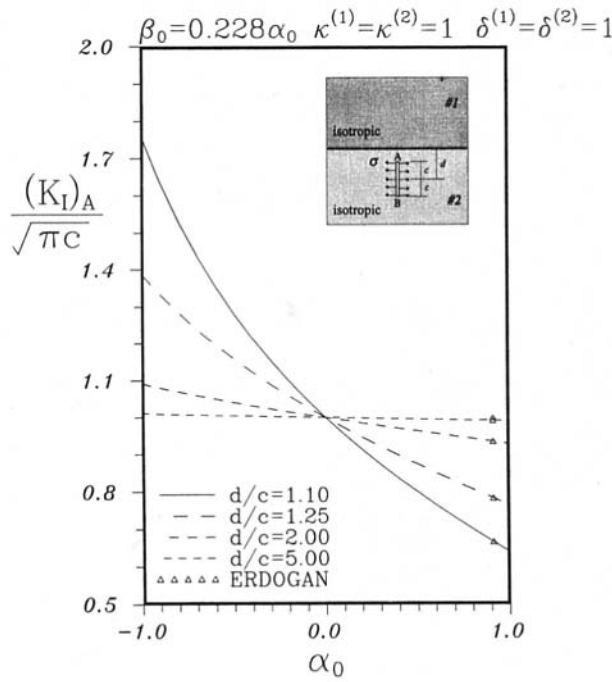


Fig. 14 Stress intensity factor at point A for dissimilar isotropic materials for various values of d/c ($\sigma = 1$)

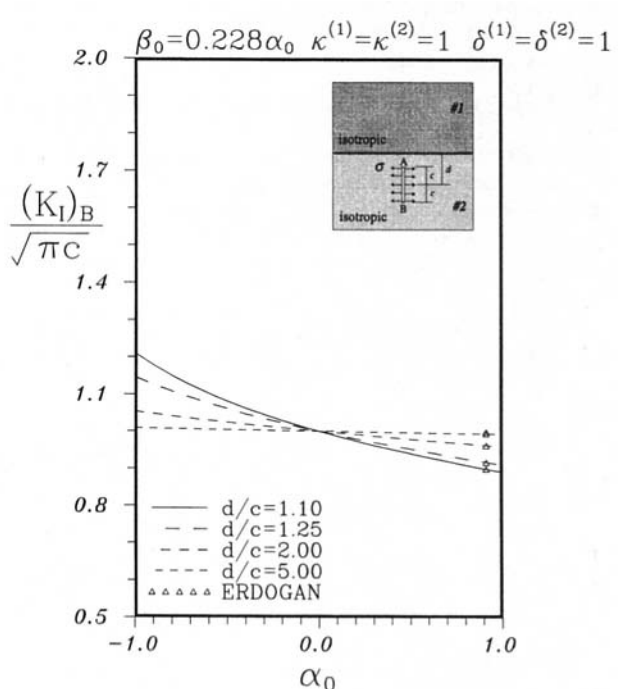


Fig. 15 Stress intensity factor at point B for dissimilar isotropic materials for various values of d/c ($\sigma = 1$)

stress intensity factors for crack faces subjected to uniform pressure σ . Both materials are taken to be isotropic, i.e., $\kappa^{(1)} = \kappa^{(2)} = 1$, $\delta^{(1)} = \delta^{(2)} = 1$. The dissimilarity of these materials is through the Dundurs' constants, $\alpha = \alpha_0$ and $\beta = \beta_0$. Note that $\alpha_0 = \beta_0 = 0.0$ corresponds to homogeneous medium. For the purpose of comparison, we select $m = 0.228$. The results obtained by Erdogan and Bircikoglu (1973) who investigated only one material combination (material #1: Aluminum $E_1 = 10^7$ psi, $\nu_1 = 0.3$ and material #2: Epoxy $E_2 = 4.45 \times 10^5$ psi, $\nu_2 = 0.35$) are also plotted in Figs. 14 and 15. Good agreement can be observed. Although results plotted in Figs. 14 and 15 are under uniform pressure loading only, we have to emphasize that these results apply also to the problem that is under uniform shear loading ($\tau = 1$). This is because the choice of $\Delta = \delta^{(1)}/\delta^{(2)}$ in plotting Fig. 14 and Fig. 15 is equal to one, hence, according to the observations of previous sections (please see Fig. 7), the aforementioned substitution of results of normal loading to shear loadings should be applied. Moreover, results of Figures 14 and 15 can also be applied to many other orthotropic bimaterial problems as long as $\Delta = 1$. For instance, let's take $\delta^{(1)} = \delta^{(2)} = 2$, or $\delta^{(1)} = \delta^{(2)} = 3$, etc., all these kinds of orthotropic bimaterial problems should the response of the stress intensity factors be exactly the same as those presented in Figs. 14 and 15.

Next, we present numerical results for the problem that material #2 being isotropic (i.e., $\kappa^{(2)} = 1$, $\delta^{(2)} = 1$) while material #1 being orthotropic. For simplicity, we present only the results for $\beta_0 = 0.0$ and $d/c = 1.1$. It is seen that the parameter $\delta^{(1)}$ has significant effect on the stress intensity factors for most values of α_0 , as shown in Figs. 16 and 17. Note that there are two extreme values of α_0 (i.e., $\alpha_0 = -1$ and $\alpha_0 = 1$) that the effects of $\delta^{(1)}$ on the stress intensity factors disappear. This is due to the fact that as $\alpha_0 \rightarrow -1$, we have $\alpha_1 = \alpha_2 = 1$ (see Eq. (29)), and from Eq. (36c),

$$N_{11}^{22} = N_{22}^{22} = -1$$

$$N_{12}^{22} = N_{21}^{22} = 0.$$

Hence, the kernel functions are reduced to the problem for a half-plane solid with traction-free boundary as $\alpha_0 \rightarrow -1$. There-

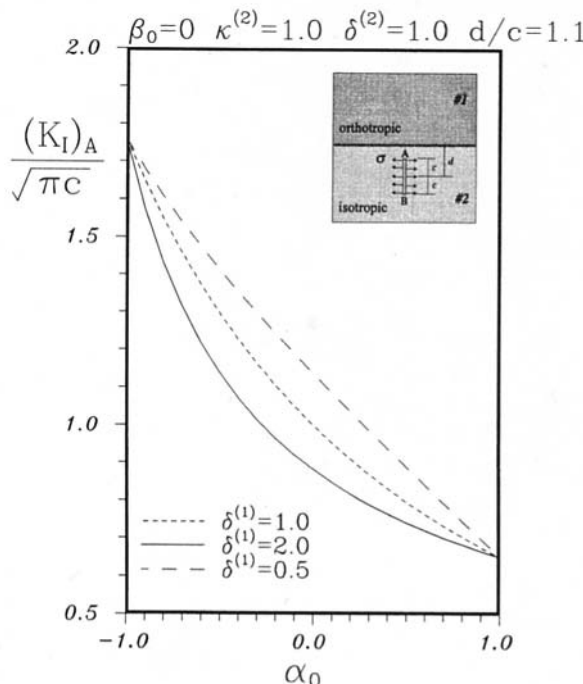


Fig. 16 Stress intensity factor at point A for dissimilar isotropic materials for various values of $\delta^{(1)}$ ($\sigma = 1$)

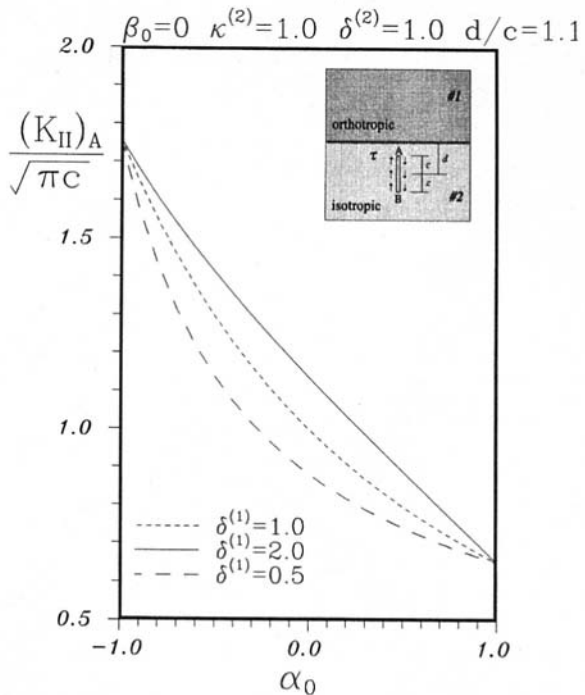


Fig. 17 Stress intensity factor at point A for dissimilar isotropic materials for various values of $\delta^{(1)}$ ($\tau = 1$)

fore results will be independent of $\delta^{(1)}$. As to the case of $\alpha_0 \rightarrow 1$, the generalized Dundurs' constants become

$$\alpha_1 = \alpha_2 = 1$$

$$\delta^{(2)-1} \beta_1 = \delta^{(2)} \beta_2 = \frac{1 - \nu^{(2)}}{2 \omega_+^{(2)}}$$

and with these values the expressions for N_{11}^{22} , N_{22}^{22} , N_{12}^{22} , and N_{21}^{22} will be given by Eq. (37). Hence, the kernel functions will this time correspond to the problem for a half-plane solid with clamped boundary as $\alpha_0 \rightarrow 1$ and results are again independent of $\delta^{(1)}$. It should be noted that the choice of $\beta_0 = 0$ in plotting Figs. 16 and 17 implies that $\mathbf{W} = \mathbf{0}$. Hence, according to the observations that have been discussed in previous section (please see Fig. 10), those results presented in Figs. 16 and 17 are actually related to each other by

$$(K_I)_A \text{ (for } \delta^{(1)} = 2.0 \text{)} = (K_{II})_A \text{ (for } \delta^{(1)} = 1/2 \text{)}$$

$$(K_I)_A \text{ (for } \delta^{(1)} = 1/2 \text{)} = (K_{II})_A \text{ (for } \delta^{(1)} = 2.0 \text{)}.$$

One last thing to be mentioned is that results of Figs. 16 and 17 that correspond to the case for $\delta^{(1)} = 1.0 = \delta^{(2)}$ apply also to other orthotropic bimaterial problems as long as the material parameter $\Delta = \delta^{(1)}/\delta^{(2)} = 1$.

Acknowledgment

This work was supported by the NSC of the Republic of China under NSC 85-2211-E-006-011.

References

- Bogy, D. B., 1970, "On the Problem of Edge-bonded Elastic Quarter-planes Loaded at the Boundary," *Int. J. Solids Structures*, Vol. 6, pp. 1287-1313.
- Chadwick, P., and Smith, G. D., 1977, "Foundations of the Theory of Surface Waves in Anisotropic Elastic Materials," *Advances in Applied Mechanics*, Vol. 17, pp. 303-376.
- Cook, T. S., and Erdogan, F., 1972, "Stresses in Bonded Materials with a Crack Perpendicular to the Interface," *Int. J. Engng. Sci.*, Vol. 10, pp. 677-697.
- Dongye, C., and Ting, T. C. T., 1989, "Explicit Expressions of Barnett-Lothe Tensors and Their Associated Tensors for Orthotropic Materials," *Quarterly of Applied Mathematics*, Vol. 47, pp. 723-734.

Dundurs, J., 1968, *Elastic Interaction of Dislocations with Inhomogeneities, Mathematical Theory of Dislocation*, ASME, New York, pp. 70–115.

Erdogan, F., 1972, "Fracture Problems in Composite Materials," *Engineering Fracture Mechanics*, Vol. 4, pp. 811–840.

Erdogan, F., and Biricikoglu, V., 1973, "Two Bonded Half Planes with a Crack Going Through the Interface," *Int. J. Engng. Sci.*, Vol. 11, pp. 745–766.

Eshelby, J. D., Read, W. T., and Shockley, W., 1953, "Anisotropic Elasticity With Applications to Dislocation Theory," *Acta Metallurgica*, Vol. 1, pp. 251–259.

Gerasoulis, A., 1982, "The Use of Piecewise Quadratic Polynomials for the Solution of Singular Integral Equations of Cauchy Type," *Computational Mathematics with Applications*, Vol. 8, pp. 15–22.

Gupta, V., Argon, A. S., and Suo, Z., 1992, "Crack Deflection at an Interface Between Two Orthotropic Media," *ASME JOURNAL OF APPLIED MECHANICS*, Vol. 59, pp. 79–87.

Hutchinson, J. W., Mear, M. E., and Rice, J. R., 1987, "Crack Paralleling an Interface Between Dissimilar Materials," *ASME JOURNAL OF APPLIED MECHANICS*, Vol. 54, pp. 828–832.

Krenk, S., 1979, "On the Elastic Constants of Plane Orthotropic Elasticity," *Journal of Composite Materials*, Vol. 13, pp. 108–116.

Miller, G. R., 1989, "Analysis of Crack Near Interfaces Between Dissimilar Anisotropic Materials," *International Journal of Engineering Science*, Vol. 27, pp. 667–678.

Muskelishvili, N. I., 1953, *Singular Integral Equations*, Noordhoff.

Stroh, A. N., 1958, "Dislocations and Cracks in Anisotropic Elasticity," *Philos. Mag.*, Vol. 7, pp. 625–646.

Sung, J. C., and Liou, J. Y., 1994, "Analysis of a Crack Embedded in a Linear Elastic Half-Plane Solid," *ASME JOURNAL OF APPLIED MECHANICS*, accepted for publication.

Sung, J. C., and Liou, J. Y., 1994, "Singularities at the Tip of a Crack Terminating Normally at an Interface Between Two Orthotropic Media," *ASME JOURNAL OF APPLIED MECHANICS*, accepted for publication.

Suo, Z., 1990, "Singularities, Interfaces and Cracks in Dissimilar Anisotropic Media," *Proceedings of the Royal Society of London*, Vol. A427, pp. 331–358.

Ting, T. C. T., 1986, "Explicit Solution and Invariance of The Singularities at an Interface Crack in Anisotropic Composites," *International Journal of Solids and Structures*, Vol. 22, pp. 763–965.

Ting, T. C. T., 1992, "Image Singularities of Green's Functions for Anisotropic Elastic Half-Spaces and Bimaterials," *The Quarterly Journal of Mechanics and Applied Mathematics*, Vol. 45, pp. 119–139.

Ting, T. C. T., and Hoang, P. H., 1984, "Singularities at the Tip of a Crack Normal to the Interface of an Anisotropic Layered Composite," *International Journal of Solids and Structures*, Vol. 20, pp. 439–454.

Zwiers, R. I., Ting, T. C. T., and Spilker, R. L., 1982, "On the Logarithmic Singularity of Free-Edge Stress in Laminated Composites Under Uniform Extension," *ASME JOURNAL OF APPLIED MECHANICS*, Vol. 49, pp. 561–569.

APPENDIX A

The vector function $f(z)$ is given by

$$2\pi i f(z) = \begin{cases} \sum_{j=1}^2 \{ \text{diag} < \ln(z_1 - z_j^D), \ln(z_2 - z_j^D) > \mathbf{B}^{(1)^{-1}} \mathbf{M}^{12} \mathbf{B}^{(2)^T} \mathbf{I}_j \mathbf{B}^{(2)^T} \} \mathbf{b}, z_k \in \#1 \\ \text{diag} < \ln(z_1 - z_1^D), \ln(z_2 - z_2^D) > \mathbf{B}^{(2)^T} \mathbf{b} - \sum_{j=1}^2 \{ \text{diag} < \ln(z_1 - \bar{z}_j^D), \\ \ln(z_2 - \bar{z}_j^D) > \mathbf{B}^{(2)^{-1}} \mathbf{M}^{22} \bar{\mathbf{B}}^{(2)^T} \mathbf{I}_j \bar{\mathbf{B}}^{(2)^T} \} \mathbf{b}, z_k \in \#2 \end{cases}$$

where

$$z_j^D = x_1^D + p_j^{(2)} x_2^D, \quad (j = 1, 2)$$

is the point where point dislocation \mathbf{b} is acting. (For convenience, only the result of \mathbf{b} acting at material #2 is given above.)

APPENDIX B

The functions of $n_{kj}^{\alpha\beta}(\gamma)$ and $\tilde{n}_{kj}^{\alpha\beta}(\gamma)$ appearing in Eq. (39) are as follows:

$$\begin{aligned} n_{11}^{11} &= -(2\omega_-^{(1)})^{-2} \{ q_-^{(1)2} + q_+^{(1)2} - q_-^{(1)2} q_+^{(1)2\gamma} - q_+^{(1)2} q_-^{(1)2\gamma} \} \\ n_{12}^{11} &= -(2\omega_-^{(1)})^{-2} \{ q_-^{(1)3} q_+^{(1)2\gamma} + q_+^{(1)3} q_-^{(1)2\gamma} - q_-^{(1)} - q_+^{(1)} \} \\ n_{21}^{11} &= -(2\omega_-^{(1)})^{-2} \{ q_-^{(1)} q_+^{(1)2\gamma} + q_+^{(1)} q_-^{(1)2\gamma} - q_-^{(1)} - q_+^{(1)} \} \\ n_{22}^{11} &= -(2\omega_-^{(1)})^{-2} \{ 2 - q_-^{(1)2} q_+^{(1)2\gamma} - q_+^{(1)2} q_-^{(1)2\gamma} \} \\ \tilde{n}_{11}^{11} &= n_{22}^{11}, \quad \tilde{n}_{12}^{11} = n_{12}^{11}, \quad \tilde{n}_{21}^{11} = n_{21}^{11}, \quad \tilde{n}_{22}^{11} = n_{11}^{11} \quad (\text{B1}) \end{aligned}$$

and

$$\begin{aligned} n_{11}^{12} &= (4\omega_-^{(1)} \omega_-^{(2)})^{-1} \{ q_+^{(2)\gamma} (q_+^{(1)2-\gamma} - q_-^{(1)2-\gamma}) \\ &\quad + q_-^{(2)\gamma} (q_-^{(1)2-\gamma} - q_+^{(1)2-\gamma}) \} \Delta^{1-\gamma} \\ n_{12}^{12} &= (4\omega_-^{(1)} \omega_-^{(2)})^{-1} \{ q_-^{(2)\gamma} q_+^{(2)\gamma} (q_+^{(1)2-\gamma} - q_-^{(1)2-\gamma}) \\ &\quad + q_+^{(2)\gamma} (q_-^{(1)2-\gamma} - q_+^{(1)2-\gamma}) \} \Delta^{2-\gamma} \\ n_{21}^{12} &= (4\omega_-^{(1)} \omega_-^{(2)})^{-1} \{ q_+^{(2)\gamma} (q_-^{(1)1-\gamma} - q_+^{(1)1-\gamma}) \\ &\quad + q_-^{(2)\gamma} (q_+^{(1)1-\gamma} - q_-^{(1)1-\gamma}) \} \Delta^{1-\gamma} \\ n_{22}^{12} &= (4\omega_-^{(1)} \omega_-^{(2)})^{-1} \{ q_-^{(2)\gamma} q_+^{(2)\gamma} (q_-^{(1)1-\gamma} - q_+^{(1)1-\gamma}) \\ &\quad + q_+^{(2)\gamma} (q_-^{(1)1-\gamma} - q_+^{(1)1-\gamma}) \} \Delta^{2-\gamma} \\ \tilde{n}_{11}^{12} &= (4\omega_-^{(1)} \omega_-^{(2)})^{-1} \{ q_-^{(2)2} q_+^{(2)\gamma} (q_-^{(1)1-\gamma} - q_+^{(1)1-\gamma}) \\ &\quad + q_+^{(2)2} q_-^{(2)\gamma} (q_+^{(1)1-\gamma} - q_-^{(1)1-\gamma}) \} \Delta^{1-\gamma} \\ \tilde{n}_{12}^{12} &= (4\omega_-^{(1)} \omega_-^{(2)})^{-1} \{ q_-^{(2)2} q_+^{(2)\gamma} (q_+^{(1)1-\gamma} - q_-^{(1)1-\gamma}) \\ &\quad + q_+^{(2)2} q_-^{(2)\gamma} (q_-^{(1)1-\gamma} - q_+^{(1)1-\gamma}) \} \Delta^{1-\gamma} \quad (\text{B2}) \end{aligned}$$

where

$$q_+^{(\alpha)} = \omega_+^{(\alpha)} + \omega_-^{(\alpha)}, \quad q_-^{(\alpha)} = \omega_+^{(\alpha)} - \omega_-^{(\alpha)}, \quad (\alpha = 1, 2). \quad (\text{B3})$$

Note that n_{kj}^{22} (and \tilde{n}_{kj}^{22}) and n_{kj}^{21} (and \tilde{n}_{kj}^{21}) can be obtained from (B1) and (B2) by interchanging the superindices (1) \rightarrow (2) and (2) \rightarrow (1), respectively, and also by replacing Δ by Δ^{-1} . When material #1 is degenerated, i.e., $\kappa_1 = 1$ then Eqs. (B1) and (B2) become

$$\begin{aligned} n_{11}^{11} &= -\gamma(2 - \gamma), \quad n_{12}^{11} = -(1 - \gamma)(2 - \gamma), \\ n_{21}^{11} &= \gamma(1 - \gamma), \quad n_{22}^{11} = (1 - \gamma)^2 \quad (\text{B4}) \end{aligned}$$

and

$$\begin{aligned} n_{11}^{12} &= (2\omega_-^{(2)})^{-1} \{ (2 - \gamma)(q_+^{(2)\gamma} - q_-^{(2)\gamma}) \} \Delta^{1-\gamma} \\ n_{12}^{12} &= (2\omega_-^{(2)})^{-1} \{ (2 - \gamma)(q_-^{(2)} q_+^{(2)\gamma} - q_+^{(2)} q_-^{(2)\gamma}) \} \Delta^{2-\gamma} \\ n_{21}^{12} &= (2\omega_-^{(2)})^{-1} \{ (1 - \gamma)(q_-^{(2)\gamma} - q_+^{(2)\gamma}) \} \Delta^{1-\gamma} \\ n_{22}^{12} &= (2\omega_-^{(2)})^{-1} \{ (1 - \gamma)(q_+^{(2)} q_-^{(2)\gamma} - q_-^{(2)} q_+^{(2)\gamma}) \} \Delta^{2-\gamma} \\ \tilde{n}_{11}^{12} &= (2\omega_-^{(2)})^{-1} \{ (1 - \gamma)(q_+^{(2)\gamma} - q_-^{(2)\gamma}) \} \Delta^{1-\gamma} \\ \tilde{n}_{12}^{12} &= (2\omega_-^{(2)})^{-1} \{ (1 - \gamma)(q_+^{(2)} q_-^{(2)\gamma} - q_-^{(2)} q_+^{(2)\gamma}) \} \Delta^{1-\gamma} \\ n_{11}^{21} &= (2\omega_-^{(2)})^{-1} \{ \gamma(q_+^{(2)\gamma} - q_-^{(2)\gamma}) \} \Delta^{-\gamma} \\ n_{12}^{21} &= (2\omega_-^{(2)})^{-1} \{ \gamma(q_+^{(2)2} q_-^{(2)\gamma} - q_-^{(2)2} q_+^{(2)\gamma}) \} \Delta^{-\gamma} \quad (\text{B5}) \end{aligned}$$

When material #2 is degenerated, i.e., $\kappa_2 = 1$, then Eq. (B2) becomes

$$\begin{aligned} n_{11}^{12} &= (2\omega_-^{(1)})^{-1} \{ \gamma(q_+^{(1)2-\gamma} - q_-^{(1)2-\gamma}) \} \Delta^{1-\gamma} \\ n_{12}^{12} &= (2\omega_-^{(1)})^{-1} \{ (1-\gamma)(q_+^{(1)2-\gamma} - q_-^{(1)2-\gamma}) \} \Delta^{2-\gamma} \\ n_{21}^{12} &= (2\omega_-^{(1)})^{-1} \{ \gamma(q_-^{(1)1-\gamma} - q_+^{(1)1-\gamma}) \} \Delta^{1-\gamma} \\ n_{22}^{12} &= (2\omega_-^{(1)})^{-1} \{ (1-\gamma)(q_+^{(1)1-\gamma} - q_-^{(1)1-\gamma}) \} \Delta^{2-\gamma} \\ \tilde{n}_{11}^{12} &= (2\omega_-^{(1)})^{-1} \{ (1-\gamma)(q_+^{(1)1-\gamma} - q_-^{(1)1-\gamma}) \} \Delta^{1-\gamma} \\ \tilde{n}_{12}^{12} &= (2\omega_-^{(1)})^{-1} \{ (2-\gamma)(q_+^{(1)1-\gamma} - q_-^{(1)1-\gamma}) \} \Delta^{1-\gamma} \end{aligned}$$

$$\begin{aligned} \tilde{n}_{21}^{12} &= (2\omega_-^{(1)})^{-1} \{ (1-\gamma)(q_-^{(1)1-\gamma} - q_+^{(1)1-\gamma}) \} \Delta^{1-\gamma} \\ \tilde{n}_{22}^{12} &= (2\omega_-^{(1)})^{-1} \{ (2-\gamma)(q_-^{(1)1-\gamma} - q_+^{(1)1-\gamma}) \} \Delta^{1-\gamma}. \end{aligned} \quad (B6)$$

When both materials become degenerate, ($\kappa_1 = 1$, $\kappa_2 = 1$), (B2) reduces to

$$\begin{aligned} n_{11}^{12} &= \gamma(2-\gamma)\Delta^{1-\gamma}, \quad n_{12}^{12} = -(1-\gamma)(2-\gamma)\Delta^{2-\gamma}, \\ n_{21}^{12} &= -\gamma(1-\gamma)\Delta^{1-\gamma}, \quad n_{22}^{12} = (1-\gamma)^2\Delta^{2-\gamma} \\ \tilde{n}_{11}^{12} &= (1-\gamma)^2\Delta^{1-\gamma}, \quad \tilde{n}_{12}^{12} = (1-\gamma)(2-\gamma)\Delta^{1-\gamma}, \\ \tilde{n}_{21}^{12} &= \gamma(1-\gamma)\Delta^{1-\gamma}, \quad \tilde{n}_{22}^{12} = \gamma(2-\gamma)\Delta^{1-\gamma}. \end{aligned} \quad (B7)$$

A Finite Element Analysis of Mode III Quasi-Static Crack Growth at a Ductile-Brittle Interface

S. Omprakash
Graduate Student.

R. Narasimhan
Assistant Professor.

Department of Mechanical Engineering,
Indian Institute of Science,
Bangalore 560012, India

Steady-state quasi-static crack growth along a bimaterial interface is analyzed under Mode III, small-scale yielding conditions using a finite element procedure. The interface is formed by an elastic-plastic material and an elastic substrate. The top elastic-plastic material is assumed to obey the J_2 incremental theory of plasticity. It undergoes isotropic hardening with either a bilinear uniaxial response or a power-law response. The results obtained from the full-field numerical analysis compare very well with the analytical asymptotic results obtained by Castañeda and Mataga (1991), which forms one of the first studies on this subject. The validity of the separable form for the asymptotic solution assumed in their analysis is investigated. The range of dominance of the asymptotic fields is examined. Field variations are obtained for a power-law hardening elastic-plastic material. It is seen that the stresses are lower for a stiffer substrate. The potential of the bimaterial system to sustain slow stable crack growth along the interface is studied. It is found that the above potential is larger if the elastic substrate is more rigid with respect to the elastic-plastic material.

1 Introduction

Ductile-brittle interfaces occur in a variety of advanced engineering materials like composites, cermets, polycrystalline intermetallic alloys, etc. Interface failure in these materials is a common occurrence caused due to the propagation and coalescence of pre-existing or nucleated cracks along the interface. Hence an understanding of the mechanics of interface failure is essential to gauge the efficiency and reliability of such components. In this work, the interface is assumed to be weaker than both the materials and hence the crack is expected to propagate along it.

The understanding of interfacial crack propagation is at a preliminary stage of development and thus the bulk of the work reported till now deal with stationary cracks in linear-elastic materials. Rice (1988) and Shih (1991) have reviewed the progress made on the mechanics of interface fracture. Some important contributions dealing with material nonlinearities in the context of a stationary crack at a bimaterial interface include those of Shih and Asaro (1988, 1989) and Zywicz and Parks (1989), on power-law hardening and perfectly plastic behavior, respectively.

In elastic-plastic materials, a slow, stable crack extension phase under monotonically increasing load or displacement conditions is often observed prior to catastrophic failure. An elastic-plastic material offers much more resistance to nonproportional straining (which occurs near the tip of a propagating crack) than to proportional ones, and this is the main source of stable crack growth. Several investigators (Chitaley and McClintock, 1971; Drugan et al., 1982, and Castañeda, 1987) have studied,

using analytical methods, the asymptotic fields near the tip of a growing crack in homogeneous elastic-plastic materials. Numerical studies of quasi-static crack growth in homogeneous elastic-plastic materials have also been carried out by many researchers (Dean and Hutchinson, 1980; Narasimhan et al., 1987).

By contrast, very few contributions have been made till now on crack propagation along the interface between two dissimilar elastic-plastic materials. The work by Castañeda and Mataga (1991) is one of the first studies on this subject. They performed an asymptotic analysis and obtained the near-tip stress and velocity fields of a crack propagating steadily and quasi-statically along the interface between a strain-hardening ductile material and a brittle material. The ductile material is characterized by a J_2 -flow theory with either linear hardening or perfect plasticity. Both the cases of antiplane shear and Mode I plane strain were considered. Drugan (1991) also derived the stress and deformation fields near the tip of a crack that is propagating quasi-statically along the interface formed by a rigid material on one side and an elastic-ideally plastic material on the other.

It is the objective of this work to perform a full-field finite element analysis of steady quasi-static crack propagation under Mode III, small-scale yielding conditions along a bi-material interface. The interface (see Fig. 1) is formed by an elastic material (material #2) and an elastic-plastic material (material #1). The latter is assumed to exhibit either linear isotropic hardening or power-law hardening.

The organization of the paper is as follows. In Sec. 2, the constitutive model that is used is presented. In Sec. 3, the finite element procedure employed to simulate steady-state crack growth along the interface is briefly described. In Sec. 4, the results obtained from the analyses are discussed. The finite element mesh used in this work is well refined near the crack tip so that an accurate modeling of the near-tip fields is achieved. This is confirmed by a good comparison between the present numerical results and the analytical (asymptotic) solution of Castañeda and Mataga (1991) for the case when material #1 displays linear isotropic hardening (see Sec. 4.1).

Contributed by the Applied Mechanics Division of THE AMERICAN SOCIETY OF MECHANICAL ENGINEERS for publication in the ASME JOURNAL OF APPLIED MECHANICS.

Discussion on this paper should be addressed to the Technical Editor, Professor Lewis T. Wheeler, Department of Mechanical Engineering, University of Houston, Houston, TX 77204-4792, and will be accepted until four months after final publication of the paper itself in the ASME JOURNAL OF APPLIED MECHANICS.

Manuscript received by the ASME Applied Mechanics Division, Mar. 4, 1993; final revision, July 15, 1994. Associate Technical Editor: D. M. Parks.

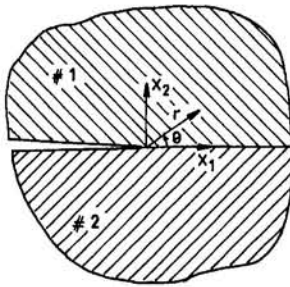


Fig. 1 Schematic representation of the bimaterial with an interface crack

The validity of the separable solution assumed in the above analytical work for the asymptotic fields is examined. The range of dominance of these fields is also investigated. The effect of the mismatch in the elastic shear modulus between the two materials on the stresses and deformations near the propagating crack tip is studied. With a view to examine the potential of the bimaterial system to sustain slow stable crack growth along the interface, the ratio of far-field J integral for steady-state crack growth to its value at initiation J_{ss}/J_c is estimated using a critical crack-tip opening displacement criterion (ductile fracture criterion). The effect of the ratio of the elastic shear modulus of the two materials on the J_{ss}/J_c ratio is investigated.

2 Constitutive Model

In this paper, a small-strain, incremental plasticity theory is employed along with the Huber-Von Mises yield condition and the associated flow rule to describe the constitutive behavior of the elastic-plastic material #1 (see Fig. 1). The material #2 which forms the other side of the interface is taken as isotropic-elastic with shear modulus G_2 .

The Huber-Von Mises yield condition for isotropic hardening under antiplane shear takes the form,

$$\Phi(\tau, \bar{\gamma}^p) = \tau_\beta \cdot \tau_\beta - \bar{\tau}^2(\bar{\gamma}^p) = 0. \quad (1)$$

Here, $\tau_1 = \sigma_{31}$ and $\tau_2 = \sigma_{32}$ are the shear stress components, and $\bar{\gamma}^p = \int \sqrt{\dot{\gamma}_1^2 + \dot{\gamma}_2^2} \cdot dt$ is the accumulated equivalent plastic strain. The notations $\gamma_1 = 2\epsilon_{31}$ and $\gamma_2 = 2\epsilon_{32}$ will be used for the engineering shear strains. For a linear hardening elastic-plastic material G'_1 is the tangent modulus under simple shear (which is a constant), and G_1 is the elastic shear modulus. For a power-law hardening material, the strain-hardening function $\bar{\tau}(\bar{\gamma}^p)$ is defined by the relation,

$$\left(\frac{\bar{\gamma}^p}{\gamma_{01}} \right) = \left(\frac{\bar{\tau}}{\tau_{01}} \right)^n - \left(\frac{\bar{\tau}}{\tau_{01}} \right). \quad (2)$$

Here, n is the strain-hardening exponent, τ_{01} is the initial yield stress, and $\gamma_{01} = \tau_{01}/G_1$ is the initial yield strain of the material under simple shear. It should be noted that $n = 1$ corresponds to the case of a purely elastic material and $n \rightarrow \infty$ pertains to the elastic-perfectly plastic limit.

The constitutive law for material #1 when it is currently experiencing elastic-plastic deformation can be expressed as

$$\tau_\alpha = G_1 \left[\delta_{\alpha\beta} - \frac{G_1}{G_1 + H} \frac{\tau_\beta \tau_\alpha}{\bar{\tau}^2} \right] \dot{\gamma}_\beta. \quad (3)$$

In the above equation, H is the plastic modulus which is defined as

$$H = \frac{d\bar{\tau}}{d\bar{\gamma}^p}. \quad (4)$$

3 Numerical Procedure

In this paper, steady-state crack growth along the interface is simulated under Mode III using the finite element procedure

based on moving crack-tip coordinates devised by Dean and Hutchinson (1980). Herein, a semi-infinite crack which has been propagating in a quasi-static manner with velocity V under Mode III small-scale yielding conditions at a bi-material interface is considered. It is assumed that the zone of inelastic deformation is contained in a small region near the crack tip in material #1 and the elastic K -field holds good at points far away from the tip. A brief description of the numerical procedure is given below.

The crack tip coordinates (X_1, X_2) and the field quantities are normalized as

$$\left. \begin{aligned} \hat{X}_\alpha &= X_\alpha / (K/\tau_{01})^2, \\ \hat{u}_3 &= u_3 / (K^2/G_1\tau_{01}), \\ \hat{\tau}_\alpha &= \tau_\alpha / \tau_{01}, \\ \hat{\gamma}_\alpha &= \gamma_\alpha / \gamma_{01}. \end{aligned} \right\} \quad (5)$$

Here, K is the remote Mode III stress intensity factor. Further, the crack is assumed to propagate steadily in the X_1 direction with velocity V , so that the time rate of change of any field quantity at a fixed material point can be expressed as

$$\frac{d}{dt} (\cdot) = (\cdot) = -V \frac{\partial}{\partial X_1} (\cdot). \quad (6)$$

By applying the principle of virtual work, and making use of the normalizations given in (5), and the steady-state condition (6), the (nonlinear) finite element equilibrium equations can be derived (see Dean and Hutchinson, 1980).

An iterative procedure (see Dean and Hutchinson, 1980) is used to solve these nonlinear equilibrium equations. In the present formulation, the stresses and plastic strains have been updated using an explicit stress update algorithm (with subincrementation), by integrating along the negative X_1 -direction (holding X_2 fixed), as suggested by the steady-state equation (6) subject to the initial state of the material point outside the elastic-plastic boundary.

To simulate steady-state crack growth along the interface, a large rectangular domain representing both the materials forming the interface is modelled with four-node rectangular finite elements with bilinear shape functions placed parallel to the interface line ($\hat{X}_2 = 0$). The crack line is located along the negative \hat{X}_1 -axis. The mesh contains a total of 1286 nodal points and 1200 four noded rectangular elements. The size of the smallest element near the crack tip is designed to be less than 1/6000 of the expected size of the plastic zone. Also, the mesh is graded in a manner such that a majority of elements are within the expected boundary of the plastic zone and relatively large size elements are employed in the far-field elastic region. The above mesh design is expected to resolve the fields inside the plastic zone and particularly near the crack tip accurately. This will be confirmed when comparisons with available analytical solutions are made in Sec. 4. Displacement boundary condition based on the elastic K -field is prescribed along the top and bottom boundaries of the mesh, while traction (from the K -field) is specified on the upstream (right) and downstream (left) boundaries of the mesh.

4 Results and Discussion

Attention is focussed on two sets of bimaterials. One set of bimaterials has both the elastic-plastic top and the elastic substrate of the same stiffness (same value of the shear modulus, i.e., $G_1 = G_2$ or $\beta = G_2/G_1 = 1$). The other combination has the substrate considerably stiffer ($\beta = G_2/G_1 = 10$).

4.1 Linear Hardening Elastic-Plastic Material and Elastic Substrate. In this section, the results obtained from the finite element analysis for the case where material #1 exhibits isotropic linear strain hardening with a tangent modulus G'_1 are

discussed. As mentioned in the Introduction, Castañeda and Mataga (1991) have recently derived an asymptotic analytical solution for this case under the conditions of both Mode III as well as Mode I plane strain. Their work involved two important assumptions. First, it was assumed that the dominant term for the stress and velocity fields near the crack tip is separable in polar coordinates r and θ (see Fig. 1). Secondly, the radial variation of the dominant term was taken to be in the form r^s , where s is the strength of singularity of the field quantities near the crack tip. Thus, on using the normalizations introduced in Eq. (5), the structure of the near-tip variation for the polar stress components proposed by Castañeda and Mataga (1991) can be written as

$$\left. \begin{aligned} \hat{\tau}_r &= A\hat{r}^s y_1(\theta), \\ \hat{\tau}_\theta &= A\hat{r}^s y_2(\theta), \end{aligned} \right\} \quad (7)$$

as $\hat{r} \rightarrow 0$. Here, A is an amplitude parameter which is undetermined by the asymptotic analysis. Further, $y_1(\theta)$ and $y_2(\theta)$ are dimensionless angular functions which are normalized such that $y_2(0) = 1$. Castañeda and Mataga (1991) solved the governing differential equations numerically and obtained the exponent s and the angular functions $y_i(\theta)$ for $\beta = 1$ and $\beta \rightarrow \infty$ for several values of $\alpha = G_1^1/G_1$.

4.1.1 Validity of the Asymptotic Solution. The validity of the asymptotic analytical solution of Castañeda and Mataga (1991) is checked by comparing their solution with the results obtained from the present full-field finite element analysis. First, the radial dependence assumed in this near-tip stress field is examined. To this end, the variation of $\log_e(\hat{\tau}_2)$ with $\log_e(\hat{X}_1)$ where \hat{X}_1 is normalized distance ahead of the propagating crack tip is shown in Fig. 2, for $\alpha = G_1^1/G_1 = 0.2$. The numerically obtained results are presented in this figure corresponding to $\beta = 1$ and 10. Also displayed in this figure are the best fit straight lines (by least squares method) to the six nearest points to the crack tip.

The strength of the singularity s was obtained directly by measuring the slope of the aforementioned best fit straight lines like those shown in Fig. 2. The s values thus obtained from the present finite element results are compared with those determined from the asymptotic analysis by Castañeda and Mataga (1991), in Table 1. It can be seen from this table that the s values computed from the finite element results match very closely with those given by Castañeda and Mataga (1991) for $\alpha = 0.2$. The computed value of s differs more from the asymptotic results with decreasing value of α . Further, it must be noted from Table 1 (see also Fig. 2) that the strength of singularity, for any particular value of α , is lower if the substrate is more rigid.

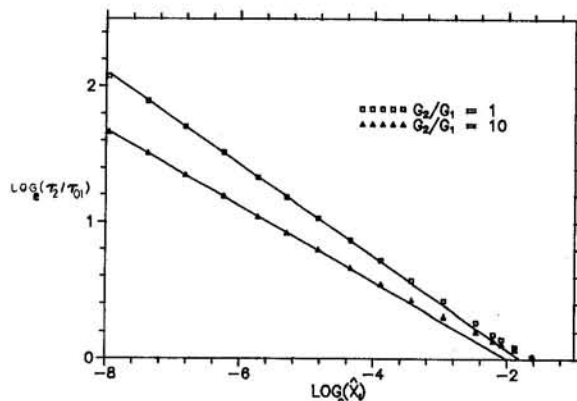


Fig. 2 Logarithmic plot of the radial stress variation for $\alpha = 0.2$ and $\beta = 1, 10$

Table 1 Strength of singularity s

α	Asymptotic ($\beta = 1$)	Numerical ($\beta = 1$)	Asymptotic ($\beta = \infty$)	Numerical ($\beta = 10$)
0.2	-0.343	-0.340	-0.277	-0.280
0.1	-0.270	-0.266	-0.207	-0.205
0.05	-0.204	-0.192	-0.153	-0.146

It is important to ascertain the range of dominance of the asymptotic solution of Castañeda and Mataga (1991). To this end, straight line fits having the exact slope s given in their paper were again made to the numerically obtained results of $\log_e(\hat{\tau}_2)$ versus $\log_e(\hat{X}_1)$ corresponding to the first few points ahead of the tip. The amplitude parameter A in Eq. (7) was determined from these straight line fits. The distance ahead of the crack tip where the difference between the points obtained from the numerical solution and the above best fit straight lines becomes significant (say, by about five percent) is a measure of the range of dominance of the asymptotic singular solution of Castañeda and Mataga (1991).

This range of dominance along with the amplitude parameter A is shown in Table 2 for various values of α and for $\beta = 1$ and 10. In interpreting the results of Table 2, it must be noted that the maximum plastic zone size which occurs ahead of the crack tip in material #1 is between 0.2 to 0.3(K/τ_{01})². It can be seen from this table that the range of dominance depends on the hardening parameter α . As α decreases (diminishing strain hardening) it can be observed that the range of dominance falls, allowing the actual fields to deviate from the asymptotic solution at a smaller distance ahead of the crack tip. For $\alpha < 0.005$, the range of dominance of the asymptotic stress variation given by Castañeda and Mataga (1991) becomes extremely small (less than 0.5 percent of the maximum plastic zone size).

Secondly, it is examined whether the variable-separable form which was assumed for the near-tip fields in the analytical asymptotic analysis, is corroborated by the finite element solution. For the variable-separable solution (Eq. (7)) to be valid, the angular distribution of $\hat{\tau}_r(\hat{r}, \theta)/A\hat{r}^s$ should be the same for any near-tip contour surrounding the crack tip. Here it is most desirable to consider circular contours surrounding the crack tip since all the points on the contour will be equidistant from the crack tip. However, this is not directly possible since the present numerical procedure employs rectangular elements parallel to the crack line (see Sec. 3). Hence, the stresses obtained from the finite element analysis (corresponding to material #1) were first smoothed using a post-processing technique and angular variations along near-tip semi-circular contours were extracted from the smoothed results.

The case $\alpha = 0.1$ and $\beta = 1$ is considered here for discussion. The value of A was determined following the procedure discussed above (see Table 2). The angular variation of the functions $y_1(\theta) = \hat{\tau}_r(\hat{r}, \theta)/A\hat{r}^s$ and $y_2(\theta) = \hat{\tau}_\theta(\hat{r}, \theta)/A\hat{r}^s$ obtained from the finite element results, are plotted along two semi-circular contours with different normalized radial distance \hat{r} from the crack tip in the upper half of the bi-material in Fig.

Table 2 Range of dominance of the asymptotic field and the amplitude parameter A under small-scale yielding

α	Range of Dominance		Amplitude Parameter A	
	$\beta = 1$	$\beta = 10$	$\beta = 1$	$\beta = 10$
0.2	0.026	0.030	0.527	0.583
0.1	0.016	0.017	0.568	0.632
0.05	0.007	0.008	0.604	0.673
0.01	0.0017	0.0013	0.681	0.746
0.005	0.0010	0.0008	0.718	0.770

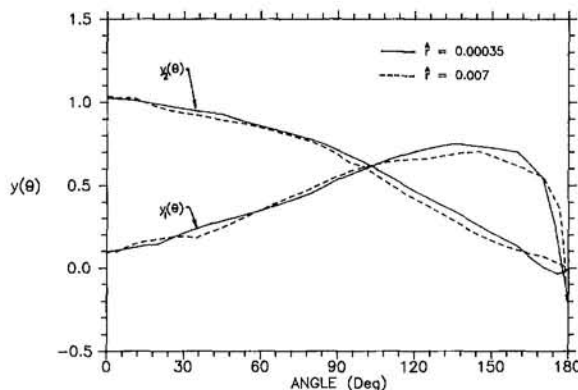


Fig. 3 Variation of the dimensionless angular functions for two different semi-circular contours for $\alpha = 0.1$ and $\beta = 1$

3. It should be noted that both these contours are well inside the plastic zone in material #1. It can be seen that there is a good agreement between the distribution of the angular functions along the two contours. This suggests that the separable form considered by Castañeda and Mataga (1991) is a reasonable assumption for the Mode III case.

4.1.2 Angular Variation of the Velocity Field. The angular variation of the normalized velocity field, $\hat{y}_1 = -\dot{u}_3/(V_{y01})$ in the top half of the bi-material is shown in Figs. 4 and 5. The centroidal values of \hat{y}_1 in the elements located along the rectangular contour shown in the inset of Fig. 4 have been used to construct these plots. In Fig. 4, the angular variation of velocity is compared for $\alpha = 0.001, 0.05$ corresponding to the case $\beta = 1$. In Fig. 5, they are compared for the same values of α pertaining to $\beta = 10$.

The angular variation for $\alpha = 0.001$ in Figs. 4 and 5 is similar to the analytical results given by Castañeda and Mataga (1991). It is observed from these figures that the distributions for $\alpha = 0.001$ and 0.05 crossover at approximately $\theta = 55$ deg. In both these figures it can be seen that the magnitude of the velocity is same for $\alpha = 0.001$ and 0.05 at $\theta = 0$. From the fact that the magnitude of velocity is larger for the case of higher strain hardening (larger α) over a substantial angular range (55 deg $< \theta < 180$ deg), it is expected that the crack profile will also be larger for this case irrespective of the value of β . On comparing Figs. 4 and 5 it is noticed that the magnitude of the velocity is lower for a stiffer substrate indicating that the crack profile for material #1 will be lesser if β is higher.

Finally, it is worth mentioning, that the velocity \dot{u}_3 at the interface line ($\theta = 0$) is smaller for a larger value of β and is

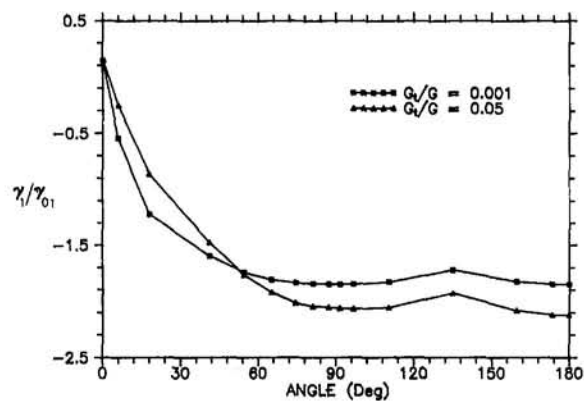


Fig. 5 Angular variation of the velocity field for $\alpha = 0.05, 0.001$ and $\beta = 10$

expected to vanish for $\beta \rightarrow \infty$ in accordance with the rigid nature of the substrate for this case.

4.2 Power-Hardening Elastic-Plastic Material and Elastic Substrate. In this section, the results obtained from the finite element analysis for the case where material #1 exhibits power-law hardening with a hardening exponent n are discussed. No asymptotic solutions are available for crack growth at a bimaterial interface when one of the materials exhibits power-law hardening. Hence, no direct comparison is possible between the present finite element results and an analytical solution for this case.

4.2.1 Near-Tip Stress Distribution. The normalized stress $\hat{\tau}_2$ is plotted with respect to normalized distance \hat{X}_1 , ahead of the propagating crack tip in Fig. 6 for two different values of the hardening exponent, $n = 10$ and $n = 5$. The cases of $\beta = 1$ and 10 are considered. It should be noted that the length scale over which the plots are shown in Fig. 6 is well inside the plastic zone in material #1.

It can be readily seen from the above figure that the stress becomes unbounded as the crack tip is approached. Also, the stress $\hat{\tau}_2$ for the bimaterial with a stiffer substrate (larger β) is significantly lower for a given value of n . As in the linear hardening case, it is found on comparing the curves corresponding to $n = 10$ and $n = 5$ in Fig. 6 that the stress at a certain normalized distance ahead of the crack tip decreases with diminishing strain hardening (larger values of hardening exponent n). As the level of hardening decreases the stress singularity falls and, in the case of a homogeneous material, the τ_2 stress ahead of the crack tip in the limit $n \rightarrow \infty$ approaches a constant value of τ_0 except, perhaps, very close to the crack tip.

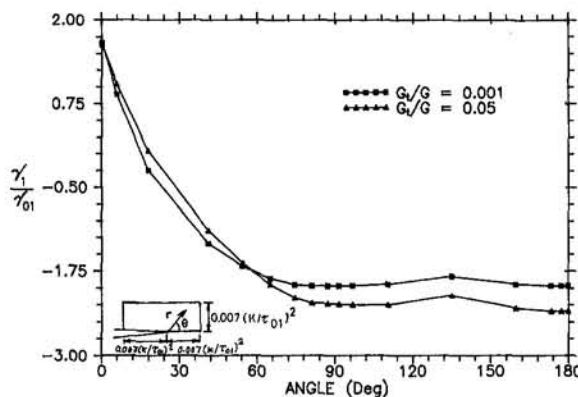


Fig. 4 Angular variation of the velocity field for $\alpha = 0.05, 0.001$ and $\beta = 1$

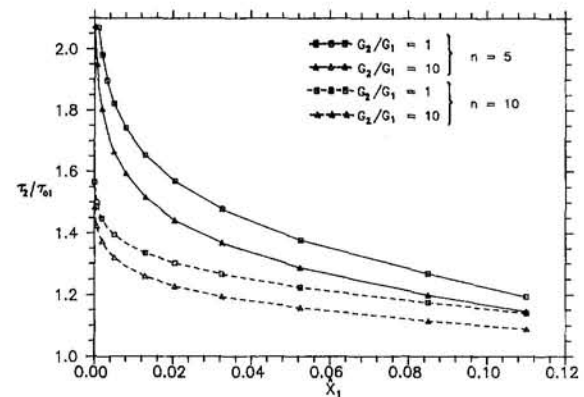


Fig. 6 Radial stress variation ahead of the crack tip for $n = 5, 10$ and $\beta = 1, 10$

The near-tip angular variation of τ_r and τ_θ in material #1 is similar to the linear hardening case (see angular functions shown in Fig. 3). It was found that a larger value of β reduces the magnitude of the stresses around the crack tip. Also, increasing n (for a fixed β) produces a significant decrease in the near-tip stress field. It is of interest to compare the near-tip angular stress variations obtained in this work corresponding to very low strain hardening (of material #1) with the asymptotic solution given by Drugan (1991). It was found from the present full-field numerical results under small-scale yielding conditions that for the case of $\beta = 10$ and low strain hardening, $\tau_1(r, \theta = 0^+) \approx 0$ near the crack tip. Drugan's asymptotic solution for the stress field reduces to that given by Chitaley and McClintock (1971) for a homogeneous elastic-perfectly plastic material under the above condition. In Fig. 7, this asymptotic solution is compared with the near-tip angular variation of τ_r , τ_θ and the equivalent stress $\tau_e = \sqrt{\tau_r^2 + \tau_\theta^2}$, obtained from the present numerical work for $n = 25$ (power hardening) and $\alpha = 0.001$ (linear hardening) and corresponding to $\beta = 10$. The numerical results are taken along the same near-tip rectangular contour shown in the inset of Fig. 4. Further, the stresses are normalized in a manner so that $\tau_e = 1$ at $\theta = 0$ to facilitate a comparison with the perfectly plastic asymptotic results. It can be seen from Fig. 7 that the near-tip angular stress variation obtained from the present work for very low strain hardening in material #1 along with a stiff substrate, follow quite well the analytical results given by Drugan (1991). It should be noted from Fig. 7 that there is a sharp upward turn in τ_e as $\theta \rightarrow 180$ deg. The numerical results for the cases indicated in Fig. 7 showed secondary plastic reloading very near the crack flank which conforms to the analytical solution of Drugan (1991).

4.2.2 Crack Profiles. The crack profiles in the two halves of the bi-material are shown in Fig. 8 for a hardening exponent of $n = 10$. The crack displacement u_3 normalized by $K^2/G_1 \tau_{01}$ is plotted against normalized distance along the crack flanks. The cases of $\beta = 1$ and $\beta = 10$ are considered. The zero datum in this figure corresponds to the original interface line.

It is found that the crack profile is almost symmetric with respect to the crack line for the case of $\beta = 1$. For a stiffer substrate, the crack profile is lesser both in the top and bottom halves. The crack displacement in material #2 decreases dramatically as β increases, whereas in material #1 the reduction is quite small. In the limiting case of a perfectly rigid substrate, the crack flank should displace only in the top half, and this profile for the Mode III condition considered in this paper should coincide with that in a homogeneous elastic-plastic material. It was found that the crack displacement is more if material #1 possesses larger strain hardening (smaller n).

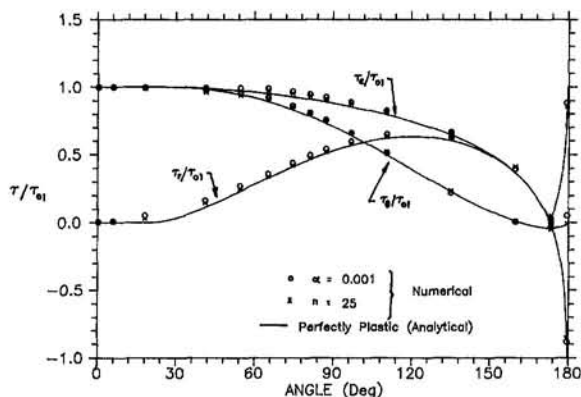


Fig. 7 Comparison of the near-tip angular stress distribution for $\alpha = 0.001$ (very low linear hardening), $n = 25$ (very low power-law hardening) and $\beta = 10$, with the analytical perfectly-plastic solution

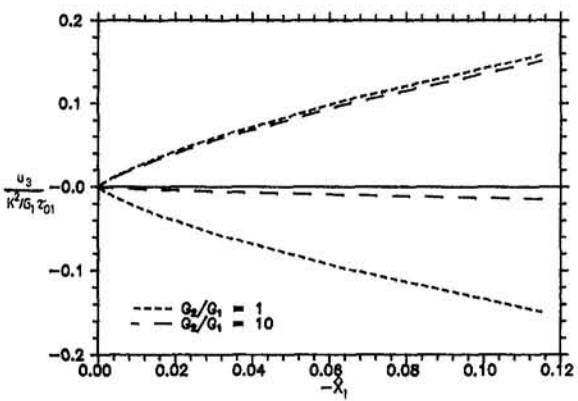


Fig. 8 Crack opening profile for $n = 10$ and $\beta = 1, 10$

4.2.3 Potential for Stable Crack Growth. It is important to compare the potential of bi-material systems with different amounts of mismatch in elastic moduli, to sustain stable crack growth at the interface. For this purpose, the ratio of the far-field J -integral for steady-state crack growth to its value at initiation, (J_{ss}/J_c) has been estimated using a critical crack-tip opening displacement criterion which applies for ductile fracture. Failure adjacent to or along an interface can be caused by a ductile failure mechanism (like microvoid growth and coalescence) or by a brittle failure mechanism (like microcracking) or by interface debonding. The dominance of a particular failure mechanism at the interface depends on the material properties, geometry of the system and the nature of applied loading. In fracture experiments using alumina bonded with pure aluminum, Dalgleish et al. (1989) observed ductile rupture in the aluminum side adjacent to the interface. On the other hand, a bimaterial combination involving alumina and an aluminum-magnesium alloy, failed by brittle fracture in the alumina side adjacent to the interface. These experiments did not show any evidence of interface debonding.

According to the critical crack-tip opening displacement criterion, crack growth will occur if the opening displacement δ at a small micro-structural distance r_c behind the tip attains a critical value δ_c . The crack profiles for steady-state crack growth shown in Fig. 8 in the upper half of the bi-material were combined with corresponding crack profiles for the stationary crack to estimate the ratio J_{ss}/J_c (see, for example, Dean and Hutchinson, 1980). For this purpose, the solution for a stationary crack at a bimaterial interface under Mode III small-scale yielding conditions was obtained using a separate finite element procedure.

In Fig. 9, the variation of the J_{ss}/J_c ratio with the microstructural parameter $\delta_c/\gamma_{01}r_c$, estimated using the critical crack-tip opening displacement criterion is shown for hardening exponent $n = 10$. A comparison is made of the J_{ss}/J_c ratio for two bimaterials with $\beta = 1$ and $\beta = 10$. The figure clearly shows that for a certain value of the microstructural parameter, the ratio J_{ss}/J_c for a bi-material with $\beta = 10$ is higher than that for $\beta = 1$. This indicates that a bimaterial with a stiffer substrate has a far greater potential to sustain stable crack growth due to ductile rupture adjacent to the interface than a bimaterial with the same elastic moduli on either side. Further, it can be seen from Fig. 9 that as $\delta_c/\gamma_{01}r_c$ increases the potential of the bimaterial system to sustain stable crack growth at the interface increases. It was found that the application of a critical stress criterion (which pertains to brittle failure) showed results which were qualitatively similar to Fig. 9.

5 Conclusions

A finite element analysis of steady quasi-static crack growth under Mode III conditions at a ductile-brittle interface has been

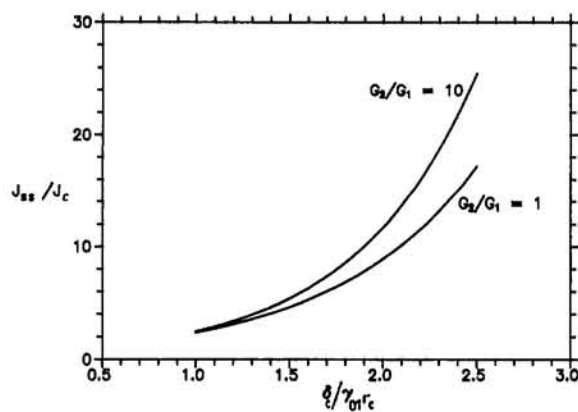


Fig. 9 Variation of J_{ss}/J_c with microstructural parameter $\delta_c/\gamma_{01}r_c$ based on a ductile fracture criterion for $n = 10$ and $\beta = 1, 10$

conducted. The ductile material is assumed to exhibit either linear isotropic hardening or power-law hardening. The following are the most important conclusions of this work.

1 The dominant term representing the asymptotic fields is found to exhibit a radial dependence of the form r^s , when the ductile material displays linear hardening. Further, the present numerical results suggest that variable-separable solution assumed for the asymptotic fields in the work of Castafielda and Mataga (1991) is reasonable for Mode III. The results obtained for the singularity order s match quite closely with those reported in their work.

2 The range of dominance of the analytical near-tip fields of Castafielda and Mataga (1991) is found to be a function of the hardening parameter α . It decreases with diminishing strain hardening.

3 From the analysis of results for the power-law hardening ductile material, it is observed that for a given value of the hardening exponent n , the stresses around the crack tip are lower for a bimaterial with a stiffer substrate.

4 The crack displacement in the ductile material is less when the substrate is stiffer. For a given ratio of $\beta = G_2/G_1$, the crack displacement (for steady-state crack growth) in the ductile material reduces with decreasing strain hardening.

5 A bimaterial system with a stiffer substrate exhibits a greater potential to sustain slow stable crack growth along the interface. This is true both when failure occurs by ductile rupture or brittle cracking adjacent to the interface.

References

Castafielda, P. P., 1987, "Asymptotic Fields in Steady Crack Growth with Linear Strain Hardening," *Journal of Mechanics and Physics of Solids*, Vol. 35, pp. 227-268.

Castafielda, P. P., and Mataga, P. A., 1991, "Stable Crack Growth along a Brittle/Ductile Interface—I. Near-tip Fields," *International Journal of Solids and Structures*, Vol. 27, No. 1, pp. 105-133.

Chitaley, A. D., and McClintock, F. A., 1971, "Elastic-Plastic Mechanics of Steady Crack Growth under Anti-plane Shear," *Journal of Mechanics and Physics of Solids*, Vol. 19, pp. 147-163.

Dalgleish, B. J., Trumble, K. P., and Evans, A. G., 1989, "The Strength and Fracture of Alumina Bonded with Aluminium Alloys," *Acta Metallurgica*, Vol. 37, pp. 1923-1931.

Dean, R. H., and Hutchinson, J. W., 1980, "Quasi-static Steady State Crack Growth in Small-Scale Yielding," in *Fracture Mechanics: Twelfth Conference, ASTM-STP-700*, pp. 383-405.

Drugan, W. J., 1991, "Near-tip fields for Quasi-static Crack Growth along a Ductile-Brittle Interface," *ASME JOURNAL OF APPLIED MECHANICS*, Vol. 58, pp. 111-119.

Drugan, W. J., Rice, J. R., and Sham, T. L., 1982, "Asymptotic Analysis of Growing Plane Strain Tensile Cracks in Elastic-Ideally Plastic Solids," *Journal of Mechanics and Physics of Solids*, Vol. 30, pp. 447-473.

Narasimhan, R., Rosakis, A. J., and Hall, J. F., 1987, "A Finite Element Study of Stable Crack Growth under Plane Stress Conditions: Part II—Influence of Hardening," *ASME JOURNAL OF APPLIED MECHANICS*, Vol. 54, pp. 846-853.

Rice, J. R., 1988, "Elastic Fracture Mechanics Concepts for Interfacial Cracks," *ASME JOURNAL OF APPLIED MECHANICS*, Vol. 55, pp. 98-103.

Shih, C. F., 1991, "Cracks on Bimaterial Interfaces: Elasticity and Plasticity Aspects," *Materials Science and Engineering*, Vol. A143, pp. 77-90.

Shih, C. F., and Asaro, G. C., 1988, "Elastic-Plastic Analysis of Cracks on Bimaterial Interfaces, Part I: Small-Scale Yielding," *ASME JOURNAL OF APPLIED MECHANICS*, Vol. 55, pp. 299-316.

Shih, C. F., and Asaro, G. C., 1989, "Elastic-Plastic Analysis of Cracks on Bimaterial Interfaces, Part II: Structure of Small Scale Yielding Fields," *ASME JOURNAL OF APPLIED MECHANICS*, Vol. 56, pp. 763-779.

Zywicz, E., and Parks, D. M., 1989, "Elastic Yield Zone Around an Interfacial Crack Tip," *ASME JOURNAL OF APPLIED MECHANICS*, Vol. 56, pp. 577-584.

Effective Thermoelastic Moduli of a Unidirectional Fiber Composite Containing Interfacial Arc Microcracks

G. P. Tandon

AdTech Systems Research, Inc.
1342 North Fairfield Road,
Dayton, OH 45432

N. J. Pagano

WL/MLBM,
Wright Patterson AFB,
Dayton, OH 45433

In this work, we have employed a variational model to examine the effect of fiber-matrix debonding on the thermoelastic response of a unidirectional composite. The model is designed to represent the concentric cylinder model of a composite representative volume element and it contains the capability to enhance the accuracy of a given numerical solution. The effect of the extent of debonding as well as fiber volume fraction on all the effective moduli of the unidirectional composite has been examined. Numerical results reported in the literature are compared with the results of the model developed in the present study to examine the quality of the model.

Introduction

The effect of debonding on the thermomechanical behavior of the composite can be studied by introducing models that simulate failure at the constituent interfaces. One such model hypothesizes that various interfacial conditions corresponding to an imperfect interface can be theoretically simulated by assigning different property values to an imaginary layer (or interphase region) (Agarwal and Bansal, 1979; Tandon and Pagano, 1988; Jasiuk and Tong, 1989). The debonding phenomenon has also been simulated by perfectly smooth interfaces (Benveniste and Aboudi, 1984; Mura et al., 1985; Pagano and Tandon, 1990) by imposing the continuity of normal displacements and tractions at the interfaces while allowing the shear traction to vanish there. Several authors (Lene and Leguillon, 1982; Benveniste, 1985; Aboudi, 1987; Steif and Hoysan, 1987; Jasiuk and Tong, 1989; Hashin, 1990) have developed models for interfacial sliding based on the approximation that interface tractions are directly proportional to the corresponding jumps in displacement. On the other hand, a fiber completely separated from the matrix can be simulated by applying zero traction boundary conditions on the interface or as a cylindrical void in the matrix material (Pagano and Tandon, 1990). Alternately, a debonded fiber can be imagined to be replaced by one bonded to the matrix but having a modified constitutive equation to simulate a material capable of carrying compression only (Takahashi and Chou, 1988). All the models discussed so far are mathematical representations of a fiber that has fully debonded from the matrix of the composite, i.e., all these approaches have implicitly assumed that the entire fiber-matrix interface has debonded. However, the actual interface may exhibit a behavior that represents partial debonding, i.e., there may exist a region of the interface where failure has taken place and the rest of the interface remains intact.

The problem of partial debonding has been addressed in the literature by use of finite element methods, where a series of coincident node pairs are generated along the interface to

model the discontinuous displacement behavior of the fiber and matrix (Shimansky et al., 1990; Sullivan et al., 1990; Nimmer et al., 1991; Robertson and Mall, 1992; Yuan, 1992). Other treatments include the use of the boundary element method employing the basic cell of a rectangular array (Achenbach and Zhu, 1989) and a hexagonal array (Achenbach and Zhu, 1990) and solving of singular integral equations using numerical methods (Selvadurai et al., 1989; Teng, 1992). A damage model for uniaxially reinforced composites weakened by an ensemble of microcracks assumed to be entirely open and confined to the fiber/matrix interface has been presented by Ju (1991). Recently, employing complex variable methods, Chao and Laws (1992) have given a proper solution for partial crack closure due to load orientation.

There are various aspects to the problem of interfacial debonding, such as the prediction of initiation, growth, and extent of debonding, and the effect of debonding on composite response, say, effective composite moduli. In the present work, we restrict our attention to the latter problem, i.e., we consider the effect of the extent of debonding as well as constituent material properties and volume fraction, on composite moduli. Our approach is to appeal to the Reissner (1950) variational theorem, which has been successfully employed to study the elastic stress fields in flat laminates (Pagano, 1978) as well as involute bodies of revolution (Pagano, 1986) and concentric cylinder assemblages (Pagano, 1991; Pagano and Brown, 1993; Pagano and Tandon, 1994). It has already been demonstrated that such models provide accurate descriptions for stress fields in the vicinity of a stress riser, even though no singularity is present owing to the solution scheme employed, so that they are appropriate for use in conjunction with an average stress failure theory, while accurate predictions of energy release rates have also been demonstrated. In order to examine the quality of the model, we will compare the results for the debonding problem treated by Yuan (1992), Teng (1992), and Sullivan et al. (1990). The variational analysis can also be easily employed to examine the internal stress field and energy release rate in the presence of interfacial debond. This would be useful in analyzing a progressive crack under changing overall loads. This work is currently in progress and will be presented elsewhere (Tandon and Pagano, 1994).

Variational Model

The medium considered is a concentric cylindrical body as shown in Fig. 1. The innermost cylinder is the fiber, the next

Contributed by the Applied Mechanics Division of THE AMERICAN SOCIETY OF MECHANICAL ENGINEERS for publication in the ASME JOURNAL OF APPLIED MECHANICS.

Discussion on this paper should be addressed to the Technical Editor, Professor Lewis T. Wheeler, Department of Mechanical Engineering, University of Houston, Houston, TX 77204-4792, and will be accepted until four months after final publication of the paper itself in the ASME JOURNAL OF APPLIED MECHANICS.

Manuscript received by the ASME Applied Mechanics Division, Sept. 20, 1993, final revision, July 29, 1994. Associate Technical Editor: G. J. Dvorak.

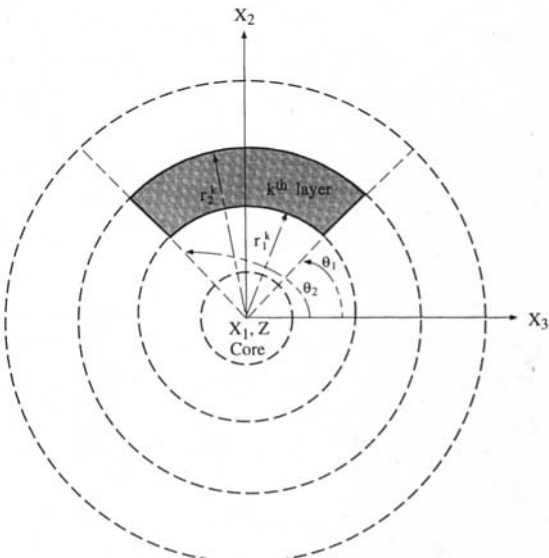


Fig. 1 Cross section of composite cylinder for analysis

ring(s) can be considered as coating(s) or interphase region(s) while the outermost ring can represent the matrix material or a material with effective composite properties. Cylindrical coordinates r, θ, z are introduced and each material is assumed to be thermoelastically cylindrically orthotropic.

The methodology that was developed by Pagano and Tandon (1994) was based on dividing the cylindrical domain in the $-r$ and $-\theta$ directions as shown in Fig. 1. The number of subdivisions was dictated by the nature of damage present, required solution accuracy and the choice of boundary conditions. A typical region bounded by the "edges" defined by $\theta = \theta_1$ and θ_2 is referred to as a sector. Each sector, in turn, is composed of a cylindrical core surrounded by a number of concentric cylindrical wedges. In subsequent discussion, any arbitrary region bounded by inner and outer radii, denoted by r_1 and r_2 , respectively, will be referred to as a layer. It will be convenient to define an index k ($k = 0, 1, \dots, N$) to represent the various layers, where $k = 0$ refers to the core and there are N concentric cylindrical layers in the model.

The stress field is assumed such that σ_z, σ_θ and $\sigma_{z\theta}$ are linear in the radial direction, r , within the layer, while the form of the remaining stress components are then derived from the elasticity equations of equilibrium (with no z -dependence). Letting $\sigma_1, \sigma_2, \sigma_3, \sigma_4, \sigma_5, \sigma_6$, represent $\sigma_z, \sigma_\theta, \sigma_r, \sigma_{rz}, \sigma_{r\theta}, \sigma_{z\theta}$, respectively, we arrive at the relations in the layer $r_1 \leq r \leq r_2$

$$\sigma_i = p_{ij} f^{(i)} \quad (i = 1, 2, \dots, 6; J = 1, 2, \dots, 4) \quad (1)$$

where p_{ij} are functions of θ only defined such that

$$p_{i\alpha}(\theta) = \sigma_i(r_\alpha, \theta) \quad (i = 1, 2, \dots, 6; \alpha = 1, 2) \quad (2)$$

and $f^{(i)}$ are known shape functions of r defined by

$$f_1^{(1)} = f_1^{(2)} = f_1^{(3)} = f_1^{(4)} = f_1^{(5)} = f_1^{(6)} = \frac{r_2 - r}{r_2 - r_1}$$

$$f_2^{(1)} = f_2^{(2)} = f_2^{(3)} = f_2^{(4)} = f_2^{(5)} = f_2^{(6)} = \frac{r - r_1}{r_2 - r_1}$$

$$f_3^{(3)} = f_3^{(5)} = \left(\frac{r_1}{r_2} - \frac{r_2}{r_1} + \frac{r}{r_1} - \frac{r}{r_2} \right) (r_2 - r_1)^{-1} + \frac{1}{r} \quad (r_1 \neq 0)$$

$$f_4^{(3)} = f_4^{(4)} = \left(\frac{r_1}{r_2^2} - \frac{r_2}{r_1^2} + \frac{r}{r_1^2} - \frac{r}{r_2^2} \right) (r_2 - r_1)^{-1} + \frac{1}{r^2} \quad (r_1 \neq 0) \quad (3)$$

with

$$p_{ij} = f^{(i)} = 0 \quad (r_1 = 0; i = 1, 2, \dots, 6 \text{ and } J = 3, 4)$$

$$p_{ij} = f^{(i)} = 0 \quad (r_1 \neq 0; i = 1, 2, 6 \text{ and } J = 3, 4 \text{ or}$$

$$i = 4, 5 \text{ and } J = 4). \quad (4)$$

In other words, the functions $f^{(i)}$ and the corresponding p_{ij} not displayed in (3) all vanish. Thus, the p functions are equal to actual stresses at $r = r_1, r_2$ and the stresses are functions of r and θ alone. In problems which do not involve elastic singularities, the assumed variation of the stress field is limited only by the thickness of the layer. Therefore, to improve the accuracy of the model, each one of the wedges or the cylindrical core can be additionally subdivided in the radial direction.

The r, θ, z components of displacement are designated as u_r, u_θ , and u_z , respectively. The general form of the displacement field consistent with stresses that only depend on r and θ is given by

$$u_r = u(r, \theta) + z(c \sin \theta + d \cos \theta)$$

$$u_\theta = v(r, \theta) + z(c \cos \theta - d \sin \theta)$$

$$u_z = w(r, \theta) - r(c \sin \theta + d \cos \theta) + \epsilon z \quad (5)$$

where c and d measure rigid-body displacements and ϵ is a constant. In the subsequent derivation of the governing equations, the integrations will give rise to weighted average displacements and displacements on the surfaces $r = r_1, r_2$. Therefore, we make the definitions

$$(\dot{q}, \ddot{q}, \bar{q}, q^*, \hat{q}) = \int_{r_1}^{r_2} q(r^{-2}, r^{-1}, 1, r, r^2) dr; \quad q = u, v, w \quad (6)$$

although every weighted integral is not defined for each displacement function. We also let

$$q_\alpha(\theta) = q(r_\alpha, \theta) \quad (\alpha = 1, 2) \quad (7)$$

with the same interpretation of q .

Reissner (1950) has shown that the governing equations of elasticity can be obtained as a consequence of the variational equation

$$\delta J = 0 \quad (8)$$

where

$$J = \int_v F dV - \int_{S'} \bar{T}_i U_i dS \quad (9)$$

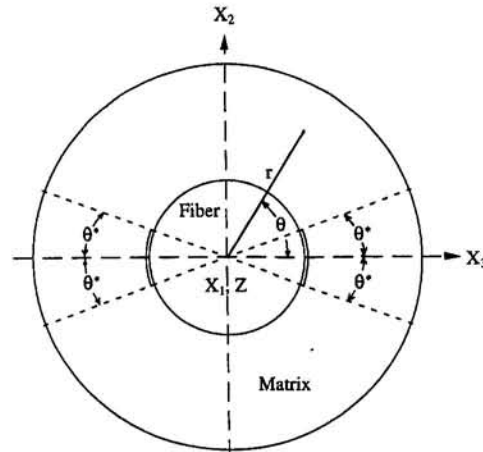


Fig. 2 Schematic of partial debonding at fiber/matrix interface (given by $\theta = \pm\theta^*, \pi \pm \theta^*$)

and

$$F = \frac{1}{2} \tau_{ij} (U_{i,j} + U_{j,i}) - W(\tau_{ij}, e_{ij}). \quad (10)$$

In these equations W is the complementary energy; τ_{ij} and U_i are the stress and displacement components, respectively, in Cartesian coordinates; e_{ij} are the mathematical free expansional or nonmechanical strains; V is the volume enclosed by S ; S' is the part of S on which one or more traction components are prescribed; \bar{T}_i are the Cartesian components of the prescribed tractions; and body forces have been neglected.

The variational equation is equivalent to the field equations and boundary conditions of linear elasticity theory provided both stresses and displacements are subject to variation in the application of (8). For a body consisting of a core region plus N cylindrical layers, the formulation leads to a system of $24N + 19$ algebraic and ordinary differential equations in θ for a like number of unknowns, which are $p_{11}, p_{12}, p_{21}, p_{22}, p_{31}, p_{32}, p_{33}, p_{34}, p_{41}, p_{42}, p_{43}, p_{51}, p_{52}, p_{53}, p_{61}, p_{62}, \bar{u}, u^*, \bar{v}, v^*, \bar{w}, w^*$, and ϵ , within each annulus; and $p_{11}, p_{12}, p_{21}, p_{22}, p_{31}, p_{32}, p_{41}, p_{42}, p_{51}, p_{52}, p_{61}, p_{62}, \bar{u}, u^*, \bar{v}, v^*, \bar{w}, w^*$ and ϵ , in the core, while $7N + 6$ boundary conditions are required at each "edge" $\theta = \theta_1, \theta_2$. Note that the interfacial displacements u_i, v_i and w_i ($i = 1, 2$) only appear in the governing equations if they are *prescribed*, hence they are not treated as dependent variables in the model.

On planes $r = \text{constant}$, the appropriate prescribed functions consist of one member of each of the following products

$$p_{31}u_1, \quad p_{41}v_1, \quad p_{51}w_1 \quad (11)$$

on surfaces $r = r_1 \neq 0$ and

$$p_{32}u_2, \quad p_{42}v_2, \quad p_{52}w_2 \quad (12)$$

on surfaces $r = r_2$, while for the core region (12) alone is applicable. Furthermore, continuity conditions can be written for the surfaces $r = \text{constant}$ which are internal to the medium. The boundary conditions on $\theta = \theta_1, \theta_2$, or "edge" conditions, can be expressed by prescribing one term from each of the following products (although this decomposition is not unique)

$$H_1^k \bar{u}_k, \quad H_2^k u_k^*, \quad H_4^k \bar{v}_k, \quad H_5^k v_k^*, \quad H_6^k \bar{w}_k, \quad H_7^k w_k^*, \quad (k = 0, 1, -N) \quad (13)$$

while if $k \neq 0$ we have, in addition, the product

$$H_3^k \bar{u}_k \quad (k = 1, 2, -N) \quad (14)$$

where for $k \neq 0$,

$$H_1 = \frac{r_2 p_{41} - r_1 p_{42} + \left(\frac{r_1}{r_2^2} - \frac{r_2}{r_1^2} \right) p_{43}}{r_2 - r_1}; \quad H_2 = \frac{p_{42} - p_{41} + \left(\frac{1}{r_1^2} - \frac{1}{r_2^2} \right) p_{43}}{r_2 - r_1}; \quad H_3 = p_{43} \quad (15)$$

and for $k = 0$,

$$H_1 = p_{41}; \quad H_2 = (p_{42} - p_{41})/r_2; \quad H_3 = 0, \quad (16)$$

while

$$H_4 = \frac{r_2 p_{21} - r_1 p_{22}}{r_2 - r_1}; \quad H_5 = \frac{p_{22} - p_{21}}{r_2 - r_1} \quad H_6 = \frac{r_2 p_{61} - r_1 p_{62}}{r_2 - r_1}; \quad H_7 = \frac{p_{62} - p_{61}}{r_2 - r_1} \quad (17)$$

hold for any value of k (recall that $k = 0$ represents the core material). In the event that the body is subdivided into sections

Table 1 Effective stiffness coefficients from present model for Nicalon/1723 glass composite ($v_f = 0.4$; θ^* = debond angle as shown in Fig. 2)

Stiffness (GPa)	$\theta^* = 0^\circ$	$\theta^* = 30^\circ$	$\theta^* = 45^\circ$	$\theta^* = 60^\circ$	$\theta^* = 90^\circ$
C_{11}	157.868	151.114	147.245	143.933	137.270
C_{22}	141.484	133.426	122.380	104.706	36.665
C_{33}	141.484	88.244	62.529	46.103	36.665
C_{12}	48.302	41.838	36.626	30.307	10.043
C_{21}	48.302	41.838	36.626	30.307	10.043
C_{13}	48.302	29.675	20.515	14.532	10.043
C_{31}	48.302	29.675	20.515	14.532	10.043
C_{23}	45.837	29.885	21.570	15.770	8.534
C_{32}	45.837	29.885	21.570	15.770	8.534
C_{44}	47.824	37.592	29.197	21.038	14.065
C_{55}	48.226	36.389	27.766	20.786	15.426
C_{66}	48.226	47.685	45.874	41.859	15.426

by planes $\theta = \text{const}$, such as in the case where internal cracks in these planes are present, the appropriate interface conditions follow directly from (13) and (14). For example, one member of each term can be specified for prescribed tractions and/or displacements while continuity is implied when *each member* of (13) and (14) is continuous. The solution to the boundary value problem is exact (in the present formulation) if the edge traction boundary conditions are consistent with the assumed r -dependence. Otherwise, further subdivision of the layer will have to be done to approximate the prescribed edge traction boundary condition.

In the longitudinal direction, we either prescribe ϵ or N_z given by

$$\frac{N_z}{(z_2 - z_1)} = \int_{\theta_1}^{\theta_2} \left[p_{11} \frac{(r_2^2 + r_1 r_2 - 2r_1^2)}{6} + p_{12} \frac{(2r_2^2 - r_1 r_2 - r_1^2)}{6} \right] d\theta. \quad (18)$$

However, the various ϵ or N_z may or may not be arbitrarily selected as this choice is affected by the boundary conditions across both interfaces of a layer (Pagano and Tandon, 1994). Also note that freedom to prescribe arbitrary sets of traction boundary conditions in boundary value problems is restricted owing to the need to constrain rigid-body displacement.

Since the field equations within each material are linear differential equations with constant coefficients, the general form of the solution for any of the dependent variables $P(\theta)$ is expressed by

$$P(\theta) = \sum_i A_i e^{\lambda_i \theta} + P_p(\theta) \quad (19)$$

within *each* layer where A_i are constants, λ_i are eigenvalues of a determinant, and $P_p(\theta)$ is a particular solution. In case of multiple roots, the homogeneous solution can be obtained by the method of reduction of order. For the class of boundary value problems treated in this work (see (21) and (27)), the general form of the particular solution is given by

$$P_p(\theta) = \sum_i K_i \theta^i + \sum_{\omega=1}^2 (L_\omega \cos \omega \theta + M_\omega \sin \omega \theta) \quad (20)$$

where each term of the particular solution is further multiplied by θ^m if the right-hand side of the nonhomogeneous linear equation happens to be the solution of the corresponding homogeneous equation (m is the multiplicity of the root of the character-

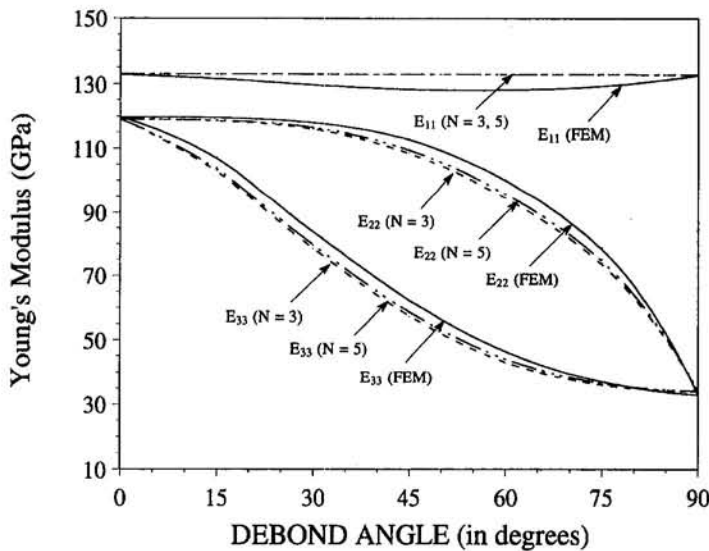


Fig. 3 The variation of effective Young's moduli, namely, E_{11} , E_{22} , and E_{33} of Nicalon/1723 glass composite with angle of debonding (FEM data from Yuan, 1992)

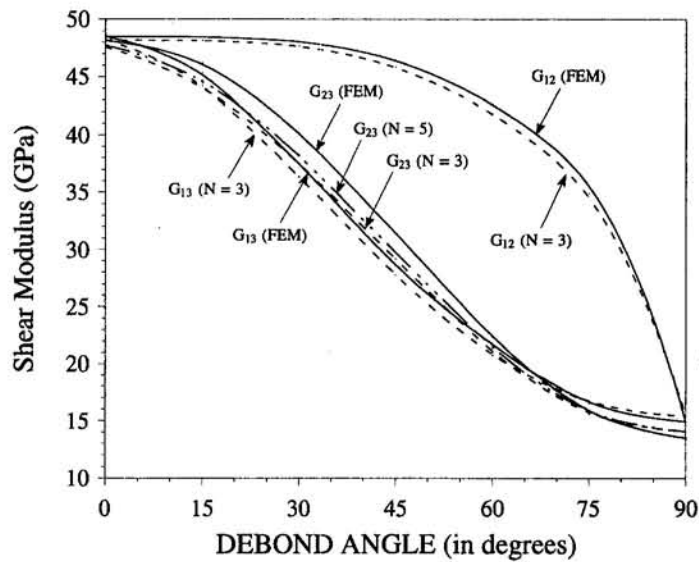


Fig. 4 The variation of effective shear moduli, namely, G_{12} , G_{13} , and G_{23} of Nicalon/1723 glass composite with angle of debonding (FEM data from Yuan, 1992)

istic equation of the homogeneous equation). This completes the boundary value problem formulation with the present model.

Effective Moduli

To define the effective thermoelastic properties of a composite, the RVE is subjected to linear surface displacement conditions

$$U_i(S) = \epsilon_{ij}^0 x_j(S) \quad (i, j = 1, 2, 3) \quad (21)$$

where x_j are the Cartesian coordinates of the outer surface S of the concentric cylinder and ϵ_{ij}^0 are constants (In the case of a homogeneous material under boundary conditions (21), the strain field would be given by ϵ_{ij}^0). The stress-strain relation for the composite can then be written as

$$\tau_i^{(c)} = C_{ij}^{(c)} (\epsilon_j^{(c)} - e_j^{(c)}) \quad (i, j = 1, 2 \dots 6) \quad (22)$$

where $C_{ij}^{(c)}$ is the effective stiffness and $e_j^{(c)}$ is the effective

expansional (nonmechanical) strain of the composite, while $\tau_i^{(c)}$ and $\epsilon_j^{(c)}$ are the composite stress and strain components, respectively. The displacement formulation leads to a direct calculation of the composite stiffness, $C_{ij}^{(c)}$. On the other hand, the RVE can be subjected to traction boundary conditions

$$T_i(S) = \tau_{ij}^0 n_j \quad (i, j = 1, 2, 3) \quad (23)$$

where n_j are the components of the unit outward normal vector and τ_{ij}^0 are constants. The traction formulation leads to the calculation of effective compliance, $S_{ij}^{(c)}$, through the relation

$$\epsilon_i^{(c)} = S_{ij}^{(c)} \tau_j^{(c)} + e_i^{(c)} \quad (i, j = 1, 2 \dots 6) \quad (24)$$

where $S_{ij}^{(c)}$ is not necessarily the inverse of $C_{ij}^{(c)}$. In Eqs. (22) and (24), standard contracted notation is used such that $\tau_1, \tau_2, \tau_3, \tau_4, \tau_5, \tau_6$ stand for $\tau_{11}, \tau_{22}, \tau_{33}, \tau_{23}, \tau_{13}, \tau_{12}$, respectively, and ϵ_i ($i = 1, 2 \dots 6$) are the respective engineering strains. Further, recalling the issues discussed earlier (Pagano and Tan-

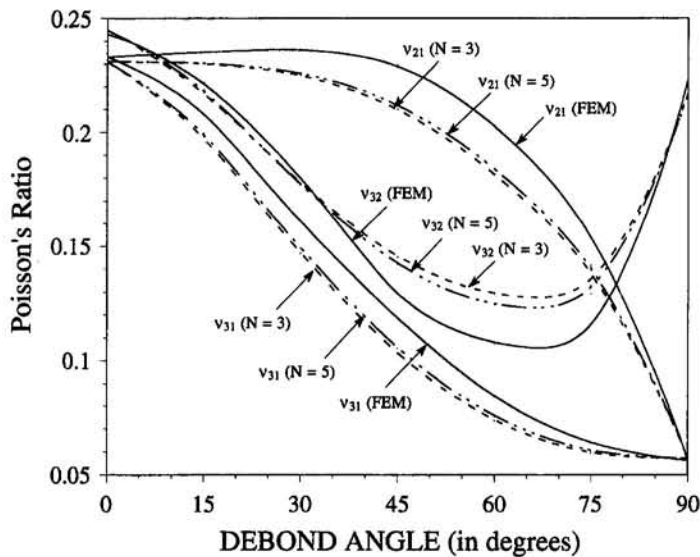


Fig. 5 The variation of effective Poisson's ratios, namely, ν_{21} , ν_{31} , and ν_{32} of Nicalon/1723 glass composite with angle of debonding (FEM data from Yuan, 1992)

don, 1990), the composite stress is obtained by volume averaging the stress tensor while the composite strains are given by constants which are their surface values at certain points on the outer boundary of the composite cylinder (these are the same as the body average strains defined by Benveniste, 1985).

Under *perfect bonding*, with the fibers aligned unidirectionally along x_1 , use of displacement (21) and traction (23) boundary conditions on the external surface of the RVE leads to upper and lower bound estimates of the elastic stiffnesses, respectively. For the composite cylinder model, upper and lower bounds for four of the five elastic moduli, namely, longitudinal Young's modulus, E_{11} ; major Poisson's ratio, ν_{13} ; longitudinal shear modulus, G_{13} ; and plane-strain bulk modulus, K_{23} coincide, whereas, bounding solutions for the transverse Young's modulus, E_{33} , are obtained. Hashin et al. (1985) have compared the analytical predictions employing CCM with numerical results using hexagonal array and have shown that the agreement between the two solutions is extremely good for all elastic properties considered. Hashin et al. (1985) further observed that the upper bound results for composite transverse Young's modulus using CCM correlated very well with experimental measurements of composite moduli for a wide range of elastic moduli and fiber volume fraction. Further comparisons of the effective elastic moduli and constituent microstresses employing CCM with existing numerical solutions are given in Tandon (1995). The results clearly demonstrate that CCM can provide a good simulation for the RVE provided the displacements are prescribed on the external surfaces. For this study, we will therefore make use of displacement boundary conditions to define the composite properties.

To evaluate the effective elastic moduli, we set the expansional strain components identically equal to zero in (22). By setting each strain component, $\epsilon_j^{(c)}$, equal to one individually, while all others are zero, we will, respectively, obtain the j th column of the $C_{ij}^{(c)}$ matrix. The effective engineering constants can now be defined by the following generalized relations between the stiffness coefficients where the symmetry of the coefficients is not assumed

$$E_{11} = C_{11} + \frac{C_{12}(C_{31}C_{23} - C_{21}C_{33})}{(C_{22}C_{33} - C_{23}C_{32})} + \frac{C_{13}(C_{32}C_{21} - C_{31}C_{22})}{(C_{22}C_{33} - C_{23}C_{32})}$$

$$E_{22} = C_{22} + \frac{C_{21}(C_{13}C_{32} - C_{12}C_{33})}{(C_{11}C_{33} - C_{13}C_{31})} + \frac{C_{23}(C_{12}C_{31} - C_{11}C_{32})}{(C_{11}C_{33} - C_{13}C_{31})}$$

$$E_{33} = C_{33} + \frac{C_{31}(C_{12}C_{23} - C_{13}C_{22})}{(C_{11}C_{22} - C_{12}C_{21})} + \frac{C_{32}(C_{13}C_{21} - C_{11}C_{23})}{(C_{11}C_{22} - C_{12}C_{21})}$$

$$\nu_{21} = \frac{(C_{12}C_{33} - C_{13}C_{32})}{(C_{11}C_{33} - C_{13}C_{31})}; \quad G_{12} = C_{66}$$

$$\nu_{31} = \frac{(C_{13}C_{22} - C_{12}C_{23})}{(C_{11}C_{22} - C_{12}C_{21})}; \quad G_{13} = C_{55}$$

$$\nu_{32} = \frac{(C_{11}C_{23} - C_{13}C_{21})}{(C_{11}C_{22} - C_{12}C_{21})}; \quad G_{23} = C_{44}. \quad (25)$$

Note that in Eqs. (25) the superscript (c) on the composite stiffness coefficients has been omitted for brevity, and in subsequent discussion will also be frequently omitted unless needed for clarity. Next, setting the composite strain components $\epsilon_j^{(c)}$ all to zero leads to the calculation of the expansional strain through

$$\epsilon_j^{(c)} = -S_{ij}^{(c)} \tau_j^{(c)} \quad (\text{with } \epsilon_j^{(c)} = 0) \quad (26)$$

where the elastic compliance $S_{ij}^{(c)}$ has already been determined and the composite stress $\tau_j^{(c)}$ can be computed as explained earlier.

Partial Debonding Problem

We will now treat the case where debonding may occur over a portion of the interface given by $\theta = \pm\theta^*, \pi \pm \theta^*$ for all values of z (θ is measured from x_3 -axis as shown in Fig. 2). A fiber completely separated from the matrix can be simulated by applying zero traction boundary conditions on the interface (Pagano and Tandon, 1990) provided the displacements are consistent with opening¹. On the other hand, continuity of all traction and displacement components exist in the bonded region. The interface boundary conditions treated in this problem thus consist of

$$\sigma_r = \sigma_{r\theta} = \sigma_{rz} = 0, \quad \text{in debonded region}$$

$$\sigma_r, \sigma_{r\theta}, \sigma_{rz}, u_r, u_{r\theta}, u_{rz} \text{ continuous; in "bonded" region.} \quad (27)$$

¹The linear elasticity solution provided here does not consider the nonlinear contact problem.

These are the theory of elasticity boundary conditions which are transformed by (2) and (7) for the present model. Additionally, we prescribe ϵ and set the fiber and matrix displacement to be the same in the longitudinal direction for the case of complete debonding. For the type of boundary value problems treated in this work (see (21) and (27)), we have continuity along the radial lines at $\theta = \pm\theta^*, \pi \pm \theta^*$. However, when $\theta^* = 90$ deg corresponding to complete debonding, rigid-body displacements have to be constrained within the fiber region.

Numerical Results

We consider a unidirectional composite aligned along x_1 for the analysis. The material properties used in the calculations, representative of Nicalon fiber and 1723 Glass matrix, both assumed to be isotropic, are listed as follows:

Material	E(GPa)	G(GPa)	$\alpha \times 10^{-6}/^\circ\text{C}$
Nicalon	200.0	77.0	3.2
1723 Glass	88.0	36.0	5.2

Two different solutions based on the present model are constructed for this study. In the first solution where $N = 3$, the matrix is modeled as two cylindrical layers which have their common interface at $r = (r_m + r_f)/2$, while the fiber is subdivided into a core and layer with their interface being located at $r_f/2$. In the second solution, we set $N = 5$ such that in the fiber region we have a core and two annular regions whereas the matrix was subdivided into three layers. The core and subsequent layer outer radii for $N = 5$ were given by $r_f/3, 2r_f/3, r_f, (2r_f + r_m)/3, (r_f + 2r_m)/3$ and r_m , respectively.

For $v_f = 0.4$, and $N = 3$, the nonzero components of the effective stiffness matrix are listed in Table 1 as a function of the angle of debonding. For both $\theta^* = 0$ deg and 90 deg, corresponding to perfect bonding and complete debonding of the interface, respectively, the composite is transversely isotropic, and there exist five independent components of C_{ij} , which may be taken as $C_{11}, C_{22}, C_{12}, C_{23}$, and C_{66} . However, for partial debonding of the interface, isotropy in the transverse 2-3 plane is lost. For all other values of θ^* (different from 0 deg and 90 deg) the number of independent C_{ij} is found to be nine corresponding to an orthotropic material. The additional stiffness components can be taken to be C_{33}, C_{13}, C_{44} , and C_{55} . The concentric cylinder had also been discretized and analyzed by Yuan (1992) using finite elements. The results from his analysis are found to be in reasonable agreement with our values listed in Table 1.

Using (25), the effective engineering constants can now be calculated. Figures 3-5 illustrate the behavior of the effective engineering constants with angle of debonding for $v_f = 0.4$ and $N = 3$ and 5 along with the values reported by Yuan (1992). The results of the present study have been shown (Pagano and Tandon, 1994) to be in excellent agreement with the elasticity solution (Pagano and Tandon, 1990) for $\theta^* = 0$ deg and 90 deg. As seen from Fig. 3, debonding at the interface is seen to have negligible effect on the longitudinal Young's modulus, E_{11} . Also, E_{33} seems to decrease gradually with increasing θ^* whereas E_{22} remains almost insensitive to debonding at small values of θ^* . At a debond angle of say 45 degrees, E_{33} reduces by approximately 44 percent of its value at $\theta^* = 0$ deg, whereas the reduction in E_{22} is only about 7 percent. Even at a debond angle of 75 deg, the reduction in E_{22} is only about 30 percent. With further increase of θ^* , E_{22} drops rapidly to its completely unbonded value. Increasing the number of rings N from 3 to 5 results in a slight increase in the effective stiffness but the improvement is small. The FEM solution obtained by Yuan (1992) seems to predict a slightly stiffer composite in the transverse plane. However, agreement between the results from the variational model and FEM solution is quite reasonable for the entire range of debonding.

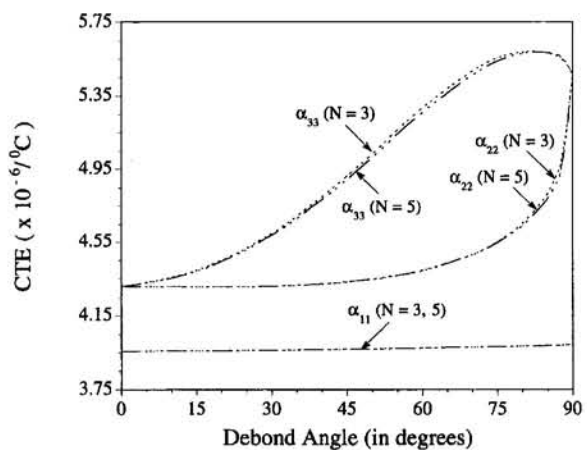


Fig. 6 The variation of effective coefficient of thermal expansion, namely, α_{11} , α_{22} , and α_{33} of Nicalon/1723 glass composite with angle of debonding

The behavior of the longitudinal shear modulus, G_{12} , is similar to that of E_{22} , whereas, the transverse shear modulus, G_{23} and longitudinal shear modulus, G_{13} behave in a manner similar to that of E_{33} , as shown in Fig. 4. The FEM solution (Yuan, 1992) again seems to predict a stiffer composite over most of the range of θ^* . The effective Poisson's ratios satisfy the relation

$$\nu_{ij}E_{jj} = \nu_{ji}E_{ii}; \quad i \neq j; \quad \text{no } i, j \text{ summation,} \quad (28)$$

thereby establishing symmetry of the effective stiffness matrix. Their variation with the angle of debonding is illustrated in Fig. 5. What is interesting to note is that the transverse Poisson's ratio, ν_{32} , passes through a minimum as θ^* is varied from 0 to 90 deg.

In Fig. 6, we have illustrated the behavior of the effective coefficients of thermal expansion (CTE) with angle of debonding for $v_f = 0.4$ and $N = 3$ and 5. The results of the present analysis are seen to be in very good agreement with the elasticity solution of a concentric cylinder for the two extremes of perfect bonding ($\theta^* = 0$ deg) and complete debonding ($\theta^* = 90$ deg). Similar to E_{11} , debonding at the interface is seen to have negligible effect on the longitudinal CTE, α_{11} . It is also interesting to note that α_{33} seems to increase gradually with increasing θ^* , with a maximum occurring close to complete separation, whereas α_{22} remains almost insensitive to debonding at small values of θ^* .

The composite cylinder model has also been employed by Teng (1992) to evaluate the stiffness reduction of a unidirectional fiber composite containing interfacial cracks under longitudinal shear loading. The resulting mixed boundary value problem lead to systems of dual series equations, which were then reduced to Fredholm integral equations of the first kind with a logarithmically singular kernel, and solved numerically. In Fig. 7 we have compared the effective longitudinal shear moduli obtained from Teng's (1992) analysis with the results from the present formulation with $N = 3$. The fiber volume fraction was kept at 0.4 while two different ratios of fiber to matrix shear moduli, namely, $G_f/G_m = 5$ and 20, were considered. As seen in Fig. 7, the results from our approximate model agree very well with the exact solutions over the entire range of debonding for both moduli ratios employing relatively small number of layers.

Finally, Sullivan, Cassin and Rosen (1990) have employed finite element analysis to model the effects of fiber/matrix debonding on the resulting transverse moduli of unidirectional composites using the repeating element of a hexagonal array. The results from the present formulation (employing a concentric cylinder RVE) are compared with their model representative of six disbonds around the fiber, with the centers of each disbond

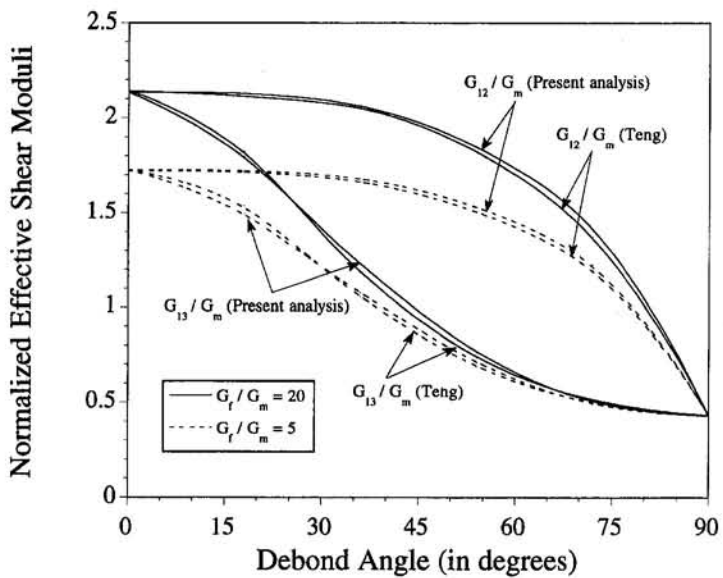


Fig. 7 Comparison of normalized effective longitudinal shear moduli from Teng's (1992) analysis with present formulation

segment positioned 60 deg apart. The fiber and material properties taken from the work of Sullivan et al. (1990) are listed as follows:

Material	E_T (GPa)	E_A (GPa)	ν_T	ν_A	G_A (GPa)
Fiber	9.9	397.2	0.45	0.41	19.9
Matrix	9.1	9.1	0.11	0.11	4.1

where subscripts T and A refer to the stated property in transverse and axial direction, respectively.

The composite transverse Young's modulus, E_{33} , and shear modulus, G_{23} , have been plotted in Fig. 8. Two fiber volume fractions were investigated, namely, 0.4 and 0.6. The results from our approximate model (with $N = 3$) are seen to agree reasonably with finite element solutions for the range of debond-

ing considered. The degradation of the effective transverse properties is seen to increase as the angle of debond grows and is more severe for the higher fiber volume fraction composite, i.e., at larger debond angles, lower fiber volume fraction results in a stiffer composite. We have further observed that the variation of E_{22} , G_{12} , G_{13} , ν_{21} , and ν_{31} , with v_f , is similar to that of E_{33} , whereas E_{11} increases linearly with increase in v_f .

Concluding Remarks

In this study, a variational model of a concentric cylinder has been utilized to examine the effect of the extent of debonding as well as fiber volume fraction, on the composite moduli of a typical glass-ceramic composite material. For a symmetrically partially debonded interface, the composite behaves as an orthotropic material. Interface debonding is seen to have negligible effect on E_{11} and α_{11} , whereas, E_{22} , G_{12} , ν_{21} , and α_{22} are almost

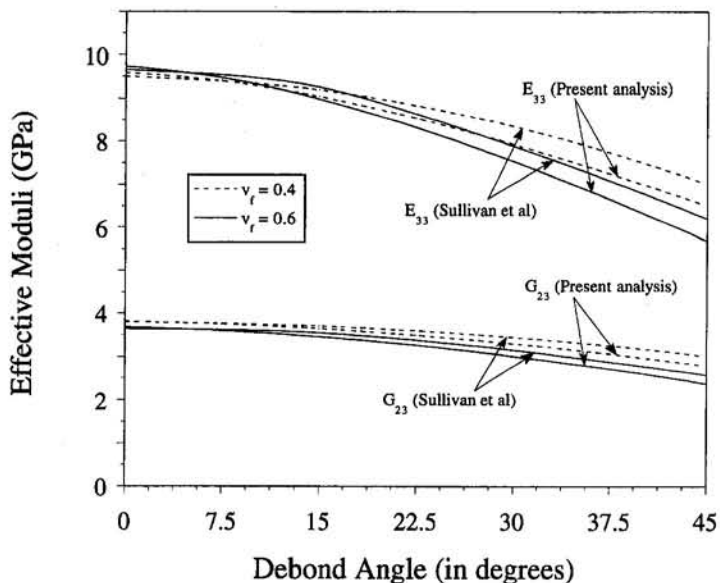


Fig. 8 Comparison of effective transverse Young's modulus, E_{33} , and transverse shear modulus, G_{23} , from the analysis of Sullivan et al. (1990) with present formulation

insensitive to debonding at small values of θ^* . Further, for small debond angles, transverse Young's modulus is seen to increase with increasing fiber volume fraction, whereas, at larger debond angles, lower fiber volume fraction results in a stiffer composite. It has been clearly demonstrated that the agreement between the results from the approximate model (employing relatively small number of layers) and existing numerical solutions (Yuan, 1992; Teng, 1992; Sullivan et al., 1990) is quite reasonable for the entire range of debonding considered. Comparison of experimental measurements of composite moduli with the results such as those presented in this study can be instrumental in the analysis of failure modes in the constituent materials of brittle matrix composites.

As mentioned earlier, the number of regions in the r -direction can be increased in order to improve the solution accuracy in the variational method. Another way to enhance correctness is to adjust the relative thickness of the subdivisions without increasing their number. Thus, it is the linear dimension in the radial direction which is the single variable controlling the accuracy of the solution in the variational method. On the other hand, in most of the numerical approaches, such as 2-D finite element or finite difference, it's the finite size of the element, or node point spacings in both r - and θ -directions, which control the accuracy of the solution. In that respect, the variational method facilitates easier control over numerical accuracy.

Finally, in this work, the variational method has been used to define the response of a composite that behaves in accordance with the concentric cylinder representative volume element. Alternately, the variational method can be coupled with a four (or more) phase model (Pagano and Brown, 1993) to look at first damage in a composite or to examine the effect of nonuniform fiber spacing, rather than using this as an RVE.

References

Aboudi, J., 1987, "Damage in Composites—Modeling of Imperfect Bonding," *Composites Science and Technology*, Vol. 28, pp. 103–128.

Achenbach, J. D., and Zhu, H., 1989, "Effect of Interfacial Zone on Mechanical Behavior and Failure of Fiber Reinforced Composites," *Journal of Mechanics and Physics of Solids*, Vol. 37, pp. 381–393.

Achenbach, J. D., and Zhu, H., 1990, "Effect of Interphases on Micro and Macromechanical Behavior of Hexagonal-Array Fiber Composites," *ASME JOURNAL OF APPLIED MECHANICS*, Vol. 57, pp. 956–963.

Agarwal, B. D., and Bansal, R. K., 1979, "Effects of an Interfacial Layer on the Properties of Fibrous Composites: A Theoretical Analysis," *Fibre Science and Technology*, Vol. 12, pp. 149–158.

Benveniste, Y., and Aboudi, J., 1984, "A Continuum Model for Fiber Reinforced Materials with Debonding," *International Journal of Solids and Structures*, Vol. 20, pp. 935–951.

Benveniste, Y., 1985, "The Effective Mechanical Behaviour of Composite Materials with Imperfect Contact Between the Constituents," *Mechanics of Materials*, Vol. 4, pp. 197–208.

Chao, R., and Laws, N., 1992, "Closure of an Arc Crack in an Isotropic Homogeneous Material due to Uniaxial Loading," *Quarterly Journal of Mechanics and Applied Mathematics*, Vol. 45, pp. 629–640.

Hashin, Z., Rosen, B. W., and Humphreys, E. A., 1985, "Fiber Composite Analysis and Design," Report DOT/FAA/CT-85/6, Vol. 1, pp. 2–24–2–37.

Hashin, Z., 1990, "Thermoelastic Properties of Fiber Composites With Imperfect Interface," *Mechanics of Materials*, Vol. 8, pp. 333–348.

Jasiuk, I., and Tong, Y., 1989, "The Effect of Interface on the Elastic Stiffness of Composites," *Mechanics of Composite Materials and Structures*, J. N. Reddy et al., eds., ASME AMD-Vol. 100, pp. 49–54.

Ju, J. W., 1991, "A Micromechanical Damage Model for Uniaxially Reinforced Composites Weakened By Interfacial Arc Microcracks," *ASME JOURNAL OF APPLIED MECHANICS*, Vol. 58, pp. 923–930.

Lene, F., and Leguillon, D., 1982, "Homogenized Constitutive Law for a Partially Cohesive Composite Material," *International Journal of Solids and Structures*, Vol. 18, pp. 443–458.

Mura, T., Jasiuk, I., and Tsuchida, B., 1985, "The Stress Field of a Sliding Inclusion," *International Journal of Solids and Structures*, Vol. 21, pp. 1165–1179.

Nimmer, R. P., Bankert, R. J., Russell, E. S., Smith, G. A., and Wright, P. K., 1991, "Micromechanical Modeling of Fiber/Matrix Interface Effects in Transversely Loaded SiC/Ti-6-4 Metal Matrix Composites," *Journal of Composites Technology and Research*, Vol. 13, No. 1, pp. 3–13.

Pagano, N. J., 1978, "Stress Fields in Composite Laminates," *International Journal of Solids and Structures*, Vol. 14, pp. 385–400.

Pagano, N. J., 1986, "Axisymmetric Stress Fields in Involute Bodies of Revolution," *Journal Spacecraft and Rockets*, Vol. 23, No. 2, pp. 165–170.

Pagano, N. J., and Tandon, G. P., 1990, "Modeling of Imperfect Bonding in Fiber Reinforced Brittle Matrix Composites," *Mechanics of Materials*, Vol. 9, pp. 49–64.

Pagano, N. J., 1991, "Axisymmetric Micromechanical Stress Fields in Composites," *Proceedings 1991 IUTAM Symposium on Local Mechanics Concepts for Composite Materials Systems*, Springer-Verlag, New York, p. 1.

Pagano, N. J., and Brown, III, H. W., 1993, "The Full-Cell Cracking Mode in Unidirectional Brittle Matrix Composites," *Composites*, Vol. 24, pp. 69–83.

Pagano, N. J., and Tandon, G. P., 1994, "2-D Damage Modes in Unidirectional Composites under Transverse Tension and/or Shear," *Mechanics of Composite Materials and Structures*, Vol. 1, No. 2, pp. 119–155.

Reissner, E., 1950, "On a Variational Theorem in Elasticity," *Journal of Mathematical Physics*, Vol. 29, p. 90.

Robertson, D. D., and Mall, S., 1992, "Fiber-Matrix Interphase Effects Upon Transverse Behavior in Metal-Matrix Composites," *Journal of Composites Technology and Research*, Vol. 14, No. 1, pp. 3–11.

Selvadurai, A. P. S., Singh, B. M., and Au, M. C., 1989, "Axial Loading of a Rigid Disc Inclusion with a Debonded Region," *International Journal of Solids and Structures*, Vol. 25, pp. 783–795.

Shimansky, R. A., Hahn, H. T., and Salamon, N. J., 1990, "The Effect of Weak Interface on Transverse Properties of a Ceramic Matrix Composite," *Materials Research Society Symposium Proceedings*, Vol. 170, pp. 193–204.

Steif, P., and Hoysan, S. F., 1987, "An Energy Method for Calculating the Stiffness of Aligned Short-Fiber Composites," *Mechanics of Materials*, Vol. 6, pp. 197–210.

Sullivan, B. J., Cassin, T. G., and Rosen, B. W., 1990, "Micromechanical Analysis of Unidirectional Composites with Unique Fiber Geometries and Fiber/Matrix Interface Conditions," *Proceedings of American Society for Composites, Fifth Technical Conference*, Technomic, Lancaster, PA, pp. 144–153.

Takahashi, K., and Chou, T. W., 1988, "Transverse Elastic Moduli of Unidirectional Fiber Composites with Interfacial Debonding," *Metallurgical Transactions A*, Vol. 19A, pp. 129–135.

Tandon, G. P., and Pagano, N. J., 1988, "A Study of Fiber-Matrix Interfacial Modeling," *Proceedings 4th Japan-US Conference on Composite Materials*, Technomic, Lancaster, PA, pp. 191–200.

Tandon, G. P., 1995, "Use of Composite Cylinder Model as Representative Volume Element for Unidirectional Fiber Composites," to appear in *Journal of Composite Materials*, Vol. 29, No. 3, pp. 388–409.

Tandon, G. P., and Pagano, N. J., 1994, "Damage Modeling of Brittle Matrix Composites Under Thermal and Transverse Loading," *Damage Mechanics in Composites*, AMD-Vol. 185, D. H. Allen and J. W. Ju, eds., ASME, New York, pp. 129–141.

Teng, H., 1992, "On Stiffness Reduction of a Fiber-Reinforced Composite Containing Interfacial Cracks Under Longitudinal Shear," *Mechanics of Materials*, Vol. 13, pp. 175–183.

Yuan, F. G., 1992, "Elastic Moduli of Fiber Reinforced Brittle Matrix Composites with Interfacial Debonding," Contract F33615-90-C-5944, Wright Laboratory, Materials Directorate, Wright Patterson AFB.

Sung Yi²

H. H. Hilton³

M. F. Ahmad⁴

Aeronautical and Astronautical
Engineering Department,
National Center for Supercomputing
Applications
and Theoretical and Applied
Mechanics Department,
University of Illinois at Urbana-Champaign,
Urbana, IL 61801-2935

Nonlinear Thermo-Viscoelastic Analysis of Interlaminar Stresses in Laminated Composites¹

A finite element formulation for analyzing interlaminar stress fields in nonlinear anisotropic viscoelastic laminated composites is presented including a hygrothermal formulation. Schapery's single integral formulation is extended to account for viscoelastic anisotropy and multiaxial stress states. Numerical results obtained from the present formulation are compared against experimental data and excellent agreement is obtained between these results. As illustrative examples, inplane and interlaminar stresses for (45/-45)_s T300/5208 laminate are also presented.

When polymeric composites are exposed to elevated temperatures and moisture environments, mechanical behaviors of polymer matrix composites are significantly affected by such ambient conditions. Environmental factors such as temperature, moisture content, oxygen, and ultraviolet radiation are significant contributors to material degradation of polymer matrix composites and these effects have received substantial attention in the literature (Crossman et al., 1978, 1979; Shen and Springer, 1979; Whiteside et al., 1983; Yeow et al., 1979). Nonlinear viscoelastic behavior has been observed in laboratory tests of polymer matrix composites (Harper and Weitsman, 1985; Hiel et al., 1984; Lou and Schapery, 1971; Tuttle and Brinson, 1986; Walrath, 1991). Under elevated load conditions, history-dependent effects can also lead to accumulation of residual stresses. It is important to examine the dimensional changes of the laminate as well as moisture and temperature induced stresses as functions of time. Elastic approaches cannot accurately predict residual stress and strain fields since material properties and strengths of polymeric matrix composites are strongly time dependent (Dillard and Brinson, 1983; Hiel et al., 1983; Lifshitz and Rotem, 1970; Yi, 1993). In composite structural design, time-dependent effects of polymer matrix composite materials must be considered in order to ensure realistic analysis and the environmental durability over the entire life span of composite structures.

Interlaminar stresses near free edges are mainly responsible for delamination failures. Numerous studies (Brewer and Lague, 1988; Dávila and Johnson, 1993; Gu and Reddy, 1992; Hiel et al., 1991; Hilton and Yi, 1993; Kim and Soni, 1984; Lin and Yi, 1991; Lucas and Odegard, 1989; O'Brien, 1982; Pipes and Pegano, 1970; Sun and Chen, 1987; Wang and Cross-

man, 1977; Wang and Choi, 1982; Yi, 1993) have been undertaken to investigate interlaminar stresses and failures of laminated composites. Hiel et al. (1991) studied the interlaminar tensile strength under static and fatigue loads including the temperature and moisture effects. Gu and Reddy (1992) studied the effect of geometric nonlinearities on free-edge stress fields. Dávila and Johnson (1993) investigated the response and failure for dropped-ply laminates tested in flat-end compression. A limited number of studies (Hilton and Yi, 1993; Lin and Yi, 1991; Yi, 1993) have been conducted for rate-dependent interlaminar stresses and delaminations. No work has been reported on interlaminar stresses for nonlinear viscoelastic composites. (After this paper was submitted and reviewed, Kennedy and Wang (1994) presented a three-dimensional finite element analysis for anisotropic Schapery-type stress strain relations and developed equally efficient recursive relations.) Henriksen (1984) has presented a two-dimensional isotropic viscoelastic finite element analysis. Lin and Yi (1991) developed the numerical procedure to analyze the viscoelastic interlaminar stresses. Later Yi (1993) proposed the modified Quadratic Delamination Criterion to account for time-dependent strengths in order to predict the delamination initiations in viscoelastic composite laminates as functions of time and loading history. Hilton and Yi (1993) have shown that the times for delamination onset occurrences in composites can be predicted probabilistically. Their analysis includes stochastic processes due to combined random loads and random delamination failure stresses as well as random anisotropic viscoelastic material properties.

In this study, based on Schapery's nonlinear constitutive relations and virtual work principle (Findley et al., 1989; Lamborn and Schapery, 1993; Lou and Schapery, 1971; Schapery, 1969), a numerical procedure is developed for the analysis of nonlinear anisotropic viscoelastic in-plane and interlaminar stresses in composite laminates during environmental exposure. Numerical results have been obtained for [45/-45]_s laminates to demonstrate the feasibility of the present approach. Other lay-up orientations can be conveniently analyzed using the present formulation.

Analysis

Lekhnitskii (1963) was the first to consider an anisotropic elastic generalized plane-strain problem. Pipes and Pagano (1970) used the following displacement field for symmetric laminates under a generalized plane-strain state:

¹ Portions of this paper were presented at the AIAA/ASME/ASCE/AHS/ASC 35th Structures, Structural Dynamics, and Materials Conference, Apr. 18-20, 1994, Hilton Head, SC.

² Post Doctoral Research Associate at the National Center for Supercomputing Applications (NCSA) and Visiting Assistant Professor of Theoretical and Applied Mechanics.

³ Professor Emeritus of Aeronautical and Astronautical Engineering (AAE) and of Supercomputing Applications (NCSA).

⁴ Research Scientist at NCSA and AAE.

Contributed by the Applied Mechanics Division of THE AMERICAN SOCIETY OF MECHANICAL ENGINEERS for publication in the ASME JOURNAL OF APPLIED MECHANICS.

Discussion on this paper should be addressed to the Technical Editor, Professor Lewis T. Wheeler, Department of Mechanical Engineering, University of Houston, Houston, TX 77204-4792, and will be accepted until four months after final publication of the paper itself in the ASME JOURNAL OF APPLIED MECHANICS.

Manuscript received by the ASME Applied Mechanics Division, May 5, 1994; final revision, Oct. 31, 1994. Associate Technical Editor: J. N. Reddy.

$$\begin{aligned}
u(x, y, z, t) &= x \cdot \epsilon_1(t) + U(y, z, t) \\
v(y, z, t) &= V(y, z, t) \\
w(y, z, t) &= W(y, z, t)
\end{aligned} \quad (1)$$

where $\epsilon_1(t)$ is the uniform extensional strain. Small displacements are considered in order to focus primarily on nonlinear material property effects.

For this case the resulting strains and stresses are independent of the x -coordinate and the equilibrium equations in the absence of body forces become

$$\begin{aligned}
\sigma_{x,x} + \tau_{xy,y} + \tau_{xz,z} &= 0 \\
\tau_{yz,x} + \sigma_{y,y} + \tau_{yz,z} &= 0 \\
\tau_{xz,x} + \tau_{zy,y} + \sigma_{z,z} &= 0
\end{aligned} \quad (2)$$

where a comma denotes partial differentiation.

Based on the time-temperature superposition principle (Williams et al., 1955), the relaxation curves can be shifted and master relaxation curves can be obtained at the reference temperature and humidity, where linear anisotropic viscoelastic relaxation moduli can be represented as

$$Q_{ij}(T_f, M_f, \zeta_{ij}) = Q_{ij}^{\infty} + \Delta Q_{ij}(T_f, M_f, \zeta_{ij}) \quad (3)$$

with no summation on i or j and with the reduced time ζ_{ij} defined by

$$\zeta_{ij}(t) = \int_0^t a_{ij}[T(s), M(s)] ds \quad (4)$$

In the above, $i, j = 1, 2, \dots, 6$, T_f and M_f are the reference temperature and moisture content, Q_{ij}^{∞} and ΔQ_{ij} are the equilibrium moduli at constant strain and transient components, respectively, and ζ_{ij} are reduced times which are related the shift factors a_{ij} . The relaxation modulus tensor has nine independent constants for a three-dimensional orthotropic material.

By using a generalized Maxwell model, the relaxation moduli can be represented in terms of exponential series such that (Hilton and Dong, 1964)

$$Q_{ij}(T_f, M_f, \zeta_{ij}) = Q_{ij}^{\infty} + \sum_{\omega=1}^{NT_{ij}} Q_{ij\omega} \cdot e^{-\zeta_{ij}/\lambda_{ij\omega}} \quad (5)$$

where $\lambda_{ij\omega}$ are relaxation times, NT_{ij} are the numbers of terms used in the series expansion and with no summation on i or j .

Introduction of the abbreviated notation leads to the following relaxation moduli Q_{ij} and reduced times ζ_{ij}

$$Q_r(T_f, M_f, \zeta_r) = Q_{ij}(T_f, M_f, \zeta_{ij}) \quad (6)$$

with no summation on i or j and with

$$\zeta_r = \zeta_{ij} \quad r = 1, \dots, 9.$$

The transformed relaxation moduli \bar{Q}_{ij} with respect to the laminate coordinates can be obtained by appropriate coordinate transformations and by using the abbreviated notation they become

$$\bar{Q}_{ij}(t) = \sum_{r=1}^9 A_{ijr} Q_r(t) \quad (7)$$

where A_{ijr} are the transformation coefficients.

A general practical constitutive theory for nonlinear viscoelastic materials was developed by Schapery (Findley et al., 1989; Lamborn and Schapery, 1993; Lou and Schapery, 1971; Schapery, 1969) from irreversible thermodynamic principles. By using free energy and entropy production, nonlinear stress relaxation can be expressed in terms of the same time-dependent properties obtained by the linear analysis. In the present study, Schapery's single integral formulation is extended to account for anisotropy and multi-axial stress states. Using the contracted

notation, the constitutive relations for nonlinear thermo-viscoelastic composite materials with respect to the laminate coordinate can be expressed as

$$\begin{aligned}
\sigma_i(t) = \sum_{r=1}^9 & \left[A_{ijr} h_r^{\infty} Q_r^{\infty} \tilde{\epsilon}_j(t) \right. \\
& \left. + A_{ijr} h_r^1 \cdot \int_0^t \Delta Q_r [\zeta_r(t) - \zeta'_r(\tau)] \frac{\partial h_r^2 \tilde{\epsilon}_j(\tau)}{\partial \tau} d\tau \right] \quad (8)
\end{aligned}$$

with

$$\tilde{\epsilon}_j(t) = \epsilon_j(t) - \epsilon_j^*(t). \quad (9)$$

In the above, σ_i are stresses and ϵ_j and ϵ_j^* are total and hydrothermal strains. Q_r^{∞} and ΔQ_r are the equilibrium moduli at constant strain and transient components defined by linear viscoelasticity. The quantities h_r^{∞} , h_r^1 , h_r^2 , and $\bar{\epsilon}_r$ are strain-dependent material properties. The reduced time ζ_r can be defined as a function of shift factor

$$\begin{aligned}
\zeta_r(t) &= \int_0^t \bar{\epsilon}_r(T, M, \epsilon) ds \\
\zeta'_r(\tau) &= \int_0^{\tau} \bar{\epsilon}_r(T, M, \epsilon) ds. \quad (10)
\end{aligned}$$

The shift functions $\bar{\epsilon}_r$ may depend on strain, temperature, and moisture contents. When the nonlinear material parameters h are set equal to one, Eq. (9) reduces to the statement of the linear Boltzmann superposition principle.

Material parameters of laminated composites are evaluated by uniaxial tests. However, under uniaxial test conditions, an individual ply within the laminate is in a multiaxial stress state and the influence of other stresses on material parameters must be considered. Hiel et al. (1984), Tuttle and Brinson (1986), and Walrath (1991) have introduced the average matrix octahedral shear stress in order to account for such multiaxial conditions. Similarly, in this present study, the octahedral shear strain $\epsilon^{m\text{oct}}$ is introduced and then nonlinear material parameters can be expressed as functions of single invariant

$$\epsilon^{m\text{oct}} = \frac{1}{9}[(\epsilon_1^m - \epsilon_2^m)^2 + (\epsilon_2^m - \epsilon_3^m)^2 + (\epsilon_3^m - \epsilon_1^m)^2] \quad (11)$$

where ϵ_1^m , ϵ_2^m , and ϵ_3^m are principal strains of the matrix.

Finite Element Formulation

Using virtual work and the constitutive integral equations, finite element equilibrium equations for nonlinear viscoelastic composite laminates can now be formulated. In the absence of body forces, the virtual work principle for element e becomes

$$\delta \pi^{(e)} = \int_{V^{(e)}} \delta \epsilon^T \sigma dV^{(e)} - \int_{\Gamma^{(e)}} \delta \mathbf{d}^{(e)T} \mathbf{T}^{(e)} d\Gamma^{(e)} = 0 \quad (12)$$

where $\delta \epsilon$ is the associated virtual strain tensor, σ the stress tensor, $\mathbf{T}^{(e)}$ the boundary tractions, $\delta \mathbf{d}^{(e)}$ the virtual displacement vector, $V^{(e)}$ the body volume, and $\Gamma^{(e)}$ is the surface on which boundary tractions are prescribed.

The displacement components $U^{(e)}$, $V^{(e)}$, $W^{(e)}$ in Eq. (1) may be approximated as

$$\left\{ \begin{array}{l} U^{(e)}(y, z, t) \\ V^{(e)}(y, z, t) \\ W^{(e)}(y, z, t) \end{array} \right\} = [\Psi^{(e)}] \{ \mathbf{d}^{(e)}(t) \} \quad (13)$$

where

$$[\Psi^{(e)}] = \begin{bmatrix} \psi_1 & 0 & 0 & \cdots & \psi_l & 0 & 0 \\ 0 & \psi_1 & 0 & \cdots & 0 & \psi_l & 0 \\ 0 & 0 & \psi_1 & \cdots & 0 & 0 & \psi_l \end{bmatrix} \quad (14)$$

$$\{\mathbf{d}^{(e)}(t)\} = [d_1^{(e)}, d_1^{(e)}, d_1^{(e)}, d_2^{(e)}, d_2^{(e)}, d_2^{(e)}, \dots, d_l^{(e)}, d_l^{(e)}, d_l^{(e)}]^T. \quad (15)$$

In the above, l is the number of nodes for each element, $[\Psi^{(e)}(y, z)]$ are the isotropic shape functions and $\{\mathbf{d}^{(e)}(t)\}$ is the element nodal displacement vector.

By substituting Eqs. (14) into (1), the displacements and their virtual counterparts within an element can be expressed in terms of axial strains and nodal displacements

$$\{\bar{u}^{(e)}\} = [\mathbf{L} \quad \Psi^{(e)}] \begin{Bmatrix} \epsilon_1(t) \\ \mathbf{d}^{(e)}(t) \end{Bmatrix} \quad (16)$$

and

$$\delta\{\bar{u}^{(e)}\} = [\mathbf{L} \quad \Psi^{(e)}] \delta \begin{Bmatrix} \epsilon_1(t) \\ \mathbf{d}^{(e)}(t) \end{Bmatrix}$$

where

$$\{\bar{u}^{(e)}\} = \begin{Bmatrix} u^{(e)}(t) \\ v^{(e)}(t) \\ w^{(e)}(t) \end{Bmatrix}$$

$$\delta\{\bar{u}^{(e)}\} = \delta \begin{Bmatrix} u^{(e)}(t) \\ v^{(e)}(t) \\ w^{(e)}(t) \end{Bmatrix} \quad (17)$$

and

$$\{\mathbf{L}\} = [x \quad 0 \quad 0]^T.$$

Differentiating Eq. (17) with respect to x_i results in the following strain-displacement relationship:

$$\{\epsilon(t)\} = [\mathbf{B}] \begin{Bmatrix} \epsilon_1(t) \\ \mathbf{d}^{(e)}(t) \end{Bmatrix}. \quad (18)$$

Similar to the stress-strain relationships, finite element equilibrium equations for nonlinear viscoelastic bodies can also be stated as hereditary integral equations. Substituting Eqs. (18) and (19) into the virtual work principle Eq. (13) yields the finite element equilibrium equations for each element

$$\sum_{r=1}^9 \left[h_r^{\alpha(e)} (\bar{u}^{(e)}) \cdot k_{mn}^{\alpha(e)} \bar{u}_n(t) + h_r^{\alpha(e)} (\bar{u}^{(e)}) \cdot \int_0^t k_{mn}^{(e)}(\mathbf{x}, \zeta_r - \zeta'_r) \times \frac{\partial h_r^{2(e)}(\bar{u}^{(e)}) \bar{u}_n^{(e)}(s)}{\partial s} ds \right] = f_m^{(e)}(t) + f_m^{\bar{h}(e)}(t) \quad (19)$$

with no summation over r and where $m, n = 1, 2, \dots, 3l + 1$. In the above, $k_{mn}^{(e)}$ is the element stiffness matrix, $\bar{u}_n^{(e)}$ is the vector of element nodal displacements and $f_m^{(e)}$ and $f_m^{\bar{h}(e)}$ are element nodal force vectors due to applied surface tractions or uniaxial strain and hydrothermal loadings, respectively. Nonlinear material parameters $h_r^{\alpha(e)}$, $h_r^{1(e)}$, $h_r^{2(e)}$, and $\bar{u}^{(e)}$ can be described as functions of displacements by using strain-displacement relationship. The element stiffness matrix and the element nodal force vectors can be defined as follows:

$$k_{mn}^{(e)} = \iint_{\Gamma^{(e)}} B_{im} A_{ijr} Q_r^\alpha B_{jn} dy dz \quad (20)$$

$$k_{mn}^{(e)}(\mathbf{x}, \zeta_r - \zeta'_r) = \iint_{\Gamma^{(e)}} B_{im} A_{ijr} \Delta Q_r(\zeta_r - \zeta'_r) B_{jn} dy dz$$

$$= \sum_{\omega=1}^{NT_r} \iint_{\Gamma^{(e)}} B_{im} A_{ijr} Q_{r\omega}^t$$

$$\times \exp[-(\zeta_r - \zeta'_r)/\lambda_{r\omega}] B_{jn} dy dz$$

$$= \sum_{\omega=1}^{NT_r} k_{mn\omega}^{(e)} \cdot \exp[-(\zeta_r - \zeta'_r)/\lambda_{r\omega}]$$

$$(\text{no summation over repeated } r) \quad (21)$$

and

$$f_m^{(e)}(t) = \iint_{\Gamma^{(e)}} [\Psi] \{\mathbf{t}(t)\} dy dz. \quad (22)$$

The residual nodal force vector due to hydrothermal loads becomes

$$\begin{aligned} f_m^{\bar{h}(e)}(t) = & \sum_{r=1}^9 \left[h_r^{\alpha(e)} \iint_{\Gamma^{(e)}} B_{im} A_{ijr} Q_r^\alpha \bar{e}_j^*(t) dy dz \right. \\ & + h_r^{1(e)} \iint_{\Gamma^{(e)}} \int_{\tau=0}^{\tau=t} B_{im} A_{ijr} Q_r^t(\zeta_r - \zeta'_r) \times \frac{\partial h_r^{2(e)} \bar{e}_j^*(\tau)}{\partial \tau} d\tau dy dz \left. \right] \quad (23) \end{aligned}$$

where \bar{e}_j^* are the transformed free hydrothermal strains.

Using an exponential series for relaxation moduli, the force vector can be rewritten as

$$\begin{aligned} f_m^{\bar{h}(e)}(t) = & - \sum_{r=1}^9 \left[h_r^{\alpha(e)} \cdot \{f_{mr}^{\alpha(e)} \cdot \theta^T(t) + f_{mr}^{\beta(e)} \cdot \theta^H(t)\} \right. \\ & + h_r^{1(e)} \sum_{\omega=1}^{NT_r} \left\{ \int_{\tau=0}^{\tau=t} f_{mr\omega}^{\alpha(e)} \cdot \exp[-(\zeta_r - \zeta'_r)/\lambda_{r\omega}] \right. \\ & \times \frac{\partial h_r^{2(e)} \theta^T(\tau)}{\partial \tau} \left. + f_{mr\omega}^{\beta(e)} \cdot \exp[-(\zeta_r - \zeta'_r)/\lambda_{r\omega}] \right. \\ & \times \left. \frac{\partial h_r^{2(e)} \theta^H(\tau)}{\partial \tau} \right\} \cdot d\tau \left. \right] \quad (24) \end{aligned}$$

where

$$f_{mr}^{\alpha(e)} = \iint_{\Gamma^{(e)}} B_{im} A_{ijr} Q_r^\alpha \bar{e}_j dy dz$$

$$f_{mr}^{\beta(e)} = \iint_{\Gamma^{(e)}} B_{im} A_{ijr} Q_r^\beta \bar{e}_j dy dz$$

$$f_{mr\omega}^{\alpha(e)} = \iint_{\Gamma^{(e)}} B_{im} A_{ijr} Q_{r\omega}^t \bar{e}_j dy dz$$

$$f_{mr\omega}^{\beta(e)} = \iint_{\Gamma^{(e)}} B_{im} A_{ijr} Q_{r\omega}^t \bar{e}_j dy dz \quad (25)$$

with no summation on r . Note that \bar{e}_j and \bar{e}_j^* are the transformed coefficients of thermal and hydroscopic expansions with respect to the xyz coordinate system.

The global matrices can be assembled from the element matrices and then the finite element equilibrium equations for the global system become

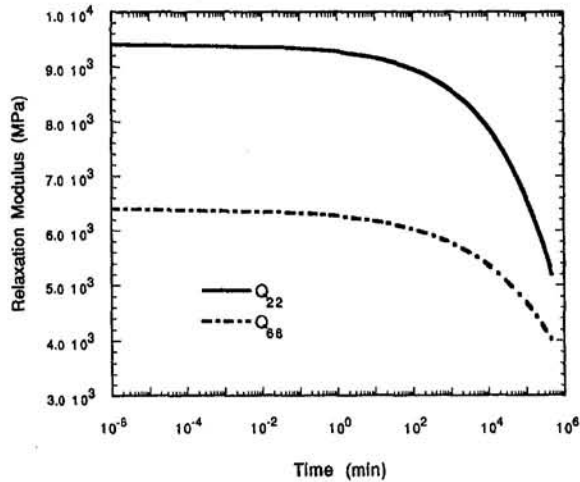


Fig. 1 Master relaxation modulus curves for T300/5208

$$\sum_{r=1}^9 \left[h_r^\infty \cdot k_{mr}^\infty \bar{u}_n(t) + h_r^1 \cdot \int_0^t k_{mr}^t[x, \zeta_r(t) - \zeta_r'(s)] \cdot \frac{\partial h_r^2 \bar{u}_n(s)}{\partial s} ds \right] = f_m(t) + f_{\bar{m}}(t). \quad (26)$$

Since the above equations are hereditary integrals, a direct integration of Eq. (27) requires enormous storage memory and computational time. To overcome these difficulties, a numerical algorithm similar to that used by Bathe (1982), Lin and Yi (1991), Oden (1971), Roy and Reddy (1988), Taylor et al. (1970), and Zak (1967) for linear viscoelastic materials is developed here for the solution of Eq. (27). The present formulation requires storage of only the previous time solution instead of all the solutions throughout the loading time history.

Let

$$\begin{aligned} \hat{q}_{nr}(t) &= h_r^2 \cdot \bar{u}_n(t) \\ \hat{\theta}_r^T(t) &= h_r^2 \cdot \theta^T(t) \\ \hat{\theta}_r^H(t) &= h_r^2 \cdot \theta^H(t) \end{aligned} \quad (27)$$

then the governing equations can be integrated step by step using a finite difference recurrence relationship for approximate calculations of derivatives of Eqs. (28). By assuming that the \hat{q}_{nr} vary linearly over each time step Δt_j , the variables \hat{q}_{nr} and their time derivatives are given by

$$\begin{aligned} \hat{q}_{nr}(t) &\simeq \frac{1}{\Delta t_j} [(t_j - t) \hat{q}_{nr}(t_{j-1}) + (t - t_{j-1}) \hat{q}_{nr}(t_j)] \\ \frac{\partial \hat{q}_{nr}(t)}{\partial t} &\simeq \frac{\Delta \hat{q}_{nr}(t_j)}{\Delta t_j} = \frac{\hat{q}_{nr}(t_j) - \hat{q}_{nr}(t_{j-1})}{\Delta t_j} \end{aligned} \quad (28)$$

with

$$\Delta t_j = t_j - t_{j-1} \quad t_{j-1} \leq t \leq t_j.$$

Similarly the hygrothermal derivatives are defined as

$$\begin{aligned} \frac{\partial \hat{\theta}_r^T(t)}{\partial t} &\simeq \frac{\Delta \hat{\theta}_r^T(t_j)}{\Delta t_j} = \frac{\hat{\theta}_r^T(t_j) - \hat{\theta}_r^T(t_{j-1})}{\Delta t_j} \\ \frac{\partial \hat{\theta}_r^H(t)}{\partial t} &\simeq \frac{\Delta \hat{\theta}_r^H(t_j)}{\Delta t_j} = \frac{\hat{\theta}_r^H(t_j) - \hat{\theta}_r^H(t_{j-1})}{\Delta t_j} \end{aligned} \quad (29)$$

If no loading is applied at time $t < 0$ then

$$\Delta \hat{\theta}_r^T(0) = \hat{\theta}_r^T(0), \quad \Delta \hat{\theta}_r^H(0) = \hat{\theta}_r^H(0). \quad (30)$$

By using finite difference approximations in Eqs. (29) and (30), Eq. (27) can be expressed in a recursive form as

$$\begin{aligned} \sum_{r=1}^9 \{ h_r^\infty k_{mr}^\infty + h_r^1 h_r^2 \sum_{\omega=1}^{NT_r} k_{mr\omega} \cdot S_{r\omega}(\Delta t_p) \} \bar{u}_n(t_p) \\ = f_m(t_p) + f_{\bar{m}}(t_p) - \sum_{r=1}^9 h_r^1 \sum_{\omega=1}^{NT_r} \{ k_{mr\omega} \\ \times S_{r\omega}(\Delta t_p) \hat{q}_{nr}(t_{p-1}) - R_{mr\omega}(t_p) \} \quad (31) \end{aligned}$$

with

$$\begin{aligned} f_{\bar{m}}(t_p) = - \sum_{r=1}^9 [h_r^\infty \cdot \{ f_{mr}^{\infty\alpha} \cdot \theta^T(t_p) \\ + f_{mr}^{\infty\beta} \cdot \theta^H(t_p) \} + h_r^1 \cdot \sum_{\omega=1}^{NT_r} \{ f_{mr\omega}^{\alpha\alpha} \cdot \Delta \hat{\theta}_r^T(t_p) \\ + f_{mr}^{\beta\beta} \cdot \Delta \hat{\theta}_r^H(t_p) \} \cdot S_{r\omega}(\Delta t_p)] \quad (32) \end{aligned}$$

$$\begin{aligned} R_{mr\omega}(t_p) = e^{-\Delta \zeta_r(t_p)/\lambda_{r\omega}} \{ R_{mr\omega}(t_{p-1}) \\ + [k_{mr\omega} \cdot \Delta \hat{q}_{nr}(t_{p-1}) - f_{mr\omega}^{\alpha\alpha} \cdot \Delta \hat{\theta}_r^T(t_{p-1}) \\ - f_{mr\omega}^{\beta\beta} \cdot \Delta \hat{\theta}_r^H(t_{p-1})] \cdot S_{r\omega}(\Delta t_{p-1}) \} \quad (33) \end{aligned}$$

$$S_{r\omega}(\Delta t_p) = \frac{1}{\Delta t_p} \int_{t_{p-1}}^{t_p} \exp[-\Delta \zeta_r(t)/\lambda_{r\omega}] d\tau$$

$$\Delta \zeta_r(t_p) = \zeta_r(t_p) - \zeta_r(t_{p-1})$$

$$R_{mr\omega}(0) = 0$$

$$S_{r\omega}(0) = 1$$

(no summation over r).

Note that Eqs. (32) are recursive and that it is possible to solve iteratively for the displacements \bar{u}_n at time t_p using only the previous solution at time t_{p-1} . In the present study, a modified Newton-Raphson technique (Oden, 1971; Taylor et al., 1970) was used to solve the above nonlinear equations.

Numerical Results

A limited number of parametric studies have been constructed in order to illustrate the nonlinear time-dependent behavior of laminated composites. Consider the laminate under a plane-strain condition in the x -direction. The laminate width is 2 cm and the laminate width-to-thickness ratio is four. The composites consist of T300/5208 graphite/epoxy. Using creep and creep recovery tests, the master compliance curves and shift

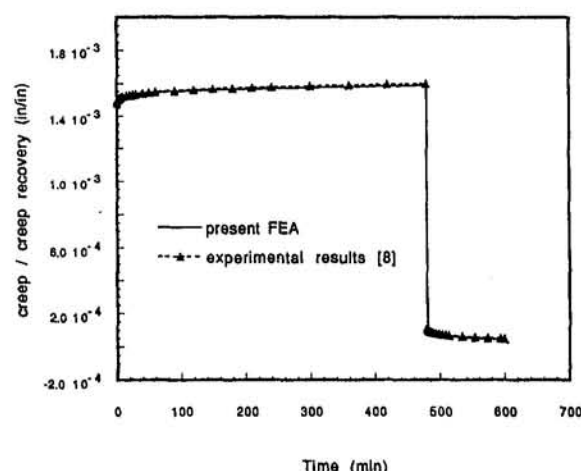


Fig. 2 Creep and creep recovery in [90]s laminate

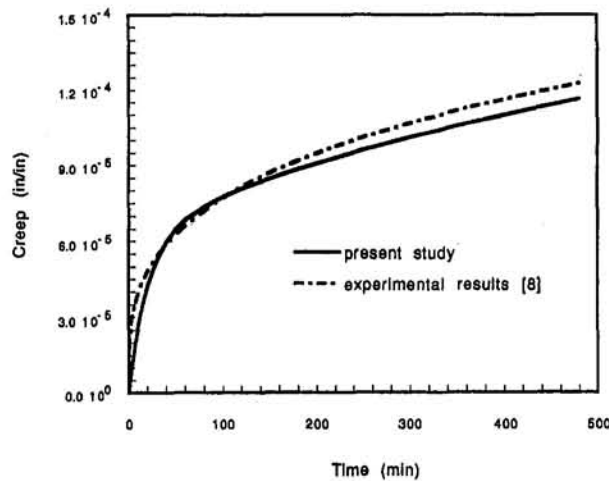


Fig. 3 Creep in [90]_s laminate

factors corresponding to various loading conditions were obtained from Tuttle and Brinson (1986).

In this study, the relaxation moduli were evaluated by Schapery's nonlinear stress-strain relationship and by relaxation/relaxation recovery analysis as extended to anisotropic relations, Eq. (9). Time-dependent Q_{22} and Q_{66} are plotted in Fig. 1. It is assumed that time function for Q_{33} is equal to the one for Q_{22} , and that $Q_{66} = Q_{44} = Q_{55}$. Q_{11} is taken to be elastic since it is generally controlled by fiber properties. Also the time functions for Q_{12} , Q_{13} , and Q_{23} are taken the same as that for Q_{22} .

Linear viscoelastic interlaminar stresses at $t = 0$ were compared with closed-form elastic solutions obtained by Yi (1993). Comparison studies between viscoelastic finite element solutions and the classical lamination solutions were also reported by Lin and Yi (1991). In this paper, a comparison study between experimental results and the present numerical solution was conducted. Creep and creep recovery data for T300/5208 graphite/epoxy composites were experimentally determined by Tuttle and Brinson (1986). At a temperature of 300°F, $\sigma_x = 13.93$ MPa (2020 psi) was applied to the 90 deg laminates. The loading was held constant for eight hours and then removed in an instantaneous elastic step and after unloading, the creep recovery was measured for two hours.

In the present study, 29-node isoparametric elements were used and the in-plane stresses, σ_x , calculated by the present method were compared with experimental results. As shown in Figs. 2-4, excellent agreement between these results was

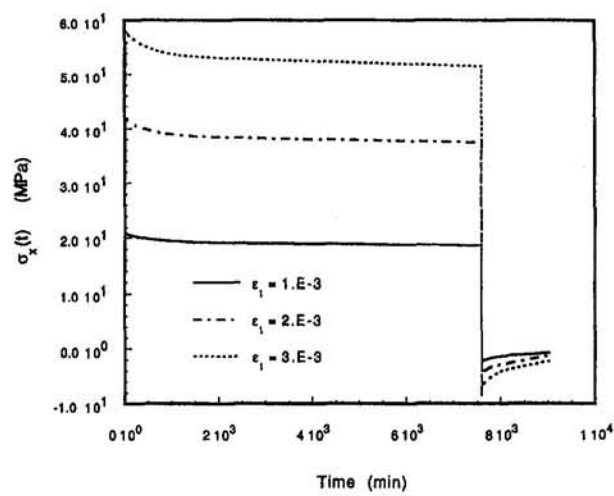


Fig. 5 Time-dependent in-plane stress σ_x in [45/-45]_s laminate

obtained. The discrepancies between these two solutions are within 3 percent. Similar errors were also observed in the compliance-relaxation modulus conversion process. The transient creep and recovery responses are magnified in Figs. 3-4.

The nonlinear time-dependent inplane and interlaminar stresses in composite laminates were studied as a function of time and loading magnitude. T300/5208 laminates with [45/-45]_s lay-ups were considered and nine-node isoparametric elements were used. The finite element model consists of 14 × 4 meshes (56 elements) in the yz cross section with a total of 784 degrees of freedom. The step-size Δt is set to 0.5 min initially and Δt increases with time. There are 55 time steps involved in the calculation of time-dependent interlaminar stresses over a period of 6.3 days. Three axial strain loading conditions such as $\epsilon_x = 0.001$, $\epsilon_x = 0.002$, and $\epsilon_x = 0.003$ were considered. At isothermal conditions ($T = 147^\circ\text{F}$), the axial strains were held constant for 5.3 days and then removed in an instantaneous step. The inplane stress σ_x which was obtained near the center of laminate was plotted in Fig. 5 and the residual stresses were observed after unloading.

The interlaminar stress distributions along the interface between the 45 deg and -45 deg layers are shown in Figs. 6-9. Normal interlaminar stresses σ_z at $t = 0$ and 7600 mins are depicted in Figs. 6 and 7, respectively. Also transverse shear stresses τ_{xz} at $t = 0$ and 7600 mins are plotted in Figs. 8 and 9, respectively. As shown in Fig. 10, the rate of stress relaxation

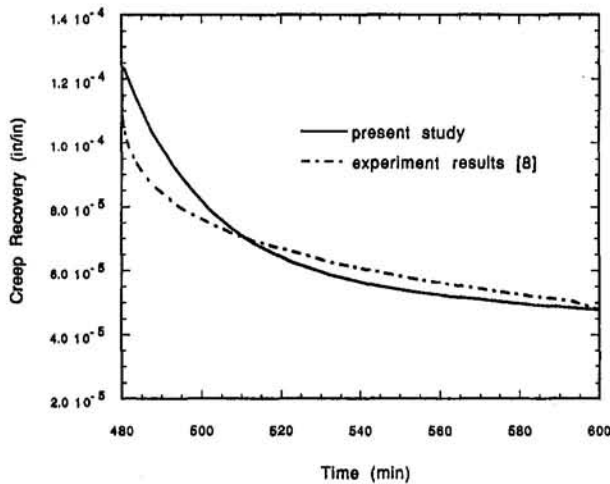


Fig. 4 Creep recovery in [90]_s laminate

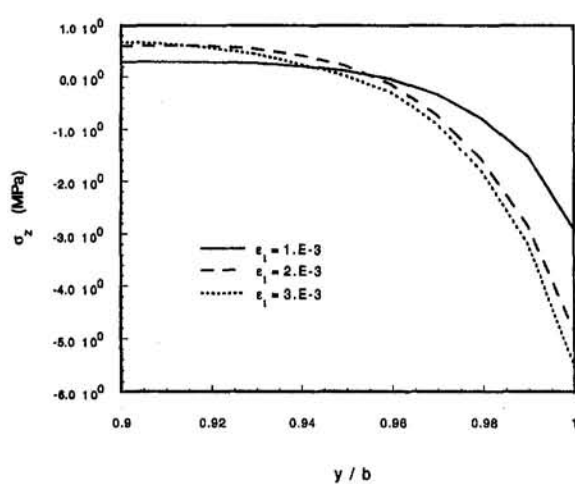


Fig. 6 Interlaminar normal stress σ_z in [45/-45]_s laminate ($t = 0$ mins)

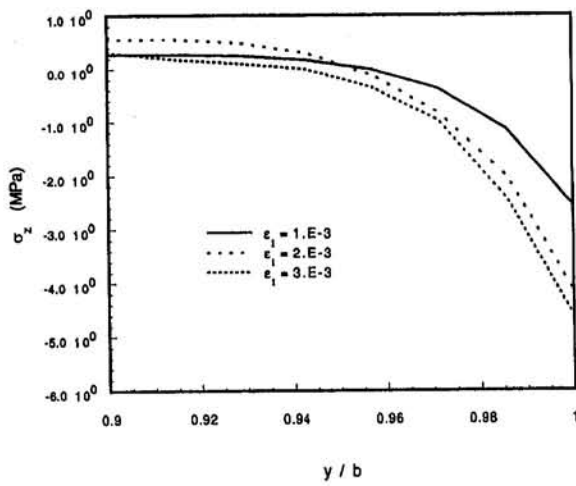


Fig. 7 Interlaminar normal stress σ_z in $[45/-45]_s$ laminate ($t = 7600$ mins)

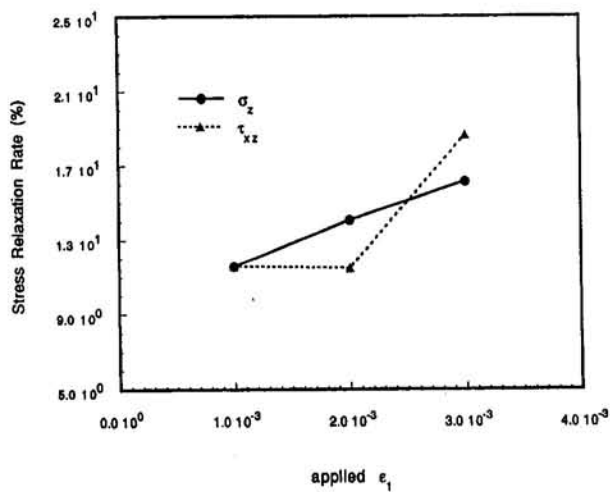


Fig. 10 Relaxation rate for constant extensional load

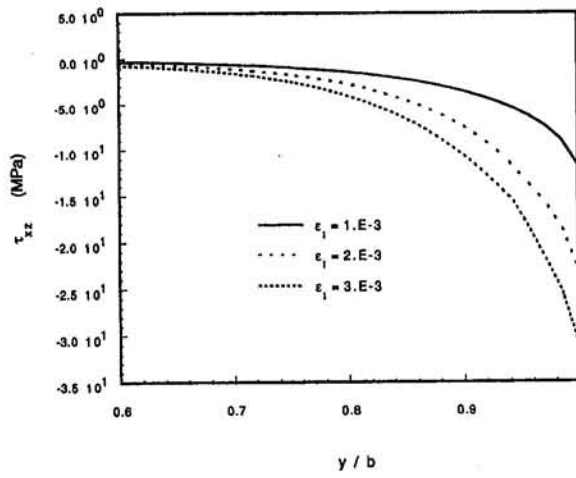


Fig. 8 Interlaminar shear stress τ_{xz} in $[45/-45]_s$ laminate ($t = 0$ mins)

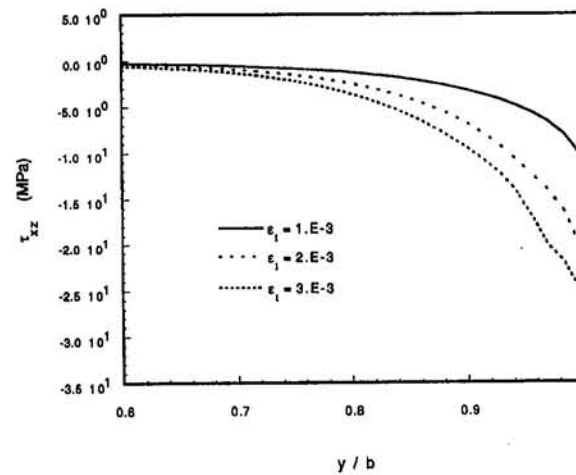


Fig. 9 Interlaminar shear stress τ_{xz} in $[45/-45]_s$ laminate ($t = 7600$ mins)

is greater at higher loading conditions. Over a period of 5.3 days, the stresses σ_z and τ_{xz} relaxed about 11.6 percent at $\epsilon_1 = 10^{-3}$ while at $\epsilon_1 = 3 \times 10^{-3}$ those stresses decreased 16.2

percent and 18.7 percent, respectively. The results show that increasing the load significantly increases nonlinear behavior.

Conclusions

Based on Schapery's nonlinear constitutive relations and virtual work principles, it is possible to develop three-dimensional nonlinear anisotropic viscoelastic stress-strain relations and an attendant finite element analysis, which was applied to the determination inplane and interlaminar stresses in composite laminates during environmental exposures. Numerical results have been obtained for $[45/-45]_s$ laminates, which demonstrate the feasibility of the present formulation. Other lay-up orientations can be conveniently analyzed using the present approach. The results indicate a strong sensitivity to the nonlinearities of the viscoelastic constitutive relations.

References

- Bathe, K., 1982, *Finite Element Procedures in Engineering Analysis*, Prentice-Hall, New York.
- Brewer, J. C., and Lagace, P. A., 1988, "Quadratic Stress Criterion for Initiation of Delamination," *Journal of Composite Materials*, Vol. 22, pp. 1141-1155.
- Crossman, F. W., Mauri, R. E., and Warren, W. J., 1978, "Moisture Altered Viscoelastic Response of Graphite/Epoxy Composite," *Advanced Composite Materials—Environmental Effects*, ASTM STP 658, J. R. Vinson, ed., ASTM, Philadelphia, pp. 205-220.
- Crossman, F. W., and Flagg, D. L., 1979, "Dimensional Stability of Composite Laminates During Environmental Exposure," *SAMPE Journal*, Vol. 15, No. 4, pp. 15-20.
- Dillard, D. A., and Brinson, H. F., 1983, "A Numerical Procedure for Predicting Creep and Delayed Failure in Laminated Composites," *Long-Term Behavior of Composites*, ASTM STP 813, T. K. O'Brien, ed., ASTM, Philadelphia, pp. 23-37.
- Dávila, C. G., and Johnson, E. R., 1993, "Analysis of Delamination Initiation in Postbuckled Dropped-Ply Laminates," *AIAA Journal*, Vol. 31, No. 4, pp. 721-727.
- Findley, W. N., Lai, J. S., and Onaran, K., 1989, *Creep and Relaxation of Nonlinear Viscoelastic Materials With an Introduction to Linear Viscoelasticity*, Dover Publications, New York.
- Gu, Q., and Reddy, J. N., 1992, "Non-linear Analysis of Free-Edge Effects in Composite Laminates Subjected to Axial Loads," *International Journal of Non-Linear Mechanics*, Vol. 276, pp. 27-41.
- Harper, B. D., and Weitsman, Y., 1985, "On the Effects of Environmental Conditioning on Residual Stresses in Composite Laminates," *International Journal of Solids and Structures*, Vol. 21, pp. 907-926.
- Henriksen, M., 1984, "Nonlinear Viscoelastic Stress Analysis—A Finite Element Approach," *Computers & Structures*, Vol. 18, pp. 133-138.
- Hiel, C., Cardon, A. H., and Brinson, H. F., 1984, "The Nonlinear Viscoelastic Response of Resin Matrix Composite Laminates," NASA Contractor Report 3772.
- Hiel, C. C., Sumich, M., and Chappell, D. P., 1991, "A Curved Beam Test Specimen for Determining the Interlaminar Tensile Strength of a Laminated Composite," *Journal of Composite Materials*, Vol. 25, pp. 854-868.

Hilton, H. H., and Dong, S. B., 1964, "An Analogy for Anisotropic, Nonhomogeneous, Linear Viscoelasticity," *Developments in Mechanics*, Pergamon Press, New York, pp. 58-73.

Hilton, H. H., and Yi, S., 1993, "Stochastic Viscoelastic Delamination Onset Failure Analysis of Composites," *Journal of Composite Materials*, Vol. 27, No. 11, pp. 1097-1113.

Kennedy, T. C., and Wang, M., 1994, "Three-Dimensional, Nonlinear Viscoelastic Analysis of Laminated Composites," *Journal of Composite Materials*, Vol. 28, pp. 902-925.

Kim, R. Y., and Soni, S. R., 1984, "Experimental and Analytical Studies On the Onset of Delamination in Laminated Composites," *Journal of Composite Materials*, Vol. 18, pp. 70-80.

Lamborn, M. J., and Schapery, R. A., 1993, "An Investigation of the Existence of a Work Potential for Fiber Reinforced Plastic," *Journal of Composite Materials*, Vol. 27, pp. 352-382.

Lekhnitskii, S. G., 1963, *Theory of Elasticity of an Anisotropic Body*, Holden-Day, San Francisco.

Lifshitz, J. M., and A. Rotem, 1970, "Time-Dependent Longitudinal Strength of Unidirectional Fibrous Composites," *Fibre Science and Technology*, Vol. 3, pp. 1-20.

Lin, K. Y., and Yi, S., 1991, "Analysis of Interlaminar Stresses in Viscoelastic Composites," *International Journal of Solids and Structures*, Vol. 27, No. 7, pp. 929-945.

Lou, Y. C., and Schapery, R. A., 1971, "Viscoelastic Characterization of a Nonlinear Fiber-Reinforced Plastic," *Journal of Composite Materials*, Vol. 5, pp. 208-234.

Lucas, J. P., and Odegard, B. C., 1989, "Moisture Effects on Mode 1 Interlaminar Fracture Toughness of Graphite Fiber Thermoplastic Matrix Composite," *Advances in Thermoplastic Matrix Composite Materials*, ASTM STP 1044, M. Newaz, ed., ASTM, Philadelphia, pp. 231-247.

O'Brien, T. K., 1982, "Characterization of Delamination Onset and Growth in a Composite Laminates," *Damage in Composite Materials*, ASTM STP 775, ASTM, Philadelphia, pp. 140-167.

Oden, J. T., 1971, *Finite Elements in Nonlinear Continua*, McGraw-Hill, New York.

Pipes, R. B., and Pagano, N. J., 1970, "Interlaminar Stresses in Composite Laminates under Uniform Axial Extension," *Journal of Composite Materials*, Vol. 4, pp. 538-548.

Roy, S., and Reddy, J. N., 1988, "A Finite Element Analysis of Adhesively Bonded Composite Joints with Moisture Diffusion and Delayed Failure," *Computers & Structures*, Vol. 29, pp. 1011-1031.

Schapery, R. A., 1969, "On the Characterization of Nonlinear Viscoelastic Materials," *Polymer Engineering and Science*, Vol. 9, No. 4, pp. 295-310.

Shen, C. H., and Springer, G. S., 1979, "Moisture Absorption of Graphite/Epoxy Composites Immersed in Liquids and in Humid Air," *Journal of Composite Materials*, Vol. 13, pp. 131-147.

Sun, C. T., and Chen, J. K., 1987, "Effect of Plasticity on Free Edge Stresses in Boron-Aluminum Composite Laminates," *Journal of Composite Materials*, Vol. 21, pp. 969-985.

Taylor, R. L., Pister, K. S., and Goudreau, G. L., 1970, "Thermomechanical Analysis of Viscoelastic Solids," *International Journal for Numerical Methods in Engineering*, Vol. 2, pp. 45-59.

Tuttle, M. E., and Brinson, H. F., 1986, "Prediction of the Long-Term Creep Compliance of General Composite Laminates," *Experimental Mechanics*, Vol. 26, No. 1, pp. 89-102.

Walrath, D. E., 1991, "Viscoelastic Response of a Unidirectional Composite Containing Two Viscoelastic Constituents," *Experimental Mechanics*, Vol. 31, No. 6, pp. 111-117.

Wang, A. S. D., and Crossman, F. W., 1977, "Edge Effects on Thermally Induced Stresses in Composite Laminates," *Journal of Composite Materials*, Vol. 11, pp. 300-301.

Wang, S. S., and Choi, I., 1982, "Influence of Fiber Orientation and Ply Thickness on Hygroscopic Boundary-Layer Stresses in Angle-Ply Composite Laminates," *Journal of Composite Materials*, Vol. 16, pp. 244-256.

Whiteside, J. B., DeLasi, R. J., and Schulte, R. L., 1983, "Distribution of Absorbed Moisture in Graphite/Epoxy Laminates After Real Time Environmental Cycling," *Long-Term Behavior of Composites*, ASTM STP 813, T. K. O'Brien, ed., ASTM, Philadelphia, pp. 192-205.

Williams, M. L., Landel, R. F., and Ferry, J. D., 1955, "The Temperature Dependence of Relaxation Mechanism in Amorphous Polymers and Other Glass-Liquids," *Journal of the American Chemical Society*, Vol. 77, pp. 3701-3707.

Yeow, Y. T., Morris, D. H., and Brinson, H. F., 1979, "Time-Temperature Behavior of a Unidirectional Graphite-Epoxy Composite," *Composite Materials: Testing and Design*, Fifth Conference, ASTM STP 674, S. W. Tsai, ed., ASTM, Philadelphia, pp. 263-271.

Yi, S., 1993, "Thermoviscoelastic Analysis of Delamination Onset and Free Edge Response in Epoxy Matrix Composite Laminates," *AIAA Journal*, Vol. 31, No. 12, pp. 2320-2328.

Zak, A. R., 1967, "Structural Analysis of Realistic Solid Propellant Materials," *J. Spacecraft and Rockets*, Vol. 5, pp. 270-275.

A Micromechanical Model for the Fiber Bridging of Macro-Cracks in Composite Plates

G. A. Kardomateas

Associate Professor,
Mem. ASME.

R. L. Carlson

Professor Emeritus.

School of Aerospace Engineering,
Georgia Institute of Technology,
Atlanta, GA 30332-0150

Recent experimental studies on the propagation of transverse cracks in composites have shown that fiber bridging is frequently present, and can be considered as the cause of increased toughness. This paper presents a model that is capable of quantifying this effect and explaining the decrease in the crack growth rate in either a monotonic or a cyclic load profile. Both Modes I and II are considered. The model is based on the elastic loading of a fiber located on the macro-crack face close to the tip and under dominantly plane strain conditions. Two fundamental cases of fiber bridging configurations are distinguished, namely when the fiber-matrix interface is intact and when the fiber-matrix interface has partially failed. Following the single fiber analysis, the model is extended to the case of multiple fibers bridging the faces of the macro-crack. The analysis is for a generally anisotropic material and the fiber lines are at arbitrary angles. Results are presented for the case of an orthotropic material with unidirectional fibers perpendicular to the crack faces. Specifically, the reduction in the stress intensity factor (relative to the nominal value) is investigated for the glass fibers in a glass/epoxy composite system. The effects of fiber debonding and pullout with friction as well as fiber breaking are accounted for in the analysis, and results with respect to a parameter representing the fiber-matrix interface friction are presented. Results are also presented regarding the partial or full fracture of the fiber bridging zone. The model can also be used to analyze the phenomenon of fiber nesting, which is similar to fiber bridging, and occurs with growing delaminations.

Introduction

In many composite structure applications, transverse cracks, usually emanating from holes or notches, extend into sizable macro-cracks growing across the fibers. Fiber bridging of the macro-crack faces has been observed to take place in polymeric matrix composites (e.g., Botsis and Shafiq, 1992) and ceramic-matrix composites (e.g., Zok et al., 1990).

The bridging of macro-cracks by fibers only partially pulled out is a significant source of toughness. The toughening mechanism behind the delamination tip is analogous to the contribution to the toughness of polymers by bridges between molecular chains. Alternatively stated, in plastics, internal stresses are transmitted through tangles of chains, and if crosslinks are present, more and more internal resistance to external loading is available.

The toughening roles played by fibers bridging a crack can be conceptually described as follows: Close to the crack tip, the crack-opening displacement is small enough to be accommodated by enhanced extension of the fiber located there: typical strains to failure are 0.003 for fiberglass and 0.01 for carbon fiber. Moving away from the crack tip, the displacement gets larger so that fiber pull-out or fiber fracture are required in order to accommodate the increasing crack displacement.

This phenomenon has been exploited in the design of various titanium and titanium aluminide alloys which have been reinforced by unidirectional SiC fibers having carbon-rich coatings. These fiber coatings contain weak graphitic films, which facil-

tate interfacial failure and extensive sliding resisted by friction (e.g. Cox et al., 1989). Such weak interfaces are beneficial in relatively brittle-matrix composites, especially the titanium aluminides, in contrast to the case of the more common ductile metal matrix and polymeric composites, in which stronger interfaces are generally believed to optimize macroscopic properties.

Despite the relatively stronger interfaces of polymeric matrix composites, fiber bridging has been observed as a source of toughening even in these materials. Moreover, another phenomenon, which is analogous to fiber bridging, appears in polymeric matrix composites with growing delaminations. This is the phenomenon of fiber nesting, which takes place because of the fibers which cross adjacent layers due to compression during the manufacturing process (Russell and Street, 1988). As the delamination extends, these nested (bridged) fibers gradually become strained and subsequently divert some of the available strain energy away from the crack tip; therefore increasing the toughness.

The fiber bridging effect on the opening of macro-cracks in composites is analogous to the effect of discrete asperities in the obstruction to crack closure in metallic materials (Beevers et al., 1984; Carlson et al., 1991). However, the fiber bridging of delaminations in composites affects the loading phase (opening of the delamination) and hence it can influence both the monotonic and cyclic growth behavior, whereas the discrete asperities effect in metallic cracks affects the unloading phase (closing of the cracks) and hence this phenomenon influences primarily the cyclic growth behavior. In both cases, the result is a reduced growth rate. In the same context, it can be argued that just as the plastic crushing of discrete asperities can result in an acceleration of fatigue crack growth in metals following a compressive excursion (Kardomateas and Carlson, 1994), the fracture of fiber bridges can similarly result in an acceleration of crack growth in composites following a tensile overload in a cyclic load sequence. Furthermore, it should be noted that fatigue crack growth of metals in an inert atmosphere may,

Contributed by the Applied Mechanics Division of THE AMERICAN SOCIETY OF MECHANICAL ENGINEERS for publication in the ASME JOURNAL OF APPLIED MECHANICS.

Discussion on this paper should be addressed to the Technical Editor, Professor Lewis T. Wheeler, Department of Mechanical Engineering, University of Houston, Houston, TX 77204-4792, and will be accepted until four months after final publication of the paper itself in the ASME JOURNAL OF APPLIED MECHANICS.

Manuscript received by the ASME Applied Mechanics Division, May 16, 1994; final revision, Oct. 18, 1994. Associate Technical Editor: I. M. Daniel.

during unloading, result in a welding of asperities, which would produce an effect similar to the bridging phenomenon discussed here (Carlson and Beevers, 1992).

Several important contributions have appeared on the bridging problem, mainly in connection with ceramic matrix composites. Specifically, Budiansky and Amazigo (1989) examined the effect of fiber bridging on the Mode I stress intensity factor in a smeared fiber force model. Rubinstein and Xu (1992) also examined the effect of fiber bridging on the Mode I stress intensity factor by using a discrete fiber representation in an isotropic material and a linear fiber force-displacement relationship. Nemat-Nasser and Hori (1987) developed asymptotic solutions for fully or partially bridged cracks. A detailed treatment of the fiber debonding with friction was provided by Hutchinson and Jensen (1990).

In the present paper, a different approach is followed, based on discrete fibers at arbitrary orientations, with allowance for fiber breaking. The analysis allows evaluation for both Mode I and II stress intensity factors and is valid for a generally anisotropic material. Also, by incorporating the capability of treating individual fibers, it is possible to examine cases in which single fibers are either fractured or have interface failures which are very different from their adjacent neighbors; such studies would be analogous to examining the effect of imperfections in structural systems. Two cases are treated separately here: either the fiber-matrix interface remains intact or has failed. For the latter case, a general nonlinear fiber force-displacement relationship is proposed.

Formulation

Let us first define the basic geometric and material parameters that will be used in formulating the model. Consider a fiber at an angle ω and at a distance c from the tip of a macro-crack in a composite body of thickness t (Figs. 1(a), (b)). The length of the macro-crack is $2a$ and the fiber is at a distance b from the center. The presence of both externally applied forces and

crack face forces is illustrated in Fig. 1(a), whereas the details of the proposed model are indicated in Fig. 1(b). Only the upper crack face is shown with the fiber developing a force with components P and Q .

Let us consider a state of plane strain, i.e., $\epsilon_{zz} = \gamma_{yz} = \gamma_{xz} = 0$. In this case, the stress-strain relations for the orthotropic body are (Lekhnitskii, 1963):

$$\begin{bmatrix} \epsilon_{xx} \\ \epsilon_{yy} \\ \epsilon_{zz} \\ \gamma_{xy} \end{bmatrix} = \begin{bmatrix} \alpha_{11} & \alpha_{12} & \alpha_{13} & \alpha_{16} \\ \alpha_{12} & \alpha_{22} & \alpha_{23} & \alpha_{26} \\ \alpha_{13} & \alpha_{23} & \alpha_{33} & \alpha_{26} \\ \alpha_{16} & \alpha_{26} & \alpha_{36} & \alpha_{66} \end{bmatrix} \begin{bmatrix} \sigma_{xx} \\ \sigma_{yy} \\ \sigma_{zz} \\ \tau_{xy} \end{bmatrix}, \quad (1)$$

where α_{ij} are the compliance constants (we have used the notation $1 \equiv x, 2 \equiv y, 3 \equiv z$).

Using the condition of plane strain, which requires that $\epsilon_{zz} = 0$, allows elimination of σ_{zz} , i.e.,

$$\sigma_{zz} = -\frac{1}{\alpha_{33}} (\alpha_{13}\sigma_{xx} + \alpha_{23}\sigma_{yy}). \quad (2)$$

The Eq. (1) can then be written in the form

$$\begin{bmatrix} \epsilon_{xx} \\ \epsilon_{yy} \\ \gamma_{xy} \end{bmatrix} = \begin{bmatrix} \beta_{11} & \beta_{12} & \beta_{16} \\ \beta_{12} & \beta_{22} & \beta_{26} \\ \beta_{16} & \beta_{26} & \beta_{66} \end{bmatrix} \begin{bmatrix} \sigma_{xx} \\ \sigma_{yy} \\ \tau_{xy} \end{bmatrix}, \quad (3)$$

where

$$\beta_{ij} = \alpha_{ij} - \frac{\alpha_{13}\alpha_{j3}}{\alpha_{33}} \quad (i, j = 1, 2, 4, 5, 6). \quad (4)$$

Problems of this type can be formulated in terms of two complex analytic functions $\Phi_k(z_k)$ ($k = 1, 2$) of the complex variables $z_k = x + s_k y$, where s_k, \bar{s}_k , $k = 1, 2$ are the roots of the algebraic equation

$$\beta_{11}s^4 - 2\beta_{16}s^3 + (2\beta_{12} + \beta_{66})s^2 - 2\beta_{26}s + \beta_{22} = 0. \quad (5)$$

It was proven by Lekhnitskii (1963) that these roots $s_1, s_2, \bar{s}_1, \bar{s}_2$ are either complex or purely imaginary, i.e., Eq. (5) cannot have real roots.

Now we proceed to the problem of studying the effect of discrete loads on a crack face in an anisotropic material.

I Concentrated Equilibrating Forces on the Two Faces of a Macro-Crack in an Anisotropic Material. As has been discussed, following Lekhnitskii (1963), the plane-strain anisotropic elasticity problem can be reduced to that of determining the two complex potentials $\Phi_k(z_k)$ of two different complex variables, $z_k = x + s_k y$, $k = 1, 2$. Notice that if the complex potentials Φ_k are regarded as functions of the complex variables z_k , they must be determined not in the region S but in regions S_k , obtained from S by the affine transformation

$$x_k = x + \alpha_k y, \quad y_k = \beta_k y \quad (k = 1, 2), \quad (6)$$

where $s_k = \alpha_k + i\beta_k$.

For a crack of length $2a$ in the z -plane (Fig. 2), Sih and Liebowitz (1968) have shown that K_I and K_{II} can be evaluated directly from $\Phi_1(z_1)$ in the limit as $z_1 \rightarrow a$; i.e.,

$$K_I + \frac{K_{II}}{s_2} = 2\sqrt{2} \left(\frac{s_2 - s_1}{s_2} \right) \lim_{z_1 \rightarrow a} \sqrt{z_1 - a} \Phi_1'(z_1). \quad (7)$$

In many extensional problems the use of conformal mapping is an efficient method for obtaining the stress intensity factors.

Let the mapping function be defined (with the usual restrictions as to analyticity and single-valuedness) by

$$z = \omega(\zeta); \quad z_k = \omega_k(\zeta_k). \quad (8)$$

Essentially, we map all three regions S, S_1, S_2 onto the $\zeta = \xi + i\eta$ plane (Fig. 2). This mapping is effected so that one and the same point on the contour of the ζ -plane region will corre-

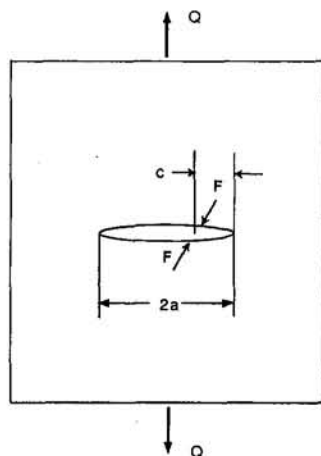


Fig. 1(a) External (global) and crack face (local) loading

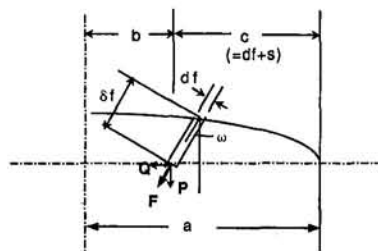


Fig. 1(b) A single fiber loading the upper crack face

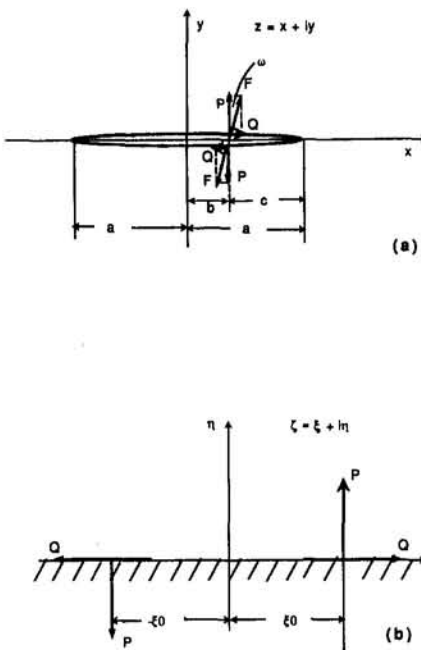


Fig. 2(a) The z -plane with the crack in an anisotropic body; (b) the transformed, ζ -plane

spond to the points on the contours of the regions S and S_k , which are related by the affine transformation (6).

Then

$$\Phi'_1(z_1) = \frac{d\Phi_1}{dz_1} \frac{d\zeta_1}{dz_1} = \frac{\Phi'_1(\zeta_1)}{\omega'_1(\zeta_1)}. \quad (9)$$

Now, corresponding to the crack tip $z = z_1 = a$ in the z -plane, there will be a point $\zeta = \zeta_c$ in the ζ -plane. Thus, Eq. (7) may be written

$$K_I + \frac{K_H}{s_2} = 2\sqrt{2} \left(\frac{s_2 - s_1}{s_2} \right) \lim_{\zeta_1 \rightarrow \zeta_c} [\omega_1(\zeta_1) - \omega_1(\zeta_c)]^{1/2} \frac{\Phi'_1(\zeta_1)}{\omega'_1(\zeta_1)}. \quad (10)$$

The above equation illustrates the fact that the stress intensity factors may be found simply from a knowledge of $\Phi'_1(z_1)$ in the vicinity of the crack tip, and that Φ_2 can be ignored if the stress intensity factors are the only desired result.

In the $z = x + iy$ plane, we have the region S in the form of an infinite plane with a crack (Fig. 2(a)), for which the equation is

$$x = a \cos \theta, -\pi < \theta < \pi; \quad y = 0. \quad (11a)$$

Since $z_k = x + s_k y$, the regions S_1 and S_2 are also planes with straight cutouts described by

$$x_k = x = a \cos \theta, -\pi < \theta < \pi; \quad y_k = y = 0, \quad (k = 1, 2). \quad (11b)$$

As has been already observed, we map all three regions S , S_1 , S_2 onto the lower half of the plane $\zeta = \xi + i\eta$. This mapping is effected so that to all three points on the contours of the regions S and S_k corresponds one and the same point on the real axis $\zeta = \xi$.

$$z = \omega(\zeta) = a \left(\frac{1 - \zeta^2}{1 + \zeta^2} \right); \quad z_k = \omega(\zeta_k). \quad (12a)$$

The functions reciprocal to the above, are

$$\zeta = \left(\frac{a - z}{a + z} \right)^{1/2}; \quad \zeta_k = \left(\frac{a - z_k}{a + z_k} \right)^{1/2}. \quad (12b)$$

Indeed, when x and y runs along the contour of the crack, taking on values $x = a \cos \theta$ and $y = 0$, then (12b) results in the values

$$\zeta = \zeta_k = \tan(\theta/2) \quad (k = 1, 2). \quad (13)$$

That is, a crack of length $2a$ in the z -plane is transformed to the entire real axis of the ζ -plane, and the infinite plane to the lower half of the ζ -plane. The crack tip $z = a$ is mapped onto the point $\zeta = 0$, and $z = -a$ is mapped onto the two infinite points on the real axis $\zeta = \pm\infty$. Therefore, the upper crack face on the z -plane is mapped onto the positive real semi-axis of the ζ -plane and the lower crack face is mapped onto the negative real semi-axis. Since one point z in the z -plane corresponds to the two points $\pm\zeta$ in the ζ -plane, a one-to-one, conformal transformation is established between the z -plane and the lower half of the ζ -plane.

For a generally anisotropic material, the function $\Phi'_1(\zeta_1)$ for two equilibrating concentrated loads on the half-plane, applied at $\zeta = \pm\zeta_0$, with components P (vertical) and Q (horizontal) is (Lekhnitskii, 1963)

$$\Phi'_1(\zeta_1) = \frac{Ps_2 + Q}{\pi i} \frac{1}{(s_1 - s_2)} \left[\frac{1}{(\zeta_0 - \zeta_1)} - \frac{1}{(-\zeta_0 - \zeta_1)} \right]. \quad (14)$$

Then, upon noting that

$$\lim_{\zeta_1 \rightarrow 0} [\omega(\zeta_1) - \omega(0)]^{1/2} \frac{1}{\omega'(\zeta_1)} = -\frac{i\sqrt{2}}{4\sqrt{a}},$$

and that

$$\lim_{\zeta_1 \rightarrow 0} \frac{1}{\zeta_0 - \zeta_1} = \frac{1}{\zeta_0} = \left(\frac{a + z_0}{a - z_0} \right)^{1/2},$$

and using (10) and (14), since $z_0 = b$, we obtain for a generally anisotropic body (at the right end of the crack):

$$K_I + \frac{K_H}{s_2} = \frac{Ps_2 + Q}{\pi s_2 \sqrt{a}} \left(\frac{a + b}{a - b} \right)^{1/2}, \quad (15a)$$

so that the stress intensity factors are given directly as

$$K_I = \frac{P}{\pi \sqrt{a}} \left(\frac{a + b}{a - b} \right)^{1/2}; \quad K_H = \frac{Q}{\pi \sqrt{a}} \left(\frac{a + b}{a - b} \right)^{1/2}. \quad (15b)$$

Hence, the relations (15) give the stress intensity factors for an anisotropic infinite sheet with a crack along the x -axis of length $2a$, centered at the origin, and having two equilibrating forces at $x = b$, one on the upper crack face and the other on the lower crack face, with y -component, P , and x -component, Q (per unit thickness).

Notice that since the loads on the crack faces are self-equilibrating, the stress intensity factors do not depend on the material constants. This observation has also been made by Sih et al. (1965); moreover, in analyzing plane center-crack problems, Sih et al. (1965) were able to conclude that "for problems involving self-equilibrating loads (on each boundary) the stress intensity factors for both the isotropic and the anisotropic materials are identical." Only if these loads are not self-equilibrating on each boundary, do the stress intensity factors depend on the elastic constants. A similar statement has been made in connection with the stress distribution in multiply connected bodies by Timoshenko and Goodier (1970). Specifically, they concluded that "the stress

distribution is independent of the elastic constants of the material if the resultant of the forces applied to each boundary are zero. The moment of these forces need not be zero.' Notice that this conclusion is of practical importance in the experimental determination of the stress distribution for any material by simply applying the optical methods on a transparent material.

Sih et al. (1965) treated the problem of a single, unbalanced, vertical force, P , on the upper crack face by using a mapping function that transforms the crack in the z -plane into a circular hole of unit radius in the ζ -plane. Since the force was unbalanced, their stress intensity factors included the material constants; however, if an equilibrating force on the lower crack face is included, then their formulas would reduce to the stress intensity factors (15), independent of the elastic constants.

Although the stress intensities are decoupled and independent of the elastic constants, the displacement relationships are not, as will be shown in the next section which considers the development of the fiber-bridging model. The basic configuration of an anisotropic infinite body loaded with remote normal stress σ_0 and in-plane shear τ_0 would also exhibit this feature of decoupled and independent of the elastic constants stress intensities, with $K_I = \sigma_0\sqrt{a}$ and $K_H = \tau_0\sqrt{a}$, but the displacements would be coupled (Sih and Chen, 1981).

Hence, it is re-emphasized that since during fiber bridging the loads on the crack faces are self-equilibrating, the stress intensity factors do not depend on the elastic constants for either the isotropic or the anisotropic material assumption.

Next, we shall use these relations in the development of the fiber bridging model.

II Development of the Fiber-Bridging Model. In terms of the stress intensity factors K_I and K_H , Sih and Liebowitz (1968) give relations for the displacement field as

$$u_x(r, \theta) = \sqrt{2r} \operatorname{Re} \left\{ \frac{1}{s_1 - s_2} [(K_I s_1 + K_H) p_2 \sqrt{\cos \theta + s_2 \sin \theta} - (K_I s_2 + K_H) p_1 \sqrt{\cos \theta + s_1 \sin \theta}] \right\}, \quad (16a)$$

$$u_y(r, \theta) = \sqrt{2r} \operatorname{Re} \left\{ \frac{1}{s_1 - s_2} [(K_I s_1 + K_H) q_2 \sqrt{\cos \theta + s_2 \sin \theta} - (K_I s_2 + K_H) q_1 \sqrt{\cos \theta + s_1 \sin \theta}] \right\}, \quad (16b)$$

where

$$p_k = \beta_{11} s_k^2 + \beta_{12} - \beta_{16} s_k; \quad q_k = \beta_{12} s_k + \frac{\beta_{22}}{s_k} - \beta_{26}, \quad k = 1, 2. \quad (16c)$$

At a distance c behind the crack tip, i.e., at $\theta = \pi$ and $r = c$, the displacements become

$$u_x = \sqrt{2c} \operatorname{Im} \left\{ \frac{1}{s_2 - s_1} [K_I(s_1 p_2 - s_2 p_1) + K_H(p_2 - p_1)] \right\}, \quad (17a)$$

$$u_y = \sqrt{2c} \operatorname{Im} \left\{ \frac{1}{s_2 - s_1} [K_I(s_1 q_2 - s_2 q_1) + K_H(q_2 - q_1)] \right\}. \quad (17b)$$

The displacements at the lower crack face, i.e., at $\theta = -\pi$, are of opposite sign.

Notice that even if a pure Mode I state of loading exists, i.e., $K_H = 0$, both normal and shear components of the displacement field u_y and u_x , respectively, are nonzero for general anisotropy. This means that the final orientations of the bridging fibers, ω_i ,

may be slightly different than the initial fiber orientations. They will be determined in the process of fiber loading, and are, therefore, unknowns to be determined.

It should also be mentioned that the length of the fiber bridging zone is assumed to be small compared to the crack length, and confined near the tip of the crack. Therefore, the displacement relations are expected to be adequate near the crack tip for the problem under consideration. In practical cases, at moderate distances from the crack tip, the fibers would actually be expected to be broken, anyway. A more accurate solution for the displacement field, valid at large distances away from the crack tip would certainly be desirable; however, it is not available at present and our future plans include exploring the theoretical aspects of obtaining a more accurate displacement field for an anisotropic crack. This would then be directly incorporated into our fiber bridging model. Future research could also include detailed finite element analyses. Please note that the same assumptions regarding the displacement field, namely use of the asymptotic near-tip formula, have been adopted in past work of other researchers, such as the discrete asperities model in metals of Beevers et al. (1984). The discrete asperities model has been applied to the closure obstruction problem, and it has been found that the features of the model can be used to correlate experimental measurements of opening stress intensity factors after tensile overloads (Carlson et al., 1991).

Now, let us represent the Mode I and Mode II contribution of the global, external load by $K_{I,GL}$ and $K_{II,GL}$, respectively. By superposition, the total stress intensity factor is

$$K_{I,II} = K_{I,II,\text{local}} + K_{I,II,GL}. \quad (18)$$

Displacement conditions at the fiber sites are needed to determine the fiber loads. The displacements at the upper macro-crack face, i.e., at $\theta = \pi$ and an arbitrary r , due to both local and global loading, is

$$u_{x,y}(r, \pi) = u_{x,y,GL} + u_{x,y,\text{local}}. \quad (19)$$

Moreover, if $c = a - b$ represents the initial distance of the fiber load point from the crack tip, this distance on the upper crack face is $c - \delta_f \sin \omega$, and the corresponding distance on the lower crack face is $c + \delta_f \sin \omega$, due to the fiber orientation at an angle ω as shown in Fig. 1(b). The quantity δ_f represents half of the final fiber interference length and will be discussed in detail in the following. Hence, including the effect of loading both the upper and lower faces of the macro-crack, and using the stress intensity factors for the global and the local load from (15), we can write the x -component of the displacement difference between the upper, $\theta = \pi$, and lower, $\theta = -\pi$, face of the macro-crack at the fiber site, $r = c$, as follows:

$$\begin{aligned} u_x(c, \pi) = & 2\sqrt{2c} \operatorname{Im} \left\{ \frac{1}{s_2 - s_1} [K_{I,GL}(s_1 p_2 - s_2 p_1) \right. \\ & \left. + K_{II,GL}(p_2 - p_1)] \right\} \\ & + 2\sqrt{2c} \left[\left(\frac{2a - c + \delta_f \sin \omega}{c - \delta_f \sin \omega} \right)^{1/2} \right. \\ & \left. + \left(\frac{2a - c - \delta_f \sin \omega}{c + \delta_f \sin \omega} \right)^{1/2} \right] \\ & \times \operatorname{Im} \left\{ \frac{1}{s_2 - s_1} \left[\frac{F \cos \omega}{2\pi\sqrt{a}} (s_1 p_2 - s_2 p_1) \right. \right. \\ & \left. \left. + \frac{F \sin \omega}{2\pi\sqrt{a}} (p_2 - p_1) \right] \right\}, \quad (20a) \end{aligned}$$

and the y -component of the displacement spread (opening) as

$$\begin{aligned}
 u_y(c, \pi) = & 2\sqrt{2c} \operatorname{Im} \left\{ \frac{1}{s_2 - s_1} [K_{I,GL}(s_1 q_2 - s_2 q_1) \right. \\
 & + K_{II,GL}(q_2 - q_1)] \left. \right\} \\
 & + 2\sqrt{2c} \left[\left(\frac{2a - c + \delta_f \sin \omega}{c - \delta_f \sin \omega} \right)^{1/2} \right. \\
 & + \left(\frac{2a - c - \delta_f \sin \omega}{c + \delta_f \sin \omega} \right)^{1/2} \left. \right] \\
 & \times \operatorname{Im} \left\{ \frac{1}{s_2 - s_1} \left[\frac{F \cos \omega}{2\pi\sqrt{a}} (s_1 q_2 - s_2 q_1) \right. \right. \\
 & \left. \left. + \frac{F \sin \omega}{2\pi\sqrt{a}} (q_2 - q_1) \right] \right\}. \quad (20b)
 \end{aligned}$$

Two separate cases of fiber bridging configurations are distinguished now.

(a) *Fiber-Matrix Interface Intact*. In this case, which is schematically shown in Fig. 3, the displacement at the fiber site is zero. The fiber is elastically stretched with a force F , therefore the fiber stress is

$$\sigma = \frac{4F}{\pi d_f^2}; \quad \sigma < \sigma_{uf}, \quad (21a)$$

where d_f is the fiber diameter. A condition of the fiber stress being below the fiber ultimate strength σ_{uf} is imposed for validity of this model.

The condition of zero displacement at the fiber site gives

$$u_x(c, \pm \pi) = u_y(c, \pm \pi) = 0. \quad (21b)$$

Taking into account (15b), (17), and (18), it is concluded that the foregoing two equations, (21b), are two linear equations in P and Q . Notice that in this case the fiber can sustain both tensile and shear stresses; the force along the fiber axis is $F = P \cos \omega + Q \sin \omega$.

In this case of an intact fiber-matrix interface, we have very effective ligament bridging. However, it is more reasonable, common, and an experimentally supported fact, that the fiber does not remain perfectly bonded to the matrix and fiber debonding occurs to some extent. This case is examined next.

(b) *Partial Fiber-Matrix Interface Debonding*. In this case, which is schematically shown in Fig. 1(b), the displacement at the fiber site is nonzero. The characterization of frictional sliding of a fiber embedded in a matrix is an issue of intense current interest. To this extent, Hutchinson and Jensen

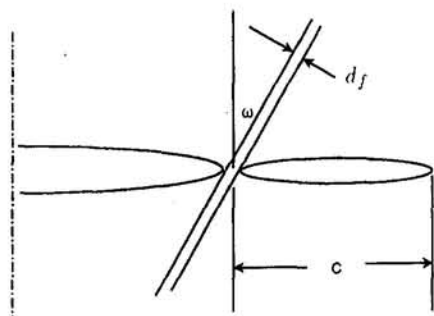


Fig. 3 The case of fiber-matrix interface intact (ligament-bridging)

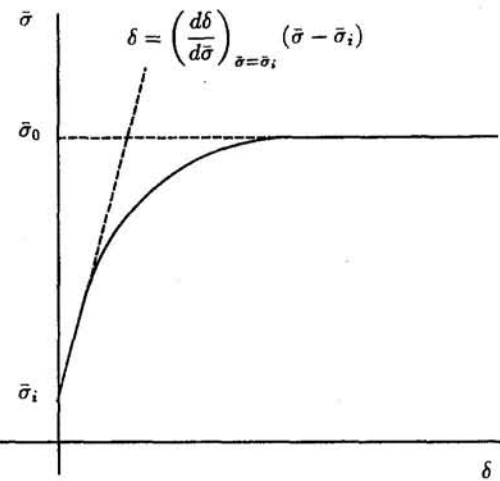


Fig. 4 Schematic of the fiber stress, σ , versus displacement, δ , curve

(1990) have developed a model that describes the interactions between components of a unidirectionally reinforced composite which is subject to debonding. The model is designed to include the effects of fiber strength, interface bond strength, and the friction force which can develop if residual compressive stresses act across the interface boundary.

The form of the fiber stress, σ , versus the pullout displacement, δ , curve with Coulomb friction is qualitatively illustrated in Fig. 4. The fiber stress versus the debond length, l , is similar in form. As shown, the debond length and pullout displacement are zero until a threshold value of stress, σ_i , is achieved. Above this value, the curves have decreasing slopes until a limiting, unstable value of stress, σ_0 , is attained. Note that if the fiber strength, σ_c , is less than σ_0 , the value of σ can abruptly decrease and then continuously decrease with increasing δ .

In the following, a_i , b_i , and \tilde{c}_i are constants that depend on the overall modulus of the composite and the elastic properties of the fibers and the matrix, and they are given in the Appendix of Hutchinson and Jensen (1990). An expression for the debond length, l , is given in terms of the coefficient of friction, μ , and the area fraction of the fiber, $\rho = [d_f/(d_f + s)]^2$, as follows

$$l = \frac{d_f}{4\mu b_1} \ln \left[\frac{\sigma_0 - \sigma_i + k_1(\sigma_i - \sigma)}{\sigma_0 - \sigma} \right], \quad (22a)$$

where

$$k_1 = \rho(1 - \rho)^{-1} a_3 \tilde{c}_3 / b_1. \quad (22b)$$

When the fiber is isotropic with $\nu_f = \nu_m$, then $a_3 = 0$ and thus $k_1 = 0$.

Moreover, the pullout displacement, δ , is given by Hutchinson and Jensen (1990) in terms of the modulus of the matrix, E_m , and the mode II toughness for the debond crack, measured by the critical value of the energy release rate, G_c :

$$\begin{aligned}
 \delta = & (b_2 + b_3) \left\{ \frac{1 - \rho}{\rho} \frac{l}{\tilde{c}_1 \tilde{c}_3} \left(\frac{2G_c}{E_m d_f} \right)^{1/2} \right. \\
 & \left. - \frac{d_f \sigma_r^-}{4\mu b_1^2 E_m} [e^{-\zeta_i} + \zeta_i - 1] \right\}, \quad (22c)
 \end{aligned}$$

where $\zeta_i = 4\mu b_1 l / d_f$ and σ_r^- is the normal stress acting across the interface just below the debond tip. For debonding with Coulomb friction,

$$\sigma_r^- = -\rho^{-1}(1 - \rho)(b_1 / \tilde{c}_3)[\sigma_0 - \sigma_i + k_1(\sigma_0 - \sigma)]. \quad (22d)$$

The previous expressions are nonlinear relations for the fiber displacement versus fiber stress law, $\delta = F(\sigma)$. Although it

seems that a nonlinear fiber load-displacement relationship would provide a more complete description of the fiber debonding process and better account for the relative sliding between the fiber and the matrix, the need for analytically tracking the problem easily has led to the use of a linear relationship between displacement and fiber load (e.g., Rubinstein and Xu, 1992). It is also easier to illustrate the use of our fiber bridging model by using a linear law.

For this purpose, a linear fiber displacement versus fiber stress law is adopted by using the initial, almost linear segment the curve in Fig. 4, as follows:

$$\delta = \left(\frac{d\delta}{d\sigma} \right)_{\sigma=\sigma_i} (\sigma - \sigma_i); \quad l = \left(\frac{dl}{d\sigma} \right)_{\sigma=\sigma_i} (\sigma - \sigma_i). \quad (23a)$$

Such an approximation should be adequate as long as we are not very close to the saturation stress, σ_0 .

The resulting expressions are much simpler if we assume that the fiber is isotropic with $\nu_f = \nu_m$ (in which case $k_1 = 0$). Under this assumption, we obtain from (22a, c) and (23a)

$$\delta = (b_2 + b_3) \frac{1 - \rho}{\rho \tilde{c}_1 \tilde{c}_3} \left(\frac{2G_c}{E_m d_f} \right)^{1/2} \frac{d_f}{4\mu b_1 (\sigma_0 - \sigma_i)} (\sigma - \sigma_i);$$

for $\sigma_i < \sigma < \sigma_0$. $(23b)$

The initiation stress σ_i is the stress required to propagate the debond crack up the fiber and is given in terms of the axial mismatch strain ϵ_z^T by

$$\frac{\sigma_i}{E_m \epsilon_z^T} = \frac{1}{\tilde{c}_1} \left(\frac{2G_c}{E_m d_f \epsilon_z^T} \right)^{1/2} - \frac{\tilde{c}_2}{\tilde{c}_1} \quad (23c)$$

In turn, the saturation stress σ_0 is given in terms of the radial mismatch strain ϵ_r^T , by

$$\sigma_0 = \rho E_f \epsilon_r^T / \nu_f. \quad (23d)$$

The initiation stress can be negative if the nondimensional combination $2G_c/(E_f \epsilon_r^T)$ is sufficiently small; in such cases, a finite length debond zone would be introduced before any overall stress is applied. In the interest of simplicity, let us take $\sigma_i = 0$ (the case of nonzero σ_i will be examined in a future publication). Furthermore, since we assume that there is a uniform distribution of fibers with spacing s and diameter d_f through the thickness, there are $1/(d_f + s)$ fibers per unit thickness, and the effective area per unit thickness is $A_f = \pi d_f^2/4(d_f + s)$. Then, (23b) gives the fiber displacement $\delta_f = \delta$ in terms of the fiber force $F_i = \sigma A_f$, in the form

$$\delta_f = -\tilde{\lambda} \frac{4F_i(d_f + s)}{\pi E_f d_f}, \quad (24a)$$

where now $\tilde{\lambda}$ is dimensionless and can be considered as a measure of the fiber-matrix friction

$$\tilde{\lambda} = (b_2 + b_3) \frac{1 - \rho}{\rho \tilde{c}_1 \tilde{c}_3} \left(\frac{2G_c}{E_m d_f} \right)^{1/2} \frac{E_f}{4\mu b_1 \sigma_0}. \quad (24b)$$

The minus sign is used because the fiber is under tension loading when the crack face is loaded with a force opposite to the one in Fig. 2(a); the force in Fig. 2(a) would generate the local stress intensity factors given by (15).

In the previous relations, d_f is the fiber diameter and s is the mean spacing between the fibers. In a representation of the form (24a), the quantity $\tilde{\lambda}$ increases for poorer bond quality that allows more fiber sliding. This quantity can vary widely depending on the class of composites under consideration. Specifically, brittle (ceramic)-matrix composites are characterized by relatively weak interfaces, in contrast to the case of the more

common polymeric-matrix composites or the ductile metal-matrix composites, in which relatively strong interfaces generally exist.

Since $2\delta_f$ is the final interference fiber height, the conditions for determining the forces P and Q are the displacements at the fiber site

$$\begin{aligned} u_x(c, \pi) - u_x(c, -\pi) &= 2\delta_f \sin \omega, \\ u_y(c, \pi) - u_y(c, -\pi) &= 2\delta_f \cos \omega. \end{aligned} \quad (25)$$

III Multiple Fiber Bridging. The single fiber analysis has been used thus far because a clear definition of the working quantities was needed. In actual fiber-bridging situations, multiple fibers are connecting the two faces of the macro-crack. Based on the single fiber analysis, an extension to multiple fibers can be directly performed. An interesting observation in connection with the multiple fiber bridging problem is that the load redistribution, which occurs among fiber bridges, as the load increases (or the crack propagates) and some fibers break in the process, is analogous to the redistribution of stresses which occurs due to the development of a crack-tip plastic zone in metallic materials. On another note, it can be observed that a similar redistribution occurs in the shear lag mechanism of load transfer in composites.

If n fibers at final angles ω_i and at distances c_i behind the tip (and b_i from the center) are bridging the faces of the macro-crack, then the first set of conditions for determining the forces P_i and Q_i are the displacement components equations at each of the fiber sites (Fig. 5). A direct extension of Eqs. (20), and using (25), gives the first equation from the x -component of the displacement spread between the upper and lower crack faces as

$$\begin{aligned} \delta_{fi} \sin \omega_i &= \sqrt{2c_i} \operatorname{Im} \left\{ \frac{1}{s_2 - s_1} [K_{I,GL}(s_1 p_2 - s_2 p_1) \right. \\ &\quad \left. + K_{II,GL}(p_2 - p_1)] \right\} \\ &\quad + \sqrt{2c_i} \sum_{j=1}^n \left[\left(\frac{2a - c_j + \delta_{fj} \sin \omega_j}{c_j - \delta_{fj} \sin \omega_j} \right)^{1/2} \right. \\ &\quad \left. + \left(\frac{2a - c_j - \delta_{fj} \sin \omega_j}{c_j + \delta_{fj} \sin \omega_j} \right)^{1/2} \right] \\ &\quad \times \operatorname{Im} \left\{ \frac{1}{s_2 - s_1} \left[\frac{F_j \cos \omega_j}{2\pi\sqrt{a}} (s_1 p_2 - s_2 p_1) \right. \right. \\ &\quad \left. \left. + \frac{F_j \sin \omega_j}{2\pi\sqrt{a}} (p_2 - p_1) \right] \right\}, \quad i = 1, \dots, n \quad (26a) \end{aligned}$$

The condition from the y -component of the displacement spread is

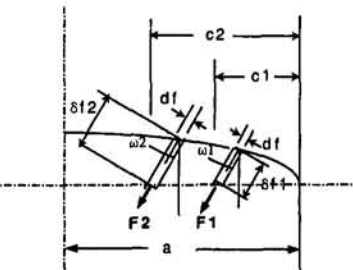


Fig. 5 Loading of multiple fibers on the upper face of the macro-crack

$$\begin{aligned}
\delta_{fi} \cos \omega_i &= \sqrt{2c_i} \operatorname{Im} \left\{ \frac{1}{s_2 - s_1} [K_{I,GL}(s_1 q_2 - s_2 q_1) \right. \\
&\quad \left. + K_{II,GL}(q_2 - q_1)] \right\} \\
&\quad + \sqrt{2c_i} \sum_{j=1}^n \left[\left(\frac{2a - c_j + \delta_{fj} \sin \omega_j}{c_j - \delta_{fj} \sin \omega_j} \right)^{1/2} \right. \\
&\quad \left. + \left(\frac{2a - c_j - \delta_{fj} \sin \omega_j}{c_j + \delta_{fj} \sin \omega_j} \right)^{1/2} \right] \\
&\quad \times \operatorname{Im} \left\{ \frac{1}{s_2 - s_1} \left[\frac{F_j \cos \omega_j}{2\pi\sqrt{a}} (s_1 q_2 - s_2 q_1) \right. \right. \\
&\quad \left. \left. + \frac{F_j \sin \omega_j}{2\pi\sqrt{a}} (q_2 - q_1) \right] \right\}, \quad i = 1, \dots, n. \quad (26b)
\end{aligned}$$

The second set of conditions is the fiber load-displacement equations, either (22) for a nonlinear law or (23), (24) for a linear law.

The quantities to be determined are the final fiber interference heights δ_{fi} and the fiber loads F_i as well as the fiber orientations ω_i ; hence there are $3n$ unknowns. For each fiber there are two displacement equations, (26a, b), and one "fiber constitutive," equation; hence we have a total of $3n$ equations. Therefore, a well-posed problem has been formulated. The only complication arises from the fact that the system of equations is non-linear.

The problem becomes linear, however, in the more common problem of a transverse crack in a zero-degree unidirectional orthotropic composite under pure Mode I loading, if the linear fiber load-displacement Eq. (24a) is used (Fig. 6). Due to symmetry, $\omega_i = 0$, and the x -displacements are zero and the corresponding relations (26a) are automatically satisfied (because the quantities in the brackets turn out to be real). Furthermore, δ_{fi} can be directly expressed in terms of F_i from the linear fiber load-displacement law. This leaves us with the n fiber loads, F_i , to be determined from the n linear equations from the normal, u_y , displacement relations at the fiber sites, (26b). The number of loaded fibers, n , is determined by imposing the condition of the fiber loads being below the fiber strength, i.e.:

$$-\frac{4F_i(d_f + s)}{\pi d_f^2} < \sigma_{uf}, \quad i = 1, \dots, n. \quad (27)$$

Hence, n is increased successively, until a state is reached where the n th fiber is under load exceeding the fracture strength.

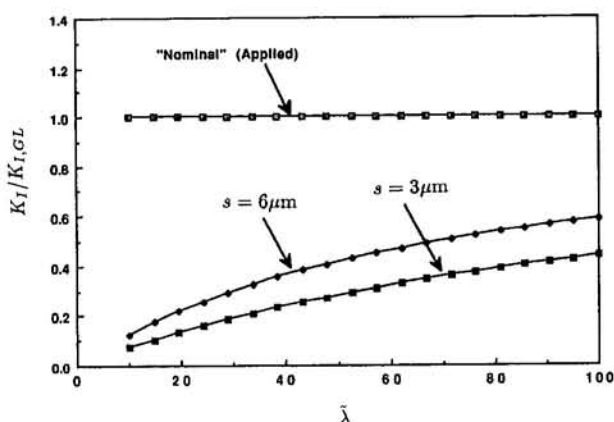


Fig. 6 The "effective" stress intensity factor, K_I , as a function of λ , which expresses the interface friction. Two values of fiber spacing, s , are considered. $K_{I,GL}$ is the nominal (applied) stress intensity factor.

In the general case of an arbitrary fiber orientation, under combined Mode I and II loading with the linear fiber load-displacement relation, again δ_{fi} can be directly expressed in terms of F_i . Furthermore, an initial guess for the final fiber orientations is the initial fiber orientations of the parent composite, ω_i^0 . This leaves us with the n fiber loads, F_i , to be determined from the n linear equations for the normal, u_y , displacements at the fiber sites. An iteration procedure can be employed to find the final orientations of the bridging fibers, ω_i , by satisfying the x -displacement equations. Since a neighborhood of the roots is identified, standard numerical techniques such as the Newton-Raphson, generalized to multiple dimensions, can be used (Press et al., 1989).

Once the fiber loads, F_i , and the fiber interference lengths, δ_{fi} , and orientations, ω_i , are determined, the local stress intensity factors can be found by using (15b), as follows:

$$\begin{aligned}
K_{I,local} &= \sum_{j=1}^n \frac{F_j \cos \omega_j}{2\pi\sqrt{a}} \left[\left(\frac{2a - c_j + \delta_{fj} \sin \omega_j}{c_j - \delta_{fj} \sin \omega_j} \right)^{1/2} \right. \\
&\quad \left. + \left(\frac{2a - c_j - \delta_{fj} \sin \omega_j}{c_j + \delta_{fj} \sin \omega_j} \right)^{1/2} \right], \quad (28a)
\end{aligned}$$

$$\begin{aligned}
K_{II,local} &= \sum_{j=1}^n \frac{F_j \sin \omega_j}{2\pi\sqrt{a}} \left[\left(\frac{2a - c_j + \delta_{fj} \sin \omega_j}{c_j - \delta_{fj} \sin \omega_j} \right)^{1/2} \right. \\
&\quad \left. + \left(\frac{2a - c_j - \delta_{fj} \sin \omega_j}{c_j + \delta_{fj} \sin \omega_j} \right)^{1/2} \right]. \quad (28b)
\end{aligned}$$

Application of the Model

The model described in the previous section has been used to analyze the effect of fiber bridging on a transverse crack in a unidirectional orthotropic plate. The linear fiber load-displacement law, Eq. 24(a), is used. It will be shown that the effect of fiber spacing and the fiber-matrix interface friction can be quantified in this model. Moreover, the response due to increasing magnitudes of tensile loads that may include partial or full fracture of the bridging zone will be investigated.

The composite system considered is a glass/epoxy with glass fibers of diameter $d_f = 11 \mu\text{m}$. Two values of spacing are considered: one with a fiber spacing of $s = 6 \mu\text{m}$ and a more closely spaced system, $s = 3 \mu\text{m}$. Notice that the fibers are at distances from the crack tip $c_j = (d_f + s)j$, $j = 1, \dots, n$. For square spacing, this would give fiber volume fractions of $V_f = 0.329$ and $V_f = 0.485$, respectively, according to the formula (e.g., Hull, 1981):

$$V_f = \frac{\pi}{4} \left(\frac{s}{d_f} + 1 \right)^{-2}.$$

The glass fibers have a modulus $E_f = 72.5 \text{ GPa}$ and an ultimate strength of $\sigma_{uf} = 3.5 \text{ GPa}$. The epoxy matrix is assumed to have a shear modulus of $G_m = 1.35 \text{ GPa}$.

The moduli in GN/m^2 and Poisson's ratios used are listed below, where 1 is the horizontal (x) direction, 2 is the vertical (y), and 3 the direction through the thickness (z).

(a) Spacing of $s = 6 \mu\text{m}$: $E_1 = E_3 = 5.1$, $E_2 = 26.2$, $G_{12} = G_{23} = 2.1$, $G_{31} = 1.9$, $\nu_{12} = 0.068$, $\nu_{23} = 0.277$, $\nu_{31} = 0.400$. The characteristic Eq. (5) gives purely imaginary roots:

$$s_1 = 0.297i, \quad s_2 = 1.609i.$$

Furthermore, Eq. (16c) gives real p_k and purely imaginary q_k .

(b) Spacing of $s = 3 \mu\text{m}$: $E_1 = E_3 = 6.5$, $E_2 = 37$, $G_{12} = G_{23} = 2.6$, $G_{31} = 2.4$, Poisson's ratios are the same as in system (a). For this material, the characteristic Eq. (5) gives again purely imaginary roots:

$$s_1 = 0.277i; \quad s_2 = 1.641i.$$

Furthermore, Eq. (16c) gives again real p_k and purely imaginary q_k .

In either a center-cracked specimen with a crack of length $2a$ or a single-edge crack specimen with a crack of length a under a remotely applied normal stress σ_0 , the stress intensity factor is the same as for an isotropic body (e.g., Sih and Chen, 1981):

$$K_{I,GL}(\sigma_0) = \sigma_0 \sqrt{a}; \quad K_{II,GL} = 0. \quad (29)$$

A crack length of $a = 10$ mm and a remotely applied stress corresponding to the typical value of fracture toughness of the epoxy matrix are assumed, i.e., $K_{I,GL} = 1.25 \text{ MN/m}^{3/2}$. The remotely applied stress, $\sigma_0 = 12.5 \text{ MPa}$, and the crack length are also the same as the ones used in the experiments of Botsis and Shafiq (1992) and Botsis and Beldica (1994). Furthermore, a fiber bridging zone of $120 \mu\text{m}$ behind the crack tip is assumed. For the spacing of $s = 6 \mu\text{m}$, a total of 20 fibers would span this distance, whereas for the spacing of $s = 3 \mu\text{m}$, there would be a total of 40 fibers in the bridging zone.

For the unidirectional case, $\omega = 0$, the local stress intensity factors are given by using (28), as follows:

$$K_{I,\text{local}} = \sum_{j=1}^n \frac{F_j}{\pi \sqrt{a}} \left(2 - \frac{c_j}{a} \right)^{1/2}; \quad K_{II,\text{local}} = 0. \quad (30)$$

Although the stress intensity factor $K_{I,GL}$ is applied and constitutes the nominal quantity indicative of the amount of crack tip loading, an "effective" stress intensity factor $K_I = K_{I,GL} + K_{I,\text{local}}$, due to the effect of fiber bridging, actually exists at the crack tip. This depends strongly of the properties of fiber-matrix interface, as is clearly seen in Fig. 6, which shows $K_I/K_{I,GL}$ as a function of the parameter $\tilde{\lambda}$, which expresses the interface friction. For a larger value of $\tilde{\lambda}$, i.e., more fiber debonding, the effective stress intensity factor is smaller.

The two curves represent the two cases of fiber spacing considered, and it is again clear that the more widely spaced fibers show a larger effective stress intensity factor than the more closely spaced system. This agrees very nicely with the experimental observation of Botsis and Shafiq (1992) that the more closely spaced system is tougher than the more widely spaced one. Specifically, for $\tilde{\lambda} = 20$, the effective K_I for $s = 6 \mu\text{m}$ is 21 percent of the nominal value, whereas for the more closely spaced $s = 3 \mu\text{m}$ system, the effective K_I is only 13 percent of the nominal value. For a weaker fiber-matrix interface bond, $\tilde{\lambda} = 100$, the effective K_I for $s = 6 \mu\text{m}$ is 59 percent of the nominal value, and, by comparison, for the more closely spaced $s = 3 \mu\text{m}$ system, the effective K_I is smaller, i.e., 44 percent of the nominal value.

In either case, the fiber stress was below the ultimate fracture stress σ_{uf} of the glass fiber, for the entire range of $\tilde{\lambda}$'s considered; this indicates that for this example only fiber debonding and no fiber fracture would occur. Botsis and Shafiq (1992) and Botsis and Beldica (1994) considered the same geometrical configuration and the same level of applied stress but in a more widely spaced glass fiber system and a larger fiber diameter. Substituting for their fiber spacing and fiber diameter, the present model would also predict fiber stresses in the bridging zone below the ultimate fracture strength of the glass fibers, and this would again agree with their experimental results, in which no fiber fracture was observed. Hence, fiber bridging can reduce significantly the stress intensity factor and hence "toughen" the material, but this depends strongly on the fiber-matrix interface and the fiber spacing. The model presented in this paper allows quantifying this important qualitative observation.

It is conceivable that an increasing remotely applied stress σ_0 would lead to fracture of either some of the most remote from the crack tip fibers, or of the entire fiber bridging zone.

Table 1 Fracture of fiber bridges

$\tilde{\lambda}^*$	$\sigma_0/\sigma_0^\dagger$	n_f^\ddagger
10.0	8.68	0
30.0	10.79	3
40.0	12.11	6
50.0	13.16	9
60.0	14.21	13
90.0	17.63	16
100.0	18.68	17

* From Eq. (24b).

† σ_0 is the applied stress corresponding to the fracture toughness of the epoxy matrix; σ_0^\dagger is the applied stress that causes fracture of at least one of the fiber bridges.

‡ Number of fiber bridges left (out of initially 20).

This was found to depend strongly on the fiber-matrix interface parameter, $\tilde{\lambda}$, as shown in Table 1. In this table, the value of the applied stress, σ_0 , that first causes fracture of the fiber bridges is calculated for the entire range of $\tilde{\lambda}$'s considered, along with the number of fiber bridges left, n_f . The case of fiber spacing $s = 6 \mu\text{m}$ is considered. The fiber bridging zone behind the crack tip consists of initially 20 fibers. It can be seen that for strong fiber-matrix interfaces, i.e., low values of $\tilde{\lambda}$, the entire fiber bridging zone breaks and no fiber bridges are left, i.e., $n_f = 0$. Notice that this implies some kind of unstable process since in this case of low $\tilde{\lambda}$, the maximum stress carried by a bridging zone with a smaller number of fibers is higher than the corresponding one with the load distributed on a larger number of fibers. However, for relatively weak fiber-matrix interfaces, that is high values of $\tilde{\lambda}$, only some of the most remote fibers break and as a result, a fiber bridging zone is still left. The applied stress that causes fracture of fiber bridges naturally increases with weaker fiber-matrix interfaces, i.e., higher values of $\tilde{\lambda}$.

Acknowledgment

The financial support of the Office of Naval Research, Mechanics Division, Grant N00014-91-J-1892, and the interest and encouragement of the Grant Monitor, Dr. Y. Rajapakse, are both gratefully acknowledged.

References

- Beevers, C. J., Carlson, R. L., Bell, K., and Starke, E. A., 1984, "A Model for Fatigue Crack Closure," *Engineering Fracture Mechanics*, Vol. 19, pp. 93-100.
- Botsis, J., and Shafiq, A. B., 1992, "Crack Growth Characteristics of an Epoxy Reinforced with Long Aligned Glass Fibers," *International Journal of Fracture*, Vol. 58, No. 1, pp. R3-R10.
- Botsis, J., and Beldica, C., 1994, "Strength Characteristics and Fatigue Crack Growth in a Composite with Long Aligned Fibers," *International Journal of Fracture*, Vol. 69, pp. 27-50.
- Budiansky, B., and Amazigo, J. C., 1989, "Toughening by Aligned, Frictionally Constrained Fibers," *Journal of the Mechanics and Physics of Solids*, Vol. 37, pp. 93-109.
- Carlson, R. L., and Beevers, C. J., 1992, "Effects of Overloads and Mixed Modes on Closure," *Conference on Theoretical Concepts and Numerical Analysis of Fatigue* A. Blom and C. J. Beevers, eds., University of Birmingham, UK, Engineering Materials Advisory Services Ltd., Warley, UK, pp. 277-297.
- Carlson, R. L., Kardomateas, G. A., and Bates, P. R., 1991, "The Effects of Overloads in Fatigue Crack Growth," *International Journal of Fatigue*, pp. 453-460.
- Cox, B. N., James, M. R., Marshall, D. B., Morris, W. L., Rhodes, C. G., and Shaw, M., 1989, "Mechanics of Failure in Titanium Aluminide Composites," *Proceedings, 10th International SAMPE Conference*, Birmingham, UK, S. Benson et al., eds., Elsevier, Holland.
- Hull, D., 1981, "An Introduction to Composite Materials," *Cambridge Solid State Science Series*, Cambridge University Press, Cambridge, UK.
- Hutchinson, J. W., and Jensen, H. M., 1990, "Models of Fiber Debonding and Pullout in Brittle Composites with Friction," *Mechanics of Materials*, Vol. 9, pp. 139-162.

Kardomateas, G. A., and Carlson, R. L., 1995, "An Analysis of the Effects of Compressive Load Excursions on Fatigue Crack Growth in Metallic Materials," *ASME JOURNAL OF APPLIED MECHANICS*, Vol. 62, pp. 240-243.

Nemat-Nasser, S., and Hori, M., 1987, "Toughening by Partial or Full Bridging of Cracks in Ceramics and Fiber Reinforced Composites," *Mechanics of Materials*, Vol. 6, pp. 245-269.

Lekhnitskii, S. G., 1963, *Theory of Elasticity of an Anisotropic Elastic Body*, Holden-Day, San Francisco.

Press, W. H., Flannery, B. P., Teukolsky, S. A., and Vetterling, W. T., 1989, *Numerical Recipes*, Cambridge University Press, Cambridge, U.K.

Rosen, B. W., 1964, "Tensile Failure of Fibrous Composites," *AIAA Journal*, Vol. 2, No. 11, Nov., pp. 1985-1991.

Rubinstein, A. A., and Xu, K., 1992, "Micromechanical Model of Crack Growth in Fiber-Reinforced Ceramics," *Journal of the Mechanics and Physics of Solids*, Vol. 40, pp. 105-125.

Russell, A. J., and Street, K. N., 1988, "A Constant ΔG Test for Measuring Mode I Interlaminar Fatigue Crack Growth Rates," *Composite Materials: Testing and Design (Eighth Conference)*, ASTM STP 972, J. D. Whitcomb, ed., American Society for Testing and Materials, Philadelphia, pp. 259-277.

Sih, G. C., and Chen, E. P., 1981, *Mechanics of fracture*, Vol. 6, Martinus Nijhoff Publishers, The Hague, pp. 9-19, 87-99.

Sih, G. C., and Liebowitz, H., 1968, "Mathematical theories of brittle fracture," *Fracture*, Vol. II, H. Liebowitz, ed., Academic Press, New York, pp. 67-190.

Sih, G. C., Paris, P. C., and Irwin, G. R., 1965, "On Cracks in Rectilinearly Anisotropic Bodies," *Int. J. Fract. Mech.*, Vol. 1, pp. 189-203.

Timoshenko, S. P., and Goodier, J. N., 1970, *Theory of Elasticity*, McGraw-Hill, New York, p. 136.

Zok, F., and Hom, C. L., 1990, "Large Scale Bridging in Brittle Matrix Composites," *Acta Metallurgica et Materialia*, Vol. 38, No. 10, pp. 1895-1904.

G. W. Hunt

A. Blackmore

Department of Civil Engineering,
Imperial College of Science,
Technology and Medicine
Imperial College Road,
London SW7 2BU U.K.

Principles of Localized Buckling for a Strut on an Elastoplastic Foundation

Localization theory for long continuous structures is extended to the buckling of a thin elastic strut supported by a bilinear elastoplastic medium. It is demonstrated that the form of localization has much in common with the buckling of struts on linear and nonlinear elastic foundations in that the localized response, which is of the greatest practical significance, is accompanied by a myriad of associated less significant solutions including periodic ones. Special shooting techniques are developed to deal with the problem of finding the localized solutions from amongst all competing possibilities.

1 Introduction

The strut on elastic foundation has proved a fundamental model of structural mechanics (Hetényi, 1946), in both nonlinear and linearized forms. Many such problems are well described after a linearization, but the strut on elastic foundation is not among them. Important localized buckle patterns are lost for example, along with the associated spatial chaos. Even nonlinear formulations sometimes miss localized solutions in favor of their periodic or homogeneous counterparts. In Thompson and Hunt (1973) for example, both linked and continuous struts on elastic foundations are analysed in depth for their periodic responses; the authors were then unaware that, if such a system is long enough (more than about twice the wavelength of the buckle for the continuous strut), a localized buckle pattern would predominate.

Softening nonlinearity is an essential ingredient of localization, and can come about either through natural geometric effects over large deflections (Hunt et al., 1993), or over small deflections with softening introduced into the foundation (Hunt and Wadee, 1991). We deal here with the associated problem of a linearized strut on a foundation with bilinear stiffness. We can take this as being identical to an elastoplastic foundation (Tvergaard and Needleman, 1980), provided that, in a natural loading sequence from zero compression, elastic unloading following finite plastic deformation is denied; however unloading back down the original elastic loading path is allowed.

The long strut on the bilinear foundation is characterized by the fact that the localized response bifurcates from a finite-amplitude periodic shape, rather than the vanishingly small amplitude of the nonlinear elastic foundation (Hunt and Wadee, 1991). Thus, while for the latter the end-shortening grows from zero as localization develops, for a bilinear foundation it is finite before the periodic form is lost: and the longer the strut, the greater this initial end-shortening. This effectively "spring loads" the system, providing the rest of the structure with the potential to unload elastically into the localized region, and gives a characteristic snap-back "C" shape to the load/end-shortening response. In a mechanism which reflects the scaling problems known to arise in localization problems in continuum

mechanics (Bažant and Cedolin, 1991), the longer the strut the more severe the snap-back.

Here we explore the response of the strut on bilinear foundation entirely in terms of the dynamical phase-space analogy (Hunt et al., 1989), that is by running the spatial differential equation as though it were in time. At a general point along the length the behavior can always be described by a linear Hamiltonian differential equation. General solutions are then derivable in closed form, and the response can be understood, at least locally, in its entirety. Multiple changes of stiffness, as might occur in a periodic or near-periodic displacement when the elastic limit is exceeded at many points simultaneously, introduces a complex sequence of bifurcations that in the limit turns out to be chaotic. In a companion paper (Blackmore and Hunt, 1996), we apply the approach to the problem of upheaval buckling, with lift-off from a stiff elastic bed into a medium which provides no restraint. Such problems could possibly enter the large-deflection range, and the full nonlinear (elastica) bending equation is therefore also included as an option.

2 Linear Equations

The full nonlinear differential equation for large deflections of a strut of bending stiffness EI , under compressive load P , resting on a linear foundation of stiffness k , is (Hunt et al., 1993),

$$EI[\ddot{y} + 4\dot{y}\dot{y}\dot{y}(1 - \dot{y}^2)^{-1} + \dot{y}^3(1 + 3\dot{y}^2)(1 - \dot{y}^2)^{-2}] + P\dot{y}(1 - \dot{y}^2)^{-1/2} + ky(1 - \dot{y}^2) = 0, \quad (1)$$

where dots denote differentiation with respect to the spatial variable x , measured along the length of the strut as shown in Fig. 1. The linearized version for small deflections is

$$EI\ddot{y} + P\dot{y} + ky = 0. \quad (2)$$

This can be nondimensionalized by writing $P = p\sqrt{kEI}$ and differentiating with respect to a new spatial variable \tilde{x} , defined by $\tilde{x} = x\sqrt{k/EI}$ (Hunt et al., 1996a), to give

$$\ddot{y} + p\dot{y} + y = 0. \quad (3)$$

From this point we shall drop the tilde, it being understood that all representations are in the nondimensionalized form.

To this we add two further parameters which allow discontinuous jumps at the corner of the bilinearity. A *stiffness ratio* ρ is first added to the third term; for a bilinear foundation of initial stiffness k_1 and final stiffness k_2 , inside the elastic limit ($y < \dot{y}$) we thus run the equation with $\rho = 1$, changing to some

Contributed by the Applied Mechanics Division of THE AMERICAN SOCIETY OF MECHANICAL ENGINEERS for publication in the ASME JOURNAL OF APPLIED MECHANICS.

Discussion on this paper should be addressed to the Technical Editor, Professor Lewis T. Wheeler, Department of Mechanical Engineering, University of Houston, Houston, TX 77204-4792, and will be accepted until four months after final publication of the paper itself in the ASME JOURNAL OF APPLIED MECHANICS.

Manuscript received by the ASME Applied Mechanics Division, Aug. 29, 1994; final revision, Jan. 17, 1995. Associate Technical Editor: S. Kyriakides.



Fig. 1 Strut on a linear elastic foundation

$\rho = k_2/k_1 < 1$ when the elastic limit is exceeded. A constant Q is also included, to allow for a lateral side load and/or for the sudden shift in the virtual origin of y that comes about with the discontinuity in stiffness, as seen later. We thus write the fundamental equation

$$\ddot{y} + p\ddot{y} + \rho y + Q = 0. \quad (4)$$

In the sense of the dynamical phase-space analogy (Hunt et al., 1989), that is by running the equation in a spatial dimension x as though it were in time t , this is all that is required to describe a strut on a bilinear foundation. We shall be particularly interested in passage through the *symmetric section* $\dot{y} = \ddot{y} = 0$, this being a key condition for localized responses (Hunt and Wadee, 1991).

2.1 Stationary Equilibrium and Linear Eigenvalues.

For all cases of Eq. (4) there is a flat (fundamental) state of equilibrium, where the derivatives of y are zero, namely,

$$y = \bar{y} = -\frac{Q}{\rho}. \quad (5)$$

Invoking the dynamical phase-space analogy, this is like a state of stationary equilibrium in time, the eigenvalues of which can be used to fully describe the linearized response. The state may be unreachable however; it may for instance lie inside the elastic limit, $y < \bar{y}$, when the corresponding equation only applies outside the limit, or vice versa.

We are interested here in parameter ranges, $0 < p < p^c = 2(P < P_1^c = 2\sqrt{k_1 EI})$, and $\rho \leq 1$. In the search for closed-form solutions to Eq. (4), we start by noting that the characteristic equation

$$\lambda^4 + p\lambda^2 + \rho = 0 \quad (6)$$

dictates four distinct forms, depending on the values of p and ρ .

2.1.1 Case A: Four Complex Conjugate Eigenvalues ($0 < \rho \leq 1$, $p^2 < 4\rho$). Here the eigenvalues $\lambda = \pm\alpha \pm i\beta$ have both real and imaginary parts, as shown in the complex plane in Fig. 2(a), and a general solution can be written

$$y = e^{\alpha x}(a \cos \beta x + b \sin \beta x) + e^{-\alpha x}(c \cos \beta x + d \sin \beta x) - Q, \quad (7)$$

where

$$\alpha = \sqrt{\frac{\sqrt{\rho} - p}{2}}, \quad \beta = \sqrt{\frac{\sqrt{\rho} + p}{4}}, \quad (8)$$

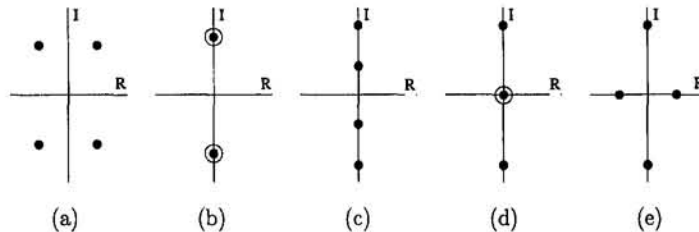


Fig. 2 Complex conjugate eigenvalues for linearized Eq. (4): (a) Case A; (b) Transitional case; (c) Case B; (d) Case D; (e) Case C

and a , b , c , and d are real constants. We note that for the differential equation running inside the elastic limit, this case holds with $\rho = 1$ and $Q = 0$.

The signs of the real parts of the eigenvalues indicate that the flat state is a four-dimensional saddle point with a two-dimensional stable, and a two-dimensional unstable, manifold (Hunt and Wadee, 1991). The symmetric section condition, $\dot{y} = \ddot{y} = 0$, occurs at a length x given by

$$x = \frac{1}{4\alpha} \ln \left(\frac{c^2 + d^2}{a^2 + b^2} \right) = \frac{1}{2\beta} \arctan \left(\frac{ad + bc}{ac - bd} \right). \quad (9)$$

We see that if $c^2 + d^2 < a^2 + b^2$, this condition is met at negative x . Thus, if a starting position $x = 0$ has the amplitude of the oscillation on the unstable manifold, $\sqrt{a^2 + b^2}$, greater than that on the stable manifold, $\sqrt{c^2 + d^2}$, and x is taken as positive, passage through the symmetric section is impossible; divergence has taken hold, and oscillations of y must grow exponentially with x .

2.1.2 Case B: Four Imaginary Eigenvalues ($0 < \rho \leq 1$, $p^2 > 4\rho$). If $\rho = 1$, as p approaches p^c from below the eigenvalues converge onto the imaginary axis as shown in Fig. 2(b). For $p > p^c$, the eigenvalues then split but remain with no real parts, as shown in Fig. 2(c). The same situation can be found after a sudden drop in ρ as the elastic limit is exceeded. The effective p^c also drops, and we can now have $p^2 > 4\rho$, leading to the general solution

$$y = a \cos \lambda_1 x + b \sin \lambda_1 x + c \cos \lambda_2 x + d \sin \lambda_2 x - Q/\rho, \quad (10)$$

where

$$\lambda_1 = \left(\frac{p}{2} - \sqrt{\frac{p^2}{4} - \rho} \right)^{1/2},$$

$$\lambda_2 = \left(\frac{p}{2} + \sqrt{\frac{p^2}{4} - \rho} \right)^{1/2}, \quad (11)$$

and a , b , c , and d are again real constants. This is shown in the complex plane in Fig. 2(c).

Equation (10) has the form of a quasi-periodic solution, and describes a trajectory on a two-dimensional torus in phase space. The symmetric section condition gives

$$x = \frac{1}{\lambda_1} \arctan \left(\frac{b}{a} \right) = \frac{1}{\lambda_2} \arctan \left(\frac{d}{c} \right) \quad (12)$$

which, from a geometrical point of view, represents the condition that the peaks of both harmonic components in Eq. (10) coincide.

2.1.3 Case C: Two Real, Two Imaginary Eigenvalues ($\rho < 0, p < 2$). For the case where $\rho < 0$ and the foundation has negative stiffness, there are two real and two imaginary eigenvalues, as shown in Fig. 2(d) (Hunt et al., 1989), with the general solution

$$y = ae^{\lambda_1 x} + be^{-\lambda_1 x} + c \cos \lambda_2 x + d \sin \lambda_2 x - Q/\rho, \quad (13)$$

where

$$\lambda_1 = \left(-\frac{p}{2} + \sqrt{\frac{p^2}{4} - \rho} \right)^{1/2},$$

$$\lambda_2 = \left(\frac{p}{2} + \sqrt{\frac{p^2}{4} - \rho} \right)^{1/2}, \quad (14)$$

and a, b, c , and d are real constants.

This corresponds to the combination of a two-dimensional saddle and a two-dimensional center. For the symmetric section condition we have

$$\frac{1}{2\lambda_1} \ln \left(\frac{b}{a} \right) = \frac{1}{\lambda_2} \arctan \left(\frac{d}{c} \right), \quad (15)$$

which indicates coincidence of a peak of the harmonic component of Eq. (13) with the peak of the exponential component.

2.1.4 Case D: Two Zero, Two Imaginary Eigenvalues ($\rho = 0, p < 2$). The case where $\rho = 0$ provides another distinct solution to Eq. (4). The characteristic Eq. (6) reduces to

$$\lambda^4 + p\lambda^2 = 0, \quad (16)$$

which has two imaginary and two coincident zero eigenvalues, and we get the general solution

$$y = a + bx + c \cos \sqrt{p}x + d \sin \sqrt{p}x - (Q/2p)x^2, \quad (17)$$

where a, b, c , and d are real constants. For the symmetric section condition we have

$$x = \frac{pb}{Q} = \frac{1}{\sqrt{p}} \arctan \left(\frac{d}{c} \right), \quad (18)$$

which represents a peak of the harmonic component of Eq. (17) coinciding with the peak of the parabolic component.

This case is of particular practical significance, being an important ingredient of the buckling of a strut on an elastic-perfectly plastic foundation, and the upheaval problem of our companion paper (Blackmore and Hunt, 1996).

2.2 Spatial Energies: Lagrangian and Hamiltonian. The Lagrange equation for a conservative mechanical system running in time is

$$\frac{d}{dt} \frac{\partial T}{\partial \dot{q}_i} + \frac{\partial V}{\partial q_i} = 0, \quad (19)$$

where T is the kinetic energy, V is the potential energy, and q_i is a typical generalized coordinate. If we replace time t with our spatial coordinate x , we can write

$$T = \dot{y}\dot{y} + \frac{1}{2}p\dot{y}^2,$$

$$V = \frac{1}{2}(\rho y^2 - \dot{y}^2) + Qy + V_0, \quad (20)$$

where V_0 is a constant to be determined later. We interpret q_i first as y , leading to the fundamental Eq. (4), and secondly as \dot{y} , giving the identity $\ddot{y} = \ddot{y}$. T and V thus provide spatial forms of kinetic and potential energy, respectively. Unlike a typical mechanical system, however, T is an indefinite quadratic form. But the system is Hamiltonian and we have a constant of the

motion $\mathcal{H} = T + V = \text{const}$, which in this analogy is a statement of conservation of spatial energy.

3 Bilinear Equations

For the strut on the bilinear foundation it is now just a case of applying the appropriate equations and conditions from above to track the response as the strut repeatedly crosses the elastic limit. Let us suppose that, for $y < \hat{y}$, Eq. (3) governs, meaning that the initial elastic foundation stiffness k_1 is positive. If we measure y from the flat fundamental equilibrium state (5) where all derivatives vanish, $Q = 0$. As the response crosses the elastic limit at $y = \hat{y}$, continuity in y and its derivatives must be maintained: The left-hand sides of Eqs. (3) and (4) must match at $y = \hat{y}$. This gives

$$Q = \hat{y}(1 - \rho) \quad (21)$$

for $y > \hat{y}$, and Eq. (5) then fixes the corresponding flat state at

$$\bar{y} = -\frac{Q}{\rho} = -\frac{\hat{y}}{\rho}(1 - \rho). \quad (22)$$

In a similar manner, to ensure continuity between the two forms for the spatial potential energy V , we must have

$$V_0 = -\frac{1}{2}\hat{y}^2(1 - \rho) \quad (23)$$

for $y > \hat{y}$. We note that $V_0 = 0$ inside the elastic limit, giving $\mathcal{H} = T + V = 0$ in the corresponding flat fundamental state. Continuity of T is always ensured, the expression of Eq. (20) undergoing no change as the elastic limit is passed.

The values of y and its derivatives at the elastic limit can also be used to calculate the constants a, b, c , and d for the appropriate general solution. Applying the associated symmetric section condition we can then predict *when we reach the elastic limit* whether a symmetric section condition (localization) will occur in the next “loop.” The arctangent functions of conditions (9), (12), (15), and (18) admit an infinite number of solutions (separated by multiples of π) which enables prediction and classification of localized solutions, as seen later.

3.1 Elastic-Hardening Foundation. Let us consider a strut on a bilinear foundation with initial stiffness $k_1 > 0$ and final stiffness $0 < k_2 < k_1$, conventionally referred to as a hardening foundation, as shown in Fig. 3(a), in which $f(y)$ is

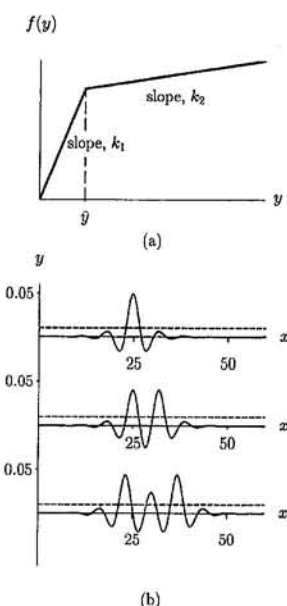


Fig. 3 (a) Bilinear foundation characteristics; (b) Examples of localized modes ($EI = k_1 = 1, k_2 = 0.1, \hat{y} = 0.01, P = 1.6$)

the resisting force per unit length. Inside the elastic limit ($y < \bar{y}$) Eq. (3) governs, and for $P < P_1^C = 2\sqrt{k_1 EI}$ ($p < p^C = 2$) general solution (7) of case A applies. Invoking the dynamical phase-space analogy, we start from close to the flat equilibrium state $y = 0$ and trace the response with positive x . Wherever the starting condition lies with respect to the stable and unstable manifolds, it can be taken that on reaching the elastic limit the system is in a state of divergence, with a more dominant destabilizing than stabilizing component to the general solution.

Outside the elastic limit governing Eq. (4) holds, with $0 < \rho < 1$, and Q given by Eq. (21). The corresponding position of the flat fundamental state of Eq. (22) is inside the elastic limit ($\bar{y} < \hat{y}$) and therefore unreachable. Depending on the value of load P there are two possibilities:

- If $P < P_2^C = 2\sqrt{k_2 EI}$, $p^2 < 4\rho$ and case A holds. Since $\bar{y} < \hat{y}$ the response will continue to be dominated by the unstable part of the general solution, divergence will be maintained albeit at a different rate, and passage through the symmetric section and hence localization are not possible.
- If $P > P_2^C = 2\sqrt{k_2 EI}$, $p^2 > 4\rho$ and case B holds. The quasi-periodic form allows passage through the symmetric section, and consequently localization is possible.

The linear eigenvalue problem hence suggests that only a periodic solution exists at $P = P_1^C$, but localized solutions can exist over the range between P_1^C and P_2^C . Multiple crossing of the elastic limit provides a variety of possible modeforms, three of the simplest, identified by the search routine described later in Section 4.2, being shown in Fig. 3(b).

Figure 4 shows the variation of maximum amplitude y_{\max} and end-shortening Δ with load P for the top example of Fig. 3(b); at the given load this form exits the elastic limit only once before the symmetric section is reached, although at the extreme of the post-buckling curve, close to the critical load P_1^C , it tends to evolve into forms involving more than one exit. Other curves exist for the other modes, but over the range of displacements illustrated here it appears that the illustrated curve represents the least energy, most likely solution in practice. The form of Fig. 4(b) becomes length dependent close to P_1^C , the eigenvector in the critical state being periodic, and end-shortening for a periodic buckle depending on both amplitude and length while that for a localized buckle depends only on amplitude. For long struts this gives a characteristic snap-back ‘‘C’’ shape to the post-buckling response, seen in the closeup of Fig. 4(b). A typical loading sequence for a perfect inextensile strut, brought about by controlling end-shortening displacement Δ , is then as follows.

Inextensibility implies that the immediate application of a small Δ induces buckling, the load rising instantly to P_1^C . Further application then produces a periodic buckle pattern, the value of Δ growing accordingly along the corresponding ‘‘neutral’’ equilibrium path at constant load, until the amplitude reaches \hat{y} ; the longer the strut, the greater the corresponding ‘‘triggering’’ value of Δ . There is then an immediate snap downwards at constant Δ (sometimes called snap-back), to a lower position on the ‘‘C’’ curve where the buckle pattern is localized, here with much the same shape as seen at the top of Fig. 3(b).

One consequence of this loading history is that, for a system free from imperfections, permanent plastic deformation is avoided. Unloading occurs suddenly as a ‘‘spring-loaded’’ buckled periodic form with amplitude \hat{y} evolves into a localized post-buckled state. The elastic unloading that occurs outside the region of localization is always back down the original loading path of Fig. 3(a).

3.2 Elastic-Perfectly Plastic Foundation. The case of $k_2 = 0$ is of particular interest, as it models the case of upheaval from an elastic bed seen in the related companion paper (Blackmore and Hunt, 1996).

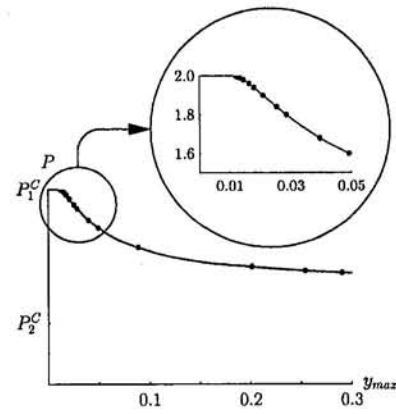


Fig. 4(a) Load versus maximum buckle amplitude

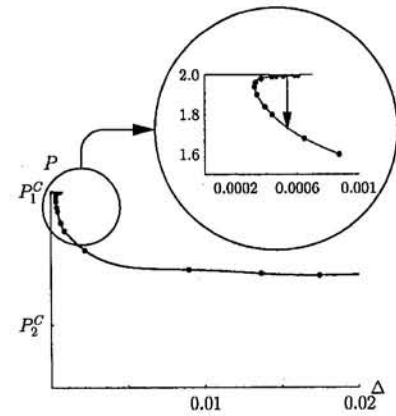


Fig. 4(b) Load versus end-shortening, with close-up showing characteristic snap-back ‘‘C’’ shape

Fig. 4 Primary mode post-buckling response ($EI = k_1 = 1$, $k_2 = 0.1$, $\bar{y} = 0.01$)

more and Hunt, 1996). Inside the elastic limit case A holds as before, while outside the strut is assumed to have lifted from the bed and case D applies. Passage through the symmetric section, and hence localization, are now possible over the range $0 < P < P_1^C$. We see from Eq. (5) that the flat fundamental state for $k_2 = 0$ is at $\bar{y} = \pm\infty$.

3.3 Elastic-Softening Foundation. If k_1 is positive but k_2 is negative we have a so-called softening foundation. The elastic limit $y = \hat{y}$ now marks a change in the form of general solution from case A to case C, and passage through the symmetric section, and localization, are again possible. Equation (22) shows that the flat fundamental state for $k_2 < 0$ lies outside the elastic limit and is thus physically realizable.

4 Numerical Experimentation

The linearized solutions developed above allow limited prediction of the displacement ‘‘history,’’ in the sense of the dynamical phase-space analogy, of a strut on a bilinear foundation. It is of course possible to track any particular solution by piecewise application of the specific general solutions given above, but only for one set of starting conditions at a time. For the system as a whole we turn to numerical runs of Eq. (4) using a fourth-order symplectic (volume-preserving) Runge-Kutta scheme (Sanz-Serna, 1988; Hunt and Wadee, 1991). When the load varies along the length, as in the application to uplift buckling with friction of Blackmore and Hunt (1996), there is no readily available general solution but the dynamical analogy accommodates the change without difficulty.

A new feature to the numerical runs is the introduction of a stepsize adjustment routine as the elastic limit is crossed, to ensure that the stiffness change is invoked tolerably close to the correct position. This is similar to the problem of landing exactly on a Poincaré section when using numerical integration techniques to compute Poincaré maps (Hénon, 1982). Successively smaller and smaller step sizes are used to home in, to a specifiable degree of accuracy, on the elastic limit itself.

4.1 Blanket Runs. In assessing the global behavior of such fourth-order autonomous systems, much can be learnt from blanketing a two-dimensional space of starts, as shown in Fig. 5. The phase space is of course four dimensional, but we can assume two of these dimensions to be fixed a priori by two (starting) boundary conditions. All allowable states of the system then appear in a two-dimensional space of starts spanning perhaps two of y and its first three derivatives: Figure 5 shows a portion of this space in the two starting variables y_0 and \dot{y}_0 . Because localized or homoclinic solutions start at, or at least close to, the flat fundamental state at $y = \dot{y} = 0$, we have confined ourselves to starts over a small region (radius 0.0001) enclosing this state, which itself is found at the center of each plot.

These plots, drawn specifically for $EI = k_1 = 1, k_2 = 0.1, P = 1.8$, emphasize that the localized solutions exist within a spiral structure: as we move in towards the center along each spiral, the same localized form is merely shifted outwards along the length. Cutting across the spiral formation reveals the large number of different waveforms that can appear, some of which are illustrated in Fig. 6. Localized modes are detected by passage through the symmetric section $\dot{y} = \ddot{y} = 0$; reversibility suggests that this acts as a mirror (Champneys and Toland, 1993), and starts from close to the flat state thence retrace the solution in reverse to end up at the flat state again. With k_2 as positive, localization involves case B solutions outside the elastic limit, and condition (12) on exit from this limit thereby defines passage through the symmetric section precisely; similarly, on subsequent reentry, a second set of symmetric-section solutions is defined by the case A condition (9).

The multiplicity of possible solutions is apparent from Fig. 5, which represent in turn passage through the symmetric section following the first exit, first reentry, second exit, etc., of the elastic limit. For the left-hand set, solutions for which

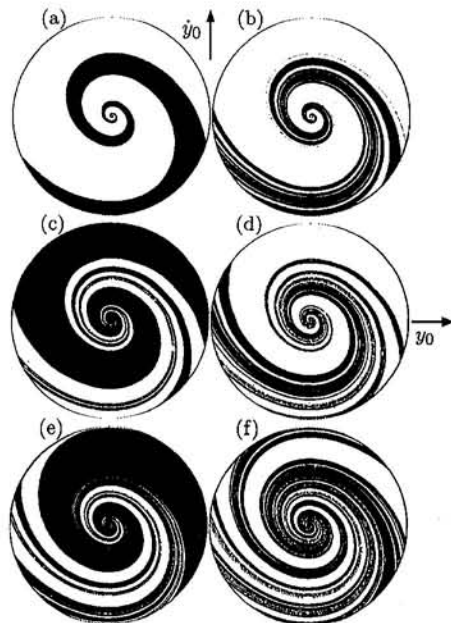


Fig. 5 Blanket runs in the (y_0, \dot{y}_0) space of starts, showing increasingly complex behavior as the strut leaves and re-enters the foundation. ($EI = k_1 = 1, k_2 = 0.1, \dot{y} = 0.01, P = 1.8$).

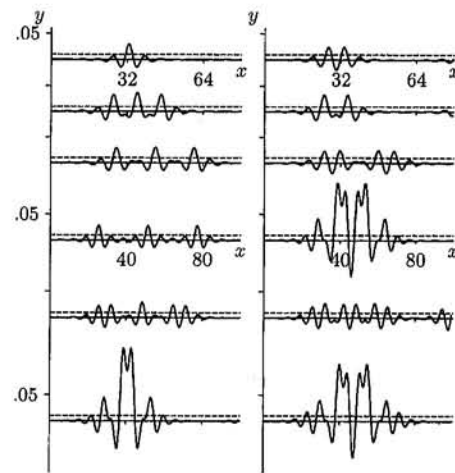


Fig. 6 Multiple possible equilibrium solutions ($EI = k_1 = 1, k_2 = 0.1, \dot{y} = 0.01, P = 1.8$). The primary mode, shown at the top left, is the least energy, most likely solution for practical circumstances.

$$\lambda_2 \arctan(b/a) - \lambda_1 \arctan(d/c) > 0, \quad (24)$$

after the first, second, etc., exit from the elastic limit are plotted in black, while those not satisfying this criterion are shown in white. For the right-hand set, those satisfying

$$\beta \ln \left(\frac{c^2 + d^2}{a^2 + b^2} \right) - 2\alpha \arctan \left(\frac{ad + bc}{ac - bd} \right) > 0 \quad (25)$$

are marked in black, and those not satisfying in white. In each case, passage through the symmetric section itself is thus marked by the border between black and white, which, in common with other examples of localization and spatial chaos (Hunt and Wadee, 1991; Champneys and Toland, 1993; Hunt et al., 1996b), has in the limit an infinitely broken fractal structure.

4.2 Localized Modes and Search Routines. Some of the infinite variety of allowable buckling modes for the strut on an elastoplastic foundation are shown in Fig. 6, where the broken horizontal line drawn at $y = \dot{y}$ indicates the elastic limit. We emphasize that not all of the modes depicted here represent realistic buckling situations; they merely indicate the number and variety of solutions available to a set of valid equilibrium equations, however these happen to be solved. From a practical point of view, the minimum energy state is found in the mode at the top left of the figure, which thus represents the most likely form in practice.

The modes are found by starting initial-value runs for Eq. (4) from close to the flat state $y = 0$, and searching systematically in the same two-dimensional space of starts as the blanket runs of Fig. 5 for positions where the appropriate symmetric section condition, either (24) or (25) depending on whether the evolution in x is exiting or entering the elastic zone, is an equality rather than an inequality. Of course this is only possible to within some numerical tolerance, but with double-precision real variables and focusing as accurately as possible, near perfect symmetry about the center of the localization is obtained in all cases shown in Fig. 6. These systematic search procedures are described in earlier publications (see, for example, Hunt and Wadee, 1991).

5 Concluding Remarks

Application of the dynamical phase-space analogy, which in essence means making constructive use of shooting techniques while maintaining an awareness of the underlying character of the dynamics, has advantages when it comes to numerical modeling of localization phenomena. Further nonlinearities like

complicated bedding relations or elastoplasticity of the strut material generate no real extra difficulty; modified equations can simply be run in x , with very much the same kind of questions being asked. Initial value problems remain unfettered by boundary constraints at the far end, and this frees the approach from the sort of assumptions—periodicity, constraint to certain wavelengths, and even of active length itself—that are often part of boundary value approaches but can hamper applicability (see, for example, Thompson and Hunt, 1973; Tvergaard and Needleman, 1980). These advantages are apparent in the application to upheaval buckling in subsea pipelines (Blackmore and Hunt, 1996). Under an active pressure or temperature rise, frictional restraint between the bed and the pipe causes the load to vary along the length, as well as restricting the length of pipe that is able to unload into the buckled regime. Both effects would be awkward to model in a boundary value formulation, but the first is simply accounted for by allowing an appropriate variation for p in the differential equation, while the second is handled with a straightforward modification to the search routine of Section 4.2. This underlines the importance of the dynamical analogy, closed-form solutions to the boundary value problem being significantly more difficult, if not impossible, to handle for a differential equation with a nonconstant coefficient.

The multiplicity of possible equilibrium states at any load, or indeed under any applied end displacement, apparently available to such spatially chaotic localization problems means that extra physical interpretation is required beyond just equilibrium considerations; we need somehow to select the most likely state from all competing possibilities, many of which may be stable in the sense of being local energy minima. For such systems, it seems that the Maxwell criterion of stability, which suggests that as a result of external disturbances a system will tend to settle in its global energy minimum, may be more realistic than any locally defined criterion; this may be particularly true when, as here, snap-back behavior is likely (Baker and Hunt, 1994).

Acknowledgments

Financial support for the second author was provided by a research studentship from the Engineering and Physical Sciences Research Council of Great Britain.

References

- Baker, G., and Hunt, G. W., 1994, "Energy Computations of Softening Phenomena," *Fracture and Damage of Quasi-Brittle Materials: Proceedings of the U.S.-Europe Workshop, Prague*, Z. P. Bažant, Z. Bittnar, M. Jirasek, and J. Mazars, eds., Sept., E & FN Spon, London, pp. 387–394.
- Bažant, Z. P., and Cedolin, L., 1991, *Stability of Structures: Elastic, Inelastic, Fracture, and Damage Theories*, Oxford University Press, New York.
- Blackmore, A., and Hunt, G. W., 1996, "The Dynamical Phase-Space Analogy as a Tool for the Analysis of Upheaval Buckling," to be published.
- Champneys, A. R., and Toland, J. F., 1993, "Bifurcation of a Plethora of Large Amplitude Homoclinic Orbits for Hamiltonian Systems," *Nonlinearity*, Vol. 6, pp. 665–721.
- Hénon, M., 1982, "On the Numerical Computation of Poincaré Maps," *Physica D*, Vol. 5, pp. 412–414.
- Hetényi, M., 1946, *Beams on Elastic Foundation*, The University of Michigan Press, Ann Arbor, MI.
- Hunt, G. W., and Wadee, M. K., 1991, "Comparative Lagrangian Formulations for Localized Buckling," *Proceedings of the Royal Society of London*, Vol. A434, pp. 485–502.
- Hunt, G. W., Bolt, H. M., and Thompson, J. M. T., 1989, "Structural Localization Phenomena and the Dynamical Phase-Space Analogy," *Proceedings of the Royal Society of London*, Vol. A425, pp. 245–267.
- Hunt, G. W., Wadee, M. K., and Shiakolas, N., 1993, "Localized Elasticity for the Strut on the Linear Foundation," *ASME JOURNAL OF APPLIED MECHANICS*, Vol. 60, pp. 1033–1038.
- Hunt, G. W., Mühlhaus, H-B., and Whiting, A. I. M., 1996a, "Evolution of Localized Folding for a Thin Elastic Layer in a Softening Visco-Elastic Medium," PAGEOP to be published.
- Hunt, G. W., Lawther, R., and Providência, P., 1996b, "Finite Element Modeling of Spatially-Chaotic Structures," to be published.
- Sanz-Serna, J. M., 1988, "Runge-Kutta Schemes for Hamiltonian Systems," *BIT*, Vol. 28, pp. 877–883.
- Thompson, J. M. T., and Hunt, G. W., 1973, *A General Theory of Elastic Stability*, Wiley, London.
- Tvergaard, V., and Needleman, A., 1980, "On the Localization of Buckle Patterns," *ASME JOURNAL OF APPLIED MECHANICS*, Vol. 47, pp. 613–619.

A Treatment of Internally Constrained Materials¹

J. Casey² and M. M. Carroll³.

An interesting point, not addressed by the author, arises in regard to invariance requirements. Recall that in continuum mechanics it is usually stated that under an arbitrary superposed rigid motion of the continuum, the Cauchy stress tensor \mathbf{T} transforms as

$$\mathbf{T}^+ = \mathbf{Q}\mathbf{T}\mathbf{Q}^T, \quad (1)$$

where the proper orthogonal tensor \mathbf{Q} (depending on time only) represents the rotation in the superposed motion. Correspondingly, the symmetric Piola-Kirchhoff stress tensor \mathbf{S} transforms as

$$\mathbf{S}^+ = \mathbf{S}. \quad (2)$$

If one is considering a material in which the stress \mathbf{T} is uniquely determined by the history of the deformation of the body, the transformation law (1) can be argued on the physical grounds that a superposed motion leaves unaltered the distance between every pair of particles of the body, always resulting in the same Lagrangian strain field \mathbf{E} . For materials with internal constraints, however, only part of the stress tensor is determined by the motion of the body. For the determinate part of the stress, the argument given above leads to a transformation law of type (1). But, can we say anything about how the indeterminate part of the stress should transform?

To pursue this question, we first recall that for a material subject to an internal constraint of the form

$$\phi(\mathbf{E}) = 0, \quad (3)$$

the stress \mathbf{S} is given by

$$\mathbf{S} = \bar{\mathbf{S}} + \lambda \frac{\partial \phi}{\partial \mathbf{E}}, \quad (4)$$

where λ is a Lagrange multiplier and the portion $\bar{\mathbf{S}}$ is prescribed by a constitutive equation. In terms of Cauchy stress, (4) may be written as

$$\mathbf{T} = \bar{\mathbf{T}} + \lambda \Gamma, \quad (5)$$

¹ By J. Casey and published in the June 1995 issue of the ASME JOURNAL OF APPLIED MECHANICS, Vol. 62, pp. 542-544.

² Department of Mechanical Engineering, University of California at Berkeley, Berkeley, CA 94720-1740. Mem. ASME.

³ School of Engineering, Rice University, Houston, TX 77251. Mem. ASME.

where

$$\bar{\mathbf{T}} = \frac{1}{J} \mathbf{F} \bar{\mathbf{S}} \mathbf{F}^T, \quad \Gamma = \frac{1}{J} \mathbf{F} \frac{\partial \phi}{\partial \mathbf{E}} \mathbf{F}^T. \quad (6)$$

Now, under superposed rigid motions of the constrained body, the tensors $\bar{\mathbf{T}}$ and $\bar{\mathbf{S}}$ transform as

$$\bar{\mathbf{T}}^+ = \mathbf{Q} \bar{\mathbf{T}} \mathbf{Q}^T, \quad \bar{\mathbf{S}}^+ = \bar{\mathbf{S}}. \quad (7)$$

Further, since the constraint itself applies to all motions (including in particular those differing from a given motion by a superposed rigid motion), we have

$$\left(\frac{\partial \phi}{\partial \mathbf{E}} \right)^+ = \frac{\partial \phi}{\partial \mathbf{E}}, \quad \Gamma^+ = \mathbf{Q} \Gamma \mathbf{Q}^T. \quad (8)$$

But, however tempting it may be, we have no grounds for asserting that the value of the Lagrange multiplier is necessarily the same for the given motion and for all motions that differ from it by a rigid motion. Indeed, the essential arbitrariness in the definition of the multiplier would surely preclude such an assumption. We conclude therefore that for a constrained material, the stress tensors \mathbf{T} and \mathbf{S} do not necessarily transform by (1) and (2), respectively.

The case of a rigid body furnishes a nice illustration. The Cauchy stress tensor in a rigid body is completely indeterminate. For such a body, any pair of motions resulting from two arbitrarily different external force systems still differ by a rigid motion. It is evident that the internal stress states in these two motions are completely independent of one another, and hence do not satisfy (1).

In closing, we remark that for researchers who prefer to use the Principle of Material Frame-Indifference rather than invariance requirements under superposed rigid motions, caution must be exercised in dealing with constrained materials. In the case of rigid bodies, for example, might not two observers looking at a single motion be expected to relate their Cauchy stress tensors by (1)?⁴ In this connection, it is interesting to note that Truesdell and Noll (1965, p. 44), in their statement of the Principle of Material Frame-Indifference, say: "Constitutive equations must be invariant under changes of frame of reference." Only if one applies the principle to the part of the stress which is supplied through a constitutive equation can an absurdity be avoided.

Reference

Truesdell, C., and Noll, W., 1965, "The Non-Linear Field Theories of Mechanics," *Handbuch der Physik*, S. Flügge, ed., Vol. III/3, Springer-Verlag, Berlin.

⁴ It may be mentioned that in accordance with the Principle of Material Frame-Indifference, the tensor \mathbf{Q} is permitted to belong to the full orthogonal group, although that point is not at issue here.